

NOVEMBER 2018

**AJNR**

VOLUME 39 • PP 1963–2166

# AJNR

## AMERICAN JOURNAL OF NEURORADIOLOGY

NOVEMBER 2018  
VOLUME 39  
NUMBER 11  
WWW.AJNR.ORG

THE JOURNAL OF DIAGNOSTIC AND  
INTERVENTIONAL NEURORADIOLOGY

Spinal epidural arteriovenous fistulas  
Neuroimaging findings of Zika virus  
Flow-diversion effect of LEO stents

Official Journal ASNR • ASFNR • ASHNR • ASPNR • ASSR



# A Complete Coil Portfolio

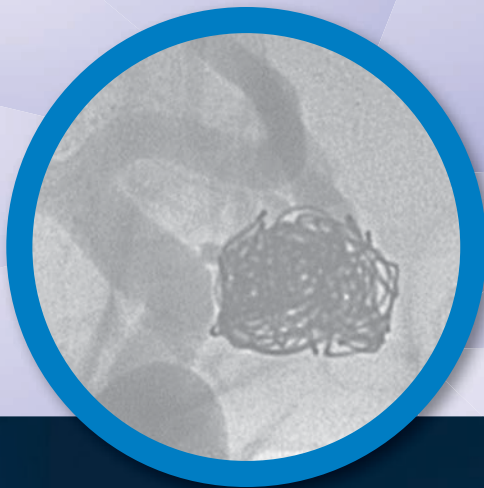
## Hydrogel Embolic Coils & Platinum Coils

MicroVention's comprehensive portfolio features clinically proven Hydrogel coils, which can be used exclusively or in combination with our trusted Platinum coils to treat a wide range of aneurysms and neurovascular lesions.

### Breakthrough Hydrogel Technology

- Less Recurrence
- Less Retreatment
- More Progressive Occlusion

*Compared to platinum coils with comparable safety<sup>1</sup>*



#### REFERENCES:

1. Taschner et al. Second-Generation Hydrogel Coils for the Endovascular Treatment of Intracranial Aneurysm; A Randomized Controlled Trial. 2018;49:00-00. DOI:10.1161/STROKEAHA.117.018707

For more information or a product demonstration,  
contact your local MicroVention representative:



**MicroVention Worldwide  
Innovation Center**  
35 Enterprise  
Aliso Viejo, CA 92656 USA  
MicroVention UK Limited  
MicroVention Europe, S.A.R.L.  
MicroVention Deutschland GmbH  
**microvention.com**

PH +1.714.247.8000

PH +44 (0) 191 258 6777

PH +33 (1) 39 21 77 46

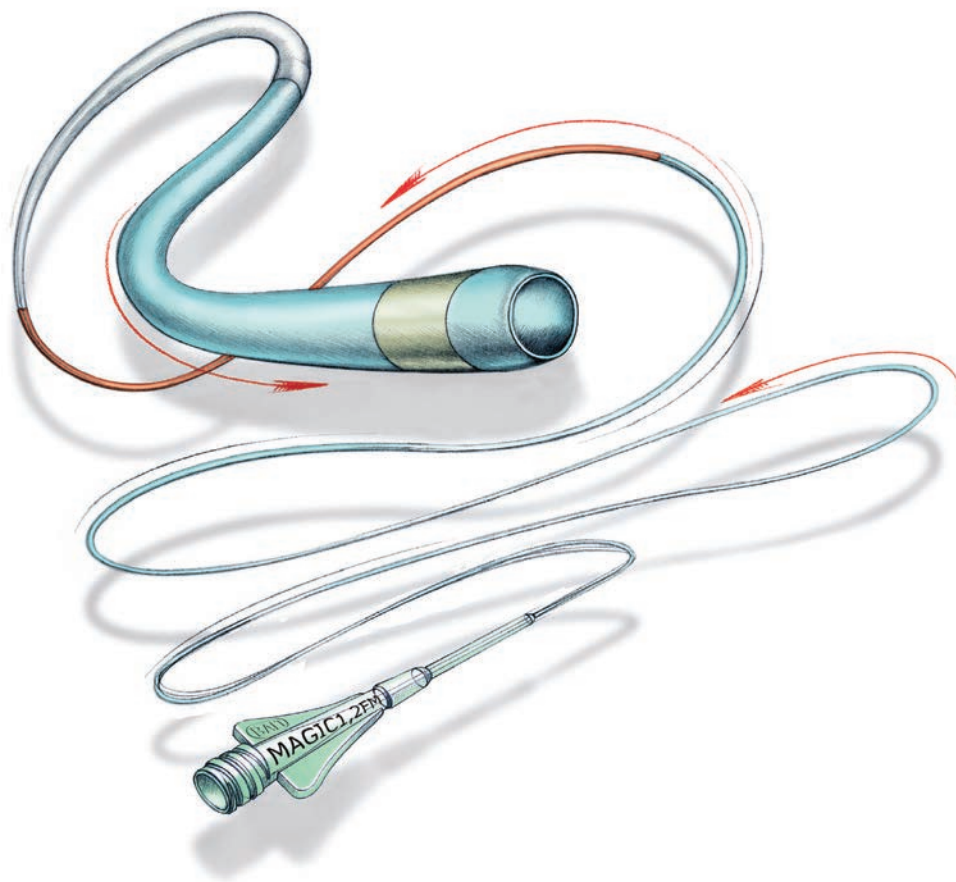
PH +49 211 210 798-0

# Magic



**FLOW-DEPENDENT MICROCATHETER**

**NOW AVAILABLE THROUGH BLOCKADE™ MEDICAL**



**ORDERMAGICS@BLOCKADEMEDICAL.COM**

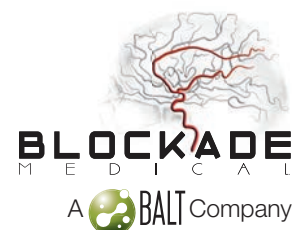
MAGIC catheters are designed for general intravascular use. They may be used for the controlled, selective regional infusion of therapeutic agents or embolic materials into vessels.<sup>1</sup>

1. Magic Catheters IFU – Ind 19

MKTG-068 Rev. A

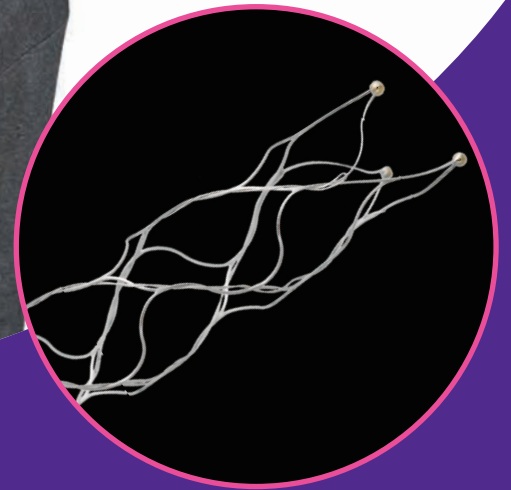
18 Technology Drive #169, Irvine Ca 92618

P 949.788.1443 | F 949.788.1444



**stryker**

Now you have **24 hours** to make a lifetime of difference in stroke patients like Nora



The Trevo Retriever is the only device cleared to **reduce disability in stroke patients up to 24 hours** from time last seen well.

For more information, visit [strykerneurovascular.com/trevo24hours](http://strykerneurovascular.com/trevo24hours)

**Trevo<sup>®</sup> XP**  
PROVUE RETRIEVER

Copyright © 2018 Stryker  
AP002078 v1.0

Redefine aspiration.

## AXS Vecta 71 Aspiration Catheter

**Big 0.071in ID aspiration lumen**  
to ingest more clot

Deliver through a 0.088in ID  
long sheath or **the new**  
**0.091in AXS Infinity LS™**  
**Plus Long Sheath**

**Packaged with  
the Scout Introducer,**  
a 0.044in lumen nitinol  
cross coil catheter that  
replaces the need for  
a 3MAX or other  
delivery catheter

**AXS Vecta™ 71**  
ASPIRATION CATHETER

# CALL FOR AJNR EDITORIAL FELLOWSHIP CANDIDATES

## 2019 Candidate Information and Requirements

ASNR and AJNR are pleased once again to join efforts with other imaging-related journals that have training programs on editorial aspects of publishing for trainees or junior staff (3–5 years after training), including Radiology (Olmsted fellowship), AJR (Figley and Rogers fellowships), JACR (Bruce J. Hillman fellowship), and Radiologia.

### GOALS

- Increase interest in editorial and publication-related activities in younger individuals.
- Increase understanding and participation in the AJNR review process.
- Incorporate into AJNR's Editorial Board younger individuals who have previous experience in the review and publication process.
- Fill a specific need in neuroradiology not offered by other similar fellowships.
- Increase the relationship between “new” generation of neuroradiologists and more established individuals.
- Increase visibility of AJNR among younger neuroradiologists.

### ACTIVITIES OF THE FELLOWSHIP

- Serve as Editorial Fellow for one year. This individual will be listed on the masthead as such.
- Review at least one manuscript per month for 12 months. Evaluate all review articles submitted to AJNR.
- Learn how electronic manuscript review systems work.
- Be involved in the final decision of selected manuscripts together with the Editor-in-Chief.
- Participate in all monthly Senior Editor telephone conference calls.
- Participate in all meetings of the Editors during the annual meetings of ASNR and RSNA and the Radiology Editors Forum as per candidate's availability. The Foundation of the ASNR will provide \$2000 funding for this activity.
- Evaluate progress and adjust program to specific needs in annual meeting or telephone conference with the Editor-in-Chief.
- Embark on an editorial scientific or bibliometric project that will lead to the submission of an article to AJNR or another appropriate journal as determined by the Editor-in-Chief. This project will be presented by the Editorial Fellow at the ASNR annual meeting.
- Serve as liaison between AJNR and ASNR's Young Professionals Network. Participate in meetings and telephone calls with this group. Design one electronic survey/year, polling the group regarding readership attitudes and wishes.
- Recruit trainees as reviewers as determined by the Editor-in-Chief.
- Organize and host a Fellows' Journal Club podcast.
- Serve as Guest Editor for an issue of AJNR's News Digest with a timely topic.

### QUALIFICATIONS

- Be a fellow in neuroradiology from North America, including Canada (this may be extended to include other countries).
- Be a junior faculty neuroradiology member (< 3 years) in either an academic or private environment.
- Be an “in-training” or member of ASNR in any other category.

### APPLICATION

- Include a short letter of intent with statement of goals and desired research project. CV must be included.
- Include a letter of recommendation from the Division Chief or fellowship program director. A statement of protected time to perform the functions outlined is desirable.
- Applications will be evaluated by AJNR's Senior Editors prior to the ASNR meeting. The name of the selected individual will be announced at the meeting.
- Applications should be received by March 1, 2019 and sent to Ms. Karen Halm, AJNR Managing Editor, electronically at khalm@asnr.org.

## AXS Infinity LS™ Plus Long Sheath

See package insert for complete indications, contraindications, warnings and instructions for use.

### INDICATIONS FOR USE

The AXS Infinity LS Plus Long Sheath is indicated for the introduction of interventional devices into the peripheral, coronary, and neuro vasculature.

### RX ONLY

### CONTRAINDICATIONS

There are no known contraindications.

### POTENTIAL ADVERSE EVENTS

- Acute vessel occlusion
- Air embolism
- Death
- Distal embolization
- Emboli
- False aneurysm formation
- Hematoma or hemorrhage at the puncture site
- Infection
- Intracranial hemorrhage
- Ischemia
- Neurological deficit including stroke
- Vessel spasm, thrombosis, dissection or perforation

### WARNINGS

Contents supplied STERILE using an ethylene oxide (EO) process. Do not use if sterile barrier is damaged. If damage is found, call your Stryker Neurovascular representative.

For single use only. Do not reuse, reprocess or resterilize. Reuse, reprocessing or resterilization may compromise the structural integrity of the device and/or lead to device failure which, in turn, may result in patient injury, illness or death. Reuse, reprocessing or resterilization may also create a risk of contamination of the device and/or cause patient infection or cross-infection, including, but not limited to, the transmission of infectious disease(s) from one patient to another. Contamination of the device may lead to injury, illness or death of the patient.

After use, dispose of product and packaging in accordance with hospital, administrative and/or local government policy.

1. Do not re-sterilize or reuse, intended for single use only. Re-sterilization and/or reuse may result in cross contamination and/or reduced performance.
2. When the long sheath is exposed to the vascular system, it should be manipulated while under high-quality fluoroscopic observation. Do not advance or retract the long sheath if resistance is met during manipulation; determine the cause of the resistance before proceeding.

### PRECAUTIONS

1. Store in a cool, dry, dark place.
2. Do not use kinked, damaged, or opened devices.
3. Use the device prior to the "Use By" date specified on the package.
4. Exposure to temperatures above 54°C (130°F) may damage device. Do not autoclave.
5. Torquing or moving the device against resistance may result in damage to the vessel or device.
6. Maintain a constant infusion of appropriate flush solution.
7. If flow through the device becomes restricted, do not attempt to clear the lumen by infusion. Remove and replace the device.
8. Examine the device to verify functionality and to ensure that its size and shape are suitable for the specific procedure for which it is to be used.
9. The AXS Infinity LS Plus Long Sheath should be used only by physicians trained in percutaneous procedures and/or interventional techniques.
10. Do not use if labeling is incomplete or illegible.

## AXS Vecta™ 71 Aspiration Catheter

See package insert for complete indications, contraindications, warnings and instructions for use.

### INDICATIONS FOR USE

The AXS Vecta™ Aspiration System, including the AXS Vecta 71 Aspiration Catheter, Aspiration Tubing Set, and VC-701 Cliq Aspirator Pump, is indicated in the revascularization of patients with acute ischemic stroke secondary to intracranial large vessel occlusive disease (within the internal carotid, middle cerebral – M1 and M2 segments, basilar, and vertebral arteries) within 8 hours of symptom onset. Patients who are ineligible for intravenous tissue plasminogen activator (IV t-PA) or who failed IV t-PA therapy are candidates for treatment.

Stryker Corporation or its divisions or other corporate affiliated entities own, use or have applied for the following trademarks or service marks: AXS Infinity LS, AXS Vecta, Stryker. All other trademarks are trademarks of their respective owners or holders.

Scout is a trademark of InNeuroCo, Inc.

Copyright © 2018 Stryker

AP002264 v1.0 | Page 2 of 2

## Trevo® XP ProVue Retrievers

See package insert for complete indications, complications, warnings, and instructions for use.

### INDICATIONS FOR USE

1. The Trevo Retriever is indicated for use to restore blood flow in the neurovasculature by removing thrombus for the treatment of acute ischemic stroke to reduce disability in patients with a persistent, proximal anterior circulation, large vessel occlusion, and smaller core infarcts who have first received intravenous tissue plasminogen activator (IV t-PA). Endovascular therapy with the device should start within 6 hours of symptom onset.
2. The Trevo Retriever is intended to restore blood flow in the neurovasculature by removing thrombus in patients experiencing ischemic stroke within 8 hours of symptom onset. Patients who are ineligible for intravenous tissue plasminogen activator (IV t-PA) or who fail IV t-PA therapy are candidates for treatment.
3. The Trevo Retriever is indicated for use to restore blood flow in the neurovasculature by removing thrombus for the treatment of acute ischemic stroke to reduce disability in patients with a persistent, proximal anterior circulation, large vessel occlusion of the internal carotid artery (ICA) or middle cerebral artery (MCA)-M1 segments with smaller core infarcts (0-50cc; for age < 80 years, 0-20cc; for age ≥ 80 years). Endovascular therapy with the device should start within 6-24 hours of time last seen well in patients who are ineligible for intravenous tissue plasminogen activator (IV t-PA) or who fail IV t-PA therapy.

### COMPLICATIONS

Procedures requiring percutaneous catheter introduction should not be attempted by physicians unfamiliar with possible complications which may occur during or after the procedure. Possible complications include, but are not limited to, the following: air embolism; hematoma or hemorrhage at puncture site; infection; distal embolization; pain/headache; vessel spasm, thrombosis, dissection, or perforation; emboli; acute occlusion; ischemia; intracranial hemorrhage; false aneurysm formation; neurological deficits including stroke; and death.

### COMPATIBILITY

3x20mm retrievers are compatible with Trevo® Pro 14 Microcatheters (REF 90231) and Trevo® Pro 18 Microcatheters (REF 90238). 4x20mm retrievers are compatible with Trevo® Pro 18 Microcatheters (REF 90238). 4x30mm retrievers are compatible with Excelsior® XT-27™ Microcatheters (150cm x 6cm straight REF 275081) and Trevo® Pro 18 Microcatheters (REF 90238). 6x5mm Retrievers are compatible with Excelsior® XT-27™ Microcatheters (119cm x 6cm straight REF 275081). Recommended minimum vessel ID for all Retriever sizes is 2.5mm. Compatibility of the Retriever with other microcatheters has not been established. Performance of the Retriever device may be impacted if a different microcatheter is used.

Balloon Guide Catheters (such as Mercor® Balloon Guide Catheter and FlowGate® Balloon Guide Catheter) are recommended for use during thrombus removal procedures.

Copyright © 2018 Stryker

AP002078 v1.0 | Page 2 of 2

### RX ONLY

### DEVICE DESCRIPTION

The AXS Vecta Aspiration System consists of the AXS Vecta 71 Aspiration Catheter, the Aspiration Tubing Set, and the VC 701 Cliq Aspirator Pump. The AXS Vecta 71 Aspiration Catheter is a single lumen, flexible, variable stiffness catheter. It has a radiopaque marker band on the distal end and a Luer hub at the proximal end. The AXS Vecta 71 Aspiration Catheter shaft has a lubricious coating at the distal end to reduce friction during use. The Scout Introducer may be used in conjunction with the AXS Vecta 71 Aspiration Catheter to facilitate in the introduction of the AXS Vecta 71 Aspiration Catheter into distal vasculature and aid in navigation to distal anatomy. The Scout Introducer has a lubricious coating at the distal end to reduce friction during use. The inner lumen of the AXS Vecta 71 Aspiration Catheters is compatible with the Scout Introducing, guide wires and micro catheters. The inner lumen of the Scout Introducer is compatible with guide wires and micro catheters of an outer diameter of less than 0.044in. Each package includes one AXS Vecta 71 Aspiration Catheter, one Scout Introducer, one hemostasis valve, and two peel-away introducers. Dimensions of the AXS Vecta 71 Aspiration Catheter and Scout Introducer are included on the individual device label. The AXS Vecta 71 Aspiration Catheters are available in 3 different lengths, the device configurations including the length of the Scout packaged with each catheter and the recommended microcatheter length is presented in the table below.

Catheter part number	INC-11129-115	INC-11129-125	INC-11129-132
Catheter inner diameter (in)	0.071	0.071	0.071
Distal catheter outer diameter (in)	0.082	0.082	0.082
Catheter working length (cm)	115	125	132
Scout Introducer length (cm)	133	143	150
Recommended compatible microcatheter length (cm)	150	160	160
Recommended compatible microcatheter outer diameter (in)	0.044 max	0.044 max	0.044 max
Recommended compatible guidewire outer diameter (in)	0.038 max	0.038 max	0.038 max

The AXS Vecta Aspiration System is recommended for use in the following vessel size ranges based on non-clinical testing:

AXS Vecta 71 Aspiration Catheter	Vessel size (mm)
INC-11129-115	2-4
INC-11129-125	2-4
INC-11129-132	2-4

### CONTRAINDICATIONS

The AXS Vecta 71 Aspiration Catheter has not been evaluated for use in the coronary vasculature. Do not use automated high-pressure contrast injection equipment with the AXS Vecta 71 Aspiration Catheter because it may damage the device.

### POTENTIAL ADVERSE EVENTS

- Acute vessel occlusion
- Air embolism
- Allergic reaction and anaphylaxis from contrast media
- Arteriovenous fistula
- Death
- Device malfunction
- Distal embolization
- Emboli
- False aneurysm formation
- Hematoma or hemorrhage at the puncture site
- Inability to completely remove thrombus
- Infection
- Intracranial hemorrhage
- Ischemia
- Kidney damage from contrast media
- Neurological deficit including stroke
- Risks associated with angiographic and fluoroscopic radiation including but not limited to: alopecia, burns ranging in severity from skin reddening to ulcers, cataracts, and delayed neoplasia
- Vessel spasm, thrombosis, dissection or perforation

### WARNINGS

Contents supplied STERILE using an ethylene oxide (EO) process. Do not use if sterile barrier is damaged. If damage is found, call your Stryker representative. For single use only. Do not reuse, reprocess or resterilize. Reuse, reprocessing or resterilization may compromise the structural integrity of the device and/or lead to device failure which, in turn, may result in patient injury, illness or death. Reuse, reprocessing or resterilization may also create a risk of contamination of the device and/or cause patient infection or cross-infection, including, but not limited to, the transmission of infectious disease(s) from one patient to another. Contamination of the device may lead to injury, illness or death of the patient.

After use, dispose of product and packaging in accordance with hospital, administrative and/or local government policy.

1. The AXS Vecta 71 Aspiration Catheter has not been evaluated for more than one (1) clot retrieval attempt.
2. The AXS Vecta 71 Aspiration Catheter was evaluated for an average duration of direct aspiration of 4 minutes.
3. This product is intended for single use only, do not re-sterilize or reuse. Re-sterilization and/or reuse may result in cross contamination and/or reduced performance.
4. When the catheter is exposed to the vascular system, it should be manipulated while under high-quality fluoroscopic observation. Do not advance or retract the catheter if resistance is met during manipulation; determine the cause of the resistance before proceeding.
5. Operators should take all necessary precautions to limit x-radiation doses to patients and themselves by using sufficient shielding, reducing fluoroscopy times, and modifying x-ray technical factors where possible.

### PRECAUTIONS

1. Store in a cool, dry, dark place.
2. Do not use kinked, damaged, or opened devices.
3. Use the device prior to the "Use By" date specified on the package.
4. Exposure to temperatures above 54°C (130°F) may damage device. Do not autoclave.
5. Torquing or moving the device against resistance may result in damage to the vessel or device.
6. Maintain a constant infusion of appropriate flush solution.
7. If flow through the device becomes restricted, do not attempt to clear the lumen by infusion. Remove and replace the device.
8. Examine the device to verify functionality and to ensure that its size and shape are suitable for the specific procedure for which it is to be used.
9. The AXS Vecta Aspiration System should be used only by physicians trained in percutaneous procedures and/or interventional techniques.
10. The Scout Introducer should be used with a guidewire and microcatheter inserted when in vasculature.
11. If using the AXS Vecta Aspiration System for thrombectomy, monitor the canister fluid level and replace the canister if the fill level reaches 75% of the canister volume.
12. Administration of anticoagulants and antiplatelets should be suspended until 24 hours post-treatment. Medical management and acute post stroke care should follow the American Stroke Association (ASA) guidelines.
13. Any neurological determination should be evaluated by urgent CT scan and other evaluations as indicated according to investigator/hospital best practice.
14. As in all surgical interventions, monitoring of intra-procedural blood loss is recommended so that appropriate management may be instituted.
15. Limit the usage of the AXS Vecta 71 Aspiration Catheter to arteries greater than the catheter's outer diameter.
16. Excessive aspiration with the distal tip of the AXS Vecta 71 Aspiration Catheter covered by the vessel wall may cause vessel injury. Carefully investigate location of the distal tip under fluoroscopy prior to aspiration.
17. There is an inherent risk with the use of angiography and fluoroscopy.
18. When transporting the VC-701 Cliq pump, utilize the pump handle.
19. Do not use if labeling is incomplete or illegible.



**Stryker Neurovascular**  
47900 Bayside Parkway  
Fremont, CA 94538

**strykerneurovascular.com**

Date of Release: SEP/2018

EX\_EN\_US

Retrievers are compatible with the Abbott Vascular DOC® Guide Wire Extension (REF 22260).

Retrievers are compatible with Boston Scientific Rotating Hemostatic Valve (REF 421242).

### SPECIFIC WARNINGS FOR INDICATION 1

- The safety and effectiveness of the Trevo Retrievers in reducing disability has not been established in patients with large core infarcts (i.e., ASPECTS ≤ 7). There may be increased risks, such as intracerebral hemorrhage, in these patients.
- The safety and effectiveness of the Trevo Retrievers in reducing disability has not been established or evaluated in patients with occlusions in the posterior circulation (e.g., basilar or vertebral arteries) or for more distal occlusions in the anterior circulation.

### SPECIFIC WARNINGS FOR INDICATION 2

- To reduce risk of vessel damage, take care to appropriately size Retriever to vessel diameter at intended site of deployment.

### SPECIFIC WARNINGS FOR INDICATION 3

- The safety and effectiveness of the Trevo Retrievers in reducing disability has not been established in patients with large core infarcts (i.e., ASPECTS ≤ 7). There may be increased risks, such as intracerebral hemorrhage, in these patients.
- The safety and effectiveness of the Trevo Retrievers in reducing disability has not been established or evaluated in patients with occlusions in the posterior circulation (e.g., basilar or vertebral arteries) or for more distal occlusions in the anterior circulation.
- Users should validate their imaging software analysis techniques to ensure robust and consistent results for assessing core infarct size.

### WARNINGS APPLIED TO ALL INDICATIONS

- Administration of IV t-PA should be within the FDA approved window (within 3 hours of stroke symptom onset).
- To reduce risk of vessel damage, adhere to the following recommendations:
  - Do not perform more than six (6) retrieval attempts in same vessel using Retriever devices.
  - Maintain Retriever position in vessel when removing or exchanging Microcatheter.
- To reduce risk of kinking/fracture, adhere to the following recommendations:
  - Immediately after unsheathing Retriever, position Microcatheter tip marker just proximal to sheath segment. Maintain Microcatheter tip marker just proximal to sheath section of Retriever during manipulation and withdrawal.
  - Do not rotate or torque Retriever.
  - Use caution when passing Retriever through stented arteries.
- The Retriever is a delicate instrument and should be handled carefully. Before use and when possible during procedure, inspect device carefully for damage. Do not use a device that shows signs of damage. Damage may prevent device from functioning and may cause complications.
- Do not advance or withdraw Retriever against resistance or significant vasospasm. Moving or torquing device against resistance or significant vasospasm may result in damage to vessel or device. Assess cause of resistance using fluoroscopy and if needed resheath the device to withdraw.

- If Retriever is difficult to withdraw from the vessel, do not torque Retriever. Advance Microcatheter distally, gently pull Retriever back into Microcatheter, and remove Retriever and Microcatheter as a unit. If undue resistance is met when withdrawing the Retriever into the Microcatheter, consider extending the Retriever using the Abbott Vascular DOC guidewire extension (REF 22260) so the Microcatheter can be exchanged for a larger diameter catheter such as a DAC® Catheter. Gently withdraw the Retriever into the larger diameter catheter.
- Administer anti-coagulation and anti-platelet medications per standard institutional guidelines.
- Users should take all necessary precautions to limit X-radiation doses to patients and themselves by using sufficient shielding, reducing fluoroscopy times, and modifying X-ray technical factors where possible.

### PRECAUTIONS

- Prescription only – device restricted to use by or on order of a physician.
- Store in cool, dry, dark place.
- Do not use open or damaged packages.
- Use by "Use By" date.
- Exposure to temperatures above 54°C (130°F) may damage device and accessories. Do not autoclave.
- Do not expose Retriever to solvents.
- Use Retriever in conjunction with fluoroscopic visualization and proper anti-coagulation agents.
- To prevent thrombus formation and contrast media crystal formation, maintain a constant infusion of appropriate flush solution between guide catheter and Microcatheter and between Microcatheter and Retriever or guidewire.
- Do not attach a torque device to the shaped proximal end of DOC® Compatible Retriever. Damage may occur, preventing ability to attach DOC® Guide Wire Extension.

DOC is a trademark of Abbott Laboratories.



**Stryker Neurovascular**  
47900 Bayside Parkway  
Fremont, CA 94538

**strykerneurovascular.com**

Date of Release: APR/2018

EX\_EN\_US



### Statement of Ownership, Management, and Circulation (All Periodicals Publications Except Requester Publications)

1. Publication Title: American Journal of Neuroradiology

2. Publication Number: 5 3 2 6 3 0

3. Filing Date: 9/19/2018

4. Issue Frequency: Monthly

5. Number of Issues Published Annually: 12

6. Annual Subscription Price: \$400--Individual (U.S)

7. Complete Mailing Address of Known Office of Publication (Not printer) (Street, city, county, state, and ZIP+4®): 800 Enterprise Drive, Suite 205, Oakbrook, IL 60523

Complete Mailing Address of Headquarters or General Business Office of Publisher (Not printer): 800 Enterprise Drive, Suite 205, Oakbrook, IL 60523

9. Full Names and Complete Mailing Addresses of Publisher, Editor, and Managing Editor (Do not leave blank)

Publisher (Name and complete mailing address): American Society of Neuroradiology, 800 Enterprise Drive, Suite 205, Oakbrook, IL 60523

Editor (Name and complete mailing address): Jeffrey Ross, AJNR, 800 Enterprise Drive, Suite 205, Oakbrook, IL 60523

Managing Editor (Name and complete mailing address): Karen Halm, AJNR, 800 Enterprise Drive, Suite 205, Oakbrook, IL 60523

10. Owner (Do not leave blank. If the publication is owned by a corporation, give the name and address of the corporation immediately followed by the names and addresses of all stockholders owning or holding 1 percent or more of the total amount of stock. If not owned by a corporation, give the names and addresses of the individual owners. If owned by a partnership or other unincorporated firm, give its name and address as well as those of each individual owner. If the publication is published by a nonprofit organization, give its name and address.)

Full Name	Complete Mailing Address
American Society of Neuroradiology	800 Enterprise Drive, Suite 205, Oakbrook, IL 60523

11. Known Bondholders, Mortgagees, and Other Security Holders Owning or Holding 1 Percent or More of Total Amount of Bonds, Mortgages, or Other Securities. If none, check box  None

Full Name	Complete Mailing Address
-----------	--------------------------

12. Tax Status (For completion by nonprofit organizations authorized to mail at nonprofit rates) (Check one)

Has Not Changed During Preceding 12 Months

Has Changed During Preceding 12 Months (Publisher must submit explanation of change with this statement)

PS Form 3526, July 2014 [Page 1 of 4 (see instructions page 4)] PSN: 7530-01-000-9931 PRIVACY NOTICE: See our privacy policy on www.usps.com.

13. Publication Title

14. Issue Date for Circulation Data Below

15. Extent and Nature of Circulation

		Average No. Copies Each Issue During Preceding 12 Months	No. Copies of Single Issue Published Nearest to Filing Date
a. Total Number of Copies (Net press run)		3287	3189
b. Paid Circulation (By Mail and Outside the Mail)	(1) Mailed Outside-County Paid Subscriptions Stated on PS Form 3541 (Include paid distribution above nominal rate, advertiser's proof copies, and exchange copies)	2693	2648
	(2) Mailed In-County Paid Subscriptions Stated on PS Form 3541 (Include paid distribution above nominal rate, advertiser's proof copies, and exchange copies)	0	0
	(3) Paid Distribution Outside the Mails Including Sales Through Dealers and Carriers, Street Vendors, Counter Sales, and Other Paid Distribution Outside USPS® (e.g., First-Class Mail®)	258	248
	(4) Paid Distribution by Other Classes of Mail Through the USPS (e.g., First-Class Mail®)	0	0
c. Total Paid Distribution (Sum of 15b (1), (2), (3), and (4))		2951	2896
d. Free or Nominal Rate Distribution (By Mail and Outside the Mail)	(1) Free or Nominal Rate Outside-County Copies included on PS Form 3541	0	0
	(2) Free or Nominal Rate In-County Copies included on PS Form 3541	0	0
	(3) Free or Nominal Rate Copies Mailed at Other Classes Through the USPS (e.g., First-Class Mail)	0	0
	(4) Free or Nominal Rate Distribution Outside the Mail (Carriers or other means)	53	37
e. Total Free or Nominal Rate Distribution (Sum of 15d (1), (2), (3) and (4))		53	37
f. Total Distribution (Sum of 15c and 15e)		3004	2933
g. Copies not Distributed (See Instructions to Publishers #4 (page #3))		283	256
h. Total (Sum of 15f and g)		3287	3189
i. Percent Paid (15c divided by 15f times 100)		98.2	98.7

16. Electronic Copy Circulation

		Average No. Copies Each Issue During Preceding 12 Months	No. Copies of Single Issue Published Nearest to Filing Date
a. Paid Electronic Copies		0	0
b. Total Paid Print Copies (Line 15c) + Paid Electronic Copies (Line 16a)			
c. Total Print Distribution (Line 15f) + Paid Electronic Copies (Line 16a)			
d. Percent Paid (Both Print & Electronic Copies) (16b divided by 16c x 100)			

I certify that 50% of all my distributed copies (electronic and print) are paid above a nominal price.

17. Publication of Statement of Ownership

The publication is a general publication, publication of this statement is required. Will be printed in the November issue of this publication.

Publication not required.

18. Signature and Title of Editor, Publisher, Business Manager, or Owner

*Karen Halm* Date: 9/19/2018

I certify that all information furnished on this form is true and complete. I understand that anyone who furnishes false or misleading information on this form or who omits material or information requested on the form may be subject to criminal sanctions (including fines and imprisonment) and/or civil sanctions (including civil penalties).



# Simplify the MOC Process



# Manage your CME Credits Online

Available to Members of Participating Societies

- American Board of Radiology (ABR)
- American College of Radiology (ACR)
- American Roentgen Ray Society (ARRS)
- American Society of Neuroradiology (ASNR)
- Commission on Accreditation of Medical Physics Educational Programs, Inc. (CAMPEP)
- Radiological Society of North America (RSNA)
- Society of Interventional Radiology (SIR)
- SNM
- The Society for Pediatric Radiology (SPR)

# CMEgateway.org

It's Easy and Free!

Log on to CME Gateway to:

- View or print reports of your CME credits from multiple societies from a single access point.
- Print an aggregated report or certificate from each participating organization.
- Link to SAMs and other tools to help with maintenance of certification.

## American Board of Radiology (ABR) participation!

By activating ABR in your organizational profile, your MOC-fulfilling CME and SAM credits can be transferred to your own personalized database on the ABR Web site.

Sign Up Today!

go to CMEgateway.org

## IMPORTANT SAFETY INFORMATION<sup>1</sup>

### WARNING: NEPHROGENIC SYSTEMIC FIBROSIS (NSF)

Gadolinium-based contrast agents (GBCAs) increase the risk for NSF among patients with impaired elimination of the drugs. Avoid use of GBCAs in these patients unless the diagnostic information is essential and not available with non-contrast MRI or other modalities. NSF may result in fatal or debilitating fibrosis affecting the skin, muscle and internal organs.

- The risk for NSF appears highest among patients with:
  - Chronic, severe kidney disease (GFR < 30 mL/min/1.73m<sup>2</sup>), or
  - Acute kidney injury.
- Screen patients for acute kidney injury and other conditions that may reduce renal function. For patients at risk for chronically reduced renal function (e.g. age > 60 years, hypertension, diabetes), estimate the glomerular filtration rate (GFR) through laboratory testing.
- For patients at highest risk for NSF, do not exceed the recommended DOTAREM dose and allow a sufficient period of time for elimination of the drug from the body prior to any re-administration.

## INDICATIONS AND USAGE

DOTAREM<sup>®</sup> (gadoterate meglumine) injection is a prescription gadolinium-based contrast agent indicated for intravenous use with magnetic resonance imaging (MRI) in brain (intracranial), spine and associated tissues in adult and pediatric patients (including term neonates) to detect and visualize areas with disruption of the blood brain barrier (BBB) and/or abnormal vascularity.

## CONTRAINDICATIONS

History of clinically important hypersensitivity reactions to DOTAREM.

## WARNINGS AND PRECAUTIONS

- Hypersensitivity Reactions: Anaphylactic and anaphylactoid reactions have been reported with DOTAREM, involving cardiovascular, respiratory, and/or cutaneous manifestations. Some patients experienced circulatory collapse and died. In most cases, initial symptoms occurred within minutes of DOTAREM administration and resolved with prompt emergency treatment.
- Before DOTAREM administration, assess all patients for any history of a reaction to contrast media, bronchial asthma and/or allergic disorders. These patients may have an increased risk for a hypersensitivity reaction to DOTAREM.
- Administer DOTAREM only in situations where trained personnel and therapies are promptly available for the treatment of hypersensitivity reactions, including personnel trained in resuscitation.
- Gadolinium Retention: Gadolinium is retained for months or years in several organs. The highest concentrations have been identified in the bone, followed by brain, skin, kidney, liver and spleen. The duration of retention also varies by tissue, and is longest in bone. Linear GBCAs cause more retention than macrocyclic GBCAs.
- Consequences of gadolinium retention in the brain have not been established. Adverse events involving multiple organ systems have been reported in patients with normal renal function without an established causal link to gadolinium retention.
- Acute Kidney Injury: In patients with chronically reduced renal function, acute kidney injury requiring dialysis has occurred with the use of GBCAs. The risk of acute kidney injury may increase with increasing dose of the contrast agent; administer the lowest dose necessary for adequate imaging.
- Extravasation and Injection Site Reactions: Ensure catheter and venous patency before the injection of DOTAREM. Extravasation into tissues during DOTAREM administration may result in tissue irritation.

## ADVERSE REACTIONS

- The most common adverse reactions associated with DOTAREM in clinical trials were nausea, headache, injection site pain, injection site coldness and rash.
- Serious adverse reactions in the Postmarketing experience have been reported with DOTAREM. These serious adverse reactions include but are not limited to: arrhythmia, cardiac arrest, respiratory arrest, pharyngeal edema, laryngospasm, bronchospasm, coma and convulsion.

## USE IN SPECIFIC POPULATIONS

- **Pregnancy:** GBCAs cross the human placenta and result in fetal exposure and gadolinium retention. Use only if imaging is essential during pregnancy and cannot be delayed.
- **Lactation:** There are no data on the presence of gadoterate in human milk, the effects on the breastfed infant, or the effects on milk production. However, published lactation data on other GBCAs indicate that 0.01 to 0.04% of the maternal gadolinium dose is present in breast milk.
- **Pediatric Use:** The safety and efficacy of DOTAREM at a single dose of 0.1 mmol/kg has been established in pediatric patients from birth (term neonates ≥ 37 weeks gestational age) to 17 years of age based on clinical data. The safety of DOTAREM has not been established in preterm neonates. No cases of NSF associated with DOTAREM or any other GBCA have been identified in pediatric patients age 6 years and younger.

You are encouraged to report negative side effects of prescription drugs to the FDA. Visit [www.fda.gov/medwatch](http://www.fda.gov/medwatch) or call 1-800-FDA-1088.

**Please see the full Prescribing Information, including the patient Medication Guide, for additional important safety information.**

**References:** 1. Dotarem [package insert]. Princeton, NJ: Guerbet LLC; Aug 2018. 2. Maravilla K et al. Comparison of Gadoterate Meglumine and Gadobutrol in the Diagnosis of Primary Brain Tumors: A Double-Blind Randomized Controlled Intraindividual Crossover Study (the REMIND Study). 2017 June 29. doi: 10.3174/ajnr.A5316. [Epub ahead of print]. 3. de Kerviler E et al. Adverse reactions to gadoterate meglumine: review of over 25 years of clinical use and more than 50 million doses. Invest Radiol 2016;51:544–51 CrossRef Medline. 4. Endrikat J et al. Safety of gadobutrol: results from 42 clinical phase II to IV studies and postmarketing surveillance after 29 million applications. Invest Radiol 2016;51: 537–43 CrossRef Medline. 5. Port M et al. Efficiency, thermodynamic and kinetic stability of marketed gadolinium chelates and their possible clinical consequences: a critical review. Biometals. 2008;21:469-90. 6. Frenzel T et al. Stability of gadolinium-based magnetic resonance imaging contrast agents in human serum at 37°C. Invest Radiol. 2008;43:817-828.

DOTAREM<sup>®</sup> is a registered trademark of Guerbet LLC, and is available by prescription only.

Gadavist<sup>®</sup> is a registered trademark of the Bayer group of companies, and is available by prescription only.

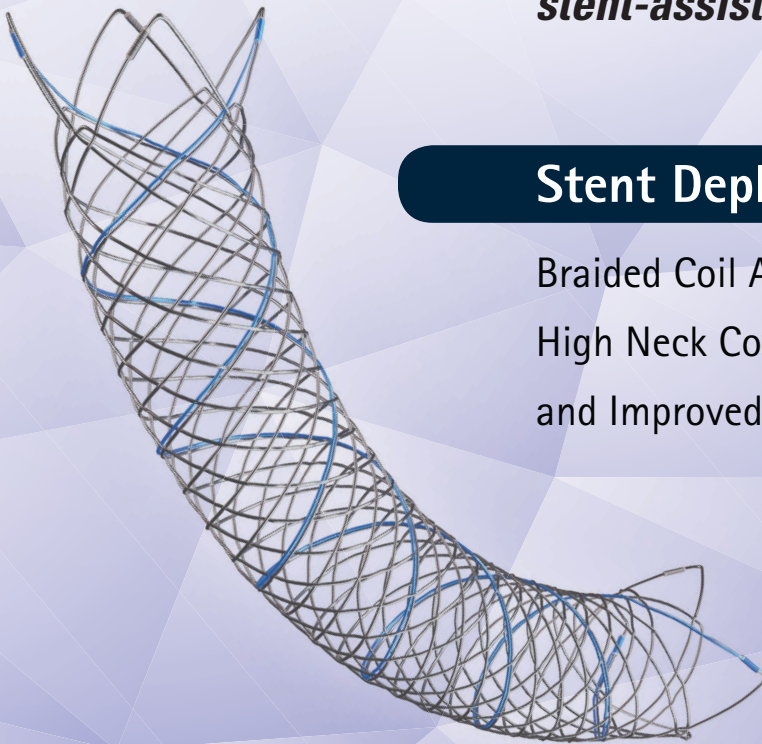


Aneurysm  
Therapy  
Solutions

# LVIS<sup>®</sup>

Intraluminal Support Device

*The first and only stent with  
Premarket Approval (PMA) for use in  
stent-assisted coil embolization*



## Stent Deployment. Refined.

Braided Coil Assist Stents with  
High Neck Coverage, Excellent Visibility  
and Improved Conformability\*

**Low-profile Visualized Intraluminal Support**



### INDICATIONS FOR USE:

The LVIS<sup>®</sup> and LVIS<sup>®</sup> Jr. devices are indicated for use with neurovascular embolization coils in patients  $\geq 18$  years of age for the treatment of wide-neck (neck width  $\geq 4$  mm or dome to neck ratio  $< 2$ ) saccular intracranial aneurysms arising from a parent vessel with a diameter  $\geq 2.0$  mm and  $\leq 4.5$  mm.

Rx Only: Federal (USA) law restricts this device to sale by or on the order of a physician.

The HydroCoil<sup>®</sup> Embolic System (HES) and MicroPlex<sup>®</sup> Coil System (MCS) are intended for the endovascular embolization of intracranial aneurysms and other neurovascular abnormalities such as arteriovenous malformations and arteriovenous fistulae. The HES and MCS are also intended for vascular occlusion of blood vessels within the neurovascular system to permanently obstruct blood flow to an aneurysm or other vascular malformation and for arterial and venous embolizations in the peripheral vasculature.

The device should only be used by physicians who have undergone pre-clinical training in all aspects of HES/MCS procedures as prescribed by MicroVention.

CE  
0297

# DOTAREM<sup>®</sup>

(gadoterate meglumine) Injection

MR

Comparison of Dotarem<sup>®</sup> to Gadavist<sup>®</sup> for Overall Visualization and Characterization in the MRI Diagnosis of Primary Brain Tumors



Despite the difference in relaxivity between these 2 GBCAs

**There Is No Measurable Difference in Clinical Benefit Observed Between Dotarem<sup>®</sup> and Gadavist<sup>®2</sup>**

as demonstrated by the **REMIND Study**, a multicenter, double-blind, randomized, controlled intraindividual crossover study.<sup>2</sup>

This study “demonstrates the non-inferiority of gadoterate meglumine [Dotarem<sup>®</sup>] versus gadobutrol [Gadavist<sup>®</sup>] for overall visualization and characterization of primary brain tumors”.<sup>2</sup> Additionally, there was no preference of the readers for either contrast agent, in most cases, regarding border delineation, internal morphology, and the qualitative degree of contrast enhancement, despite quantitative mean lesion percentage enhancement being higher with gadobutrol.<sup>2</sup>

- For all readers in the REMIND Study, more than 90% of patients presented with good or excellent overall lesion visualization and characterization with either Dotarem<sup>®</sup> or Gadavist<sup>®</sup>.<sup>2</sup>
- The REMIND Study also demonstrated a low incidence of immediate reported AEs with Dotarem<sup>®</sup> and with Gadavist<sup>®</sup>, as shown in multiple previous studies.<sup>2,3,4</sup>
- Dotarem<sup>®</sup> is the only imaging contrast with macrocyclic and ionic structure for high thermodynamic and kinetic stability.<sup>5,6</sup>
- Dotarem<sup>®</sup> is not only trusted for high molecular stability<sup>5,6</sup>; the REMIND Study demonstrates that it is as effective as Gadavist<sup>®</sup> for MRI diagnosis of primary brain tumors.<sup>2</sup>

Please see Important Safety information on opposite page. For more information on Dotarem<sup>®</sup>, please see Full Prescribing Information including Boxed Warning and Medication Guide.

Guerbet | 

**COMMITTED**

Learn more at  
[RemindStudy.com](https://RemindStudy.com)



Not for sale within the territory of the United States

# BRILLIANT HIGH-FLYER

## ACCERO® Stent

- Self-expanding braided stent
- BlueXide® surface finishing
- Excellent opening behaviour & adaptability
- Brilliant visibility

[www.acandis.com](http://www.acandis.com)

**acandis**®

ENGINEERING STROKE SOLUTIONS

# AJNR

## AMERICAN JOURNAL OF NEURORADIOLOGY

NOVEMBER 2018  
VOLUME 39  
NUMBER 11  
WWW.AJNR.ORG

Publication Preview at [www.ajnr.org](http://www.ajnr.org) features articles released in advance of print. Visit [www.ajnrblog.org](http://www.ajnrblog.org) to comment on AJNR content and chat with colleagues and AJNR's News Digest at <http://ajnrdigest.org> to read the stories behind the latest research in neuroimaging.

1963 **PERSPECTIVES** *K. Schaller and M.I. Vargas*

### EDITORIAL

 1964 **The Woven EndoBridge Finally Coming Home across the Atlantic: What to Expect?** *W.J. van Rooij, et al.*

### REVIEW ARTICLE

 1967 **Neuroimaging Findings of Zika Virus–Associated Neurologic Complications in Adults** *L.C. Hygino da Cruz Jr, et al.*

ADULT BRAIN

### PRACTICE PERSPECTIVES

1975 **Characteristics of MR Neuroimaging Services Billed by Radiologists versus Nonradiologists** *P.E. Sharp, et al.*

### RESEARCH PERSPECTIVES

  1981 **Optimization of Acquisition and Analysis Methods for Clinical Dynamic Susceptibility Contrast MRI Using a Population-Based Digital Reference Object** *N.B. Semmineh, et al.*

ADULT BRAIN

### GENERAL CONTENTS

  1989 **Impact of Ischemic Lesion Location on the mRS Score in Patients with Ischemic Stroke: A Voxel-Based Approach** *M. Ernst, et al.*

ADULT BRAIN

  1995 **Detection of Leukocortical Lesions in Multiple Sclerosis and Their Association with Physical and Cognitive Impairment: A Comparison of Conventional and Synthetic Phase-Sensitive Inversion Recovery MRI** *Y. Forslin, et al.*

ADULT BRAIN

2001 **Do All Patients with Multiple Sclerosis Benefit from the Use of Contrast on Serial Follow-Up MR Imaging? A Retrospective Analysis** *R.R. Mattay, et al.*

ADULT BRAIN

2007 **The Central Vein: FLAIR Signal Abnormalities Associated with Developmental Venous Anomalies in Patients with Multiple Sclerosis** *D.M. Rogers, et al.*

ADULT BRAIN

   2014 **Systematic Assessment of Multispectral Voxel-Based Morphometry in Previously MRI-Negative Focal Epilepsy** *R. Kotikalapudi, et al.*

ADULT BRAIN

AJNR (Am J Neuroradiol ISSN 0195–6108) is a journal published monthly, owned and published by the American Society of Neuroradiology (ASNR), 800 Enterprise Drive, Suite 205, Oak Brook, IL 60523. Annual dues for the ASNR include \$170.00 for journal subscription. The journal is printed by Cadmus Journal Services, 5457 Twin Knolls Road, Suite 200, Columbia, MD 21045; Periodicals postage paid at Oak Brook, IL and additional mailing offices. Printed in the U.S.A. POSTMASTER: Please send address changes to American Journal of Neuroradiology, P.O. Box 3000, Denville, NJ 07834, U.S.A. Subscription rates: nonmember \$410 (\$480 foreign) print and online, \$320 online only; institutions \$470 (\$540 foreign) print and basic online, \$935 (\$1000 foreign) print and extended online, \$380 online only (basic), extended online \$825; single copies are \$35 each (\$40 foreign). Indexed by PubMed/Medline, BIOSIS Previews, Current Contents (Clinical Medicine and Life Sciences), EMBASE, Google Scholar, HighWire Press, Q-Sensei, RefSeek, Science Citation Index, SCI Expanded, Meta/CZI and ReadCube. Copyright © American Society of Neuroradiology.

	2022	Does the Presence or Absence of DESH Predict Outcomes in Adult Hydrocephalus? <i>A.K. Ahmed, et al.</i>	ADULT BRAIN	
	2027	Prospective Multicenter Study of Changes in MTT after Aneurysmal SAH and Relationship to Delayed Cerebral Ischemia in Patients with Good- and Poor-Grade Admission Status <i>A. Murphy, et al.</i>	ADULT BRAIN	
		2034 Vessel Wall MRI for Targeting Biopsies of Intracranial Vasculitis <i>S.R. Zeiler, et al.</i>	ADULT BRAIN	
		2037 Hemodynamic Impairment Measured by Positron-Emission Tomography Is Regionally Associated with Decreased Cortical Thickness in Moyamoya Phenomenon <i>J.J. Lee, et al.</i>	ADULT BRAIN	
	2045	Engorgement of Deep Medullary Veins in Neurosarcoidosis: A Common-Yet-Underrecognized Cerebrovascular Finding on SWI <i>C. Zamora, et al.</i>	ADULT BRAIN	
	2051	Subtraction CTA: An Alternative Imaging Option for the Follow-Up of Flow-Diverter-Treated Aneurysms? <i>M.P. Duarte Conde, et al.</i>	INTERVENTIONAL	
		2057 Flow-Diversion Effect of LEO Stents: Aneurysm Occlusion and Flow Remodeling of Covered Side Branches and Perforators <i>F. Cagnazzo, et al.</i>	INTERVENTIONAL	
		2064 Treatment of Intracranial Aneurysms with Self-Expandable Braided Stents: A Systematic Review and Meta-Analysis <i>F. Cagnazzo, et al.</i>	INTERVENTIONAL	
	2070	Outcomes of Stent Retriever versus Aspiration-First Thrombectomy in Ischemic Stroke: A Systematic Review and Meta-Analysis <i>C.O.A. Tsang, et al.</i>	INTERVENTIONAL	
	2077	Balloon-Guide Catheters Are Needed for Effective Flow Reversal during Mechanical Thrombectomy <i>O. Nikoubashman, et al.</i>	INTERVENTIONAL	
		2082 Low Wall Shear Stress Is Associated with Local Aneurysm Wall Enhancement on High-Resolution MR Vessel Wall Imaging <i>W. Xiao, et al.</i>	INTERVENTIONAL ADULT BRAIN	
	2088	Usefulness of Vessel Wall MR Imaging for Follow-Up after Stent-Assisted Coil Embolization of Intracranial Aneurysms <i>S. Kim, et al.</i>	INTERVENTIONAL ADULT BRAIN	
	2095	Spinal Epidural Arteriovenous Fistula with Perimedullary Venous Reflux: Clinical and Neuroradiologic Features of an Underestimated Vascular Disorder <i>M. Mull, et al.</i>	INTERVENTIONAL SPINE	
	2103	Facial Venous Malformations Are Associated with Cerebral Developmental Venous Anomalies <i>W. Brinjikji, et al.</i>	HEAD & NECK	
	2108	MR Venous Flow in Sigmoid Sinus Diverticulum <i>M.R. Amans, et al.</i>	HEAD & NECK	
	2114	MR Imaging in Menière Disease: Is the Contact between the Vestibular Endolymphatic Space and the Oval Window a Reliable Biomarker? <i>G. Conte, et al.</i>	HEAD & NECK	
	2120	Corticopallidal Connectome of the Globus Pallidus Externus in Humans: An Exploratory Study of Structural Connectivity Using Probabilistic Diffusion Tractography <i>S.S. Grewal, et al.</i>	FUNCTIONAL	
			2126 Expanding the Distinctive Neuroimaging Phenotype of ACTA2 Mutations <i>F. D'Arco, et al.</i>	PEDIATRICS
	2132	Cerebral Blood Flow and Marrow Diffusion Alterations in Children with Sickle Cell Anemia after Bone Marrow Transplantation and Transfusion <i>M.T. Whitehead, et al.</i>	PEDIATRICS	
		2140 Aberrant Structural Brain Connectivity in Adolescents with Attentional Problems Who Were Born Prematurely <i>O. Tymofiyeva, et al.</i>	PEDIATRICS FUNCTIONAL	
	2148	Spinal Coccidioidomycosis: MR Imaging Findings in 41 Patients <i>R.N. Crete, et al.</i>	SPINE	
	2154	MR Neurography of the Lumbosacral Plexus for Lower Extremity Radiculopathy: Frequency of Findings, Characteristics of Abnormal Intraneural Signal, and Correlation with Electromyography <i>J.L. Chazen, et al.</i>	SPINE	
	2161	Fluoroscopically Guided Facet Injections: Comparison of Intra-Articular and Periarticular Steroid and Anesthetic Injection on Immediate and Short-Term Pain Relief <i>L.M. Kershen, et al.</i>	SPINE	

ONLINE FEATURES

E112 Standards of Practice in Acute Ischemic Stroke Intervention: International Recommendations *L. Pierot, et al.*

LETTERS

E118 Comment on “Blood Flow Mimicking Aneurysmal Wall Enhancement: A Diagnostic Pitfall of Vessel Wall MRI Using the Postcontrast 3D Turbo Spin-Echo MR Imaging Sequence” *M. Edjlali, et al.*

E119 Reply *J. Hodel, et al.*

E120 MRI Findings Suggestive of Herpes Simplex Encephalitis in Patients with Anti-NMDA Receptor Encephalitis *M. Scheel, et al.*

E121 Reply *T. Zhang, et al.*

E123 Methodologic Issues on Interrater Reliability Regarding Structural and DTI-Based Corticospinal Tract Asymmetry *F. Jalalvandi, et al.*

E124 Reply *O. Foesleitner, et al.*

BOOK REVIEWS *R.M. Quencer, Section Editor*

Please visit [www.ajnrblog.org](http://www.ajnrblog.org) to read and comment on Book Reviews.



Sagittal T2- and contrast-enhanced T1-weighted images (left and center) show extensive congestive thoracic myelopathy and dilated perimedullary veins. Right, Spinal CE-MRA (MIP) shows an arterIALIZED lumbar epidural pouch and thoracic arterIALIZED perimedullary veins.



Indicates Editor's Choices selection



Indicates Fellows' Journal Club selection



Indicates open access to non-subscribers at [www.ajnr.org](http://www.ajnr.org)



Indicates article with supplemental on-line table



Indicates article with supplemental on-line photo



Indicates article with supplemental on-line video



Evidence-Based Medicine Level 1



Evidence-Based Medicine Level 2

### Official Journal:

American Society of Neuroradiology  
American Society of Functional Neuroradiology  
American Society of Head and Neck Radiology  
American Society of Pediatric Neuroradiology  
American Society of Spine Radiology

### EDITOR-IN-CHIEF

#### Jeffrey S. Ross, MD

Professor of Radiology, Department of Radiology,  
Mayo Clinic College of Medicine, Phoenix, AZ

### SENIOR EDITORS

#### Harry J. Cloft, MD, PhD

Professor of Radiology and Neurosurgery,  
Department of Radiology, Mayo Clinic College of  
Medicine, Rochester, MN

#### Thierry A.G.M. Huisman, MD

Radiologist-in-Chief, Texas Children's Hospital,  
Houston, TX

#### Yvonne W. Lui, MD

Associate Professor of Radiology,  
Chief of Neuroradiology,  
New York University School of Medicine,  
New York, NY

#### C.D. Phillips, MD, FACR

Professor of Radiology, Weill Cornell Medical  
College, Director of Head and Neck Imaging,  
New York-Presbyterian Hospital, New York, NY

#### Pamela W. Schaefer, MD

Clinical Director of MRI and Associate Director of  
Neuroradiology, Massachusetts General Hospital,  
Boston, Massachusetts, Associate Professor,  
Radiology, Harvard Medical School, Cambridge, MA

#### Charles M. Strother, MD

Professor of Radiology, Emeritus, University of  
Wisconsin, Madison, WI

### STATISTICAL SENIOR EDITOR

#### Bryan A. Comstock, MS

Senior Biostatistician,  
Department of Biostatistics,  
University of Washington, Seattle, WA

### ARTIFICIAL INTELLIGENCE DEPUTY EDITOR

#### Christopher G. Filippi, MD

Professor and Vice Chair of Biomedical and  
Translational Science,  
Donald and Barbara Zucker School of Medicine at  
Hofstra/Northwell,  
Lenox Hill Hospital and Greenwich Village  
Healthplex, New York, NY

### EDITORIAL BOARD

Ashley H. Aiken, Atlanta, GA  
Lea M. Alhilali, Phoenix, AZ  
Kubilay Aydin, Istanbul, Turkey  
John D. Barr, Dallas, TX  
Ari Blitz, Baltimore, MD  
Barton F. Branstetter IV, Pittsburgh, PA  
Jonathan L. Brisman, Lake Success, NY  
Keith Cauley, Danville, PA  
James Y. Chen, San Diego, CA  
Asim F. Choudhri, Memphis, TN  
Daniel Chow, Irvine, CA  
J. Matthew Debnam, Houston, TX  
Seena Dehkharghani, New York, NY  
Yonghong Ding, Rochester, MN  
Clifford J. Eskey, Hanover, NH  
Saeed Fakhra, Phoenix, AZ  
Massimo Filippi, Milan, Italy  
Reza Forghani, Montreal, Quebec, Canada  
Nils D. Forkert, Calgary, Alberta, Canada  
Wende N. Gibbs, Los Angeles, CA  
Christine M. Glastonbury, San Francisco, CA  
John L. Go, Los Angeles, CA  
Philipp Göllitz, Erlangen, Germany  
Allison Grayev, Madison, WI  
Brent Griffith, Detroit, MI  
Ajay Gupta, New York, NY  
Rakesh Kumar Gupta, Haryana, India  
Lotfi Hacein-Bey, Sacramento, CA  
Christopher P. Hess, San Francisco, CA  
Andrei Holodny, New York, NY  
Benjamin Huang, Chapel Hill, NC  
Mahesh V. Jayaraman, Providence, RI  
Valerie Jewells, Chapel Hill, NC  
Christof Karmonik, Houston, TX  
Timothy J. Kaufmann, Rochester, MN  
Hillary R. Kelly, Boston, MA  
Toshibumi Kinoshita, Akita, Japan  
Kenneth F. Layton, Dallas, TX  
Alexander Lerner, Los Angeles, CA  
Michael Lev, Boston, MA  
Karl-Olof Lovblad, Geneva, Switzerland  
Franklin A. Marden, Chicago, IL  
Joseph C. McGowan, Merion Station, PA  
Stephan Meckel, Freiburg, Germany  
Christopher J. Moran, St. Louis, MO  
Takahisa Mori, Kamakura City, Japan  
Suresh Mukherji, Ann Arbor, MI  
Alexander J. Nemeth, Chicago, IL  
Renato Hoffmann Nunes, Sao Paulo, Brazil  
Sasan Partovi, Cleveland, OH  
Laurent Pierot, Reims, France  
Jay J. Pillai, Baltimore, MD  
Whitney B. Pope, Los Angeles, CA  
Joana Ramalho, Lisbon, Portugal  
Otto Rapalino, Boston, MA

Álex Rovira-Cañellas, Barcelona, Spain  
Paul M. Ruggieri, Cleveland, OH  
Amit M. Saindane, Atlanta, GA  
Erin Simon Schwartz, Philadelphia, PA  
Lubdha M. Shah, Salt Lake City, UT  
Maksim Shapiro, New York, NY  
Timothy Shepherd, New York, NY  
Mark S. Shiroishi, Los Angeles, CA  
Bruno P. Soares, Baltimore, MD  
Maria Vittoria Spampinato, Charleston, SC  
Khin Khin Tha, Sapporo, Hokkaido, Japan  
Krishnamoorthy Thamburaj, Hershey, PA  
Cheng Hong Toh, Taipei, Taiwan  
Aquila S. Turk, Charleston, SC  
Anja G. van der Kolk, Madison, WI  
Willem Jan van Rooij, Tilburg, Netherlands  
Arastoo Vossough, Philadelphia, PA  
Elysa Widjaja, Toronto, Ontario, Canada  
Max Wintermark, Stanford, CA  
Ronald L. Wolf, Philadelphia, PA  
Kei Yamada, Kyoto, Japan  
Carlos Zamora, Chapel Hill, NC  
Vahe M. Zohrabian, New Haven, CT

### EDITORIAL FELLOW

Alireza Radmanesh, New York, NY

### SPECIAL CONSULTANTS TO THE EDITOR

#### AJNR Blog Editor

Neil Lall, Denver, CO

#### Case of the Month Editor

Nicholas Stence, Aurora, CO

#### Case of the Week Editors

Juan Pablo Cruz, Santiago, Chile  
Sapna Rawal, Toronto, Ontario, Canada

#### Classic Case Editor

Sandy Cheng-Yu Chen, Taipei, Taiwan

#### Health Care and Socioeconomics Editor

Pina C. Sanelli, New York, NY

#### Physics Editor

Greg Zaharchuk, Stanford, CA

#### Podcast Editor

Wende N. Gibbs, Los Angeles, CA

#### Twitter Editor

Jennifer McCarty, Houston, TX

Founding Editor  
Juan M. Taveras

Editors Emeriti  
Mauricio Castillo, Robert I. Grossman,  
Michael S. Huckman, Robert M. Quencer

Managing Editor  
Karen Halm

Assistant Managing Editor  
Laura Wilhelm

Communications Coordinator  
Rebecca Artz

Marketing and Social Media Manager  
Kylie Mason

Executive Director, ASNR  
Mary Beth Hepp



Title: Venice in Autumn. Venice is a group of 118 small islands surrounded by canals and connected by bridges, renowned for its languorous beauty, history, carnival, and architecture.

*Karl Schaller and Maria Isabel Vargas, Neurosurgery Division and Neuroradiology Division of the Geneva University Hospitals, Geneva, Switzerland*

## The Woven EndoBridge Finally Coming Home across the Atlantic: What to Expect?

W.J. van Rooij, S.B.T. van Rooij, H.G. Kortman, and J.P. Peluso



The Woven EndoBridge (WEB; Sequent Medical, Aliso Viejo, California) is an intrasaccular flow diverter primarily developed for wide-neck bifurcation aneurysms without the need for supporting stents and concomitant dual-antiplatelet therapy. The WEB consists of a self-expanding, oblong or spheric braid of platinum-cored nitinol wires intended to implant inside the aneurysmal sac, and it can be electrothermally detached. Since its introduction in 2010, the WEB has evolved from a high-profile dual-layer to a low-profile single-layer construction that can be delivered through a 0.017-inch microcatheter in sizes up to 7 mm.<sup>1</sup> To date, more than 6000 WEBs have been implanted worldwide, most of these in Europe.

In the United States, FDA approval is expected soon, and our American colleagues will then have an exciting new tool available for endovascular treatment of intracranial aneurysms. The extensive European experience with the WEB provides for a flying start in the United States.

In this article, we share our personal experience with the WEB after having treated almost 300 aneurysms with the device.

### How Did We Start?

In 2014, we evaluated our results of stent-assisted coiling and found that stent placement in 45 patients with acutely ruptured aneurysms resulted in permanent neurologic deficit or death in 10 (22%), in 5 due to thromboembolic complications and in 5 due to early rebleed in the postoperative period despite the aneurysms being adequately coiled.<sup>2</sup> In February 2015, we considered an alternative for stent-assisted coiling in the new-generation WEB with a single layer, suitable for a 0.021-inch microcatheter. We started to use the WEB in wide-neck unruptured aneurysms without supporting stents or balloons, and our first results were encouraging. To further master the technique of the WEB, we gradually expanded the indication to all aneurysms suitable for the WEB; in general, small aneurysms from 3 to 10 mm, regardless of neck size or location.<sup>3-5</sup>

The Figure is a graphic display of the use of the WEB, coils, additional supporting devices, and flow diverters for endovascu-

lar treatment of intracranial aneurysms in our practice during 2013–2017.

### Access and Periprocedural Anticoagulation

We use a biaxial approach with a short (11 cm) 6F sheath and a Benchmark (Penumbra, Alameda, California) guiding catheter positioned in the petrous carotid artery or V3 segment of the vertebral artery. Only with very tortuous vessels do we use a 90-cm-long sheath (Neuron Max; Penumbra) with a 6F or 5F distal-access guiding catheter.

In our hospital (St Elisabeth Hospital Tilburg, The Netherlands), all admitted patients receive subcutaneous heparin, 2500 U twice daily, as a thrombotic prophylaxis. In patients with ruptured aneurysms, we use no other anticoagulation than heparin in the pressure bags for flushing (5000 U/L). In patients with unruptured aneurysms, heparin, a 2500–5000 U bolus, is given at the beginning of the procedure. Antiplatelet medication is not routinely administered.

In case of a thromboembolic complication, we try to remove the thrombus with thrombosuction or a stent retriever, and for peripheral emboli, tirofiban is used. When antiplatelet medication is considered necessary, aspirin, 500 mg, is given intravenously, later followed by prasugrel or clopidogrel (Plavix).

### WEB Sizing and Technique of Implantation

The aneurysm is measured from 3D rotational images. Oversizing the WEB is imperative to assure anchoring the device to the aneurysm walls. In general, the WEB is oversized by 1–2 mm from the mean width of the aneurysm in 2 perpendicular planes. Because compression in the diameter results in increased height, the height is chosen 1–2 mm less than the actual aneurysm height. In regularly shaped aneurysms, WEB sizing is straightforward. In irregularly shaped aneurysms, some spatial awareness is helpful. Throughout our experience with WEB sizing, our sizing failure rate is about 25%, which has not improved with time.

In the sizes of 4–7 mm, there is overlap between the WEB 21 and 17 systems. In general, the WEB 17 performs better in tortuous and difficult anatomy and the WEB 21 is more stable. Our personal preference is WEB 17 in the smallest sizes, 3–4 mm, and WEB 21 in the larger sizes, 5–8 mm.

The VIA 17 and 21 Microcatheters (Sequent Medical) are specifically developed for the WEB. These catheters can be steam-shaped when necessary (about 1 in 10 in our practice) and are stable during WEB delivery. The technique of WEB implantation is as follows: The tip of the microcatheter is positioned in the dome of the aneurysm. Then, the first part of the WEB is slowly unsheathed by microcatheter withdrawal until half of the WEB is deployed. At that point, the WEB has become soft, and puncture of the aneurysm wall with the distal marker has become highly unlikely. Next, the microcatheter is slightly pushed forward to ensure that the WEB is in the fundus of the aneurysm. At this point, the WEB can be completely deployed by further retracting the microcatheter while keeping the WEB in place.

The position of the WEB is checked with an angiographic run. Sometimes a rotational angiographic run may be helpful to eval-

Received June 1, 2018; Accepted June 27.

From the Department of Radiology (W.J.v.R., H.G.K., J.P.P.), Elisabeth Tweesteden Ziekenhuis, Tilburg, The Netherlands; and Department of Radiology (S.B.T.v.R.), Noordwest Ziekenhuisgroep, Alkmaar, The Netherlands.

Please address correspondence to W.J. van Rooij, MD, PhD, Department of Radiology, Elisabeth Tweesteden Ziekenhuis, Hilvarenbeekseweg 60, 5022GC Tilburg, The Netherlands; e-mail: wjvanrooij@gmail.com



Indicates article with supplemental on-line Appendix.

<http://dx.doi.org/10.3174/ajnr.A5798>

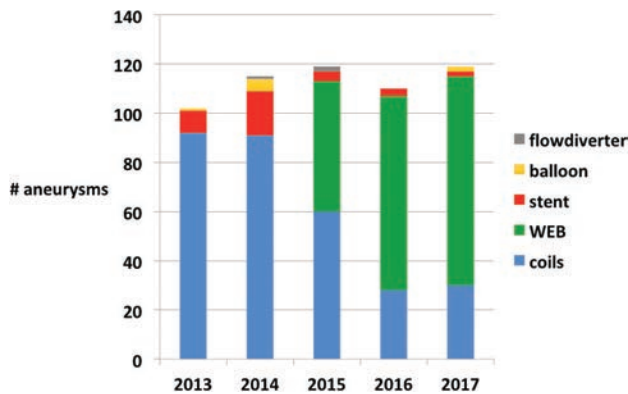


**FIGURE.** Evolution of devices used for endovascular treatment of intracranial aneurysms between 2013 and 2017.

uate the WEB position in relation to the aneurysm neck and parent vessels. We never use VasoCT (Philips Healthcare, Best, the Netherlands) for this purpose because this is time-consuming and we are somewhat afraid to recapture the WEB after several minutes have passed; possible thrombus formed inside the WEB may be fragmented and dispersed.

When a good WEB position is confirmed, the device is detached and the procedure is terminated, despite the possible presence of some flow inside the WEB and aneurysm.

The Appendix contains several links to videos of WEB treatments of intracranial aneurysms.

#### **Use of Additional Devices**

Additional coils are only rarely necessary to occlude the aneurysm or part of it. In most irregularly shaped aneurysms, the WEB can be used to cork the neck. Parts of the aneurysm not covered with the WEB will then thrombose anyway.

We never use a supporting balloon during WEB placement. In 2 cases with previously treated aneurysms, a stent was placed as a bailout procedure to stabilize the WEB after it tilted on detachment.

#### **Imaging Follow-Up after WEB Treatment**

Because many aneurysms still show some filling immediately after WEB placement, initial occlusion rates, as with coiling, cannot be given. We perform angiography after 3 months to confirm the absence of residual filling inside the WEB. Further follow-up is scheduled with 3T MRA.<sup>6</sup> Because the WEB acts like a Faraday cage, possible residual flow may remain undetected. Fortunately, residual flow at 3 months is extremely rare; we encountered only a few cases in larger aneurysms.

#### **Additional Applications of the WEB**

The WEB can also be applied for parent vessel occlusion of both large and small arteries.<sup>7</sup> For ICA occlusion, 2 WEBs are sufficient to occlude the artery. As opposed to detachable balloons, the WEB can be placed exactly in the desired position in the parent artery without fear of premature detachment. We maximally oversize the WEB in larger arteries such as the ICA or V4. The occlusion of small vessels such as the PICA (distal flow aneurysm) or the distal posterior cerebral artery (dissecting aneurysm) can be performed with the smallest WEB 17 devices.

The WEB can also be used in previously treated aneurysms.<sup>8</sup> In wide-neck remnants, stents can be avoided. In large and giant partially thrombosed aneurysms, results with the WEB are as poor as with other techniques; the WEB will migrate into intraluminal thrombus just like coil meshes do.

#### **Clinical and Imaging Results and Implications for Practice**

Our published results with the WEB, both for ruptured and unruptured aneurysms, are good with a reopening/retreatment rate of 7%, about 95% adequate occlusion, and no bleeds or rebleeds during follow-up. We encountered only 1 procedural rupture without clinical sequelae. Most thromboembolic complications were due to catheterization and not to the WEB.<sup>1,3-5,7</sup>

Clinical results in our practice have improved since the WEB replaced stent-assisted coiling, especially in ruptured aneurysms.<sup>2,4</sup> The simple periprocedural anticoagulation protocol without antiplatelet medication is a great advantage.

The WEB procedure is a single-catheter treatment and is usually straightforward and quick. After gradually gaining confidence with the WEB, we now treat most aneurysms (about 70%) with this device (Figure). Only large aneurysms and shallow aneurysms are treated otherwise. In our practice, stents and flow diverters are never used in ruptured aneurysms and only rarely in unruptured aneurysms (Figure).

Although the use of the WEB has some technical issues, these can readily be learned by anyone with some experience with endovascular aneurysm treatment. The procedure is similar to simple coiling. Proper training on phantoms and proctoring of first cases can essentially avoid a learning curve. We recommend that first-time users start with simple aneurysms rather than with complex wide-neck aneurysms. Simple aneurysms can be wide-neck as long as there is sufficient height to accommodate oversizing in width. With growing confidence, more challenging aneurysms can be treated, sometimes surprisingly easily.

#### **Improvements and Perspectives**

The development of the WEB is ongoing. More shallow sizes are being developed, and experiments are being performed with changes in the WEB shape; for example, a hybrid version between Single-Layer and Single-Layer Sphere. The larger WEB sizes, 9–11 mm, may become available in lower profiles suitable for a 0.027-inch instead of a 0.033-inch microcatheter.

To reduce the proportion of incorrect sizing of about 1 in 4, an automated 3D software program would be a valuable tool.

The WEB is now marketed as an expensive device, comparable with the price of stent-assisted coiling. With growing popularity, prices are likely to drop.

In summary, in our practice, the WEB has rapidly gained popularity and largely replaced the use of coils, stents, and flow diverters. The avoidance of dual antiplatelet medication is a great advantage over stents and flow diverters, resulting in fewer thromboembolic complications and fewer early rebleeds. The easy, quick, and safe technique has a convincing advantage over balloon- or stent-assisted coil treatments.

Disclosures: Willem Jan van Rooij—*RELATED: Consulting Fee or Honorarium:* Terumo, MicroVention; *Other:* Terumo, MicroVention, *Comments:* Proctoring WEB cases.\* Sanne van Rooij—*RELATED: Grants:* Noordwest Ziekenhuisgroep Alkmaar, and unrestricted grant from MicroVention; *Comments:* 20% of resident salary during 2 years.\* Jo P. Peluso—*RELATED: Consultancy:* Proctoring WEB cases.\* \*Money paid to individual.

## REFERENCES

1. van Rooij SB, Peluso JP, Sluzewski M, et al. **The new low-profile WEB 17 system for treatment of intracranial aneurysms: first clinical experiences.** *AJNR Am J Neuroradiol* 2018;39:859–63 CrossRef Medline
2. Bechan RS, Sprengers ME, Majoie CB, et al. **Stent-assisted coil embolization of intracranial aneurysms: complication in acutely ruptured versus unruptured aneurysms.** *AJNR Am J Neuroradiol* 2016;37:502–07 CrossRef Medline
3. van Rooij WJ, Peluso JP, Bechan RS, et al. **WEB treatment of ruptured intracranial aneurysms.** *AJNR Am J Neuroradiol* 2016;37:1679–83 CrossRef Medline
4. van Rooij SB, van Rooij WJ, Peluso JP, et al. **WEB treatment of ruptured intracranial aneurysms: a single center cohort of 100 patients.** *AJNR Am J Neuroradiol* 2017;38:2282–87 CrossRef Medline
5. van Rooij SB, van Rooij WJ, Peluso JP, et al. **The Woven EndoBridge (WEB) as primary treatment for unruptured intracranial aneurysms.** *Interv Neuroradiol* 2018 Jan 1. [Epub ahead of print] CrossRef Medline
6. van Rooij S, Peluso JP, Sluzewski M, et al. **Mid-term 3T-MRA follow-up of intracranial aneurysms treated with the Woven EndoBridge (WEB).** *Interv Neuroradiol* 2018 Jan 1. [Epub ahead of print] CrossRef Medline
7. van Rooij WJ, Sluzewski M, Bechan RS, et al. **Therapeutic internal carotid or vertebral artery occlusion using the WEB device.** *Interv Neuroradiol* 2016;22:365–67 CrossRef Medline
8. van Rooij SB, van Rooij WJ, Sluzewski M et al. **The Woven EndoBridge (WEB) for recurrent aneurysms: clinical and imaging results.** *Interv Neuroradiol* 2018 Sep 12 [Epub ahead of print]

# Neuroimaging Findings of Zika Virus–Associated Neurologic Complications in Adults

L.C. Hygino da Cruz Jr, O.J.M. Nascimento, F.P.P.L. Lopes, and I.R.F. da Silva



## ABSTRACT

**SUMMARY:** When the first suspected cases of neurologic disorders associated with the Zika virus were noticed in Brazil in late 2015, several studies had been conducted to understand the pathophysiology of the disease and its associated complications. In addition to its well-established association with microcephaly in neonates, the Zika virus infection has also been suggested to trigger other severe neurologic complications in adults, such as Guillain-Barré syndrome, radiculomyelitis, and meningoencephalitis. Hence, the Zika virus should be deemed a global threat that can cause devastating neurologic complications among individuals in all age ranges. The aim of this review was to further describe neuroimaging findings of Zika virus infection and associated neurologic complications found in adults.

**ABBREVIATIONS:** ADEM = acute disseminated encephalomyelitis; DENV = dengue fever; ELISA = enzyme-linked immunosorbent assay; GBS = Guillain-Barré syndrome; IgM = immunoglobulin M; PRNT = plaque-reduction neutralization test; TM = transverse myelitis; ZIKV = Zika virus

The Zika virus (ZIKV) is an arthropod-borne virus (arbovirus) mainly transmitted by 2 species of mosquitoes, *Aedes aegypti* and *Aedes albopictus*. The virus was first identified in 1947 in Rhesus monkeys living in the Zika forest in Uganda. During the following decades, cases of human infection were subsequently reported in East and West Africa, Southeast Asia, and, finally, the Americas.<sup>1</sup> Other modes of transmission of the virus have been described, such as sexual intercourse, blood transfusion, and vertical (mother-to-child) transmission. No other arboviruses are thought to be transmitted sexually, and the transmission can occur before, during, or after the onset of symptoms and from asymptomatic patients.<sup>2,3</sup>

The first major reported outbreaks of ZIKV infection were described in French Polynesia in 2013 and 2015. At that time, some neurologic disabilities in infants of infected pregnant women were observed; however, the maternal-fetal transmission was not suspected at that time. Later, further evidence regarding

the transmission of the virus was reported in addition to its possible connection to other neurologic complications in adults.<sup>1,3</sup>

It has been speculated that 500,000–1.5 million people in Brazil have been infected with the ZIKV since the outbreak started.<sup>4</sup> French Polynesian visitors are believed to have brought ZIKV to Brazil during the 2014 Fédération Internationale de Football Association World Cup.<sup>1</sup> In Brazil, the first case of autochthonous transmission of ZIKV infection was reported in April 2015.<sup>5</sup> By the end of 2016, across 1840 municipalities in Brazil, 161,241 cases of probable ZIKV infection were identified, 64,311 of which have been confirmed.<sup>5</sup> In the first months of the outbreak, the diagnosis of ZIKV was challenging because its most commonly reported symptoms closely resemble those of other endemic, viral, and exanthematous diseases such as dengue fever (DENV) and chikungunya. Several reports of severe neurologic complications likely to be associated with ZIKV infection have been published during the past 3 years, culminating on February 1, 2016, with a declaration from the World Health Organization of a public health emergency of international concern.<sup>6</sup>

In addition to its association with microcephaly, the ZIKV infection is also related to other neurologic complications mostly found in adults. Some authors have described a concomitant increase in the incidence of both Guillain-Barré syndrome (GBS) and ZIKV infection.<sup>7–9</sup> Association with other neurologic complications in adults has also been suggested, including meningoencephalitis,<sup>10</sup> transverse myelitis (TM),<sup>11</sup> and ophthalmologic diseases.<sup>12</sup>

MR imaging plays a key role in assessing the CNS and is, therefore, recommended for the diagnosis and follow-up of patients

From the Department of Radiology (L.C.H.C., F.P.P.L.L.), Clínica de Diagnóstico por Imagem, Rio de Janeiro, Brazil; Alta Excelência Diagnóstica (L.C.H.C.), Rio de Janeiro, Brazil; Radiology Department (L.C.H.C.), Americas Medical City, Rio de Janeiro, Brazil; Neurology Department (O.J.M.N.), Universidade Federal Fluminense, Niterói, Brazil; and Department of Neurological Sciences (I.R.F.d.S.), Rush University Medical Center, Chicago, Illinois.

This work was supported by the Conselho Nacional de Desenvolvimento e Pesquisa and Fundação de Amparo à Pesquisa do Estado do Rio de Janeiro.

Please address correspondence to L.C. Hygino da Cruz Jr, MD, Avenue Pasteur, 162 apto, 401 Botafogo, Rio de Janeiro, RJ, Brazil CEP: 22290-240; e-mail: celsohygino@hotmail.com

Indicates open access to non-subscribers at www.ajnr.org

<http://dx.doi.org/10.3174/ajnr.A5649>

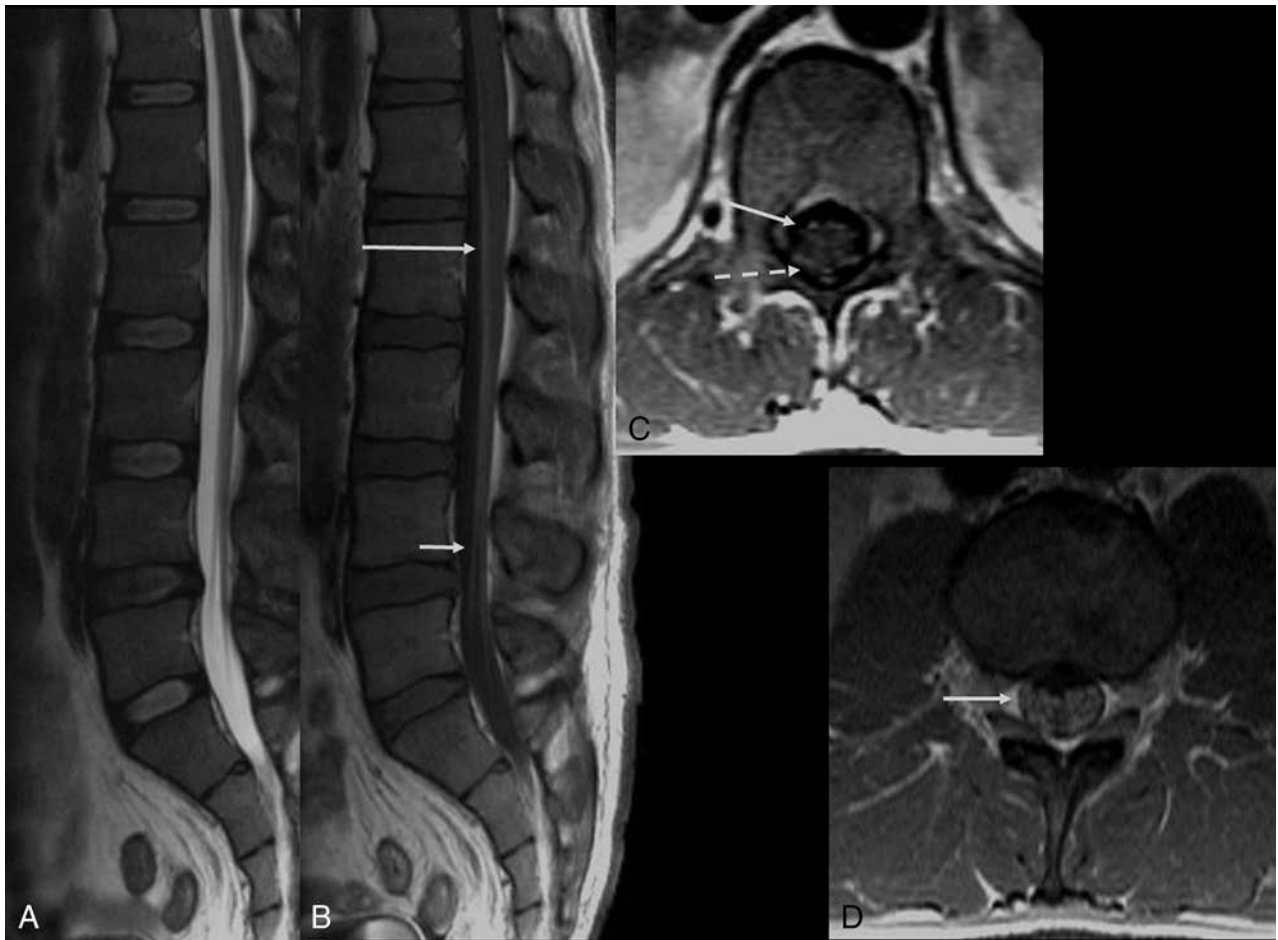


**FIG 1.** Guillain-Barré syndrome in a patient with Zika virus infection. Spine MR imaging of a 35-year-old man with progressive ascending paralysis. The conus medullaris and cauda equina nerve roots appear normal on the sagittal T2-weighted image (A). Postcontrast enhancement is noted in the conus medullaris (*long arrow*) and cauda equina nerve roots (*short arrow*) following the injection of a gadolinium-based contrast agent in the sagittal T1-weighted image (B). Postgadolinium axial T1-weighted image demonstrates enhancement in both anterior (*solid arrow*) and posterior (*dashed arrow*) nerve roots (C) as well as in the nerve roots of the cauda equina (D, *arrow*).

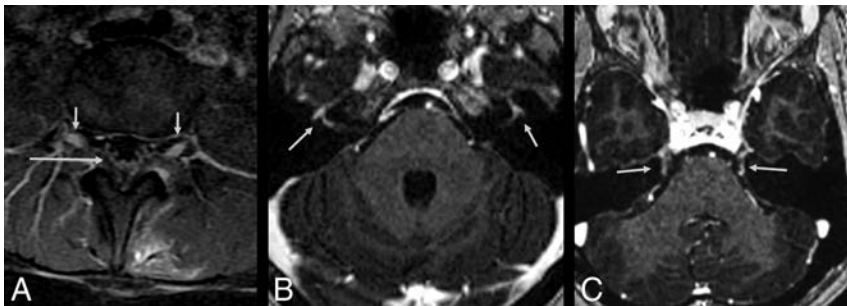


**FIG 2.** A 30-year-old woman with Zika virus infection with Guillain-Barré syndrome. Postcontrast sagittal T1-weighted image demonstrates enhancement in the cauda equina nerve roots (*long arrow*) and lumbar spine ganglia bilaterally (*short arrows*) following injection with a gadolinium-based contrast agent (A). Axial postcontrast, fat-suppressed T1-weighted MR imaging shows gadolinium enhancement of the facial nerves (B, *arrows*). Axial postcontrast, fat-suppressed T1-weighted MR imaging shows gadolinium enhancement of the trigeminal nerves (C, *arrows*).

### Vectors, Transmission, and Laboratory Diagnosis

The major vector of ZIKV worldwide is the mosquito *Aedes aegypti*, followed by *Aedes albopictus*. However, due to widespread distribution, the virus has been recently isolated from other mosquitoes, including the *Aedes furcifer*, *Aedes vittatus*, *Aedes taylori*, and *Aedes hirsutus*. The ZIKV is primarily transmitted between individuals through infected mosquito bites, establishing a transmission cycle between humans and mosquitoes. The transmission sources of ZIKV described so far are mosquito bites and human-to-human

transmission (via body fluids). MR imaging involves no ionizing radiation and has the advantage of greater tissue differentiation, allowing a better evaluation of the CNS and providing useful data for eventual differential diagnoses.

The aim of this study was to describe the MR imaging findings of neurologic disorders in adult patients with ZIKV infection.

transmission (via body fluids).

It is extremely difficult to differentiate solely on the basis of clinical grounds the acute infections caused by ZIKV, DENV, and chikungunya virus. All of them might present in most patients with an acute exanthematous fever, usually associated with a maculopapular skin rash, conjunctivitis, and a painful syndrome, nor-

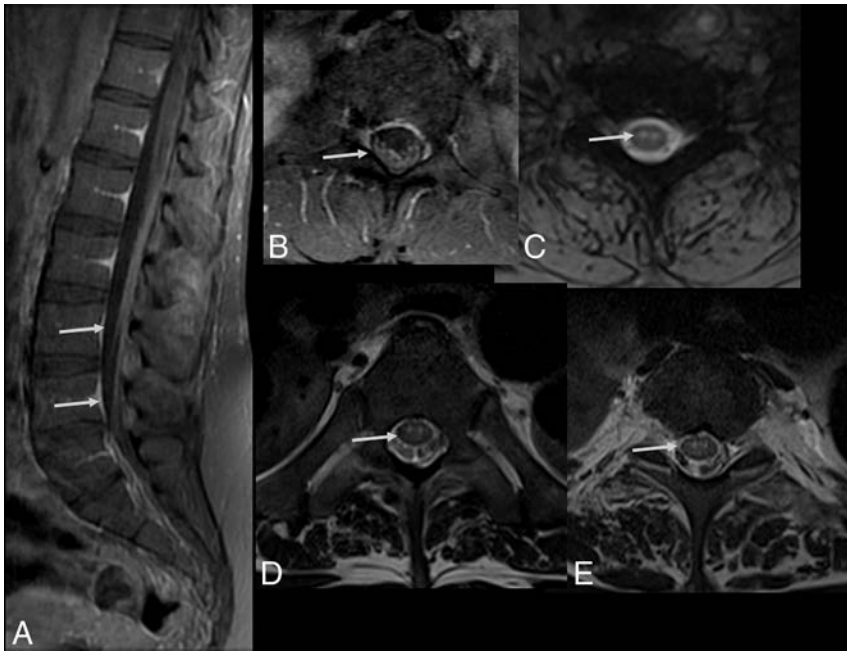


**FIG 3.** Spine MR imaging of a 35-year-old man with Zika virus infection and Guillain-Barré syndrome presenting with progressive ascending paralysis that evolved to respiratory distress and decreased level of consciousness. The patient had skin rashes preceded by flulike symptoms 1 week before the development of neurologic symptoms. Postcontrast enhancement is seen in the cauda equina nerve roots (arrows) on sagittal (A) and axial (B) T1-weighted spine images following gadolinium-based contrast agent injection. Axial gradient-echo T2-weighted (C) and FSE T2-weighted (D and E) spine images reveal hyperintensity (arrow) in the anterior horns of the cervical (C) and thoracic spinal cord (D).



**FIG 4.** Acute myelitis in a patient with Zika virus infection. Spine MR imaging of a 38-year-old woman with unsteadiness and weakness in the lower limbs. Hyperintense, ill-defined lesions are seen in sagittal (A, arrows) and axial (C and D, arrows) T2-weighted images of the cervicothoracic and middle thoracic spinal cord, causing mild expansion of the cord (A). The lesions demonstrate contrast enhancement in the postgadolinium sagittal T1-weighted image (B, arrows).

mally comprising headache, myalgia, and arthralgia, with subtle differences in the presentation.<sup>7</sup> The rash might be more prominent with ZIKV, whereas DENV leads to more pronounced

IgM pentamer is considered too large to cross the blood-brain barrier and its positivity in the CSF suggests recent intrathecal antibody synthesis and direct CNS penetration of ZIKV.<sup>18,19</sup> As suggested by

headaches and generalized pain, with chikungunya virus frequently causing incapacitating arthralgia and/or arthritis.<sup>7</sup> Thus, laboratory diagnosis is essential during an outbreak of arbovirosis, even more so in places with endemic cases.

Since the ZIKV infection has become a global health problem, the World Health Organization has published several algorithms for an accurate diagnosis of the disease.<sup>13</sup> The criterion standard for laboratory diagnosis of ZIKV infection relies mostly on the demonstration of the virus in body fluids by real-time reverse-transcription polymerase chain reaction analysis to detect the viral RNA; however, its positivity is very transient, usually persisting no longer than 5–7 days in the blood and CSF.<sup>14</sup> Some studies have suggested a prolonged positivity in urine<sup>8</sup> and semen<sup>15</sup> for a few weeks to months.

The problem is that some of the neurologic manifestations in adults are considered postinfectious autoimmune phenomena (such as GBS, TM, and acute disseminated encephalomyelitis [ADEM]), and by the time of the development of clinical symptoms, viral RNA might be already undetectable. ZIKV immunoglobulin M (IgM) antibody capture enzyme-linked immunosorbent assay (ELISA) might remain positive in the blood and CSF samples for a longer period,<sup>13,14</sup> but its use is further complicated in regions with endemic DENV because cross-reactivity is known to occur.<sup>13</sup> The plaque-reduction neutralization test (PRNT) can be performed to help differentiate anti-ZIKV antibodies from cross-reacting antibodies, but with a low specificity, excessive cost, and performance only in specialized, experienced laboratories because no commercial kit is available.<sup>16</sup> Consequently, since December 2016, the Centers for Disease Control and Prevention no longer recommend the use of the PRNT in areas with endemic presence of other flaviviruses, owing to its low accuracy.<sup>14</sup>

In an effort to improve diagnostic accuracy, a Brazilian study has shown that cross-reactivity might be overcome by using a ZIKV IgM antibody capture ELISA of both CSF and serum in cases of ZIKV-associated neurologic complications.<sup>17</sup>

This finding is based on the fact that the

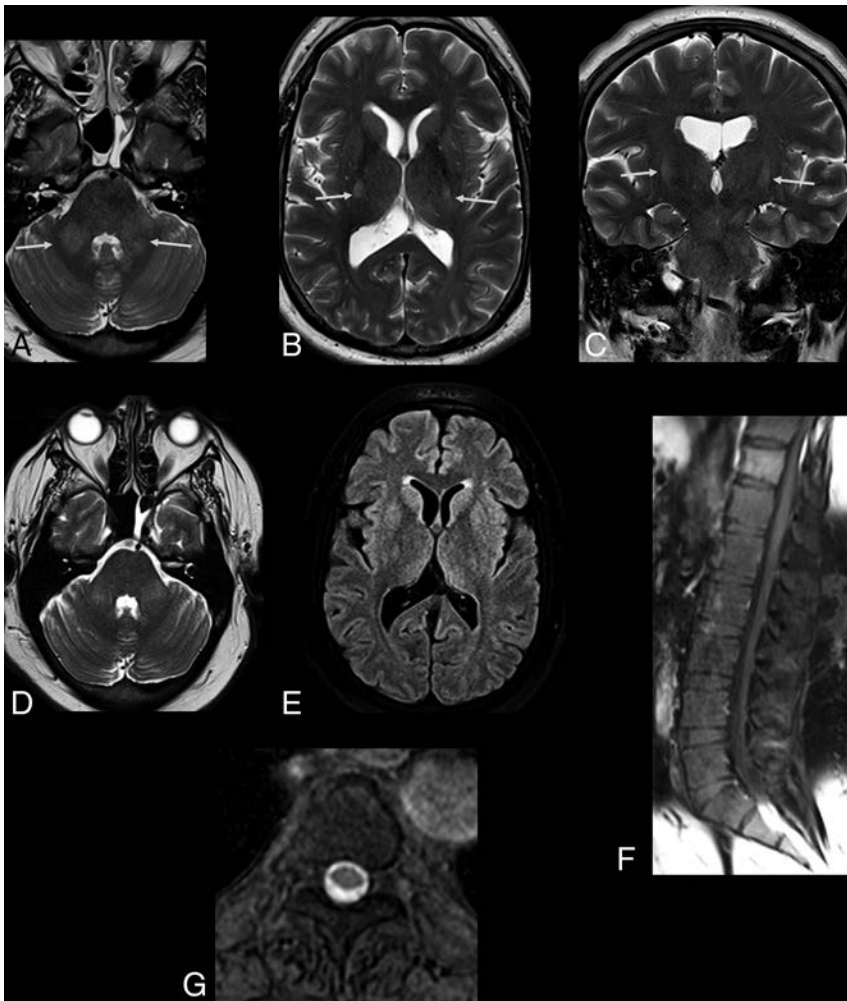


**FIG 5.** The same patient as in Fig 3. Zika virus-related Guillain-Barré syndrome associated with brain stem encephalitis and myelitis (encephaloradiculomyelitis). Brain MR imaging of a 35-year-old man positive for Zika infection with Guillain-Barré syndrome who presented with progressive ascending paralysis evolving to respiratory distress and decreased level of consciousness. The patient had skin rashes preceded by flulike symptoms 1 week before the development of neurologic symptoms. Axial and coronal T2-weighted brain images show bilateral hyperintensity (arrows) in the middle cerebellar peduncles (A) and corticospinal tracts bilaterally (B and C). Brain and spine MR imaging performed 2 months after treatment demonstrate improvement of the middle cerebellar peduncle and corticospinal tract hyperintensity (D and E). An absence of contrast enhancement is seen in the conus medullaris and cauda equina nerve roots in the postcontrast sagittal fat-suppressed T1-weighted image (F). Axial T2-weighted spine image reveals improvement of the hyperintensity in the anterior horns of the thoracic spinal cord (G).

this study, in areas with endemic DENV infection, a serum dengue IgM for serotypes 1–4 should be performed to check for cross-reactivity.<sup>17</sup> If both the serum ZIKV and DENV IgM have positive findings, then CSF IgM for both viruses is tested; the results are considered diagnostic if they are positive for ZIKV alone.<sup>17</sup> Another recent study from Brazil using CSF and blood samples from neonates with ZIKV-associated microcephaly has further supported these findings, showing a 100% correlation between positive CSF ZIKV serologies and PRNT.<sup>20</sup>

### Neurologic Disorders Associated with Zika Virus Infection in Adults

**Guillain-Barré Syndrome.** Guillain-Barré syndrome is an acute, immune-mediated polyneuropathy affecting mainly the peripheral nerves and often following a prior infection. Several reports

have described a probable, temporal association between the exponential increase in the number of GBS cases and ZIKV infection in areas of recent ZIKV outbreaks.<sup>5,8,17,21</sup> Other arboviruses, especially the dengue and chikungunya viruses, have also been associated with an increased incidence of GBS in previous studies.

Parra et al<sup>8</sup> described a series of patients with GBS and positive reverse-transcription polymerase chain reaction for ZIKV in Colombia and showed that most patients presented with an electrophysiologic pattern of acute inflammatory demyelinating polyneuropathy, which was similar to the pattern observed in a prospective cohort in Brazil.<sup>17</sup> Conversely, in a case-control study conducted in the French Polynesia, the acute motor axonal neuropathy subtype was the most prevalent presentation.<sup>21</sup> Some experts believe that the diverging findings might be explained by differences in performing electrophysiologic testing, rather than some major clinical phenomena.<sup>22</sup>

In some cases of ZIKV-related GBS, the temporal profile of neurologic symptoms is different from that observed in classic, postinfectious GBS. According to a report, neurologic symptoms are present in almost half of the cases during or immediately after the development of the clinical viral syndrome associated with ZIKV infection.<sup>8</sup> Recently, cases of ZIKV-associated acute transient polyneuritis have been reported in Brazilian patients.<sup>23</sup> Also, a case of chronic inflammatory demyelinating polyneuropathy has been reported.<sup>24</sup> Nevertheless, GBS secondary

to ZIKV seems to present with a similar clinical outcome and prognosis compared with more classic triggers for this polyneuropathy, with a fairly similar response to traditional therapies, such as intravenous immunoglobulin.<sup>7,8,17,21,25</sup>

MR imaging is mainly performed to rule out other clinical conditions presenting with acute flaccid paralysis. The findings on MR imaging are like those described in classic GBS, and nerve root enhancement of the cauda equina is often seen in postgadolinium T1-weighted imaging sequences. The involvement of the posterior nerve roots is commonly observed. However, in several cases, diffuse nerve root enhancement may also be observed (Fig 1). Spine MR imaging may also reveal bilateral abnormalities in the lumbar spinal ganglia, characterized by increased signal intensity in T2-weighted images and contrast enhancement. In addition, postcontrast enhancement of cra-

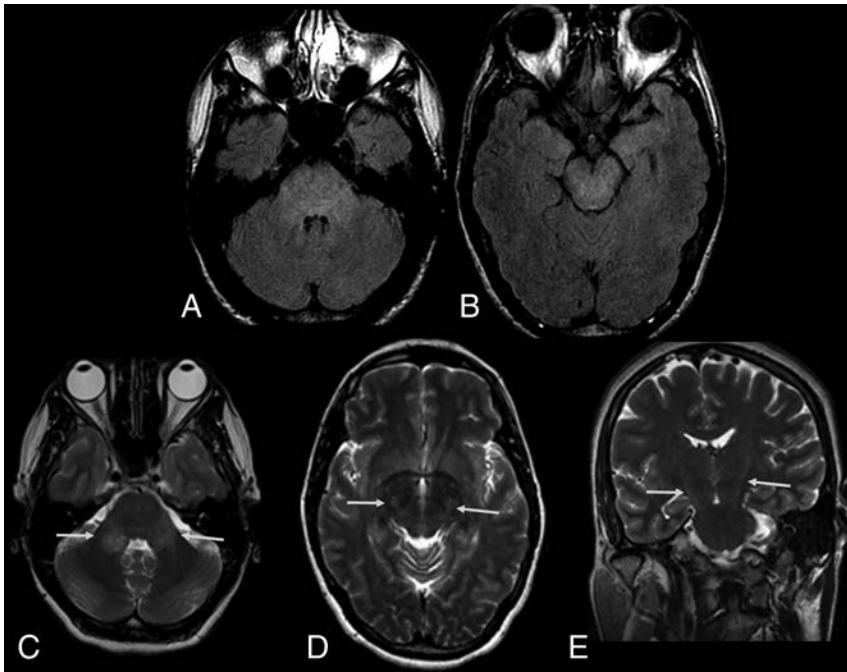


**FIG 6.** Zika virus–related brain stem encephalitis in a 40-year-old man. Axial fluid-attenuated inversion recovery image shows diffuse hyperintensity in the brain stem, especially in the pons and cerebral peduncle (A and B). Axial T2-weighted images show bilateral hyperintensity in the middle cerebellar peduncles (C, arrows). Hyperintensity is also seen in the corticospinal tracts bilaterally in axial (D) and coronal (E) T2-weighted images. These lesions showed no enhancement on postcontrast T1-weighted images (not shown).

nial nerves may also be noticeable, particularly in the facial and trigeminal nerves (Fig 2).

**Myelitis.** Despite the current absence of definitive evidence of an association between myelitis and ZIKV infection, a few reports have suggested that this association is likely to occur. Flaviviruses are neurotropic viruses, and DENV, Japanese encephalitis virus, and West Nile virus infections are often related to the occurrence of extensive transverse and longitudinal myelitis.<sup>26</sup> Clinically, patients with these infections often present with fast-developing acute flaccid paralysis.

Spinal cord involvement in ZIKV can vary, and previous reports have described different forms of involvement.<sup>11,17,27,28</sup> Clinical symptoms are diverse and depend on the location and extension of the lesion. We can speculate that ZIKV might also specifically affect the anterior horns of the spinal cord (Fig 3), leading to a motor neuron syndrome, similar to the West Nile virus.<sup>26</sup> Other forms of spinal involvement have been

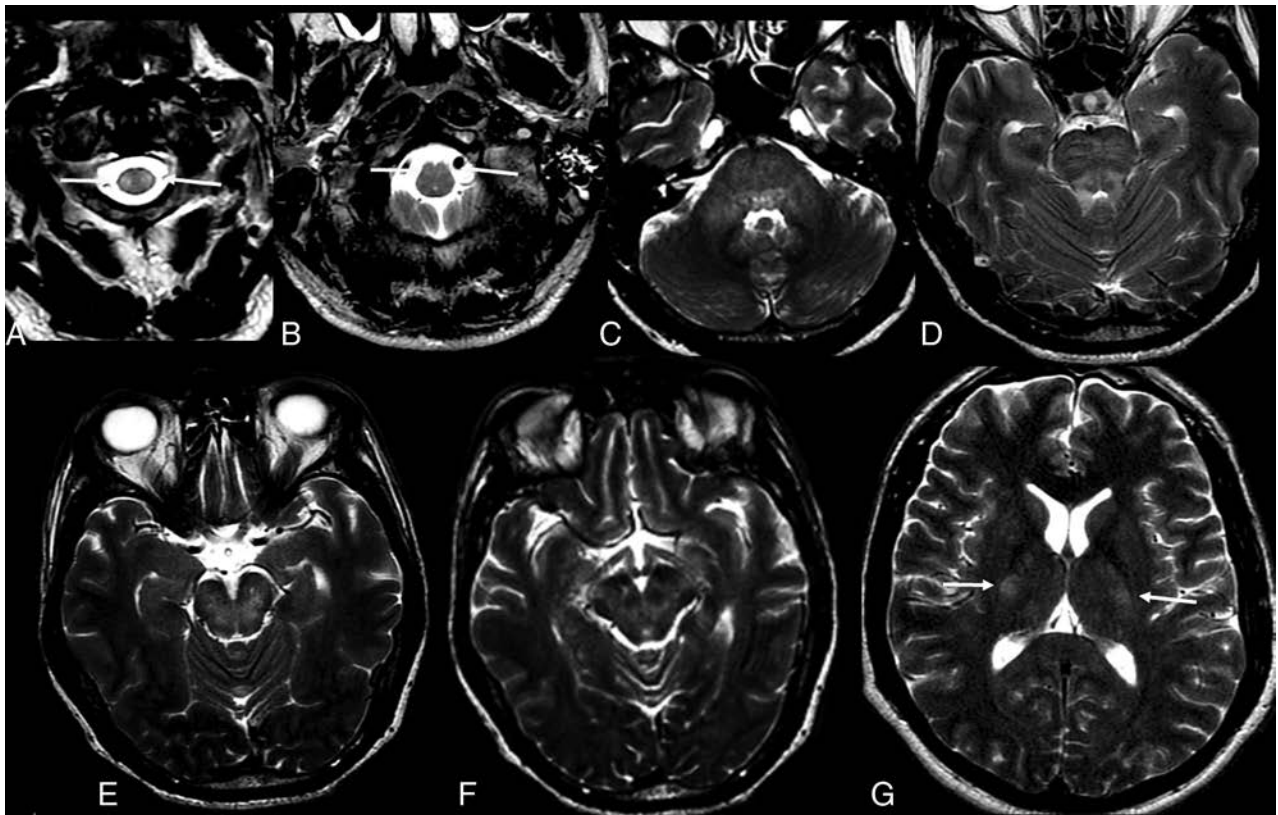


**FIG 7.** Axial T2-weighted images of a 52-year-old man with Zika virus–related brain stem encephalitis and myelitis. Hyperintense lesions are seen in the upper portion of the lateral columns of the cervical spine (A, arrow) and anterior portion of the medulla bilaterally (B, arrow). The brain stem is diffusively involved (C–G), as are the middle cerebellar peduncles (C) and the bilateral corticospinal tracts (G, arrows).

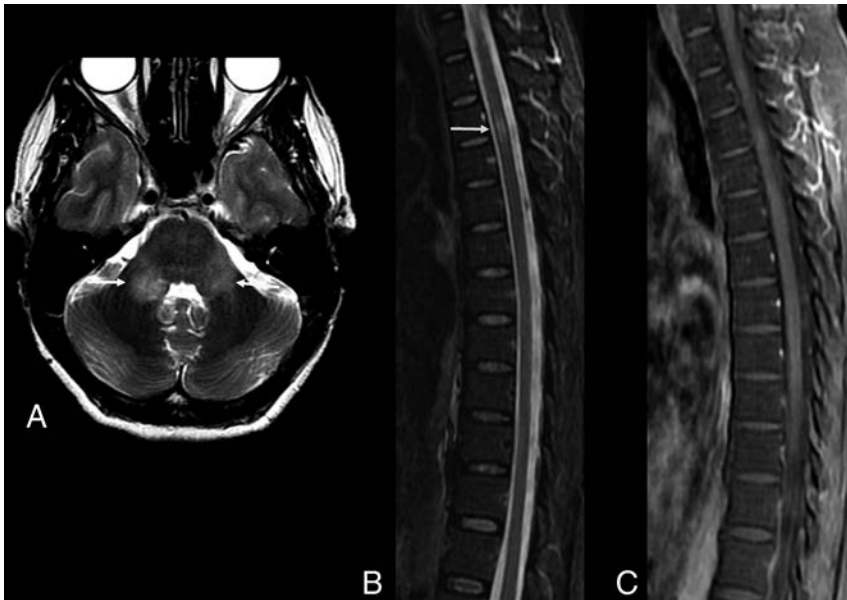


**FIG 8.** Brain and spine MR imaging of a 48-year-old woman with Zika virus infection and encephalitis and myelitis. Axial T2-weighted image of the brain shows hyperintensity of the middle cerebellar peduncles bilaterally (A, arrows). Short tau inversion recovery sagittal image (B) demonstrates a hyperintense lesion in the upper portion of the anterior spine without enhancement in the sagittal postcontrast T1-weighted image (C). Follow-up MR imaging was performed 2 weeks later.

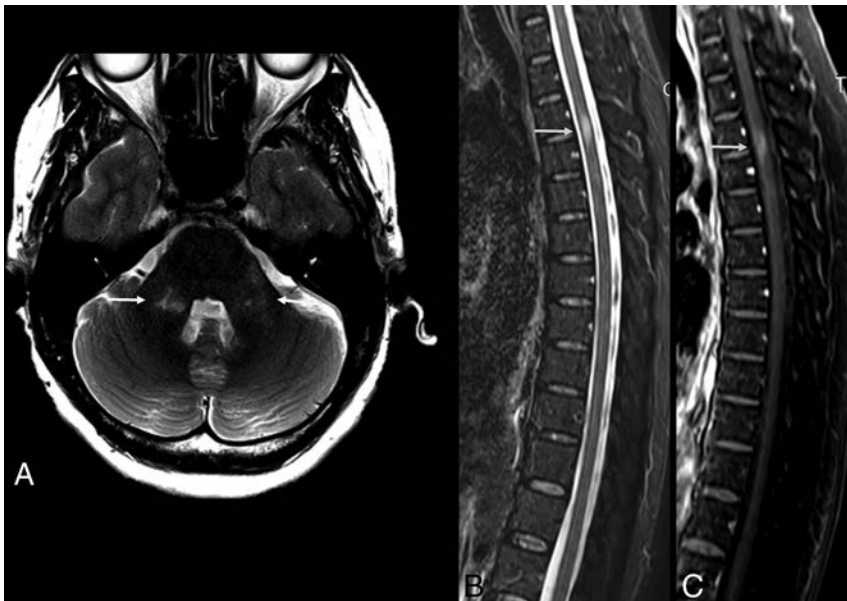


**FIG 9.** The same patient as in Fig 8. Follow-up scans (2 weeks after infection) of the brain and spine MR imaging of a 48-year-old woman with Zika virus infection and encephalitis and myelitis. Improvement of the cerebellar lesions is seen (A, arrows). However, the anterior spinal cord is enlarged (B, arrow) and shows contrast enhancement (C, arrow).

described, such as those present in acute transverse myelitis, which usually involves the spinal cord in  $>3$  segments lengthwise and more than two-thirds of its surface area.<sup>17,28</sup>

Myelitis can also be identified as diffuse lesions with varying sizes that may affect any portion of the spinal cord. Contrast enhancement may be seen in acute lesions. The spinal cord may be enlarged (Fig 4) due to edema.<sup>11,27</sup>

**Meningoencephalitis.** Meningoencephalitis is a well-known and common presentation of Japanese encephalitis<sup>29</sup> and West

Nile virus infections,<sup>26</sup> but it is, surprisingly, a relatively rare complication involving other flaviviruses, including the ZIKV.<sup>30,31</sup> The patients affected with meningoencephalitis present clinically with progressive somnolence, seizures, and focal deficits, and in rare cases, their condition may evolve into deep coma or brain death. As demonstrated in previous studies, cases of viral encephalitis (irrespective of the causing agent) may show no abnormalities on imaging examinations. Among a few available reports of ZIKV infection, no specific neuroimaging pattern has been found suggesting the occurrence of this condition.

Previous reports have revealed the presence of asymmetric subcortical hyperintense lesions in meningoencephalitis, which may show restricted diffusion.<sup>28</sup> Japanese encephalitis and West Nile viruses more commonly affect the deep gray matter, brain stem, and cerebellum; in contrast, a recent report has shown the involvement of the cortical and subcortical junctions, particularly the cingulate and superior frontal gyri.<sup>28</sup> Cortical lesions in other infections by flaviviruses have also been demonstrated but are less frequent. In another study, diffuse and confluent lesions in the basal ganglia, thalamus, and white matter have been related to ZIKV infection-related encephalitis.<sup>31</sup> Some patients may also present with bilaterally increased signal intensity in the middle cerebellar peduncles and corticospinal tracts (Fig 5). Other patients have been shown to present with brain stem involvement characterizing rhombencephalitis (Figs 6 and 7).

Frequently, evidence of different forms of presentation may coexist in the same patient, including GBS, myelitis, and meningoencephalitis. In a prospective study conducted in Brazil, cases of concomitant central and peripheral nervous system involvement were observed in some adults with acute ZIKV infection.<sup>17</sup>

**Acute Disseminated Encephalomyelitis.** Acute disseminated encephalomyelitis is an immune-mediated inflammatory demyelinating disorder targeting mostly the white matter of the brain and, less frequently, the gray matter and the spinal cord. It is characterized by an acute or subacute encephalopathy with multiple neurologic deficits and is typically monophasic and self-limiting. Although infrequent, recurrent and multiphasic forms may also

occur. Clinical symptom onset generally develops within 3 weeks after a viral infection or vaccination. However, in some cases, it is not possible to prove such a relationship. The diagnosis is based on clinical and imaging findings, as well as on excluding other conditions that can mimic ADEM. Although it can occur at any age, it is more common in children and young adults.

Similar to observations of other viral infections, ZIKV infection may also be related to ADEM.<sup>32,33</sup> The imaging findings described are like those observed in other related causes of ADEM, such as multifocal and asymmetric lesions, affecting the brain and the spinal cord. The clinical course of ADEM-ZIKV cases was very similar to that of the most typical ADEM cases, characterized as a self-limited and monophasic course, appearing weeks after the viral infection.

MR imaging findings reveal multiple ill-defined, asymmetric, hyperintense lesions on T2-weighted and FLAIR images (Fig 8), which demonstrate contrast enhancement in T1-weighted postgadolinium images.<sup>28</sup> Figure 9 shows follow-up MR imaging performed 2 weeks after the infection.

### Differential Diagnoses

Some MR imaging findings in ZIKV infection have an appearance like that of other flavivirus infections. The West Nile virus may also present with abnormalities resembling the ones described in ZIKV infections. Previous reports have demonstrated increased signal intensity in both the middle cerebellar peduncle and anterior horns of the spinal cord, as well as contrast enhancement of the lumbosacral nerve roots.<sup>26</sup> These imaging features are identical to those observed in some cases of ZIKV infection.<sup>17,26</sup> The same pattern may be observed in patients infected with the Japanese encephalitis virus.<sup>29</sup> On the other hand, in this particular presentation of patients infected with ZIKV, a slight hyperintensity in bilateral cortical spinal tracts may also be seen (Figs 5–7). Thus, the differential diagnosis of the entities presenting with the imaging findings described above may only be established with further laboratory analysis.

Nerve root enhancement seems to be the most common imaging finding related to ZIKV infection, while it has also been reported that involvement of the lumbosacral nerve roots is mostly related to GBS.<sup>8,17</sup> In our opinion, the posterior nerve roots are equally involved in ZIKV infection, as are the anterior nerve roots. However, the anterior nerve roots are preferentially involved in GBS. In endemic areas, the identification of diffuse involvement of the cauda equina may be used to suggest the diagnosis of ZIKV.

### CONCLUSIONS

In addition to the extensive congenital abnormalities previously described, ZIKV may be associated with a substantially increased incidence of a broad spectrum of life-threatening neurologic syndromes in adults. Unfortunately, no specific neuroimaging finding can be related to this viral infection. In addition, some observed abnormalities are very similar to those seen in other flavivirus infections. However, in combination with clinical information, neuroimaging can be used to suggest the possibility of ZIKV infection, especially in endemic areas. Thus, the MR imaging findings of these neurologic syndromes, in association with

serum and CSF analysis as well as molecular and serologic testing, may play a significant role in the diagnosis of ZIKV infection.

### REFERENCES

1. Faria NR, Azevedo RD, Kraemer MU, et al. **Zika virus in the Americas: early epidemiological and genetic findings.** *Science* 2016; 352:345–49 CrossRef Medline
2. Mead PS, Hills SL, Brooks JT. **Zika virus as a sexually transmitted pathogen.** *Curr Opin Infect Dis* 2018;31:39–44 CrossRef Medline
3. Sánchez-Montalvá AA, Pou D, Sulleiro E, et al. **Zika virus dynamics in body fluids and risk of sexual transmission in a non-endemic area.** *Trop Med Int Health* 2018;23:92–100 CrossRef Medline
4. Araujo AQ, Silva MT, Araujo AP. **Zika virus-associated neurological disorders: a review.** *Brain* 2016;139:2122–30 CrossRef Medline
5. Ferreira da Silva IR, Frontera JA, Moreira do Nascimento OJ. **News from the battlefield: Zika virus-associated Guillain-Barré syndrome in Brazil.** *Neurology* 2016;87:e180–81 CrossRef Medline
6. WHO statement on the first meeting of the International Health Regulations Emergency Committee on Zika virus and observed increase in neurological disorders and neonatal malformations. <http://www.who.int/mediacentre/news/statements/2016/emergency-committee-zika-microcephaly/en/>. Accessed May 13, 2017
7. Nascimento OJ, da Silva IR. **Guillain-Barré syndrome and Zika virus outbreaks.** *Curr Opin Neurol* 2017;30:500–07 CrossRef Medline
8. Parra B, Lizarazo J, Jiménez-Arango JA, et al. **Guillain-Barré syndrome associated with Zika virus infection in Colombia.** *N Engl J Med* 2016;375:1513–23 CrossRef Medline
9. Guillain-Barré syndrome: Brazil. February 8, 2016. <http://www.who.int/csr/don/8-february-2016-gbs-brazil/en/>. Accessed July 17, 2016
10. Carreaux G, Maquart M, Bedet A, et al. **Zika virus associated with meningoencephalitis.** *N Engl J Med* 2016;374:1595–96 CrossRef Medline
11. Mécharles S, Herrmann C, Poullain P, et al. **Acute myelitis due to Zika virus infection.** *Lancet* 2016;387:1481 CrossRef Medline
12. Furtado JM, Espósito DL, Klein TM, et al. **Uveitis associated with Zika virus infection.** *N Engl J Med* 2016;375:394–96 CrossRef Medline
13. World Health Organization. Laboratory testing for Zika virus infection. March 23, 2016. [http://apps.who.int/iris/bitstream/10665/204671/1/WHO\\_ZIKV\\_LAB\\_16.1\\_eng.pdf?ua=1](http://apps.who.int/iris/bitstream/10665/204671/1/WHO_ZIKV_LAB_16.1_eng.pdf?ua=1). Accessed July 17, 2016
14. Centers for Disease Control and Prevention. Fact Sheet for Healthcare Providers: Interpreting Zika MAC-ELISA Test Results. CDC. Updated May 3, 2017. <https://www.cdc.gov/zika/pdfs/interpreting-zika-mac-elisa-results.pdf>. Accessed April 13, 2017
15. de Laval F, Matheus S, Labrousse T, et al. **Kinetics of Zika viral load in semen.** *N Engl J Med* 2017;377:697–99 CrossRef Medline
16. Roehrig JT, Hombach J, Barrett AD. **Guidelines for plaque-reduction neutralization testing of human antibodies to dengue viruses.** *Viral Immunol* 2008;21:123–32 CrossRef Medline
17. da Silva IR, Frontera JA, Bispo de Filippis AM, et al. **Neurologic complications associated with the Zika virus in Brazilian adults.** *JAMA Neurol* 2017;74:1190–98 CrossRef Medline
18. Cordeiro MT, Pena LJ, Brito CA, et al. **Positive IgM for Zika virus in the cerebrospinal fluid of 30 neonates with microcephaly in Brazil.** *Lancet* 2016;387:1811–12 CrossRef Medline
19. Tunkel AR, Glaser CA, Bloch KC, et al; Infectious Diseases Society of America. **The management of encephalitis: clinical practice guidelines by the Infectious Diseases Society of America.** *Clin Infect Dis* 2008;47:303–27 CrossRef Medline
20. Cordeiro MT, Brito CA, Pena LJ, et al. **Results of a Zika virus (ZIKV) immunoglobulin M-specific diagnostic assay are highly correlated with detection of neutralizing anti-ZIKV antibodies in neonates with congenital disease.** *J Infect Dis* 2016;214:1897–904 CrossRef Medline
21. Cao-Lormeau VM, Blake A, Mons S, et al. **Guillain-Barré syndrome outbreak associated with Zika virus infection in French**

- Polynesia: a case-control study.** *Lancet* 2016;387:1531–39 CrossRef Medline
22. Uncini A, Shahrizaila N, Kuwabara S. **Zika virus infection and Guillain-Barré syndrome: a review focused on clinical and electrophysiological subtypes.** *J Neurol Neurosurg Psychiatry* 2017;88:266–71 CrossRef Medline
  23. Nascimento OJ, Frontera JA, Amitrano DA, et al. **Zika virus infection-associated acute transient polyneuritis.** *Neurology* 2017;88:2330–32 CrossRef Medline
  24. Leonhard SE, Munts AG, van der Eijk AA, et al. **Acute-onset chronic inflammatory demyelinating polyneuropathy after Zika virus infection.** *J Neurol Neurosurg Psychiatry* 2017 Nov 24. [Epub ahead of print] CrossRef Medline
  25. Muñoz LS, Parra B, Pardo CA; Neuroviruses Emerging in the Americas Study. **Neurological implications of Zika virus infection in adults.** *J Infect Dis* 2017;216:S897–905 CrossRef Medline
  26. Petropoulou KA, Gordon SM, Prayson RA, et al. **West Nile virus meningoencephalitis: MR imaging findings.** *AJNR Am J Neuroradiol* 2005;26:1986–95 Medline
  27. Palacios E, Clavijo-Prado C, Ruiz A, et al. **Longitudinal extensive transverse myelitis and Zika virus: a diagnostic challenge in a hospital in Colombia** [in English and Spanish]. *Neurologia* 2016 Oct 21. [Epub ahead of print] CrossRef Medline
  28. Zare Mehrjardi M, Carteaux G, Poretti A, et al. **Neuroimaging findings of postnatally acquired Zika virus infection: a pictorial essay.** *Jpn J Radiol* 2017;35:341–49 CrossRef Medline
  29. Kumar S, Misra UK, Kalita J, et al. **MRI in Japanese encephalitis.** *Neuroradiology* 1997;39:180–84 CrossRef Medline
  30. Schwartzmann PV, Ramalho LN, Neder L, et al. **Zika virus meningoencephalitis in an immunocompromised patient.** *Mayo Clin Proc* 2017;92:460–66 CrossRef Medline
  31. Soares CN, Brasil P, Carrera RM, et al. **Fatal encephalitis associated with Zika virus infection in an adult.** *J Clin Virol* 2016;83:63–65 CrossRef Medline
  32. Niemeyer B, Niemeyer R, Borges R, et al. **Acute disseminated encephalomyelitis following Zika virus infection.** *Eur Neurol* 2017;77:45–46 CrossRef Medline
  33. Brito Ferreira ML, Antunes de Brito CA, Moreira AJP, et al. **Guillain-Barre syndrome, acute disseminated encephalomyelitis and encephalitis associated with Zika virus infection in Brazil: detection of viral RNA and isolation of virus during late infection.** *Am J Trop Med Hyg* 2017;97:1405–09 CrossRef Medline

# Characteristics of MR Neuroimaging Services Billed by Radiologists versus Nonradiologists

 P.E. Sharp,  N.U. Lall,  D.R. Hughes,  P.P. Harkey, and  R. Duszak, Jr

## ABSTRACT

**BACKGROUND AND PURPOSE:** Although most neuroimaging examinations are interpreted by radiologists, many nonradiologists provide interpretation services. We studied day of the week, site of service, and patient complexity differences for common Medicare MR neuroimaging examinations interpreted by radiologists versus nonradiologists.

**MATERIALS AND METHODS:** Using carrier claims files for a 5% sample of Medicare beneficiaries from 2012 to 2014, we identified all claims for brain and lumbar spine MR imaging examinations. Services were categorized by physician specialty, day of the week, and the site of service. Patient complexity was calculated using Charlson Comorbidity Indices. The  $\chi^2$  was performed to test statistical significance.

**RESULTS:** A provider specialty could be identified for 568,423 brain and lumbar spine MR imaging examinations. Of weekday examinations, radiologists interpreted 475,288 (92.3%), and nonradiologists, 39,510 (7.7%). Of weekend examinations, radiologists interpreted 52,028 (97.0%) and nonradiologists 1597 (3.0%). Radiologists interpreted 145,904 (98.7%) examinations in the inpatient hospital and emergency department settings versus 1882 (1.3%) by nonradiologists. Of all examinations, 44,547 of those interpreted by radiologists (8.4%) were on the most clinically complex patients versus 2139 (5.2%) for nonradiologists. All interspecialty differences for day of the week, the site of service, and patient complexity were statistically significant ( $P < .001$ ).

**CONCLUSIONS:** Although radiologists interpret most common MR neuroimaging examinations for Medicare beneficiaries, in contrast to nonradiologists, they disproportionately render those services on weekends, in higher acuity sites, and on more complex patients. To optimize access and minimize disparities in necessary neuroimaging, quality metrics should consider such service characteristics.

**ABBREVIATION:** CCI = Charlson Comorbidity Index

Although radiologists interpret most neuroimaging examinations in the United States, a small-but-increasing proportion of those studies are interpreted by nonradiologists—most notably by neurologists, neurosurgeons, and orthopedic surgeons.<sup>1-10</sup> Writing about the changing provider marketplace in which imaging services are interpreted, Levin et al<sup>10</sup> noted an increasing proportion of in-office imaging being performed by nonradiologists; all the while, radiologists continued to render interpretations in increasing volumes for more acutely ill hospital inpatients and

patients in the emergency department. Anecdotally, others have similarly lamented that nonradiologists disproportionately render imaging services during daytime hours and on weekdays, leaving after-hours and weekend work for their radiologist counterparts.<sup>11</sup> Recent work supports this anecdote, at least with regard to lower extremity venous duplex examinations.<sup>12</sup>

Although a large body of literature exists comparing the market share of interpretation by radiologists versus nonradiologists for a variety of diagnostic and interventional radiology services, little work, to date, has focused on how those specialty differences vary by time and location.<sup>13-16</sup> Recent work suggests that emerging pay-for-performance models could unintentionally compromise patient access, particularly in areas where different specialty groups render similar services.<sup>17</sup> Further investigation into potential specialist variation—and the drivers thereof—could potentially help inform policy initiatives to ensure consistent and equitable access of all patients to high-quality services, regardless of time, date, geography, or patient complexity.

Focusing on common MR neuroimaging examinations, the

Received May 30, 2018; accepted after revision July 25.

From the Department of Radiology and Imaging Sciences (P.E.S., P.P.H., R.D.), Emory University School of Medicine, Atlanta, Georgia; Department of Radiology (N.U.L.), Ochsner Health System, New Orleans, Louisiana; Neiman Health Policy Institute (D.R.H.), Reston, Virginia; and School of Economics (D.R.H.), Georgia Institute of Technology, Atlanta, Georgia.

Previously presented as an abstract at: Annual Meeting of the American Roentgen Ray Society, April 30 to May 5, 2017; New Orleans, Louisiana.

Please address correspondence to Paige Sharp, MD, Department of Radiology and Imaging Sciences, Emory University School of Medicine, 1364 Clifton Rd NE Atlanta, Georgia 30322; e-mail: pesharp@emory.edu; @PaigeESharp

<http://dx.doi.org/10.3174/ajnr.A5807>

**Summary of differences in volumes of MR neuroimaging examinations interpreted by radiologists versus nonradiologists in a 5% national Medicare sample**

	Day of Week <sup>a</sup>		Site of Service <sup>a</sup>				Patient Complexity <sup>a</sup> (Mean CCI)
	Weekday	Weekend	ED	Inpatient	Outpatient	Office	
Radiologists	475,288	52,028	21,393	124,511	227,055	152,487	0.58
Nonradiologists	39,510	1597	303	1579	2180	36,890	0.40

**Note:**—ED indicates emergency department.  
<sup>a</sup>  $P < .001$ .

purpose of this study was to compare differences in the frequency of interpretations by radiologists versus nonradiologists as a function of the day of the week (weekday versus weekend), the site of service, and patient complexity.

**MATERIALS AND METHODS**

Our retrospective use of Medicare administrative claims data was performed under an exemption from the institutional review board of the American College of Radiology.

Under a Data Use Agreement from the Centers for Medicare and Medicaid Services, we acquired carrier claims patient-level 5% Medicare Research Identifiable Files for 2011 through 2014. These datasets contain details associated with all fee-for-service claims for a 5% national sample of Medicare enrollees, representing approximately 2.5 million beneficiaries each year. Specifically included in the dataset is information about patient demographics (eg, age, sex), Current Procedural Terminology codes, and International Classification of Diseases codes associated with all services, as well as the date, site, and rendering provider of each service.<sup>18</sup>

All professional and global billed claims for brain MR imaging (Current Procedural Terminology codes 70551, 70552, and 70553) and lumbar spine MR imaging (Current Procedural Terminology codes 72148, 72149, and 72158) services were initially identified. For each claim, the date of interpretation as attested by the billing physician was mapped to a specific day of week (eg, Sunday, Monday). Using previously described methods for Medicare claims-based analyses, we then mapped provider specialty and the site of service using the respective identification codes.<sup>14,16,19-22</sup> Radiologists were collectively identified using provider specialty codes for diagnostic radiology ( $n = 30$ ), nuclear medicine ( $n = 36$ ), and interventional radiology ( $n = 94$ ). Some provider specialties could not be determined (eg, those billing using generic multispecialty clinic codes), and these were grouped into an “undetermined specialty” category. All other specialty codes were mapped to a “nonradiologist” category. Similarly, the site of service codes were used to map services to the private office ( $n = 11$ ), inpatient hospital ( $n = 21$ ), outpatient hospital ( $n = 22$ ), and hospital emergency department ( $n = 23$ ) settings. All far less frequent sites of service were grouped together.

Charlson Comorbidity Index (CCI) scoring is widely used in the health services research literature as a surrogate for patient complexity and is calculated by combining specific International Classification of Diseases-attributable diagnoses from the patient’s medical history from the prior year.<sup>23,24</sup> Higher scores indicate higher mortality risk (eg, a score of zero indicates no comorbid diagnoses for services during the previous year). Using each beneficiary’s claims data for a single year before each MR

imaging claim (ie, 2011 through 2013), we calculated Charlson Comorbidity Index scores. These scores were grouped into 0, 1, 2, or 3+ (the latter to account for the relatively small number of patients with CCI values of >3 in our cohort).

We next compiled descriptive statistics for both brain and lumbar spine MR imaging services by specialty group in relation to the day of the week, the site of service, and the CCI.  $\chi^2$  testing was used to assess statistical significance. Because the first year of our data was required for calculation of CCI for subsequent years, these analyses span 2012–2014.

All analyses were performed using SAS, Version 9.3 for Windows (SAS Institute, Cary, North Carolina). Statistical tests were 2-sided with an  $\alpha$  level of .05.

**RESULTS**

A total of 345,880 brain MR imaging examinations were identified within the Medicare Research Identifiable Files national 5% cohort between 2012 and 2014. Of these, 308,728 (89.3%) were interpreted by radiologists, 14,569 (4.2%) were interpreted by nonradiologists, and 22,583 (6.5%) were interpreted by providers whose specialties could not be identified. The former 2 groups formed the basis of our brain MR imaging analysis.

A total of 279,073 lumbar spine MR imaging examinations were identified within our cohort. Of these, 218,588 (78.3%) were interpreted by radiologists, 26,538 (9.5%) were interpreted by nonradiologists, and 33,947 (12.2%) were interpreted by providers whose specialties could not be identified. The former 2 groups compose the basis of our lumbar spine MR imaging analysis.

When we considered brain and lumbar spine MR neuroimaging examinations together, radiologists interpreted 527,316 (84.4%) examinations and nonradiologists interpreted 41,107 (6.6%) examinations. There were 56,530 (9.0%) examinations for which a provider specialty could not be determined. Patients undergoing one or both of these services by a provider with an identifiable specialty composed our study cohort. Summary results are outlined in the Table.

**Interpreting Provider by Day of Week**

Of the 323,297 brain MR imaging examinations that could be attributed to unique provider specialties, 286,052 (88.5%) were performed on a weekday, and 37,245 (11.5%) on a weekend. Of brain MR imaging performed on weekdays, radiologists interpreted 272,282 (95.2%), while nonradiologists interpreted 13,770 (4.8%). For brain MR imaging performed on weekends, these proportions shifted to 36,446 (97.9%) by radiologists and 799 (2.1%) by nonradiologists (Fig 1A).

Of the 245,126 lumbar spine MR imaging examinations that could be attributed to unique provider specialties, 228,746 (93.3%) were performed on a weekday, and 16,380 (6.7%) on a

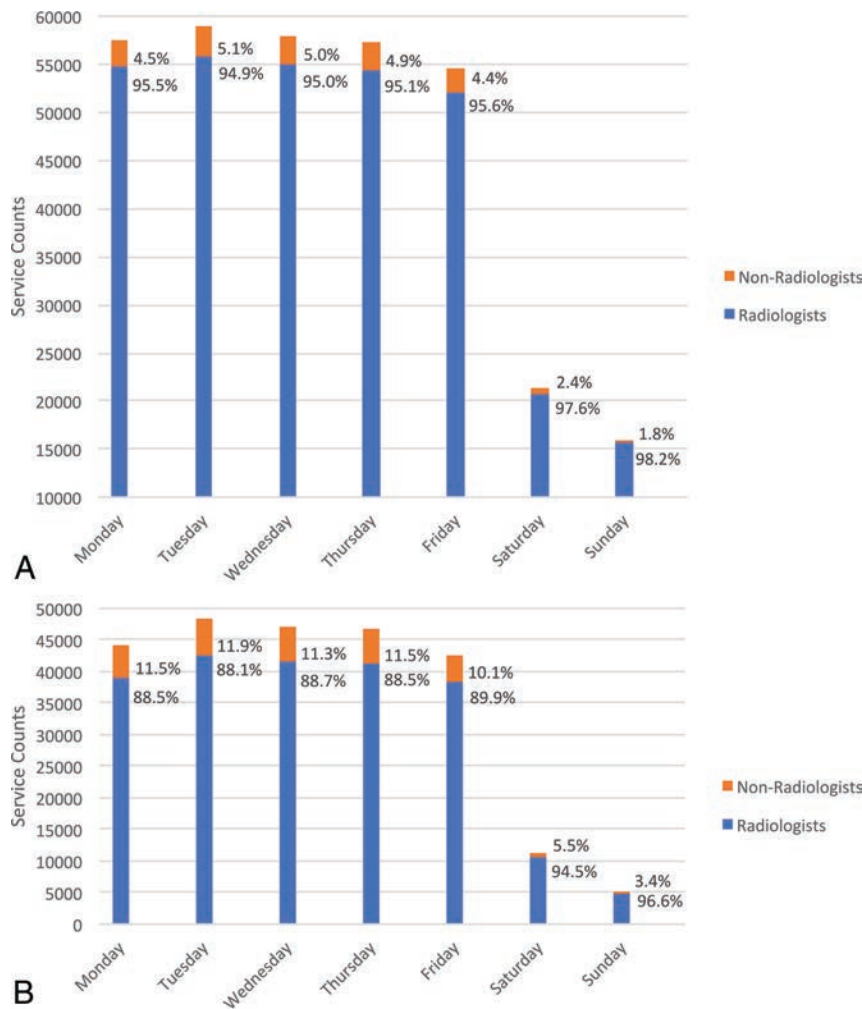


**FIG 1.** Breakdown of service counts by radiologists versus nonradiologists as billing providers in a 5% national sample of Medicare fee-for-service beneficiaries from 2012 through 2014 by day of week for brain MR imaging (A) and lumbar spine MR imaging (B) examinations.

weekend. Of lumbar spine MR imaging performed on weekdays, radiologists interpreted 203,006 (88.7%), while nonradiologists interpreted 25,740 (11.3%). For lumbar spine MR imaging performed on weekends, these proportions shifted to 15,582 (95.1%) by radiologists and 798 (4.9%) by nonradiologists (Fig 1B).

In total, for studies performed during the week, radiologists interpreted 475,288 (92.3%) and nonradiologists 39,510 (7.7%). Of weekend examinations, radiologists interpreted 52,028 (97.0%) and nonradiologists 1597 (3.0%). All of these differences were statistically significant ( $P < .001$ ).

#### Interpreting Provider by Site of Service

Radiologists interpreted 98.4% (16,088) of all brain MR imaging examinations performed in the emergency department setting, 98.7% (105,145) of those performed in the inpatient setting, and 98.8% (119,920) of those performed in the outpatient hospital setting. Nonradiologists, in contrast, interpreted <2% of brain MR imaging examinations performed in any of these sites of service; they interpreted 1.6% (265) of studies performed in the emergency department setting, 1.3% (1395) in the inpatient setting, and 1.2% (1432) in the outpatient hospital setting. Conversely, nonradiologists interpreted 14.6% (11,447) of the brain

MR imaging in the office setting. Those services rendered in private offices comprised 78.7% of all brain MR imaging interpreted by nonradiologists. The percentages of services by specialty group and sites of service are outlined in Fig 2A.

Radiologists similarly interpreted 99.3% (5305) of all lumbar spine MR imaging examinations performed in the emergency department setting, 99.1% (19,366) of those performed in the inpatient setting, and 99.3% (107,135) of those performed in the outpatient hospital setting. Nonradiologists, in contrast, interpreted <1% of lumbar spine MR imaging examinations performed in any of these sites of service: they interpreted 0.7% (38) of studies performed in the emergency department, 0.9% (184) in the inpatient setting, and 0.7% (748) in the outpatient hospital setting. Conversely, nonradiologists interpreted 22.9% (25,443) of the lumbar spine MR imaging in the office setting. Those services rendered in private offices comprised 96.3% of all lumbar spine MR imaging interpreted by nonradiologists. The percentages of services by specialty group and sites of service are outlined in Fig 2B.

In total, radiologists interpreted 145,904 (98.7%) examinations in the inpatient hospital and emergency department setting versus 1882 (1.3%)

for nonradiologists. In contrast, nonradiologists interpreted 19.5% of examinations in the office setting versus 80.5% for radiologists. All of these differences were statistically significant ( $P < .001$ ).

#### Interpreting Provider by Patient Comorbidities

We found statistically significant differences ( $P < .001$ ) in the overall complexity of patients for whom brain MR imaging examinations were interpreted by radiologists versus nonradiologists. Specifically, 79.0% of patients whose brain MR imaging was interpreted by radiologists had a CCI of 0 (indicating an absence of any of the indexed comorbidities) versus 83.1% for nonradiologists. Conversely, 11.0% of patients whose brain MR imaging was interpreted by radiologists had a CCI of  $\geq 3$  versus 7.2% for nonradiologists. The results within each CCI subset were statistically significant as well ( $P < .001$ ). Overall, the mean CCI was 0.67 for brain MR imaging interpretation services rendered by radiologists and 0.48 for those rendered by nonradiologists ( $P < .001$ ). Comorbidity differences by specialty provider group are outlined in Fig 3A.

Similarly, we found statistically significant differences ( $P < .001$ ) in the overall complexity of patients whose lumbar spine MR imaging was interpreted by radiologists versus nonradiolo-

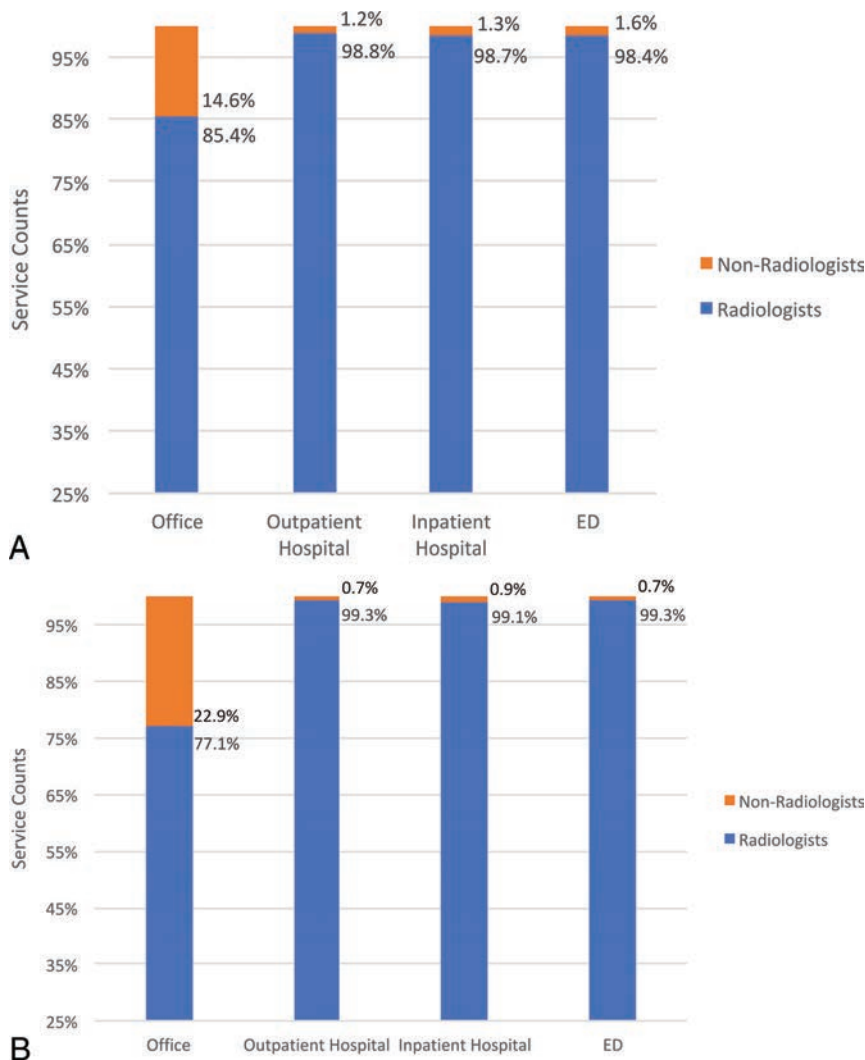


**FIG 2.** Breakdown of service counts by radiologists versus nonradiologists as billing providers in a 5% national sample of Medicare fee-for-service beneficiaries from 2012 through 2014 by site of service for brain MR imaging (A) and lumbar spine MR imaging (B) examinations.

gists. Specifically, 83.3% of patients whose lumbar spine MR imaging was interpreted by radiologists had a CCI of 0 versus 85.6% for nonradiologists. Conversely, 7.1% of patients whose lumbar MR imaging was interpreted by radiologists had a CCI of  $\geq 3$  versus 5.1% for nonradiologists. The results within each CCI subset were statistically significant as well ( $P < .001$ ). Overall, the mean CCI was 0.46 for lumbar MR imaging interpretation services rendered by radiologists and 0.36 for those rendered by nonradiologists ( $P < .001$ ). Comorbidity differences by specialty provider group are outlined in Fig 3B.

In total, radiologists and nonradiologists rendered interpretations for a similar percentage of low-acuity patients with 80.8% of brain and lumbar spine MR imaging interpreted by radiologists performed on patients with a CCI of 0 versus 84.7% for nonradiologists. Of examinations interpreted by radiologists, 44,547 (8.4%) were for patients with a CCI of  $\geq 3$  versus 2139 (5.2%) by nonradiologists. All of these differences were statistically significant ( $P < .001$ ).

## DISCUSSION

Using individual claims data for a representative national sample of  $>2$  million Medicare beneficiaries, we confirmed prior agree-

gate data-based observations that radiologists interpret most brain and lumbar MR imaging examinations in Medicare beneficiaries.<sup>5</sup> The additional encounter-level nature of our analysis, however, allowed us to confirm temporal, location, and patient complexity differences in the services rendered by radiologists versus nonradiologists. Indeed, we found that radiologists disproportionately provide services to Medicare beneficiaries at less opportune times, in higher acuity settings, and on more complex patients compared with nonradiologists. Our observations regarding common MR neuroimaging studies comport closely with those reported recently by Prabhakar et al<sup>12</sup> concerning lower extremity venous duplex examinations interpreted by radiologists versus nonradiologists.

The proportion of both brain MR imaging and lumbar spine MR imaging examinations interpreted by radiologists increased from weekdays to weekends (from 95.2% to 97.9% and 88.7% to 95.1%, respectively). As a result, there was a corresponding  $>50\%$  relative decrease in the proportion of brain MR imaging (from 4.8% to 2.1%) and lumbar spine MR imaging (from 11.3% to 4.9%) interpreted by nonradiologists on weekends relative to weekdays. As our society continues to prioritize patient access as a health care reform imperative, radiologists appear to demonstrate value by providing services at less op-

portune times to individuals who fall ill on weekends or who may not be able to take time off work to seek elective imaging.<sup>10,11</sup>

Correspondingly, our results demonstrate that radiologists interpret the greatest share of brain and lumbar spine MR imaging examinations performed in 24/7/365 environments such as the hospital inpatient and emergency department settings, which are generally associated with a higher acuity of care. In contrast, most brain and lumbar spine MR imaging examinations interpreted by nonradiologists were performed in comparably lower acuity private office settings. Of note, the office environment was the only setting in which nonradiologists interpreted  $>2\%$  of brain MR imaging or  $>1\%$  of lumbar spine MR imaging. Although our dataset does not permit us to identify specific times of service (claims are only dated but not timed), the round-the-clock nature of the inpatient hospital and emergency department settings strongly suggests that radiologists likely provide a disproportionate fraction of services during late evening and overnight hours as well.

Although claims data do not permit us to definitively assert explanations for our observations, it is possible that self-referral plays a role in the disproportionate number of studies interpreted

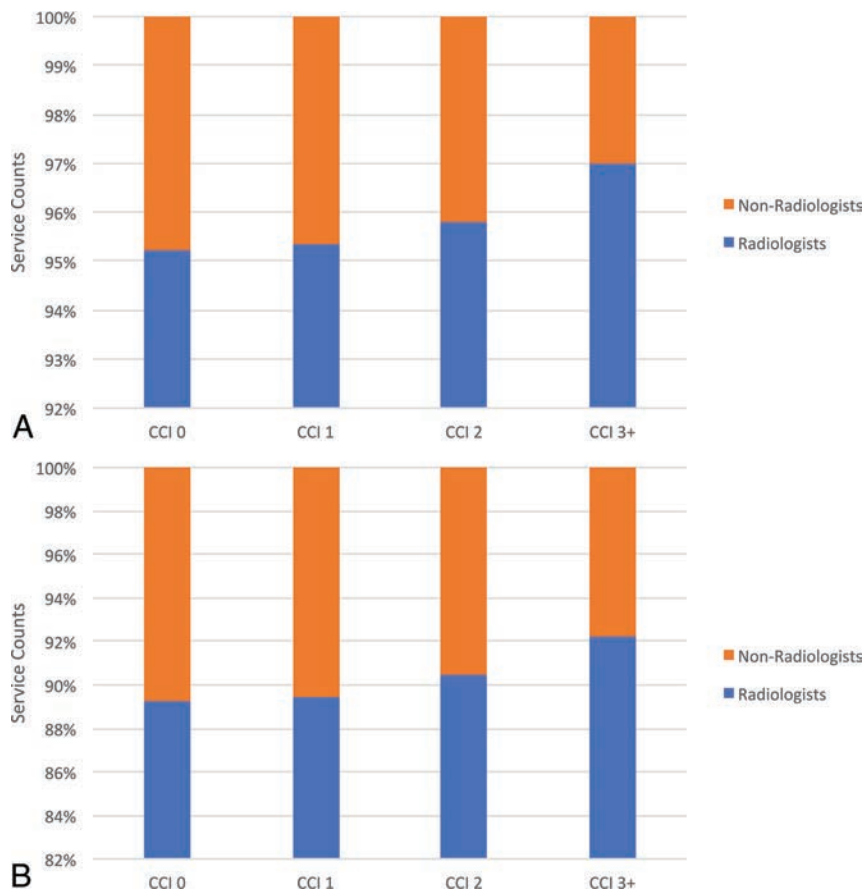


**FIG 3.** Breakdown of service counts by radiologists versus nonradiologists as billing providers in a 5% national sample of Medicare fee-for-service beneficiaries from 2012 through 2014 by patient complexity for brain MR imaging (A) and lumbar spine MR imaging (B) examinations.

by nonradiologists in the office setting. Patients seen in the clinic environment by neurologists, neurosurgeons, or orthopedic surgeons have been shown more likely to be referred to the in-office imaging centers managed by themselves or their partners.<sup>25,26</sup> This phenomenon could compound the effect that such office practices have on the overall proportion of in-office imaging examinations, but our analysis of administrative claims data does not permit us to assert causation—or even association.

Similar to differences in the day of week and site of services, our work highlights another area in which aggregate claims-based “turf battle” articles do not tell the entire story: patient complexity.<sup>5</sup> When we compared the most complex patients (CCI of 3+) in Medicare with the least complex (CCI of 0), there was a 37% relative reduction in the interpretations provided by nonradiologists for brain MR imaging and a 27% relative reduction for lumbar spine MR imaging. Correspondingly, we found that as patient complexity increased, the proportion of examinations interpreted by radiologists increased. At present, Medicare Physician Fee Schedule rates are patient-complexity neutral (eg, pay for brain MR imaging is the same regardless of whether a patient presents with uncomplicated headache or follow-up for a tumor after surgery and radiation). Our findings suggest that as our society moves increasingly to value-based payments, complexity adjustments may be appropriate to ensure appropriate incentives for providers caring for our most vulnerable patients.

Our analysis, based on Medicare claims, has several limitations. First, our findings may not necessarily be generalizable to patients with commercial insurance or even to Medicare beneficiaries undergoing other types of imaging studies. Second, we acknowledge that we were unable to identify the time of day for individual services (eg, MR imaging performed at 1 AM versus 1 PM is indistinguishable in claims data). However, the drastically increased proportion of examinations interpreted by radiologists in round-the-clock environments suggests that specialty differences also exist after hours during the week as well. Additionally, the exclusion of examinations with non-specialty-specific provider codes (eg, a generic multispecialty clinic designation) precluded our ability to identify a provider specialty for 9.0% of relevant MR neuroimaging examinations. It is conceivable, though we believe unlikely, that this exclusion would introduce bias into our reported results. Finally, the nature of claims data prevented us from making any assessments on the quality of interpretations. Such an analysis would require institutional-level data.

## CONCLUSIONS

Radiologists interpret most brain and lumbar spine MR imaging examinations performed on Medicare patients. Although some nonradiologists provide interpretation services as well, their work is disproportionately rendered on weekdays, in private office settings, and for less complex patients. Given that radiologists render the overwhelming majority of services on weekends, in sites of higher patient acuity, and to more complex patients, emerging quality metrics should consider such service characteristics to optimize equitable patient access to neuroimaging services.

## REFERENCES

- Levin DC, Matteucci T. **Do radiologists control imaging studies? Survey results from 198 academic institutions.** *Radiology* 1989; 170(3 Pt 1):879–81 CrossRef Medline
- Levin DC, Matteucci T. **“Turf battles” over imaging and interventional procedures in community hospitals: survey results.** *Radiology* 1990;176:321–24 CrossRef Medline
- Sunshine JH, Bansal S, Evens RG. **Radiology performed by nonradiologists in the United States: who does what?** *AJR Am J Roentgenol* 1993;161:419–29; discussion 430–31 CrossRef Medline
- Flanders AE, Flanders SJ, Friedman DP, et al. **Performance of neuro-radiologic examinations by nonradiologists.** *Radiology* 1996;198: 825–30 CrossRef Medline
- Rao VM, Levin DC, Spettell CM, et al. **Who performs neuroimaging? Results from the 1993 National Medicare Database.** *Radiology* 1997; 204:443–45 CrossRef Medline

6. Maitino AJ, Levin DC, Parker L, et al. **Practice patterns of radiologists and nonradiologists in utilization of noninvasive diagnostic imaging among the Medicare population 1993–1999.** *Radiology* 2003;228:795–801 CrossRef Medline
7. Levin DC, Rao VM, Parker L, et al. **Who gets paid for diagnostic imaging, and how much?** *J Am Coll Radiol* 2004;1:931–35 CrossRef Medline
8. Babiarz LS, Yousem DM, Parker L, et al. **Volume of neuroradiology studies read by neurologists: implications for fellowship training.** *J Am Coll Radiol* 2011;8:477–82 CrossRef Medline
9. Babiarz LS, Yousem DM, Parker L, et al. **Who collects professional fees for neuroradiology interpretation, radiologists or nonradiologists?** *J Am Coll Radiol* 2012;9:498–505 CrossRef Medline
10. Levin DC, Rao VM, Parker L, et al. **Analysis of radiologists' imaging workload trends by place of service.** *J Am Coll Radiol* 2013;10:760–63 CrossRef Medline
11. Weekend Hours Mean Stat Requests for Radiologists. Diagnostic Imaging. <http://www.diagnosticimaging.com/blog/weekend-hours-mean-stat-requests-radiologists>. Accessed December 12, 2017
12. Prabhakar AM, Gottumukkala RV, Wang W, et al. **Day of week, site of service, and patient complexity differences in venous ultrasound interpreted by radiologists versus nonradiologists.** *J Am Coll Radiol* 2018 May 7. [Epub ahead of print] CrossRef Medline
13. Kroll H, Duszak R, Nsiah E, et al. **Trends in lumbar puncture over 2 decades: a dramatic shift to radiology.** *AJR Am J Roentgenol* 2015;204:15–19 CrossRef Medline
14. Rosenkrantz AB, Bilal NH, Hughes DR, et al. **National specialty trends in billable diagnostic ultrasound in the ED: analysis of Medicare claims data.** *Am J Emerg Med* 2014;32:1470–75 CrossRef Medline
15. Moreno CC, Hemingway J, Johnson AC, et al. **Changing abdominal imaging utilization patterns: perspectives from Medicare beneficiaries over two decades.** *J Am Coll Radiol* 2016;13:894–903 CrossRef Medline
16. Duszak R Jr, Bilal N, Picus D, et al. **Central venous access: evolving roles of radiology and other specialties nationally over two decades.** *J Am Coll Radiol* 2013;10:603–12 CrossRef Medline
17. Roberts ET, Zaslavsky AM, McWilliams JM. **The value-based payment modifier: program outcomes and implications for disparities.** *Ann Intern Med* 2018;168:255–65 CrossRef Medline
18. Rosenkrantz AB, Hughes DR, Duszak R. **Medicare claims data resources: a primer for policy-focused radiology health services researchers.** *J Am Coll Radiol* 2017;14:1538–44 CrossRef Medline
19. Duszak R Jr, Parker L, Levin DC, et al. **Evolving roles of radiologists, nephrologists, and surgeons in endovascular hemodialysis access maintenance procedures.** *J Am Coll Radiol* 2010;7:937–42 CrossRef Medline
20. Duszak R Jr, Walls DG, Wang JM, et al. **Expanding roles of nurse practitioners and physician assistants as providers of nonvascular invasive radiology procedures.** *J Am Coll Radiol* 2015;12:284–89 CrossRef Medline
21. Rosman DA, Nsiah E, Hughes DR, et al. **Regional variation in Medicare payments for medical imaging: radiologists versus nonradiologists.** *AJR Am J Roentgenol* 2015;204:1042–48 CrossRef Medline
22. Prabhakar AM, Misono AS, Hemingway J, et al. **Medicare utilization of CT angiography from 2001 through 2014: continued growth by radiologists.** *J Vasc Interv Radiol* 2016;27:1554–60 CrossRef Medline
23. Charlson ME, Pompei P, Ales KL, et al. **A new method of classifying prognostic comorbidity in longitudinal studies: development and validation.** *J Chronic Dis* 1987;40:373–83 CrossRef Medline
24. Quan H, Sundararajan V, Halfon P, et al. **Coding algorithms for defining comorbidities in ICD-9-CM and ICD-10 administrative data.** *Med Care* 2005;43:1130–39 CrossRef Medline
25. Hillman BJ, Joseph CA, Mabry MR, et al. **Frequency and costs of diagnostic imaging in office practice—a comparison of self-referring and radiologist-referring physicians.** *N Engl J Med* 1990;323:1604–08 CrossRef Medline
26. Gazelle GS, Halpern EF, Ryan HS, et al. **Utilization of diagnostic medical imaging: comparison of radiologist referral versus same-specialty referral.** *Radiology* 2007;245:517–22 CrossRef Medline

# Optimization of Acquisition and Analysis Methods for Clinical Dynamic Susceptibility Contrast MRI Using a Population-Based Digital Reference Object

 N.B. Semmineh,  L.C. Bell,  A.M. Stokes,  L.S. Hu,  J.L. Boxerman, and  C.C. Quarles



## ABSTRACT

**BACKGROUND AND PURPOSE:** The accuracy of DSC-MR imaging CBV maps in glioblastoma depends on acquisition and analysis protocols. Multisite protocol heterogeneity has challenged standardization initiatives due to the difficulties of in vivo validation. This study sought to compare the accuracy of routinely used protocols using a digital reference object.

**MATERIALS AND METHODS:** The digital reference object consisted of approximately 10,000 simulated voxels recapitulating typical signal heterogeneity encountered in vivo. The influence of acquisition and postprocessing methods on CBV reliability was evaluated across 6912 parameter combinations, including contrast agent dosing schemes, pulse sequence parameters, field strengths, and postprocessing methods. Accuracy and precision were assessed using the concordance correlation coefficient and coefficient of variation.

**RESULTS:** Across all parameter space, the optimal protocol included full-dose contrast agent preload and bolus, intermediate (60°) flip angle, 30-ms TE, and postprocessing with a leakage-correction algorithm (concordance correlation coefficient = 0.97, coefficient of variation = 6.6%). Protocols with no preload or fractional dose preload and bolus using these acquisition parameters were generally less robust. However, a protocol with no preload, full-dose bolus, and low (30°) flip angle performed very well (concordance correlation coefficient = 0.93, coefficient of variation = 8.7% at 1.5T and concordance correlation coefficient = 0.92, coefficient of variation = 8.2% at 3T).

**CONCLUSIONS:** Schemes with full-dose preload and bolus maximize CBV accuracy and reduce variability, which could enable smaller sample sizes and more reliable detection of CBV changes in clinical trials. When a lower total contrast agent dose is desired, use of a low flip angle, no preload, and full-dose bolus protocol may provide an attractive alternative.

**ABBREVIATIONS:** ASFN = American Society of Functional Neuroradiology; API = accuracy and precision index; BSW = Boxerman-Schmainda-Weisskoff; BTIP = brain tumor imaging protocol; CCC = concordance correlation coefficient; CV = coefficient of variation; DRO = digital reference object; FA = flip angle; GV =  $\gamma$ -variate fit; rCBV = relative CBV

DSC-MR imaging CBV mapping has been used in the brain since the early 1990s<sup>1,2</sup> with multiple neuro-oncology applications, including distinction of tumor from nontumor, glioma grading, biopsy guidance, and assessing response to treatment.<sup>3-17</sup> However, disagreement persists about the best way to perform DSC-MR imaging and stems primarily from contrast

agent extravasation through blood-brain barrier deficiencies characteristic of high-grade gliomas. This contrast agent extravasation introduces both pronounced T1 effects and magnetic susceptibility differences between tumor cells and the extravascular extracellular space, thereby rendering DSC-MR imaging signal a reflection not only of the vascular volume fraction but also cell volume fraction and the vascular permeability. Although sensitivity to these additional physiologic attributes has enabled appropriately acquired DSC-MR imaging to distinguish tumor types,<sup>18</sup> it has confounded the accuracy of CBV measures, prompting the development of leakage-correction strategies including preload contrast agent administration, pulse sequence acquisition parameters balancing T1 and T2<sup>+</sup> sensitivities, and postprocessing techniques for correcting the leakage-contaminated signal.<sup>19-22</sup>

The National Cancer Institute (Quantitative Imaging Network; [https://imaging.cancer.gov/programs\\_resources/specialized\\_initiatives/qin.htm](https://imaging.cancer.gov/programs_resources/specialized_initiatives/qin.htm)), the Radiological Society of North America (Quantitative Imaging Biomarkers Alliance; <https://www.rsna.org/>)

Received March 8, 2018; accepted after revision June 8.

From the Department of Imaging Research (N.B.S., L.C.B., A.M.S., C.C.Q.), Barrow Neurological Institute, Phoenix, Arizona; Department of Radiology (L.S.H.), Mayo Clinic Arizona, Phoenix, Arizona; and Department of Diagnostic Imaging (J.L.B.), Rhode Island Hospital, Providence, Rhode Island.

This work was supported by the National Institutes of Health/National Cancer Institute (R01 CA213158), the Arizona Biomedical Research Commission (ADHS16-162414), and the Barrow Neurological Foundation (R01CA221938, C.C.Q., L.S.H., J.L.B., and U01CA220378, L.S.H.)

Please address correspondence to Chad Quarles, PhD, Barrow Neurological Institute, 350 W Thomas Rd, Phoenix, AZ 85013; e-mail: Chad.Quarles@BarrowNeuro.org; @nbsemmin

 Indicates open access to non-subscribers at [www.ajnr.org](http://www.ajnr.org)

<http://dx.doi.org/10.3174/ajnr.A5827>

QIBA/), and the National Brain Tumor Society (Jumpstarting Brain Tumor Drug Development Coalition Imaging Standardization Steering Committee; <https://www.itnonline.com/content/new-standardized-brain-tumor-mri-recommendations-announced>) have tried to standardize DCE-MR imaging methodology. The American Society of Functional Neuroradiology (ASFNR) published a white paper with a recommended DSC-MR imaging protocol based on practice patterns and literature data.<sup>23</sup> Such effort is challenged by the relative paucity of data from systematic evaluations of the influence of DSC-MR imaging methodology on CBV accuracy and has relied on anecdotal evidence, including the cor-

relation of CBV with glioma grade,<sup>24</sup> fractional tumor burden in cases of postradiation enhancement,<sup>16</sup> and patient survival in the setting of conventional and antiangiogenic therapies.<sup>12</sup> Stereotactic biopsies with coregistered CBV maps have demonstrated general concordance between CBV estimates and histology. While prior in vivo studies evaluated the impact of DSC-MR imaging acquisition parameters and methodologies on CBV data in a small number of patients with high-grade gliomas,<sup>25</sup> their influence on the underlying CBV accuracy has not been evaluated, likely due to the impracticality of multiple bolus injections in individual patients.

To facilitate the rigorous evaluation of the impact of DSC-MR imaging parameters on CBV accuracy, we recently developed and validated a population-based digital reference object (DRO) that recapitulates for glioblastoma the biophysical basis and inter- and intrasubject heterogeneity of DSC-MR imaging data.<sup>26</sup> The DRO consists of DSC-MR imaging signals computed across a range of relevant physiologic and acquisition parameters, and clinical relevance was ensured through use of training and validation datasets acquired from multiple patients with glioblastomas. Accordingly, the DRO provides a reliable ground truth for determining the impact of DSC-MR imaging acquisition and postprocessing

methods on CBV accuracy. In this study, we used the DRO to evaluate the accuracy and precision of routinely used DSC-MR imaging protocols for glioblastoma, in which the choice of acquisition parameters, including preload and bolus dose, flip angle (FA), TE, and TR, can greatly impact the sensitivity of the acquired signals on T1 and T2<sup>+</sup> contrast agent leakage effects. Additionally, the accuracy of postprocessing leakage-correction methods<sup>24,27</sup> may also depend on the degree of T1 and T2<sup>+</sup> contrast agent leakage effects, further affecting CBV accuracy. Given the interrelated nature of acquisition and postprocessing methods, we used the DRO to evaluate CBV accuracy across a range of commonly used DSC-MR imaging methods, identifying combinations of acquisition parameters yielding particularly high CBV accuracy and precision and potentially guiding future DSC-MR imaging consensus initiatives.

## MATERIALS AND METHODS

We evaluated CBV fidelity across a range of relevant DSC-MR imaging parameters using a validated DRO that computes MR imaging signal intensities for heterogeneous 3D tissue structures, accounting for the relevant underlying DSC-MR imaging contrast mechanisms.<sup>26</sup> Parameter inputs were ex-

**Table 1: Summary of investigated parameter space<sup>a</sup>**

Parameter	Values
Preload + bolus (fractional dose)	(0 + 1), (1/4 + 3/4), (1/2 + 1/2), (1/4 + 1), (1/2 + 1), (1 + 1)
Flip angle	30°, 60°, 90°
TR (sec)	1.0, 1.5, 2.0
TE (ms)	20, 30, 40, 50
Field strength	1.5T, 3T
Upper time limit, integration (sec)	180, 150, 120, 90
Postprocessing leakage correction	Uncorrected, BSW, BD, GV, BLS

**Note:**—BD indicates bidirectional; BLS, baseline subtraction.

<sup>a</sup> The dose values are presented as a fraction of a standard contrast agent dose (0.1 mmol/kg).

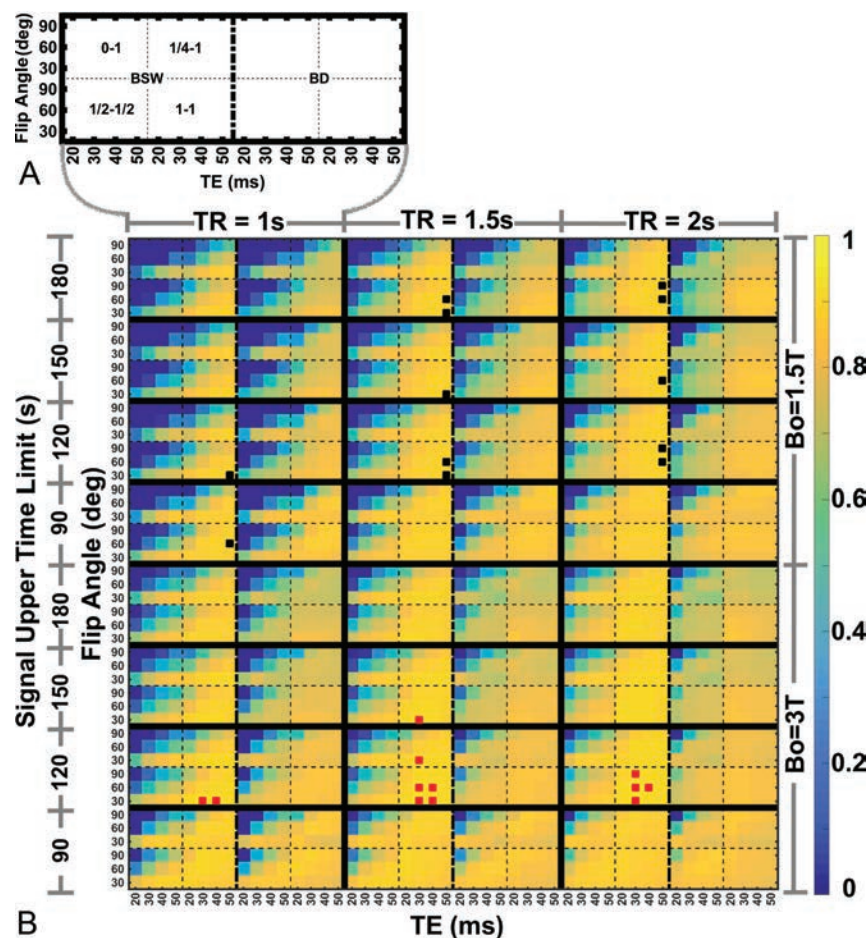


**FIG 1.** A, Parameter space encompassing 3 flip angles, 4 TEs, 4 contrast agent preload and bolus dose combinations, and 2 postprocessing leakage-correction methods. B, Heat map shows CBV accuracy and the precision index for the parameter space shown in A repeated for 3 TRs, 2 B<sub>0</sub> values, and 4 data truncation time points. The top 1% best-performing parameter combinations are indicated by black (B<sub>0</sub> = 1.5T) and red (B<sub>0</sub> = 3T) marks.

**Table 2: Comparison of the accuracy and precision index, coefficient of variation, and concordance correlation coefficient for all dosing schemes using intermediate and low flip angle protocols at 1.5T and 3T**

Dosing Scheme (Preload + Bolus)	Intermediate Flip Angle <sup>a</sup>						Low Flip Angle <sup>b</sup>					
	1.5T			3T			1.5T			3T		
	CCC	CV%	API	CCC	CV%	API	CCC	CV%	API	CCC	CV%	API
(0 + 1)	0.30	21.7	0.08	0.55	12.4	0.43	0.93	8.7	0.84	0.92	8.2	0.83
(1/4 + 3/4)	0.51	13.3	0.38	0.74	8.8	0.65	0.94	8.9	0.85	0.94	7.8	0.86
(1/2 + 1/2)	0.61	12.7	0.48	0.76	9.2	0.67	0.91	10.6	0.80	0.90	8.7	0.82
(1/4 + 1)	0.86	7.9	0.78	0.93	6.8	0.86	0.96	7.7	0.89	0.97	7.0	0.90
(1/2 + 1)	0.90	7.7	0.82	0.96	6.8	0.89	0.96	7.5	0.89	0.97	6.8	0.91
(1 + 1)	0.94	7.4	0.86	0.97	6.6	0.91	0.96	7.4	0.89	0.98	6.8	0.91

<sup>a</sup> FA = 60°, TE = 30 ms, TR = 1.5 sec.

<sup>b</sup> FA = 30°, TE = 50 ms, TR = 1.5 sec, B<sub>0</sub> = 1.5T; FA = 30°, TE = 30 ms, TR = 1.5 sec, B<sub>0</sub> = 3T.

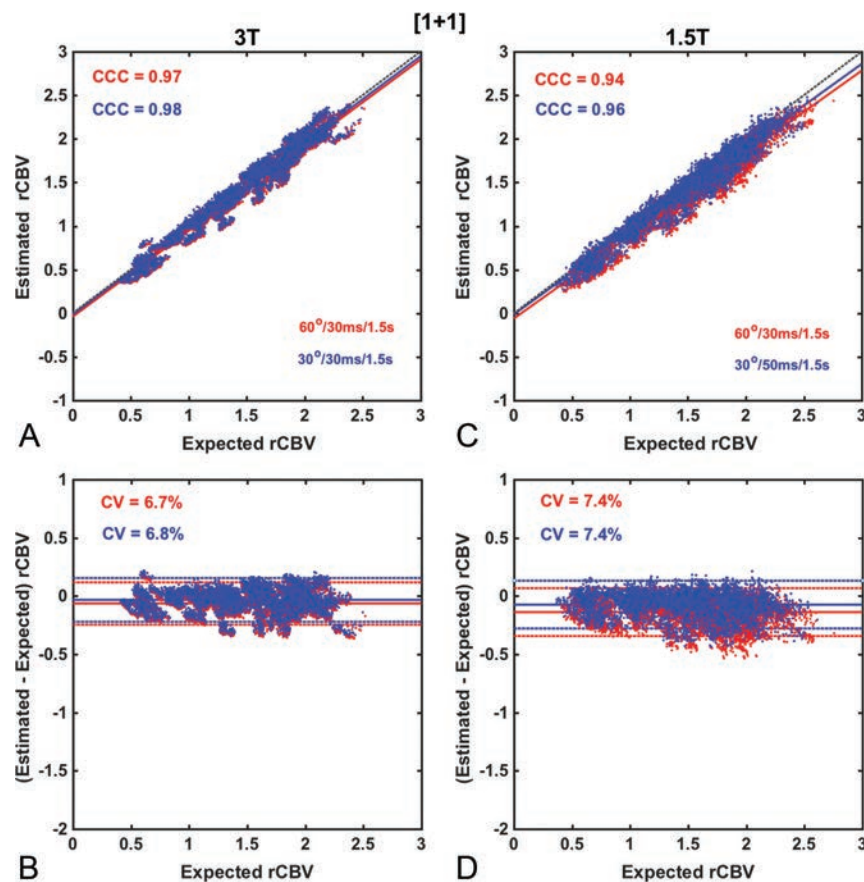


**FIG 2.** Scatter- and Bland-Altman plots comparing CBV estimates for the (1 + 1) dosing scheme at 3T (A and B) and at 1.5T (C and D) using intermediate (red) and low (blue) flip angle protocols. At 3T, both protocols yield equivalent accuracy and precision (API = 0.91), whereas at 1.5T, the low flip angle protocol provides slightly higher accuracy and precision (API = 0.89) compared with the use of an intermediate flip angle (API = 0.86). Leakage correction was applied using BSW.

tracted from voxelwise training data from 23 patients with glioblastomas (>40,000 voxels). To ensure that the simulated signals accurately represented the magnitude and distribution of contrast agent-induced T1 and T2\* changes within typical glioblastomas, we chose model parameters so that the distribution of percentage signal recovery and the mean SD of signal intensities across the DRO matched those in the patient training dataset. The training process yielded approximately 10,000 DRO voxels that agreed with the in vivo data. The DRO was validated against a separate set of patients with glioblastomas imaged with pulse sequences and contrast agent dosing schemes differing from those in the training dataset.

To investigate the influence of acquisition and postprocessing methods on the reliability of CBV measurements, we compared tumor CBV simulated with and without contrast agent leakage effects for the most commonly used DSC-MR imaging methods, including the following: 6 preload and bolus injection combinations, 3 flip angles, 3 TRs, 2 B<sub>0</sub> values, 4 TEs, and 4 upper time limits for postprocessing integration (with a constant prebolus time). Furthermore, we compared the uncorrected CBV estimates with 4 postprocessing leakage-correction methods: Boxerman-Schmainda-Weisskoff (BSW),<sup>24</sup> bidirectional,<sup>27</sup>  $\gamma$ -variate fit, and post-bolus baseline subtraction.<sup>25</sup> Note that while baseline subtraction correction is typically applied to low flip angle data that predominantly exhibit T2\* leakage effects, we implemented a version that corrects both T1 and T2\* effects. Because baseline subtraction correction arbitrarily forces all signals to return to baseline, it was applied to both normal and tumor signals in the DRO. The investigated parameter space is summarized in Table 1. Across all parameter space, the concordance correlation coefficient (CCC) and the coefficient of variation (CV) between the simulated tumor CBV and the ground truth (the CBV values not confounded by leakage effects)

were computed as a marker of accuracy and precision, respectively. To aid in the identification of the optimal protocol, we computed an accuracy and precision index (API) that combines the CCC and CV:  $API = CCC - |CV|/100$ . Accordingly, API values of 1 (CCC = 1, CV/100 = 0) reflect the ideal agreement. Protocols compliant with a recently published consensus brain tumor imaging protocol (BTIP)<sup>28</sup> were highlighted because these can be most easily incorporated into clinical trial imaging protocols. Note that dosing schemes that are labeled “BTIP compliant” are those that align with the recommended dosing requirements and not necessarily the timing between the contrast agent injection and the postcontrast T1-weighted scan.

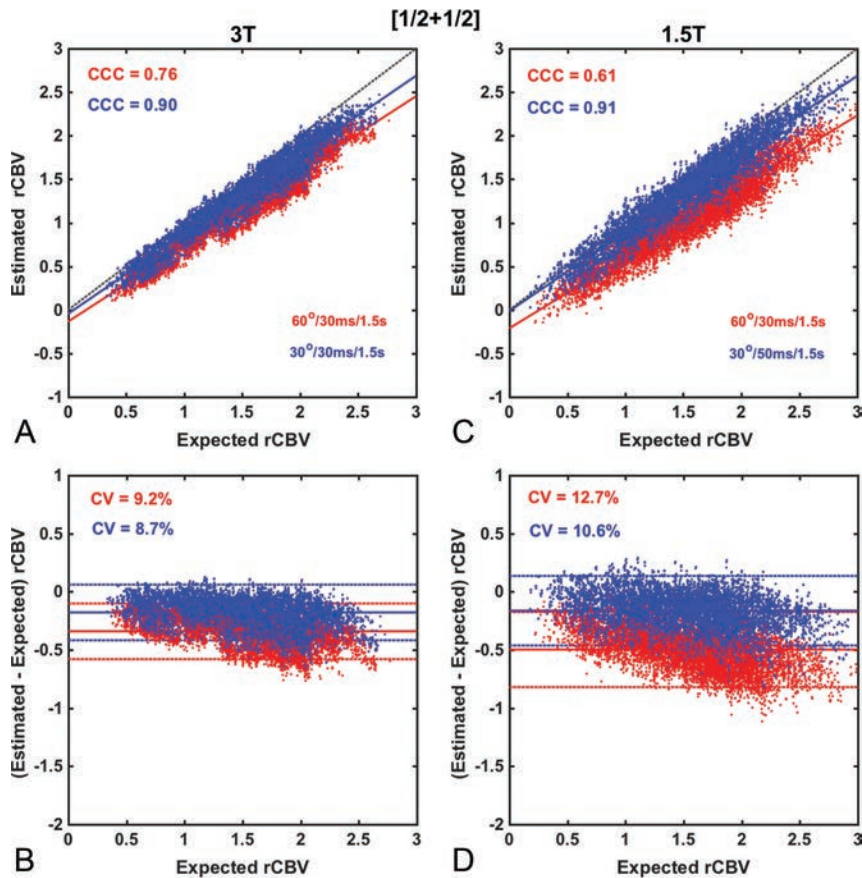


**FIG 3.** Scatter- and Bland-Altman plots comparing CBV estimates for the  $(\frac{1}{2} + \frac{1}{2})$  dosing scheme at 3T (A and B) and at 1.5T (C and D) using the intermediate (red) and low flip angle (blue) protocols. At both 3T and 1.5T, CBV values measured using an intermediate flip angle were consistently underestimated, yielding lower accuracy and precision (API = 0.67 and 0.48), respectively. The use of the low flip angle protocol improved both CBV accuracy and precision at 3T (API = 0.82) and 1.5T (API = 0.80). Leakage correction was applied using BSW.

## RESULTS

Figure 1 shows the API heat map across the parameter space in Table 1. The heat map in Fig 1 is segmented horizontally by  $B_0$  (top half:  $B_0 = 1.5T$ ; bottom half:  $B_0 = 3T$ ). Within each  $B_0$  segment, the heat map is further segmented vertically by the acquisition time limit (4 segments) and horizontally by TR (3 segments). For each acquisition time limit and TR combination, the heat map is further segmented, as shown in Fig 1A, horizontally by the leakage-correction method (2 segments for BSW and bidirectional;  $\gamma$ -variate fit, baseline subtraction, and uncorrected are excluded). Finally, each leakage-correction segment is split into 4 subplots ( $2 \times 2$ ) by contrast agent dosing [clockwise from top left:  $(0 + 1)$ ,  $(\frac{1}{4} + 1)$ ,  $(1 + 1)$ ,  $(\frac{1}{2} + \frac{1}{2})$ ], where the first and second numeric values [eg,  $(1 + 1)$ ] represent the preload and bolus-injection dose as a fraction of a total standard dose (0.1 mmol/kg). Each of these subplots shows the variation horizontally by TE (4 squares) and vertically by flip angle (3 squares). This singular figure demonstrates the API for 2304 possible parameter combinations (of the 8640 tested). The uncorrected  $\gamma$ -variate fit and baseline subtraction results are not included in Fig 1B (or in subsequent figures or tables) because their associated CCC, CV, and API values were substantially lower than those for BSW and bidirectional. For simplicity, the  $(\frac{1}{4} + \frac{3}{4})$  and  $(\frac{1}{2} + 1)$  contrast agent

dosing schemes were not incorporated in the heat map, but their results are summarized in Table 2.

Several results can be observed from the heat map. First, at both field strengths,  $(1 + 1)$  contrast agent dosing provides the highest API and the least sensitivity (more consistent API values) to variations in TR, TE, and flip angle, compared with other dosing schemes. Across all parameter combinations, the top 1% of API values ( $>0.89$ ) are derived from protocols that rely on  $(1 + 1)$  contrast agent dosing at both field strengths, as indicated by the black (1.5T) and red (3T) boxes. Although the top 1% of parameter combinations incorporate BSW leakage correction, both BSW and bidirectional leakage correction methods yielded similar APIs. Note that the top 1% is an arbitrary threshold, and the difference in utility of CBV maps derived from methods yielding slightly lower APIs (eg, top 1% versus the top 3%–5%) may not be clinically meaningful. Second, the API varies more substantially for acquisitions using  $(0 + 1)$  and  $(\frac{1}{2} + \frac{1}{2})$  contrast agent dosing schemes, indicating greater sensitivity to contrast agent leakage effects and CNR losses related to low contrast agent dose. Third, for data acquired without or with small contrast agent preloads, a low flip angle ( $30^\circ$ ) maximizes the API. Fourth, the number of data points incorporated

after the first pass into the CBV acquisition and analysis has minimal impact on API values, with a slight preference for shorter data lengths using the BSW correction.

Figures 2–5 compare the accuracy and precision of CBV measures using scatterplots (top) and Bland-Altman plots (bottom) for commonly used contrast agent dosing protocols [Fig 2:  $(1 + 1)$ , Fig 3:  $(\frac{1}{2} + \frac{1}{2})$ , Fig 4:  $(\frac{1}{4} + 1)$ , Fig 5:  $(0 + 1)$ ], field strengths (1.5T and 3T), and flip angles (low  $30^\circ$  versus intermediate  $60^\circ$ ). The BSW leakage-correction method was applied to all data. For each flip angle, the TE was selected to maximize the API, yielding 4 parameter combinations: 1.5T, FA/TE =  $30^\circ/50$  ms and FA/TE =  $60^\circ/30$  ms; 3T, FA/TE =  $30^\circ/30$  ms and FA/TE =  $60^\circ/30$  ms. The first goal of this analysis was to evaluate CBV accuracy when data are acquired using the ASFNr parameter recommendations (represented by the intermediate flip angle protocol) and variable dosing protocols and field strengths. The second was to compare this performance with that derived from the low flip angle case, which provided the overall highest CBV accuracy and precision.

Across the entire range of parameters, the highest CBV accuracy and precision (API = 0.91) was found for DSC-MR imaging data collected at 3T with a  $(1 + 1)$  dosing scheme and either an intermediate or low flip angle (Fig 2). At 1.5T, the CCC and CV

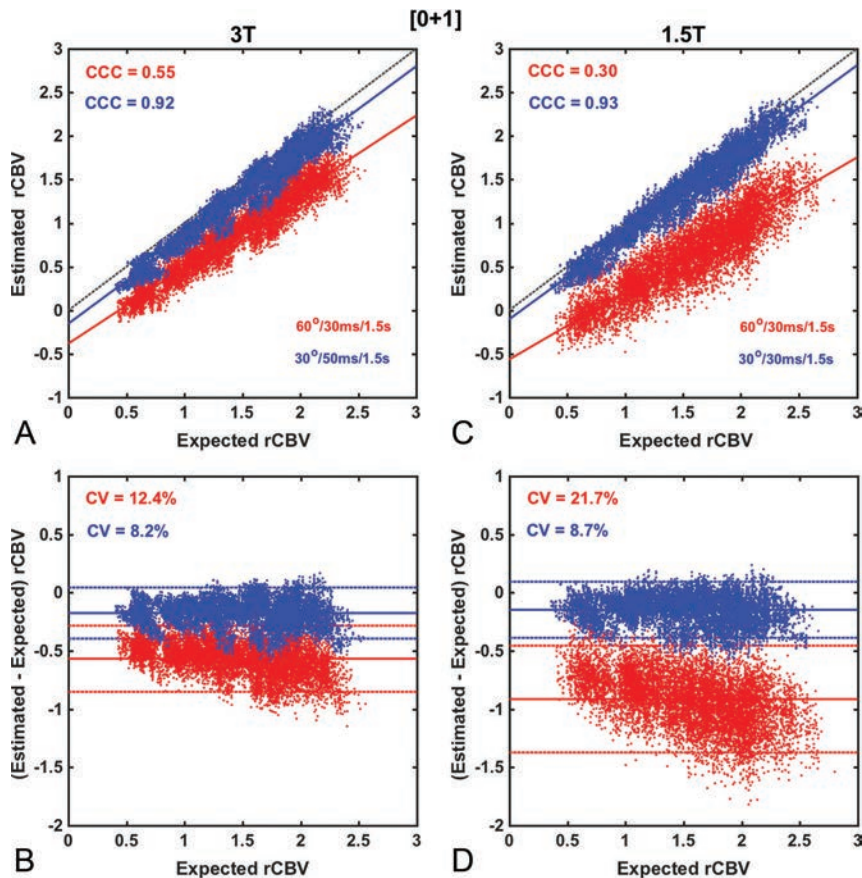


**FIG 4.** Scatter- and Bland-Altman plots comparing CBV estimates for the (0 + 1) dosing scheme at 3T (A and B) and at 1.5T (C and D), using the intermediate (red) and low (blue) flip angle protocols. At both 3T and 1.5T, CBV measured using an intermediate flip angle yielded poor accuracy and precision (API = 0.43 and 0.08), respectively. Whereas the use of a low flip angle substantially improved CBV reliability at both 3T (API = 0.83) and 1.5T (API = 0.84), respectively. Leakage correction was applied using BSW.

values were only slightly lower than those at 3T, yielding similar API values (0.86 and 0.89 for intermediate and low flip angles, respectively).

For the (1/2 + 1/2) dosing scheme, illustrated in Fig 3, CBV measured using the intermediate flip angle protocol was consistently underestimated due to residual (uncorrected) T1 leakage effects, yielding moderately lower accuracy and precision (API = 0.67) at 3T and poor performance (API = 0.48) at 1.5T. The use of a low flip angle improved the API at both 3T (API = 0.82) and 1.5T (API = 0.80) due to reduced T1 sensitivity. However, the API for this dosing scheme was consistently lower than the (1 + 1) dosing scheme.

As illustrated in Fig 4, the use of an intermediate flip angle at 3T without a preload (0 + 1) dosing scheme substantially reduced both accuracy and precision (API = 0.43). This poor performance was exacerbated at 1.5T (API = 0.08). These results are consistent with previous studies demonstrating the necessity of preload when using moderate and high flip angles.<sup>25,29,30</sup> By comparison, the use of the low flip angle protocol at 3T without preload introduces a relatively minor penalty (API = 0.83) compared with the (1 + 1) dosing scheme (API = 0.91). At 1.5T, CBV measured using the low flip angle protocol provided a substantial improvement compared with the intermediate flip angle in both accuracy and precision (API = 0.84).

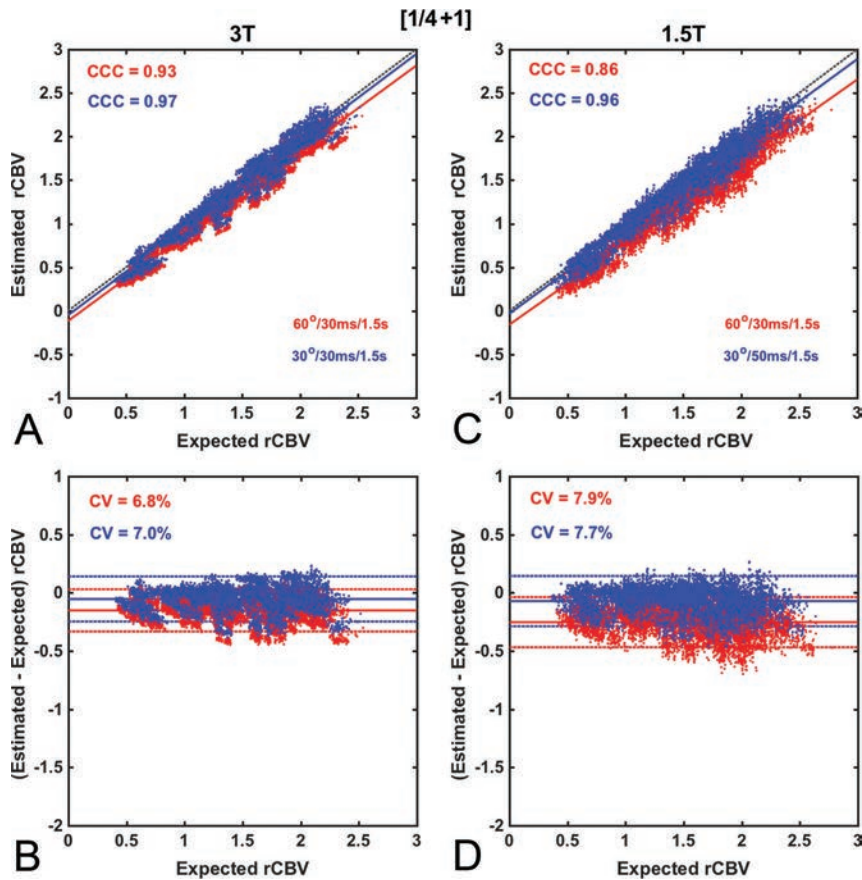
Figure 5 shows CBV accuracy and precision for DSC-MR imaging acquired with (1/4 + 1) contrast agent dosing. At 3T, both the intermediate and low flip angle protocols provide excellent accuracy (API values of 0.86 and 0.90, respectively), comparable with that for the (1 + 1) dosing scheme at 3T (API = 0.91). At 1.5T, the intermediate flip angle protocol yielded intermediate accuracy and precision (API = 0.78), whereas the low flip angle protocol yielded an API value (0.89) comparable with that for the (1 + 1) dosing scheme at 3T.

Table 2 compares CCC, CV, and API for the intermediate and low flip angle protocols at both field strengths and all dosing schemes. Across all dosing schemes and field strengths, the low FA provided equivalent or better API values compared with CBV data acquired with an intermediate FA. For BTIP-compliant dosing schemes (0 + 1), (1/4 + 3/4), (1/2 + 1/2), and (1 + 1), the (1 + 1) dosing yielded the highest accuracy and precision for both intermediate and low FA acquisitions and at both field strengths. With an intermediate FA, single total-dose protocols (0 + 1), (1/4 + 3/4), and (1/2 + 1/2) at 1.5T and the no preload protocol (0 + 1) at 3T have poor performance, with moderately good performance for split-dose protocols (1/4 + 3/4) and (1/2 + 1/2) at 3T. For non-BTIP-compliant dosing schemes (1/4 + 1) and (1/2 + 1), low and intermediate FA acquisitions yielded excellent results at 3T, and very good results at 1.5T, comparable with the optimal (1 + 1) dosing protocol.

## DISCUSSION

The computational analysis presented herein confirms that it is possible to acquire highly accurate and precise relative CBV (rCBV) measurements in glioblastoma with proper selection of DSC-MR imaging methodology. To date, recommendations on optimal DSC-MR imaging acquisition protocols, such as the ASFNR white paper,<sup>23</sup> have relied on susceptibility contrast theory, clinical experience, and limited studies involving correlation with stereotactic biopsies,<sup>16,31</sup> but this study establishes the limits of accuracy and precision using a computational approach across a wide range of parameters and, accordingly, may be used to inform the aforementioned standardization initiatives.

While the DRO used in this study can quantitatively assess rCBV accuracy for any combination of acquisition and postprocessing parameters, the overwhelming number of permutations makes identifying a single optimal approach challenging. For



**FIG 5.** Scatter- and Bland-Altman plots comparing CBV estimates for the  $(\frac{1}{4} + 1)$  dosing scheme at 3T (A and B) and 1.5T (C and D) using the intermediate (red) and low (blue) flip angle protocols. At 3T, both the intermediate and low flip angle protocols provide excellent accuracy (API = 0.86 and 0.90, respectively), comparable with that for  $(1 + 1)$  dosing at 3T (API = 0.91). Similar accuracy and precision levels were achieved at 1.5T using the low flip angle protocol (API = 0.89), but not the intermediate flip angle (API = 0.78). Leakage correction was applied using BSW.

example, the heat maps illustrate that there are many unique parameter combinations that yield reasonably accurate rCBV estimates. However, for many of these combinations, minor parameter modification (eg, changing flip angles or TEs) yields substantially decreased accuracy and/or precision. Such isolated “local maximums” reflect specific parameter subsets that may suffice for singular distributions of T1 and T2\* leakage effects but that are not broadly effective when those distributions are altered, such as greater sensitivity to T1 effects due to higher flip angles. While the DRO captures the full range of T1 and T2\* leakage effects that would be encountered across patients, the distribution of these effects within a single patient could be unique. Accordingly, our strategy for identifying the most robust DSC-MR imaging protocol included accuracy, precision, and consistency across localized parameter space (eg, a consistent API as the TE is varied), ensuring the identification of optimal methods both across and within patients.

Across all parameter space, the combination of preload scheme and acquisition parameters yielding the most robust rCBV estimates included full-dose preload and bolus  $(1 + 1)$ , with either the recommended ASFNR (intermediate flip angle) or low flip angle pulse sequence parameters. This finding is consistent with a prior *in vivo* study that demonstrated that the  $(1 + 1)$

dosing scheme provided the most robust distinction between tumor and normal tissue rCBV.<sup>25</sup> Most important, this dosing scheme maintains BTIP compliance because the postcontrast T1-weighted images can be acquired between preload and bolus contrast agent injections. The  $(1 + 1)$  dosing scheme requires double the standard dose of contrast agent (0.2 mmol/kg), and given the growing concern for long-term gadolinium deposition within the brain following repeat use of gadolinium-based contrast agents, we also investigated the accuracy of lower-dose schemes. Lower-dose, BTIP-compliant dosing schemes using the intermediate flip angle protocol introduced bias and lower precision compared with the  $(1 + 1)$  scheme. Lower preload doses yielded more error because they are not as effective at reducing T1 leakage effects before the primary bolus injection.

For dosing schemes using less than a full dose for the primary bolus, the relative magnitude of T1 leakage effects with respect to the expected T2\* changes are larger than would be observed with the  $(1 + 1)$  scheme and appear to partially confound leakage-correction algorithms. A lower primary bolus dose scheme [eg,  $(\frac{1}{2} + \frac{1}{2})$ ] also lowers the contrast-to-noise ratio and decreases precision. This reduction in precision

could yield greater within- and across-subject rCBV variability, confounding the assessment of treatment response, determination of thresholds for clinical use (eg, differentiating between tumor recurrence and radiation effects), and the sample size needed for clinical trials. These errors are magnified at 1.5T compared with 3T, which has further implications for clinical trial design. Although lower-dose protocols have reduced accuracy and precision, prior single-site studies have demonstrated their clinical utility for differentiating tumor recurrence and posttreatment radiation effects<sup>29</sup> and detecting rCBV changes following bevacizumab therapy.<sup>32</sup>

Another major finding of this work is that DSC-MR imaging data acquired with a low flip angle provide comparable or improved CBV accuracy across all dosing schemes and field strengths. As highlighted in Table 2, the acquisition protocol using a single total-dose contrast agent administration,  $[(0 + 1), (\frac{1}{4} + \frac{3}{4}), (\frac{1}{2} + \frac{1}{2})]$ , which yielded only a slighted reduced API, was a low flip angle scheme (FA = 30°, TR = 1.5 sec; TE = 50 ms at 1.5T and TE = 30 ms at 3T). The corresponding CCC values exceeded 0.9 at both 1.5T and 3T but exhibited slightly higher CV values due to a lower contrast-to-noise ratio compared with the  $(1 + 1)$  double-dose protocol. The similarity of the API values across

these single total-dose protocols, when combined with a low flip angle, indicates that the preload does not improve CBV fidelity and may not be needed in clinical practice. The use of a (0 + 1) dosing scheme with a low FA has the benefit of maintaining BTIP compliance and requiring only a single bolus injection, thereby simplifying perfusion scan protocols and increasing their consistency across patients and clinical trial sites. Given the potential ramifications of this finding on DSC-MR imaging recommendations, it would be highly relevant to compare, in the same patients, the agreement and CBV map quality from data acquired with this low flip angle alternative and the ASFNr recommendations (using the double-dose protocol). Given that DSC-MR imaging data acquired with TE = 50 ms (the optimal TE at 1.5T) could be more sensitive to EPI-related artifacts and exhibit lowered contrast to noise, in vivo studies should be performed to confirm CBV map quality and interpretability. Paulson and Schmainda<sup>25</sup> found that the use of a low flip angle and a 50-ms TE reduced the difference between tumor and normal tissue rCBV.

Similar to clinical results,<sup>25</sup> leakage-correction models based on contrast agent kinetics, such as the BSW or bidirectional methods, provide the highest rCBV accuracy compared with no leakage correction or arbitrary curve fitting, like  $\gamma$ -variate. While the latter provides curves that, in appearance, resemble traditional first-pass data, they cannot reliably correct the signal because of the underlying complexity of simultaneous and competing T1 and T2\* leakage effects. The highest accuracy and precision were found when DSC-MR imaging data were corrected using the BSW approach. The bidirectional correction was similarly accurate but with lower precision. In future work, we will expand these studies to investigate model-independent and MTT-insensitive leakage-correction methods<sup>19,33,34</sup> and methods that rely on biophysical models applied to multiecho data.<sup>35,36</sup>

## CONCLUSIONS

By leveraging a validated DRO, we characterized the influence of DSC-MR imaging methodology on CBV accuracy and precision and identified optimal protocols for clinical use. Our results support, to a large extent, the ASFNr recommendations on DSC-MR imaging best practices,<sup>23</sup> particularly at 3T and when paired with the (1 + 1) dosing protocol, which should encourage its broader acceptance and standardization. Taken together, the results indicate that for clinical trials, a (1 + 1) dosing scheme provides highly accurate and consistent CBV estimates, enabling smaller sample sizes for detecting treatment-related changes in CBV. For clinical surveillance scans, in which a lower total gadolinium dose is desirable, the low flip angle option without preload or the (1/4 + 1) dosing scheme is a viable alternative, providing reasonably robust CBV measures. An added advantage of these schemes is that they perform well at both 1.5T and 3T. Such considerations may inform standardization initiatives for the acquisition and analysis of DSC-MR imaging data in clinical trials and routine patient care.

Disclosures: Natenael B. Semmineh—RELATED: Grant: National Institutes of Health, Arizona Biomedical Research Commission, and Barrow Neurological Foundation, Comments: This work was supported by National Institutes of Health/National Cancer Institute (R01 CA213158), the Arizona Biomedical Research Commission (ADHS16-162414), and the Barrow Neurological Foundation.\* Christopher C. Quarles—RELATED: Grant: National Institutes of Health.\* Leland S. Hu—RELATED: Grant: National Institutes of Health/National Cancer Institute.\* \*Money paid to the institution.

## REFERENCES

- Belliveau JW, Kennedy DN Jr, McKinstry RC, et al. **Functional mapping of the human visual cortex by magnetic resonance imaging.** *Science* 1991;254:716–19 Medline
- Aronen HJ, Cohen MS, Belliveau JW, et al. **Ultrafast imaging of brain tumors.** *Top Magn Reson Imaging* 1993;5:14–24 Medline
- Prah MA, Al-Gizawiy MM, Mueller WM, et al. **Spatial discrimination of glioblastoma and treatment effect with histologically-validated perfusion and diffusion magnetic resonance imaging metrics.** *J Neurooncol* 2018;136:13–21 CrossRef Medline
- Liu TT, Achrol AS, Mitchell LA, et al. **Magnetic resonance perfusion image features uncover an angiogenic subgroup of glioblastoma patients with poor survival and better response to antiangiogenic treatment.** *Neuro Oncol* 2017;19:997–1007 CrossRef Medline
- Law M, Yang S, Wang H, et al. **Glioma grading: sensitivity, specificity, and predictive values of perfusion MR imaging and proton MR spectroscopic imaging compared with conventional MR imaging.** *AJNR Am J Neuroradiol* 2003;24:1989–98 Medline
- Sugahara T, Korogi Y, Shigematsu Y, et al. **Value of dynamic susceptibility contrast magnetic resonance imaging in the evaluation of intracranial tumors.** *Top Magn Reson Imaging* 1999;10:114–124 Medline
- Lev MH, Rosen BR. **Clinical applications of intracranial perfusion MR imaging.** *Neuroimaging Clin N Am* 1999;9:309–31 Medline
- Aronen HJ, Gazit IE, Louis DN, et al. **Cerebral blood volume maps of gliomas: comparison with tumor grade and histologic findings.** *Radiology* 1994;191:41–51 Medline
- Nasser M, Gahramanov S, Netto JP, et al. **Evaluation of pseudoprogression in patients with glioblastoma multiforme using dynamic magnetic resonance imaging with ferumoxytol calls RANO criteria into question.** *Neuro Oncol* 2014;16:1146–54 CrossRef Medline
- Shiroishi MS, Boxerman JL, Pope WB. **Physiologic MRI for assessment of response to therapy and prognosis in glioblastoma.** *Neuro Oncol* 2016;18:467–78 CrossRef Medline
- Boxerman JL, Ellingson BM. **Response assessment and magnetic resonance imaging issues for clinical trials involving high-grade gliomas.** *Top Magn Reson Imaging* 2015;24:127–36 CrossRef Medline
- Schmainda KM, Zhang Z, Prah M, et al. **Dynamic susceptibility contrast MRI measures of relative cerebral blood volume as a prognostic marker for overall survival in recurrent glioblastoma: results from the ACRIN 6677/RTOG 0625 multicenter trial.** *Neuro Oncol* 2015;17:1148–56 CrossRef Medline
- Harris RJ, Cloughesy TF, Hardy AJ, et al. **MRI perfusion measurements calculated using advanced deconvolution techniques predict survival in recurrent glioblastoma treated with bevacizumab.** *J Neurooncol* 2015;122:497–505 CrossRef Medline
- Boxerman JL, Ellingson BM, Jeyapalan S, et al. **Longitudinal DSC-MRI for distinguishing tumor recurrence from pseudoprogression in patients with a high-grade glioma.** *Am J Clin Oncol* 2017;40:228–34 CrossRef Medline
- Raghavan D, Boxerman J, Rogg J, et al. **Glioblastoma multiforme: utilization of advanced MRI techniques for preoperative planning.** *Med Health R* 2012;95:42–43 Medline
- Hu LS, Heiserman JE, Dueck AC, et al. **Reevaluating the imaging definition of tumor progression: perfusion MRI quantifies recurrent glioblastoma tumor fraction, pseudoprogression, and radiation necrosis to predict survival.** *Neuro Oncol* 2012;14:919–30 CrossRef Medline
- Schmainda KM, Rand SD, Joseph AM, et al. **Characterization of a first-pass gradient-echo spin-echo method to predict brain tumor grade and angiogenesis.** *AJNR Am J Neuroradiol* 2004;25:1524–32 Medline
- Mangla R, Kolar B, Zhu T, et al. **Percentage signal recovery derived from MR dynamic susceptibility contrast imaging is useful to differentiate common enhancing malignant lesions of the brain.** *AJNR Am J Neuroradiol* 2011;32:1004–10 CrossRef Medline
- Quarles CC, Ward BD, Schmainda KM. **Improving the reliability of**

- obtaining tumor hemodynamic parameters in the presence of contrast agent extravasation. *Magn Reson Med* 2005;53:130716 Medline
20. Uematsu H, Maeda M, Sadato N, et al. **Blood volume of gliomas determined by double-echo dynamic perfusion-weighted MR imaging: a preliminary study.** *AJNR Am J Neuroradiol* 2001;22:1915–19 Medline
  21. Johnson G, Wetzel SG, Cha, et al. **Measuring blood volume and vascular transfer constant from dynamic, T(2)\*-weighted contrast-enhanced MRI.** *Magn Reson Med* 2004;51:96–68 Medline
  22. Heiland, Benner T, Debus J, et al. **Simultaneous assessment of cerebral hemodynamics and contrast agent uptake in lesions with disrupted blood-brain-barrier.** *Magn Reson Imaging* 1999;17:21–27 Medline
  23. Welker K, Boxerman J, Kalnin A, et al; American Society of Functional Neuroradiology MR Perfusion Standards and Practice Subcommittee of the ASFNRC Clinical Practice Committee. **ASFNRC recommendations for clinical performance of MR dynamic susceptibility contrast perfusion imaging of the brain.** *AJNR Am J Neuroradiol* 2015;36:E41–51 CrossRef Medline
  24. Boxerman J, Schmainda KM, Weisskoff RM. **Relative cerebral blood volume maps corrected for contrast agent extravasation significantly correlate with glioma tumor grade, whereas uncorrected maps do not.** *AJNR Am J Neuroradiol* 2006;27:859–67 Medline
  25. Paulson ES, Schmainda KM. **Comparison of dynamic susceptibility-weighted contrast-enhanced MR methods: recommendations for measuring relative cerebral blood volume in brain tumors.** *Radiology* 2008;249:601–13 Medline
  26. Semmineh NB, Stokes AM, Bell LC, et al. **A population-based digital reference object (DRO) for optimizing dynamic susceptibility contrast (DSC)-MRI methods for clinical trials.** *Tomography* 2017;3:41–49 CrossRef Medline
  27. Leu, K, Boxerman JL, Cloughesy TF, et al. **Improved leakage correction for single-echo dynamic susceptibility contrast perfusion MRI estimates of relative cerebral blood volume in high-grade gliomas by accounting for bidirectional contrast agent exchange.** *AJNR Am J Neuroradiol* 2016;37:1440–46 CrossRef Medline
  28. Ellingson BM, Bendszus M, Boxerman J, et al; Jumpstarting Brain Tumor Drug Development Coalition Imaging Standardization Steering Committee. **Consensus recommendations for a standardized brain tumor imaging protocol in clinical trials.** *Neuro Oncol* 2015;17:1188–98 CrossRef Medline
  29. Hu LS, Baxter LC, Pinnaduwage DS, et al. **Optimized preload leakage-correction methods to improve the diagnostic accuracy of dynamic susceptibility-weighted contrast-enhanced perfusion MR imaging in posttreatment gliomas.** *AJNR Am J Neuroradiol* 2010;31:40–48 CrossRef Medline
  30. Kassner A, Annesley DJ, Zhu XP, et al. **Abnormalities of the contrast re-circulation phase in cerebral tumors demonstrated using dynamic susceptibility contrast-enhanced imaging: a possible marker of vascular tortuosity.** *J Magn Reson Imaging* 2000;11:103–13 Medline
  31. Barajas RF Jr, Hodgson JG, Chang JS, et al. **Glioblastoma multiforme regional genetic and cellular expression patterns: influence on anatomic and physiologic MR imaging.** *Radiology* 2010;254:564–76 CrossRef Medline
  32. Leu K, Enzmann DR, Woodworth DC, et al. **Hypervascular tumor volume estimated by comparison to a large-scale cerebral blood volume radiographic atlas predicts survival in recurrent glioblastoma treated with bevacizumab.** *Cancer Imaging* 2014;14:31 CrossRef Medline
  33. Emblem KE, Bjornerud A, Mouridsen K, et al. **T(1)- and T(2)(\*)-dominant extravasation correction in DSC-MRI: part II-predicting patient outcome after a single dose of cediranib in recurrent glioblastoma patients.** *J Cereb Blood Flow Metab* 2011;31:2054–64 CrossRef Medline
  34. Bjornerud A, Sorensen AG, Mouridsen K, et al. **T1- and T2\*-dominant extravasation correction in DSC-MRI, Part I: theoretical considerations and implications for assessment of tumor hemodynamic properties.** *J Cereb Blood Flow Metab* 2011;31:2041–53 CrossRef Medline
  35. Stokes AM, Semmineh N, Quarles CC. **Validation of a T1 and T2\* leakage correction method based on multiecho dynamic susceptibility contrast MRI using MION as a reference standard.** *Magn Reson Med* 2016;76:613–25 CrossRef Medline
  36. Schmiedeskamp H, Andre JB, Straka M, et al. **Simultaneous perfusion and permeability measurements using combined spin- and gradient-echo MRI.** *J Cereb Blood Flow Metab* 2013;33:732–43 CrossRef Medline

# Impact of Ischemic Lesion Location on the mRS Score in Patients with Ischemic Stroke: A Voxel-Based Approach

M. Ernst, A.M.M. Boers, N.D. Forkert, O.A. Berkhemer, Y.B. Roos, D.W.J. Dippel, A. van der Lugt, R.J. van Oostenbrugge, W.H. van Zwam, E. Vettorazzi, J. Fiehler, H.A. Marquering, C.B.L.M. Majoie, and S. Gellissen, on behalf of the MR CLEAN trial investigators (www.mrclean-trial.org)



## ABSTRACT

**BACKGROUND AND PURPOSE:** Previous studies indicated that ischemic lesion volume might be a useful surrogate marker for functional outcome in ischemic stroke but should be considered in the context of lesion location. In contrast to previous studies using the ROI approach, which has several drawbacks, the present study aimed to measure the impact of ischemic lesion location on functional outcome using a more precise voxelwise approach.

**MATERIALS AND METHODS:** Datasets of patients with acute ischemic strokes from the Multicenter Randomized Clinical Trial of Endovascular Therapy for Acute Ischemic Stroke in the Netherlands (MR CLEAN) were used. Primary outcome was functional outcome as assessed by the modified Rankin Scale 3 months after stroke. Ischemic lesion volume was determined on CT scans 3–9 days after stroke. Voxel-based lesion-symptom mapping techniques, including covariates that are known to be associated with functional outcome, were used to determine the impact of ischemic lesion location for outcome.

**RESULTS:** Of the 500 patients in the MR CLEAN trial, 216 were included for analysis. The mean age was 63 years. Lesion-symptom mapping with inclusion of covariates revealed that especially left-hemispheric lesions in the deep periventricular white matter and adjacent internal capsule showed a great influence on functional outcome.

**CONCLUSIONS:** Our study confirms that infarct location has an important impact on functional outcome of patients with stroke and should be considered in prediction models. After we adjusted for covariates, the left-hemispheric corticosubcortical fiber tracts seemed to be of higher functional importance compared with cortical lesions.

**ABBREVIATIONS:** FU-NCCT = follow-up noncontrast CT; ILV = ischemic lesion volume; VLSM = voxel-based lesion-symptom mapping

It is very desirable to improve prediction of functional outcome after an ischemic stroke to rapidly inform patients and their

relatives and to optimize patient management, care, and rehabilitation strategies.<sup>1,2</sup> Several studies aimed to forecast functional outcome of patients at an early stage after acute ischemic stroke using clinical and imaging data.<sup>3,4</sup> With regard to stroke studies, it would be of major interest to replace clinical study end points with a validated surrogate end point. Within this context, image-based surrogate end points would be easier and more reliable to assess and would allow performing phase II stroke studies with a smaller sample size. Previous studies indicated that ischemic lesion volume (ILV) as a surrogate marker for functional outcome might be useful but should be considered in the context of lesion location.<sup>5–8</sup>

Voxel-based lesion-symptom mapping (VLSM) techniques have been frequently used to investigate the relationship between lesion topography and functional outcome.<sup>5,7</sup> VLSM compares functional outcome scores between patients with and without le-

Received April 16, 2018; accepted August 7.

From the Departments of Diagnostic and Interventional Neuroradiology (M.E., J.F., S.G.) and Medical Biometry and Epidemiology (E.V.), University Medical Center Hamburg-Eppendorf, Hamburg, Germany; Departments of Radiology and Nuclear Medicine (A.M.M.B., O.A.B., H.A.M., C.B.L.M.M.), Biomedical Engineering and Physics (A.M.M.B., H.A.M.), and Neurology (Y.B.R.), Academic Medical Center, Amsterdam, the Netherlands; Department of Robotics and Mechatronics (A.M.M.B.), University of Twente, Enschede, the Netherlands; Department of Radiology and Hotchkiss Brain Institute (N.D.F.), University of Calgary, Calgary, Alberta, Canada; Departments of Neurology (O.A.B., D.W.J.D.) and Radiology (A.v.d.L.), Erasmus MC University Medical Center, Rotterdam, the Netherlands; Department of Neurology (R.J.v.O.), Maastricht University Medical Center and Cardiovascular Research Institute, Maastricht, the Netherlands; Department of Radiology and Cardiovascular Research Institute Maastricht (W.H.v.Z.), Maastricht University Medical Center, Maastricht, the Netherlands; and Department of Radiology (O.A.B.), Maastricht University Medical Center, Maastricht, the Netherlands.

The MR CLEAN trial was partly funded by the Dutch Heart Foundation and by nominal, unrestricted grants from AngioCare, Medtronic/Covidien, Medac, Lamepro, Penumbra, Stryker, and Top Medical/Concentric.

Please address correspondence to Marielle Ernst, MD, Department of Diagnostic and Interventional Neuroradiology, University Medical Center Hamburg-Eppendorf, Haus Ost 22 (O 22), Martinistr 52, 20246 Hamburg, Germany; e-mail: m.ernst@uke.de

Indicates article with supplemental on-line tables.

Indicates article with supplemental on-line photos.

<http://dx.doi.org/10.3174/ajnr.A5821>

sions on a voxelwise basis. In this approach, patients are divided for each voxel into 2 groups according to whether they have a lesion at that voxel location.<sup>9</sup> VLSM methods have been used to examine motor recovery,<sup>10</sup> spatial neglect,<sup>11</sup> and aphasia<sup>9,12</sup> in patients with chronic stroke, and the 1-month modified Rankin Scale score was used in patients with subacute stroke (2–3 days).<sup>5</sup> These studies have provided insight into clinical deficits linked to lesions in particular brain regions but did not include important factors known to be associated with functional outcome after stroke such as age, sex, ILV, recanalization status, and treatment technique.

We aimed to investigate the impact of stroke lesion topography on functional outcome (3-month mRS) with and without accounting for factors known to be associated with functional outcome after stroke using a large data base of well-characterized patients with acute ischemic stroke.

## **MATERIALS AND METHODS**

### **Study Population**

The analyses are based on data from the Multicenter Randomized Clinical Trial of Endovascular Treatment of Acute Ischemic Stroke in the Netherlands (MR CLEAN), which evaluated the effect of intra-arterial treatment versus usual care alone in patients with stroke with acute large-vessel occlusion in the anterior circulation. The main results and design of the study have been reported before.<sup>13,14</sup>

### **Inclusion and Exclusion Criteria**

We included all patients with a follow-up noncontrast CT (FU-NCCT) scan 3–9 days after stroke. Patients with FU-NCCT scans of poor quality due to motion or beam-hardening artifacts or technical errors precluding automatic registration or segmentation were excluded. Patients with decompressive hemicraniectomy and considerable brain shift secondary to mass effect were excluded as well. Moreover, we excluded patients with previous stroke, an mRS score of >0 at baseline, or mRS = 6 three months after stroke to remove potential confounds from death unrelated to the stroke. As a result, the patient population of this substudy differed from the total MR CLEAN population.

### **Ethics Statement**

The MR CLEAN study protocol was approved by the Medical and Ethical Review Committee (Medisch Ethische Toetsings Commissie of Erasmus MC, Rotterdam, the Netherlands) and the research board of each participating center. All patient records and images were anonymized before analysis, and written informed consent was obtained from all patients or their legal representatives as a part of the original trial protocol.

### **Ischemic Lesion Segmentation**

Binary masks of the ischemic lesions on 3- to 9-day FU-NCCT were created using a validated automatic method.<sup>15</sup> An intensity-based region-growing algorithm implemented in Matlab (MathWorks, Natick, Massachusetts) iteratively examined all neighboring voxels of a segmented volume to determine whether these neighboring voxels should be included in the segmentation. A voxel was included if the difference in its intensity and the average intensity of the segmented volume was smaller than a predefined

threshold. The region-growing was repeated for multiple thresholds. The range of thresholds was 1.5–4.5 HU with steps of 0.5 HU, resulting in 7 repeated segmentations. If needed, the segmentations were adjusted by an experienced observer with >5 years' experience in neuroradiology (M.E.), blinded to clinical information and treatment as well as further imaging. Subsequently, the ILV was calculated.

### **Functional Outcome**

Functional outcome was assessed by the mRS at 3 months after stroke onset. The mRS is one of the most widely used end points for stroke severity in clinical trials in acute stroke, shown to be valid and reliable.<sup>16</sup> It captures the patient's functional outcome on an ordinal scale that ranges from 0 to 6, where zero indicates no symptoms and 6 denotes a patient's death.

### **Statistical Analysis**

Two-tailed Wilcoxon rank sum tests were used to evaluate differences in continuous variables between patients with left-versus-right hemispheric strokes. Categorical variables were compared using the Pearson  $\chi^2$  test. Backward stepwise regression was performed to investigate the relation among age, sex, ILV, admission National Institutes of Health Stroke Scale score, occlusion site, collateral score, pretreatment Alberta Stroke Program Early CT Score, time to treatment, treatment technique (intra-arterial treatment, intravenous administration of alteplase, or conservative treatment), and recanalization status with functional outcome. Successful recanalization was defined as a modified Arterial Occlusive Lesion score  $\geq 2$  or, if missing, as a modified Thrombolysis in Cerebral Infarction score of 2b–3.<sup>17</sup> All analyses were performed in SPSS 21 (IBM, Armonk, New York).

### **Voxel-Based Lesion-Symptom Mapping**

Voxelwise analysis requires that all images be in the same coordinate space to allow comparison of voxels between groups. Therefore, after ischemic lesion segmentation, each of the FU-NCCT images was coregistered to the standard Montreal Neurological Institute<sup>18</sup> atlas space using an affine transformation and subsequent nonlinear transformation implemented in the NiftyReg toolkit (<https://www.nitrc.org/projects/niftyreg/>).<sup>19</sup> The average CT atlas template described by Rorden et al<sup>20</sup> served as a reference image. This template was based on healthy individuals with ages similar to those commonly seen in stroke (mean, 65 years of age). All coregistration results were visually checked for quality and adjusted if needed. Statistical maps of lesion contribution related to functional outcome were generated using VLSM, Version 2.55 (<http://160.129.198.244/resources.html>). For each voxel, patients were divided into 2 groups according to whether they had a lesion at that voxel location. In VLSM maps, high *t*-scores indicate that a lesion in that specific voxel has a very significant effect on functional outcome. We limited our analysis to voxels that were affected in  $\geq 10$  individuals (10%). Resulting *t*-score maps were thresholded ( $P < .01$ ) on the basis of cluster size and permutation method (2000 permutations;  $P < .05$ ) to correct for multiple comparisons. To evaluate the impact of predefined brain regions on mRS, we calculated median, mean, minimum, and maximum *t*-score values for each anatomic ROI provided by the Harvard-Oxford cortical and subcortical structural atlas<sup>21</sup> and the Johns

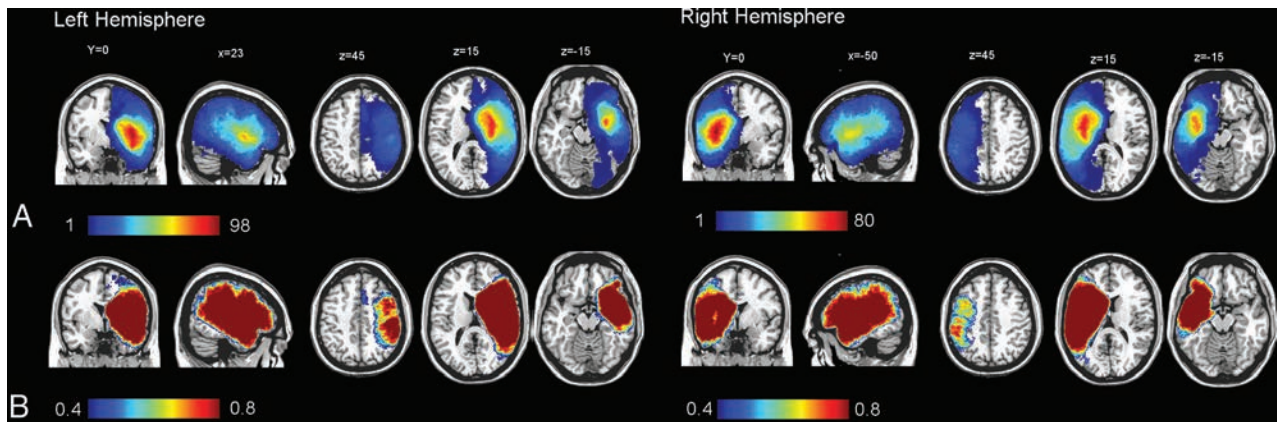


**FIG 1.** Incidence of lesions within each voxel for all patients with right and left hemispheric stroke (A) and a statistical power map between 40% and 80% for  $\alpha = 0.01$  for 3-month mRS (B).

**Table 1: Demographic differences between patients with left-versus-right hemispheric strokes<sup>a</sup>**

	Left (n = 122)	Right (n = 94)	P Value
Age (yr)	62.4 ± 11.8	63.3 ± 14.1	.57
Male sex (%)	80 (66)	55 (59)	.23
Admission NIHSS	20 [14–23]	16 [14–19]	.44
ILV (cm <sup>3</sup> )	65.9 ± 62.9	81.5 ± 71.5	.13
3-Month mRS	3 [2–4]	3 [2–4]	.81
Treated with tPA (%)	115 (94)	86 (92)	.43
Treated with EVT (%)	58 (62)	45 (48)	.96
Recanalized	64 (53)	49 (52)	.51
Time to treatment (min)	97.7 ± 52.0	107.7 ± 71.2	.44
SICH (%)	1 (1)	4 (4)	.11
ASPECTS	9 [7–10]	9 [7–10]	.16

**Note:**—EVT indicates endovascular thrombectomy; SICH symptomatic intracranial hemorrhage.

<sup>a</sup> Values are means or median [25th–75th percentiles].

**Table 2: VLSM results of regions with mean *t*-values of >4.00<sup>a</sup>**

Region	Mean	Median	SD	Max	Min
Left superior longitudinal fasciculus	4.85	4.86	0.50	6.21	3.06
Left corticospinal tract	4.45	4.42	1.53	8.06	2.36
Left uncinate fasciculus	4.44	4.19	1.12	7.04	2.93
Left central opercular cortex	4.37	4.48	0.97	6.81	2.43
Right corticospinal tract	4.32	4.45	0.86	6.23	2.39
Left inferior fronto-occipital fasciculus	4.26	4.04	1.23	7.14	2.38
Left anterior thalamic radiation	4.09	4.10	0.71	6.58	2.36
Right frontal operculum cortex	4.08	4.06	0.39	5.06	2.66
Left planum temporale	4.03	4.05	0.41	5.30	2.52

**Note:**—Min indicates minimum; Max, maximum.

<sup>a</sup> Mean, median, minimum, maximum, and SD of *t*-scores calculated for each anatomic ROI provided by the Harvard-Oxford cortical and subcortical structural atlas and Johns Hopkins University International Consortium of Brain Mapping Diffusion Tensor-81 white matter labels.

Hopkins University International Consortium of Brain Mapping Diffusion Tensor-81 white matter labels,<sup>22</sup> distributed as part of the FMRIB Software Library (FSL; <http://www.fmrib.ox.ac.uk/fsl>).<sup>23</sup> In a second step, we repeated the VLSM and recalculated the *t*-score maps, adjusting for the variables found to be significantly associated with functional outcome in a backward stepwise regression analysis.

## RESULTS

### Patient Characteristics

Of the 500 patients included in MR CLEAN, 353 patients had a 3- to 9-day FU-NCCT scan (On-line Fig 1). Sixty-nine patients were excluded because of technical errors and insufficient scan quality

precluding automatic registration or segmentation. Moreover, patients were excluded because of hemispherectomy (21 patients), severe swelling (3 patients), previous stroke or mRS of >0 at baseline (22 patients), or mRS = 6 three months after stroke (22 patients).

All analyses were based on the final dataset comprising 216 patients.

On-line Table 1 shows the baseline and follow-up characteristics of patients included in this study and of the original MR CLEAN population for comparison. The patients in this study had a mean age of 63 years, and 63% were men. The overall mean ILV was 73 mL.

### Backward Stepwise Regression Analysis

The odds for a good outcome (lower mRS) were significantly higher given male sex and successful recanalization status (OR = 2.58; 95% CI, 1.16–6.01;  $P = .023$ ; OR = 2.03; 95% CI, 1.05–4.04;  $P = .038$ , respectively) and significantly lower given a high ILV, older age, long time to treatment, and a high NIHSS score (OR = 0.71; 95% CI, 0.62–0.79;

$P < .001$ ; OR = 0.64; 95% CI, 0.46–0.88;  $P = .007$ ; OR = 0.78; 95% CI, 0.60–0.98;  $P = .043$ ; OR = 0.79; 95% CI, 0.70–0.88;  $P < .001$ , respectively). Odds ratios and confidence intervals of the variables in the final model are shown in On-line Fig 2. These variables were used as covariates in subsequent VLSM analysis. The discriminative power of the final regression model was very good (area under the curve = 0.890; 95% CI, 0.846–0.933) (On-line Fig 3).

### Voxel-Based Lesion-Symptom Mapping

Figure 1 shows the incidence of lesions within each voxel for all patients with stroke as well as the statistical power for  $\alpha = 0.01$  by

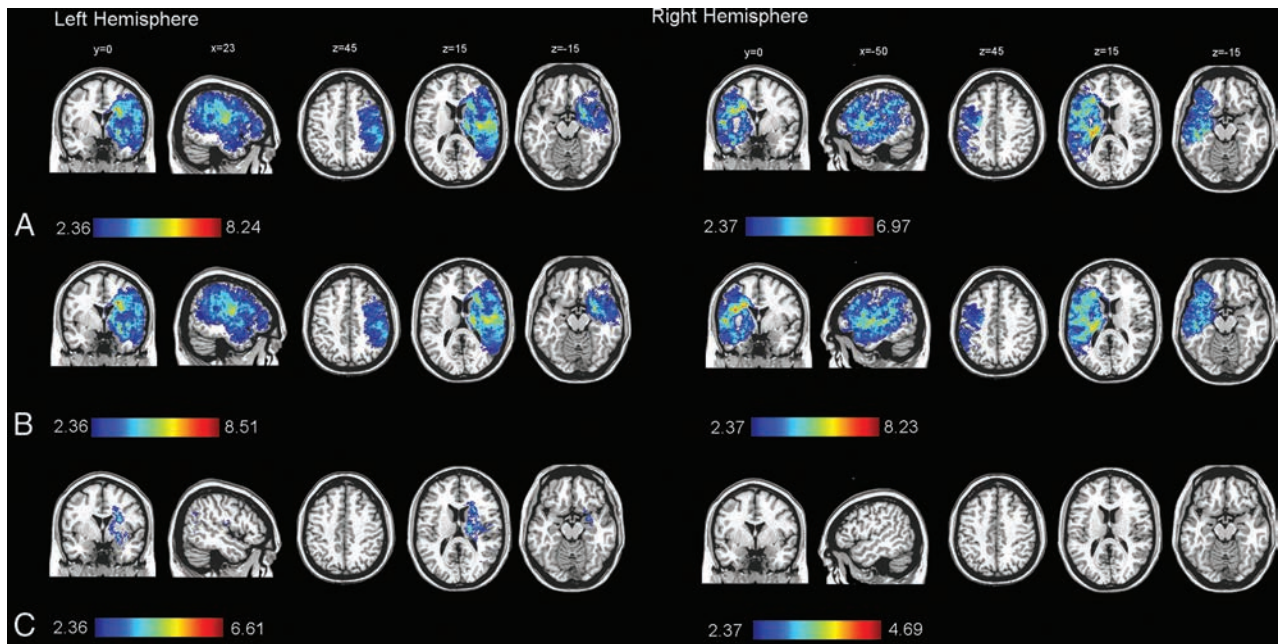


**FIG 2.** Voxel-based lesion-symptom mapping of lesion impact on the modified Rankin Scale score calculated separately for each hemisphere (*right side*,  $n = 94$ ; *left side*,  $n = 122$ ) using no covariates (A); sex and age as covariates (B); and sex, age, and ischemic lesion volume as covariates (C). The color range indicates  $t$ -scores thresholded at a 1% false discovery rate. Higher  $t$ -scores (red) indicate areas strongly associated with functional outcome (mRS).

**Table 3: VLSM results after inclusion of sex, age, and ischemic lesion volume<sup>a</sup>**

Region	Mean	Median	SD	Max	Min
Left corticospinal tract	3.86	4.11	0.97	5.90	2.36
Left inferior fronto-occipital fasciculus	3.29	3.36	0.55	4.84	2.36
Left uncinate fasciculus	3.25	3.28	0.56	4.86	2.39
Left anterior thalamic radiation	3.04	3.01	0.42	4.62	2.36
Left superior longitudinal fasciculus	2.65	2.62	0.21	3.68	2.36

**Note:**—Min indicates minimum; Max, maximum.

<sup>a</sup> Mean, median, minimum, maximum, and SD of  $t$ -scores calculated for each anatomic ROI provided by the Harvard-Oxford cortical and subcortical structural atlas and Johns Hopkins University International Consortium of Brain Mapping Diffusion Tensor-81 white matter labels.

color-coded overlays. The distribution of stroke lesions was comparable for the left and right hemispheres, with a slightly higher incidence and higher power in the left hemisphere (maximum incidences,  $n = 98$ ) than the right hemisphere (maximum incidences,  $n = 80$ ). Table 1 shows the demographic differences between patients with left and right ischemic strokes. VLSM revealed a significant contribution of brain regions comprising the motor pathway, such as the left and right corticospinal tracts. Moreover, injury involving the opercular cortex, the left superior longitudinal fasciculus, and anterior thalamic radiation was associated strongly with mRS (Table 2). A full list of mean, median, minimal, and maximal  $t$ -score values of all template ROIs is provided in On-line Table 2.

After we included sex, age, and ILV as covariates, the left deep periventricular white matter and adjacent internal capsule showed a great influence on mRS (Fig 2 and Table 3). When we included sex and age as covariates, larger regions of brain tissue in the right hemisphere (245 versus 263  $\text{cm}^3$ ) and in the left hemisphere (267 versus 272  $\text{cm}^3$ ) were significantly associated with mRS (Fig 2). The volume of voxels significantly associated with mRS was 250  $\text{cm}^3$  in the right hemisphere and 247  $\text{cm}^3$  in the left hemisphere with sex, age, and time to treatment as covariates

(On-line Fig 4). When we included sex, age, and the NIHSS as covariates, the volume of voxels significantly associated with mRS was reduced to 217  $\text{cm}^3$  in the right hemisphere and 230  $\text{cm}^3$  in the left hemisphere. When we included sex, age, and recanalization status as covariates, the volume of voxels significantly associated with mRS was reduced to 155  $\text{cm}^3$  in the right hemisphere and 236  $\text{cm}^3$  in

the left hemisphere. When ILV was included as a covariate, only voxels defined by injury to the left deep periventricular white matter and adjacent internal capsule (31.6  $\text{cm}^3$ ) were associated with mRS.

## DISCUSSION

By means of a voxelwise approach, our data demonstrate the influence of ischemic lesion location on functional outcome in patients with acute large-vessel-occlusion ischemic stroke. After we included covariates in the model, the left deep periventricular white matter and adjacent internal capsule showed a definite influence on mRS 3 months after stroke.

Our findings are in line with those in previous studies mapping corticospinal tract lesions to motor impairment and motor function recovery in patients with ischemic stroke.<sup>5,7,24,25</sup> In a previous study analyzing the ILV in motor-related brain structures (primary motor cortex, putamen, supplementary motor area, corticospinal tract, and cerebellum), patients who achieved functional independence (mRS 0–2) had a higher rate of MCA recanalization at 24 hours, a smaller final infarct volume, and less infarct growth. However, the multivariable analysis showed that

the best predictor of outcome in terms of mRS was the degree of ischemic damage in the ipsilateral corticospinal tract, which classified the patients with 78% accuracy.<sup>26</sup> In a following voxel-based analysis, the voxels of the brain linked to persistent disability were clustered in an area centered in the deep periventricular white matter and in the adjacent internal capsule.<sup>24</sup> The strategic functional importance of this area might be because it represents an important crossroad for many cortico-subcortical and long-range intrahemispheric association fiber tracts, including the corticospinal tract. Our findings support the hypothesis of greater impact of the cortical spinal tract over cortical lesions because reorganization at the cortical level remains insufficient for the patient's recovery in case of damage to the main motor outflow tract.<sup>26,27</sup> Although the mRS is currently the most commonly used outcome scale in stroke studies, it is mainly determined by motor disability and is relatively insensitive to cognitive dysfunction. The analysis of other functional outcome parameters such as the NIHSS, Barthel Index, or Glasgow Outcome Scale should be examined in future studies using VLSM.

The voxelwise approach allowed a more precise analysis of lesion location compared with previous studies using the ROI approach,<sup>28</sup> which is an intrinsic limitation implying an anatomic a priori localization of the supposed relevant brain area.

In contrast to previous studies that mirrored right-sided lesions onto left-sided ones to increase statistical power,<sup>5,25</sup> our study distinguished brain areas of the right and left hemispheres. This distinction is important given that the association between lesion location and outcome in terms of mRS is likely to be influenced by the side of the lesion.<sup>7,29</sup> Similar to the findings of Wu et al,<sup>7</sup> lesion location in the right hemisphere was no longer significantly associated with poor mRS scores after including ILV as a covariate in the model. In contrast to Wu et al, including age and sex into our model increased the number of voxels associated with mRS not only in the right hemisphere but also in the left hemisphere. This finding suggests that for a given sex and age, ischemic lesion location influences the risk of disability.

An important strength of our study was the adjustment for factors known to be associated with functional outcome after stroke. We showed that even after we adjusted for these predictors of functional outcome, infarcted voxels in the motor pathways remained independently associated with functional outcome. This finding highlights the importance of taking both lesion location and ILV into account to augment stroke-outcome prediction models.

In contrast to previous studies that used acute MR imaging,<sup>5,7</sup> the current study is the first to apply the voxel-based approach in FU-NCCTs of patients with stroke. This is important because CT is still the most common and widely available diagnostic imaging technique. However, there are limitations to CT used for determining lesion size, and high-resolution MR imaging can provide more precise results.<sup>30</sup>

With regard to the acquisition time of the FU-NCCT, the current study measured ILV in imaging acquired at the subacute time point of 3–9 days after stroke onset because it shows better association with acute imaging. Thus, a recent MR CLEAN substudy reported that the growth of ILV was common 24 hours after symptom onset.<sup>31</sup> Moreover, previous studies observed a good

association between subacute and chronic ILV, as well as a similar correlation between mRS and chronic and subacute volume, and recommended assessing ILV 3–6 days after stroke onset.<sup>32–34</sup> The exclusive use of FU-NCCTs that were acquired after stroke treatment distinguishes our approach from a study that analyzed acute DWI in an inhomogeneous group of patients with stroke undergoing MR imaging partly before and partly after revascularization therapy.<sup>7</sup>

The use of FU-NCCT 3–9 days after stroke and the exclusion of patients with hemispherectomy and brain shift as well as death before follow-up limit the generalizability of our study. However, these patients are generally known to have unfavorable functional outcome, while the analyzed patients with stroke are those whose outcome is more difficult to predict.

## CONCLUSIONS

Our study confirms that infarct location has an important impact on the outcome of patients with acute ischemic stroke and should be considered in prediction models. In the presented voxelwise approach, lesions in the periventricular white matter and internal capsule showed a strong influence on functional outcome, measured by the mRS, which underlines the importance of white matter injury to stroke pathology.

Disclosures: Anna M.M. Boers—UNRELATED: Stock/Stock Options: Nico.lab, Nils D. Forkert—UNRELATED: Grants/Grants Pending: Natural Sciences and Engineering Research Council of Canada, National Institutes of Health, Heart and Stroke Foundation, MS Society.\* Olvert A. Berkhemer—UNRELATED: Consultancy: Stryker, Comments: The Academic Medical Center received funds from Stryker for consultations by Olvert A. Berkhemer.\* Diederik W.J. Dippel—UNRELATED: Consultancy: Stryker, Bracco Imaging, Comments: Erasmus MC received funds from Stryker and Bracco Imaging for consultations by Diederik W.J. Dippel.\* Grants/Grants Pending: The MR CLEAN trial was partly funded by the Dutch Heart Foundation and by unrestricted grants from AngioCare, Medtronic/Covidien/ev3, Medac GmbH/Lampro, Penumbra, Stryker, and Top Medical/Concentric.\* Aad van der Lugt—UNRELATED: Consultancy: Stryker.\* Grants/Grants Pending: Dutch Heart Foundation, Dutch Brain Foundation, Stryker, Medtronic, Penumbra, Wim H. van Zwam—UNRELATED: Payment for Lectures Including Service on Speakers Bureaus: Stryker, Cerenovus.\* Jens Fiehler—UNRELATED: Consultancy: Acandis, Boehringer Ingelheim, Cerenovus, Covidien, Medtronic, MicroVention, Penumbra, Route 92 Medical, Stryker; Grants/Grants Pending: Acandis, Medtronic, MicroVention, Stryker.\* Henk A. Marquering—OTHER RELATIONSHIPS: cofounder and shareholder of Nico.lab, Charles B.L.M. Majoie—RELATED: Grant: Dutch Heart Foundation\*; UNRELATED: Grants/Grants Pending: European Commission, CardioVasculair Onderzoek Nederland/Dutch Heart Foundation, Stryker\*. \*Money paid to the institution.

## REFERENCES

1. Kwakkel G, Veerbeek JM, Harmeling-van der Wel BC, et al; Early Prediction of functional Outcome after Stroke (EPOS) Investigators. **Diagnostic accuracy of the Barthel Index for measuring activities of daily living outcome after ischemic hemispheric stroke: does early poststroke timing of assessment matter?** *Stroke* 2011;42:342–46 CrossRef Medline
2. Heiss WD, Kidwell CS. **Imaging for prediction of functional outcome and assessment of recovery in ischemic stroke.** *Stroke* 2014;45:1195–201 CrossRef Medline
3. Kwakkel G, Wagenaar RC, Kollen BJ, et al. **Predicting disability in stroke—a critical review of the literature.** *Age Ageing* 1996;25:479–89 CrossRef Medline
4. Kemmling A, Flottmann F, Forkert ND, et al. **Multivariate dynamic prediction of ischemic infarction and tissue salvage as a function of time and degree of recanalization.** *J Cereb Blood Flow Metab* 2015; 35:1397–405 CrossRef Medline
5. Cheng B, Forkert ND, Zavaglia M, et al. **Influence of stroke infarct**

- location on functional outcome measured by the Modified Rankin Scale.** *Stroke* 2014;45:1695–702 CrossRef Medline
6. Munsch F, Sagnier S, Asselineau J, et al. **Stroke location is an independent predictor of cognitive outcome.** *Stroke* 2016;47:66–73 CrossRef Medline
  7. Wu O, Cloonan L, Mocking SJ, et al. **Role of acute lesion topography in initial ischemic stroke severity and long-term functional outcomes.** *Stroke* 2015;46:2438–44 CrossRef Medline
  8. Forkert ND, Verleger T, Cheng B, et al. **Multiclass support vector machine-based lesion mapping predicts functional outcome in ischemic stroke patients.** *PLoS One* 2015;10:e0129569 CrossRef Medline
  9. Bates E, Wilson SM, Saygin AP, et al. **Voxel-based lesion-symptom mapping.** *Nat Neurosci* 2003;6:448–50 CrossRef Medline
  10. Lo R, Gitelman D, Levy R, et al. **Identification of critical areas for motor function recovery in chronic stroke subjects using voxel-based lesion symptom mapping.** *Neuroimage* 2010;49:9–18 CrossRef Medline
  11. Karnath HO, RENNIG J, Johannsen L, et al. **The anatomy underlying acute versus chronic spatial neglect: a longitudinal study.** *Brain* 2011;134(Pt 3):903–12 CrossRef Medline
  12. Magnusdottir S, Fillmore P, den Ouden DB, et al. **Damage to left anterior temporal cortex predicts impairment of complex syntactic processing: a lesion-symptom mapping study.** *Hum Brain Mapp* 2013;34:2715–23 CrossRef Medline
  13. Berkhemer OA, Fransen PS, Beumer D, et al. **A randomized trial of intraarterial treatment for acute ischemic stroke.** *N Engl J Med* 2015; 372:11–20 CrossRef Medline
  14. Fransen PS, Beumer D, Berkhemer OA, et al; MR CLEAN Investigators. **MR CLEAN, a multicenter randomized clinical trial of endovascular treatment for acute ischemic stroke in the Netherlands: study protocol for a randomized controlled trial.** *Trials* 2014;15:343 CrossRef Medline
  15. Boers AM, Marquering HA, Jochem JJ, et al; MR CLEAN Investigators. **Automated cerebral infarct volume measurement in follow-up noncontrast CT scans of patients with acute ischemic stroke.** *AJNR Am J Neuroradiol* 2013;34:1522–27 CrossRef Medline
  16. Banks JL, Marotta CA. **Outcomes validity and reliability of the modified Rankin scale: implications for stroke clinical trials: a literature review and synthesis.** *Stroke* 2007;38:1091–96 CrossRef Medline
  17. Zaidat OO, Yoo AJ, Khatri P, et al; Cerebral Angiographic Revascularization Grading (CARG) Collaborators, STIR Revascularization working group, STIR Thrombolysis in Cerebral Infarction (TICI) Task Force. **Recommendations on angiographic revascularization grading standards for acute ischemic stroke: a consensus statement.** *Stroke* 2013;44:2650–63 CrossRef Medline
  18. Mazziotta J, Toga A, Evans A, et al. **A four-dimensional probabilistic atlas of the human brain.** *J Am Med Inform Assoc* 2001;8:401–30 CrossRef Medline
  19. Modat M, Ridgway GR, Taylor ZA, et al. **Fast free-form deformation using graphics processing units.** *Comput Methods Programs Biomed* 2010;98:278–84 CrossRef Medline
  20. Rorden C, Bonilha L, Fridriksson J, et al. **Age-specific CT and MRI templates for spatial normalization.** *Neuroimage* 2012;61:957–65 CrossRef Medline
  21. Desikan RS, Ségonne F, Fischl B, et al. **An automated labeling system for subdividing the human cerebral cortex on MRI scans into gyral based regions of interest.** *Neuroimage* 2006;31:968–80 CrossRef Medline
  22. Mori S, Wakana S, van Zijl PC, et al. *MRI Atlas of Human White Matter.* Amsterdam: Elsevier; 2005
  23. Smith SM, Jenkinson M, Woolrich MW, et al. **Advances in functional and structural MR image analysis and implementation as FSL.** *Neuroimage* 2004;23(Suppl 1):S208–19 CrossRef Medline
  24. Cuingnet R, Rosso C, Chupin M, et al. **Spatial regularization of SVM for the detection of diffusion alterations associated with stroke outcome.** *Med Image Anal* 2011;15:729–37 CrossRef Medline
  25. Phan TG, Demchuk A, Srikanth V, et al. **Proof of concept study: relating infarct location to stroke disability in the NINDS rt-PA trial.** *Cerebrovasc Dis* 2013;35:560–65 CrossRef Medline
  26. Rosso C, Colliot O, Pires C, et al. **Early ADC changes in motor structures predict outcome of acute stroke better than lesion volume.** *J Neuroradiol* 2011;38:105–12 CrossRef Medline
  27. Seitz RJ, Sondermann V, Wittsack HJ, et al. **Lesion patterns in successful and failed thrombolysis in middle cerebral artery stroke.** *Neuroradiology* 2009;51:865–71 CrossRef Medline
  28. Ernst M, Boers AM, Aigner A, et al. **Association of computed tomography ischemic lesion location with functional outcome in acute large vessel occlusion ischemic stroke.** *Stroke* 2017;48:2426–33 CrossRef Medline
  29. Rangaraju S, Streib C, Aghaebrahim A, et al. **Relationship between lesion topology and clinical outcome in anterior circulation large vessel occlusions.** *Stroke* 2015;46:1787–92 CrossRef Medline
  30. Price CJ, Friston KJ. **Functional imaging studies of neuropsychological patients: applications and limitations.** *Neurocase* 2002;8:345–54 CrossRef Medline
  31. Buckner A, Boers AM, Bot JCJ, et al; MR CLEAN Trial Investigators (Multicenter Randomized Clinical Trial of Endovascular Treatment for Acute Ischemic Stroke in the Netherlands). **Associations of ischemic lesion volume with functional outcome in patients with acute ischemic stroke: 24-hour versus 1-week imaging.** *Stroke* 2017;48: 1233–40 CrossRef Medline
  32. Beaulieu C, de Crespigny A, Tong DC, et al. **Longitudinal magnetic resonance imaging study of perfusion and diffusion in stroke: evolution of lesion volume and correlation with clinical outcome.** *Ann Neurol* 1999;46:568–78 CrossRef Medline
  33. Ebinger M, Christensen S, De Silva DA, et al; Echoplanar Imaging Thrombolytic Evaluation Trial Investigators. **Expediting MRI-based proof-of-concept stroke trials using an earlier imaging end point.** *Stroke* 2009;40:1353–58 CrossRef Medline
  34. Tourdias T, Renou P, Sibon I, et al. **Final cerebral infarct volume is predictable by MR imaging at 1 week.** *AJNR Am J Neuroradiol* 2011; 32:352–58 CrossRef Medline

# Detection of Leukocortical Lesions in Multiple Sclerosis and Their Association with Physical and Cognitive Impairment: A Comparison of Conventional and Synthetic Phase-Sensitive Inversion Recovery MRI

Y. Forslin, Å. Bergendal, F. Hashim, J. Martola, S. Shams, M.K. Wiberg, S. Fredrikson, and T. Granberg



## ABSTRACT

**BACKGROUND AND PURPOSE:** Cortical lesions are common in multiple sclerosis and are included in the latest diagnostic criteria. The limited sensitivity of cortical MS lesions on conventional MR imaging can be improved by phase-sensitive inversion recovery. Synthetic MR imaging could provide phase-sensitive inversion recovery without additional scanning, but the use of synthetic phase-sensitive inversion recovery remains to be validated. We aimed to compare the ability and clinical value of detecting leukocortical lesions with conventional and synthetic phase-sensitive inversion recovery in MS.

**MATERIALS AND METHODS:** Twenty-one patients with MS prospectively underwent conventional and synthetic phase-sensitive inversion recovery, 3D T1-weighted, and T2 FLAIR imaging. Two neuroradiologists independently performed blinded phase-sensitive inversion recovery lesion assessments; a consensus rating with all sequences was considered the criterion standard. Lesion volumes were segmented. All participants underwent standardized cognitive and physical examinations and Fatigue Severity Scale assessment. Results were analyzed with multiple linear regressions.

**RESULTS:** Interrater and criterion standard agreement for leukocortical lesions was excellent for both conventional and synthetic phase-sensitive inversion recovery (intraclass correlation coefficient = 0.79–0.97). Leukocortical lesion volumes for both sequences were associated with lower information-processing speed ( $P \leq .01$ ) and verbal fluency ( $P \leq .02$ ). Both phase-sensitive inversion recovery sequences showed a positive effect on the association when combining volumes of leukocortical lesions and white matter lesions with information-processing speed ( $P \leq .005$ ) and verbal fluency ( $P \leq .03$ ). No associations were found between leukocortical lesion volumes and physical disability or fatigue.

**CONCLUSIONS:** Synthetic and conventional phase-sensitive inversion recovery have a sensitivity similar to that of leukocortical MS lesions. The detected leukocortical lesions are associated with cognitive dysfunction and thus provide clinically relevant information, which encourages assessment of cortical MS involvement at conventional field strengths.

**ABBREVIATIONS:** DIR = double inversion recovery; EDSS = Expanded Disability Status Scale; ICC = intraclass correlation coefficient; LCL = leukocortical lesions; PSIR = phase-sensitive inversion recovery;  $R_1$  = longitudinal relaxation rate;  $R_2$  = transverse relaxation rate

Multiple sclerosis is a chronic inflammatory and degenerative disease affecting the central nervous system and is the leading nontraumatic cause of neurologic disability in young adults.<sup>1</sup>

In recent years, there has been an increased awareness of the gray matter involvement in MS. Cortical MS lesions are closely associated with cognitive impairment<sup>2,3</sup> and contribute to cognitive deficits independent of white matter lesions.<sup>4–6</sup> Cortical lesions are also an independent predictor of conversion from clinically isolated syndrome to MS.<sup>7</sup> Thus, there is a need for feasible imaging techniques that can also monitor disease evolution and treatment response in the cerebral gray matter.<sup>8,9</sup>

While MS lesions in white matter are readily visualized with MR imaging, conventional MR imaging techniques have a low sensitivity for the detection of gray matter MS pathology, which hinders accurate assessment of the total lesion burden.<sup>5</sup> Newer MR imaging sequences such as double inversion recovery (DIR) and phase-sensitive inversion recovery (PSIR) are 1.5–5 times more sensitive than conventional MR imaging sequences in the

Received May 22, 2018; accepted after revision August 2.

From the Departments of Clinical Science, Intervention and Technology (Y.F., Å.B., F.H., J.M., S.S., M.K.W., T.G.) and Clinical Neuroscience (S.F.), Karolinska Institutet, Stockholm, Sweden; and Departments of Radiology (Y.F., F.H., J.M., S.S., M.K.W., T.G.) and Neurology (S.F.), Karolinska University Hospital, Stockholm, Sweden.

This work was supported by Karolinska Institutet and Stockholm County Council through an ALF grant.

Please address correspondence to Yngve Forslin, MD, Department of Clinical Neuroscience, CI-46, Karolinska University Hospital, 141 86 Stockholm, Sweden; e-mail: yngve.forslin@ki.se

Indicates open access to non-subscribers at www.ajnr.org

Indicates article with supplemental on-line photo.

<http://dx.doi.org/10.3174/ajnr.A5815>

detection of cortical lesions.<sup>4</sup> Leukocortical lesions (LCL) are located at the interface between the white matter and the cortex. LCL have the highest detection rate among cortical lesions and are thus a feasible potential imaging biomarker for cognitive deficits that could be readily available for clinical practice.<sup>10,11</sup>

Synthetic MR imaging is a time-efficient MR imaging technique that provides simultaneous quantitative measurements of the longitudinal relaxation rate ( $R_1$ ), the transverse relaxation rate ( $R_2$ ), and proton-density with correction for field inhomogeneities.<sup>12</sup> The technique is based on a double-echo saturation-recovery turbo spin-echo sequence applied with 4 repetitions in which the slice acquisition order is changed for each repetition. In practice, this provides 2 different TEs and 4 different TIs for each voxel. Both the magnitude and phase data are saved, providing a total of 16 complex images that are used to fit the T1- and T2-relaxation curves with a computationally efficient least-squares approach. From this simultaneous relaxometry, synthetic MR imaging can provide synthesized images with a wide range of TEs, TRs, and TIs. Thus, it is possible to obtain multiple spin-echo MR imaging weightings from a single acquisition. The technique has been shown to provide proton-density-, T1-, and T2-weighted images with diagnostic quality in MS.<sup>13-15</sup> Furthermore, it is also possible to synthesize images with inversion pulses and by specifying the TRs, TEs, and TIs as a T1-weighted inversion recovery with phase-sensitive reconstruction; the technique makes it possible to obtain PSIR images from the same sequence without additional scanning time.<sup>14</sup> This feature makes the technique attractive to apply in the monitoring of pathologies such as MS, in which the detection of cortical lesions on PSIR may be especially clinically important.

We aimed to compare the sensitivity of conventional and synthetic PSIR in detecting leukocortical MS lesions and to evaluate its clinical value in terms of their associations with clinical disability. We hypothesized that synthetic PSIR would have a sensitivity comparable with that of conventional PSIR and that the volume of LCL detected with synthetic PSIR would correlate with cognitive and physical disability.

## MATERIALS AND METHODS

### Study Population

We prospectively recruited a sample of 21 patients at the MS outpatient clinic at the Department of Neurology, Karolinska University Hospital in Huddinge, Stockholm, Sweden. The inclusion criterion was a diagnosis of MS according to the concurrent diagnostic criteria,<sup>16</sup> and the exclusion criteria were contraindications for MR imaging, neurologic comorbidities, or a history of head trauma. The cohort was representative of the MS population in our region, represented by all clinical subtypes: 13 relapsing-remitting, 7 secondary-progressive, and 1 primary-progressive.<sup>17</sup> The demography of the study population is further detailed in Table 1.

### Image Acquisition

All participants were scanned on the same Magnetom Trio 3T MR imaging scanner (Siemens, Erlangen, Germany) using a 12-channel head coil. The imaging protocol included a multidynamic multiecho turbo spin-echo sequence for synthetic MR imaging, conventional PSIR images, and additionally a 3D T1-weighted MPRAGE and T2-weighted FLAIR images. Synthetic PSIR images were achieved by

**Table 1: Demography of the study population<sup>a</sup>**

	Patients with MS
Female/male	14/7
Age (yr)	44.5 ± 12
Disease duration (yr)	14.5 ± 9.7
MS subtype (RR/SP/PP) (No.)	13/7/1
Disease-modifying therapy (No.) (%)	14 (67%)
EDSS score (median) (interquartile range)	2.0 (2.0)
Symbol Digit Modalities Test, z scores (median) (interquartile range)	-0.48 (1.46)
Verbal Fluency Test z scores	-0.37 ± 1.37
Fatigue Severity Scale score	4.53 ± 1.79

**Note:**—RR indicates relapsing-remitting; SP, secondary-progressive; PP, primary-progressive.

<sup>a</sup> Values reported as mean ± SD unless otherwise specified.

applying a phase-sensitive reconstruction on the T1 inversion recovery parameters from synthetic MR imaging as specified in Table 2. The PSIR reconstruction is performed instantaneously in the synthetic MR imaging software after reading the DICOM images and fitting the quantitative maps (which takes <20 seconds on a standard workstation). All acquisition parameters are detailed in Table 2. None of the sequences were acquired with motion correction to accurately reflect clinical image acquisitions.

### Radiologic Evaluation

The radiologic lesion assessments were performed independently by 2 neuroradiologists (F.H. and J.M.), blinded to all clinical information to avoid biased assessments. Using conventional and synthetic PSIR, the neuroradiologists identified juxtacortical lesions and assessed any adjacent cortical involvement, thus reclassifying the lesions as LCL. To compare the performance of conventional and synthetic PSIR and to avoid bias by the influence of other MR imaging sequences, the neuroradiologists initially assessed only these 2 sequences. For each patient, the conventional and synthetic PSIR images were assessed at 2 separate sessions separated by 12 weeks. For half of the participants (randomly assigned), the conventional PSIR image was presented in the first session, and the synthetic PSIR image, in the second session, and vice versa for the other half of the participants. A consensus agreement, considered to be the ground truth, was performed an additional 12 weeks later jointly by the 2 raters. For the consensus rating, both conventional and synthetic PSIR images were available, together with 3D T1-weighted MPRAGE and T2-weighted FLAIR images.

### Lesion Segmentations

WM lesion volumes were segmented on conventional FLAIR images using the lesion probability algorithm in the Lesion Segmentation Toolbox 2.0.12 (Technische Universität München, Munich, Germany) for Statistical Parametric Mapping 12 (SPM12; <http://www.fil.ion.ucl.ac.uk/spm/software/spm12>).<sup>18</sup> The resulting WM lesion probability masks were binarized in the FMRIB Software Library 5.0.9 (FSL; (<http://www.fmrib.ox.ac.uk/fsl>)) using a binarization threshold of 0.1.<sup>19</sup> A resident in radiology (Y.F.) then performed manual corrections of the automatic WM lesion segmentations using ITK-SNAP, Version 3.4.0 ([www.itksnap.org](http://www.itksnap.org)).<sup>20</sup> On the basis of the identified LCL in the consensus agreement assessment, a neuroradiologist (F.H.) manually segmented the LCL in ITK-SNAP on both conventional and synthetic PSIR images separately.

**Table 2: Image-acquisition parameters**

Sequence Type	Synthetic PSIR	Conventional PSIR	MPRAGE	FLAIR
Acquisition plane	2D axial	2D axial	3D sagittal	3D sagittal
Matrix	256 × 204	256 × 204	256 × 256	256 × 256
In-plane resolution (mm)	0.9 × 0.9	0.9 × 0.9	1.0 × 1.0	1.0 × 1.0
Slices (No.)	34	34	176	160
Slice thickness (mm)	3.0	3.0	1.0	1.0
Distance factor	0.5	0.5	—	—
Flip angle	120°	120°	9°	120°, T2 variable
TR (ms)	4820 <sup>a</sup> (6000 <sup>b</sup> )	6000	2300	6000
TE (ms)	22/100 <sup>a</sup> (10 <sup>b</sup> )	10	2.98	388
TI (ms)	150/580/2000/4130 <sup>a</sup> (500 <sup>b</sup> )	500	900	2100
Acquisition time (min:sec)	7:47	3:32	5:15	7:02

**Note:**— TR indicates repetition time; TE, echo time; TI, inversion time.

<sup>a</sup> Synthetic MRI is based on a single quantitative acquisition that is then used to generate synthetic images post hoc.

<sup>b</sup> Settings for the generation of synthetic PSIR are in parentheses.

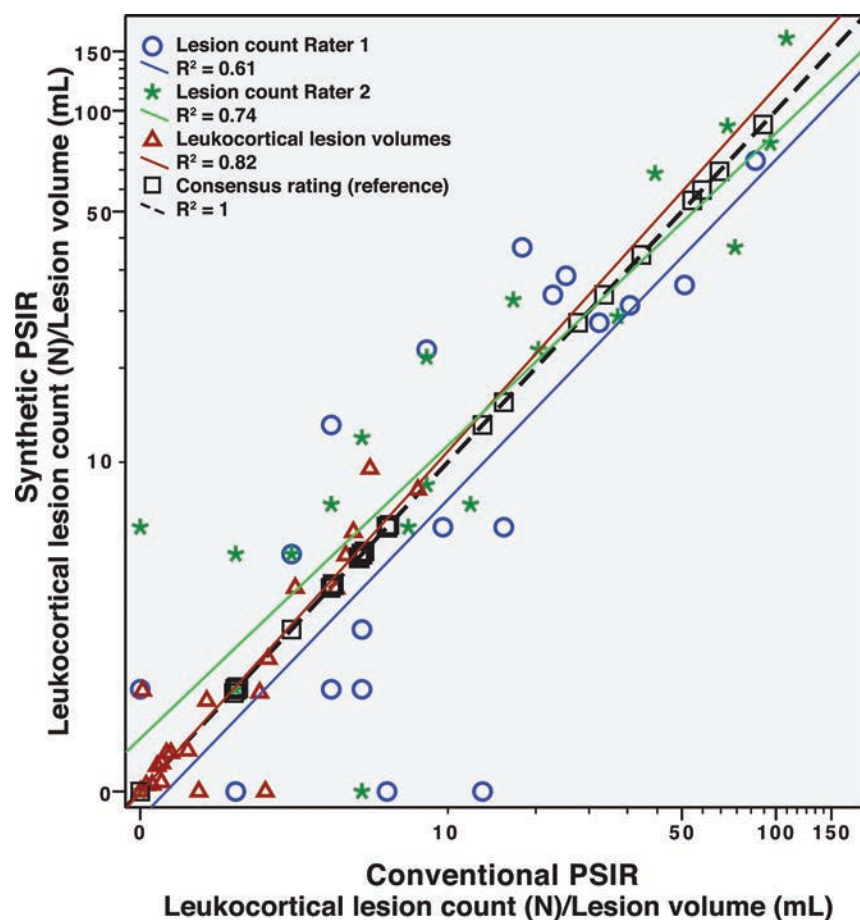


**FIG 1.** Leukocortical lesion count and volume on conventional and synthetic PSIR.

### Clinical Assessments

Physical disability was assessed with the Expanded Disability Status Scale (EDSS) by an experienced MS neurologist (S.F.). Cognitive testing was performed by an experienced neuropsychologist (Å.B.) with the Symbol Digit Modalities Test, the F-A-S Verbal Fluency Test, and the Fatigue Severity Scale. The testing was performed on the same day as the MR imaging. All cognitive scores were converted into z scores normalized to age and sex.

### Statistics

Normality of data was assessed using the Shapiro-Wilk test. Lesion counts and volumes were positively skewed. Differences in

lesion count/volume on conventional and synthetic PSIR images were therefore compared using the Wilcoxon signed rank test. Interrater agreement was evaluated using the intraclass coefficient (ICC); ICC ratings of <0.40, 0.40–0.59, 0.60–0.74, and 0.75–1.0 were considered weak, fair, good, or excellent according to statistical convention.<sup>21</sup> Standard multiple linear regression was used to evaluate associations between the EDSS, Fatigue Severity Scale, Symbol Digit Modalities Test, and Verbal Fluency Test z scores (dependent variables) and LCL volume (independent variable). Fatigue and verbal fluency z scores were normally distributed, while Symbol Digit Modalities Test z scores were negatively skewed and therefore underwent a reflect and logarithmic transformation [ $\text{Lg}10(\text{largest score in data} + 1) - \text{data}$ ] to obtain a normal distribution for the regression analysis; EDSS scores were positively skewed and underwent logarithmic transformation to achieve normal distribution. In a second step, WM lesion volumes were added to the analyses to look for any positive interaction between the 2 lesion metrics.  $P < .05$  was considered statistically significant, which after correction for the false discovery rate according to the

Benjamini-Hochberg method, corresponded to an adjusted level of  $P < .030$ .<sup>22</sup>

## RESULTS

### Lesion Counts and Volumes

The ICC between the 2 raters was excellent for LCL for both conventional PSIR (0.79,  $P < .001$ ) and synthetic PSIR (0.87,  $P < .001$ ). Both raters also had excellent agreement with the consensus rating on both conventional (ICC = 0.91 and 0.97, respectively, for each rater,  $P < .001$ ) and synthetic PSIR (ICC = 0.92 and 0.94,  $P < .001$ ). There was no significant difference in the number of

**Table 3: Comparison of leukocortical lesion counts and volumes on conventional and synthetic PSIR<sup>a</sup>**

	Conventional PSIR	Synthetic PSIR	P Value Conventional vs Synthetic PSIR <sup>b</sup>	Consensus Rating	P Value Conventional/Synthetic PSIR vs Consensus Rating <sup>b</sup>
Leukocortical lesion count, Rater 1 (No.)	7 ± 17	5 ± 26	.47	5 ± 30	.14/.06
Leukocortical lesion count, Rater 2 (No.)	7 ± 34	7 ± 29	.08	5 ± 30	.008/.96
Leukocortical lesion volume (mL)	0.53 ± 2.46	0.32 ± 2.89	.17		

<sup>a</sup> All values are given as median ± interquartile range.

<sup>b</sup> P value by the Wilcoxon signed rank test.

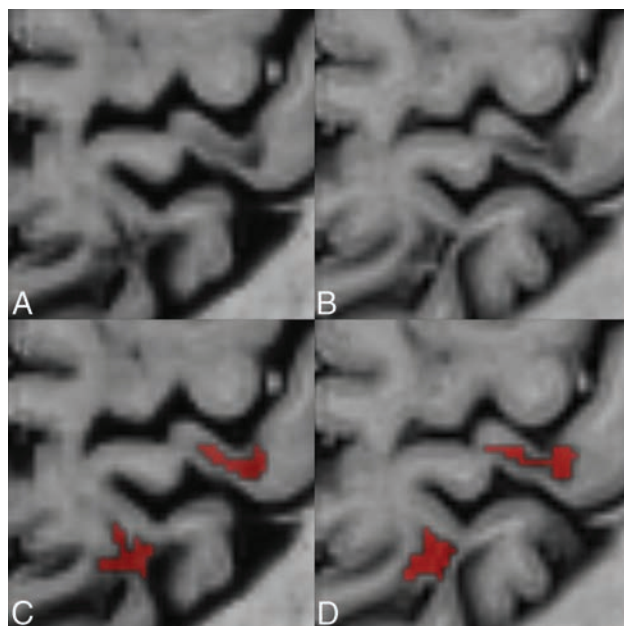


**FIG 2.** Comparison between conventional and synthetic phase-sensitive inversion recovery. A comparison between conventional (B and D) and synthetic phase-sensitive inversion recovery (A and C) illustrates 2 leukocortical MS lesions in a 40-year-old female patient with MS. Lower row illustrates the manual segmentation of the lesions by a neuroradiologist.

detected LCL between conventional and synthetic PSIR ( $P = .47$  and  $P = .08$ , respectively, for each rater). Figure 1 illustrates the relation of the individual lesion ratings and the consensus rating as well as the relation between conventional and synthetic PSIR. The 2 raters seemed to have relatively larger differences in their LCL counts in patients with fewer lesions. When we compared each individual rating with the consensus rating, one of the raters showed a small-but-significant difference between the individual and consensus rating in the LCL count on conventional PSIR ( $P = .008$ , by the Wilcoxon signed rank test). There was no significant difference between the manually segmented LCL volumes on conventional and synthetic PSIR ( $P = .17$ ). A detailed comparison of the lesion counts and volumes is presented in Table 3. Figure 2 illustrates the appearance of 2 leukocortical lesions on conventional and synthetic PSIR.

### Associations with Dysfunction

Multiple linear regression showed that higher volumes of LCL were associated with lower Symbol Digit Modalities Test z scores, reflecting information-processing speed, both with measurements from conventional ( $\beta = -0.62$ ,  $P = .003$ , adjusted  $R^2 = 0.35$ ) and synthetic PSIR ( $\beta = -0.55$ ,  $P = .010$ , adjusted  $R^2 = 0.26$ ). Similarly, higher volumes of LCL on conventional PSIR

( $\beta = -0.51$ ,  $P = .019$ , adjusted  $R^2 = 0.22$ ) were associated with lower Verbal Fluency Test z scores, and a similar trend was seen for synthetic PSIR ( $\beta = -0.43$ ,  $P = .054$ , adjusted  $R^2 = 0.14$ ). Using both the LCL and WM lesion volumes from conventional MR imaging, we saw a positive effect on the association for both the Symbol Digit Modalities Test ( $\beta = -0.66$ ,  $P = .001$ , adjusted  $R^2 = 0.41$ ) and the Verbal Fluency Test ( $\beta = -0.52$ ,  $P = .015$ , adjusted  $R^2 = 0.24$ ). An increased association was similarly observed for synthetic PSIR with the Symbol Digit Modalities Test ( $\beta = -0.58$ ,  $P = .005$ , adjusted  $R^2 = 0.31$ ) and the Verbal Fluency Test ( $\beta = -0.47$ ,  $P = .030$ , adjusted  $R^2 = 0.18$ ).

There were no statistically significant associations between EDSS scores and conventional PSIR ( $\beta = 0.45$ ,  $P = .18$ ) or synthetic PSIR ( $\beta = 0.60$ ,  $P = .12$ ). Neither were there any associations between fatigue and volumes of LCL on conventional PSIR ( $\beta = 0.04$ ,  $P = .88$ ) or synthetic PSIR ( $\beta = -0.03$ ,  $P = .89$ ).

### DISCUSSION

In this prospective cohort of 21 patients with MS, we show that synthetic PSIR based on the multiparametric synthetic MR imaging technique shows a performance comparable with that of conventional PSIR in detecting leukocortical MS lesions. We further show that larger volumes of LCL on both synthetic and conventional PSIR are associated with lower cognitive performance, thus suggesting that the finding of LCL on PSIR is clinically valuable.

Visualization of cortical pathology in vivo improves the diagnostic accuracy in MS and its differential diagnoses.<sup>23</sup> A single-center study and a larger multicenter study have demonstrated that including cortical lesions in the criteria for dissemination in space in clinically isolated syndrome increases the specificity in the prediction of those who later convert to MS.<sup>7,24</sup> Our results support the potential clinical feasibility of including the combined term “cortical/juxtacortical lesions” in the evaluation of dissemination in space in the latest MAGNIMS criteria for MS diagnostics and the latest revision of the diagnostic criteria for MS.<sup>9,23</sup>

Including cortical lesions in the diagnostic algorithms for MS has also been previously proposed,<sup>7</sup> though a histopathologic validation study later showed a fairly low cortical lesion detection rate of merely 18% with double inversion recovery.<sup>25</sup> However, PSIR has been suggested to be superior to DIR in detecting cortical MS lesions.<sup>26</sup> The excellent agreement of LCL on both conventional and synthetic PSIR in the current study indicates that the proposed rating of LCL on PSIR may give a robust assessment of cortical disease involvement in MS.<sup>27,28</sup> Nevertheless, we found that there was less difference in the LCL count between the 2 different PSIR sequences than between the raters and the consensus rating. This might be because the consensus rating generated a

larger total lesion burden when the overall sensitivity and specificity increased with the combination of all available sequences. Combining different sequences, as performed for the criterion standard, was subjectively the preferred approach by the raters in the current study to accurately delineate cortical involvement, which supports previously proposed multimodal reading protocol approaches.<sup>4,29-31</sup>

Synthetic MR imaging has previously been shown to provide proton-density-, T1-, and T2-weightings in diagnostic quality (as illustrated in the On-line Figure)<sup>13-15</sup> as well as automatic volumetrics,<sup>13</sup> with a single acquisition. The image quality of synthetic FLAIR images has, however, been shown to be hampered by artifacts.<sup>13</sup> We here show that it is possible to obtain diagnostic synthetic PSIR images from the same acquisition without additional scanning, thus providing a clinically feasible way to visualize leukocortical MS pathology, relevant for the latest revision of the MS criteria.<sup>23</sup> Nevertheless, if the purpose would be to solely acquire a PSIR contrast, the conventional PSIR would be a faster approach (3 minutes and 32 seconds versus 7 minutes and 47 seconds) but without the additional imaging information provided with synthetic MR imaging.

In terms of the clinical importance of LCL, we found a significant association between higher LCL volume (measured on both synthetic and conventional PSIR) and lower cognitive scores. The good correspondence of both PSIR methods with the cognitive scores is expected because both sequences had similar detection rates and volumes of LCL. This association was increased when adding WM lesion volume to the analyses for both sequences, showing the clinical importance of also detecting LCL with the PSIR methods used here. However, no associations with physical disability or fatigue were found, suggesting that the LCL burden is more related to cognitive disabilities. To further expand our understanding of the pathologic meaning of the imaging findings on conventional/synthetic MR imaging, future studies may investigate the association with biofluid markers of interest in MS.

This study has some limitations: The sample size is relatively small, making it unfeasible to perform additional analyses within the different MS subtypes. The sparse number of raters makes the interrater assessment less robust. Furthermore, a histopathologic validation was not possible in this in vivo study. A comparison with an ultra-high-field strength MR imaging scanner for the ground truth would have been a more optimal validation, but that was, unfortunately, not available for the purpose of the study and synthetic MR imaging has yet to be applied at 7T. A slice distance factor of 0.5 was used to avoid interslice talk. A complementing 3D acquisition approach, as used for the consensus agreement, could be valuable to further increase the detection of smaller lesions such as purely intracortical lesions. With this in mind, we harmonized the spatial resolutions for conventional and synthetic PSIR so that the comparability of the LCL detection rate was not confounded by partial volume effects.

## CONCLUSIONS

Synthetic MR imaging provides PSIR with a sensitivity similar to that of conventional PSIR in terms of the detection of leukocortical MS lesions. The leukocortical burden detected with synthetic PSIR is associated with cognitive deficits and, therefore, is of clin-

ical relevance in MS. Our results highlight the value of evaluating leukocortical MS lesions, even without the use of ultra-high-field scanners and suggest that either synthetic or conventional PSIR could be a part of a multimodal approach with additional 3D-based sequences, applied to meet the new demands of the latest revision of the MS diagnostic criteria.

## ACKNOWLEDGMENTS

We thank Russell Ouellette for valuable comments on the manuscript.

Disclosures: Yngve Forslin, Åsa Bergendal, Farouk Hashim, Juha Martola, Sara Shams, Tobias Granberg, Maria Kristoffersen-Wiberg—*RELATED*: Grant: ALF Grant\* from Karolinska Institutet and Stockholm City Council. \*Money paid to the institution. Sten Fredrikson—*UNRELATED*: Board Membership: Merck, Sanofi Genzyme, Teva Pharmaceutical Industries, Novartis, Roche; *Consultancy*: Merck, Sanofi Genzyme, Teva Pharmaceutical Industries, Novartis, Roche; *Payment for Lectures Including Service on Speakers Bureaus*: Merck, Sanofi Genzyme, Teva Pharmaceutical Industries, Novartis, Roche; *Payment for Development of Educational Presentations*: Merck, Sanofi Genzyme, Teva Pharmaceutical Industries, Novartis, Roche.

## REFERENCES

1. Peterson JW, Trapp BD. **Neuropathobiology of multiple sclerosis.** *Neuro Clin* 2005;23:107-29, vi-vii Medline
2. Chiaravalloti ND, DeLuca J. **Cognitive impairment in multiple sclerosis.** *Lancet Neurol* 2008;7:1139-51 CrossRef Medline
3. Odenthal C, Coulthard A. **The prognostic utility of MRI in clinically isolated syndrome: a literature review.** *AJNR Am J Neuroradiol* 2015;36:425-31 CrossRef Medline
4. Nelson F, Poonawalla AH, Hou P, et al. **Improved identification of intracortical lesions in multiple sclerosis with phase-sensitive inversion recovery in combination with fast double inversion recovery MR imaging.** *AJNR Am J Neuroradiol* 2007;28:1645-49 CrossRef Medline
5. Geurts JJ, Bö L, Pouwels PJ, et al. **Cortical lesions in multiple sclerosis: combined postmortem MR imaging and histopathology.** *AJNR Am J Neuroradiol* 2005;26:572-77 Medline
6. Calabrese M, Agosta F, Rinaldi F, et al. **Cortical lesions and atrophy associated with cognitive impairment in relapsing-remitting multiple sclerosis.** *Arch Neurol* 2009;66:1144-50 Medline
7. Filippi M, Rocca MA, Calabrese M, et al. **Intracortical lesions: relevance for new MRI diagnostic criteria for multiple sclerosis.** *Neurology* 2010;75:1988-94 CrossRef Medline
8. Rocca MA, Amato MP, De Stefano N, et al; MAGNIMS Study Group. **Clinical and imaging assessment of cognitive dysfunction in multiple sclerosis.** *Lancet Neurol* 2015;14:302-17 CrossRef Medline
9. Filippi M, Rocca MA, Ciccarelli O, et al; MAGNIMS Study Group. **MRI criteria for the diagnosis of multiple sclerosis: MAGNIMS consensus guidelines.** *Lancet Neurol* 2016;15:292-303 CrossRef Medline
10. Nelson F, Datta S, Garcia N, et al. **Intracortical lesions by 3T magnetic resonance imaging and correlation with cognitive impairment in multiple sclerosis.** *Mult Scler* 2011;17:1122-29 CrossRef Medline
11. Nielsen AS, Kinkel RP, Madigan N, et al. **Contribution of cortical lesion subtypes at 7T MRI to physical and cognitive performance in MS.** *Neurology* 2013;81:641-49 CrossRef Medline
12. Warrantes JB, Leinhard OD, West J, et al. **Rapid magnetic resonance quantification on the brain: optimization for clinical usage.** *Magn Reson Med* 2008;60:320-29 CrossRef Medline
13. Granberg T, Uppman M, Hashim F, et al. **Clinical feasibility of synthetic MRI in multiple sclerosis: a diagnostic and volumetric validation study.** *AJNR Am J Neuroradiol* 2016;37:1023-29 CrossRef Medline
14. Hagiwara A, Hori M, Yokoyama K, et al. **Synthetic MRI in the detection of multiple sclerosis plaques.** *AJNR Am J Neuroradiol* 2017;38:257-63 CrossRef Medline

15. Krauss W, Gunnarsson M, Nilsson M, et al. **Conventional and synthetic MRI in multiple sclerosis: a comparative study.** *Eur Radiol* 2018;28:1692–1700 [CrossRef Medline](#)
16. Polman CH, Reingold SC, Banwell B, et al. **Diagnostic criteria for multiple sclerosis: 2010 revisions to the McDonald criteria.** *Ann Neurol* 2011;69:292–302 [CrossRef Medline](#)
17. Lublin FD, Reingold SC, Cohen JA, et al. **Defining the clinical course of multiple sclerosis: the 2013 revisions.** *Neurology* 2014;83:278–86 [CrossRef Medline](#)
18. Schmidt P, Gaser C, Arsic M, et al. **An automated tool for detection of FLAIR-hyperintense white-matter lesions in multiple sclerosis.** *Neuroimage* 2012;59:3774–83 [CrossRef Medline](#)
19. Smith SM, Jenkinson M, Woolrich MW, et al. **Advances in functional and structural MR image analysis and implementation as FSL.** *Neuroimage* 2004;23(Suppl 1):S208–19 [CrossRef Medline](#)
20. Yushkevich PA, Piven J, Hazlett HC, et al. **User-guided 3D active contour segmentation of anatomical structures: significantly improved efficiency and reliability.** *Neuroimage* 2006;31:1116–28 [CrossRef Medline](#)
21. Cicchetti D. **Guidelines, criteria, and rules of thumb for evaluating normed and standardized assessment instrument in psychology.** *Psychological Assessment* 1994;6:284–90 [CrossRef](#)
22. Benjamini Y, Hochberg Y. **Controlling the false discovery rate: a practical and powerful approach to multiple testing.** *Journal of the Royal Statistical Society Series B (Methodological)* 1995;57:289–300
23. Thompson AJ, Banwell BL, Barkhof F, et al. **Diagnosis of multiple sclerosis: 2017 revisions of the McDonald criteria.** *Lancet Neurol* 2018;17:162–73 [CrossRef Medline](#)
24. Preziosa P, Rocca MA, Mesaros S, et al. **Diagnosis of multiple sclerosis: a multicentre study to compare revised McDonald-2010 and Filippi-2010 criteria.** *J Neurol Neurosurg Psychiatry* 2018;89:316–18 [CrossRef Medline](#)
25. Seewann A, Kooi EJ, Roosendaal SD, et al. **Postmortem verification of MS cortical lesion detection with 3D DIR.** *Neurology* 2012;78:302–08 [CrossRef Medline](#)
26. Sethi V, Yousry TA, Muhlert N, et al. **Improved detection of cortical MS lesions with phase-sensitive inversion recovery MRI.** *J Neurol Neurosurg Psychiatry* 2012;83:877–82 [CrossRef Medline](#)
27. Nielsen AS, Kinkel RP, Tinelli E, et al. **Focal cortical lesion detection in multiple sclerosis: 3 Tesla DIR versus 7 Tesla FLASH-T2.** *J Magn Reson Imaging* 2012;35:537–42 [CrossRef Medline](#)
28. Mainero C, Benner T, Radding A, et al. **In vivo imaging of cortical pathology in multiple sclerosis using ultra-high field MRI.** *Neurology* 2009;73:941–48 [CrossRef Medline](#)
29. Favaretto A, Poggiali D, Lazzarotto A, et al. **The parallel analysis of phase sensitive inversion recovery (PSIR) and double inversion recovery (DIR) images significantly improves the detection of cortical lesions in multiple sclerosis (MS) since clinical onset.** *PLoS One* 2015;10:e0127805 [CrossRef Medline](#)
30. Nelson F, Poonawalla A, Datta S, et al. **Is 3D MPRAGE better than the combination DIR/PSIR for cortical lesion detection at 3T MRI?** *Mult Scler Relat Disord* 2014;3:253–57 [CrossRef Medline](#)
31. Maranzano J, Rudko DA, Arnold DL, et al. **Manual segmentation of MS cortical lesions using MRI: a comparison of 3 MRI reading protocols.** *AJNR Am J Neuroradiol* 2016;37:1623–28 [CrossRef Medline](#)

# Do All Patients with Multiple Sclerosis Benefit from the Use of Contrast on Serial Follow-Up MR Imaging? A Retrospective Analysis

R.R. Mattay, K. Davtayan, M. Bilello, and A.C. Mamourian

## ABSTRACT

**BACKGROUND AND PURPOSE:** Patients with multiple sclerosis routinely have MR imaging with contrast every 6–12 months to assess response to medication. Multiple recent studies provide evidence of tissue deposition of MR imaging contrast agents, questioning the long-term safety of these agents. The goal of this retrospective image-analysis study was to determine whether contrast could be reserved for only those patients who show new MS lesions on follow-up examinations.

**MATERIALS AND METHODS:** We retrospectively reviewed brain MRIs of 138 patients. To increase our sensitivity, we used a previously described computerized image-comparison software to evaluate the stability or progression of multiple sclerosis white matter lesions in noncontrast FLAIR sequences. We correlated these findings with evidence of contrast-enhancing lesions on the enhanced T1 sequence from the same scan.

**RESULTS:** Thirty-three scans showed an increase in white matter lesion burden. Among those 33 patients, 14 examinations also demonstrated enhancing new lesions. While we found a single example of enhancement of a pre-existing white matter lesion that appeared unchanged in size, that same examination showed an overall increase in lesion burden with enhancement of other, new lesions. Thus, we found that all patients with enhancing lesions had evidence of progression on their noncontrast imaging.

**CONCLUSIONS:** Because all enhancing lesions were associated with new lesions on unenhanced imaging and progression was only evident in 24% of patients, in patients with relapsing-remitting MS, it is reasonable to consider reserving contrast for only those patients with evidence of progression on noncontrast MR images.

**ABBREVIATIONS:** GBCA = gadolinium-based contrast agents; RRMS = relapsing-remitting MS

Multiple sclerosis is a nervous system disease caused by immune-mediated myelin loss with an unpredictable course, usually characterized by clinical remission, relapse, and progression. Symptoms frequently correlate with a change in the number or volume of MS lesions in the central nervous system.<sup>1</sup> Serial clinical assessments have underestimated disease activity and lesion burden when correlated with findings on serial brain MR imaging.<sup>2</sup> According to the guidelines outlined in the Standardized MR Imaging Protocol for Multiple Sclerosis,<sup>3</sup> MR imaging using standard FLAIR, T1-weighted, and T2-weighted pulse sequences with and without injection of gadolinium-based contrast

agents (GBCA) is currently the preferred technique for the long-term monitoring of patients with MS.

Contrast-enhancing lesions indicate that there is acute active inflammatory disease and subsequent blood-brain barrier disruption,<sup>4</sup> while noncontrast images identify progression of lesion burden. It has already been shown that new lesions typically enhance after administration of gadolinium-based contrast agents for approximately 3–4 weeks after their development,<sup>5</sup> and after the resolution of enhancement, these lesions are radiologically defined as chronic.<sup>6</sup> Although pathologic specimens have also shown evidence of perivascular inflammatory infiltrates in chronic lesions in patients with MS, the blood-brain barrier either remains intact or is only minimally damaged; therefore, the lesion no longer enhances on MR imaging.<sup>7</sup> There has been recent evidence that noncontrast, susceptibility-based imaging can be used to detect a paramagnetic rim representing the presence of macrophages and other paramagnetic inflammatory species indicative of ongoing inflammation in some of these chronic lesions. However, these studies all used high-resolution imaging with a

Received March 15, 2018; accepted after revision July 26.

From the Department of Radiology, Hospital of the University of Pennsylvania, Philadelphia, Pennsylvania.

Please address correspondence to Raghav R. Mattay, MD, Hospital of the University of Pennsylvania, Division of Neuroradiology, 219 Dulles, 3400 Spruce St, Philadelphia, PA 19104; e-mail: rrmattay@gmail.com

<http://dx.doi.org/10.3174/ajnr.A5828>

7T scanner, which currently is primarily limited to research protocols.<sup>8-15</sup>

Considerable histopathologic evidence has linked leptomeningeal inflammation with subpial cortical demyelination in patients with MS.<sup>16-21</sup> While cortical lesions have been difficult to detect on in vivo MR imaging,<sup>22</sup> recent studies have shown foci of leptomeningeal enhancement in patients with MS using specific delayed-acquisition postcontrast T2 FLAIR sequences.<sup>23,24</sup> These findings have also been correlated with cortical volume loss.<sup>25</sup> However, leptomeningeal enhancement has been shown to be unrelated to white matter lesion load and enhancement,<sup>24</sup> and the same study showed that 85% of foci of leptomeningeal enhancement persisted on follow-up with no change in morphology, shape, or size, despite the patient receiving disease-modifying therapy. While cortical volume loss and leptomeningeal enhancement are promising new biomarkers in understanding the progression and pathophysiology of this disease, they do not provide immediate information on response to currently available treatments, and MR imaging pulse sequences used for their detection and quantification are not routinely used in clinical practice.

Currently, the consensus is that follow-up scans can be ordered when clinically indicated<sup>3</sup>; however, the standard of care followed in many large MS centers is to acquire regular, scheduled enhanced MR imaging. The intent is not only to analyze treatment effectiveness but also provide evidence for treatment decisions because these scans may reveal contrast-enhancing lesions in the absence of clinical symptoms.<sup>26</sup> These routine contrast-enhanced studies are performed as often as every 6 months.<sup>5</sup>

MS typically presents in young adults between 20 and 50 years of age, with a peak onset around 30 years of age<sup>27</sup> and the median time to death of approximately 30 years from disease onset.<sup>28</sup> This means that in their lifetimes, patients with MS on a 6-month imaging schedule will have  $\geq 60$  contrast-enhanced MR images.

While there exists an accepted literature on gadolinium risk for patients with severely impaired renal function, there is now emerging evidence that retained intracranial gadolinium-related deposits appear after intravenous administration of GBCA in patients with normal renal function after contrast-enhanced MR imaging. This finding suggests that we explore avoiding unnecessary the use of MR imaging contrast agents. In light of recent studies that have shown that gadolinium tissue deposition takes place even in those without intracranial abnormalities and with normal renal function,<sup>29-33</sup> the FDA has recently issued a warning precaution on all GBCA.<sup>34</sup> Although we await the results of systematic studies to better characterize the nature of this tissue deposition from the use of GBCA and, more importantly, to determine whether it results in adverse effects, it seems prudent, in the meantime, to limit their use and develop new strategies to monitor disease progression in this potentially vulnerable population of patients with MS. One such proposed strategy is the use of additional noncontrast MR imaging techniques, such as DTI-based fractional anisotropy, which has been shown to be helpful in detection of MS lesion acuity without gadolinium.<sup>35</sup>

To a similar end, we designed the current study to determine whether the nonenhanced MR imaging is reliable for selecting only those patients who need additional imaging with contrast when characterizing progression of MS. As previously mentioned,

new lesions typically only enhance for approximately 3–4 weeks after their development. Therefore, even with imaging intervals as short as every 6 months, all new, enhancing lesions that develop in that timeframe are not captured.<sup>5</sup> Also, enhancing lesions are not sufficiently sensitive for a sole measure of disease activity.<sup>36</sup>

We wondered, then, whether the findings on nonenhanced MS follow-up MR images could be used as a reliable predictor for the presence of enhancing lesions. If this were established with enough certainty, it would offer patients an option of forgoing gadolinium-based contrast agent administration in specific situations. While both enhanced and unenhanced sequences have proved useful together in maximizing the sensitivity and reliability in detecting a change in the stable disease state versus progression, we designed this study to examine whether there could be enhancing white matter lesions in patients when the unenhanced FLAIR sequence is stable—that is, no evidence of new or enlarging existing lesions. While we recognize that standard FLAIR imaging is imperfect for the detection of lesions, we re-examined this question using a 3D-FLAIR sequence along with computer-aided detection software, which we find increases the sensitivity of FLAIR to new lesions.<sup>37</sup>

## MATERIALS AND METHODS

After receiving institutional review board approval for the study, a list of 197 sequential, unique identifying numbers of follow-up brain MR images was generated from September 19, 2017, to October 31, 2017. All cases were available on our PACS for review, and the list contained cases that were imaged with MR imaging using a specific, proprietary multisequence MS protocol that was performed on one of several of our 3T scanners, Siemens Verio, Skyra, and Trio (Siemens, Erlangen, Germany). Our department 3D lab then processed the MR images obtained in this fashion using an in-house computer-assisted detection software system.<sup>17</sup> This program takes the 3D FLAIR images from the current and prior studies and applies an imaging-processing pipeline, including coregistration, skull stripping, and inhomogeneity correction. Then the program computes both forward and backward differences between the 2 time point datasets and subsequently creates composite images that display the coregistered current and prior studies, as well as a third image that shows new MS lesions in red and resolving lesions in green (Fig 1). The software is routinely run by our departmental 3D lab, and this program then sends the DICOM image files directly back to the PACS.

While this program has not received a formal FDA certification, the paired, matching source multiplanar reformats from each of the 3D-FLAIR scans are available to imagers at the time of interpretation along with the computer-processed composite images indicating change. These composite images together with the source images have been found helpful in clinical practice for identifying new lesions, particularly among confluent lesions, which are then confirmed or refuted on the source imaging. However, these synthetic composite images are not used in isolation for establishing the diagnosis.

Of the 197 patients imaged with our MS protocol, 53 were excluded because they did not have any prior studies or the prior examination was not acquired with the necessary 3D-FLAIR sequence used for image analysis, usually because the previous ex-

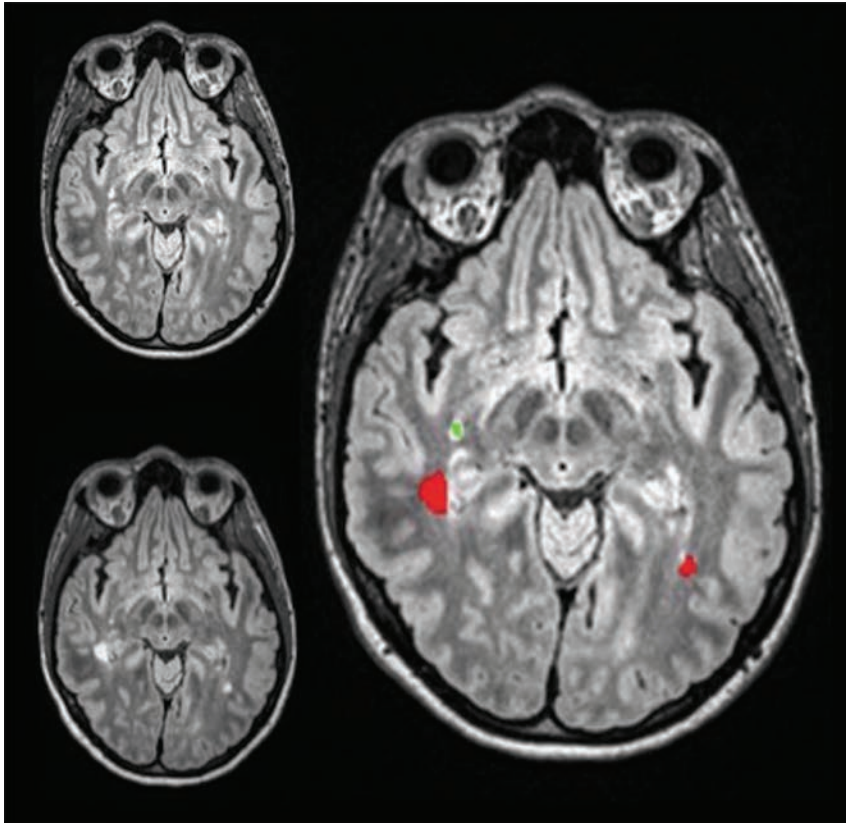


**FIG 1.** Prior FLAIR MR imaging in the upper left-hand corner, current FLAIR MR imaging in the lower left-hand corner, and the coregistered composite image on the right displaying new lesions in red, while lesions that regressed are green.

**Patients on IMT at the time of their most recent scan**

Type of IMT	No. of Patients
Fingolimod	11
Glatiramer acetate	36
Interferon $\beta$ -1a	23
Ocrelizumab	1
Dimethyl fumarate	1
Teriflunomide	9
Natalizumab	1

**Note:**—IMT indicates immune-modulating therapy.

aminations were performed at an outside institution. An additional 2 patients were excluded because they did not receive or declined contrast for their scan. Another 2 were excluded due to nondiagnostic imaging or the absence of critical sequences. We eliminated, in total, 57 cases from consideration for these reasons.

The composite images of the remaining 140 patients were then reviewed independently by 2 investigators to determine the lesion burden of white matter lesions on the most recent scan compared with the prior one. This was characterized in terms of increase, decrease, or stability on the basis of the nonenhanced FLAIR sequence, often supported by proton-density sequences. The source images used to create the composite images were reviewed at the same time by the investigators to validate the computer-generated markings because artifactual lesions in the posterior fossa and parasellar region are commonplace. Then each of the investigators recorded their decision regarding lesion enhancement based on the contrast-enhanced T1-weighted sequence. The presence of any parenchymal enhancing lesions, with or without

changes on the FLAIR scan, were recorded. The imaging findings of each of the study observers were then correlated with the report generated by the attending radiologist at the time of the initial interpretation, and agreement or differences with the final report were recorded.

The independent assessments of the 2 investigators were recorded on an Excel (Microsoft, Redmond, Washington) spreadsheet, and their findings for all variables were compared to determine whether there were any differences. Sixteen cases were identified with differences between the observers' findings or that were discordant with the initial report. These were then reviewed by a third more senior investigator (a neurologist with a Certificate of Added Qualification with 27 years' experience) to resolve any differences. The senior investigator agreed 14 times with investigator A and 2 times with investigator B.

Among these 140 cases, 3 were identified in which there was enhancement of a pre-existing lesion. All of these were also reviewed by the third, more senior investigator. Two of the 3 cases were excluded from the study because the findings

indicated a pathologic process other than multiple sclerosis. In one case, the findings were most consistent with progressive multifocal leukoencephalopathy, and in the second, the findings were consistent with a low-grade brain tumor based on prolonged mass effect and persistent, stable enhancement.

Of the final 138 patients included in the data analysis, 39 were men and 99 were women, and the entire cohort had a mean age of  $49.1 \pm 13.3$  years. Forty-one patients had specific mention of a clinical diagnosis of a certain type of MS in the electronic medical record at some point in their history. Four had secondary-progressive MS, 3 had possible primary-progressive MS, 33 had relapsing-remitting MS (RRMS), and one was thought to have secondary-progressive MS or RRMS. For the remaining 97 patients, we could not find a specific classification of MS mentioned in the clinical record. We assume that the overwhelming majority of these remaining patients had RRMS, in keeping with the expectation that 85% of patients will meet the criteria for this diagnosis.<sup>38</sup>

Data on 133 patients regarding whether they were on immune-modulating therapy was collected. Of these patients, 82 were on immune-modulating therapy at the time of their most recent scan (Table).

**RESULTS**

Thirty-three scans (24%) showed an increase in white matter lesion burden, 102 scans (74%) showed stable lesion burden, and 3 scans (2%) showed a decrease in lesion burden. Of the scans that showed an increased lesion burden, 31 demonstrated new discrete

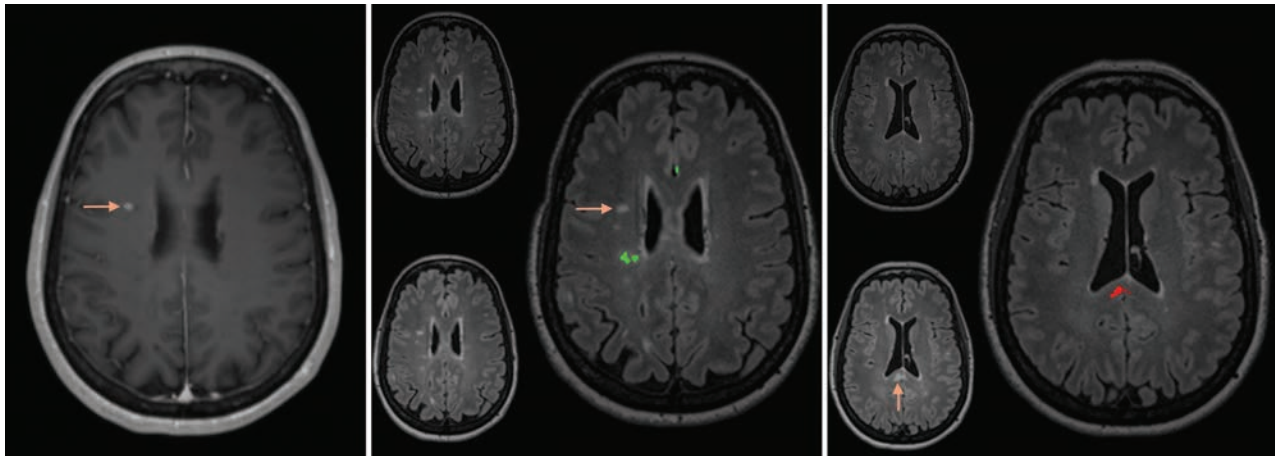


**FIG 2.** *Left:* Contrast-enhanced T1 MR imaging shows enhancement of a pre-existing lesion in the right centrum semiovale (*arrow*). *Middle:* The composite image from the coregistering software shows no growth of this corresponding lesion on FLAIR between the prior and current study (*arrow*). Additionally, 1 lesion had slightly regressed in the right posterior corona radiata (green on the composite image). *Right:* The composite image using the coregistering software at a more inferior level shows evidence of a new lesion in the splenium of the corpus callosum (*arrow* and red on composite image on the *right*).

lesions, while 2 demonstrated only enlargement of pre-existing lesions.

Fourteen scans (10%) demonstrated enhancing new lesions, all of which also demonstrated an increase in lesion burden. In 1 patient, there was enhancement of a single pre-existing lesion that appeared unchanged in size, but the same scan showed an overall increase in lesion burden with enhancement of other, new lesions (Fig 2). In short, we could not find, among the 138 follow-up studies reviewed, a single case that demonstrated abnormal parenchymal enhancement without increased lesion burden.

Of note, in the 1 instance of enhancement of a pre-existing lesion, no specific phenotype of MS was indicated in the clinical history.

## DISCUSSION

While prudent use of contrast is a cornerstone of practice for every responsible radiology department, this still allows considerable latitude when risk is perceived as nearly nonexistent and the expected small gains in sensitivity support its use. With the emerging evidence of T1 shortening in brain tissue linked to contrast administration and recent FDA warnings regarding the use of MR imaging contrast, it is an appropriate time to consider an evidence-based approach to the use of MR imaging contrast in common clinical situations. In addition, there is also a responsibility to minimize cost because contrast agents add to the examination cost due to the price of the agent itself and the added time for administration, image generation, and interpretation.

We decided to focus on the imaging of patients with multiple sclerosis because their exposure to contrast agents can be substantial because their imaging often starts at a young age and continues for decades. While there have been a few other studies examining FLAIR signal characteristics of specific, individual lesions in patients with MS and their prediction of lesion enhancement, none of these studies examine our specific question regarding the relationship of enhancement based on each patient's change in the entire white matter lesion load.<sup>39,40</sup>

On the basis of the results in our patient group reported here,

enhancing lesions were found in 10% of the follow-up scans. This is well within the expected range for our patients based on clinical experience. Lesion burden progression was evident in 24% of our subjects, also not surprising on the basis of clinical experience, and all patients with enhancing lesions also had evidence of progression.

When considered from the perspective of minimizing contrast use, one could argue that contrast administration could be withheld in those patients with stable lesions on the basis of our results. Contrast could also be selectively administered to only those patients with evidence of progression on their noncontrast imaging. Additionally, this decision to administer contrast in those patients with progression may also be influenced by whether the additional findings of enhancing lesions would then alter the clinical management of the patient. In our experience, it is not currently feasible to complete the interpretation of the imaging with the processed imaging components while the patient waits in the scanner for a decision, so with this approach, patients would need to come back for their enhanced imaging.

Because our patient population consists almost entirely of patients with RRMS and there may be differences among the different phenotypes of MS, our findings may not be generalized to all types of MS. However, this approach could be reserved for patients with known RRMS, and that would still include >80% of patients with MS.

Adoption of this approach would then avoid unnecessary use of contrast. While we can only suggest this as a probability not proved by this study, it is likely that this proposed change in practice would provide a substantial cost savings to the health system and patients by shortening examination time, reducing examination complexity, and minimizing patients' risks. However, to make a more definitive claim regarding cost savings, it would be necessary to systematically quantify the true cost and complexity required for the remaining one-quarter of patients with evidence of lesion progression returning for contrast administration.

While this proposed approach may be somewhat novel, we

believe these findings at least offer patients with RRMS a choice: completing the MR imaging examination with contrast in 1 session or imaging without contrast with the awareness that additional imaging may be necessary at a later date. This choice may be influenced by personal concern regarding receiving contrast, difficulty in returning for contrast imaging based on factors such as distance and work schedule, as well as obtaining insurance approval. However, one would think that some agreement could be reached with insurers based on the assurance that the overall number of enhanced studies and accompanying additional costs would be reduced.

While a larger study with more patients and a larger proportion of patients with progressive MS would be ideal, this study population, we believe, provides evidence that supports a larger-but-anecdotal clinical experience that enhancement is seen only with progression. The number of cases reviewed (i.e. >100) is in keeping with other studies published in the literature.<sup>41</sup> Furthermore, there are precedents for the use of imaging with marginally lower sensitivity to minimize overall risk and cost such as the use of MRA rather than CTA for aneurysm screening in patients with a family history of aneurysms.

There were 2 cases in the study group that appeared to have a disease process in addition to MS. One had imaging findings of a brain stem tumor; the other had findings of progressive multifocal leukoencephalopathy, which rarely occurs in patients with MS treated with immune modulators. Although excluded from the analysis, with our proposed approach, both patients would have received contrast had they been imaged initially with noncontrast MR imaging because of the new white matter findings in one and unresolving mass effect in the second.

One additional limitation of this study is the nature of our postcontrast imaging. We do not routinely use pulse sequences that maximize visualization of contrast enhancement, such as magnetization transfer or fat-suppressed T1-weighted postcontrast imaging mainly due to our choice of imaging all these patients at 3T, because that allows generation of high-quality FLAIR volume images for the postprocessing software to improve detection of progression. We also recognize that this type of software is not available at most imaging centers, but there are other, similar products available,<sup>42</sup> and we were intent on maximizing detection of progression for this study. We believe that this approach improves detection of new white matter lesions and may have contributed to our overall finding that enhancement of lesions was only evident when there was progression. However, we cannot say that careful review of FLAIR, proton-density, and T2-weighted scans performed in a consistent manner using landmarks determined from sagittal scans such as the anterior/posterior commissure line without computer processing would not have provided identical results.

Finally, we did not include spine imaging in this study and recognize that many sites, including our own, include cervical and thoracic imaging on routine follow-up. On the basis of our experience that enhancing cord lesions are much less common than brain lesions and that there is considerable variability in the quality of spinal cord imaging between examinations, we elected to focus on brain imaging to evaluate a substantial number of cases with enhancing lesions. It seems very likely that this same ap-

proach (ie, enhancement only for patients with progression) could be used for spinal cord imaging because the underlying biology of MS in the brain and cord should be comparable. Nevertheless, we did not directly examine that question in this study. We also did not include findings of leptomeningeal enhancement or cortical lesions because these require specialized imaging sequences that are not routine at our institution and their significance is still being evaluated.

## CONCLUSIONS

In our study of patients with MS undergoing routine MR imaging using a 3D-FLAIR acquisition and processed images that highlight new lesions, we found that all cases with enhancing brain lesions had evidence of progression on the noncontrast imaging. Because progression was only evident in 24% of our cases, approximately three-quarters of the patients having follow-up scans did not benefit from contrast enhancement. We believe that this has implications regarding the need for contrast enhancement in all follow-up scans in this patient population.

## REFERENCES

1. Rovira À, Wattjes MP, Tintoré M, et al; MAGNIMS study group. **Evidence-based guidelines: MAGNIMS consensus guidelines on the use of MRI in multiple sclerosis-clinical implementation in the diagnostic process.** *Nat Rev Neurol* 2015;11:471–82 [CrossRef](#) [Medline](#)
2. Traboulsee A, Simon JH, Stone L, et al. **Revised recommendations of the Consortium of MS Centers Task Force for a standardized MRI protocol and clinical guidelines for the diagnosis and follow-up of multiple sclerosis.** *AJNR Am J Neuroradiol* 2016;37:394–401 [CrossRef](#) [Medline](#)
3. Simon JH, Li D, Traboulsee A, et al. **Standardized MR imaging protocol for multiple sclerosis: Consortium of MS Centers consensus guidelines.** *AJNR Am J Neuroradiol* 2006;27:455–61 [Medline](#)
4. Rovira A, Auger C, Alonso J. **Magnetic resonance monitoring of lesion evolution in multiple sclerosis.** *Ther Adv Neurol Disord* 2013; 6:298–310 [CrossRef](#) [Medline](#)
5. Cotton F, Weiner HL, Jolesz FA, et al. **MRI contrast uptake in new lesions in relapsing-remitting MS followed at weekly intervals.** *Neurology* 2003;60:640–46 [CrossRef](#) [Medline](#)
6. Absinta M, Sati P, Reich DS. **Advanced MRI and staging of multiple sclerosis lesions.** *Nat Rev Neurol* 2016;12:358–68 [CrossRef](#) [Medline](#)
7. Frischer JM, Bramow S, Dal-Bianco A, et al. **The relation between inflammation and neurodegeneration in multiple sclerosis brains.** *Brain* 2009;132(Pt 5):1175–89 [CrossRef](#) [Medline](#)
8. Hammond KE, Metcalf M, Carvajal L, et al. **Quantitative *in vivo* magnetic resonance imaging of multiple sclerosis at 7 Tesla with sensitivity to iron.** *Ann Neurol* 2008;64:707–13 [CrossRef](#) [Medline](#)
9. Absinta M, Sati P, Gaitan MI, et al. **Seven-Tesla phase imaging of acute multiple sclerosis lesions: a new window into the inflammatory process.** *Ann Neurol* 2013;74:669–78 [CrossRef](#) [Medline](#)
10. Mehta V, Pei W, Yang G, et al. **Iron is a sensitive biomarker for inflammation in multiple sclerosis lesions.** *PLoS One* 2013;8:e57573 [CrossRef](#) [Medline](#)
11. Pitt D, Boster A, Pei W, et al. **Imaging cortical lesions in multiple sclerosis with ultra-high-field magnetic resonance imaging.** *Arch Neurol* 2010;67:812–18 [CrossRef](#) [Medline](#)
12. Bagnato F, Hametner S, Yao B, et al. **Tracking iron in multiple sclerosis: a combined imaging and histopathological study at 7 Tesla.** *Brain* 2011;134:3602–15 [CrossRef](#) [Medline](#)
13. Bian W, Harter K, Hammond-Rosenbluth KE, et al. **A serial *in vivo* 7T magnetic resonance phase imaging study of white matter lesions in multiple sclerosis.** *Mult Scler* 2013;19:69–75 [CrossRef](#) [Medline](#)
14. Yao B, Bagnato F, Matsuura E, et al. **Chronic multiple sclerosis**

- lesions: characterization with high-field-strength MR imaging. *Radiology* 2012;262:206–15 CrossRef Medline
15. Hagemeyer J, Heininen-Brown M, Poloni GU, et al. **Iron deposition in multiple sclerosis lesions measured by susceptibility-weighted imaging filtered phase: a case control study.** *J Magn Reson Imaging* 2012;36:73–83 CrossRef Medline
  16. Choi SR, Howell OW, Carassiti D, et al. **Meningeal inflammation plays a role in the pathology of primary progressive multiple sclerosis.** *Brain* 2012;135(Pt 10):2925–37 CrossRef Medline
  17. Lucchinetti CF, Popescu BF, Bunyan RF, et al. **Inflammatory cortical demyelination in early multiple sclerosis.** *N Engl J Med* 2011;365:2188–97 CrossRef Medline
  18. Popescu BF, Lucchinetti CF. **Meningeal and cortical grey matter pathology in multiple sclerosis.** *BMC Neurol* 2012;12:11 CrossRef Medline
  19. Magliozzi R, Howell OW, Reeves C, et al. **A gradient of neuronal loss and meningeal inflammation in multiple sclerosis.** *Ann Neurol* 2010;68:477–93 CrossRef Medline
  20. Magliozzi R, Howell O, Vora A, et al. **Meningeal B-cell follicles in secondary progressive multiple sclerosis associate with early onset of disease and severe cortical pathology.** *Brain* 2007;130(Pt 4):1089–104 Medline
  21. Howell OW, Reeves CA, Nicholas R, et al. **Meningeal inflammation is widespread and linked to cortical pathology in multiple sclerosis.** *Brain* 2011;134(Pt 9):2755–71 CrossRef Medline
  22. Daams M, Geurts JJ, Barkhof F. **Cortical imaging in multiple sclerosis: recent findings and ‘grand challenges.’** *Curr Opin Neurol* 2013;26:345–52 CrossRef Medline
  23. Eisele P, Griebbe M, Szabo K, et al. **Investigation of leptomeningeal enhancement in MS: a postcontrast FLAIR MRI study.** *Neurology* 2015;84:770–75 CrossRef Medline
  24. Absinta M, Vuolo L, Rao A, et al. **Gadolinium-based MRI characterization of leptomeningeal inflammation in multiple sclerosis.** *Neurology* 2015;85:18–28 CrossRef Medline
  25. Zivadinov R, Ramasamy DP, Vaneckova M, et al. **Leptomeningeal contrast enhancement is associated with progression of cortical atrophy in MS: a retrospective, pilot, observational longitudinal study.** *Mult Scler* 2017;23:1336–45 CrossRef Medline
  26. Miller DH, Barkhof F, Nauta JJ. **Gadolinium enhancement increases the sensitivity of MRI in detecting disease activity in multiple sclerosis.** *Brain* 1993;116:1077–94 CrossRef Medline
  27. Milo R, Kahana E. **Multiple sclerosis: geoepidemiology, genetics and the environment.** *Autoimmun Rev* 2010;9:A387–94 CrossRef Medline
  28. Brønnum-Hansen H, Koch-Henriksen N, Stenager E. **Trends in survival and cause of death in Danish patients with multiple sclerosis.** *Brain* 2004;127(Pt 4):844–50 CrossRef Medline
  29. Kanda T, Ishii K, Kawaguchi H, et al. **High signal intensity in the dentate nucleus and globus pallidus on unenhanced T1-weighted MR images: relationship with increasing cumulative dose of a gadolinium-based contrast material.** *Radiology* 2014;270:834–41 CrossRef Medline
  30. Kanda T, Fukusato T, Matsuda M, et al. **Gadolinium-based contrast agent accumulates in the brain even in subjects without severe renal dysfunction: evaluation of autopsy brain specimens with inductively coupled plasma mass spectroscopy.** *Radiology* 2015;276:228–32 CrossRef Medline
  31. McDonald RJ, McDonald JS, Kallmes DF, et al. **Intracranial gadolinium deposition after contrast-enhanced MR imaging.** *Radiology* 2015;275:772–82 CrossRef Medline
  32. Murata N, Gonzalez-Cuyar LF, Murata K, et al. **Macrocyclic and other non-group I gadolinium contrast agents deposit low levels of gadolinium in brain and bone tissue: preliminary results from 9 patients with normal renal function.** *Invest Radiol* 2016;51:447–53 CrossRef Medline
  33. McDonald RJ, McDonald JS, Kallmes DF, et al. **Gadolinium deposition in human brain tissues after contrast-enhanced MR imaging in adult patients without intracranial abnormalities.** *Radiology* 2017;285:546–54 CrossRef Medline
  34. FDA Drug Safety Communication: FDA warns that gadolinium-based contrast agents (GBCAs) are retained in the body; requires new class warnings. <https://www.fda.gov/Drugs/DrugSafety/ucm589213.htm>. Accessed March 5, 2018
  35. Gupta A, Al-Dasuqi K, Xia F, et al. **The use of noncontrast quantitative MRI to detect gadolinium-enhancing multiple sclerosis brain lesions: a systematic review and meta-analysis.** *AJNR Am J Neuroradiol* 2017;38:1317–22 CrossRef Medline
  36. Wattjes MP, Rovira À, Miller D, et al; MAGNIMS study group. **Evidence-based guidelines: MAGNIMS consensus guidelines on the use of MRI in multiple sclerosis—establishing disease prognosis and monitoring patients.** *Nat Rev Neurol* 2015;11:597–606 CrossRef Medline
  37. Bilello M, Arkuszewski M, Nucifora P, et al. **Multiple sclerosis: identification of temporal changes in brain lesions with computer-assisted detection software.** *Neuroradiol J* 2013;26:143–50 CrossRef Medline
  38. Dutta R, Trapp BD. **Relapsing and progressive forms of multiple sclerosis: insights from pathology.** *Curr Opin Neurol* 2014;27:271–78 CrossRef Medline
  39. Treabă CA, Bălașa R, Podeanu DM, et al. **Cerebral lesions of multiple sclerosis: is gadolinium always irreplaceable in assessing lesion activity?** *Diagn Interv Radiol* 2014;20:178–84 CrossRef Medline
  40. Guranda M, Essig M, Poulin A, et al. **Fluid-attenuated inversion recovery signal intensity as a predictor of gadolinium enhancement in relapsing-remitting multiple sclerosis.** *Int J MS Care* 2018;20:62–66 CrossRef Medline
  41. Elster AD, Mirza W. **MR imaging in chronic partial epilepsy: role of contrast enhancement.** *AJNR Am J Neuroradiol* 1991;12:165–70 Medline
  42. Dworkin JD, Linn KA, Oguz I, et al; North American Imaging in Multiple Sclerosis Cooperative. **An automated statistical technique for counting distinct multiple sclerosis lesions.** *AJNR Am J Neuroradiol* 2018;39:626–33 CrossRef Medline

# The Central Vein: FLAIR Signal Abnormalities Associated with Developmental Venous Anomalies in Patients with Multiple Sclerosis

D.M. Rogers, L.M. Shah, and R.H. Wiggins III

## ABSTRACT

**BACKGROUND AND PURPOSE:** Demyelination is a recently recognized cause of FLAIR hyperintensities associated with developmental venous anomalies. Our purpose was to quantify the prevalence of white matter signal abnormalities associated with developmental venous anomalies in patients with multiple sclerosis compared with controls.

**MATERIALS AND METHODS:** A retrospective, blinded, multireader study compared the prevalence of FLAIR hyperintense signal abnormalities adjacent to developmental venous anomalies in patients with MS compared with controls (patients with developmental venous anomalies without MS). Study findings were positive if a central vein was demonstrated using FLAIR and contrast-enhanced fat-saturated T1 sequences. Imaging parameters also included developmental venous anomaly location, developmental venous anomaly drainage, white matter lesion size, and depth of white matter lesions. Clinical parameters included age, sex, and the presence of confounding variables (hypertension, diabetes, migraines, and/or vasculopathy).

**RESULTS:** FLAIR signal abnormality was present around 47.3% (35/74) of developmental venous anomalies in patients with MS, and 13.5% (10/74) of developmental venous anomalies in the control group ( $P < .001$ ). The multivariate logistic regression model controlling for covariates (including migraines, hypertension, diabetes mellitus, vasculopathy, age, sex, and drainage direction of developmental venous anomalies) showed that the odds of FLAIR hyperintensity around developmental venous anomalies was 6.7-fold higher in patients with MS (relative risk MS = 6.68; 95% CI, 2.79–15.97;  $P < .001$ ).

**CONCLUSIONS:** The association of developmental venous anomalies and FLAIR hyperintensities was more common in patients with MS, which suggests that the underlying demyelinating pathologic process of MS may be the cause of this propensity in patients with MS. Impaired venous drainage in the territory of developmental venous anomalies may predispose to development of these lesions, and an associated central vein is helpful in understanding an atypical location of MS plaques.

**ABBREVIATIONS:** CCSVI = chronic cerebrospinal venous insufficiency; DVA = developmental venous anomaly

Developmental venous anomalies (DVAs) are the most common congenital cerebral vascular malformation.<sup>1</sup> They have a pathognomonic “umbrella” or “medusa” appearance on contrast-enhanced T1 or T2\* sequences due to numerous small medullary veins converging on a central collector vein, which may drain into a superficial cortical vein, dural venous sinus, or the deep venous system via a subependymal vein.<sup>2</sup> Because DVAs are usually asymptomatic and represent the sole venous outflow to

the brain parenchyma that they supply, they are known as “do not touch” lesions.<sup>3,4</sup>

Signal abnormalities on conventional FLAIR sequences are commonly observed in the drainage territory of DVAs. Prior studies have found the prevalence of white matter FLAIR hyperintensity near incidental DVAs to range from 11.6% to 30.7%.<sup>5–8</sup> These FLAIR signal abnormalities tend to be larger and occur more frequently in older patients.<sup>5–8</sup> Determining the etiology of the MR signal abnormalities around DVAs has been problematic because they are usually asymptomatic, and biopsy of such a lesion is unreasonably invasive. Edema or gliosis or both resulting from altered hemodynamics within the brain parenchyma drained by a DVA have been hypothesized as causes of the FLAIR signal abnormality around incidentally discovered DVAs, which is supported by findings on dynamic susceptibility contrast-enhanced perfusion-weighted imaging, in which CBV, CBF, TTP, and MTT are elevated.<sup>9–13</sup>

Received May 31, 2018; accepted after revision August 9.

From the Department of Radiology and Imaging Sciences, University of Utah Health Sciences Center, Salt Lake City, Utah.

Please address correspondence to Douglas M. Rogers, MD, 30 North 1900 East, #1A071, Salt Lake City, UT 34132-2140; e-mail: Douglas.rogers@hsc.utah.edu; @rogersmdouglas

<http://dx.doi.org/10.3174/ajnr.A5819>

However, sequelae of demyelination have recently been recognized as another cause of signal abnormality surrounding DVAs in patients with multiple sclerosis. Two case series have described tumefactive demyelination occurring adjacent to DVAs in patients with MS.<sup>14,15</sup> MS plaques have long been known to occur in a perivenular distribution (eg, Dawson fingers), and the development of 3T FLAIR\* and 7T MR imaging has demonstrated that almost all MS plaques have a central vein.<sup>16-18</sup> Gaitán et al<sup>17</sup> showed on dynamic contrast-enhanced 7T MR imaging that small MS plaques enhance centrifugally from a central vein, and the “central vein sign” has been identified by the North American Imaging in Multiple Sclerosis Cooperative as an imaging feature with potential prospective diagnostic utility for the diagnosis of MS.<sup>18</sup>

DVAs are a common incidental finding on contrast-enhanced brain MR imaging. Two prior studies reported the prevalence of DVAs in patients with MS as 12.1% and 12.6%, respectively.<sup>19,20</sup> Our hypothesis is that demyelination is a pathologic cause of DVA-associated FLAIR hyperintensities in patients with MS. The purpose of this retrospective study was to compare the prevalence of DVA-associated FLAIR hyperintensities with a central vein in patients with MS and patients without MS who had incidentally detected DVAs. A greater prevalence of FLAIR signal abnormalities adjacent to DVAs in patients with MS compared with controls and/or the presence of other distinguishing features (such as lesion enhancement in patients with MS) would support the underlying demyelinating pathologic process of MS as the cause of this propensity in the MS group.

## MATERIALS AND METHODS

This was an institutional review board–exempted retrospective study comparing the prevalence of white matter signal abnormalities on the FLAIR sequence adjacent to DVAs in patients with MS and patients without MS incidentally found to have DVAs.

### Subjects and Imaging

Using a radiology report search engine (Montage; Nuance Communications, Burlington, Massachusetts), we searched brain MR imaging studies obtained at an academic university hospital using the terms “developmental venous anomaly (or DVA)” AND “multiple sclerosis (or MS)” for the study group, and “developmental venous anomaly (or DVA)” for the control group.

For inclusion criteria, FLAIR and T1 postcontrast images of adequate quality must have been available for interpretation, and a clearly delineated DVA must have been present. Additionally, for the study group, the patients must have had a clinical diagnosis of relapsing-remitting MS by a neurologist and met the revised 2017 McDonald criteria for MS diagnosis.<sup>21</sup> Cases were excluded that had adjacent postoperative changes, vascular malformation, or hemorrhage (such as a cavernous malformation), as defined by susceptibility blooming artifacts adjacent to the DVA on gradient recalled-echo or susceptibility-weighted imaging.

For the study group, our search resulted in 81 DVAs found in 78 patients with MS with brain MR imaging studies performed between 2013 and 2017. One case was excluded due to an adjacent cavernous malformation, and 6 were excluded due to association with adjacent confluent white matter lesions (this imaging crite-

**Table 1: Study and control population characteristics**

Characteristic	Multiple Sclerosis (n = 74)	Controls (n = 74)	P Value
Mean age (SD) (yr)	45.1 (13.5)	50.7 (18.4)	.036
Sex: female	49 (66.2%)	37 (50.0%)	.045
MRI field strength 3T	18 (24.3%)	11 (14.9%)	
MRI field strength 1.5T	56 (75.7%)	63 (85.1%)	
DVA location			
Lobar	49 (66.2%)	51 (68.9%)	
Basal ganglia	6 (8.1%)	5 (6.7%)	
Cerebellum	18 (24.3%)	15 (20.3%)	
Brain stem	1 (1.4%)	3 (4.1%)	
DVA drainage			
Superficial	50 (67.5%)	46 (62.1%)	
Deep	21 (28.4%)	25 (33.8%)	
Both	3 (4.1%)	3 (4.1%)	
Hypertension	13 (17.6%)	15 (20.3%)	
Diabetes	3 (4.1%)	6 (8.1%)	
Migraines	10 (13.5%)	10 (13.5%)	
Intracranial vasculitis	1 (1.4%)	1 (1.4%)	

rión is discussed later in the Materials and Methods section). These exclusions left 74 DVAs in the final MS study population.

For the control group, the 78 most recent brain MR imaging cases (from March to September 2017) with a DVA and without MS were analyzed, yielding 79 clearly delineated DVAs in 78 patients. Five cases were excluded due to the presence of an adjacent cavernous malformation for a final cohort of 74 DVAs. These scans were obtained for myriad reasons, most commonly to evaluate a neoplasm elsewhere in the brain or as a staging scan for possible malignancy.

Diagnostic MR imaging was performed on Prisma, Aera, Avanto, and Espree 1.5T scanners, or Prisma and Verio 3T scanners (Siemens, Erlangen, Germany). Most scans were obtained with a magnetic field strength of 1.5T (80.4%), and the remainder were obtained at 3T (19.6%). There was no significant difference in the number of studies performed at 1.5 T and 3T between the study and control groups (Table 1). While there was some mild variability, a typical 2D-FLAIR sequence had a TR of 9000 ms and a TE of 110 ms with 5-mm slice thickness and no gap. FLAIR sequences were performed with chemical fat saturation. Typical contrast-enhanced 2D-T1 sequences had a TR of 600 ms and a TE of 10 ms with 5-mm slice thickness and no gap.

### Image Analysis and Chart Review

Two radiologists, a senior neuroradiologist with 25 years of experience and a senior resident with 4 years of experience, performed a blinded and randomized review of the images on a PACS. In cases of disagreement, a second blinded neuroradiologist with 15 years of experience served as a tie-breaker. Criteria for a positive study were adapted from the central vein sign as described in the 2016 consensus statement from the North American Imaging in Multiple Sclerosis Cooperative.<sup>18</sup> In contrast to criteria used in the literature in which FLAIR hyperintensity in the vicinity of the DVA was used, we decided to use a stricter central vein criterion as subsequently described because it is more specific for demyelination. While Sati et al<sup>18</sup> assessed the central vein and associated FLAIR hyperintense plaques on a single 3T FLAIR\* sequence, we localized lesions with side-by-side comparison of conventional FLAIR and T1 postcontrast images.

**Table 2: Results**

Variable	Multiple Sclerosis (n = 74)	Controls (n = 74)	P Value
Positive FLAIR hyperintensity with a central vein	35 (47.3%)	10 (13.5%)	<.001
FLAIR hyperintensity depth			
Juxtacortical	13 (37.1%)	5 (50.0%)	
Subcortical	12 (37.5%)	3 (30.0%)	
Periventricular	10 (28.6%)	2 (20.0%)	
Mean FLAIR hyperintensity width (SD) (mm)	8.5 (7.3)	8.0 (4.5)	
Enhancing lesions	4 (11.4%)	0 (0%)	
Location of DVA with associated FLAIR hyperintensity			
Lobar	29 (82.9%)	10 (100%)	
Basal ganglia	2 (5.7%)	0 (0%)	
Cerebellum	4 (11.4%)	0 (0%)	
Brain stem	0 (0%)	0 (0%)	
Drainage of DVA with associated FLAIR hyperintensity			
Superficial	23 (65.7%)	6 (60%)	
Deep	12 (34.3%)	2 (20%)	
Both	0 (0%)	2 (20%)	

Criteria for positive FLAIR signal abnormality adjacent to a DVA with a central vein were the following:

1) The DVA vessel must pass through the FLAIR hyperintense lesion so that it is directly abutting it, approximately equidistant from the edges of the lesion and passing through it at no more than 2 locations.

2) The FLAIR hyperintense lesion is at least 3 mm in all planes.

3) Studies were excluded if the DVA-associated FLAIR hyperintense lesion merged with another parenchymal lesion (eg, a superficial DVA extending toward multiple large periventricular plaques). While these studies might represent DVA-associated lesions, they were not included to avoid the possibility of chance associations with adjacent lesions in patients with MS who may have an overall higher burden of white matter disease.

4) Care was taken not to count flow-related FLAIR signal within the vessel itself as a surrounding parenchymal abnormality.

Imaging parameters included DVA location (lobar, basal ganglia, cerebellum, or brain stem), DVA drainage direction (superficial, deep, or both), the presence of an associated white matter lesion meeting the aforementioned central vein criteria, width of the white matter lesion measured in millimeters, and depth of the white matter lesion (juxtacortical, subcortical, or periventricular). The DVA drainage direction was defined as the confluent draining vessel extending either toward the surface of the brain (superficial), toward the ventricles (deep), or both. “Juxtacortical” was defined as a lesion that directly abuts the cortex, while a “periventricular” lesion directly abuts the lateral, third or fourth ventricles.

Clinical electronic medical record chart review was performed to confirm that study group patients had been diagnosed with MS by a neurologist and met the revised 2017 McDonald criteria for the diagnosis of MS. Clinical parameters documented on the electronic medical record review included patient age and sex, duration since the time of diagnosis of MS, and potential confounding variables for white matter FLAIR hyperintensities such as hypertension, diabetes, migraines, and/or intracranial vasculitis.

## Data Analysis

Comparisons between the groups for dichotomous outcomes were performed using the  $\chi^2$  test if the minimum expected cell frequency assumption was met (80% of the cells have expected frequencies of at least 5 and no cell has an expected frequency of <1). The McNemar test was used for paired data. For comparison of paired groups on an interval-scaled variable, a *t* test was performed. Poisson regression was used for a binary outcome, with a robust variance estimate. A multivariate logistic regression model was created with positive FLAIR signal around DVAs as an outcome while controlling for covariates (including migraines, hypertension, diabetes mellitus, vasculopathy, age, sex, and DVA drainage direction). Interrater

reliability was measured using the  $\kappa$  coefficient, which is the proportion of agreement beyond expected chance agreement.

## RESULTS

Study and control population characteristics are compared in Table 1. Of note, the MS study group was slightly younger than the control population ( $P = .036$ ), with a female preponderance ( $P = .045$ ). There were no significant differences in MR imaging field strength, DVA location, or DVA drainage in the study and control populations. Clinical parameters, including the presence of hypertension, diabetes, migraines, and/or intracranial vasculitis, were also not significantly different in the study and control populations.

FLAIR signal abnormality meeting the central vein criteria was present adjacent to 47.3% (35/74) of DVAs in patients with MS and adjacent to 13.5% (10/74) of DVAs in the control group ( $P < .001$ ) (Table 2). A multivariate logistic regression model controlling for covariates (including migraines, hypertension, diabetes mellitus, vasculopathy, age, sex, and drainage direction of DVAs) showed that the odds of FLAIR hyperintensity around DVAs was 6.7-fold higher in patients with MS (relative risk MS = 6.68; 95% CI, 2.79–15.97;  $P < .001$ ). In patients with MS, 11.4% (4/35) of the lesions demonstrated enhancement compared with none in the control group. There was no significant difference in FLAIR signal surrounding DVAs according to sex in the patients with MS ( $P = .504$ ) or in the control subjects ( $P = .197$ ). There was a 1.4-fold increase in FLAIR signal surrounding DVAs in controls for every 10-year increase in age (relative risk MS = 1.40; 95% CI, 1.01–1.94;  $P = .047$ ). No such age-related association was present in the MS cohort. The mean number of years between the diagnosis of patients with MS and current imaging was  $10.3 \pm 8.6$  years (range, 1–37 years). All except 4 patients with MS were on disease-modulating immunotherapy. Two of these patients had DVA-associated FLAIR hyperintensities, neither of which demonstrated enhancement. Examples of FLAIR hyperintense lesions adjacent to DVAs in patients with MS are shown in Fig 1, and

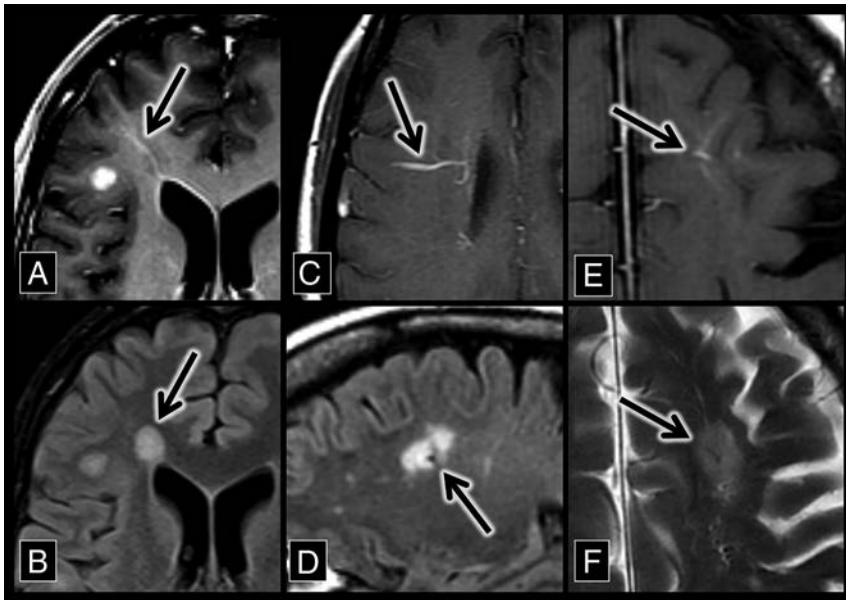


**FIG 1.** Developmental venous anomaly–associated lesions in patients with MS. *A*, An axial contrast-enhanced T1 sequence shows a right frontal lobe DVA (arrow) with surrounding T1 hypointensity. *B*, An axial FLAIR sequence shows hyperintensity (arrow) that corresponds to the DVA and associated T1 hypointensity in *A*. *C*, An axial contrast-enhanced T1 sequence shows a right frontal lobe DVA (arrow). *D*, A sagittal FLAIR sequence shows a flow void with adjacent hyperintensity (the central vein sign, arrow), which corresponds to the DVA in *C*. *E*, An axial contrast-enhanced T1 sequence shows a left frontal lobe DVA (arrow). *F*, An axial T2 sequence shows a flow void with adjacent hyperintensity (the central vein sign, arrow), which corresponds to the DVA in *E*.

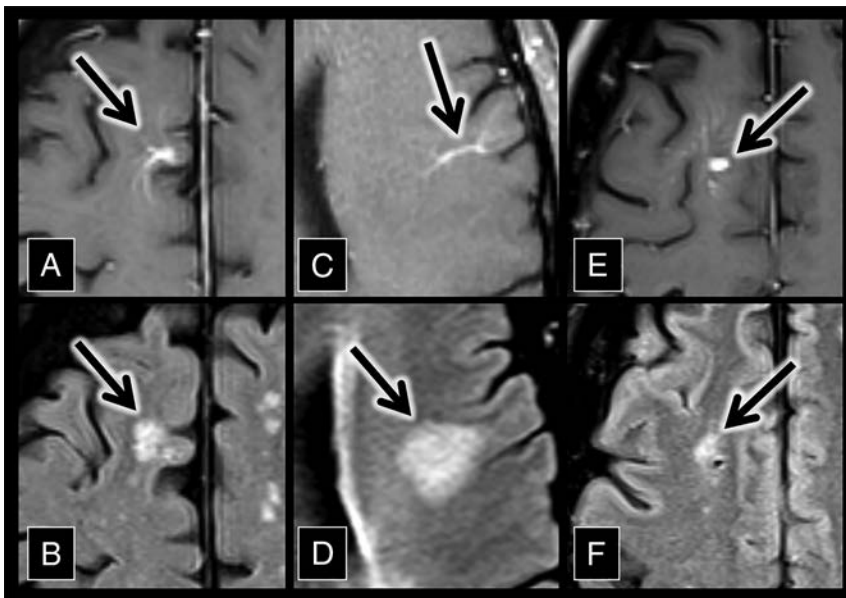


**FIG 2.** Developmental venous anomaly–associated lesions in the control group. *A*, An axial contrast-enhanced T1 sequence shows a right frontal lobe DVA (arrow). *B*, An axial FLAIR sequence shows hyperintensity (arrow) adjacent to the DVA in *A*. *C*, An axial contrast-enhanced T1 sequence shows a left frontal lobe DVA (arrow). *D*, An axial FLAIR sequence shows hyperintensity (arrow) adjacent to the DVA in *C*. *E*, An axial contrast-enhanced T1 sequence shows a right frontal lobe DVA (arrow). *F*, An axial FLAIR sequence shows hyperintensity (arrow) adjacent to the DVA in *E*.

FLAIR hyperintense lesions in the control group are shown in Fig 2.

For the cases of MS, the interrater reliability for the detection of FLAIR signal surrounding a DVA was 0.865 (95% CI, 0.748–0.979). For the control cases, the interrater reliability for detection

of FLAIR signal surrounding a DVA was 0.874 (95% CI, 0.702–1). This corresponds to excellent agreement.<sup>22</sup>

## DISCUSSION

In our study, FLAIR signal abnormalities adjacent to DVAs were found to be significantly more prevalent in patients with MS compared with the control group of patients without MS (47.3%–13.5%,  $P < .001$ ). Multivariate logistic regression accounting for multiple possible confounding variables found that white matter lesions are 6.7 times more likely around DVAs in patients with MS compared with controls (95% CI, 2.79–15.97;  $P < .001$ ). The underlying pathologic process in both the control group and in some of the patients with MS is likely perivenular gliosis secondary to vascular congestion, venous hypertension, and chronic hypoxia in the territory of the DVA, as described in the neuropathology literature and previously depicted with MR perfusion.<sup>9–13,23–25</sup>

However, the significantly higher proportion of DVA-associated FLAIR abnormalities in patients with MS combined with the presence of lesion enhancement in some cases suggests an additional underlying pathologic cause (eg, sequelae of demyelination caused by multiple sclerosis) of these signal abnormalities in patients with MS. To be clear, these results do not imply that demyelination is the underlying cause of the signal abnormalities in the control group or healthy patients with DVAs. The underlying cause of the leukoaraiosis on FLAIR sequences in each case is indistinguishable when they are chronic lesions (Figs 1 and 2). However, advanced MR imaging techniques such as perfusion MR imaging have the potential of distinguishing DVA-associated FLAIR hyperintensity due to demyelination prospectively, and are an exciting avenue for further research.

The association of DVAs with demyelination in patients with MS has clinical utility, particularly in cases in which there is imaging overlap between active demyelination and possible central nervous system neoplasms (Fig 3).<sup>14</sup>

A noninvasive diagnostic strategy in these cases is short-term follow-up imaging because the enhancement of an actively demyelinating lesion will fade with time, persisting chronically as a DVA-associated FLAIR hyperintensity. The association of DVAs and FLAIR hyperintensities in

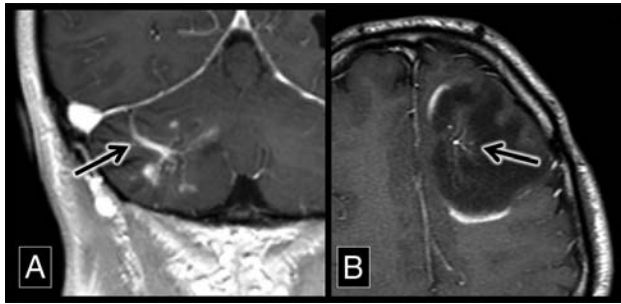


**FIG 3.** Demyelinating lesions around developmental venous anomalies with enhancement. *A*, A coronal contrast-enhanced T1 sequence shows a superficially draining right cerebellar DVA (arrow) associated with enhancing parenchymal lesions. This was biopsy-proved demyelination. *B*, An axial contrast-enhanced T1 sequence shows a left frontal lobe DVA (arrow) with surrounding T1 hypointensity and discontinuous peripheral enhancement, typical of demyelination in a patient with MS.

patients with MS can also be useful to explain why demyelinating plaques may appear in atypical locations such as the basal ganglia. MS plaques classically appear along normally distributed veins (such as at the calloseseptal interface) but also can be seen in areas of the brain where there is variant venous anatomy.

Previously reported theories may explain why FLAIR hyperintensities adjacent to DVAs are more common in patients with MS. The first is that patients with MS are predisposed to develop demyelination around DVAs due to their local inefficient venous drainage.<sup>9-13</sup> MS plaques form when lymphocytes and monocytes cross the blood-brain barrier across venous channels, leading to perivenular cuffing.<sup>26,27</sup> It is here that they react to autoantigens such as myelin basic protein, inciting an inflammatory response leading to perivenular demyelination.<sup>28,29</sup> Jung et al<sup>9</sup> previously showed on MR imaging perfusion that MTT and TTP are prolonged around most DVAs, suggestive of venous congestion in the parenchyma supplied by these DVAs. We hypothesize that the local venous congestion in the territory of a DVA predisposes to blood-brain barrier breakdown and lymphocytic infiltration, leading to demyelination in these regions. Previously published pathology-proved cases also support this hypothesis.<sup>14,30</sup> It is unknown whether DVAs carry a greater risk for developing surrounding demyelination compared with normally distributed veins (such as calloseseptal medullary veins). However, our finding that nearly half of DVAs in patients with MS have associated FLAIR hyperintensity, combined with the previously published findings supporting venous congestion in these regions, raises this possibility. Further investigation of DVA-associated signal abnormalities in patients with MS with MR imaging perfusion may help prove this theory.

It is critical that we address the controversial entity chronic cerebrospinal venous insufficiency (CCSVI), given the volume of medical literature and social media attention devoted to it. The CCSVI theory suggests that patients with MS are more likely to have stenosis of cerebrospinal venous outflow tracts, leading to intracranial venous reflux.<sup>31,32</sup> In theory, a higher prevalence of global cerebral venous insufficiency in patients with MS superimposed on the impaired drainage of DVAs could lead to a higher rate of DVA-associated FLAIR hyperintensities in patients with MS compared with controls. However, CCSVI has largely been

debunked as an underlying cause of MS lesions because there has been only a weak association between the CCSVI sonographic criteria proposed by Zamboni et al<sup>32</sup> and MS, and multiple studies have found no statistically significant difference in venous drainage between patients with MS and controls.<sup>33-38</sup> While global venous insufficiency in patients with MS seems unlikely on the basis of the current literature, this does not mean that local impairment of venous drainage in the territory of a DVA cannot be an exacerbating factor in MS.

There was an approximately 2:1 ratio of females to males in the MS group, while it was a 1:1 ratio in the control group. This ratio supports the previously reported epidemiology of MS.<sup>39</sup> This difference was accounted for in the statistical analysis with a multivariate logistic regression model. We do not hypothesize that sex is an independent risk factor for the development of white matter lesions adjacent to DVAs, and sex predilection for these lesions has not been reported in the literature. In our study, of the 10 patients positive for DVA-associated FLAIR hyperintensity in the control group, 6 were male (60%). We found no statistical correlation of sex and FLAIR hyperintensity surrounding DVAs in patients with MS or controls.

In our study, the MS group was slightly younger than the control group. This is likely because patients with MS present for imaging due to symptoms at a younger age than the background population. This discrepancy was accounted for in the statistical analysis with a multivariate logistic regression model. Additionally, we are reporting a higher prevalence of DVA-associated signal abnormalities in the younger MS group; it has been reported in the literature that these signal abnormalities are more common in older patients.<sup>5</sup> Similarly, univariate regression analysis showed that older control patients were more likely to have FLAIR hyperintensities adjacent to DVAs ( $P = .047$ ). No association between patient age and the prevalence or size of DVA-associated signal abnormalities was seen in the MS group.

We acknowledge the limitations of this retrospective study. There may be a selection bias because a radiology report search tool was used for initial inclusion in the study. Cases in which smaller DVAs may not have been perceived by the prospectively interpreting radiologist or cases in which a DVA was identified but not included in a radiology report were not included in our study. We used a T1 postcontrast sequence to detect DVAs, which is potentially less sensitive compared with T2\* sequences (such as SWI or 3T FLAIR\*). Additionally, our 5-mm slice thickness may also be less sensitive compared with thinner slice techniques. However, being present in both cohorts of patients somewhat mitigates these biases. One might hypothesize that because patients with MS may have more white matter disease compared with controls, a chance association with DVAs is more likely. However, this was corrected for by adherence to our exclusion criteria, which specifically omitted cases in which there were confluent white matter lesions adjacent to the DVA.

## CONCLUSIONS

Because statistically more FLAIR hyperintensities were found to surround DVAs in patients with MS compared with controls, our results suggest that the underlying demyelinating pathologic process of MS may be the cause of this propensity in patients with MS.

We hypothesize that impaired venous drainage in the territory of DVAs predisposes to the development of these lesions in patients with MS, and further prospective evaluation of these lesions with MR perfusion is a logical next step. This imaging feature is helpful in distinguishing tumefactive demyelinating lesions and central nervous system neoplasms and in understanding atypical locations of MS plaques at sites of variant venous anatomy.

## REFERENCES

- Sarwar M, McCormick WF. **Intracerebral venous angioma: case report and review.** *Arch Neurol* 1978;35:323–25 CrossRef Medline
- Truwit CL. **Venous angioma of the brain: history, significance, and imaging findings.** *AJR Am J Roentgenol* 1992;159:1299–307 CrossRef Medline
- Garner TB, Del Curling O Jr, Kelly DL Jr, et al. **The natural history of intracranial venous angiomas.** *J Neurosurg* 1991;75:715–22 CrossRef Medline
- Töpper R, Jürgens E, Reul J, et al. **Clinical significance of intracranial developmental venous anomalies.** *J Neurol Neurosurg Psychiatry* 1999;67:234–38 CrossRef Medline
- Santucci GM, Leach JL, Ying J, et al. **Brain parenchymal signal abnormalities associated with developmental venous anomalies: detailed MR imaging assessment.** *AJNR Am J Neuroradiol* 2008;29:1317–23 CrossRef Medline
- San Millán Ruiz D, Delavelle J, Yilmaz H, et al. **Parenchymal abnormalities associated with developmental venous anomalies.** *Neuroradiology* 2007;49:987–95 CrossRef Medline
- Umino M, Maeda M, Matsushima N, et al. **High-signal-intensity abnormalities evaluated by 3D fluid-attenuated inversion recovery imaging within the drainage territory of developmental venous anomalies identified by susceptibility-weighted imaging at 3 T.** *Jpn J Radiol* 2014;32:397–404 CrossRef Medline
- Linscott LL, Leach JL, Zhang B, et al. **Brain parenchymal signal abnormalities associated with developmental venous anomalies in children and young adults.** *AJNR Am J Neuroradiol* 2014;35:1600–07 CrossRef Medline
- Jung HN, Kim ST, Cha J, et al. **Diffusion and perfusion MRI findings of the signal-intensity abnormalities of brain associated with developmental venous anomaly.** *AJNR Am J Neuroradiol* 2014;35:1539–42 CrossRef Medline
- Iv M, Fischbein NJ, Zaharchuk G, et al. **Association of developmental venous anomalies with perfusion abnormalities on arterial spin labeling and bolus perfusion-weighting imaging.** *J Neuroimaging* 2015;25:243–50 CrossRef Medline
- Camacho DL, Smith JK, Grimme JD, et al. **Atypical MR imaging perfusion in developmental venous anomalies.** *AJNR Am J Neuroradiol* 2004;25:1549–52 Medline
- Sharma A, Zipfel GJ, Hildebolt C, et al. **Hemodynamic effects of developmental venous anomalies with and without cavernous malformations.** *AJNR Am J Neuroradiol* 2013;34:1746–51 CrossRef Medline
- Hanson EH, Roach CJ, Ringdahl EN, et al. **Developmental venous anomalies: appearance on whole-brain CT digital subtraction angiography and CT perfusion.** *Neuroradiology* 2011;53:331–41 CrossRef Medline
- Rogers DM, Peckham ME, Shah LM, et al. **Association of developmental venous anomalies with demyelinating lesions in patients with multiple sclerosis.** *AJNR Am J Neuroradiol* 2018;39:97–101 CrossRef Medline
- Ma M, Chen JY, Plowey ED, et al. **Tumefactive demyelination associated with developmental venous anomaly: report of two cases.** *Clin Imaging* 2017;43:194–98 CrossRef Medline
- Samaraweera AP, Clarke MA, Whitehead A, et al. **The central vein sign in multiple sclerosis lesions is present irrespective of the T2\* sequence at 3 T.** *J Neuroimaging* 2017;27:114–21 CrossRef Medline
- Gaitán MI, Sati P, Inati SJ, et al. **Initial investigation of the blood-brain barrier in MS lesions at 7 Tesla.** *Mult Scler* 2013;19:1068–73 CrossRef Medline
- Sati P, Oh J, Constable RT, et al. **The central vein sign and its clinical evaluation for the diagnosis of multiple sclerosis: a consensus statement from the North American Imaging in Multiple Sclerosis Cooperative.** *Nat Rev Neurol* 2016;12:714–22 CrossRef Medline
- Zhao G, Li DK, Traboulsee T, et al. **Developmental venous anomalies (venous angiomas) on MRI are more common in patients with multiple sclerosis.** In: *Proceedings of the International Society for Magnetic Resonance in Medicine Scientific Meeting and Exhibition and the Annual Meeting of the Society for MR Radiographers & Technologists*, Kyoto, Japan. May 15–21, 2004
- Sasani MR, Dehghan AR, Ali Reza N. **The relationship of multiple sclerosis and cerebral developmental venous anomaly with an advantageous role in the multiple sclerosis diagnosis.** *Iran J Neurol* 2017;16:168–72 Medline
- Thompson AJ, Banwell BL, Barkhof F, et al. **Diagnosis of multiple sclerosis: 2017 revisions of the McDonald criteria.** *Lancet Neurol* 2018;17:162–73 CrossRef Medline
- Landis JR, Koch GG. **The measurement of observer agreement for categorical data.** *Biometrics* 1977;33:159–74 CrossRef Medline
- Moody DM, Brown WR, Challa VR, et al. **Periventricular venous collagenosis: association with leukoaraiosis.** *Radiology* 1995;194:469–76 CrossRef Medline
- Keith J, Gao FQ, Noor R, et al. **Collagenosis of the deep medullary veins: an underrecognized pathologic correlate of white matter hyperintensities and periventricular infarction?** *J Neuropathol Exp Neurol* 2017;76:299–312 CrossRef Medline
- Brown WR, Moody DM, Challa VR, et al. **Venous collagenosis and arteriolar tortuosity in leukoaraiosis.** *J Neurol Sci* 2002;203–204:159–63 CrossRef Medline
- Matthews PM, Roncaroli F, Waldman A, et al. **A practical review of the neuropathology and neuroimaging of multiple sclerosis.** *Pract Neurol* 2016;16:279–87 CrossRef Medline
- Tanaka R, Iwasaki Y, Koprowski H. **Ultrastructural studies of perivascular cuffing cells in multiple sclerosis brain.** *Am J Pathol* 1975;81:467–78 Medline
- Adams CW. **The onset and progression of the lesion in multiple sclerosis.** *J Neurol Sci* 1975;25:165–82 CrossRef Medline
- Minagar A, Alexander JS. **Blood-brain barrier disruption in multiple sclerosis.** *Mult Scler* 2003;9:540–49 CrossRef Medline
- Jung G, Schröder R, Lanfermann H, et al. **Evidence of acute demyelination around a developmental venous anomaly: magnetic resonance imaging findings.** *Invest Radiol* 1997;32:575–77 CrossRef Medline
- Singh AV, Zamboni P. **Anomalous venous blood flow and iron deposition in multiple sclerosis.** *J Cereb Blood Flow Metab* 2009;29:1867–78 CrossRef Medline
- Zamboni P, Galeotti R, Menegatti E, et al. **Chronic cerebrospinal venous insufficiency in patients with multiple sclerosis.** *J Neurol Neurosurg Psychiatry* 2009;80:392–99 Medline
- Zamboni P, Menegatti E, Galeotti R, et al. **The value of cerebral Doppler venous haemodynamics in the assessment of multiple sclerosis.** *J Neurol Sci* 2009;282:21–27 CrossRef Medline
- Krogias C, Schröder A, Wiendl H, et al. **“Chronic cerebrospinal venous insufficiency” and multiple sclerosis: critical analysis and first observation in an unselected cohort of MS patients [in German].** *Nervenarzt* 2010;81:740–46 CrossRef Medline
- Doepf F, Paul F, Valdueza JM, et al. **No cerebrocervical venous congestion in patients with multiple sclerosis.** *Ann Neurol* 2010;68:173–83 CrossRef Medline Medline
- Comi G, Battaglia MA, Bertolotto A, et al; CoSMo Collaborative Study Group. **Observational case-control study of the prevalence of chronic cerebrospinal venous insufficiency in multiple sclerosis: results from the CoSMo study.** *Mult Scler* 2013;19:1508–17 CrossRef Medline

37. Traboulsee AL, Knox KB, Machan L, et al. **Prevalence of extracranial venous narrowing on catheter venography in people with multiple sclerosis, their siblings, and unrelated healthy controls: a blinded, case-control study.** *Lancet* 2014;383:138–45 CrossRef Medline
38. Jedynak W, Cieszanowski A. **Is there any relation between chronic cerebrospinal venous insufficiency and multiple sclerosis? A critical review.** *Pol J Radiol.* 2014;79:131–36 CrossRef Medline
39. Alonso A, Hemán MA. **Temporal trends in the incidence of multiple sclerosis: a systematic review.** *Neurology* 2008;71:129–35 CrossRef Medline

# Systematic Assessment of Multispectral Voxel-Based Morphometry in Previously MRI-Negative Focal Epilepsy

R. Kotikalapudi, P. Martin, J. Marquetand, T. Lindig, B. Bender, and N.K. Focke



## ABSTRACT

**BACKGROUND AND PURPOSE:** Voxel-based morphometry is widely used for detecting gray matter abnormalities in epilepsy. However, its performance with changing parameters, smoothing and statistical threshold, is debatable. More important, the potential yield of combining multiple MR imaging contrasts (multispectral voxel-based morphometry) is still unclear. Our aim was to objectify smoothing and statistical cutoffs and systematically compare the performance of multispectral voxel-based morphometry with existing T1 voxel-based morphometry in patients with focal epilepsy and previously negative MRI.

**MATERIALS AND METHODS:** 3D T1-, T2-, and T2-weighted FLAIR scans were acquired for 62 healthy volunteers and 13 patients with MR imaging negative for focal epilepsy on a Magnetom Skyra 3T scanner with an isotropic resolution of 0.9 mm<sup>3</sup>. We systematically optimized the main voxel-based morphometry parameters, smoothing level and statistical cutoff, with T1 voxel-based morphometry as a reference. As a next step, the performance of multispectral voxel-based morphometry models, T1+T2, T1+FLAIR, and T1+T2+FLAIR, was compared with that of T1 voxel-based morphometry using gray matter concentration and gray matter volume analysis.

**RESULTS:** We found the best performance of T1 at 12 mm and a T-threshold (statistical cutoff) of 3.7 for gray matter concentration analysis. When we incorporated these parameters, after expert visual interpretation of concordant and discordant findings, we identified T1+FLAIR as the best model with a concordant rate of 46.2% and a concordant rate/discordant rate of 1.20 compared with T1 with 30.8% and 0.67, respectively. Visual interpretation of voxel-based morphometry findings decreased concordant rates from 38.5%–46.2% to 15.4%–46.2% and discordant rates from 53.8%–84.6% to 30.8%–46.2% and increased specificity across models from 33.9%–40.3% to 46.8%–54.8%.

**CONCLUSIONS:** Multispectral voxel-based morphometry, especially T1+FLAIR, can yield superior results over single-channel T1 in focal epilepsy patients with a negative conventional MR imaging.

**ABBREVIATIONS:** AUC = area under the curve; C<sub>R</sub> = concordant rate; D<sub>R</sub> = discordant rate; EEG = electroencephalography; GMC = gray matter concentration; GMV = gray matter volume; S<sub>p</sub> = specificity; VBM = voxel-based morphometry

In focal epilepsy, detection of a focal lesion in MR imaging increases the odds of seizure-free outcome after an operation by 2.5–3 times.<sup>1</sup> A common epileptogenic lesion is focal cortical dys-

plasia, which has notable morphologic characteristics on MR imaging.<sup>2</sup> However, pure visual analysis, especially in subtle cases, can be challenging. Also, many histopathologically proven focal cortical dysplasias escape visual detection.<sup>3</sup> Failure to identify these lesions can often label patients as having negative MR imaging for focal cortical dysplasia. These patients have poor surgical outcomes or may not even be referred for a potential epilepsy surgery.<sup>4</sup>

During the past decade, multiple MR imaging postprocessing methods have been applied to improve lesion detection in epilepsy,<sup>5</sup> of which the most common applications are based on voxel-based morphology (VBM), usually using T1-weighted images (single-channel T1 VBM). VBM enables a voxelwise comparison between 2 groups of subjects and can highlight areas of statistically significant differences.<sup>6</sup> This approach is commonly applied in the presurgical evaluation of epilepsy, comparing a single patient against a group of healthy controls. Martin et al, in 2015,<sup>5</sup> reviewed various studies that have reported the potential use of VBM based on T1

Received February 5, 2018; accepted after revision August 6.

From the Departments of Diagnostic and Interventional Neuroradiology (R.K., T.L., B.B.) and Neurology and Epileptology (R.K., P.M., J.M., N.K.F.), Hertie Institute for Clinical Brain Research, University Hospital Tübingen, Tübingen, Germany; and Department of Clinical Neurophysiology (R.K., N.K.F.), University Hospital Göttingen, Göttingen, Germany.

This work was funded by the University of Tübingen/Applied Clinical Research (321-0-1) and Deutsche Forschungsgemeinschaft (FO750/5-1).

Please address correspondence to Raviteja Kotikalapudi, Department of Clinical Neurophysiology, University Hospital Göttingen, Robert-Koch-Str 40, 37075 Göttingen, Germany; e-mail: raviteja.kotikalapudi@gmail.com

Indicates open access to non-subscribers at www.ajnr.org

Indicates article with supplemental on-line tables.

Indicates article with supplemental on-line photos.

<http://dx.doi.org/10.3174/ajnr.A5809>

within a sensitivity range of 60%–100%, whereas its application in identifying structural abnormalities in cryptogenic epilepsy remains challenging, with a sensitivity between 10% and 38%. Also, past studies used variable smoothing (between 5 and 14 mm)<sup>7–9</sup> and statistical cutoffs to elucidate VBM findings.<sup>10,11</sup> Studies have shown that changing smoothing kernel size<sup>9</sup> and statistical thresholds have a direct impact on the VBM findings,<sup>10</sup> also affecting the specificity of the results.<sup>10</sup>

Recently, multispectral VBM (ie, the combination of multiple MR imaging contrast sequences) was proposed and made available in SPM8/SPM12 (<http://www.fil.ion.ucl.ac.uk/spm/software/spm12>) within its unified segmentation framework (New Segment). This approach enables combining different MR image contrasts. Lindig et al, in 2018,<sup>12</sup> showed that multispectral VBM improves tissue segmentation for gray matter, white matter, and CSF and improves lesion detection in MR imaging positive for focal epilepsy compared with T1 VBM. However, it is still unclear whether multispectral VBM is beneficial in the more challenging cohort of MR imaging negative for epileptogenic lesions.

In this study, we wanted to objectify the selection of smoothing and statistical cutoffs with reference to the established and frequently used T1 VBM. This enabled us to systematically compare the diagnostic value of T1 and multispectral VBM using multiple image contrast combinations, T1+T2, T1+FLAIR, and T1+T2+FLAIR, in patients with focal epilepsy, but negative conventional MR imaging (ie, previously MRI-negative).

## MATERIALS AND METHODS

### Subjects

We recruited 62 healthy volunteers (number of controls,  $N_c$ ; 36 women, 26 men; mean age, 27.5 years) and 13 patients with MR imaging negative for cryptogenic epilepsy (number of patients,  $N_p$ ; 6 women, 7 men; mean age, 35.9 years) with a lobar clinical hypothesis of epilepsy origin. The clinical hypothesis was established through multiexpert consensus in the monthly epilepsy case conference, which uses all available clinical information in the presurgical epilepsy program (On-line Table 1). The multispectral VBM results analyzed in this work were not used in forming the clinical hypothesis. All patients had undergone video-electroencephalography (EEG) telemetry and neuropsychological assessment, and 6 of them had undergone PET/CT. After an epilepsy case conference for each of the 13 patients, 7 were identified as candidates for further intracranial EEG and possible subsequent epilepsy surgery due to medically refractory seizures (for clinical details see On-line Table 1). To date, intracranial EEG was performed in 5 patients and was offered to 2 patients who have not yet decided. Of the 5 patients with implants, 3 patients (patients 1, 2, and 6) had undergone an operation; in 2 patients with implants (patients 4 and 11), surgery was declined due to suspected multifocal epileptogenesis. In postsurgical patients, histopathology revealed evidence of hippocampal sclerosis in 1 patient (patient 2), but this patient did not achieve postoperative seizure freedom (Engel class II). The histopathologic tests of the other 2 operated patients (patients 1 and 6) were unremarkable, and to date, 1 patient (patient 1) is seizure-free without anticonvulsive medication (Engel I). The other patient (patient 6) had postoperative seizure freedom, but only for 1 year. All subjects were scanned on a 3T MR

imaging scanner (Magnetom Skyra; Siemens, Erlangen, Germany) at the University Hospital Tübingen. The acquisition protocol was previously reported<sup>12</sup> and consists of 0.9-mm<sup>3</sup> isotropic 3D T1-weighted MPRAGE (= T1), 3D T2-weighted sampling perfection with application-optimized contrasts by using different flip angle evolutions (SPACE sequence; Siemens) (= T2), and 3D inversion recovery prepared SPACE sequence (= FLAIR).

### Image Processing

At first, all scans were converted from DICOM to NIfTI format using MRIConvert (<https://lcn.uoregon.edu/downloads/mriconvert>). The postprocessing was performed with SPM12 in a Matlab R2016a (MathWorks, Natick, Massachusetts) environment and with an in-house Matlab code. We used VBM based on T1 images only (T1 VBM) as a reference. This was compared with multispectral VBM combinations based on multiple MR images (ie, T1+T2, T1+FLAIR, and T1+T2+FLAIR). For multispectral VBM, T2 images (T2 and FLAIR channels) were coregistered to their respective T1 images using linear coregistration with 12 *df* and a normalized mutual information cost function. Segmentation was performed with default settings of bias regularization of 0.001 and a bias cutoff full width at half maximum of 60 mm. As a next step, the segmented GM images were normalized to the Montreal Neurological Institute space by using the Diffeomorphic Anatomical Registration Through Exponentiated Lie Algebra (DARTEL, part of SPM) toolbox, with an isotropic resolution of 1.5 mm<sup>3</sup>.<sup>13</sup> To correct for regional volume changes in normalization, we modulated images to preserve the quantity of GM tissue (gray matter volume [GMV]) within a voxel and unmodulated images for preserving the concentration of GM tissue (gray matter concentration [GMC]). Finally, spatially normalized images were smoothed, using a Gaussian kernel with a range from 4- to 16-mm full width at half maximum in a step size of 2. The smoothed GMC and GMV images were further analyzed using SPM12.

### Statistical Analysis

We used the general linear model from SPM12 to analyze regional increased differences in the smoothed GMC and GMV images. The general linear model analysis was performed using the factorial design specification (2-sample *t* test) in SPM12 to compare each patient against the control cohort (patient comparison) and each control in a leave-one-out cross-validation against the remainder of the controls after removing the subject in question (control comparison). We included age and sex as covariates for GMC. Total intracranial volume was also included as a covariate for GMV. The resulting statistical maps (*t*-contrast maps, subject > controls, ie, increase of GM) were thresholded with *T*-score cutoffs from 2.5 to 6 in step sizes of 0.1. The suprathreshold clusters at each smoothing level and each *T*-threshold were used for reporting the results.

### Objective Diagnostic Performance Assessment

We created a brain mask by summation of normalized unmodulated GM and WM images from T1 segmentation. Voxel intensities <0.5 were excluded to remove nonbrain areas. On the basis of the expert clinical hypothesis, the lobes of the hypothesis were identified for each patient in the Montreal Neurological Institute structural atlas provided with FSL, Version 5.0

(<http://www.fmrib.ox.ac.uk/fsl>).<sup>14,15</sup> For each patient, “concordant lobes” were defined as the atlas lobes/regions (for example, left frontal lobe) that are identified as the lobes of clinical hypothesis. The lobes that are not a part of the clinical hypothesis for each patient were defined as “discordant lobes.” For controls, because no epileptogenic lesions are expected, all atlas regions were defined as discordant.

### Analysis

Every suprathreshold cluster was considered as a concordant or a discordant finding provided one-third or greater of the suprathreshold cluster overlapped the respective lobar ROI (concordant or discordant).

The concordant rate ( $C_R$ ) was calculated as

$$C_R = \left( \frac{N_{CON}}{N_P} \right) \times 100.$$

The discordant rate ( $D_R$ ) was calculated as

$$D_R = \left( \frac{N_{DIS}}{N_P} \right) \times 100.$$

For controls, each suprathreshold cluster was considered a non-epileptogenic finding provided one-third or greater of the cluster overlapped the control cortical mask (excluding likely artifactual findings outside the brain). Specificity ( $S_p$ ) was calculated as

$$S_p = \left( \frac{N_{NF}}{N_C} \right) \times 100.$$

$N_{CON}$ ,  $N_{DIS}$  and  $N_{NF}$  in the above equations refer to the number of patients with concordant and discordant findings and the number of controls with no findings, respectively.

### Diagnostic Assessment

To determine the ideal parameters (smoothing level and T-threshold), we generated receiver operating characteristic curves at each smoothing level by plotting  $100 - S_p$  versus  $C_R$  for all T-thresholds. The area under the curve (AUC) was calculated using a trapezoidal integration function in Matlab as a performance index for each smoothing kernel width. For comparing single-versus-multispectral VBM, we considered the smoothing level with the best performance (the highest AUC across all smoothing levels; 4–16 mm) for T1 as a reference.

### Determining T-Threshold, $S_p$ , and $C_R$

For this reference smoothing kernel,  $S_p$  and  $C_R$  values at T-thresholds of 2.5–6 were plotted.<sup>8</sup> We considered the T-threshold in which the remainder of  $C_R - S_p$  was the smallest but still positive. This point was referred to as the “optimized T-threshold.” At this threshold, a balanced trade-off between these 2 diagnostic indices ( $C_R$  and  $S_p$ ) can be achieved. At this defined T-threshold and the reference smoothing level,  $S_p$ ,  $C_R$ , and  $D_R$  values were reported for all VBM models. Later, the Euclidean distance (ED) (Fig 1D) of the pair  $S_p$ ,  $C_R$  from (100, 100) was calculated for all VBM models as

$$ED = \sqrt{(100 - S_p)^2 + (100 - C_R)^2}.$$

### Visual Interpretation of VBM Findings

On the basis of the minimum Euclidean distance value across models and analysis, we selected analysis findings for visual interpretation. Visual analysis was performed to verify VBM findings in patients and controls. At the reference smoothing kernel and the optimized T-threshold, all findings across models were inverse-transformed to native space using the deformation utility in SPM12 for each subject separately (“back-normalization”). To group clusters in a close spatial relation, we applied a smoothing of 8-mm full width at half maximum to the transformed cluster maps and considered all clusters connected at a statistical value of  $>0.5$  as a single cluster for the visual review process. Later, these clusters (native space findings) across all models were combined for each subject. Finally, native space findings were overlaid on corresponding patient native T1 and coregistered T2 and FLAIR scans. An expert board-certified neuroradiologist (B.B.) inspected each finding without prior knowledge of the lobar hypothesis and labeled each cluster as the following: 1, potentially epileptogenic and visible; 2, potentially epileptogenic but not visible; 3, nonepileptogenic; 4, unclear/not visible or ambiguous; and 5, artifacts. For visual inspection of controls, each cluster was categorized into the following: 1, visible and nonepileptogenic; 2, unclear/not visible; and 3, artifacts. The reviewer used the non-epileptogenic label when the finding was visible but likely not epileptogenic, such as microangiopathy or perivascular spaces. VBM clusters were rated as unclear when the finding was not sufficiently visible to confirm these findings as potentially epileptogenic, nonepileptogenic, or artifacts. As part of the visual analysis, we reviewed all clusters again to ascertain the correctness of the automated lobar classification and to flag them as either concordant or discordant clusters. This step was needed in only 1 case in which 63.2% of voxels were in the concordant lobar mask. Hence, this cluster was eventually marked as a concordant finding.

## RESULTS

### VBM Automated Results: Smoothing Parameters in GMC and GMV

For all models in the GMC analysis, the ideal smoothing was found to be 12 mm. T1+FLAIR showed the best AUC of 0.42 at 12 mm in comparison with T1 (0.35), T1+T2 (0.29), and T1+T2+FLAIR (0.36). For the GMV analysis, the ideal smoothing was also at 12-mm full width at half maximum of different smoothing levels as shown in Fig 1A, -B and On-line Table 2.

### T-Threshold, Concordant Rate, and Specificity

We found the intersection of  $C_R$  and  $S_p$  across different T-thresholds at 3.7 for 12 mm in GMC analysis (Fig 1C). At this T-threshold, T1+T2 and T1+FLAIR showed  $C_R$ ,  $S_p$  at 46.2, 40.3 and 46.2, 37.1, respectively, compared with T1 at 38.5, 33.9. The ratio of  $C_R/D_R$  was also higher for T1+T2 and T1+FLAIR at 0.86 and 0.75, respectively, compared with T1. The Euclidean distances for all models were in the range of 80.37–90.29. The performance details of all models are presented in Table 1. For the GMV analysis, a lower T-threshold of 3.0 was found at 12 mm as the intersection point for  $C_R$  and  $S_p$ . The concordant rate across models was between 7.7% and 38.5%, with specificity between 9.7% and

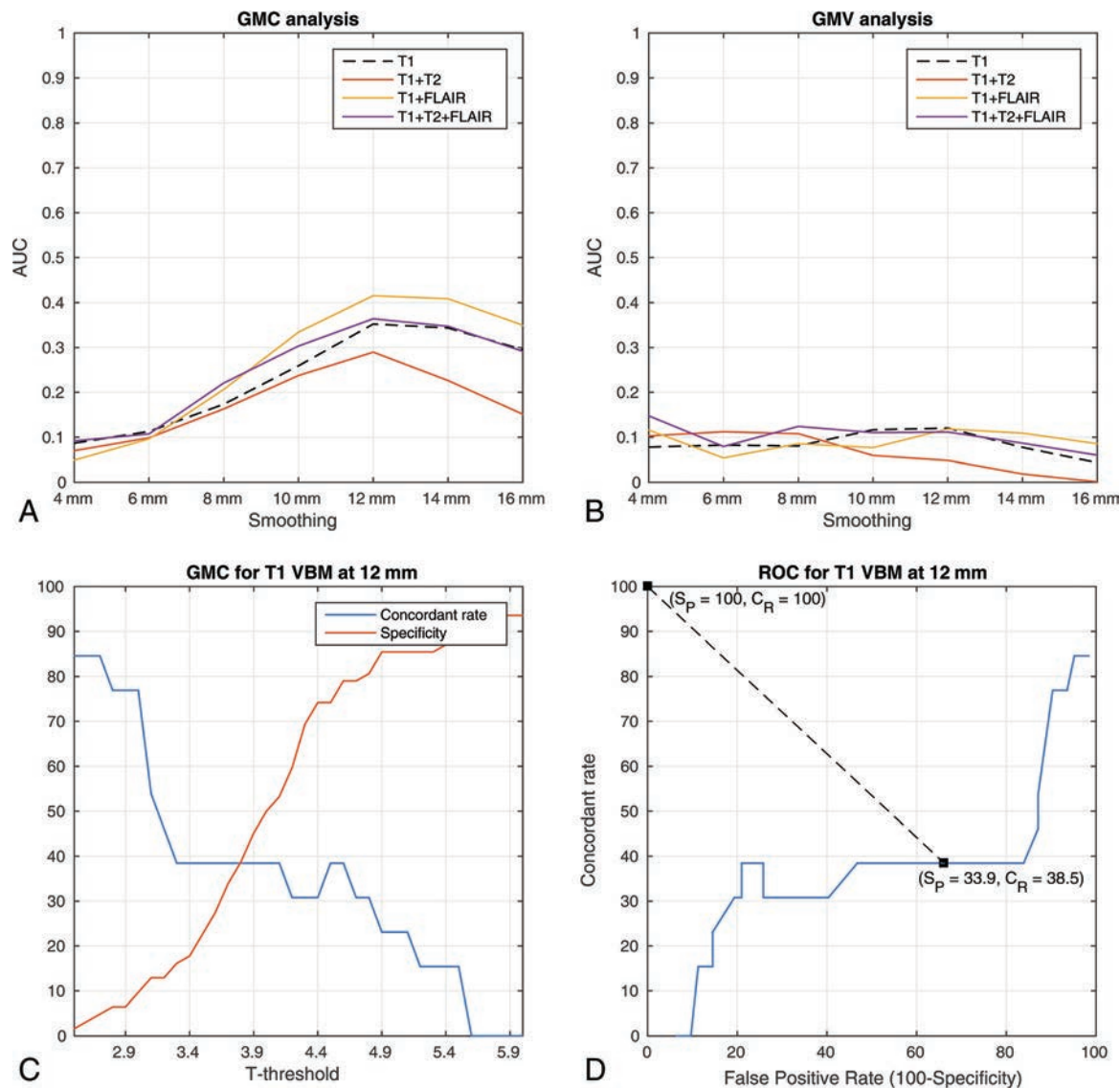


**FIG 1.** Diagnostic performance of different VBM models. A and B, The area under the curve for different smoothing kernels for gray matter concentration and volume. C, An example of an intersection plot for T1 VBM for the concordant rate and specificity against statistical cutoffs. D, An example of a receiver operating characteristic curve for T1 VBM at 12-mm smoothing for GMC. The Euclidean distance is calculated from the optimized T-threshold (3.7 in GMC analysis), where  $C_R, S_p = 38.5, 33.9$  to  $C_R, S_p = 100, 100$ . False positive rate =  $100 - S_p$ .

**Table 1: GMC analysis for VBM models at 12 mm and a T-threshold of 3.7<sup>a</sup>**

Model	Concordant Rate (%)	Specificity (%)	Discordant Rate (%)	Euclidean Distance (Range, 0–141.14)	Concordant Rate/Discordant Rate
T1	38.5	33.9	84.6	90.29	0.46
T1+T2	46.2	40.3	53.8	80.37	0.86
T1+FLAIR	46.2	37.1	61.5	82.77	0.75
T1+T2+FLAIR	46.2	35.5	76.9	84.00	0.60

<sup>a</sup>For VBM GMC automated analysis (prior to visual interpretation), values of concordant rate, specificity, discordant rate, Euclidean distance from  $C_R = S_p = 100$ , and concordant/discordant ratio are provided for all models: namely, T1, T1+T2, T1+FLAIR, and T1+T2+FLAIR. The smoothing level and T-threshold are 12 mm and 3.7, respectively.

21%.  $C_R/D_R$  across models was between 0.10 and 0.50. The Euclidean distances were in the range of 105.32–123.66. All details for GMV analysis are provided in Table 2.

### Visual Interpretation Results of VBM Findings

Visual interpretation was performed for GMC analysis at 12-mm full width at half maximum and a T-threshold of 3.7. The highest concordant rate was found for T1+FLAIR at 46.2% in compar-

ison with T1 at 30.8%. Also, T1+FLAIR showed the highest  $C_R/D_R$  ratio at 1.20 compared with T1 (0.67) and the rest of the models. Only T1+FLAIR and T1+T2+FLAIR showed more or equal concordant-to-discordant findings. The discordant finding rate dropped from 53.8%–84.6% to 30.8%–46.2% after visual interpretation. All results for visual interpretation of patient findings are presented in Table 3. In the visual interpretation of controls, 14.5%–21% of findings were marked as nonepileptogenic, while

**Table 2: GMV analysis for VBM models at 12 mm and a T-threshold of 3.0<sup>a</sup>**

Model	Concordant Rate (%)	Specificity (%)	Discordant Rate (%)	Euclidean Distance (Range, 0–141.14)	Concordant Rate/Discordant Rate
T1	23.1	21.0	84.6	110.25	0.27
T1+T2	7.7	17.7	76.9	123.66	0.10
T1+FLAIR	38.5	9.7	84.6	109.25	0.46
T1+T2+FLAIR	38.5	14.5	76.9	105.32	0.50

<sup>a</sup> For VBM GMV automated analysis (prior to visual interpretation), values of concordant rate, specificity, discordant rate, Euclidean distance from  $C_R = S_P = 100$ , and concordant/discordant ratio are provided for all models: namely, T1, T1+T2, T1+FLAIR, and T1+T2+FLAIR. The smoothing level and T-threshold are 12 mm and 3.0, respectively.

**Table 3: Patients—visual analysis results for GMC<sup>a</sup>**

Model	Potentially Epileptogenic (and Visible)	Potentially Epileptogenic (and Not Visible)	Potentially Epileptogenic (Combined)	Nonepileptogenic	Unclear	Artifacts
Concordant lobe (%)						
T1	15.4	15.4	30.8	7.7	15.4	0
T1+T2	15.4	0	15.4	7.7	15.4	0
T1+FLAIR	15.4	30.8	46.2	7.7	23.1	0
T1+T2+FLAIR	15.4	15.4	30.8	7.7	23.1	0
Discordant lobe (%)						
T1	7.7	38.5	46.2	7.7	30.8	15.4
T1+T2	7.7	23.1	30.8	0	23.1	0
T1+FLAIR	7.7	30.8	38.5	7.7	30.8	7.7
T1+T2+FLAIR	7.7	23.1	30.8	0	30.8	7.7

<sup>a</sup> Visual interpretation results of GMC analysis of patients are provided. The results contain percentages of patients scored by the reviewer as potentially epileptogenic and visible, potentially epileptogenic and not visible, potentially epileptogenic (number of patients with potentially epileptogenic and visible/not visible or both), nonepileptogenic, unclear, and artifacts. The results are reported for both concordant and discordant lobes.

**Table 4: Controls—visual analysis results for GMC<sup>a</sup>**

Models	All Lobes (%)			
	Nonepileptogenic	Unclear	Artifacts	Corrected Specificity (Excluding Artifacts and Nonepileptogenic)
T1	14.5	53.2	22.6	46.8
T1+T2	21.0	45.2	17.7	54.8
T1+FLAIR	16.1	50.0	19.4	50.0
T1+T2+FLAIR	16.1	48.4	25.8	51.6

<sup>a</sup> Visual interpretation results for GMC analysis for controls are presented. Results contain the percentage of controls scored by the reviewer as nonepileptogenic, unclear, and artifacts. Finally, corrected specificity is reported as the percentage of controls that did not have unclear findings—that is, all findings identified as artifacts/nonepileptogenic lesions and patients with no findings (VBM specificity prior to visual analysis).

45.2%–53.2% were marked as unclear (Table 4); 17.7%–25.8% of controls also had findings that were classified as artifacts. The overall specificity after visual interpretation across models was between 46.8% and 54.8%.

## DISCUSSION

In this study, we identified ideal analysis parameters, namely smoothing and T-threshold (statistical cutoff), with reference to T1 VBM. Incorporating these parameters, we systematically compared T1 and multispectral VBM using a combination of T1, T2, and FLAIR images for detecting gray matter structural abnormalities in patients with MR imaging previously negative for focal epilepsy. We objectified the main VBM parameters, smoothing and statistical cutoffs, with reference to the classic T1 VBM. Furthermore, by systematically comparing multispectral VBM models against T1 VBM and using visual inspection of VBM findings, we found T1+FLAIR as the best performing model based on the concordant rate, specificity, and concordant-to-discordant ratio.

## Smoothing and Statistical Cutoff

There is a wide variation in parameters in VBM studies for lesion detection in epilepsy for smoothing kernel sizes ranging from 5 to 14 mm<sup>7-9,16-18</sup> and for a statistical cutoff from  $P < .001$  uncorrected (corresponding to a statistical cutoff T of approximately 3.2 in our sample) to  $P < .05$  family wise error–corrected (corresponding to a statistical cutoff T of approximately 5.1 in our sample)<sup>10</sup> as well as comparisons at multiple statistical cutoffs.<sup>8</sup> We provide a systematic comparison of the 2 main parameters focused on patients with focal epilepsy, but negative conventional MRI, given that this is the main target cohort for advanced lesion detection in epilepsy. For the most frequently used T1-only approach, we found that a smoothing of 12-mm full width at half maximum and a threshold of  $T = 3.7$  provide the highest AUC and best diagnostic balance between concordant rate and specificity. Most interesting, our recommendation of a 12-mm smoothing kernel is similar to that in a previous study conducted by Salmond et al.<sup>19</sup> In line with this study, we found a low specificity with decreased diagnostic performance (AUC, Fig 1A and On-line Table 2) at 4 mm across all models.

Second, as expected, the concordant rate decreased and specificity increased with respect to increasing statistical cutoffs (Fig 1C). This finding is in agreement with a previous study on a lesional cohort based on Z-scores.<sup>8</sup> We aimed for a balance between sensitivity/ $C_R$  and specificity (maximal AUC, intersection of  $C_R$  and  $S_P$ ). It is debatable whether a different approach with maximized sensitivity could also be clinically useful, dealing with little or no specificity. However, in our view, a VBM approach should have at least some

degree of specificity to be informative in the difficult context of MRI-negative patients, in which invasive diagnostics and invasive EEG are commonly performed and carry low-but-non-negligible risks for patients. Martin et al<sup>10</sup> found that the best odds ratio for predicting postoperative seizure freedom was achieved by the VBM variant with the best specificity, namely the normalized FLAIR signal. Nonetheless, our results will also provide guidance if other groups want to select their analysis parameters with a different intention, either maximizing sensitivity or specificity (On-line Figs 1 and 2).

### Gray Matter Concentration versus Volume Analysis

We found that gray matter concentration analysis revealed better results for both single- and multispectral models in comparison with volume analysis. This is in agreement with a previous study in a different cohort in which gray matter concentration was found to be better in detecting epileptogenic lesions in MRI-negative and MRI-positive patients.<sup>10</sup> The only difference between the 2 analyses is the additional step of modulation, which is intended to preserve the original tissue volume.<sup>6</sup> The exact reason for this diagnostic difference remains speculative. It is possible that epileptogenic lesions and focal cortical dysplasias are better characterized by local changes of tissue composition, and global volume effects attenuate the effect size (eg, “compensating” gray matter increase in the lesions with atrophy in the surrounding area). Whether superiority of GMC over GMV analysis remains true for different MR imaging pulse sequences with different tissue contrasts needs to be determined.

### Visual Interpretation of VBM Findings

After visual interpretation of control findings, we found a specificity range between 46.8% and 54.8% across all models. We cannot draw a direct comparison with previous studies because our VBM models, smoothing and statistical cutoffs, are different from those in past studies.<sup>10,16,20</sup> However, we are in line with our previous study on 50 controls, in which a specificity of 42% was reported for T1 gray matter concentration analysis<sup>10</sup> at  $P < .05$  (family-wise error). Moreover, 12.1%–16.1% of controls had only visible (nonepileptogenic/artifacts) findings (ie, controls who had visible findings but no unclear findings). This finding contributed to an increase in specificity after visual analysis (Table 4). In a previous study based on the morphometric analysis program, approximately 25% of findings in controls (13 of 52) were marked as nonepileptogenic normal variants,<sup>20</sup> similar to our results. Across models, after visual analysis, we observed a drop in concordant and discordant rates (Tables 1 and 3). In a previous study based on an MR imaging cohort negative for epileptogenic lesions, after visual analysis, the concordant rate for FLAIR and T1 VBM dropped from 28.6% and 14.3% to 14.3% and 0%, respectively.<sup>21</sup> This result shows that visual interpretation of VBM findings is needed before considering these for epilepsy surgery. Nevertheless, we and others have previously shown that VBM findings carry a positive odds ratio for a good outcome after epilepsy surgery and are, thus, clinically relevant.<sup>10,20</sup>

### Effect of Multispectral VBM

After visual inspection, the highest concordant rate was confirmed for multispectral T1 + FLAIR at 46.2% in comparison with T1 (30.8%) and the other models. This is in line with a previous study in patients with lesional epilepsy, in which multispectral

**Table 5: Nonvisible findings—visual analysis results for GMC<sup>a</sup>**

Models	All Lobes (%)	
	Controls	Patients
T1	53.2	61.5
T1+T2	45.2	30.8
T1+FLAIR	50.0	61.5
T1+T2+FLAIR	48.4	46.2

<sup>a</sup>Rates of findings not visible—that is, unclear findings in controls and unclear/potentially epileptogenic and not visible findings in patients across all lobes for all models (%) are reported.

T1 + FLAIR also showed a superior performance compared with T1.<sup>12</sup> Similarly, the enhanced performance of FLAIR-VBM (concordant rate, 14.3%) over T1 (0%) was also found in a study cohort of children with cryptogenic epilepsy.<sup>21</sup> Additionally, intensity-normalized FLAIR-VBM<sup>11</sup> showed positive odds of 7.3 for a successful surgical outcome in comparison with T1 VBM in 129 patients with MR imaging negative for epilepsy.<sup>10</sup> This finding indicates that inclusion of a new channel, FLAIR in this case, can contribute to increasing concordant rates in a cohort with MR imaging negative for focal epilepsy. Overall these results show that multispectral VBM is superior to T1 VBM, but there still is a need for new modalities and approaches to be explored (eg, based on [resting-state] functional imaging, alternative tissue contrasts like MP2RAGE/diffusion imaging, and higher magnetic fields).

### Discordant Findings in Patients

All VBM variants had a relevant number of findings discordant with the primary clinical hypothesis, but these differed substantially among the variants. Only T1 + FLAIR showed more concordant-than-discordant findings, with the highest concordant-to-discordant ratio among all models and approximately 2 times more than in T1. In a previous study, Martin et al<sup>10</sup> showed that only normalized FLAIR-VBM had more concordant than discordant findings in MRI-negative patients against T1. In the same study, only normalized FLAIR-VBM had no discordant findings in the group of 15 patients with MR imaging positive for focal cortical dysplasia. We are not aware of any other VBM-based study addressing discordant findings in the cryptogenic epilepsy cohort; 30.8%–46.2% of patients still had discordant findings that were marked as potentially epileptogenic. In this most challenging epilepsy surgery cohort (MR imaging negative for focal epilepsy), the definition of an epileptogenic zone is often limited because fast propagation of epileptogenic activity can be difficult to detect in scalp video-EEG.<sup>22,23</sup> Furthermore, patients can have >1 epileptogenic zone/lesion, and our hypotheses were derived from noninvasive data (especially video telemetry EEG) in many cases (On-line Table 1). Thus, VBM findings initially considered discordant may still be real and clinically relevant. We also provided the concordant and discordant findings in patients for all VBM models that were visually confirmed as potentially epileptogenic as in On-line Table 3.

### Nonvisible Findings

Patients and controls also had findings marked as not visible (Table 5). The biologic meaning of these findings that are not visible, is difficult to assess. They can be due to subtle artifacts beyond the visible threshold (eg, field inhomogeneities or movement) or minor differences in cortical morphology without direct pathologic mean-

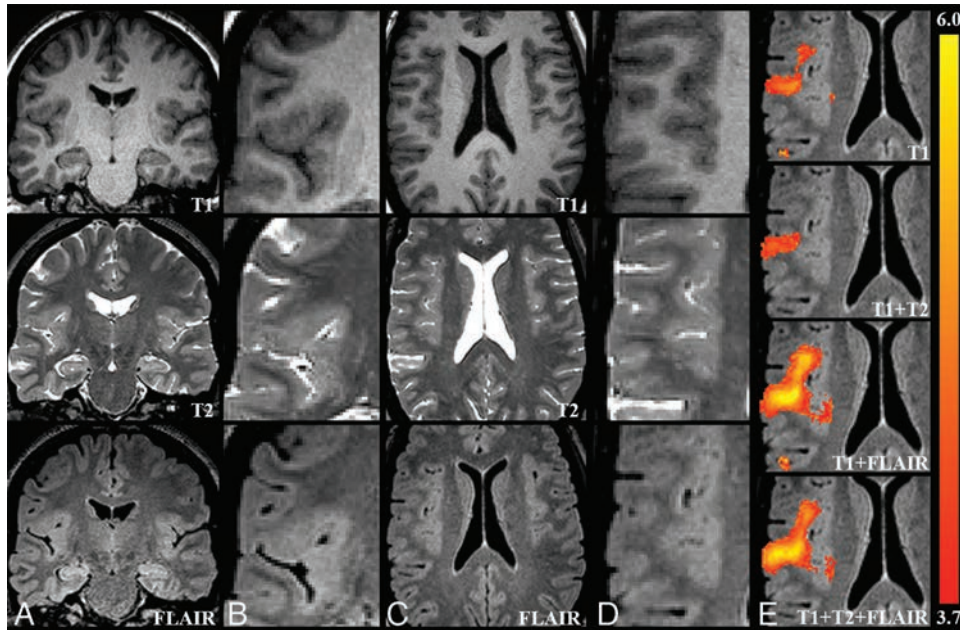


**FIG 2.** Sample case (patient 4). A and C, An overview in the native space T1, T2, and FLAIR images. B and D, Zoomed-in images focusing on a possible epileptogenic lesion. A subtle disruption of cortical morphology is visible in this figure, more prominent on FLAIR images. This finding is concordant with the clinical hypothesis supported by noninvasive and intracranial EEG, indicating seizure onset in the right frontal lobe. The possible lesion was detected as increased GM by all VBM models, but the extent and effect size were clearly better for the VBM models, including FLAIR (E).

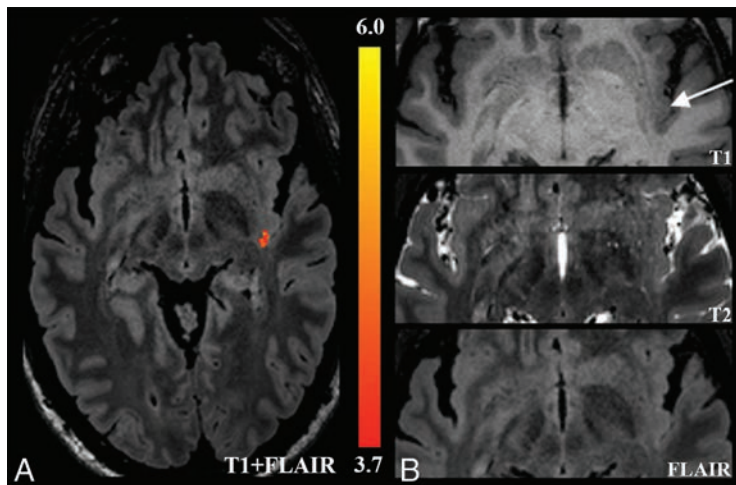


**FIG 3.** Sample case (patient 13). A, A VBM finding detected only by T1+FLAIR in the left temporoinsular region overlaid on the native space FLAIR image. B, Magnified images of T1, T2, and FLAIR suggesting a blurred gray-white matter junction (arrow). This finding is concordant with the clinical hypothesis of seizure onset.

ing. In patients, these findings can also represent subtle epileptogenic lesions that escape visual detection. In a direct comparison, the frequency of detecting a nonvisible finding was only slightly higher in patients than in controls (for some models), making it likely that these findings are largely nonspecific. However, more clinical data and follow-up are needed to draw further conclusions from such nonvisible findings.

### Diagnostic Value of Multispectral FLAIR-VBM in Focal Epilepsy

A major advantage of multispectral VBM lies in simultaneously including FLAIR along with T1. It takes only an extra 5–7 minutes

to acquire 3D-FLAIR. Additionally, processing time for T1 and T1+FLAIR VBM differs only in the extra step of coregistration for the latter. Second, many lesions in focal epilepsy (focal cortical dysplasia, hippocampal sclerosis, tumors) have a prolonged T2-relaxation, resulting in hyperintense signal and increased visibility on a FLAIR image.<sup>2,21</sup> Thus, it is not surprising that FLAIR-based methods could detect those lesions better than T1 alone.<sup>11,12</sup> For example, Fig 2 shows the presumed lesion to be more visible on FLAIR than on T1 images. All VBM models eventually detect this abnormality, but the coverage and effect size were best in VBM models that include FLAIR. The finding is in concordance with the clinical lobar hypothesis, which was in the right frontal lobe, indicated by noninvasive EEG and intracranial EEG.

Another example is shown in Fig 3, where only T1+FLAIR VBM detects a subtle structural abnormality in the left temporoinsular region. In comparison with the right side, a subtle blurring of GM-WM is visible at the left temporal operculum/posterior insula. This finding is in concordance with the clinical lobar hypothesis of bilateral temporal onset. In both cases, it is likely that the suspected abnormalities are segmented as gray matter and, consequently, increase the gray matter probability when the FLAIR image is added. Furthermore, the improved tissue classification by multimodal segmentation may improve the lesion detection.<sup>12,24,25</sup> Of the 3 patients with operations, 1 patient (patient 6) had findings concordant with the lobar clinical hypothesis in the left temporal region detected by T1

and T1+FLAIR but not coinciding with the resected area. The patient was seizure-free for only 1 year before seizures resumed, raising the possibility of a partial resection and prompting further clinical investigations.

### Limitations

Five of 6 patients with concordant findings did not have surgical resection; the 1 patient with a resection did not have the finding in the resection area and later had seizure relapse. Hence, a histopathologic confirmation was not possible. Low rates of surgical resection as well as reduced chances of seizure freedom are typical for patients with MR imaging negative for epilepsy.<sup>1</sup> Nonetheless, a visual review of the findings by an expert radiologist blinded to the clinical hypothesis shows clear improvement in the concordant/discordant ratio for multispectral VBM. This indicates that these findings can be of diagnostic relevance. However, our study cannot assess whether multispectral VBM will eventually improve the surgical outcome. This will require longitudinal multimodal studies by large multicenter collaborations. Our results can guide the choice of sequences and analysis parameters for such projects.

### CONCLUSIONS

We provide optimized VBM parameters, specifically smoothing and statistical cutoff (T-threshold), for lesion detection in MR imaging previously negative for focal epilepsy with T1 VBM as a reference. We systematically compared multispectral VBM with T1 VBM. We found a smoothing level of 12 mm and a T-threshold of 3.7 for GMC analysis as ideal parameters. With these parameters, after we visually confirmed VBM findings, multispectral VBM T1+FLAIR yielded results superior to those of all other models. We also found VBM an important computational advancement, which, after a careful visual interpretation, can aid the presurgical evaluation of focal epilepsy. We recommend multispectral VBM, especially T1+FLAIR, as currently the best VBM model in detecting increased gray matter structural abnormalities in patients with MR imaging previously negative for focal epilepsy.

Disclosures: Benjamin Bender—UNRELATED: Expert Testimony: Medtronic\*. Niels K. Focke—RELATED: Grant: Deutsche Forschungsgemeinschaft/Deutsche Forschungsgemeinschaft, Comments: Deutsche Forschungsgemeinschaft grant FO750/5–1; UNRELATED: Consultancy: Bial, Eisai; Payment for Lectures Including Service on Speakers Bureaus: UCB; Payment for Development of Educational Presentations: Bial. \*Money paid to the institution.

### REFERENCES

1. Téllez-Zenteno JF, Hernández Ronquillo L, Moien-Afshari F, et al. **Surgical outcomes in lesional and non-lesional epilepsy: a systematic review and meta-analysis.** *Epilepsy Res* 2010;89:310–18 CrossRef Medline
2. Blümcke I, Thom M, Aronica E, et al. **The clinicopathologic spectrum of focal cortical dysplasias: a consensus classification proposed by an ad hoc Task Force of the ILAE Diagnostic Methods Commission.** *Epilepsia* 2011;52:158–74 CrossRef Medline
3. Wang ZL, Alexopoulos AV, Jones SE, et al. **The pathology of magnetic-resonance-imaging-negative epilepsy.** *Mod Pathol* 2013;26:1051–58 CrossRef Medline
4. Spencer SS, Berg AT, Vickrey BG, et al; Multicenter Study of Epilepsy Surgery. **Predicting long-term seizure outcome after resective epilepsy surgery: the multicenter study.** *Neurology* 2005;65:912–18 CrossRef Medline
5. Martin P, Bender B, Focke NK. **Post-processing of structural MRI for individualized diagnostics.** *Quant Imaging Med Surg* 2015;5:188–203 CrossRef Medline
6. Ashburner J, Friston KJ. **Voxel-based morphometry: the methods.** *Neuroimage* 2000;11(6 Pt 1):805–21 CrossRef Medline
7. Huppertz HJ, Grimm C, Fauser S, et al. **Enhanced visualization of blurred gray-white matter junctions in focal cortical dysplasia by voxel-based 3D MRI analysis.** *Epilepsy Res* 2005;67:35–50 CrossRef Medline
8. Colliot O, Bernasconi N, Khalili N, et al. **Individual voxel-based analysis of gray matter in focal cortical dysplasia.** *Neuroimage* 2006;29:162–71 CrossRef Medline
9. Keller SS, Roberts N. **Voxel-based morphometry of temporal lobe epilepsy: an introduction and review of the literature.** *Epilepsia* 2008;49:741–57 CrossRef Medline
10. Martin P, Winston GP, Bartlett P, et al. **Voxel-based magnetic resonance image postprocessing in epilepsy.** *Epilepsia* 2017;58:1653–64 CrossRef Medline
11. Focke NK, Symms MR, Burdett JL, et al. **Voxel-based analysis of whole brain FLAIR at 3T detects focal cortical dysplasia.** *Epilepsia* 2008;49:786–93 CrossRef Medline
12. Lindig T, Kotikalapudi R, Schweikardt D, et al. **Evaluation of multimodal segmentation based on 3D T1-, T2- and FLAIR-weighted images: the difficulty of choosing.** *Neuroimage* 2018;170:210–21 CrossRef Medline
13. Ashburner J. **A fast diffeomorphic image registration algorithm.** *Neuroimage* 2007;38:95–113 CrossRef Medline
14. Mazziotta J, Toga A, Evans A, et al. **A probabilistic atlas and reference system for the human brain: International Consortium for Brain Mapping (ICBM).** *Philos Trans R Soc Lond B Biol Sci* 2001;356:1293–322 CrossRef Medline
15. Collins DL, Holmes CJ, Peters TM, et al. **Automatic 3-D model-based neuroanatomical segmentation.** *Hum Brain Mapp* 1995;3:190–208 CrossRef
16. Focke NK, Bonelli SB, Yogarajah M, et al. **Automated normalized FLAIR imaging in MRI-negative patients with refractory focal epilepsy.** *Epilepsia* 2009;50:1484–90 CrossRef Medline
17. Kassubek J, Huppertz HJ, Spreer J, et al. **Detection and localization of focal cortical dysplasia by voxel-based 3-D MRI analysis.** *Epilepsia* 2002;43:596–602 CrossRef Medline
18. Bonilha L, Montenegro MA, Rorden C, et al. **Voxel-based morphometry reveals excess gray matter concentration in patients with focal cortical dysplasia.** *Epilepsia* 2006;47:908–15 CrossRef Medline
19. Salmond C, Ashburner J, Vargha-Khadem F, et al. **Distributional assumptions in voxel-based morphometry.** *Neuroimage* 2002;17:1027–30 CrossRef Medline
20. Wang ZI, Jones SE, Jaisani Z, et al. **Voxel-based morphometric magnetic resonance imaging (MRI) postprocessing in MRI-negative epilepsies.** *Ann Neurol* 2015;77:1060–75 CrossRef Medline
21. Riney CJ, Chong WK, Clark CA, et al. **Voxel based morphometry of FLAIR MRI in children with intractable focal epilepsy: implications for surgical intervention.** *Eur J Radiol* 2012;81:1299–305 CrossRef Medline
22. Alarcón G, Kissani N, Dad M, et al. **Lateralizing and localizing values of ictal onset recorded on the scalp: evidence from simultaneous recordings with intracranial foramen ovale electrodes.** *Epilepsia* 2001;42:1426–37 Medline
23. Spencer SS, Williamson PD, Bridgers SL, et al. **Reliability and accuracy of localization by scalp ictal EEG.** *Neurology* 1985;35:1567–75 CrossRef Medline
24. Viviani R, Pracht ED, Brenner D, et al. **Multimodal MEMPRAGE, FLAIR, and R2\* segmentation to resolve dura and vessels from cortical gray matter.** *Front Neurosci* 2017;11:258 CrossRef Medline
25. Viviani R, Stöcker T, Stingl JC. **Multimodal FLAIR/MPRAGE segmentation of cerebral cortex and cortical myelin.** *Neuroimage* 2017;152:130–41 CrossRef Medline

# Does the Presence or Absence of DESH Predict Outcomes in Adult Hydrocephalus?

<sup>1</sup>A.K. Ahmed, <sup>2</sup>M. Luciano, <sup>3</sup>A. Moghekar, <sup>4</sup>J. Shin, <sup>5</sup>N. Aygun, <sup>6</sup>H.I. Sair, <sup>7</sup>D. Rigamonti, and <sup>8</sup>A.M. Blitz

## ABSTRACT

**BACKGROUND AND PURPOSE:** The DESH (disproportionately enlarged subarachnoid-space hydrocephalus) pattern of “tight high-convexity and medial subarachnoid spaces, and enlarged Sylvian fissures with ventriculomegaly” is used to determine which patients undergo an operation for adult hydrocephalus at many centers. Our aim was to review adult hydrocephalus cases when DESH has not been a criterion for an operation to determine the prevalence of DESH among the cohort and compare the surgical outcomes in the presence or absence of DESH.

**MATERIALS AND METHODS:** A retrospective cohort study was conducted at a single institution (Johns Hopkins Hospital) to include patients surgically treated for adult hydrocephalus between 2003 and 2014 drawn from a data base of patients who had undergone standardized hydrocephalus protocol MR imaging. Preoperative imaging was reviewed by 2 blinded neuroradiologists to characterize the presence of DESH. Preoperative and postoperative clinical symptomatology was recorded. Frequencies were compared using the Fisher exact test, and nonparametric means were compared using the Mann-Whitney *U* Test.

**RESULTS:** One hundred thirty-three subjects were identified and included (96 DESH absent, 37 DESH present). Shunting led to significant improvement in gait and urinary and cognitive symptoms for the overall cohort and for patients with and without DESH ( $P < .05$ ). The Fisher exact test did not demonstrate any significant differences in either gait or urinary or cognitive symptom improvement between patients with or without DESH ( $P > .05$ ).

**CONCLUSIONS:** The current study demonstrated symptom improvement in patients with adult hydrocephalus following shunting, with no significant differences between subjects with and without DESH. Thus, shunt insertion for patients with adult hydrocephalus should not rely solely on the presence of preoperative DESH findings.

**ABBREVIATIONS:** DESH = disproportionately enlarged subarachnoid-space hydrocephalus; iNPH = idiopathic normal pressure hydrocephalus; MMSE = Mini-Mental State Examination; NPH = normal pressure hydrocephalus; TUG = Timed Up and Go test

Adult hydrocephalus, the communicating form known as normal pressure hydrocephalus (NPH) in the elderly population, is associated with the classic triad of gait, cognitive, and urinary disturbances.<sup>1,2</sup> Shunting is the mainstay of treatment, but the accurate neuroradiologic diagnosis of shunt-responsive adult hydrocephalus may be difficult. As described by the NPH guidelines study group, there is no single standard for the imaging evaluation of idiopathic NPH (iNPH).<sup>3-5</sup>

The Study of Idiopathic Normal Pressure Hydrocephalus on Neurologic Improvement (SINPHONI) developed MR imaging-based diagnostic criteria for adult hydrocephalus, termed “disproportionately enlarged subarachnoid-space hydrocephalus” (DESH).<sup>2</sup> DESH is defined as “tight high-convexity and medial subarachnoid spaces, and enlarged Sylvian fissures with ventriculomegaly.” Hashimoto et al<sup>2</sup> reported that the DESH criteria, on coronal MR imaging, are a defining characteristic for iNPH. The DESH pattern is used to aid in the surgical selection of patients in some centers and is given particular weight in some geographic areas.<sup>6</sup>

The aim of the present study was to review adult hydrocephalus cases at a single institution (Johns Hopkins Hospital), where the presence or absence of DESH has not been used as a surgical criterion, to determine the prevalence of DESH among the cohort, characterize adult hydrocephalus cases by the presence of DESH criteria, and compare the outcomes of patients with and without DESH following shunting treatment.

Received April 17, 2018; accepted after revision August 10.

From the Departments of Neurosurgery (A.K.A., M.L., D.R.), Neurology (A.M.), and Radiology and Radiological Sciences (N.A., H.I.S., A.M.B.), Division of Neuroradiology, Johns Hopkins University School of Medicine, Baltimore, Maryland; and Department of Radiology (J.S.), University of California, San Francisco, School of Medicine, San Francisco, California.

Please address correspondence to Ari M. Blitz, MD, Division of Neuroradiology, Johns Hopkins Hospital, 600 North Wolfe St, Phipps B-126 Baltimore, MD 21287; e-mail: Ablitz1@jhmi.edu

<http://dx.doi.org/10.3174/ajnr.A5820>

## MATERIALS AND METHODS

### Study Design and Inclusion Criteria

A retrospective chart review was conducted, following institutional review board approval (NA\_00067508), which included patients who underwent treatment for adult hydrocephalus at a single institution from 2003 to 2014 selected from a data base of patients who have undergone a standardized hydrocephalus protocol clinical high-resolution MR imaging, including sagittal MPRAGE (TR, 2300 ms; TE, 1.88 ms; inversion recovery, 900; 144 partitions; 0.9-mm isotropic voxels). Patients undergoing an operation had a preoperative Evans index of  $>0.3$  and symptoms of potential hydrocephalus. The inclusion criteria for screening consisted of patients 18–80 years if age with symptomatic and radiographically confirmed adult hydrocephalus treated by surgical shunting, with sufficient preoperative imaging and a detailed medical record describing preoperative and postoperative symptoms. All included patients underwent high-resolution imaging through the hydrocephalus center for evaluation of potential adult hydrocephalus.

### Hydrocephalus Classification

All preoperative images were de-identified and reviewed by 2 neuroradiologists blinded to clinical features, with discrepancies resolved through consensus, and scored for the presence or absence of all DESH criteria, based on the previously published criteria.<sup>4</sup> However, previous reports did not include cutoff measurements for Sylvian fissure enlargement according to the DESH criteria. Consistent with the literature definition of DESH, the presence of Sylvian fissure enlargement was a qualitative observation made after thorough review of the relevant literature. The authors chose not to classify Sylvian fissure enlargement by measurement, to avoid inconsistencies with previous reports describing the DESH classification.<sup>3–5</sup> In an effort to include a pure sample of DESH cases and controls negative for DESH, we excluded patients who had partial features of DESH without fulfilling all criteria from this study. Excluded patients were those with either tight high-convexity and medial subarachnoid spaces without enlarged Sylvian fissures or patients with enlarged Sylvian fissures in the absence of tight high-convexity and medial subarachnoid spaces.

### Recorded Data

Following retrospective review of medical records for adult patients surgically treated for hydrocephalus, demographic (age at treatment and sex) data, symptomatology, and treatment were recorded. Imaging, gait, urinary dysfunction, dementia, Mini-Mental State Examination (MMSE) scores, Timed Up and Go test (TUG) scores,<sup>7</sup> Tinetti scores, and depression status were recorded preoperatively and postoperatively. Baseline gait was recorded on a scale of 0–4: 0, no gait abnormality; 1, minor gait abnormality on uneven surfaces or with regard to pace; 2, recent history of falls; 3, requiring cane or walker assistance; and 4, wheelchair-bound. Urinary function was recorded as the following: 0, no urinary dysfunction; 1, urinary urgency, hesitancy, ambiguous dysfunction, or noted by others; 2, rare urinary dysfunction; 3, frequent urinary dysfunction; and 4, incontinent. Cognitive symptoms were recorded as the following: 0, no cognitive symptoms; 1, infrequent forgetfulness or ambiguous cogni-

tive symptoms; 2, mild cognitive symptoms; 3, frequent cognitive symptoms; and 4, severe cognitive impairment in activities of daily living.

Because many studies of adult hydrocephalus suggest 1 year of follow-up,<sup>2–8</sup> postoperative clinical outcomes were recorded close to the 1-year postoperative follow-up visit and at the last known clinical follow-up. Postoperative gait, and urinary and cognitive symptoms were graded by 3 criteria: 1, worsening of symptoms; 2, no improvement (ie, same as baseline); or 3, improvement in symptoms at the last known clinical follow-up.

### Statistical Analysis

Frequencies were compared using the Fisher exact test, and non-parametric means were compared using the Mann-Whitney *U* test. A *P* value  $< .05$  was considered significant. Analysis was performed by using STATA SE 12 (StataCorp, College Station, Texas).

## RESULTS

### Patient Demographics and Baseline Characteristics

Patients surgically treated for adult hydrocephalus during an 11-year period (2003–2014) were included. Following blinded neuroradiology review of preoperative imaging for 162 adult patients surgically treated for hydrocephalus, 29 patients had partial features of DESH without fulfilling the complete DESH criteria and were excluded from this study. Of the remaining 133, ninety-six (72.2%) did not meet any DESH criteria and 37 (27.8%) had all DESH features present (Figure and Table 1). Of the 133 patients included in this study, 68.4% were men. The mean age at shunting was 71.7 years (range, 53–80 years) (Table 1).

### Clinical Presentation

Preoperatively, 14 (10.5%) patients presented with a normal gait, 18 (13.5%) presented with gait abnormalities on an uneven surface or slow pace, 54 (40.6%) had a history of falls, 39 (29.3%) required an assisted gait, and 8 (6%) were wheelchair-bound. Of the 133 patients, those with preoperative findings of DESH ( $n = 37$ ) had greater preoperative gait dysfunction compared with those without DESH ( $n = 96$ ) ( $P < .05$ ). Of those with preoperative DESH findings, only 2.7% had a normal gait compared with 13.5% of those without DESH (Table 2).

Of the cohort of 131 patients in whom urinary function was known, 43 (32.8%) had no preoperative urinary dysfunction; 18 (13.7%) had urgency, anxiety, or ambiguous symptoms; 43 (32.8%) had rare or intermittent symptoms; 16 (12.2%) had urinary dysfunction often; and 10 (7.6%) had urinary incontinence at presentation. There were no significant differences between patients with or without DESH, regarding preoperative urinary dysfunction ( $P > .05$ ).

Similar to urinary dysfunction, there were no significant differences between patients with and without DESH with respect to preoperative dementia. In both groups, 15.8% had no dementia, preoperatively ( $P > .05$ ) (Table 2).

The mean score for the MMSE was 26.5 (95% CI, 7–30); for the Tinetti, it was 21.4 (95% CI, 6–28); and for the TUG, it was 19.07 (95% CI, 4.5–82); 55.3% of patients presented with depression and 56.4% presented with headaches. MMSE, Tinetti, TUG,

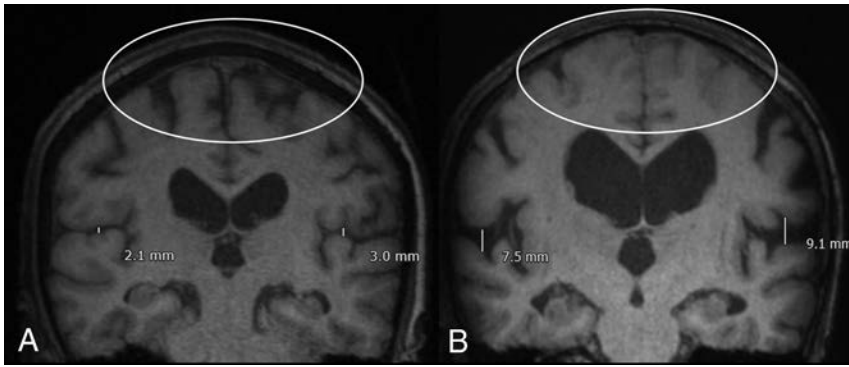


**FIGURE.** Characteristic imaging and classification for patients with adult hydrocephalus. A, Absence of DESH. B, DESH present: Sylvian fissure enlargement and tight high-convexity effacement are present. Both patients were treated with ventricular shunting and had improvement in symptoms. A scaled measurement of the Sylvian fissure is provided to illustrate the extent of fissure enlargement in this representative case. However, consistent with the defining features of DESH in the literature,<sup>3-5</sup> quantitative measurement was not used as scoring criterion during blinded neuroradiologist review.

**Table 1: Demographics and baseline characteristics**

Demographics and Characteristics	
Mean age (range) (yr)	71.7 (53–80)
Sex	68.4% Male, 32.6% female
Hydrocephalus classification (n = 133)	
No DESH (No.) (%)	96 (72.2%)
DESH (No.) (%)	37 (27.8%)

depression, and headache status were not significant between patients with and without DESH ( $P > .05$  for all) (Table 2).

### Clinical Outcomes following Treatment

Clinical outcomes were recorded close to the 1-year follow-up visit ( $254.3 \pm 37.9$  days) and at the last known follow-up visit ( $1248.3 \pm 103.3$  days) after the operation. There were no significant differences in any of the clinical outcomes recorded between these postoperative time points ( $P > .05$  for all). Gait status was known for 113 patients following shunting treatment. Excluding those with a normal gait at baseline ( $n = 7$ ), 84% (89/106) demonstrated gait improvement of some kind following shunting. For patients with and without preoperative DESH with preoperative gait deficits, 80% (24/30) and 85.5% (65/76) had some magnitude of improvement in gait following shunting, respectively. Although shunting led to significant gait improvement for the overall cohort, for patients with and without DESH ( $P < .05$  for all), the Fisher exact test did not demonstrate any significant differences in the magnitude or proportion of gait improvement based on the presence or absence of DESH ( $P > .05$ ).

Following shunting treatment, 89.9% (71/79) of patients with preoperative urinary dysfunction and 75% (30/40) with preoperative dementia symptoms had some magnitude of improvement following shunting. Shunting led to significant improvement in urinary and dementia symptoms for the overall cohort and for patients with and without DESH ( $P < .05$ ). The Fisher exact test did not demonstrate any significant differences in the proportion of either urinary or dementia symptom improvement between patients with or without DESH ( $P > .05$ ) (Table 3). The Fisher exact test also did not demonstrate any demographically significant differences with respect to sex or age for patients with known

baseline and postoperative gait, urinary, and dementia symptoms ( $P > .05$  for all).

The number of patients with known postoperative status for the MMSE, Tinetti, and TUG was limited and therefore not found to be statistically significant compared with preoperative values.

### DISCUSSION

The communicating form of adult hydrocephalus in the elderly, NPH, is associated with the classic triad of gait, cognitive, and urinary disturbances. A third of NPH cases are classified as idiopathic, not secondary to trauma, surgery, meningitis, or other abnormalities of the arachnoid mater.<sup>8,9</sup> Ventricular shunting may provide symptom relief

in cases of NPH, which can be difficult to distinguish from vascular dementias and neurodegenerative diseases of the elderly. Thus, the treatment of NPH relies partly on accurate neuroimaging diagnosis and characterization.<sup>10,11</sup>

Kitagaki et al<sup>9</sup> demonstrated that the Sylvian fissure CSF volume and ventricular volume were greater in patients with iNPH compared with other dementias (ie, Alzheimer disease). Patients with iNPH also had decreased CSF in the superior convexity and medial subarachnoid spaces. This study supported enlarged basal cisterns and Sylvian fissures, with focally dilated sulci, as responsive to shunting. Narita et al<sup>12</sup> showed that presurgical high-convexity tightness, callosal angle, and Sylvian fissure dilation were significantly associated with clinical improvement. Following multiple linear regression, high-convexity tightness alone predicted clinical improvement at 1 year. However, 92% of patients had high-convexity tightness (rated as  $\geq 2$ ), and 100% had Sylvian fissure dilation (rated as  $\geq 2$ ). Similar to findings in the current study, findings in patients with DESH did improve following shunting, but the study of Narita et al<sup>12</sup> excluded patients with no DESH findings who were treated by shunting.

In a study by Mostafa et al,<sup>13</sup> 72 patients negative for DESH and 31 patients positive for DESH with adult hydrocephalus were assessed for shunt responsiveness—compared with 96 and 37 patients in the current study, respectively. In this study of the 103 patients included, 78 demonstrated symptomatic improvement at 1 year after shunting. Most interesting, of those who improved, 69% were negative for DESH findings and only 31% were positive for DESH with significance between both groups ( $P < .001$ ). The positive and negative predictive values for DESH findings predicting shunt responsiveness were 77% and 25%, respectively. This finding suggests that though the presence of DESH may predict shunt responsiveness, its absence does not preclude symptom improvement following shunting. The authors did not directly compare surgical outcomes of patients positive and negative for DESH, leaving open the possibility that DESH features were significant contributors to prognosis.

In the current study, patients positive for DESH had improvement in urinary, gait, and dementia symptoms following shunt

**Table 2: Preoperative clinical presentation**

	Overall	No DESH	DESH	P Value (No DESH vs DESH)
Gait (No.)	133	96	37	
Normal gait	14	13	1	>.05
Gait abnormality with uneven surfaces or pace	18	15	3	>.05
History of falls	54	40	14	>.05
Assisted gait (ie, walker)	39	23	16	>.05
Wheelchair-bound	8	5	3	>.05
Urinary dysfunction (No.)	131	94	37	
No dysfunction	43	31	12	>.05
Urgency, anxiety, or ambiguous symptoms not otherwise classified	19	16	3	>.05
Rare or intermittent symptoms	43	30	13	>.05
Urinary symptoms often	16	11	5	>.05
Urinary incontinence (requiring adult diapers)	10	6	4	>.05
Dementia (No.)	133	96	37	
No dementia	22	16	6	>.05
Forgetfulness	33	28	5	>.05
Mild dementia	47	33	14	>.05
Moderate dementia	21	14	7	>.05
Severe dementia	10	5	5	>.05
MMSE <sup>a</sup> (mean) (95% CI)	26.5 (7–30)	27.1 (16–30)	21.3 (7–28)	>.05
Tinetti (proportion)	21.4 (6–28)	21.63 (6–28)	21.3 (7–28)	>.05
TUG (mean) (95% CI)	19.07 (4.5–82)	18.63 (4.5–60)	19.5 (9.7–82)	>.05
Depression (proportion)	52/94 (55.3%)	40/73 (54.8%)	12/21 (57.1%)	>.05
Headache (proportion)	44/78 (56.4%)	36/62 (58.1%)	8/16 (50%)	>.05

<sup>a</sup> The MMSE score was available for 26/96 patients with preoperative findings without DESH and 34/37 patients with DESH.

**Table 3: Outcomes following treatment for adult hydrocephalus at last known follow-up (1248.3 ± 103.3 days following surgery)<sup>a</sup>**

	Overall	No DESH	DESH	P Value <sup>b</sup> (No DESH vs DESH)
Gait (No.)	113	84	29	
Improvement	89	65	24	>.05
No improvement	13	8	5	>.05
Worse	4	3	1	>.05
Normal findings at baseline	7	6	1	>.05
P value <sup>b</sup>	<.05	<.05	<.05	
Improvement compared with baseline				
Urinary dysfunction (No.) (%)	119	84	35	
Improvement	71	50	21	>.05
No improvement	6	3	3	>.05
Worse	2	2	0	>.05
Normal findings at baseline	40	29	11	>.05
P value <sup>b</sup>	<.05	<.05	<.05	
Improvement compared with baseline				
Dementia (No.) (%)				
Improvement	30	24	6	>.05
No improvement	7	4	3	>.05
Worse	3	3	0	>.05
Normal findings at baseline	7	4	3	>.05
P value <sup>b</sup>	<.05	<.05	<.05	
Improvement compared with baseline				
MMSE	27.5 (17–30)	27.7 (16–30)	27.4 (17–30)	>.05
Tinetti	25 (8–28)	24.9 (5–28)	25 (15–28)	>.05
TUG	13.5 (6–25.7)	14.6 (7.5–57)	12.9 (10.9–19)	>.05

<sup>a</sup> Columns compare the proportion improved among a cohort (ie, overall, DESH, No DESH); rows compare proportional improvement between those with and without DESH.

<sup>b</sup> The Fisher exact test was performed for those with preoperative symptoms, excluding those with normal findings at baseline. Findings are significant.

treatment. However, the data also demonstrated shunt responsiveness in the absence of DESH findings. Unlike previous literature, in our study, gait, dementia, and urinary symptoms improved in groups with DESH and without DESH following shunting, with no significant differences between groups. The DESH findings of tight high-convexity and medial subarachnoid spaces and enlarged Sylvian fissures with ventriculomegaly<sup>2</sup> may

therefore encompass only a portion of shunt-responsive adult hydrocephalus.

Limitations of this work include a sample size from a single institution, and those inherent in retrospective studies. In particular, outcome data available in the medical record for subjects in the study were limited and not homogeneous among all subjects. Because patients who fulfilled only partial features of DESH were

excluded from this study, the findings presented cannot be generalized to all patients with adult hydrocephalus. The exclusion of patients with poor clinical documentation or insufficient follow-up is unavoidable when collecting meaningful data but introduces the potential for bias in the inclusion of subjects. Our data suggest that if there is prognostic significance for the DESH pattern below the power of our study, it is not of sufficient magnitude to warrant significant weighting for the selection of individual patients for an operation. Future prospective studies in this area are required, including rigorous preoperative and postoperative clinical and radiographic evaluation.

## CONCLUSIONS

Normal-pressure hydrocephalus, a communicating form of adult hydrocephalus, is associated with the classic triad of gait, cognitive, and urinary disturbances in elderly patients. The DESH findings of tight high-convexity and medial subarachnoid spaces and enlarged Sylvian fissures with ventriculomegaly can be used for the diagnosis of NPH but may only encompass a portion of shunt-responsive adult hydrocephalus. The current study demonstrated urinary and dementia symptom improvement in both the presence and absence of DESH following shunting, with no significant differences between groups. Thus, shunt insertion for patients with adult hydrocephalus should not rely solely on the presence of preoperative DESH findings.

Disclosures: Abhay Moghekar—UNRELATED: Board Membership: I serve on the medical advisory board of the Hydrocephalus Association. It is an unpaid position; Travel/Accommodations/Meeting Expenses Unrelated to Activities Listed: Hydrocephalus Association, Comments: travel to the annual meeting advisory board meeting of the Hydrocephalus Association. Nafi Aygun—UNRELATED: Royalties: Elsevier, Cambridge University Press; Payment for Development of Educational Presentations: American College of Radiology. Ari M. Blitz—RELATED: Support for Travel to Meetings for the Study or Other Purposes: International Society for Hydrocephalus and CSF Disorders, Comments: partial reimbursement for travel for an educational talk on a related subject; UNRELATED: Grants/Grants Pending: National Institutes of Health, Comments: coinvestigator of FAIN U01DC013778 and R21 NS096497, prior grant support via the Principal Investigator Dr Daniele Rigamonti from Aesculab\*; Payment for Lectures Including Service on Speakers Bureaus: French-Israeli Radiology course, Comments: partial reimbursement for travel for educational talks. \*Money paid to the institution.

## REFERENCES

1. Adams RD, Fisher CM, Hakim S, et al. **Symptomatic occult hydrocephalus with “normal” cerebrospinal-fluid pressure: a treatable syndrome.** *N Engl J Med* 1965;273:117–26 CrossRef Medline
2. Hashimoto M, Ishikawa M, Mori E, et al; Study of INPH on neurologic improvement (SINPHONI). **Diagnosis of idiopathic normal pressure hydrocephalus is supported by MRI-based scheme: a prospective cohort study.** *Cerebrospinal Fluid Res* 2010;7:18 CrossRef Medline
3. Marmarou A, Bergsneider M, Klinge P, et al. **The value of supplemental prognostic tests for the preoperative assessment of idiopathic normal-pressure hydrocephalus.** *Neurosurgery* 2005;57(3 Suppl):S17–28; discussion ii-v Medline
4. Relkin N, Marmarou A, Klinge P, et al. **Diagnosing idiopathic normal-pressure hydrocephalus.** *Neurosurgery* 2005;57(3 Suppl):S4–16; discussion ii-v Medline
5. Keong NC, Pena A, Price SJ, et al. **Imaging of normal pressure hydrocephalus: theories, techniques, and challenges.** *Neurosurg Focus* 2016;41:E11 CrossRef Medline
6. Mori E, Ishikawa M, Kato T, et al; Japanese Society of Normal Pressure Hydrocephalus. **Guidelines for management of idiopathic normal pressure hydrocephalus: second edition.** *Neurol Med Chir (Tokyo)* 2012;52:775–809 CrossRef Medline
7. Mendes GAS, de Oliveira MF, Pinto FCG. **The Timed Up and Go Test as a diagnostic criterion in normal pressure hydrocephalus.** *World Neurosurg* 2017;105:456–61 CrossRef Medline
8. Gallagher RM, Marquez J, Osmotherly P. **Cognitive and upper limb symptom changes from a tap test in Idiopathic Normal Pressure Hydrocephalus.** *Clin Neurol Neurosurg* 2018;10:92–96.
9. Kitagaki H, Mori E, Ishii K, et al. **CSF spaces in idiopathic normal pressure hydrocephalus: morphology and volumetry.** *AJNR Am J Neuroradiol* 1998;19:1277–84 Medline
10. Matsumae M, Kikinis R, Möröcz IA, et al. **Age-related changes in intracranial compartment volumes in normal adults assessed by magnetic resonance imaging.** *J Neurosurg* 1996;84:982–91 CrossRef Medline
11. Gammal TE, Allen MB, Brooks BS, et al. **MR evaluation of hydrocephalus.** *AJR Am J Roentgenol* 1987;149:807–13 CrossRef Medline
12. Narita W, Nishio Y, Baba T, et al. **High-convexity tightness predicts the shunt response in idiopathic normal pressure hydrocephalus.** *AJNR Am J Neuroradiol* 2016;37:1831–37 CrossRef Medline
13. Mostafa T, Craven C, Patel NA, et al. **DESH negative normal pressure hydrocephalus: can patients still benefit from shunt insertion?** *Fluids and Barriers of the CN* 2015;12(Suppl 1):O52 CrossRef

# Prospective Multicenter Study of Changes in MTT after Aneurysmal SAH and Relationship to Delayed Cerebral Ischemia in Patients with Good- and Poor-Grade Admission Status

A. Murphy, T.-Y. Lee, T.R. Marotta, J. Spears, R.L. Macdonald, R.I. Aviv, A. Baker, and A. Bharatha

## ABSTRACT

**BACKGROUND AND PURPOSE:** Patients with aneurysmal SAH and good clinical status at admission are considered at a lower risk for delayed cerebral ischemia. Prolonged MTT may be associated with an increased risk. It is unclear whether this is dependent on clinical status. Our purpose was to determine whether increased MTT within 3 days of aneurysmal SAH compared with baseline is associated with a higher risk of delayed cerebral ischemia in patients with good (World Federation of Neurosurgical Societies I–III) versus poor (World Federation of Neurosurgical Societies IV–V) admission status.

**MATERIALS AND METHODS:** This prolonged MTT was a multicenter, prospective cohort investigation of 87 patients with aneurysmal SAH. MTT was measured at admission before aneurysm treatment (MTT<sub>1</sub>) and following repair (MTT<sub>2</sub>) within 3 days of admission; MTT<sub>diff</sub> was calculated as the difference between MTT<sub>2</sub> and MTT<sub>1</sub>. Changes in MTT across time were assessed with repeated measures analyses. Risk of delayed cerebral ischemia or death was determined with multivariate logistic regression analysis.

**RESULTS:** In patients with a good grade ( $n = 49$ ), MTT was prolonged in patients who developed delayed cerebral ischemia, with MTT<sub>diff</sub> significantly greater ( $0.82 \pm 1.5$ ) compared with those who did not develop delayed cerebral ischemia ( $-0.14 \pm 0.98$ ) ( $P = .03$ ). Prolonged MTT was associated with a significantly higher risk of delayed cerebral ischemia or death (OR = 3.1; 95% CI, 1.3–7.4;  $P = .014$ ) on multivariate analysis. In patients with poor grades ( $n = 38$ ), MTT<sub>diff</sub> was not greater in patients who developed delayed cerebral ischemia; MTT<sub>1</sub> was significantly prolonged compared with patients with a good grade.

**CONCLUSIONS:** Patients in good clinical condition following aneurysmal SAH but with increasing MTT in the first few days after aneurysmal SAH are at high risk of delayed cerebral ischemia and warrant close clinical monitoring.

**ABBREVIATIONS:** aSAH = aneurysmal SAH; DCI = delayed cerebral ischemia; GCS = Glasgow Coma Scale; ICP = intracranial pressure; MTT<sub>1</sub> = MTT before aneurysm treatment; MTT<sub>2</sub> = MTT after repair; MTT<sub>diff</sub> = the difference between MTT before aneurysm treatment and after repair; WFNS = World Federation of Neurosurgical Societies

Identifying patients at high risk of delayed cerebral ischemia (DCI) after aneurysmal subarachnoid hemorrhage (aSAH) is

important for guiding medical and endovascular management and could help improve disposition planning. Management algorithms are largely based on admission clinical status and the volume of SAH.<sup>1,2</sup> The World Federation of Neurosurgical Societies (WFNS) has a commonly used scale to assess presentation clinical status.<sup>3</sup> Higher WFNS grades (IV–V) are associated with a higher risk of DCI and death,<sup>3–4</sup> while a good grade (WFNS I–III) at admission indicates lower risk.<sup>5</sup>

Early perfusion abnormalities before DCI symptoms could help identify patients at risk.<sup>6</sup> Specifically, delayed MTT measured with CTP may be associated with higher risk.<sup>7</sup> Absolute thresholds have been cited but depend on physiologic variability between individuals and technical aspects of acquisition and post-

Received March 25, 2018; accepted after revision July 26.

From the Division of Diagnostic and Interventional Neuroradiology (A.M., T.R.M., A. Bharatha), Department of Medical Imaging, Division of Neurosurgery (R.L.M.), Departments of Anesthesia and Critical Care Medicine (A. Baker), Labatt Family Centre of Excellence in Brain Injury and Trauma Research (R.L.M.), Keenan Research Centre for Biomedical Science (R.L.M.), and the Li Ka Shing Knowledge Institute (R.L.M.), St. Michael's Hospital, Toronto, Ontario, Canada; Lawson Health Research Institute and Robarts Research Institute (T.-Y.L.), University of Western Ontario, London, Ontario, Canada; Division of Neurosurgery (T.R.M., J.S., A. Bharatha), Department of Surgery, St. Michael's Hospital, University of Toronto, Toronto, Ontario, Canada; Departments of Physiology and Surgery (R.L.M.) and Medical Imaging (A. Bharatha), University of Toronto, Toronto, Ontario, Canada; and Department of Medical Imaging (R.I.A.), Sunnybrook Hospital, Toronto, Ontario, Canada.

A.M. was supported by an RSNA Research Fellow Grant. Portions of this work were supported by the Innovation Fund of the Alternative Funding Plan for the Academic Health Sciences Centres of Ontario (St. Michael's Hospital, Sunnybrook Hospital) to A. Bharatha and R.I.A.

Please address correspondence to Aditya Bharatha, MD, FRCPC, St. Michael's Hospital, University of Toronto, 30 Bond St, Room 3-077CC, Toronto, ON, M5B 1W8 Canada; e-mail: BharathaA@smh.ca

<http://dx.doi.org/10.3174/ajnr.A5844>

processing.<sup>8</sup> Hence, early changes in cerebral perfusion within individuals may be a more accurate marker.

The purpose of this study was to determine whether prolonged MTT within 3 days of aSAH is associated with a higher risk of DCI in patients with good (WFNS I–III) and poor (WFNS IV–V) clinical status on admission. Secondly, we assessed the pattern of MTT changes before and after aneurysm treatment in patients with good and poor grades.

## MATERIALS AND METHODS

### Study Population

This was a prospective multicenter cohort investigation of patients with aSAH between 2015 and 2017. Power analysis performed for logistic regression analysis with DCI as a binary response variable showed that 83 patients were required to achieve 80% power at .05 significance. Inclusion criteria were aSAH and age older than 18 years. Exclusion criteria were the following: no aneurysm, prior aneurysm treatment, poor scan quality, no baseline CTP, severe renal dysfunction, or contrast allergy. Consecutive patients presenting with aSAH at 2 institutions (St. Michael's Hospital and Sunnybrook Hospital, Toronto, Ontario, Canada) were screened. Institutional ethics approval and informed consent were obtained.

### Clinical Data

Patient demographics, WFNS grade (good grade = I–III; poor grade = IV–V), Glasgow Coma Scale (GCS) score, hypertension, and smoking status were recorded at admission. The type of aneurysm treatment (clipping or coiling) was documented. Intracranial pressure (ICP) measurements were obtained at scanning when available.

DCI was defined according to a previously published consensus statement and considered present with new focal neurologic impairment or a decrease of at least 2 points in the GCS score not apparent immediately after aneurysm treatment and not attributed to other causes.<sup>9</sup> Death within 2 weeks of admission was additionally noted. Timing of medical and endovascular treatment for DCI was reviewed to confirm occurrence after the onset of symptoms.

### CT

Each patient had a noncontrast CT, CTA, and CTP on admission (before aneurysm treatment) and within 3 days of admission (after aneurysm treatment). Admission noncontrast CT images were assessed to determine the Modified Fisher Scale grade<sup>10</sup> and for hydrocephalus and intraparenchymal hematoma. CTAs were assessed for angiographic vasospasm (the presence of large-artery vessel narrowing at baseline or on a subsequent study compared with baseline).

CTP was performed on either 256-slice or 64-slice scanners (Revolution or VCT; GE Healthcare, Milwaukee, Wisconsin) (256-slice: 14 cm of coverage with 80 kV; 75–150 Smart mA dose modulation; noise index, 8; rotation time, 1 second; and Adaptive Statistical Iterative Reconstruction (ASIR), 50%; 64-slice: shuttle mode, 16 × 5 mm slices [8 cm of coverage] with 80 kV and 100 milliamper second (mAs)).

CTP cine images were analyzed on CT Perfusion 5 (Prototype

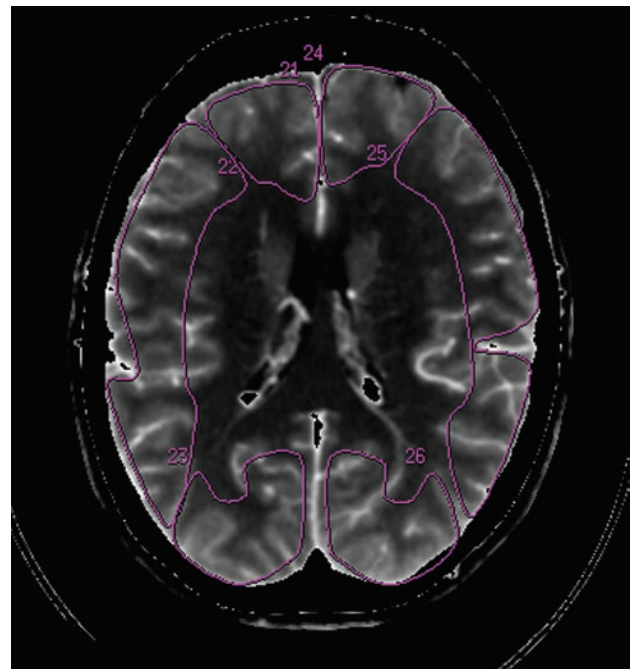


**FIG 1.** Example of cortical vascular territory ROIs drawn on the average map before gray-white matter segmentation.

of CTP 4D; GE Healthcare) by research assistants with expertise in CTP analysis blinded to clinical data. Arterial input ROIs were chosen to maximize the slope of the arterial time-density curve, usually the anterior cerebral artery or MCA. Venous ROIs were placed on the superior sagittal sinus to maximize the area under the venous time-density curve.<sup>11</sup> CTP functional maps for each slice, including MTT, CBF, and an average map (average of all the cine images of the same slice), were generated.

Slices with extensive coil artifacts were excluded. ROIs were drawn to define the anterior cerebral artery, MCA, and posterior cerebral artery vascular territories and the basal ganglia and thalamus on each slice, avoiding hematomas and External ventricular drain (EVD) tracts (Fig 1). Segmentation of gray and white matter was achieved using a threshold range of Hounsfield units. Blood flow and blood volume thresholding was performed to exclude vascular structures by eliminating pixels with blood flow of >100 mL/min/100 g and blood volume of >8 mL/100 g from the segmented gray and white matter masks.<sup>12</sup> The ROIs were automatically propagated to MTT maps, and MTT was calculated as the weighted average of the gray matter volume from all ROIs on all slices. MTT on the CTP performed at admission before aneurysm treatment was MTT1, and at 3 days after treatment, it was MTT2.

### Statistical Analysis

Characteristics of the study population were compared using an independent *t* test for continuous variables or  $\chi^2$  analysis for categorical variables.

To study the interaction between MTT changes associated with DCI and clinical grade, we dichotomized patients into 2 groups (good grade, WFNS I–III; and poor grade, WFNS IV–V) at presentation. Repeated measures linear regression analysis was performed to assess differences between MTT1 and MTT2 and the interaction between temporal changes in MTT and grade. Post hoc analysis was

**Table 1: Characteristics of the study population**

	All (n = 87)	Good Grade (n = 49)	Poor Grade (n = 38)	P Value
Age (mean) (SD) (yr)	58.5 (13.2)	57.5 (12.8)	59.4 (13.9)	.554
Female (No.) (%)	58 (67)	34 (69)	24 (63)	.541
Smoking (No.) (%)	28 (32)	15 (31)	13 (34)	.722
Hypertension (No.) (%)	41 (47)	19 (39)	22 (58)	.076
GCS score (mean) (SD)	11.2 (4.6)	14.5 (0.8)	6.8 (3.8)	<.001
mFisher grade (No.) (%)				<.001
1	7 (8)	7 (14)	0 (0)	
2	26 (30)	21 (43)	5 (13)	
3	6 (7)	6 (12)	0 (0)	
4	58 (55)	15 (31)	33 (87)	
Aneurysm treatment (No.) (%)				.015
Clip	11 (13)	7 (14)	4 (11)	
Coil	70 (81)	42 (86)	28 (74)	
None	6 (6)	0 (0)	6 (16)	
Intracerebral hematoma (No.) (%)	64 (74)	8 (16)	15 (40)	.03
Hydrocephalus (No.) (%)	57 (66)	27 (55)	30 (79)	.02
Intracranial pressure (mean) (SD) <sup>a</sup>	28.7 (28.0)	15.3 (7.9)	36.8 (31.1)	.005
Angiographic vasospasm (No.) (%)				.377
CT 1	1 (1)	1 (2)	0	
CT 2	10 (11)	6 (12)	4 (11)	
DCI (No.) (%)	13 (15)	9 (18)	4 (11)	.309
Death (No.) (%)	12 (14)	0 (0)	12 (34)	<.001
DCI or death (No.) (%)	25 (28)	9 (18)	16 (42)	.015

Note:—mFisher indicates modified Fisher Scale; CT 1, before aneurysm treatment; CT 2, after aneurysm treatment.

<sup>a</sup> Data available in 15/49 patients with good grades and 31/38 with poor grades.

**Table 2: Mean MTT values**

	Good Grade			Poor Grade		
	All	No DCI	DCI	All	No DCI	DCI or Death
MTT 1 (SD)	6.3 (1.4)	6.2 (1.3)	6.6 (1.9)	7.7 (2.3) <sup>a</sup>	7.3 (1.7) <sup>a</sup>	8.3 (3.0) <sup>a</sup>
MTT 2 (SD)	6.3 (1.7)	6.1 (1.5)	7.4 (2.5)	6.4 (1.9)	6.5 (2.1)	6.0 (0.8)
MTT <sub>diff</sub> (SD)	0.03 (1.2)	-0.14 (0.98)	0.82 (1.6)	-0.75 (1.7)	-0.75 (1.8)	-0.78 (1.6)

<sup>a</sup> Significantly greater than MTT1 in patients with good grades ( $P < .05$ ).

performed with paired *t* tests for patients with good and poor grades. The difference between MTT before aneurysm treatment and after repair (MTT<sub>diff</sub>) was calculated. Differences between groups were assessed with independent *t* test analysis.

Logistic regression analysis was used to assess predictors of DCI or death. First, univariate analysis was used to identify significant clinical predictors. Multivariate analysis was then performed to assess the risk of DCI or death associated with MTT<sub>diff</sub> for patients with good and poor grades, in combination with clinical factors identified as significant on independent univariate analysis. Receiver operating characteristic curve analysis with calculation of the Youden Index was performed to determine optimal thresholds of MTT1, MTT2, and MTT<sub>diff</sub>. Statistical analysis was performed with the SPSS statistics package, Version 24 (IBM, Armonk, New York). Results were considered significant at  $P < .05$ .

## RESULTS

### Characteristics of Study

Eighty-seven patients were included. One hundred two were screened, and 15 were excluded for the following indications: no baseline CTP ( $n = 6$ ), rebleed of previously coiled aneurysm ( $n = 2$ ), nonaneurysmal SAH ( $n = 5$ ), CTP of insufficient quality ( $n = 1$ ), and no SAH on baseline ( $n = 1$ ) (Table 1).

Forty-nine of 87 (56%) had good grades on admission, and 38/87 (44%) had poor grades. Patients with poor grades had lower

GCS scores, higher Modified Fisher Scale scores, higher ICP, and higher incidences of intraparenchymal hematoma, hydrocephalus, and untreated aneurysm. Death within 2 weeks occurred in 12 patients, all of whom had poor grades. While the rate of DCI was similar between patients with good and poor grades, patients with poor grades had significantly higher rates of death and DCI when considered together.

### Temporal Trends in MTT

There was a significant interaction between MTT and clinical grade ( $P = .009$ ), indicating that changes between MTT1 and MTT2 are different for patients with poor and good grades. MTT1 was significantly higher in patients with a poor grade compared with patients with a good grade with and without DCI or death ( $P < .05$ ). There was no difference in MTT2 (Table 2 and Figs 2 and 3).

In patients with a good grade, different trends were observed between MTT1 and MTT2 in patients with and without DCI ( $P = .03$ ) (Table 2). The mean difference between MTT2 and MTT1 was positive in patients who developed DCI ( $0.82 \pm 1.6$ ), indicating increasing (worsening) MTT in the first few days after aSAH. This difference was

significantly greater than the MTT<sub>diff</sub> in patients without DCI ( $-0.14 \pm 0.98$ ,  $P = .03$ ), which showed an average decrease (improvement) in MTT.

In patients with a poor grade, similar trends were observed between MTT1 and MTT2 in patients with and without DCI ( $P = .969$ ). MTT significantly decreased between MTT1 and MTT2 in patients who developed DCI or death and those who did not (MTT1,  $8.3 \pm 3.0$  seconds, versus MTT2,  $6.0 \pm 0.8$  seconds;  $P = .03$ ). In pooled analysis combining patients with good and poor grades, we did not find a statistically significant trend in the change in MTT between patients who did or did not develop DCI.

### Univariate Analysis: Predictors of DCI or Death

Univariate analysis showed that WFNS, ICP, GCS, and intraparenchymal hematoma were significant predictors of DCI or death (Table 3). In patients with a good grade, MTT<sub>diff</sub> was associated with a higher risk of DCI (OR = 2.1; 95% CI, 1.0–4.1;  $P = .04$ ). Patients with poor grades had no significantly increased risk of DCI or death with increasing MTT (OR = 0.99; 95% CI, 0.6–1.6;  $P = .97$ ).

### Multivariate Analysis: Predictors of DCI or Death

Increasing MTT between MTT1 and MTT2 (higher MTT<sub>diff</sub>), intraparenchymal hematoma, and higher WFNS scores remained

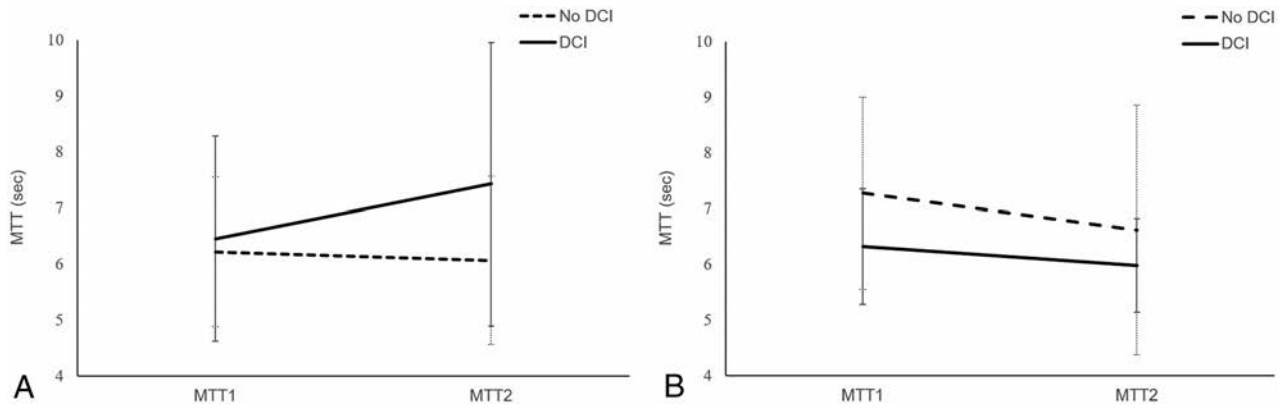


**FIG 2.** Average MTT values in patients with good (A) and poor (B) grades with and without DCI. Note that the displayed y-axis MTT has been truncated (4–8 seconds in A and 5–7.5 seconds in B) to physiologic ranges to allow better visualization of the trends. *Error bars* represent the SDs (reflecting interindividual variation in MTT).

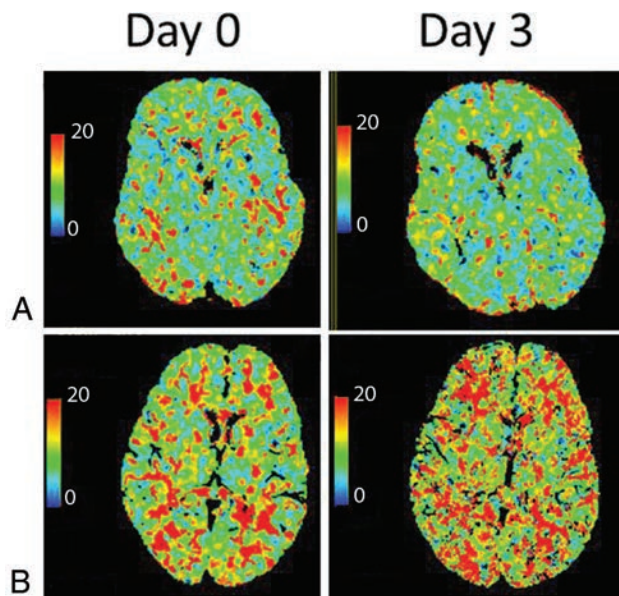


**FIG 3.** Representative MTT maps at days 0 and 3. A, Patient with good grade (WFNS I) who did not develop DCI. MTT on day 0 = 6.8 second; MTT on day 3 = 6.8 second. B, Patient with good grade (WFNS I) who developed DCI on day 5. MTT on day 0 = 7.4 second; MTT on day 3 = 10.2 second.

significant predictors of DCI or death on multivariate analysis (Table 4). Subgroup analysis of patients with good and poor grades showed that higher  $MTT_{diff}$  (worsening MTT between MTT1 and MTT2) was significantly associated with an increased risk of DCI in patients with a good grade (OR = 3.1; 95% CI, 1.3–7.4;  $P = .014$ ).

### MTT Thresholds

In patients with a poor grade, there was a higher baseline MTT threshold (MTT1, >9.6 seconds) compared with patients with a good grade (MTT1, >6.5 seconds), whereas the MTT2 thresholds are similar regardless of clinical grade.  $MTT_{diff}$  thresholds also differed depending on the clinical grade, with patients with a good grade showing a positive threshold ( $MTT_{diff} > 0.2$ ) and patients with a poor grade showing a negative threshold ( $MTT_{diff}$  more than  $-0.33$ ) (Table 5).

### DISCUSSION

In this study, we showed that increasing (worsening) MTT in the first few days after aSAH was associated with an increased risk of DCI or death in patients with a good grade. Roughly every 1-second increase in global MTT was associated with a  $3\times$  greater risk of DCI in patients with a good clinical status, and this risk remained significant on multivariate analysis. In contrast, patients with a poor grade (WFNS IV–V) tended to show decreasing (improving) MTT in the first few days after aSAH in those with and without subsequent DCI or death.

Some management algorithms rely on clinical status for triaging patients to high or low risk for DCI and poor outcome.<sup>2,13</sup> Patients in good clinical condition may undergo less frequent neurologic monitoring and may be transferred out of intensive care units earlier.<sup>1</sup> Consensus statements have identified CTP as a potential screening tool, though specific recommendations for its integration are lacking.<sup>14,15</sup> Our data support the use of CTP in the first few days after aSAH before the typical onset of DCI, to identify patients who, despite good clinical status, remain at an elevated risk of DCI. Multivariate analysis showed that increasing MTT remained a significant risk factor for DCI in patients with a good grade.

MTT changes that we observed occurred before DCI symptoms. This “therapeutic window” could allow optimization of therapy in high-risk patients. Effective options for the prevention of DCI are currently limited to nimodipine and maintenance of euvolemia.<sup>16</sup> Once DCI has been established, hypertensive therapy is considered first-line treatment in many centers, though there is a lack of evidence showing clinical benefit.<sup>16–18</sup> Targeted application of therapies in individuals at higher risk might improve the clinical efficacy, though currently evidence is lacking. In addition, new prophylactic treatment studies might incorporate  $MTT_{diff}$  as a biomarker for imaging selection or for monitoring treatment efficacy.<sup>13,19,20</sup>

While MTT on admission was significantly higher in patients with a poor-versus-good grade, it was not a significant predictor of DCI or death in either univariate or multivariate models. This finding may reflect the limitations of a single-measurement MTT,<sup>22</sup> compared with temporal changes of MTT in an individual. Technical differences may also have an impact.<sup>22</sup> In our study, CTP data were acquired at 2 different tertiary care centers

**Table 3: Univariate analysis**

	All			Good Grade			Poor Grade		
	OR	95% CI	P Value	OR	95% CI	P Value	OR	95% CI	P Value
Female	1.4	0.5–3.9	.504	0.86	0.18–4.0	.85	2.5	0.61–10.2	.2
Age	1.0	0.97–1.04	.512	0.96	0.90–1.0	.19	0.1	0.99–1.1	.09
Smoking	1.74	0.61–5.0	.303	0.86	0.18–4.0	.85	3.6	0.80–16.4	.096
Hypertension	1.5	0.59–3.80	.4	0.75	0.17–3.2	.7	4.44	1.12–17.7	.03 <sup>a</sup>
Hydrocephalus	0.66	0.24–1.8	.421	0.98	0.23–4.2	.98	0.78	0.16–3.9	.77
Hematoma	0.11	0.31–0.84	.021 <sup>a</sup>	0.065	0.01–0.38	.002 <sup>a</sup>	1.15	0.31–4.3	.832
GCS score	0.88	0.79–0.97	.01 <sup>a</sup>	0.92	0.38–2.2	.85	0.92	0.77–1.1	.36
WFNS score	1.44	1.08–1.92	.013 <sup>a</sup>						
mFisher Scale score	1.14	0.74–1.77	.554	0.48	0.21–1.1	.08	1.8	0.58–5.8	.3
Intracranial pressure	1	1.0–1.1	.013 <sup>a</sup>	1.0	1.0–1.1	.03	0.89	0.68–1.2	.41
MTT1	1.3	1.0–1.6	.055	1.1	0.69–1.8	.66	1.21	0.89–1.6	.22
MTT2	1.16	0.87–1.55	.326	1.4	0.98–2.1	.06	0.85	0.51–1.4	.52
MTT <sub>diff</sub>	1.24	0.82–1.86	.305	2.1	1.0–4.1	.04 <sup>a</sup>	0.99	0.6–1.6	.97

Note:—mFisher indicates modified Fisher Scale.

<sup>a</sup> Significant.

**Table 4: Multivariate analysis**

	All			Good Grade			Poor Grade		
	OR	95% CI	P Value	OR	95% CI	P Value	OR	95% CI	P Value
WFNS grade	3.08	1.03–9.22	.04						
GCS score	1.2	0.87–2.8	.31	0.57	0.17–1.9	.36	1.11	0.88–1.4	0.38
Hematoma	0.15	0.03–0.72	.02	0.03	0.003–0.34	.005	1.2	0.18–7.6	.87
MTT <sub>diff</sub>	1.67	1.01–2.8	.04	3.1	1.3–7.4	.014	0.91	0.52–1.6	.73

**Table 5: Optimal MTT thresholds and sensitivity and specificity (determined by the Youden Index) for DCI/death<sup>a</sup>**

Clinical Grade	MTT1	MTT2	MTT <sub>diff</sub>
All	9.5 (26, 95)	5.5 (67, 48)	0.06 (47, 75)
Good	6.5 (56, 73)	5.0 (100, 35)	0.2 (73, 37)
Poor	9.6 (64, 90)	5.4 (88, 46)	−0.33 (43, 65)

<sup>a</sup> MTT values in seconds with corresponding sensitivity and specificity (%).

with different CT scanners, though all postprocessing was performed at the same core laboratory with standardized methodology.

We chose to analyze MTT because it has been previously shown to be a sensitive perfusion parameter for prediction and detection of DCI,<sup>23–25</sup> and it takes into account fluctuations in both CBF and CBV (MTT = CBV / CBF as per the central volume principle). Prolonged MTT may be reflective of vasospasm in both proximal vessels surrounding the circle of Willis (angiographic vasospasm) or distal parenchymal arterioles (microcirculation). Autoregulatory disturbances likely have a role in the development of DCI (or are precursors to DCI) and may occur independent of large-artery vasospasm.<sup>26</sup> In this cohort, very few patients showed angiographic vasospasm at MTT1 or MTT2; the incidence was similar between patients with good and poor grades and unlikely to be a significant cause of early MTT elevation (Table 1).

Elevations in MTT during the first few days after aSAH potentially reflect an element of early brain injury, a global brain injury that occurs in the first few days following aSAH and may be associated with DCI. The underlying etiology of early brain injury may involve inadequate physiologic compensation for acute ICP elevations from aneurysm rupture, with cellular injury, edema, blood-brain barrier disruption, and microvascular disturbances.<sup>27,28</sup> Clinical manifestations may not be clear on early physical examination until abrupt changes in neurologic status

are manifested as DCI. We showed a significant interaction between clinical grade and MTT, indicating that MTT changes are different between patients with good and poor grades. While MTT generally worsened in patients with a good grade who subsequently went on to DCI, it improved in patients with a poor grade with DCI. This seemingly paradoxical result might be accounted for by the effects of early brain injury or the effects of untreated ICP/hydrocephalus, both of which could result in prolonged MTT.<sup>29</sup> In our cohort, EVDs were present in 60% of patients with a poor grade at MTT1, and an additional 8 patients (21%) had interval EVD insertion before MTT2. In both groups, we observed improving MTT between MTT1 and MTT2, suggesting that corrected hydrocephalus is not the only explanation for MTT improvement in these patients.

In patients with a poor grade, high MTT at admission of >9.6 seconds (as determined by the Youden Index threshold analysis; Table 5) portends increased risk of subsequent DCI or death. Elevated ICP can lead to delayed MTT. As ICP normalizes (for example, following CSF diversion), MTT decreases as cerebral perfusion improves; this change could lead to improvement or reperfusion injury that exacerbates early brain injury.

With respect to early within-individual changes in MTT, there are other limited published data. In a study by Rogriguez-Régent et al,<sup>30</sup> CTP between day 0 and day 4 was analyzed in 47 patients with aSAH. Early deterioration in perfusion parameters was significantly correlated with an increased risk of delayed infarct burden on CT/MR imaging. However, their study focused on imaging outcome, whereas ours focused on clinical deterioration of DCI. Because therapeutic maneuvers may prevent patients with DCI from developing infarction, we think that our study provides important evidence about the relationship of early deterioration in MTT to the development of clinical DCI, which is the current target for clinical intervention. Our study also included a larger

cohort of patients and explored the influence of clinical grade on early perfusion changes.

Limitations include a relatively low percentage of DCI in this cohort compared with the literature, which, in the context of the sample size, could influence the power of the results. In addition, the clinical teams were not blinded to the results of CTA/CTP; however, they did not have access to quantitative CTP data, only qualitative color maps. This is mitigated by the fact that this study included strict clinical definitions of DCI, which were not influenced by imaging results. There was a relatively high rate of patients with poor grades in this study, likely due to the prospective study design in which patients with poor presentation of clinical status were not excluded. Clinical detection of DCI in patients with poor grades is challenging, and this issue could introduce errors in the diagnosis of DCI in these patients. We chose to include death in combination with DCI in patients with a poor grade because this is a measurable outcome in patients with a comatose or nearly comatose state, but this could also introduce error. Finally, CT perfusion includes iodinated contrast (risks for renal injury and allergic reaction) and ionizing radiation (risk of radiation injury and induced cancer); however, these risks are low using optimal imaging protocols.

## CONCLUSIONS

In patients with a good grade (WFNS I–III), increased MTT in the early period after SAH (around day 3) compared with a baseline study performed at presentation is associated with a significantly higher risk of subsequent development of DCI. Patients with a poor grade (WFNS IV–V) did not show an increased risk of DCI with increasing MTT. Early changes in MTT may be a useful imaging biomarker for the risk of DCI in patients with a good grade.

## ACKNOWLEDGMENTS

The authors thank the following individuals for their contributions to this investigation: Kyle Burgers, Elton Law, Feng Su, Marjorie Ho, Rita Vittorino, Vy Nguyen, Yang-mei Li, Pascal Tyrrell, Kuan Liu, and Yaesh Randeree.

Disclosures: Amanda Murphy—RELATED: Grant: RSNA Research Fellow Grant.\* Ting-Yim Lee—UNRELATED: Grants/Grants Pending: GE Healthcare, Comments: research study on dual-energy CT scanning of metal objects in the extremities\*; Royalties: GE Healthcare, Comments: for the CT perfusion license agreement\*. Thomas R. Marotta—UNRELATED: Consultancy: Medtronic, Comments: proctor for the Pipeline Embolization Device; Patents (Planned, Pending or Issued): eCLIPS; Stock/Stock Options: Evasc. Robert L. Macdonald—UNRELATED: Board Membership: Brain Aneurysm Foundation, Canadian Institutes of Health Research; Employment: Edge Therapeutics; Stock/Stock Options: Edge Therapeutics. Richard I. Aviv—RELATED: Grant: Sunnybrook Alternate Funding Plan. Comments: grant is for 46,000, grant was peer reviewed.\* Aditya Bharatha—RELATED: Grant: Ontario Alternate Funding Plan Innovation Grant.\* \*No money paid to the institution.

## REFERENCES

1. de Oliveira Manoel AL, Jaja BN, Germans MR, et al; SAHIT collaborators. **The VASOGRADE: a simple grading scale for prediction of delayed cerebral ischemia after subarachnoid hemorrhage.** *Stroke* 2015;46:1826–31 CrossRef Medline
2. de Oliveira Manoel AL, Turkel-Parrella D, Duggal A, et al. **Managing aneurysmal subarachnoid hemorrhage: it takes a team.** *Cleve Clin J Med* 2015;82:177–92 CrossRef Medline
3. Teasdale GM, Drake CJ, Hunt W, et al. **A universal subarachnoid**

4. **hemorrhage scale: report of a committee of the World Federation of Neurological Societies.** *J Neurol Neurosurg Psychiatry* 1988;51:1457.
5. de Rooij NK, Greving JP, Rinkel GJE, et al. **Early prediction of delayed cerebral ischemia after subarachnoid hemorrhage: development and validation of a practical risk chart.** *Stroke* 2013;44:1288–94 CrossRef Medline
6. Crobeddu E, Mittal MK, Dupont S, et al. **Predicting the lack of development of delayed cerebral ischemia after aneurysmal subarachnoid hemorrhage.** *Stroke* 2012;43:697–701 CrossRef Medline
7. Lagares A, Cicuendez M, Ramos A, et al. **Acute perfusion changes after spontaneous SAH: a perfusion CT study.** *Acta Neurochir (Wien)* 2012;154:402–05; discussion 411–12 CrossRef Medline
8. Murphy A, Manoel AL, Burgers K, et al. **Early CT perfusion changes and blood-brain barrier permeability after aneurysmal subarachnoid hemorrhage.** *Neuroradiology* 2015;57:767–73 CrossRef Medline
9. Sanelli PC, Ugorec I, Johnson CE, et al. **Using quantitative CT perfusion for evaluation of delayed cerebral ischemia following aneurysmal subarachnoid hemorrhage.** *AJNR Am J Neuroradiol* 2011;32:2047–53 CrossRef Medline
10. Vergouwen MD, Vermeulen M, van Gijn J, et al. **Definition of delayed cerebral ischemia after aneurysmal subarachnoid hemorrhage as an outcome event in clinical trials and observational studies: proposal of a multidisciplinary research group.** *Stroke* 2010;41:2391–95 CrossRef Medline
11. Frontera JA, Claassen J, Schmidt JM, et al. **Prediction of symptomatic vasospasm after subarachnoid hemorrhage: the modified Fisher scale.** *Neurosurgery* 2006;59:21–27 CrossRef Medline
12. Lee TY, Menon BK, Goyal M, et al. **Quantitative CBF measurement with CT perfusion: is it correct to correct the partial volume averaged arterial input curve with venous output curve?** *Stroke* 2013;44:e174–228
13. Kudo K, Terae S, Katoh C, et al. **Quantitative cerebral blood flow measurement with dynamic perfusion CT using the vascular-pixel elimination method: comparison with H2(15)O positron emission tomography.** *AJNR Am J Neuroradiol* 2003;24:419–26 Medline
14. Macdonald RL. **Delayed neurological deterioration after subarachnoid haemorrhage.** *Nat Rev Neurol* 2014;10:44–58 CrossRef Medline
15. Connolly ES Jr, Rabinstein AA, Carhuapoma JR, et al; American Heart Association Stroke Council; Council on Cardiovascular Radiology and Intervention; Council on Cardiovascular Nursing; Council on Cardiovascular Surgery and Anesthesia; Council on Clinical Cardiology. **Guidelines for the management of aneurysmal subarachnoid hemorrhage: a guideline for healthcare professionals from the American Heart Association/American Stroke Association.** *Stroke* 2012;43:1711–37 CrossRef Medline
16. Diringner MN, Bleck TP, Claude Hemphill J 3rd, et al; Neurocritical Care Society. **Critical care management of patients following aneurysmal subarachnoid hemorrhage: recommendations from the Neurocritical Care Society's Multidisciplinary Consensus Conference.** *Neurocrit Care* 2011;15:211–40 CrossRef Medline
17. Francoeur CL, Mayer SA. **Management of delayed cerebral ischemia after subarachnoid hemorrhage.** *Crit Care* 2016;20:277 CrossRef Medline
18. Muench E, Horn P, Bauhuf C, et al. **Effects of hypervolemia and hypertension on regional cerebral blood flow, intracranial pressure, and brain tissue oxygenation after subarachnoid hemorrhage.** *Crit Care Med* 2007;35:1844–51; quiz 1852 Medline
19. Gathier CS, van den Bergh WM, Slooter AJ; HIMALAIA-Study Group. **HIMALAIA (Hypertension Induction in the Management of Aneurysmal subArachnoid haemorrhage with secondary Ischaemia): a randomized single-blind controlled trial of induced hypertension vs. no induced hypertension in the treatment of delayed cerebral ischemia after subarachnoid hemorrhage.** *Int J Stroke* 2014;9:375–80 CrossRef Medline
20. Meyer R, Deem S, Yanez ND, et al. **Current practices of triple-H prophylaxis and therapy in patients with subarachnoid hemorrhage.** *Neurocrit Care* 2011;14:24–36 CrossRef Medline
21. Hänggi D, Etminan N, Macdonald RL, et al. **NEWTON: nimodip-**

- ine microparticles to enhance recovery while reducing toxicity after subarachnoid hemorrhage. *Neurocrit Care* 2015;23:274–84 CrossRef Medline
21. Sanelli PC, Jou A, Gold R, et al. **Using CT perfusion during the early baseline period in aneurysmal subarachnoid hemorrhage to assess for development of vasospasm.** *Neuroradiology* 2011;53:425–34 CrossRef Medline
  22. Kudo K, Sasaki M, Yamada K, et al. **Differences in CT perfusion maps generated by different commercial software: quantitative analysis by using identical source data of acute stroke patients.** *Radiology* 2010;254:200–09 CrossRef Medline
  23. Mir DI, Gupta A, Dunning A, et al. **CT perfusion for detection of delayed cerebral ischemia in aneurysmal subarachnoid hemorrhage: a systematic review and meta-analysis.** *AJNR Am J Neuroradiol* 2014;35:866–71 CrossRef Medline
  24. Cremers CH, van der Schaaf IC, Wensink E, et al. **CT perfusion and delayed cerebral ischemia in aneurysmal subarachnoid hemorrhage: a systematic review and meta-analysis.** *J Cereb Blood Flow Metab* 2014;34:200–07 CrossRef Medline
  25. Etminan N, Beseoglu K, Heiroth HJ, et al. **Early perfusion computerized tomography imaging as a radiographic surrogate for delayed cerebral ischemia and functional outcome after subarachnoid hemorrhage.** *Stroke* 2013;44:1260–66 CrossRef Medline
  26. Santos GA, Petersen N, Zamani AA, et al. **Pathophysiologic differences in cerebral autoregulation after subarachnoid hemorrhage.** *Neurology* 2016;86:1950–56 CrossRef Medline
  27. Sabri M, Lass E, Macdonald RL. **Early brain injury: a common mechanism in subarachnoid hemorrhage and global cerebral ischemia.** *Stroke Res Treat* 2013;2013:394036 CrossRef Medline
  28. Cahill J, Calvert WJ, Calvert JW, et al. **Mechanisms of early brain injury after subarachnoid hemorrhage.** *J Cereb Blood Flow Metab* 2006;26:1341–53 CrossRef Medline
  29. van Asch CJ, van der Schaaf IC, Rinkel GJ. **Acute hydrocephalus and cerebral perfusion after aneurysmal subarachnoid hemorrhage.** *AJNR Am J Neuroradiol* 2010;31:67–70 CrossRef Medline
  30. Rodriguez-Régent C, Hafsa M, Turc G, et al. **Early quantitative CT perfusion parameters variation for prediction of delayed cerebral ischemia following aneurysmal subarachnoid hemorrhage.** *Eur Radiol* 2016;26:2956–63 CrossRef Medline

# Vessel Wall MRI for Targeting Biopsies of Intracranial Vasculitis

S.R. Zeiler, Y. Qiao, C.A. Pardo, M. Lim, and B.A. Wasserman



## ABSTRACT

**SUMMARY:** Central nervous system vasculitides are elusive diseases that are challenging to diagnose because brain biopsies have high false-negative rates. We sought to test the ability of contrast-enhanced, high-resolution 3D vessel wall MR imaging to identify vascular inflammation and direct open biopsies of intracranial target vessels and adjacent brain parenchyma. Eight of 9 specimens revealed vascular inflammation. We conclude that vessel wall MR imaging can identify inflamed intracranial vessels, enabling precise localization of biopsy targets.

**ABBREVIATIONS:** CNSV = CNS vasculitis; VWMRI = vessel wall MR imaging

We operationally define central nervous system vasculitis (CNSV) as any inflammatory vasculopathy producing non-atheromatous inflammation of intracranial vessels either directly (eg, primary CNS vasculitis) or indirectly via inflammation of CNS parenchyma with secondary vascular involvement (eg, as seen with infections, tumors, and certain autoimmune conditions). A variety of pathogenic processes leading to CNSV may have similar or overlapping clinical presentations and can mimic noninflammatory vasculopathies on conventional MR imaging or CT (eg, atherosclerosis, dissection, and reversible cerebrovascular vasoconstriction syndrome).<sup>1,2</sup> Thus, a biopsy should be performed for a definitive diagnosis and to identify the cause of the underlying inflammation,<sup>1,3,4</sup> especially because immunosuppressive therapy has adverse effects.<sup>5</sup>

Unfortunately, despite MR imaging and digital subtraction angiography (DSA) having high sensitivities for CNSV (60%–100%), specificity estimates range from 14% to 60%<sup>6,7</sup> and 19% to 36%<sup>7–9</sup> for DSA and MR imaging, respectively. For MR imaging, this sensitivity is likely secondary to flow artifacts and partial volume averaging constraints.<sup>10</sup> Furthermore, intracranial blood

vessel biopsy has a high false-negative rate (<50%)<sup>9,11</sup> because of patchy involvement of relevant pathology.<sup>3,12,13</sup>

We hypothesized that vessel wall MR imaging (VWMRI)<sup>14</sup> can identify inflamed intracranial vessels and precisely localize biopsy targets, thus aiding in the diagnosis of CNSV and its attendant pathology.

## MATERIALS AND METHODS

### Patients

We present 9 patients (On-line Tables 1 and 2) consecutively admitted to the Johns Hopkins stroke service between 2012 and 2016 for ischemic stroke with clinical concern for CNSV and no reasonable explanation for a noninflammatory cause.<sup>4</sup> Work-up for hypercoagulable state, rheumatologic disease, malignancy, cardiac dysfunction, and infection was unremarkable for all patients except patient 6, which revealed Varicella zoster virus immunoglobulin G in the CSF. All 9 patients referred with intent to biopsy underwent VWMRI and subsequent biopsy and were therefore included in this prospective study and consecutively entered into our data base. The institutional review board approved this study and provided an exemption to allow the inclusion of de-identified data for patients from whom we did not receive written consent because the VWMRI was performed as part of clinical care.

### MR Imaging Examination Protocol

VWMRI examinations were performed up to 7 days before biopsy (mean, 2.2 days) on a 3T MR imaging scanner (Magnetom Skyra; Siemens, Erlangen, Germany) using a 32-channel head coil. Fiducial markers were placed, and a standardized MR imaging protocol was implemented for all patients that included a 3D time-of-

Received December 22, 2017; accepted after revision June 17, 2018.

From the Department of Neurology (S.R.Z., C.A.P.), The Russell H. Morgan Department of Radiology and Radiological Sciences (Y.Q., B.A.W.), and Departments of Pathology (C.A.P.) and Neurosurgery (M.L.), Johns Hopkins University, Baltimore, Maryland.

Please address correspondence to B.A. Wasserman, MD, Park E367, 600 North Wolfe St, Baltimore, MD 21287; e-mail: bwasser@jhmi.edu

Indicates open access to non-subscribers at [www.ajnr.org](http://www.ajnr.org)

Indicates article with supplemental on-line tables.

Indicates article with supplemental on-line photos.

<http://dx.doi.org/10.3174/ajnr.A5801>

flight MRA (acquired resolution,  $0.5 \times 0.5 \times 0.55 \text{ mm}^3$ ), pre- and postcontrast 3D VWMRI (acquired resolution,  $0.5 \times 0.5 \times 0.5 \text{ mm}^3$ ), and a 3D contrast-enhanced MRA (acquired resolution,  $0.52 \times 0.52 \times 1.04 \text{ mm}^3$ ) of the intracranial vessels (On-line Fig 1). Diffusion-weighted images of the brain were obtained for all patients, and susceptibility-weighted images (acquired resolution,  $0.70 \times 0.70 \times 1.50 \text{ mm}^3$ ) were obtained for 5 of the 9 examinations. Postcontrast T1 echo-spoiled gradient-echo images were obtained for surgical navigation.

The 3D-VWMRI sequence design was previously described, and T1-weighting was implemented to highlight contrast enhancement (TR/TE, 800/25 ms; turbo factor, 30; echo spacing, 5.6 ms; generalized autocalibrating partially parallel acquisition acceleration, 2; FOV,  $160 \times 160 \text{ mm}^2$ ; number of averages, 1.4).<sup>14,15</sup> VWMRI was acquired in a coronal plane (112 slices [56 mm]; 9.5-minute acquisition time) and, after contrast administration, was oriented in multiple planes (axial [80 slices, 40 mm; 7.5-minute acquisition time], coronal, and in some cases, sagittal) to enable greater coverage of intracranial vessels, including distal branches. Contrast-enhanced MRA images were acquired during the intravenous administration of gadobutrol (Gadavist; Bayer Schering Pharma, Berlin, Germany; 0.1 mmol/kg) with arterial and venous phase acquisitions, and postcontrast VWMRI acquisitions began 5 minutes after contrast administration.

### MR Imaging Analysis

All MR imaging examinations were analyzed by a neuroradiologist (B.A.W.) using a PACS. 3D-VWMRI was reconstructed in multiple obliquities and was used to visually identify vascular inflammation (present/absent) based on segmental, concentric enhancement of the vessel wall and/or circumferential, periaxial enhancement following a vessel segment. Evidence of atherosclerotic features including calcification, a fibrous cap and lipid core, or focal, noncircumferential wall thickening excluded the diagnosis of vasculitis. The 3D-TOF MRA and contrast-enhanced MRA acquisitions were reconstructed and coregistered with the VWMRI sequence to isolate the vessel of interest in long and short axes. Because the lumen of very small vessels could not always be identified on VWMRI, small-vessel involvement was suspected on the basis of the linear configuration of inflammatory enhancement (Figure) and was corroborated by the identification of a lumen on the reconstructed contrast-enhanced MRA and TOF MRA source images or the susceptibility-weighted images when available. Diffusion-weighted imaging (on present and prior examinations) was used to exclude foci of enhancement due to subacute infarction. The inflamed vessel segments were then reviewed with the neurology and neurosurgical services to reach a consensus on a vessel target that avoided eloquent areas, was superficial, and was preferably venous.

### Biopsy Procedure

Open biopsy was performed with the patient under general anesthesia using fiducial markers. The target vessel and adjacent brain parenchyma were biopsied with the aid of an image-guidance system (Brainlab Cranial Navigation Systems; Brainlab, Feldkirchen, Germany). M.L. was able to identify and biopsy a vessel at the identified coordinates.

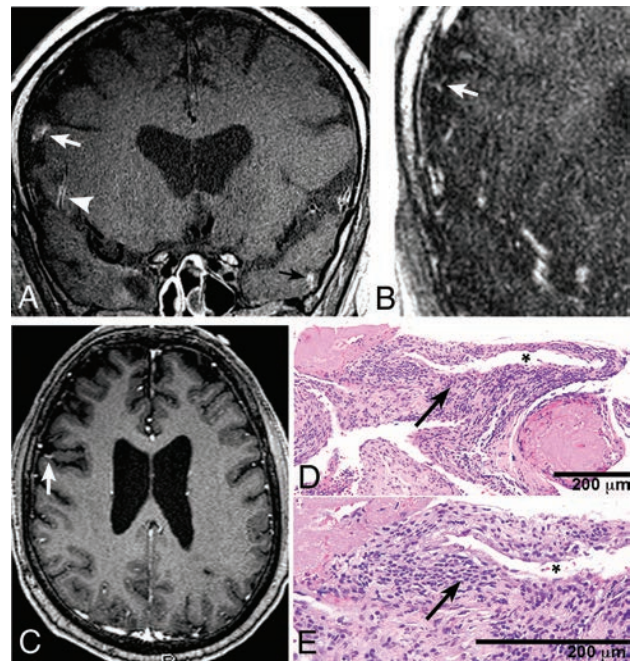


**FIGURE.** High-resolution vessel wall MR imaging protocol for identifying a surgical target in a 33-year-old man with suspected intracranial vasculitis. A coronal reconstruction of a 3D-VWMRI sequence (acquired resolution, 0.5 mm isotropic, A) shows evidence of vasculitis, including circumferential enhancement and thickening of the wall of a small branch of the right MCA (white arrowhead) and of small cortical veins (arrow). The right frontal cortical vein (white arrow), confirmed to be a vein on the venous phase of the contrast-enhanced MRA (B), was selected as the target. Note that the vessel is identified on the 3D echo-spoiled gradient-echo sequence (C, arrow) acquired for surgical navigation but does not appear abnormal (D and E). Hematoxylin-eosin-stained biopsy section shows significant transmural inflammation (arrows) of the blood vessel wall. The lumen is indicated by asterisks.

## RESULTS

### Biopsy Results

The targeted blood vessel and surrounding brain tissue were obtained from each patient (On-line Table 2). Blood vessel biopsy analysis from 8 of the 9 patients revealed vascular inflammation via direct tissue examination (Figure and On-line Fig 2). The etiology of CNSV for patients 1, 2, 3, and 9 was primary CNS angitis; for patient 4, it was amyloid- $\beta$ -related angitis; and for patient 6, it was Varicella zoster virus vasculitis. Although we confirmed perivascular inflammation for patients 7 and 8, we were unable to find a cause. Brain biopsy specimens showed no evidence of parenchymal inflammation in all except patient 7. The vessel specimen from patient 5 did not reveal inflammation but instead a multitude of thickened blood vessels with amyloid deposition. There were no postoperative complications.

Standard MR imaging T1 postcontrast studies (Figure and On-line Fig 2) as well as MRA, CTA, and DSA studies (On-line Table 1) did not prospectively identify the target pathology that was identified by VWMRI and eventually biopsied.<sup>16</sup>

## DISCUSSION

We present the first reported study to use 3D-VWMRI at 3T for identifying CNSV. Notably, we show that VWMRI can be used to direct biopsies of inflamed intracranial vessels with high accuracy

(89% in our series), which is a substantial improvement over the standard approach (sensitivities as low as 36% in prior studies).<sup>3,7,9,17</sup> The success of our study was largely attributable to our ability to implement a 3D high-resolution VWMRI sequence that enables evaluation of a large volume of intracranial vessels, maximizing the number of potential targets that could then be reviewed for accessibility and safety.

There are several limitations of this study: 1) Although the VWMRI sequence was acquired using a TR of 800 ms to produce T1-weighting, some inherent proton-density weighting could not be eliminated, and this issue accounted for areas of mild hyperintense signal from remote white matter ischemic injury. We acquired precontrast VWMRI to help distinguish this hyperintensity from true enhancement surrounding small parenchymal vessels. Consequently, we confirmed vascular enhancement only when postcontrast signal was unequivocally high, so vessels with milder postcontrast signal were excluded from consideration. 2) The 3D-VWMRI sequence can result in inadequate flow suppression, depending on the size and orientation of the vessel.<sup>18</sup> We acquired the 3D-VWMRI sequence in multiple planes, so most vessels were captured in the long axis relative to the scan orientation. Furthermore, we used contrast-enhanced MRA images to confirm patency of the lumen. 3) Shifting of vascular structures from the craniotomy and opening of the dura could lead to false-negative specimen analyses. Nevertheless, in our cohort, every patient except patient 5 was confirmed to have CNSV on biopsy. VWMRI was unable to distinguish inflammation located in the transmural or perivascular space.

## CONCLUSIONS

Our data indicate that VWMRI can be used to target and improve the yield of biopsy in patients with CNSV. We suggest that biopsy remains instrumental in tailoring therapy because VWMRI was unable to distinguish among primary, infectious, and/or any etiology leading to perivascular inflammation.

Disclosures: Ye Qiao—UNRELATED: Patents (Planned, Pending or Issued): 3D high-resolution intracranial vessel wall imaging technique, US Patent Application 13/922,111. Michael Lim—UNRELATED: Consultancy: Bristol-Myers Squibb, Merck, Tocagen, Stryker; Grants/Grants Pending: Bristol-Myers Squibb, Accuray, Agenus\*; Patents (Planned, Pending or Issued): for radiation and immunotherapy. Bruce A. Wasserman—OTHER RELATIONSHIPS: Patent No. 13/922,111 for the 3D high-resolution vessel wall MRI technique used in this study. No financial gain (ie, no royalties or licenses). \*Money paid to the institution.

## REFERENCES

- Birnbaum J, Hellmann DB. **Primary angitis of the central nervous system.** *Arch Neurol* 2009;66:704–09 Medline
- Jennette JC, Falk RJ, Bacon PA, et al. **2012 revised International Chapel Hill Consensus Conference Nomenclature of Vasculitides.** *Arthritis Rheum* 2013;65:1–11 CrossRef Medline
- Salvarani C, Brown RD Jr, Calamia KT, et al. **Primary central nervous system vasculitis: analysis of 101 patients.** *Ann Neurol* 2007;62:442–51 CrossRef Medline
- Marsh EB, Zeiler SR, Levy M, et al. **Diagnosing CNS vasculitis: the case against empiric treatment.** *Neurologist* 2012;18:233–38 CrossRef Medline
- Néel A, Pagnoux C. **Primary angitis of the central nervous system.** *Clin Exp Rheumatol* 2009;27:S95–107 Medline
- Kadkhodayan Y, Alreshaid A, Moran CJ, et al. **Primary angitis of the central nervous system at conventional angiography.** *Radiology* 2004;233:878–82 CrossRef Medline
- Chu CT, Gray L, Goldstein LB, et al. **Diagnosis of intracranial vasculitis: a multi-disciplinary approach.** *J Neuropathol Exp Neurol* 1998;57:30–38 CrossRef Medline
- Calabrese LH, Duna GF. **Evaluation and treatment of central nervous system vasculitis.** *Curr Opin Rheumatol* 1995;7:37–44 Medline
- Duna GF, Calabrese LH. **Limitations of invasive modalities in the diagnosis of primary angitis of the central nervous system.** *J Rheumatol* 1995;22:662–67 Medline
- Antiga L, Wasserman BA, Steinman DA. **On the overestimation of early wall thickening at the carotid bulb by black blood MRI, with implications for coronary and vulnerable plaque imaging.** *Magn Reson Med* 2008;60:1020–28 CrossRef Medline
- Cupps TR, Moore PM, Fauci AS. **Isolated angitis of the central nervous system: prospective diagnostic and therapeutic experience.** *Am J Med* 1983;74:97–105 Medline
- Alreshaid AA, Powers WJ. **Prognosis of patients with suspected primary CNS angitis and negative brain biopsy.** *Neurology* 2003;61:831–33 CrossRef Medline
- Miller DV, Salvarani C, Hunder GG, et al. **Biopsy findings in primary angitis of the central nervous system.** *Am J Surg Pathol* 2009;33:35–43 CrossRef Medline
- Qiao Y, Steinman DA, Qin Q, et al. **Intracranial arterial wall imaging using three-dimensional high isotropic resolution black blood MRI at 3.0 Tesla.** *J Magn Reson Imaging* 2011;34:22–30 CrossRef Medline
- Qiao Y, Guallar E, Suri FK, et al. **MR imaging measures of intracranial atherosclerosis in a population-based study.** *Radiology* 2016;280:860–68 CrossRef Medline
- Salvarani C, Brown RD Jr, Calamia KT, et al. **Angiography-negative primary central nervous system vasculitis: a syndrome involving small cerebral vessels.** *Medicine (Baltimore)* 2008;87:264–71 CrossRef Medline
- Berlit P, Kraemer M. **Cerebral vasculitis in adults: what are the steps in order to establish the diagnosis? Red flags and pitfalls.** *Clin Exp Immunol* 2014;175:419–24 CrossRef Medline
- Jara H, Yu BC, Caruthers SD, et al. **Voxel sensitivity function description of flow-induced signal loss in MR imaging: implications for black-blood MR angiography with turbo spin-echo sequences.** *Magn Reson Med* 1999;41:575–90 CrossRef Medline

# Hemodynamic Impairment Measured by Positron-Emission Tomography Is Regionally Associated with Decreased Cortical Thickness in Moyamoya Phenomenon

J.J. Lee, J.S. Shimony, H. Jafri, A.R. Zazulia, R.G. Dacey, Jr., G.R. Zipfel, and C.P. Derdeyn



## ABSTRACT

**BACKGROUND AND PURPOSE:** Impaired cerebrovascular reactivity has been associated with decreased cortical thickness in patients with arterial occlusive diseases. This study tests the hypothesis that severe hemodynamic impairment, indicated by increased oxygen extraction fraction ratios on positron-emission tomography with  $^{15}\text{O}$  tracers, is associated with decreased cortical thickness in patients with Moyamoya phenomenon.

**MATERIALS AND METHODS:** Patients with unilateral or bilateral idiopathic Moyamoya phenomenon were recruited. Oxygen extraction fraction ratio maps were generated from cerebral images of  $\text{O}^{[15]\text{O}}$  counts divided by  $\text{H}_2\text{[}^{15}\text{O]}$  counts with normalization by corresponding cerebellar counts. The normal range of the oxygen extraction fraction ratio was estimated from historically available healthy control subjects. Cortical thickness was estimated from T1-weighted MR imaging and FreeSurfer. Regional samples of oxygen extraction fraction ratios and cortical thicknesses were drawn using FreeSurfer parcellations, retaining only parcellations from the vascular territory of the middle cerebral artery.

**RESULTS:** Complete MR imaging and PET datasets were available in 35 subjects, including 23 women; the mean age at scanning was 44 years. Patients with Moyamoya phenomenon had a significantly increased regional oxygen extraction fraction ratio compared with 15 healthy control subjects ( $P < .001$ ). Regional oxygen extraction fraction ratio and age were significant predictors of cortical thickness ( $P < .001$  for each) in a generalized linear mixed-effects model. Using hemisphere averages and patient averages, we found that only age was a significant predictor of cortical thickness ( $P < .001$ ).

**CONCLUSIONS:** Chronic hemodynamic impairment, as indicated by a higher regional oxygen extraction fraction ratio, was significantly predictive of reduced cortical thickness in mixed-effects analysis of FreeSurfer regions. This phenomenon may be related to reversible metabolic down-regulation.

**ABBREVIATIONS:** OEF = oxygen extraction fraction; OEFR = oxygen extraction fraction ratio; SEM = standard error of measurement

Chronic hemodynamic impairment from basal artery occlusive disease may lead to regional reductions in cortical thickness. Fierstra et al<sup>1</sup> examined patients with unilateral occlusive

cerebrovascular disease using  $\text{CO}_2$  reactivity and diminished blood oxygen level–dependent responses as a marker for regional hemodynamic impairment. They demonstrated that regions with steal physiology and a reduced blood oxygen level–dependent response to  $\text{CO}_2$  had cortical thickness ( $2.40 \pm 0.03$  mm standard error of measurement [SEM]) that increased 5.1% after successful surgical revascularization ( $2.53 \pm 0.03$  mm SEM).

Received February 12, 2018; accepted after revision August 6.

From the Mallinckrodt Institute of Radiology (J.J.L., J.S.S., H.J., A.R.Z.) and Departments of Neurology (A.R.Z., G.R.Z.) and Neurosurgery (R.G.D., G.R.Z.), Washington University, St Louis, Missouri; and Department of Radiology (C.P.D.), University of Iowa, Iowa City, Iowa.

This work was supported by the National Institute of Neurological Disorders and Stroke RO1 NS051631 (C.P.D.). Support for the research imaging center where the MR studies were performed was provided by UL1 RR024992-01, TL1 RR024995-01, and KL2 RR 024994-01 from the National Center for Research Resources, a component of the National Institutes of Health, and the National Center for Research Resources Roadmap for Medical Research, P30NS048056. J.S.S. was also supported by the Eunice Kennedy Shriver National Institute of Child Health & Human Development of the National Institutes of Health under Award Number U54 HD087011 to the Intellectual and Developmental Disabilities Research Center at Washington University.

The content of this work is solely the responsibility of the authors and does not necessarily represent the official view of the National Center for Research Resources or the National Institutes of Health.

Clinical trial registration information: <http://www.clinicaltrials.gov>. Unique identifier: NCT00629915.

Please address correspondence to John J. Lee, MD, PhD, Mallinckrodt Institute of Radiology, Washington University School of Medicine, 4525 Scott Ave, Campus Box 8225, St Louis, MO 63110; e-mail: [jjlee@wustl.edu](mailto:jjlee@wustl.edu); [@jjleeWustlEdu](mailto:@jjleeWustlEdu)

Indicates open access to non-subscribers at [www.ajnr.org](http://www.ajnr.org)

Indicates article with supplemental on-line tables.

<http://dx.doi.org/10.3174/ajnr.A5812>

Methods to categorize hemodynamic impairment are based on the response of the cerebrovasculature to vasodilatory challenges, measurements of increased blood volume, mean transit time, or measurements of an increased oxygen extraction fraction (OEF).<sup>2</sup> The diminished blood oxygen level–dependent response to CO<sub>2</sub> is likely a response of pre-existing autoregulatory vasodilation in response to reduced perfusion pressure.<sup>2</sup> OEF measurement uses <sup>15</sup>O radiotracers to quantify oxygen extracted from blood by the brain. When cerebral blood flow falls, the OEF can increase from a normal baseline of 40% up to 80% to maintain normal oxygen metabolism and brain function.<sup>3,4</sup> Increased OEF has been shown to be a powerful predictor of stroke in patients with atherosclerotic carotid artery occlusion.<sup>2,5-7</sup>

Quantitative OEF requires radial artery cannulation, multiple levels of calibrations, and the assumption that first-passage of the bolus of radiolabels along the radial artery is an accurate proxy for first-passage of the bolus through the cerebral circulation. For chronic carotid occlusive disease, methods of OEF estimation using emission counts and normalization against reference values have had comparable predictive values for clinical outcomes and improved receiver operating characteristics.<sup>8,9</sup> In this work, we used the ratio of count-based OEF (OEFR) in the cerebral regions to count-based OEF in the cerebellum for all analyses.<sup>10</sup>

This study sought to test the hypothesis that chronic hemodynamic impairment, as identified by an OEFR, is associated with decreased cortical thickness in patients with Moyamoya phenomenon.<sup>1</sup>

## MATERIALS AND METHODS

### Patients

Technically sufficient MR imaging, PET imaging, and clinical data were obtained from 35 patients enrolled in a prospective, blindly adjudicated study of hemodynamic factors and stroke risk.<sup>11</sup> Inclusion criteria were unilateral or bilateral Moyamoya phenomenon by angiography. Patients with prior surgical revascularization were included if the contralateral hemisphere was affected and untreated or if there were recurrent symptoms in the treated hemisphere. In analyses, data were excluded if the encompassing hemisphere demonstrated cortical infarction or hemorrhage. These inclusion and exclusion criteria and their applicability to cerebral hemispheres as well as individual patients were based on criteria used in previous cortical thickness studies of Moyamoya phenomenon by Fierstra et al.<sup>1</sup> On enrollment, patients traveled to Washington University Medical Center for a detailed neurologic history, physical examination, interviews for baseline demographics and stroke risk factors, MR imaging, and PET imaging.

The present data are a subset of data from a prospective natural history study by Derdeyn et al.<sup>11</sup> Of the 50 subjects in the previous study, 15 were excluded from this study because of the following: technically incomplete imaging necessary for this study, bilateral infarctions, bilateral hemorrhages, or surgical treatment with improvement. Methodologic differences between the prior study and this one included the following: use of FreeSurfer (<http://surfer.nmr.mgh.harvard.edu>)<sup>12-14</sup> automated cortical parcellations, classification of regions most likely to be in the

MCA vascular territory, granular identification of regional peaks of OEFR, and use of generalized linear mixed models.

Solely for purposes of estimating the range of normal values for OEFR, technically sufficient, historically available PET data from Grubb et al<sup>6</sup> were gathered from 15 subjects, including 8 women, who had previously been recruited for healthy control PET measurements; the mean age for this cohort was 48 ± 18 years. All control subjects had normal neurologic examination findings and normal brain MR imaging findings. Cortical thickness assessments were not technically feasible in the historical data. Written, informed consent was obtained for all patients and healthy subjects according to guidelines of the Washington University institutional review boards.

### PET Imaging

All PET imaging was performed at a single ECAT EXACT HR+ scanner (Siemens, Erlangen, Germany). Scanning began with transmission acquisitions from [<sup>68</sup>Ge]/[<sup>68</sup>Ga] sources for attenuation correction. Subjects inhaled 1 or 2 breaths from tubing connected to a shielded canister containing room air and 100 mCi (nominal) of O[<sup>15</sup>O]. Emission scanning began simultaneously, lasting 120 seconds. After waiting at least 15 minutes, a bolus of 75 mCi (nominal) of H<sub>2</sub>[<sup>15</sup>O] was injected through an antecubital intravenous cannula, and emissions were scanned for 120 seconds. Following filtered back-projection reconstruction with corrections for normalization, attenuation, and scatter, reconstructed images had 2.0 × 2.0 × 2.4 mm resolution in an FOV of 128 × 128 × 63 voxels. Dynamic oxygen and water image frames were temporally summed over 40 seconds starting from the time of tracer arrival into the FOV; then they were Gaussian-filtered to the measured point-spread function of the scanner, 7.3 × 7.3 × 5.3 mm full width at half maximum.<sup>15,16</sup>

### MR Imaging

All MR imaging studies used the same 3T system (Magnetom Tim Trio; Siemens). MR imaging was performed within 24 hours of PET scanning, in most cases within 1 hour after the conclusion of PET studies. All except 4 patients were scanned by MPRAGE series (TR, 2000 ms; TE, 2.97 ms) with a sagittal orientation, 1 × 1 × 1 mm resolution, and 208 × 256 × 144 FOV. Some MPRAGE scans had 1.25 × 1.25 × 1.3 mm resolution. For detecting white matter lesions, FLAIR series (TR, 4000 ms; TE, 294 ms; 0.9 × 0.9 × 5.0 mm resolution; 256 × 256 × 26 FOV) and T2-weighted imaging (TR, 3200 ms; TE, 319 ms; turbo spin-echo; 0.45 × 0.45 × 5.0 mm resolution; 416 × 512 × 26 FOV) were also obtained.

### Analysis of OEFR and Cortical Thickness

All ROIs made use of the Destrieux parcellations, *aparc.a2009s+aseg*, obtained from *recon-all* in FreeSurfer (Linux GNU stable, Version 5 20130513).<sup>12-14,17</sup> Fully regional analyses used cortical regions numbered 11101–11175 and 12101–12175 and cerebellar regions 7, 8, 46, and 47 as discovered by *recon-all* and using additional selection criteria detailed below. The FMRIB Linear Image Registration Tool (FLIRT, Version 5; <http://www.fmrib.ox.ac.uk/fsl/flwiki/FLIRT>)<sup>18</sup> created coregistrations of all tracer studies from PET onto FreeSurfer-generated T1.mgz images us-

ing mutual information cost functions. The `mri_segstats` application from FreeSurfer provided statistical results for all regions. The regions provided sampling of emission counts directly from  $O[^{15}O]$  and  $H_2[^{15}O]$ , both cortical and cerebellar, and OEFRs were calculated from regional mean counts normalized by the corresponding measurements in the cerebellum. All cerebellar regions were bilaterally pooled according to patient identity to avoid possible artifacts from crossed cerebellar diaschisis.

To increase the specificity of analysis, we manually classified the Destrieux regions<sup>17</sup> according to vascular territories previously reported by van der Zwan et al.<sup>19</sup> van der Zwan et al had empirically determined estimates of the volumetric extent of the anterior, middle, and posterior cerebral arterial circulations by injecting colored Araldite F mixtures (Kirkside Products, Osborne Park, Western Australia) into arterial sources of unfixed human brains obtained at routine postmortem. The largest volumetric extent of the middle cerebral artery territory was identified by visual inspection with Destrieux parcellations on the Montreal Neurological Institute 305 atlas. By submitting a subset of Destrieux region numbers 11101–11175 and 12101–12175 to `mri_segstats`, we obtained estimates of OEFRs for 60 parcellations per hemisphere most likely to correspond to the MCA territories. All OEFR measurements were matched with cortical thickness measurements from identical, coregistered sampling volumes in the images; the correspondence was ensured throughout analyses of regions, hemispheres, and patients. The PET data from historical, healthy control subjects did not include high-resolution MPRAGE; consequently, the Montreal Neurological Institute 305 atlas was coregistered to the historical PET images, and mapped Destrieux regions were subsequently sampled to obtain OEFRs.

Analysis with granularity for hemispheres facilitates comparison of this work with the limited number of existing cortical thickness reports. Granularity for patient identity facilitates comparison with existing Moyamoya phenomenon case series. Thus, measurements made on Destrieux regions for MCA territories within a hemisphere were pooled by hemispheres and patient identities and analyzed separately.

All registration results and OEFR calculations were individually reviewed as maps coregistered to T1.mgz anatomy as well as surface inflation maps. Regions of cortical infarction noted in clinical histories and MR imaging were marked for exclusion from further analyses. Most artifacts identified in quality-control reviews were associated with infarcted areas previously identified by exclusion criteria. All processing pipelines and analyses were coded in Matlab (Mathworks, Natick, Massachusetts) for reproducibility.

### Statistical Analyses

The historical healthy control data solely provided confidence intervals for estimating normal OEFR. *T* tests for differences of regional OEFR between controls and patients with Moyamoya phenomenon were 2-tailed and heteroscedastic because these measurements were drawn from distinct studies, clinical categories, and subjects (`ttest2` from Matlab R2017a). Generalized linear mixed-effects models used normal priors without link functions (`fitglm` from Matlab). Mixed-effect models appropriately describe the hierarchic covariance structures of measurements made

by regions, hemispheres, and subjects and the repeated measurements necessarily made on hierarchic data. In this work, mixed-effects models tested the OEFR, age, and sex as predictors of cortical thickness.<sup>15,20</sup> Intercepts, OEFR, age, and sex always had fixed effects. Intercepts and OEFR were explored using Akaike and Bayesian information criteria as random effects and grouped by patient identity to account for covariance structures between regions for a given patient. There were no other adjustments for multiple measurements. The significance level was always 95%. Analyses computed joint covariances of fixed effects and covariance parameters and assessed the Hessian of the objective function at convergence. The maximum pseudolikelihood algorithm estimated model parameters with 10–100 iterations.

### RESULTS

On-line Table 1 lists demographic, clinical, diagnostic, and treatment results both from Derdeyn et al<sup>11</sup> and this study. The natural history study of 50 patients by Derdeyn et al used OEFRs in hemispheres as a biomarker. This study examined a subset of 35 patients with technically adequate imaging, after imposing additional inclusion and exclusion criteria described in the Materials and Methods, to enable FreeSurfer-based regional analyses. The elevated regional OEFR in this study is defined to exceed the upper 95% confidence limit of regional OEFR measured in the control group of healthy subjects described in the Materials and Methods and quantified below. Characteristics listed in On-line Table 1 indicate the generalizability of these study results.

On-line Table 1 reports partitioning of patient census and measurements into unilateral and bilateral Moyamoya phenomenon in the category of vasculopathy on angiography. Of 10 patients with unilateral Moyamoya phenomenon, only 1 patient did not have an elevated regional OEFR; however, the hemisphere with Moyamoya phenomenon was excluded because of resolved symptoms after surgical revascularization. Of 25 patients with bilateral Moyamoya disease, 3 had an elevated regional OEFR.

Thirteen hemispheres in 13 patients were excluded from analyses in accordance with predetermined criteria, described in the Materials and Methods, applied to hemispheres. Of the remainder, 9 hemispheres in 9 patients were excluded for cortical infarction in the middle cerebral artery territory. Three hemispheres in 3 patients were excluded for basal ganglia hemorrhage. Three patients had prior surgical unilateral revascularization procedures. One of these revascularized hemispheres was excluded for basal ganglia hemorrhage; another hemisphere was excluded for absence of recurrent symptoms after surgical treatment. A total of 57 hemispheres in 35 patients were included in analyses.

### Imaging OEFR and Cortical Thickness

Figure 1A–D shows regional OEFRs fused with T1 anatomy and cortical thickness embedded in inflated surface maps for 4 patients randomly sampled from the patient cohort. Matlab function random-sampled patient identities following inclusion and exclusion selections. Higher regional OEFR was associated with a thinner cortex on visual inspection. However, venous sinuses and adjacent regions with partial volume averaging have artifactually elevated OEFRs arising from venous tracer activities because the

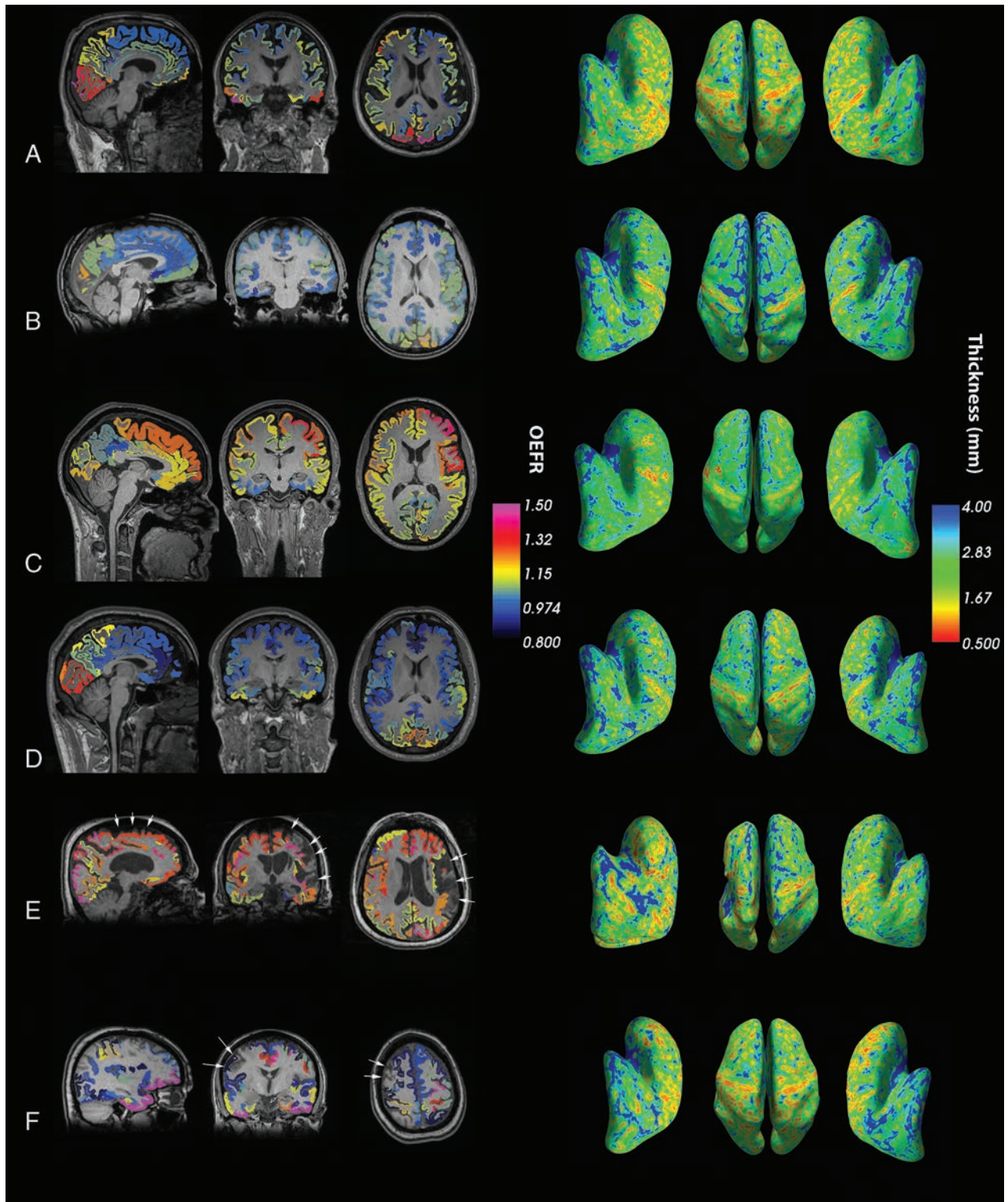


**FIG 1.** Representative views of OEFRs averaged over Destrieux parcellations, T1-anatomy, and cortical thickness on inflated surface maps. A–D, Four patients without infarction or hemorrhage were selected randomly from the patient cohort for visualization. E, This patient exemplifies the rationale for excluding infarcted hemispheres. Extensive encephalomalacia distorts cortical parcellations and confounds calculations on cortical and pial anatomy by FreeSurfer (arrows). F, This patient demonstrates paradoxically decreased OEFR around a region of infarction (arrows). The validity and significance of such decreases near infarcted areas are unknown. Consequently, all hemispheres ipsilateral to infarctions or hemorrhages were excluded. Modal color maps are identical for all subfigures and views.

OEFR method does not correct for cerebral blood volumes. Restricting analyses to MCA regions mitigates these artifacts. Figure 1E, -F demonstrates confounding artifacts in hemispheres with

infarction or hemorrhage. Anatomic pathology such as encephalomalacia presented challenges to the parcellation algorithms in FreeSurfer. Consequently, automated identifying of regions be-

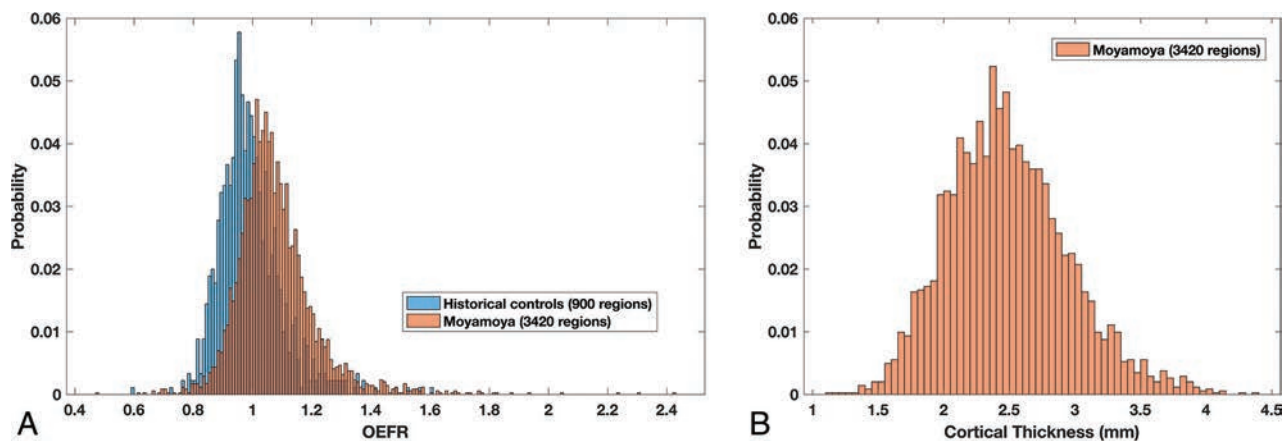


**FIG 2.** A, Histogram of OEFR from Destrieux FreeSurfer regions within MCA vascular territories from 15 historically obtained healthy control subjects. Superimposed is the histogram of OEFR from anatomically corresponding regions from 35 patients with Moyamoya phenomenon. Following applying exclusion criteria, there are 900 regions from controls and 3420 regions from patients. B, Histogram of cortical thickness from the same 3420 MCA regions in patients with Moyamoya phenomenon.

comes unreliable, and partial volume averaging with adjacent nonviable tissues made OEFR estimates uninterpretable.

### Distributions of OEFR and Cortical Thickness

A historical dataset of 15 healthy subjects provided 900 Destrieux regions from MCA territories for use in estimating confidence intervals for the normal range of OEFRs.<sup>15</sup> The distribution of OEFRs is shown in Fig 2A in blue. The mean OEFR was 0.995 with 95% CI, 0.776–1.213, and values above 1.213 were considered elevated. For patients with Moyamoya phenomenon, after inclusion and exclusion selections, 3420 Destrieux MCA regions had OEFRs distributed as shown in Fig 2A in orange. The mean OEFR was 1.076 with 95% CI, 0.805–1.357. The 2-tailed *t* test rejects the null hypothesis of equal means with unequal variances between healthy controls and patients with 95% CI, 0.07–0.090. For all patients with Moyamoya phenomenon, the 3420 regions had cortical thicknesses distributed according to Fig 2B with a mean of  $2.49 \pm 0.01$  mm SEM and 95% CI, 1.57–3.41. There were 376 hemodynamically impaired Moyamoya regions with elevated OEFRs of  $>1.213$ ; their cortical thicknesses had a mean of  $2.34 \pm 0.02$  mm SEM and 95% CI, 1.47–3.21. On-line Table 1 enumerates how demographics, categoric clinical presentations, and angiographic confirmation of unilateral Moyamoya phenomena or bilateral Moyamoya disease varied with respect to OEFR and nominal elevations of OEFR.

### Mixed-Effects Models

Figure 3 and On-line Table 2 detail results from generalized linear mixed-effects models. For measurements with granularity for Destrieux FreeSurfer regions within MCA territories, 3420 regions had OEFRs ranging from 0.479 to 2.43; age, 25–72 years; time from symptom onset to scanning from 0.1 to 87 months; and cortical thickness ranging from 1.10 to 4.38 mm. The best model, reported in the Wilkinson Notation in On-line Table 2, had 5 fixed-effects coefficients and 70 random-effects coefficients for the intercept and OEFR for each patient grouping. The groupings described interhemispheric covariance patterns computed with 4 parameters in full Cholesky form. For the Destrieux FreeSurfer regions within MCA territories, OEFR and age were significant

predictors of cortical thickness at the 5%  $\alpha$  level with  $P < .001$ . After we removed the OEFR and time from onset to scanning from the mixed model, only age was a significant predictor.

For measurements with granularity for hemispheres, 57 hemispheres had OEFRs from 0.917 to 1.32 and cortical thickness from 1.94 to 2.81 mm. The best model had 35 random-effects coefficients for the intercept for each patient grouping and an isotropic covariance pattern with 2 parameters. Only age was a significant predictor of cortical thickness, regardless of whether OEFR or time to scanning was included in the mixed model.

For measurements with granularity for patients (1 or 2 hemispheres), 35 patients had an OEFR from 0.932 to 1.32 and cortical thickness from 2.01 to 2.81 mm. In numeric analyses, the data did not support any random effects. Only age was a significant predictor of cortical thickness regardless of inclusions of OEFR or time to scanning in the mixed model.

### DISCUSSION

The present data support the observation that cortical thickness is reduced in chronic hemodynamic impairment.<sup>1,11,21</sup> This study aimed to maintain continuity with the larger body of cortical thickness research, including the study of Moyamoya phenomenon by Fierstra et al.<sup>1,21</sup> Patients with Moyamoya phenomenon from Fierstra et al, with steal phenomena before surgical revascularization, had a hemispheric mean thickness of  $2.40 \pm 0.03$  mm SEM. Patients with Moyamoya phenomenon in this study had FreeSurfer regions characterized by increased OEF, and their mean thickness was  $2.34 \pm 0.02$  mm SEM. However, this work differs from the prior studies of Fierstra et al, in 3 important ways. First, hemodynamic impairment in the previous studies was identified by regions that demonstrated paradoxically reduced blood oxygen level–dependent signal after CO<sub>2</sub> challenge (steal phenomenon).<sup>1</sup> Hemodynamic impairment in the present work was identified by increased OEFRs. These 2 physiologies are fundamentally different, though both likely reflect responses to reduced perfusion pressure or blood flow.<sup>2</sup> Second, in the original 2010 study of Fierstra et al, all patients had unilateral occlusive disease, and the comparison was made between brain regions with steal

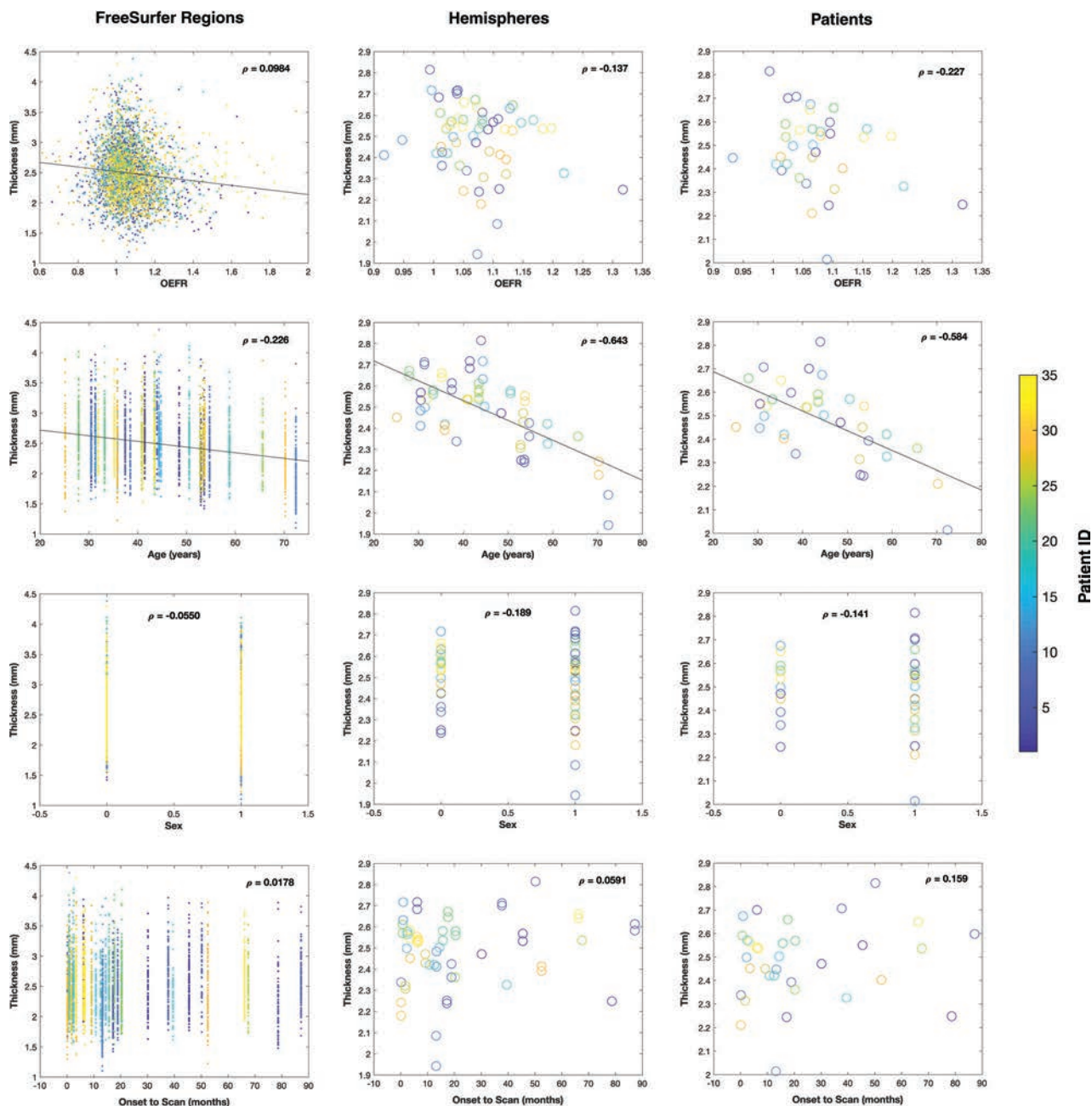


**FIG 3.** Plots of data arranged by granularity of measurements (FreeSurfer regions, hemispheres, patients) in columns and mappings of predictors (OEFR, age, sex, and time from symptom onset to scanning) of cortical thickness in rows. For sex, male = 0 and female = 1. The color map indicates patient identities. Lines of regression between model parameters and cortical thickness correspond to significant predictors.  $\rho$  denotes the partial correlation coefficient between the plotted parameter and cortical thickness. The *top-left* panel excludes a data point with OEFR = 0.479 and 4 data points with an OEFR of >2 to clarify the distribution of regional data with respect to OEFR and thickness. All plots exclude regions and hemispheres ipsilateral to infarctions or hemorrhages as detailed in the Materials and Methods.

phenomenon on the affected hemisphere and unaffected contralateral regions with each patient serving as his or her own control.<sup>21</sup> In the present analysis, we included patients with bilateral and unilateral disease and idiopathic Moyamoya phenomenon. Third, we used mixed-effects models to examine OEFR and cortical thickness with explicit considerations for the hierarchy of FreeSurfer regions, hemispheres, and patient identities. We also selectively examined MCA territories, and included age, sex, and time between symptom onset and scanning in our models.

We used values of OEFR from Destrieux parcellation regions

confined to MCA territories. Distal internal carotid occlusive disease was most likely to affect flow to these regions. We recognize that patients in this series may have had greater flow reduction to one or the other territory and some may have had posterior cerebral artery involvement. Averaging over entire hemispheres shifted the significance of regressions from OEFR and age to only age, a well-studied predictor for cortical thickness.<sup>20</sup> Diagnosis and surgical treatment options for patients with Moyamoya phenomenon may benefit from FreeSurfer-based regional measurements of OEF, OEFR, or cortical thickness.

Carotid disease and chronic hemodynamic impairment are associated with reduced cognitive function. Subclinical stroke represents the major potential confound for this association.<sup>22</sup> In baseline data from the Randomized Evaluation of Carotid Occlusion and Neurocognition (RECON) study, Marshall et al<sup>23</sup> reported a strong association between increased OEF and reduced baseline neurocognitive status. Patients with increased OEF on study entry were much more likely to have neurocognitive impairment than patients with a normal OEF.

Finally, there is good evidence that cortical thickness is dynamic.<sup>24,25</sup> Increases in gray matter volume and cortical thickness have been reported with learning new functions. These changes can be measured within days and are postulated to reflect neuronal changes, such as spine and synapse turnover,<sup>26</sup> given the time course.<sup>24</sup> Changes in the microvasculature are possible (eg, reduced capillary density, vasoconstriction), but difficult to explain. The associations of cortical thickness with age that we observed are well-described and provide further evidence of the external validity of our methods and observations; however, associations of cortical thickness with sex are likely confounded by the predominance of women with Moyamoya phenomenon in our study cohort.<sup>11,20,27,28</sup> The alternative explanations for reduced cortical thickness would generally not be reversible. These would include selective neuronal loss, submillimeter cortical infarctions, and white matter infarction leading to reduced cortical activity.

## CONCLUSIONS

Our data support the hypothesis that chronic hemodynamic impairment measured by PET is regionally associated with reduced cortical thickness. The effects of regional chronic hemodynamic impairment are significant and comparable with age for explaining reduced cortical thickness; age is a well-studied predictor of cortical thickness in healthy adults. Given the evidence from other studies that cortical thickness decreases are reversible, it is possible that decreases reflect metabolic down-regulation that may, in turn, be associated with reversible cognitive impairment. Future studies that incorporate serial measurements of oxygen metabolism and neuropsychological testing will be required to test these hypotheses.

For enhanced reproducibility, analysis software, unit tests, and summary data are provided at <https://github.com/jjleewustledu/Hemodynamic-Impairment-Measured-by-PET-is-Regionally-Associated-with-Cortical-Thickness-in-Moyamoya>.

Disclosures: John J. Lee—*RELATED: Grant:* National Institutes of Health, *Comments:* Supported by National Institute of Neurological Disorders and Stroke RO1 NS051631. Support for the research imaging center where the MR imaging studies were performed was provided by 1UL1RR024992-01, 1TL1RR024995-01, and 1KL2RR 024994-01 from the National Center for Research Resources, a component of the National Institutes of Health, and the National Institutes of Health Roadmap for Medical Research and P30NS048056\*. Joshua S. Shimony—*UNRELATED: Expert Testimony:* expert testimony in regard to the use of DTI in the diagnosis of traumatic brain injury; *Grants/Grants Pending:* National Institutes of Health \*. Gregory R. Zipfel—*UNRELATED: Consultancy:* Gerson Lehrman Group, *Comments:* consulting on a medical topic outside that discussed in the present article; *Expert Testimony:* Wais, Vogelstein, Forman and Offutt; Darby & Gaza; Zeigler Cohen & Koch; Hyde, Love, and Overby; Boyle Brasher LLC, *Comments:* expert witness for a variety of medical conditions; *Grants/Grants Pending:* National Institutes of Health.\* \*Money paid to institution.

## REFERENCES

1. Fierstra J, Maclean DB, Fisher JA, et al. **Surgical revascularization reverses cerebral cortical thinning in patients with severe cerebrovascular steno-occlusive disease.** *Stroke* 2011;42:1631–37 CrossRef Medline
2. Derdeyn CP, Grubb RL Jr, Powers WJ. **Cerebral hemodynamic impairment: methods of measurement and association with stroke risk.** *Neurology* 1999;53:251–51 CrossRef Medline
3. McHenry LC Jr, Fazekas JF, Sullivan JF. **Cerebral hemodynamics of syncope.** *Am J Med Sci* 1961;241:173–78 Medline
4. Derdeyn CP, Videen TO, Yundt KD, et al. **Variability of cerebral blood volume and oxygen extraction: stages of cerebral haemodynamic impairment revisited.** *Brain* 2002;125:595–607 CrossRef Medline
5. Powers WJ, Clarke WR, Grubb RL Jr, et al; CROSS Investigators. **Extracranial-intracranial bypass surgery for stroke prevention in hemodynamic cerebral ischemia: the Carotid Occlusion Surgery Study randomized trial.** *JAMA* 2011;306:1983–92 CrossRef Medline
6. Grubb RL Jr, Derdeyn CP, Fritsch SM, et al. **Importance of hemodynamic factors in the prognosis of symptomatic carotid occlusion.** *JAMA* 1998;280:1055–60 CrossRef Medline
7. Yamauchi H, Fukuyama H, Nagahama Y, et al. **Significance of increased oxygen extraction fraction in five-year prognosis of major cerebral arterial occlusive diseases.** *J Nucl Med* 1999;40:1992–98 Medline
8. Derdeyn CP, Videen TO, Simmons NR, et al. **Count-based PET method for predicting ischemic stroke in patients with symptomatic carotid arterial occlusion.** *Radiology* 1999;212:499–506 CrossRef Medline
9. Powers WJ. William M. Feinberg award for excellence in clinical stroke: hemodynamics and stroke risk in carotid artery occlusion. *Stroke* 2014;45:3123–28 CrossRef Medline
10. Jiang TT, Videen TO, Grubb RL Jr, et al. **Cerebellum as the normal reference for the detection of increased cerebral oxygen extraction.** *J Cereb Blood Flow Metab* 2010;30:1767–76 CrossRef Medline
11. Derdeyn CP, Zipfel GJ, Zazulia AR, et al. **Baseline hemodynamic impairment and future stroke risk in adult idiopathic Moyamoya phenomenon: results of a prospective natural history study.** *Stroke* 2017;48:894–99 CrossRef Medline
12. Dale AM, Fischl B, Sereno MI. **Cortical surface-based analysis, I: segmentation and surface reconstruction.** *Neuroimage* 1999;9:179–94 CrossRef Medline
13. Fischl B, Sereno MI, Dale AM. **Cortical surface-based analysis, II: inflation, flattening, and a surface-based coordinate system.** *Neuroimage* 1999;9:195–207 CrossRef Medline
14. Fischl B. **FreeSurfer.** *Neuroimage* 2012;62:774–81 CrossRef Medline
15. Derdeyn CP, Videen TO, Grubb RL Jr, et al. **Comparison of PET oxygen extraction fraction methods for the prediction of stroke risk.** *J Nucl Med* 2001;42:1195–97 Medline
16. Karakatsanis N, Sakellios N, Tsantilas NX, et al. **Comparative evaluation of two commercial PET scanners, ECAT EXACT HR+ and Biograph 2, using GATE.** *Nuclear Instruments and Methods in Physics Research A* 2006;569:368–72 CrossRef
17. Destrieux C, Fischl B, Dale A, et al. **Automatic parcellation of human cortical gyri and sulci using standard anatomical nomenclature.** *Neuroimage* 2010;53:1–15 CrossRef Medline
18. Smith SM, Jenkinson M, Woolrich MW, et al. **Advances in functional and structural MR image analysis and implementation as FSL.** *Neuroimage* 2004;23:S208–19 CrossRef Medline
19. van der Zwan A, Hillen B, Tulleken CAF, et al. **Variability of the territories of the major cerebral arteries.** *J Neurosurg* 1992;77:927–40 CrossRef Medline
20. Salat DH, Buckner RL, Snyder AZ, et al. **Thinning of the cerebral cortex in aging.** *Cereb Cortex* 2004;14:721–30 CrossRef Medline
21. Fierstra J, Poulblanc J, Han JS, et al. **Steal physiology is spatially associated with cortical thinning.** *J Neurol Neurosurg Psychiatry* 2010;81:290–93 CrossRef Medline
22. Romero JR, Beiser A, Seshadri S, et al. **Carotid artery atherosclerosis,**

- MRI indices of brain ischemia, aging, and cognitive impairment: the Framingham Study.** *Stroke* 2009;40:1590–96 CrossRef Medline
23. Marshall RS, Festa JR, Cheung YK, et al. **Cerebral hemodynamics and cognitive impairment: baseline data from the RECON trial.** *Neurology* 2012;78:250–55 CrossRef Medline
  24. Driemeyer J, Boyke J, Gaser C, et al. **Changes in gray matter induced by learning: revisited.** *PLoS One* 2008;3:e2669 CrossRef Medline
  25. Bermudez P, Lerch JP, Evans AC, et al. **Neuroanatomical correlates of musicianship as revealed by cortical thickness and voxel-based morphometry.** *Cereb Cortex* 2009;19:1583–96 CrossRef Medline
  26. Trachtenberg JT, Chen BE, Knott GW, et al. **Long-term in vivo imaging of experience-dependent synaptic plasticity in adult cortex.** *Nature* 2002;420:788–94 CrossRef Medline
  27. Gautam P, Cherbuin N, Sachdev PS, et al. **Sex differences in cortical thickness in middle aged and early old-aged adults: personality and total health through life study.** *Neuroradiology* 2013;55:697–707 CrossRef Medline
  28. Fjell AM, Westlye LT, Amlien I, et al. **High consistency of regional cortical thinning in aging across multiple samples.** *Cereb Cortex* 2009;19:2001–12 CrossRef Medline

# Engorgement of Deep Medullary Veins in Neurosarcoidosis: A Common-Yet-Underrecognized Cerebrovascular Finding on SWI

C. Zamora, S.-C. Hung, C. Tomingas, C. Atkinson, and M. Castillo

## ABSTRACT

**SUMMARY:** We describe the prevalence and potential significance of deep medullary vein engorgement on SWI in patients with neurosarcoidosis, a finding that has not been described previously. Engorgement was evaluated for possible associations with meningeal or perivascular disease, intracranial hemorrhage, and venous thrombosis, as well as with modified Rankin Scale scores at the time of MR imaging and at follow-up. Deep medullary vein engorgement was seen in 7 of 21 patients and was more common in men. Patients with venous engorgement had a significantly increased incidence of microhemorrhages, perivascular disease, and hydrocephalus. There was no association with the degree of leptomeningeal disease, venous dural sinus thrombosis, or modified Rankin Scale scores. In conclusion, deep medullary vein engorgement was common in our patients with neurosarcoidosis. Although its pathophysiology remains uncertain, it could be related to venous or perivenous abnormalities and may represent a useful secondary finding of cerebrovascular disease.

**ABBREVIATION:** DMVE = deep medullary vein engorgement

Sarcoidosis is a multisystem disease characterized by formation of noncaseating granulomas.<sup>1</sup> Neurologic manifestations occur in 5% of patients, and mortality can be as high as 11% in the 10 years after initial diagnosis.<sup>2,3</sup> Neurosarcoidosis has a predilection for perivascular dissemination but can also lead to parenchymal, leptomeningeal, or pachymeningeal disease and may result in a granulomatous angiitis.<sup>4,5</sup> CNS complications can be diverse and are a function of the nature and extent of tissues involved. Patients can have cranial neuropathies, neuroendocrine dysfunction due to involvement of the pituitary-hypothalamic axis, aseptic meningitis, and myelopathy, among other symptoms. A relatively rare-but-ominous complication is hydrocephalus, which is associated with high mortality.<sup>6</sup> Intracranial hemorrhage is also associated with a poor prognosis and has been reported as a possible sequela of vascular disease.<sup>5,7,8</sup>

We have noted that some patients with neurosarcoidosis show a characteristic pattern of deep medullary vein engorgement (DMVE) on SWI, which, to our knowledge, has not been previously described. Our purpose was to report the prevalence of this finding and to establish whether there may be an association with

an increased frequency of intracranial hemorrhage, hydrocephalus, or worse neurologic outcomes.

## Case Series

**Subjects.** This retrospective study was approved by our institutional review board, which waived the requirement for informed consent. We searched our electronic medical records system between January 2013 and December 2017 and included all consecutive adult patients ( $n = 21$ ; 10 men; mean age,  $46 \pm 14$  years) diagnosed with probable or definite neurosarcoidosis based on the criteria of Zajicek et al.<sup>9</sup> We only included patients after 2013 because that was the year when we started using SWI routinely at our institution.

## Clinical Variables

General demographic information and clinical characteristics were extracted from the patients' charts at the time of initial MR imaging. Modified Rankin Scale scores were determined from neurology consults and/or clinical visits at the time of initial MR imaging and at last follow-up.<sup>10</sup>

## Imaging Evaluation

Routine multisequence pre- and postcontrast MR imaging scans were evaluated by a neuroradiologist with a Certificate of Added Qualification for the presence of DMVE, leptomeningeal or dural disease, discrete perivascular nodular enhancement (distinct from the engorged vessel), venous thrombosis, hydrocephalus,

Received April 6, 2018; accepted after revision June 18.

From the Division of Neuroradiology, Department of Radiology, University of North Carolina School of Medicine, Chapel Hill, North Carolina.

Please address correspondence to Carlos Zamora, MD, Division of Neuroradiology, Department of Radiology, University of North Carolina School of Medicine, CB 7510, 3320 Old Infirmary, Chapel Hill, NC 27599-7510; e-mail: carlos\_zamora@med.unc.edu

<http://dx.doi.org/10.3174/ajnr.A5783>

and hemorrhage. Microhemorrhages were defined as  $<1$  cm, and macrohemorrhages were  $\geq 1$  cm. Imaging was performed on 1.5T or 3T MR imaging scanners (Avanto, Trio, Skyra, or Aera, Siemens, Erlangen, Germany). Typical parameters for SWI were the following: TE, 40 ms; TR, 49 ms at 1.5T; and TE, 20 ms; TR, 28 ms

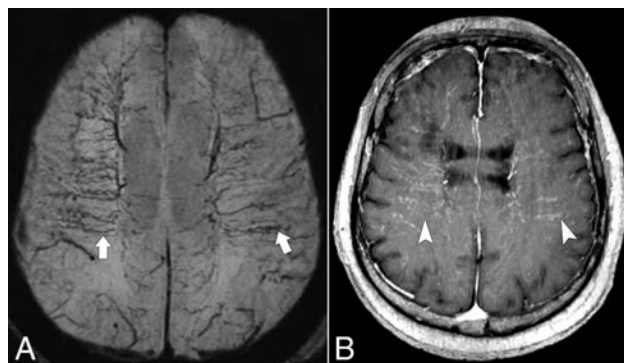


**FIG 1.** A 46-year-old man with word-finding difficulties, seizures, and vision loss. SWI minimum-intensity-projection images (A) demonstrates engorged and tortuous deep medullary veins perpendicular to the long axis of the lateral ventricles (arrows), with a fanned configuration around the frontal horns. Thick-slab (12-mm) postcontrast MPRAGE MIP image (B) shows corresponding enhancement (arrowheads). There is also ventriculomegaly.

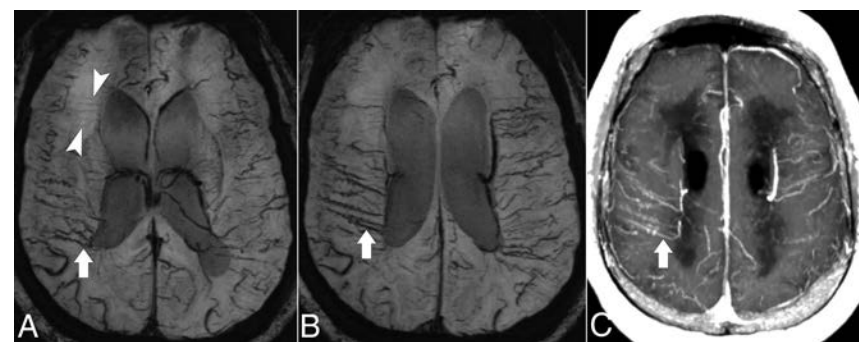


**FIG 2.** A 48-year-old man presenting with confusion. SWI minimum-intensity-projection images (A and B) show engorged and tortuous deep medullary veins bilaterally (arrows). Note thinner and relatively faint deep medullary veins in the right frontal lobe (arrowheads in A). There is also corresponding enhancement in the postcontrast MPRAGE MIP image (arrow in C).

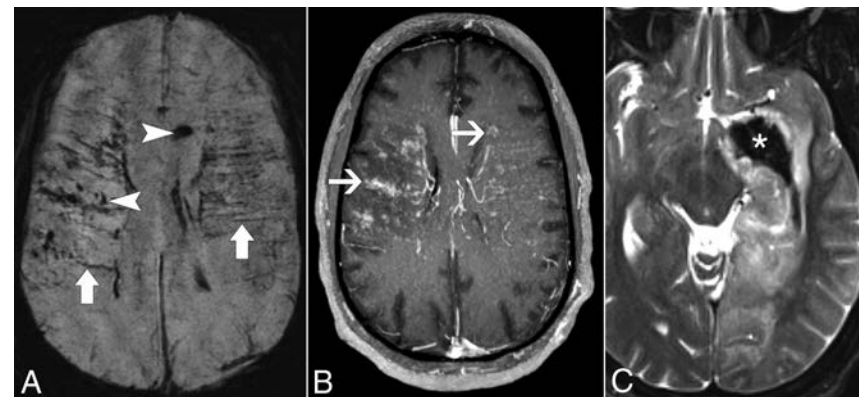


**FIG 3.** A 23-year-old man presenting with severe headaches, nausea, vomiting, and confusion. SWI minimum-intensity-projection image (A) demonstrates engorged deep medullary veins bilaterally (thick arrows) with corresponding enhancement on the postcontrast MPRAGE MIP image (B). There are numerous microhemorrhages bilaterally (arrowheads in A) and a macrohemorrhage in the left temporal lobe (asterisk in C) with surrounding edema seen on the T2 image. Note extensive nodular perivascular enhancement in B (thin arrows).

at 3T; section thickness, 2 mm; flip angle, 15°; FOV, 220 × 220 mm; and matrix size, 256 × 256. Venous thrombosis was evaluated using contrast-enhanced MPRAGE,<sup>11</sup> with the following parameters: TE, 2.54 ms; TR, 1900 ms; section thickness, 1 mm; flip angle, 9°; FOV, 250 × 250 mm; matrix size, 256 × 256. Minimum and maximum intensity projections were postprocessed at slice thicknesses of 16 and 12 mm for SWI and MPRAGE, respectively. The median time (interquartile range) from symptom onset to the first MR imaging that included SWI was 36.4 months (9–47 months) in the group with DMVE and 28.5 months (3–47 months) in the group without DMVE.

### Statistical Analysis

The normality of data distribution was evaluated with the Shapiro-Wilk test. Distributions were summarized using the mean  $\pm$  SD or median (interquartile range). Categorical data were expressed as counts or percentages. We used the  $\chi^2$  and Fisher exact tests for categorical variables and the independent 2-sample *t* test to compare means of normally distributed data. The Mann-Whitney *U* test was used to compare variables that were not normally distributed. *P* values  $< .05$  were considered significant. Statistical analysis was performed with SPSS, Version 24 (IBM, Armonk, New York).

### Deep Medullary Vein Engorgement

DMVE was present in 7 (33%) of 21 patients and appeared as enlarged and tortuous medullary veins in a parallel configuration at the level of the corona radiata and a radial orientation around the frontal horns and atria (Fig 1A and Fig 2A, -B). This was bilateral and symmetric in all except 1 patient and showed corresponding enhancement on post-contrast MPRAGE (Fig 1B and Fig 2C). DMVE was more common in men (29%) compared with women (5%,  $P = .013$ ). There was no significant association between DMVE and patient age ( $P = .813$ ). DMVE persisted in 5 patients who had follow-up MR imaging despite treatment with corticosteroids or immunomodulatory drugs (mean follow-up duration, 803  $\pm$  549 days).

### Intracranial Hemorrhage

Microhemorrhages were present in 7 (33%) of 21 patients and were more prevalent with DMVE ( $P = .009$ ). Five (71%) of 7 patients with DMVE and 2 (14%) of 14 patients without DMVE had microhemorrhages. There was a single macrohemorrhage in a patient with DMVE who also had microhemorrhages (Fig 3); however, the presence of macrohemorrhage per se was not significant ( $P = .147$ ). Thirteen patients had MR imaging follow-up at a mean of 803  $\pm$

**Basic demographics, symptoms, MRI findings, and modified Rankin Scale scores of patients with neurosarcoidosis**

Characteristics	Total (%)	DMVE (+) (%)	DMVE (-) (%)	P Value
No.	21	7	14	
Age (mean ± SD) (yr)	46 ± 14	45 ± 13	47 ± 16	.813
Sex (M/F)	10/11	6/1	4/10	.013 <sup>a</sup>
Symptoms				
Headache	8 (38%)	4 (57%)	4 (29%)	.346
Vision loss	5 (24%)	1 (14%)	4 (29%)	.624
Seizure	3 (14%)	0 (0%)	3 (21%)	.521
Extremity weakness	3 (14%)	1 (14%)	2 (14%)	1
Cranial neuropathy	2 (10%)	0 (0%)	2 (14%)	.533
Gait instability	3 (14%)	2 (29%)	1 (7%)	.247
Bowel/bladder dysfunction	4 (19%)	3 (43%)	1 (7%)	.088
Others	4 (19%)	1 (14%)	3 (21%)	
Intracranial hemorrhage				
Microhemorrhage	7 (33%)	5 (71%)	2 (14%)	.009 <sup>a</sup>
Macrohemorrhage	1 (5%)	1 (14%)	0 (0%)	.147
Enhancing disease				
Leptomeningeal	13 (62%)	4 (57%)	9 (64%)	.751
Pachymeningeal	8 (38%)	3 (43%)	5 (36%)	.751
Perivascular	3 (14%)	3 (43%)	0 (0%)	.008 <sup>a</sup>
Venous thrombosis	2 (10%)	1 (14%)	1 (7%)	.599
Hydrocephalus	6 (29%)	4 (57%)	2 (14%)	.040 <sup>a</sup>
Modified Rankin Scale score (mean)				
At initial MRI (n = 20)		3.2 ± 0.75	2.1 ± 1.5	.125
At follow-up (n = 18)		2.4 ± 1.1	1.5 ± 1.1	.167

<sup>a</sup> Statistically significant.

549 days. There was 1 instance of a new microhemorrhage in a patient with DMVE at follow-up, but this occurrence was not statistically significant ( $P = .118$ ). There was no significant association between intracranial hemorrhage and patient age ( $P = .704$ ) or perivascular nodular enhancement ( $P = .186$ ).

**Meningeal and Perivascular Disease**

Thirteen (62%) of 21 patients had leptomeningeal enhancement: mild/localized ( $n = 7$ ), moderate ( $n = 1$ ), and severe/extensive ( $n = 5$ ). There was no difference in the overall prevalence of leptomeningeal enhancement between patients with and without DMVE ( $P = .751$ ). When only patients with leptomeningeal enhancement were considered, there was no difference in the presence of severe leptomeningeal disease between patients with and without DMVE ( $P = .569$ ). There was also no difference in the prevalence of dural sarcoidosis between patients with and without DMVE ( $P = .751$ ). Areas of discrete perivascular nodular enhancement were found in 3 (43%) of 7 patients with DMVE and were not seen in those without DMVE ( $P = .008$ ). When present, these tended to be scattered and isolated except for 1 patient with extensive disease (Fig 3).

**Venous Thrombosis**

There was 1 patient without DMVE who had thrombosis of the superior sagittal sinus and 1 patient with DMVE who had a non-occlusive chronic thrombus in the torcula ( $P = .599$ ). Although there was no definite cortical or deep cerebral venous thrombosis, we noticed a relative paucity of cortical veins along the cerebral hemispheres in some patients. To account for this as a potential cause for the engorgement, we compared the number of cortical veins at the level of the body of the lateral ventricles between

patients with and without DMVE and there was no significant difference ( $P = .707$ ).

**Hydrocephalus**

Hydrocephalus was present in 6 (29%) of 21 patients and was significantly more common in patients with DMVE (4 of 7 patients, 57%) than in those without (2 of 14 patients, 14%;  $P = .04$ ). There was no significant association between hydrocephalus and patient age ( $P = .222$ ), leptomeningeal enhancement ( $P = .201$ ), or perivascular nodular enhancement ( $P = .844$ ). A summary of imaging variables is presented in the Table.

**Clinical Characteristics and Neurologic Status**

As can be seen in the Table, symptoms were similar in both groups: Patients without DMVE presented with headaches ( $n = 4$ ), vision loss ( $n = 4$ ), seizures ( $n = 3$ ), extremity weakness ( $n = 2$ ), cranial neuropathies ( $n = 2$ ), gait instability ( $n = 1$ ), hypopituitarism ( $n = 1$ ), bladder dysfunction ( $n = 1$ ), memory issues ( $n = 1$ ), and catatonia ( $n = 1$ ). Patients in the group with DMVE presented with headaches ( $n = 4$ ), gait instability ( $n = 2$ ), bowel and/or bladder dysfunction ( $n = 3$ ), vision loss ( $n = 1$ ), extremity weakness ( $n = 1$ ), and word-finding difficulties ( $n = 1$ ).

Modified Rankin Scale scores were obtained at the time of first MR imaging in 20 of 21 patients. In 1 patient, information on neurologic status was not available. Mean scores were higher (worse) in patients with DMVE ( $3.2 \pm 0.75$ ) compared with those without DMVE ( $2.1 \pm 1.5$ ), but the difference was not significant ( $P = .125$ ). Of 18 patients available for clinical follow-up (mean follow-up duration,  $725 \pm 551$  days), mean scores were also higher in those with DMVE; however, the difference was not significant ( $P = .167$ ).

**Laboratory Findings**

Because this was a retrospective study, laboratory results at the time of scanning were limited. CSF analysis in 3 patients with DMVE and 5 patients without DMVE showed no significant differences in angiotensin-converting enzyme ( $P = .393$ ) or protein ( $P = .786$ ) levels or pleocytosis ( $P = .464$ ). The CSF angiotensin-converting enzyme level was elevated in 1 patient with DMVE and 1 patient without DMVE, and the CSF protein level was elevated in 2 of 3 patients in the first group and 4 of 5 patients in the second group. The serum angiotensin-converting enzyme was available for 2 patients with DMVE and 7 patients without DMVE and was within normal limits except for 1 patient in each group.

**DISCUSSION**

Deep medullary veins constitute the major draining route of cerebral white matter.<sup>12</sup> They have a typical perpendicular arrangement relative to the long axis of the lateral ventricles and a radial

distribution along the atria and frontal horns, with a fine and uniform caliber and several zones of convergence that lead to the subependymal veins and ultimately the dural sinuses.<sup>13</sup>

In this study, we found that DMVE is a common finding in neurosarcoidosis, though not as yet recognized as a distinct cerebrovascular manifestation.<sup>5</sup> It was significantly more common in men, consistent with cerebrovascular manifestations of sarcoidosis being more frequent in this group.<sup>5</sup> DMVE came to our attention owing to its conspicuity on SWI, a sequence that is now widely available and was originally developed as a means for MR venography.<sup>14</sup> A recent review showed 1 case with mild periatrinal DMVE in a typical radial configuration on SWI; however, the presence of engorgement itself was not described.<sup>5</sup>

The pathophysiology of engorgement is uncertain but does not appear to be directly caused by downstream venous occlusion because dural sinuses and deep cerebral veins were patent in almost all our patients. Although there was no evident cortical thrombosis, we did notice a relative paucity of cortical veins along the cerebral hemispheres in some patients from both groups, which raised the question of whether abnormalities in the cortical veins could explain the appearance of DMVE. We did not find a significant difference in the number of visualized cortical veins between groups, but this could be an effect of sample size, and a difference may manifest itself in a larger population. Previous studies have proposed congestion of deep medullary veins as a potential indirect sign of dural sinus thrombosis.<sup>12,15-17</sup> However, other than 2 cases published by Taoka et al<sup>12</sup> and D'Amore et al,<sup>17</sup> most reports do not convincingly demonstrate the characteristic parallel or radial anatomy seen in our patients. Comparison with such studies is limited because they lacked SWI. In our cohort, 1 patient with DMVE had chronic nonocclusive thrombus in the torcula, and we do not know whether it may have contributed to vascular engorgement. Thrombus can also show prominent hypointense signal on SWI<sup>18</sup> and could potentially be difficult to distinguish from venous engorgement solely on the basis of that sequence. Although attributing our finding to venous engorgement rather than thrombosis was relatively straightforward based on its SWI appearance and lack of "blooming" artifacts, we also confirmed it by the corresponding contrast enhancement.

There was a higher incidence of perivascular space involvement in the group of patients with DMVE than in those without. Neurosarcoidosis is thought to spread to the CNS via the hematogenous route and has a tendency to disseminate along perivascular spaces, though the reason for this particular distribution is unknown.<sup>19</sup> Recent studies have drawn attention to the presence of a glial-based vascular or "glymphatic" pathway for cerebral clearance of solutes and metabolic by-products that is heavily dependent on aquaporin-4 water channels.<sup>20-24</sup> In vivo and ex vivo experiments have shown rapid periarterial influx of CSF driven by arterial pulsations into the brain parenchyma, subsequent exchange with interstitial fluid, and final paravascular clearance along draining veins.<sup>23</sup> Whether the glymphatic system plays a role in patients with neurosarcoidosis who have parenchymal or perivascular disease has not been established to date, and we do not know whether such a pathway could have influenced the development of DMVE. There is also significant controversy regarding the direction of interstitial fluid clearance and the specific

anatomic space where it occurs, with other studies demonstrating primarily intramural outflow along the basement membranes of arteries and not veins.<sup>25</sup> This is an area of intense research,<sup>26</sup> and it is likely that evidence of the role of the glymphatic system in the pathogenesis of autoimmune and inflammatory disorders of the CNS will continue to accumulate in the near future.

Histopathologically, granulomatous infiltration of arterial and venous walls and perivascular tissues in neurosarcoidosis can be indistinguishable from primary CNS angiitis.<sup>5</sup> Notably, venous involvement is more common around the ventricles,<sup>27</sup> territory drained by the medullary veins. In some cases, there may be an inflammatory infiltrate with extensive endothelial damage in the absence of granulomas.<sup>28</sup> These pathologic alterations may result in narrowing or obliteration of the vessel lumina<sup>19</sup> and may possibly contribute to the engorged appearance of deep medullary veins through some degree of venous impedence.

Previous reports of primary CNS angiitis have shown a similar pattern of radial enhancement of deep medullary veins.<sup>29,30</sup> However, it is difficult to assess how much of the linear enhancement in those patients was related to venous engorgement versus perivascular disease because no SWI was performed and findings resolved after treatment. In our study, contrast enhancement was likely a combination of perivascular disease superimposed on engorged vessels. While most patients with DMVE did not show discrete perivascular nodular enhancement, small intramural or transmural changes may have been present but beyond the capabilities of conventional MR imaging to resolve. Furthermore, there was no difference in leptomeningeal enhancement between patients with and without DMVE, and those with marked leptomeningeal disease burden were not more likely to fall into either category.

Deep medullary veins can also be prominent in ischemic stroke, in which mild prominence of deep medullary veins has been linked to hypoperfusion and poor outcomes.<sup>31,32</sup> In that setting, they are presumed to be a manifestation of an increased regional oxygen extraction fraction leading to elevated deoxyhemoglobin in the draining veins. Studies have also suggested that this finding may be a predictor of hemorrhagic transformation in patients treated with intravenous tissue plasminogen activator.<sup>33,34</sup> A similar appearance has also been described in Moyamoya disease, in which it has been correlated with severity.<sup>35</sup> However, this so-called "brush sign" is relatively subtle, and none of the published cases have shown the degree of tortuosity and engorgement that was evident in our patients, in whom the process appears to be longstanding and potentially irreversible. Therefore, it is unlikely that the presence of DMVE is a direct result of perfusion changes in neurosarcoidosis. Nevertheless, we did not perform perfusion imaging, and additional research may be worthwhile.

Intracranial hemorrhage is rare in neurosarcoidosis and typically presents as microhemorrhages, likely a reflection of small-vessel disease.<sup>5,7,36</sup> Hemorrhage is thought to result from destruction of the vessel wall by granulomatous inflammation, and 1 previous report documented venous rupture on histopathology.<sup>36</sup> In our study, most patients with DMVE had microhemorrhages. These were significantly more common in this group and did not seem to be an effect of patient age. Notably, there was 1

instance of macrohemorrhage that occurred in a patient with DMVE.

Hydrocephalus is seen in 10% of patients with neurosarcoidosis and is associated with high mortality.<sup>6,37</sup> It can result from decreased CSF resorption, obstruction from meningeal or subependymal disease, or adhesions with ventricular entrapment.<sup>2,38,39</sup> We found that hydrocephalus was much more frequent in patients with DMVE, and it is possible that these are manifestations of a more aggressive sarcoid phenotype. We did explore whether patients with DMVE had worse neurologic outcomes, but there was no significant difference in modified Rankin Scale scores at initial evaluation or follow-up.

The main limitations of this study are inherent in its retrospective nature, with heterogeneity in follow-up times and treatment paradigms. Studies were performed on different field magnets, which likely had an effect on the conspicuity of DMVE. Additionally, conventional postcontrast MR imaging likely underestimates vascular/perivascular disease in the background of engorged enhancing vessels. Finally, sample size was relatively small, and it is possible that specific clinical associations may come to light in larger studies.

In conclusion, DMVE is a frequent manifestation of neurosarcoidosis and was seen in about one-third of patients. It does not appear to be secondary to venous thrombosis in most patients and could be an indirect effect of venous and perivenous inflammation resulting in increased venous impedance. In our cohort, this finding was associated with an increased prevalence of microhemorrhages and hydrocephalus, but patients with this finding did not have worse neurologic outcomes. Being a relatively common finding, DMVE might prompt the reader to consider a diagnosis of neurosarcoidosis in challenging cases.

Disclosures: Carlos Zamora—UNRELATED: Royalties: Lippincott Williams & Wilkins and Thieme, Comments: royalties for authorship, *Neuroradiology Companion*, 5th ed, and *The Comprehensive Neurosurgery Board Preparation Book*.

## REFERENCES

1. Sakthivel P, Bruder D. **Mechanism of granuloma formation in sarcoidosis.** *Curr Opin Hematol* 2017;24:59–65 CrossRef Medline
2. Smith JK, Matheus MG, Castillo M. **Imaging manifestations of neurosarcoidosis.** *AJR Am J Roentgenol* 2004;182:289–95 CrossRef Medline
3. Joubert B, Chapelon-Abrie C, Biard L, et al. **Association of prognostic factors and immunosuppressive treatment with long-term outcomes in neurosarcoidosis.** *JAMA Neurol* 2017;74:1336–44 CrossRef Medline
4. Fritz D, Voortman M, van de Beek D, et al. **Many faces of neurosarcoidosis: from chronic meningitis to myelopathy.** *Curr Opin Pulm Med* 2017;23:439–46 CrossRef Medline
5. Bathla G, Watal P, Gupta S, et al. **Cerebrovascular manifestations of neurosarcoidosis: an underrecognized aspect of the imaging spectrum.** *AJNR Am J Neuroradiol* 2018;39:1194–1200 CrossRef Medline
6. van Rooijen JM, Mijnhout GS, Aalders TT, et al. **Hydrocephalus, a rare manifestation of sarcoidosis.** *Clin Pract* 2011;1:e66 CrossRef Medline
7. Travers F, Maltête D, Morisse-Pradier H, et al. **Intracranial hemorrhage in neurosarcoidosis.** *J Neurol Sci* 2014;341:185–86 CrossRef Medline
8. Libman RB, Sharfstein S, Harrington W, et al. **Recurrent intracerebral hemorrhage from sarcoid angiitis.** *J Stroke Cerebrovasc Dis* 1997;6:373–75 CrossRef Medline
9. Zajicek JP, Scolding NJ, Foster O, et al. **Central nervous system sarcoidosis: diagnosis and management.** *QJM* 1999;92:103–17 CrossRef Medline
10. Cohen Aubart F, Bouvry D, Galanaud D, et al. **Long-term outcomes of refractory neurosarcoidosis treated with infliximab.** *J Neurol* 2017;264:891–97 CrossRef Medline
11. Liang L, Korogi Y, Sugahara T, et al. **Evaluation of the intracranial dural sinuses with a 3D contrast-enhanced MP-RAGE sequence: prospective comparison with 2D-TOF MR venography and digital subtraction angiography.** *AJNR Am J Neuroradiol* 2001;22:481–92 Medline
12. Taoka T, Fukusumi A, Miyasaka T, et al. **Structure of the medullary veins of the cerebral hemisphere and related disorders.** *Radiographics* 2017;37:281–97 CrossRef Medline
13. Hooshmand I, Rosenbaum AE, Stein RL. **Radiographic anatomy of normal cerebral deep medullary veins: criteria for distinguishing them from their abnormal counterparts.** *Neuroradiology* 1974;7:75–84 CrossRef Medline
14. Reichenbach JR, Venkatesan R, Schillinger DJ, et al. **Small vessels in the human brain: MR venography with deoxyhemoglobin as an intrinsic contrast agent.** *Radiology* 1997;204:272–77 CrossRef Medline
15. Vogl TJ, Bergman C, Villringer A, et al. **Dural sinus thrombosis: value of venous MR angiography for diagnosis and follow-up.** *AJR Am J Roentgenol* 1994;162:1191–98 CrossRef Medline
16. Cromb  D, Haven F, Gille M. **Isolated deep cerebral venous thrombosis diagnosed on CT and MR imaging: a case study and literature review.** *JBR-BTR* 2003;86:257–61 Medline
17. D'Amore A, Conte G, Vighianesi A, et al. **Elderly patient with dural sinus thrombosis leading to abnormal medullary veins and cerebral venous infarctions.** *Radiol Case Rep* 2012;7:655 CrossRef Medline
18. Mittal S, Wu Z, Neelavalli J, et al. **Susceptibility-weighted imaging: technical aspects and clinical applications, Part 2.** *AJNR Am J Neuroradiol* 2009;30:232–52 CrossRef Medline
19. Mirfakhraee M, Crofford MJ, Guinto FC Jr, et al. **Virchow-Robin space: a path of spread in neurosarcoidosis.** *Radiology* 1986;158:715–20 CrossRef Medline
20. Louveau A, Plog BA, Antila S, et al. **Understanding the functions and relationships of the glymphatic system and meningeal lymphatics.** *J Clin Invest* 2017;127:3210–19 CrossRef Medline
21. Louveau A, Smirnov I, Keyes TJ, et al. **Structural and functional features of central nervous system lymphatic vessels.** *Nature* 2015;523:337–41 CrossRef Medline
22. Iliff JJ, Nedergaard M. **Is there a cerebral lymphatic system?** *Stroke* 2013;44:S93–95 CrossRef Medline
23. Iliff JJ, Wang M, Liao Y, et al. **A paravascular pathway facilitates CSF flow through the brain parenchyma and the clearance of interstitial solutes, including amyloid  $\beta$ .** *Sci Transl Med* 2012;4:147ra111 CrossRef Medline
24. Engelhardt B, Carare RO, Bechmann I, et al. **Vascular, glial, and lymphatic immune gateways of the central nervous system.** *Acta Neuropathol* 2016;132:317–38 CrossRef Medline
25. Albargothy NJ, Johnston DA, MacGregor-Sharp M, et al. **Convective influx/glymphatic system: tracers injected into the CSF enter and leave the brain along separate periarterial basement membrane pathways.** *Acta Neuropathol* 2018 May 12. [Epub ahead of print] CrossRef Medline
26. Bacyinski A, Xu M, Wang W, et al. **The paravascular pathway for brain waste clearance: current understanding, significance and controversy.** *Front Neuroanat* 2017;11:101 CrossRef Medline
27. Brown MM, Thompson AJ, Wedzicha JA, et al. **Sarcoidosis presenting with stroke.** *Stroke* 1989;20:400–05 CrossRef Medline
28. Mochizuki I, Kubo K, Hond T. **Widespread heavy damage of capillary endothelial cells in the pathogenesis of sarcoidosis: evidence by monoclonal von Willebrand factor immunohistochemistry in the bronchus and lung of patients with sarcoidosis.** *Sarcoidosis Vasc Diffuse Lung Dis* 2014;31:182–90 Medline
29. Hassan AS, Trobe JD, McKeever PE, et al. **Linear magnetic resonance enhancement and optic neuropathy in primary angiitis of the central nervous system.** *J Neuroophthalmol* 2003;23:127–31 CrossRef Medline

30. Ganta K, Malik AM, Wood JB, et al. **Radial contrast enhancement on brain magnetic resonance imaging diagnostic of primary angiitis of the central nervous system: a case report and review of the literature.** *J Med Case Rep* 2014;8:26 CrossRef Medline
31. Yu X, Yuan L, Jackson A, et al. **Prominence of medullary veins on susceptibility-weighted images provides prognostic information in patients with subacute stroke.** *AJNR Am J Neuroradiol* 2016;37:423–29 CrossRef Medline
32. Mucke J, Möhlenbruch M, Kickingereder P, et al. **Asymmetry of deep medullary veins on susceptibility weighted MRI in patients with acute MCA stroke is associated with poor outcome.** *PLoS One* 2015;10:e0120801 CrossRef Medline
33. Terasawa Y, Yamamoto N, Morigaki R, et al. **Brush sign on 3-T T2\*-weighted MRI as a potential predictor of hemorrhagic transformation after tissue plasminogen activator therapy.** *Stroke* 2014;45:274–76 CrossRef Medline
34. Hermier M, Nighoghossian N, Derex L, et al. **Hypointense transcallosal veins at T2\*-weighted MRI: a marker of hemorrhagic transformation risk in patients treated with intravenous tissue plasminogen activator.** *J Cereb Blood Flow Metab* 2003;23:1362–70 CrossRef Medline
35. Horie N, Morikawa M, Nozaki A, et al. **“Brush sign” on susceptibility-weighted MR imaging indicates the severity of moyamoya disease.** *AJNR Am J Neuroradiol* 2011;32:1697–702 CrossRef Medline
36. O’Dwyer JP, Al-Moyeed BA, Farrell MA, et al. **Neurosarcoidosis-related intracranial haemorrhage: three new cases and a systematic review of the literature.** *Eur J Neurol* 2013;20:71–78 CrossRef Medline
37. Krumholz A, Stern BJ. **Neurologic manifestations of sarcoidosis.** *Handb Clin Neurol* 2014;119:305–33 CrossRef Medline
38. Nozaki K, Judson MA. **Neurosarcoidosis.** *Curr Treat Options Neurol* 2013;15:492–504 CrossRef Medline
39. Ginat DT, Dhillon G, Almast J. **Magnetic resonance imaging of neurosarcoidosis.** *J Clin Imaging Sci* 2011;1:15 CrossRef Medline

# Subtraction CTA: An Alternative Imaging Option for the Follow-Up of Flow-Diverter-Treated Aneurysms?

 M.P. Duarte Conde,  A.M. de Korte,  F.J.A. Meijer,  R. Aquarius,  H.D. Boogaarts,  R.H.M.A. Bartels, and  J. de Vries

## ABSTRACT

**BACKGROUND AND PURPOSE:** This was a pilot study to explore the diagnostic accuracy and safety of subtraction CTA combined with a single-energy metal artifact reduction algorithm (SEMAR) compared to DSA for the evaluation of intracranial aneurysm occlusion after flow diverter treatment.

**MATERIALS AND METHODS:** We included patients treated with a flow diverter for an unruptured intracranial aneurysm between November 2015 and November 2016. The patient cohort comprised 2 groups: those who underwent follow-up imaging 1 month after flow-diverter treatment and those with a known residual intracranial aneurysm after flow diverter treatment who underwent imaging at regular follow-ups. Full-brain subtraction CTA was performed on a 320–detector row CT system. A low-dose non-enhanced volume acquisition was followed by a contrast-enhanced volume CTA. Iterative and noise-reduction filters, SEMAR, and <sup>SURE</sup>Subtraction algorithms were applied. DSA was performed on a flat panel C-arm angiography system. Standard posteroanterior, lateral, 3D, and detailed 2D acquisitions were performed. Imaging was independently scored by 2 clinicians. Aneurysm occlusion (Raymond scale) was our primary outcome parameter.

**RESULTS:** Thirteen intracranial aneurysms were evaluated with subtraction CTA and DSA. Nine aneurysm remnants were demonstrated by both subtraction CTA and DSA. The sensitivity and specificity of subtraction CTA for the detection of aneurysm occlusion were 100% (95% CI, 82.41%–100%) and 100% (95% CI, 67.55%–100%), respectively. Agreement between readers was perfect ( $\kappa = 1.0$ ). The smallest neck remnant detected on subtraction CTA was 1.2 mm. No complications occurred.

**CONCLUSIONS:** Subtraction CTA with single-electron metal artifact reduction is effective in the reduction of metal artifacts of flow diverters and might therefore be a viable alternative in the assessment of intracranial aneurysm occlusion after flow diverter treatment.

**ABBREVIATIONS:** IA = intracranial aneurysm; FD = flow diverter; sCTA = subtraction CTA; SEMAR = single-electron metal artifact reduction

Flow diverters (FDs) are being increasingly used to treat complex intracranial aneurysms (IAs).<sup>1–3</sup> These stentlike implants initially disrupt the blood flow into the IA and eventually facilitate parent artery reconstruction through endothelialization of the FD. Ideally this will lead to IA occlusion and rupture prevention.<sup>2,4</sup>

Although complete IA occlusion is the goal of the FD treatment, it is only achieved in around 75%–80% of cases.<sup>5</sup> Identification of aneurysm remnants after FD treatment is therefore

important because remnants can still rupture and cause a subarachnoid hemorrhage.<sup>6</sup> Digital subtraction angiography is considered the criterion standard to assess IA occlusion and IA remnants after FD treatment. However, this technique is invasive and has a low but not negligible complication rate.<sup>7–9</sup>

Subtraction CT angiography (sCTA), in which a noncontrast acquisition is subtracted from a contrast-enhanced acquisition, might be a good alternative to DSA in the follow-up of patients treated with FDs. This technique has already been shown to produce results comparable with those of DSA in the detection and classification of IAs in the preoperative setting.<sup>10,11</sup> Detection of small IAs and IAs adjacent to bony structures is even more accurate in sCTA.<sup>11</sup> Additional advantages of sCTA compared with DSA are lower costs,<sup>12,13</sup> a less invasive procedure,<sup>7–9</sup> and a lower radiation dose for the patient.<sup>14</sup> One major disadvantage of using sCTA in the follow-up of patients treated with FDs is that the metal wires of the implant can produce artifacts, which can hamper IA assessment.

With the introductions of new metal artifact–reduction algo-

Received May 13, 2018; accepted after revision August 9.

From the Departments of Neurosurgery (M.P.D.C., A.M.d.K., R.A., H.D.B., R.H.M.A.B., J.d.V.), Radiology and Nuclear Medicine (F.J.A.M.), and Pathology (R.A.), Radboud University Medical Center, Nijmegen, the Netherlands.

Mariana P. Duarte Conde and Antonius M. de Korte contributed equally to this article. This work was supported by Stryker Neurovascular.

Please address correspondence to A.M. de Korte, MD, Radboud University Medical Center, Department of Neurosurgery, PO Box 9101, 6500 HB Nijmegen, the Netherlands; e-mail: Thomas.dekorte@radboudumc.nl

<http://dx.doi.org/10.3174/ajnr.A5817>

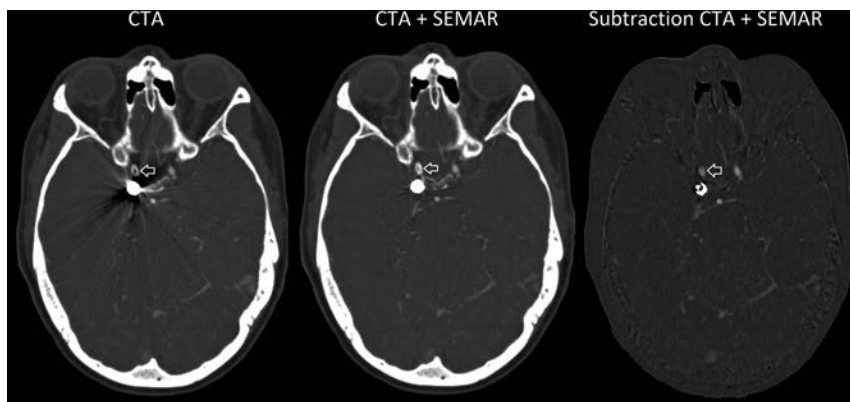


**FIG 1.** A patient with 3 aneurysms treated with either a flow diverter or coils. Axial view in which both a flow diverter (arrows) and coils are visible to illustrate the effect of single-energy metal artifact reduction. Non-SEMAR CTA (left), CTA with SEMAR (middle), and subtraction CTA with SEMAR (right) demonstrate the effects of SEMAR on metal artifacts.

rithms like single-energy metal artifact reduction (SEMAR) and subtraction algorithms (<sup>SURE</sup>Subtraction; Toshiba Medical Systems, Tokyo, Japan) for second-generation 320–detector row CT scanners,<sup>15</sup> it now seems that we might overcome this problem. The SEMAR algorithm uses several back-projection steps to extract metal objects from the raw data. Next, metal artifacts are filtered out by forward-projection through <sup>SURE</sup>Subtraction algorithms. The corrected raw data are then reconstructed, and metal components without artifacts are placed back into the image. This algorithm, in combination with subtraction algorithms, has shown promising results regarding artifact reduction in several fields of medicine but has not been evaluated for assessing aneurysm occlusion after FD implantation.<sup>16–19</sup>

The goal of our study was to answer the following question: Can sCTA combined with a SEMAR algorithm effectively reduce metal artifacts of FDs, making it a viable alternative to DSA in the postoperative follow-up of patients treated with FDs? To answer our research question, we performed a pilot study to evaluate the diagnostic accuracy of sCTA compared with DSA for the evaluation of IA occlusion after FD placement.

## MATERIALS AND METHODS

### Study Population

A pilot study was performed at our Department of Neurosurgery. Ethics committee approval was obtained, and all patients gave written informed consent. Patients treated with a FD for an unruptured IA were included in our series. The patient cohort comprised 2 groups: those who were treated between November 2015 and November 2016 receiving follow-up imaging 1 month after FD treatment and those with a known residual IA after earlier FD treatment who received imaging at regular follow-ups (which was between November 2015 and November 2016).

Exclusion criteria were the following: younger than 18 years of age, retreatment for a previously coiled IA, the presence of an SAH, a known allergy or contraindication to the use of contrast agents, renal insufficiency, pregnancy, or the current clinical condition not allowing inclusion. Renal function was checked before (<3 months) and 3 days after the procedure. sCTA and DSA were performed within 24 hours of each other.

### Digital Subtraction Angiography

DSA was performed on a flat panel C-arm angiography system (Allura Xper FD20; Philips Healthcare, Best, the Netherlands). Before all acquisitions, a system-specific air calibration of the C-arm system was performed. Standard posteroanterior and lateral acquisitions were obtained using a diagnostic catheter via the transfemoral route. After standard 2D acquisitions, a 3D rotational acquisition was performed using a cerebral soft-tissue protocol (XperCT; Philips Healthcare) with selective contrast bolus injection via the ICA using a power injector (Angiomat Illumena; Covidien/Mallinckrodt, Lake Forest, California).

3D reconstructions were generated and analyzed on a workstation (XtraVision; Philips Healthcare). 3D reconstructions were used to assess the best working projections for following detailed 2D acquisitions. At the end of the procedure, the arterial puncture wound was closed with an Angio-Seal (St. Jude Medical, Minnetonka, Minnesota) or by manual compression. An average of 50 mL of contrast material (300 mg of iodine/mL, iomeprol, Iomeron; Bracco, Milan, Italy) was used per procedure. The estimated radiation dose for the entire DSA (all acquisitions) was 10 mSv.

### Subtraction CTA

Full-brain sCTA was performed on a wide-detector CT system (320–detector row CT scanner, Aquilion ONE Vision Edition; Toshiba Medical Systems). The scanning protocol included a low-dose nonenhanced volume acquisition at 120 kV and 100 mAs followed by a contrast-enhanced volume CTA at 120 kV and 22 mAs using a bolus-tracked 50-mL contrast agent bolus (300 mg of Iomeron). Iterative and noise-reduction filters, SEMAR, and <sup>SURE</sup>Subtraction algorithms were applied (Fig 1). The estimated radiation dose was 2.6 mSv as reported by the scanner after each acquisition.

### Image Analysis

Studies were independently scored by 1 neuroradiologist (F.J.A.M., reader 1 with 12 years experience) and 1 neurosurgeon (M.P.D.C., reader 2 with 3 years experience). Neither of these 2 readers were involved in the treatment of the patients. Both sCTA and DSA studies were reviewed on a dedicated clinical workstation (Impax, Version 6.6; Agfa HealthCare, Mortsel, Belgium).

All variables were dichotomized to assess the diagnostic accuracy of sCTA compared with DSA as the reference standard. Intracranial aneurysm occlusion rate, based on the Raymond scale, was used as the primary study parameter and was categorized as either completely occluded (Raymond grade 1) or incompletely occluded (Raymond grade  $\geq 2$ ).

We assessed the following secondary outcome measures: Device deployment, wall apposition, and neck coverage were scored as “complete” or “incomplete.” Proximal and distal vessel patency

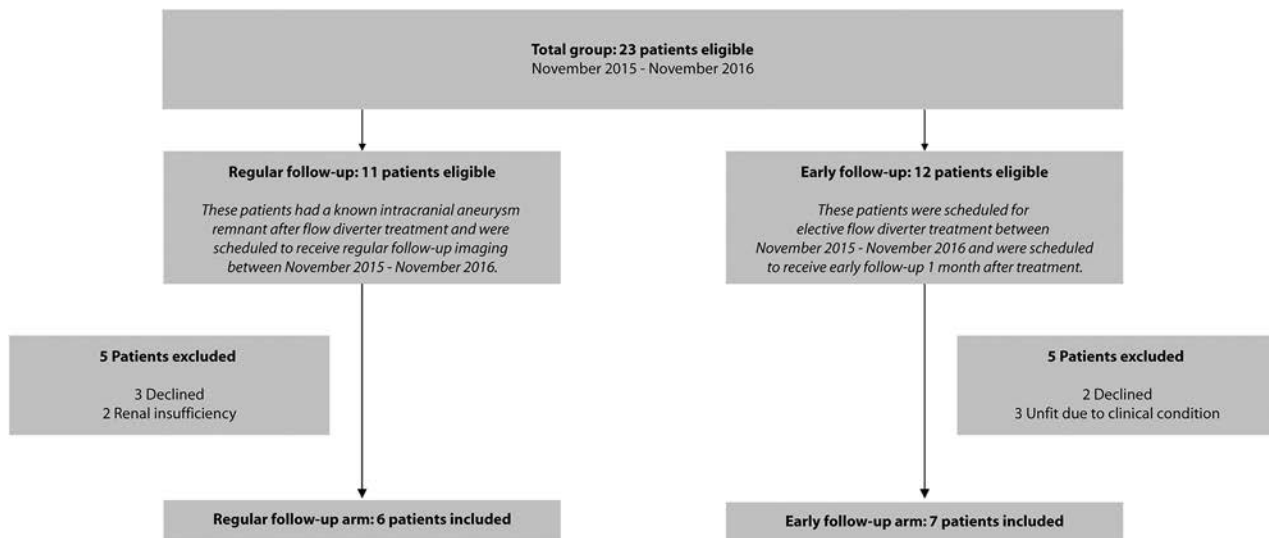


**FIG 2.** Description of study cohort.

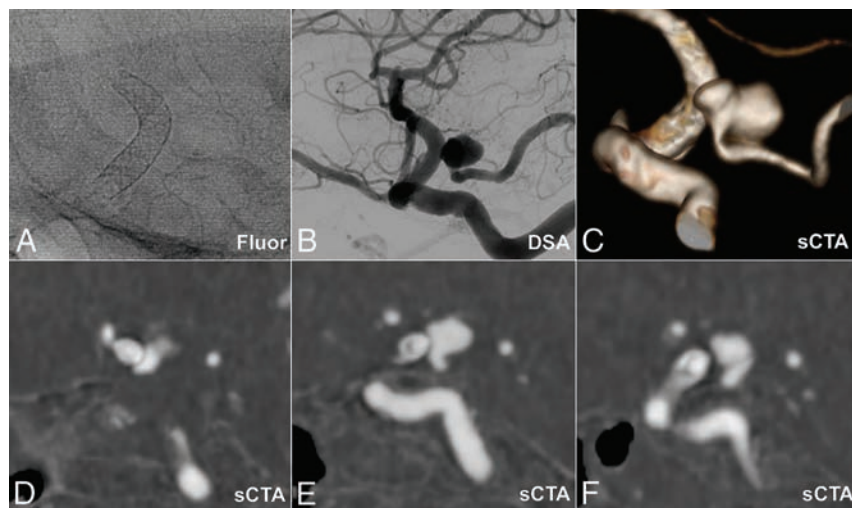


**FIG 3.** Residual aneurysm located at the origin of the posterior communicating artery after flow diverter placement in the internal carotid artery. Fluoroscopy (A) with a flow diverter clearly visible, DSA (B), subtraction CTA 3D view (C), and subtraction CTA thin-slice 1-mm MIPs (D–F).

was compared with pretreatment vessel diameter and scored as either “nonstenotic” ( $\leq 25\%$  stenosis) or “stenotic” ( $> 25\%$  stenosis). Side-branch patency was scored as “unchanged” or “changed” compared with pretreatment DSA.

Statistical analysis was performed on initial scoring. In case of discrepancies, readers were asked to re-evaluate these specific cases in a second reading to see whether consensus between sCTA and DSA scoring could be reached. These consensus readings were used solely for descriptive analysis and not for statistical analysis because of the great bias after the initial reading.

### Statistical Analysis

Statistical analyses were performed using SPSS statistical software (Version 22.0; IBM, Armonk, New York). The sensitivity and specificity of sCTA compared with DSA regarding the primary outcome measure were calculated.  $\kappa$  statistics were calculated for interrater reliability regarding the primary outcome measure.

$\kappa$  values were scored according to the method of Fleiss et al<sup>20</sup>:  $< 0.4$ , positive but poor agreement;  $0.41$ – $0.75$ , good agreement; and  $> 0.75$  excellent agreement. Descriptive statistics were used for patient and aneurysm characteristics and secondary parameters.

## RESULTS

### Included Patients

Between November 2015 and November 2016, twenty-three patients were treated with a flow diverter at our Department of Neurosurgery. Thirteen patients (8 women and 5 men) were enrolled in this study (Fig 2). Seven patients were newly treated and underwent early follow-up imaging 1 month after treatment to assess IA closure. The remaining 6 patients had a

known IA remnant and were included at their regular follow-up moment. Five patients declined to participate in the study, and 2 patients were excluded due to their renal function. Three patients were excluded due to their clinical condition. These patients had neurologic deterioration after FD treatment either due to mass effect or ischemic events.

The average age of patients was  $60 \pm 8$  years (range, 44–76 years). Treated IAs originated from the internal carotid artery (54%,  $n = 7$ ), middle cerebral artery (23%,  $n = 3$ ), posterior communicating artery (8%,  $n = 1$ ), vertebral artery (8%,  $n = 1$ ), and posterior inferior cerebellar artery (8%,  $n = 1$ ).

All patients had been treated previously with a Surpass FD (Stryker Neurovascular, Kalamazoo, Michigan). Eleven patients were treated with 1 FD and 2 patients were retreated with an additional FD due to persistent IA filling after the initial FD treatment. sCTA and DSA were performed within 24 hours of each other in every patient. No complications occurred.

### Primary Outcome

In all cases, sCTA and DSA provided adequate images for diagnostic evaluation. Nine incomplete IA occlusions were demonstrated by both sCTA and DSA (Figs 3–5).

The sensitivity and specificity of sCTA for the detection of IA occlusion were 100% (95% CI, 82.41%–100%) and 100% (95% CI, 67.55%–100%), respectively (Table). Agreement between readers was perfect ( $\kappa = 1.0$ ). The smallest neck remnant detected on sCTA was 1.2 mm (Fig 6).

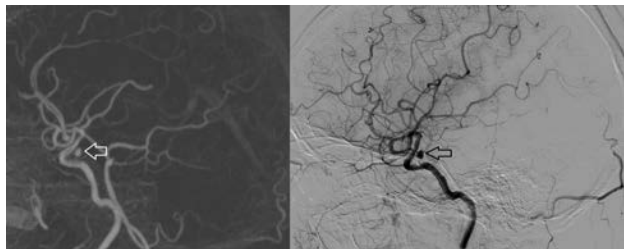


**FIG 4.** Residual aneurysm (arrows) located at the right carotid artery after flow-diverter placement in the internal carotid artery. Sagittal view of 45-mm-slice MIPs on subtraction CTA (left) and DSA (right).

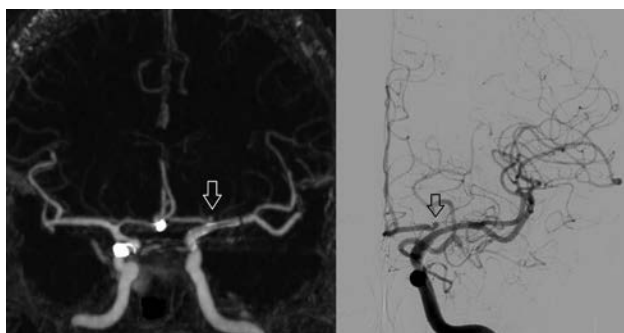


**FIG 5.** Residual aneurysm (arrows) located at the left anterior cerebral artery after flow-diverter placement in the internal carotid artery and middle cerebral artery. Coronal view of 20-mm-slice MIPs on subtraction CTA (left) and posteroanterior-acquisition DSA (right). Two previously coiled aneurysms on the contralateral carotid artery and anterior communicating artery can be seen on the subtraction CTA.

### Secondary Outcomes

Agreement between sCTA and DSA regarding the secondary parameters is presented in the Table. Five disagreements in 4 secondary parameters occurred.

### DISCUSSION

We strived to answer the following question: Can sCTA, combined with a SEMAR algorithm, effectively reduce metal artifacts of FDs, making them a viable alternative to DSA in the postoperative follow-up of patients treated with FDs? In this pilot study, we showed that sCTA in combination with a SEMAR algorithm was effective in the reduction of metal artifacts of FDs and that the diagnostic accuracy of sCTA with a SEMAR was similar compared with DSA for the evaluation of IA occlusion after FD placement.

To our knowledge, this is the first study in which an alternative imaging technique has been shown to be comparable with DSA after FD treatment; in recent studies, contrast-enhanced MRA,<sup>21–23</sup> 3D TOF-MRA,<sup>21,22</sup> C-arm conebeam CT,<sup>24,25</sup> and CTA<sup>22</sup> were all inferior to DSA due to metal artifacts originating from the FD wires. Although a recent study comparing contrast-enhanced MRA with DSA demonstrated good imaging of the aneurysm sac after FD treatment, the assessability of the stent lumen, however, remained difficult due to metal artifacts.<sup>23</sup>

Besides IA occlusion, we also assessed several secondary parameters such as device deployment, device malapposition, parent artery stenosis, and side-branch patency. Although 5 disagreements between DSA and sCTA occurred in these secondary parameters (Table), none would have led to discrepancies in clinical decision-making. Disagreements were not clearly in favor of 1 of the 2 modalities. For example, in 1 case, a side branch was missed by 1 reader on sCTA but not on DSA. However, in another case, both readers scored wall apposition as incomplete on sCTA but complete on DSA in 1 subject. A second reading of this case confirmed incomplete wall apposition on DSA, which demonstrated the potential of sCTA in the follow-up of patients treated with FDs.

The SEMAR algorithm has been an important addition to the sCTA technique. Despite only recently becoming commercially available, it has already led to successful results in several fields of medicine. The algorithm was able to reduce metal artifacts in

### Number of discrepancies between sCTA and DSA for both readers

Intracranial Aneurysm Feature	Discrepancies between sCTA and DSA		Comments
	Reader 1	Reader 2	
Aneurysm closure (Raymond I)	0	0	NA
Complete device deployment	0	1	Device deployment was scored complete on sCTA but incomplete on DSA; a second reading of this case confirmed complete device deployment on DSA
Complete wall apposition	1	1	In 1 patient, both readers scored wall apposition incomplete on sCTA but complete on DSA; a second reading of this case confirmed incomplete wall apposition on DSA
Complete neck coverage	0	0	NA
Vessel patency distal (nonstenotic)	1	0	Vessel patency was scored nonstenotic on sCTA but stenotic on DSA in 1 case; a second reading confirmed nonstenosis on DSA
Vessel patency proximal (nonstenotic)	0	0	NA
Side branch patency (no change)	0	1	In 1 case, a side branch was missed on follow-up sCTA; a second reading of the case confirmed a patent side branch on sCTA

**Note:**—NA indicates not applicable.

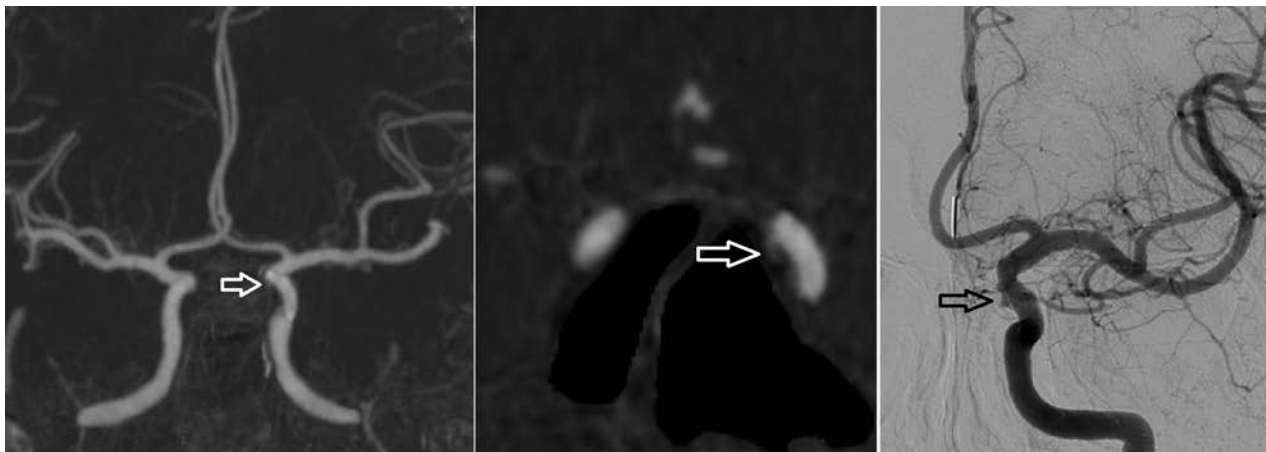


**FIG 6.** Small residual aneurysm (arrows) located at the left carotid artery after flow-diverter placement in the internal carotid artery. Coronal view of 20-mm-slice MIP on subtraction CTA (left), coronal subtraction CTA thin-slice 1-mm MIP (middle), and posteroanterior-acquisition DSA (right).

patients with dental implants<sup>26</sup> and hip prostheses.<sup>17</sup> Additionally, the SEMAR was also able to improve image quality in patients treated with coils for IA aneurysms and abdominal aneurysms (Fig 1).<sup>16,18</sup> These results demonstrate the importance of SEMAR when using sCTA, and we think it might also be a useful tool for follow-up imaging when patients with IAs have been treated with surgical clips or detachable coils. This should be studied in future research.

This study has several limitations. First, because this was a pilot study, we used a small patient cohort and thus gathered limited data. However, we were able to collect a relatively high number of nonoccluded IAs by selecting patients with either a known aneurysm remnant as well as by performing a short follow-up after FD implantation. A large, prospective study is necessary to confirm the results of this pilot study.

Second, blinded scoring of sCTA and DSA studies would have improved the methodology of this study. However, with a limited study population, it will remain extremely difficult for readers to be completely blinded because they will likely recognize individual cases by the size, shape, and location of the IA.

Third, we only included patients treated with a Surpass FD device and results may not translate to other FDs because not all FDs are made from the same material. However, the cobalt chromium wires of the Surpass FD are expected to result in more pronounced metal artifacts compared with nitinol stents, which would make this a worst-case scenario.

## CONCLUSIONS

Subtraction CTA with the SEMAR is effective in the reduction of metal artifacts of FDs and might, therefore, be a viable alternative in the assessment of IA occlusion after FD treatment.

Disclosures: J. de Vries - RELATED: Consultancy: Stryker Neurovascular.\* H.D. Boogaarts - RELATED: Consultancy: Stryker Neurovascular.\* \*Money paid to the institution.

## REFERENCES

1. Becske T, Kallmes DF, Saatci I, et al. Pipeline for uncoilable or failed aneurysms: results from a multicenter clinical trial. *Radiology* 2013; 267:858–68 CrossRef Medline
2. De Vries J, Boogaarts J, Van Norden A, et al. New generation of flow

diverter (Surpass) for unruptured intracranial aneurysms: a prospective single-center study in 37 patients. *Stroke* 2013;44:1567–77 CrossRef Medline

3. Lylyk P, Miranda C, Ceratto R, et al. Curative endovascular reconstruction of cerebral aneurysms with the Pipeline embolization device: the Buenos Aires experience. *Neurosurgery* 2009;64:632–42; discussion 642–43; quiz N6 CrossRef Medline
4. Wakhloo AK, Gounis MJ. Revolution in aneurysm treatment: flow diversion to cure aneurysms: a paradigm shift. *Neurosurgery* 2014; 61(Suppl 1):111–20 CrossRef Medline
5. Brinjikji W, Murad MH, Lanzino G, et al. Endovascular treatment of intracranial aneurysms with flow diverters: a meta-analysis. *Stroke* 2013;44:442–47 CrossRef Medline
6. Feuerberg I, Lindquist C, Lindqvist M, et al. Natural history of postoperative aneurysm rests. *J Neurosurg* 1987;66:30–34 CrossRef Medline
7. Dawkins AA, Evans AL, Wattam J, et al. Complications of cerebral angiography: a prospective analysis of 2,924 consecutive procedures. *Neuroradiology* 2007;49:753–59 CrossRef Medline
8. Thiex R, Norbash AM, Frerichs KU. The safety of dedicated-team catheter-based diagnostic cerebral angiography in the era of advanced noninvasive imaging. *AJNR Am J Neuroradiol* 2010;31: 230–34 CrossRef Medline
9. Cloft HJ, Joseph GJ, Dion JE. Risk of cerebral angiography in patients with subarachnoid hemorrhage, cerebral aneurysm, and arteriovenous malformation: a meta-analysis. *Stroke* 1999;30:317–20 CrossRef Medline
10. Luo Z, Wang D, Sun X, et al. Comparison of the accuracy of subtraction CT angiography performed on 320-detector row volume CT with conventional CT angiography for diagnosis of intracranial aneurysms. *Eur J Radiol*;2012;81:118–22 CrossRef Medline
11. Ramasundara S, Mitchell PJ, Dowling RJ. Bone subtraction CT angiography for the detection of intracranial aneurysms. *J Med Imaging Radiat Oncol* 2010;54:526–33 CrossRef Medline
12. Harrison MJ, Johnson BA, Gardner GM, et al. Preliminary results on the management of unruptured intracranial aneurysms with magnetic resonance angiography and computed tomographic angiography. *Neurosurgery* 1997;40:947–55; discussion 955–57 CrossRef Medline
13. Dehdashti AR, Binaghi S, Uske A, et al. Comparison of multislice computerized tomography angiography and digital subtraction angiography in the postoperative evaluation of patients with clipped aneurysms. *J Neurosurg* 2006;104:395–403 CrossRef Medline
14. Manninen AL, Isokangas JM, Karttunen A, et al. A comparison of radiation exposure between diagnostic CTA and DSA examination. *AJNR Am J Neuroradiol* 39:2051–56 Nov 2018 www.ajnr.org

- tions of cerebral and cervicocerebral vessels. *AJNR Am J Neuroradiol* 2012;33:2038–42 CrossRef Medline
15. Golshani B, Lazzaro MA, Raslau F, et al. **Surveillance imaging after intracranial stent implantation: non-invasive imaging compared with digital subtraction angiography.** *Neurointerv Surg* 2013;5:361–65 CrossRef Medline
  16. Kidoh M, Utsunomiya D, Ikeda O, et al. **Reduction of metallic coil artefacts in computed tomography body imaging: effects of a new single-energy metal artefact reduction algorithm.** *Eur Radiol* 2016;26:1378–86 CrossRef Medline
  17. Yasaka K, Maeda E, Hanaoka S, et al. **Single-energy metal artifact reduction for helical computed tomography of the pelvis in patients with metal hip prostheses.** *Jpn J Radiol* 2016;34:1–8 CrossRef Medline
  18. Pan YN, Chen G, Li AJ, et al. **Reduction of metallic artifacts of the post-treatment intracranial aneurysms: effects of single energy metal artifact reduction algorithm.** *Clin Neuroradiol* 2017 Nov 16. [Epub ahead of print] CrossRef Medline
  19. Asano Y, Tada A, Shinya T, et al. **Utility of second - generation single-energy metal artifact reduction in helical lung computed tomography for patients with pulmonary arteriovenous malformation after coil embolization.** *Jpn J Radiol* 2018;36:285–294 CrossRef Medline
  20. Fleiss J, Levin B, Cho Paik M. *Statistical Methods for Rates and Proportions.* Hoboken: John Wiley Sons; 2003:800
  21. Attali J, Benaissa A, Soize S, et al. **Follow-up of intracranial aneurysms treated by flow diverter: comparison of three-dimensional time-of-flight MR angiography (3D-TOF-MRA) and contrast-enhanced MR angiography (CE-MRA) sequences with digital subtraction angiography as the gold standard.** *J Neurointerv Surg* 2016;8:81–86 CrossRef Medline
  22. Toni F, Marliani AF, Cirillo L, et al. **3T MRI in the evaluation of brain aneurysms treated with flow-diverting stents: preliminary experience.** *Neuroradiol J* 2009;22:588–99 CrossRef Medline
  23. Patzig M, Forbrig R, Ertl L, et al. **Intracranial aneurysms treated by flow-diverting stents: long-term follow-up with contrast-enhanced magnetic resonance angiography.** *Cardiovasc Intervent Radiol* 2017;40:1713–22 CrossRef Medline
  24. Yu SC, Lee KT, Lau TW, et al. **Intravenous C-arm conebeam CT angiography following long-term flow-diverter implantation: technologic evaluation and preliminary results.** *AJNR Am J Neuroradiol* 2016;37:481–86 CrossRef Medline
  25. Yang P, Ahmed A, Schafer S, et al. **Low-dose volume-of-interest C-arm CT imaging of intracranial stents and flow diverters.** *AJNR Am J Neuroradiol* 2016;37:648–54 CrossRef Medline
  26. Yasaka K, Kamiya K, Irie R, et al. **Metal artefact reduction for patients with metallic dental fillings in helical neck computed tomography: comparison of adaptive iterative dose reduction 3D (AIDR 3D), forward-projected model-based iterative reconstruction solution (FIRST) and AIDR 3D with single-energy metal artefact reduction (SEMAR).** *Dentomaxillofac Radiol* 2016;45:20160114 CrossRef Medline

# Flow-Diversion Effect of LEO Stents: Aneurysm Occlusion and Flow Remodeling of Covered Side Branches and Perforators

 F. Cagnazzo,  M. Cappucci,  C. Dargazanli,  P.-H. Lefevre,  G. Gascou,  C. Riquelme,  R. Morganti,  V. Mazzotti,  A. Bonafe, and  V. Costalat



## ABSTRACT

**BACKGROUND AND PURPOSE:** Flow diversion with intermediate-porosity stents (braided stents) has been recently reported for distally located small aneurysms. The aim of this study was to evaluate the flow-diversion effect of LEO stents on covered vessels and for aneurysms treated with sole stent-placement therapy.

**MATERIALS AND METHODS:** We retrospectively evaluated the following outcomes: 1) remodeling of covered side branches and perforators (extra-aneurysmal flow remodeling), and 2) the occlusion rate of aneurysms treated with sole stent-placement therapy (intra-aneurysmal flow remodeling).

**RESULTS:** Seventy-six patients with 98 covered vessels were studied. Overall, 89 covered arteries (91%) were normal, 7 showed narrowing (7%), and 2 (2%) were occluded (1 posterior communicating artery and 1 MCA) without related complications (mean DSA follow-up, 14 months). Univariate and multivariate analyses highlighted smoking ( $P = .03$ ) and the length of follow-up ( $P = .002$ ) as factors associated with arterial remodeling. Of the 17 Sylvian (lenticulostriate arteries) and 7 basilar perforators, 1 (4%) group of Sylvian perforators covered with double stents had asymptomatic remodeling. Ten aneurysms (mean size, 3.5 mm) were treated with LEO stents as stent monotherapy (5 recanalized after coiling and 5 directly treated with the LEO). Complete occlusion (Raymond-Roy I) was achieved in 70% of aneurysms (mean follow-up, 14 months). The Raymond-Roy I occlusion rate among recanalized aneurysms and those directly treated with LEO stents was 80% and 60%, respectively ( $P = .9$ ).

**CONCLUSIONS:** The rate of flow remodeling on the covered arteries and perforators was 9% and 4%, respectively, and was clinically irrelevant in all cases. Complete occlusion of aneurysms treated with sole stent-placement therapy was 70%. These data stress the flow-diversion properties of LEO stents.

**ABBREVIATIONS:** PcomA = posterior communicating artery; RR = Raymond-Roy; SAC = stent-assisted coiling

LEO stents (Balt Extrusion, Montmorency, France) are self-expanding closed-cell stents produced by braiding individual strands of nitinol onto a mandrel.<sup>1</sup> Based on the braided morphology, LEO stents have a relatively small pore size (cell size of approximately 0.9 mm) that gives a higher metal coverage ratio compared with other self-expandable stents, allowing a certain grade of flow-diverting hemodynamic effect.<sup>2</sup> Accordingly, LEO

stents have been recently reported as stent monotherapy for the treatment of small and complex intracranial aneurysms based on their flow-modification capacity and their biologic effects.<sup>3,4</sup> The deployment of low-porosity flow-diverter stents across side branches or perforators has a potential risk of occlusion and related symptomatic ischemic lesions.<sup>5,6</sup> Because of their intermediate porosity, braided stents could provide flow-change patterns similar to those provided by conventional flow-diverter devices, both on the aneurysm and covered side branches and perforators.<sup>3</sup> However, the extra-aneurysmal flow modifications, the fate of vessels covered by LEO stents, and the related clinical sequelae have been poorly investigated in the literature.

We present a retrospective series of 76 intracranial aneurysms and 98 side branches covered by LEO stents with the aim of investigating the following: 1) the flow-diversion effect on the aneurysms treated with LEO stents as a stent monotherapy, 2) the flow remodeling of the covered side branches and perforators, and 3) the clinical events related to the flow changes on the investigated vessels.

Received March 6, 2018; accepted after revision July 30.

From the Neuroradiology Department (F.C., M.C., C.D., P.-H.L., G.G., C.R., A.B., V.C.), University Hospital Gui-de-Chauliac, Centre Hospitalier Universitaire de Montpellier, Montpellier, France; and Section of Statistics (R.M., V.M.), University Hospital of Pisa, Pisa, Italy.

Please address correspondence to Federico Cagnazzo, MD, Neuroradiology Department, CHU Gui-de-Chauliac, 80 Ave Augustin Fliche, 34000 Montpellier, France; e-mail: f.cagnazzo86@gmail.com

 Indicates article with supplemental on-line tables.

 Indicates article with supplemental on-line photo.

<http://dx.doi.org/10.3174/ajnr.A5803>

## MATERIALS AND METHODS

### Patient Selection

Our hospital institutional review board (Centre Hospitalier Universitaire de Montpellier) approved this retrospective study. Our institutional prospectively maintained data base (January 2011 to January 2018) was retrospectively reviewed by 2 and, in case of inconsistency, by 3 investigators independently. The inclusion criteria were the following: 1) intracranial aneurysms treated with a LEO placed across side branches or perforators, and 2) intracranial aneurysms treated with stent monotherapy in which LEO devices were used as intermediate-porosity flow diverters. Only patients examined with DSA at follow-up were included in this series. Flow diversion with the LEO as stent monotherapy was performed to treat the following: 1) small aneurysms with a complex morphology not amenable to simple coil embolization, balloon remodeling, or stent-assisted coiling (SAC); 2) distally located recanalized aneurysms requiring retreatment and difficult to treat with conventional coiling (for the unstable position of the microcatheter) or with flow diversion (for the presence of important branches or perforators); and 3) dissecting aneurysms not amenable to different treatments. The treatment strategy was chosen by multidisciplinary consensus (vascular neurosurgeons and interventional neuroradiologists).

### Antiplatelet Therapy

For unruptured aneurysms, antiplatelet therapy included daily dual-antiplatelet medication with aspirin (Kardelic), 75 mg, and clopidogrel (Plavix), 75 mg, starting 5 days before treatment. The therapy was maintained for 3–6 months. Thereafter, based on the clinical and radiologic evaluation, the patients were switched to aspirin. VerifyNow P2Y<sub>12</sub> assay (Accumetrics, San Diego, California) was used to test the platelet inhibition: both P2Y<sub>12</sub> reaction unit and aspirin reaction units were tested. When LEO stents were used in patients with acutely ruptured aneurysms, an intravenous bolus of abciximab (0.125 mg/kg) was administered a few minutes before stent deployment, and standard dual-antiplatelet therapy was started the day after. Concurrent with the procedure, in both unruptured and ruptured aneurysms, intravenous heparinization was performed (activated clotting time maintained above 250 seconds).

### Description of Technique

All patients were treated under general anesthesia via a transfemoral approach. Through a long femoral sheath (triaxial approach), a 6F guiding catheter was advanced into the carotid or vertebrobasilar system. Vessels and aneurysms were analyzed via biplane and 3D rotational angiography. The LEO stent was unsheathed under roadmap guidance through the dedicated Vasco microcatheter (Balt). VasoCT (Philips Healthcare, Best, the Netherlands) with diluted iodinated contrast medium was used to assess stent apposition to the arterial wall.<sup>7,8</sup>

### Clinical and Imaging Assessment

Usually, the angiographic follow-up was performed with MRA at 6 months and DSA at 12 and 24 months. Flow remodeling was examined with DSA. Flow remodeling was examined on

the following arteries covered by LEO stents (On-line Table 1): ophthalmic artery, anterior choroidal artery, posterior communicating artery (PcomA), A1 segment (stent from the ICA to M1), A2 segment (stent from the A1 to the contralateral A2, or stent from the A1 to the ipsilateral A2 in cases of an absent or hypoplastic contralateral A1), callosomarginal and orbitofrontal arteries, middle cerebral artery (M2), superior cerebellar artery, anterior inferior cerebellar artery, and posterior cerebellar artery. Covered anterior communicating arteries and related perforators were not considered in this study. Perforator arteries covered by the LEO were divided into 2 groups: Sylvian perforator (lenticulostriate arteries) and basilar artery perforators. Perforating arteries were grouped as 1 entity per case (group of perforators) and were counted accordingly. The native arterial configuration was based on preoperative angiography. The flow remodeling was recorded as follows: 1) normal artery (no change in flow or caliber), 2) reduced in caliber/narrowing, and 3) occluded. Parent vessel stenosis was not considered as extra-aneurysmal flow remodeling. The ischemic complications related to covered vessels were detected on MR imaging at follow-up. Clinical follow-up information was obtained at the time of the follow-up clinic visits at 6, 12, and 24 months.

The aneurysm occlusion rate was defined on the basis of the Raymond-Roy (RR) classification: complete occlusion (class I), residual neck (class II), and incomplete occlusion or residual aneurysm (class III).<sup>9</sup>

### Statistical Analysis

Categorical data were described by frequency, whereas quantitative data were described by mean and SD. The dependent variable was the angiographic outcome of the covered artery, and it was divided into “normal” and “occlusion/narrowing.” The  $\chi^2$  test was used to evaluate the qualitative risk factors for occlusion/narrowing (location, hypertension, smoking, number of stents, covered artery arising from the inner or outer curve or from a linear stent, and sex). The *t* test (2-tailed) was applied to assess quantitative risk factors (length of follow-up and age). Although the number of events was <20, two variables (smoking and length of follow-up) were significantly associated with arterial occlusion/narrowing in univariate analysis and were analyzed together in a binary logistic regression (multivariate analysis) to assess the independent contribution of each risk factor. The results of the regression model were calculated by the Wald test and expressed using *P* values and related odds ratios. All statistical analyses, descriptive and inferential, were performed with SPSS, Version 24 (IBM, Armonk, New York).

## RESULTS

### Population Characteristics

In the 7-year period, 76 consecutive patients (51 women, 25 men; mean age, 54.5 ± 10.5 years) with 98 side branches and 24 groups of perforators (17 Sylvian perforators and 7 basilar perforators) covered with LEO stents were included in this study (details in On-line Tables 2 and 3).

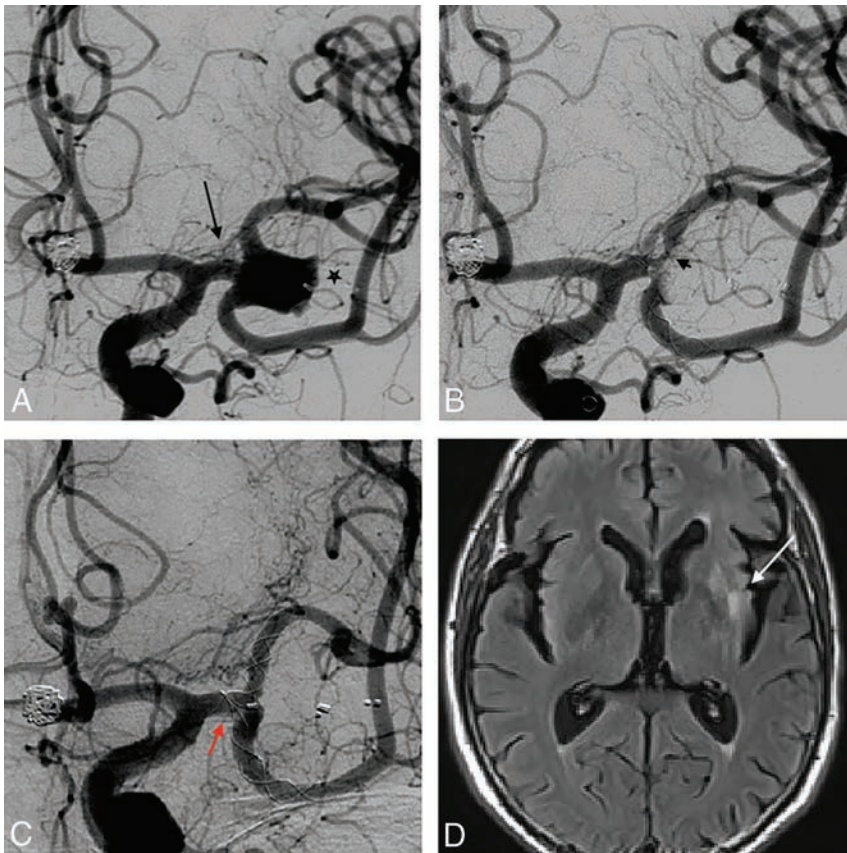


**FIG 1.** A, Procedural angiogram of a 63-year-old man showing a 9-mm left MCA aneurysm recanalized after treatment with a Woven EndoBridge (WEB; Sequent Medical, Aliso Viejo, California) device (black star). This image also shows the lenticulostriate arteries arising from the M1 (black arrow). B, The working projection demonstrates the implantation of 2 LEO stents (Y-configuration) into the M2 branches and a second WEB into the aneurysm. There is a small incomplete wall stent apposition in the superior M2 branch, probably related to a small arterial dissection (short black arrow). C, A 13-month DSA image shows total occlusion of the aneurysm and remodeling of the lenticulostriate arteries covered with 2 overlapped LEOs (red arrow). D, MR imaging reveals small and asymptomatic ischemic lesions in the left basal ganglia (white arrow).

### Treatment-Related Complications

Successful stent deployment was observed in all except 2 cases. A minor misopening of the proximal part of the stent was seen on plain x-rays and confirmed by the VasoCT. Due to the minor malapposition of the stents, no additional maneuvers were performed and there were no related complications. Overall, in-stent acute thrombosis was seen in 9 cases and was completely resolved after abciximab injection in all except 1 case. Small and asymptomatic ischemic lesions in the basal ganglia were reported in 2 patients (1 case is described in Fig 1). Finally, there were 2 cases of asymptomatic ICA dissections.

Two cases of asymptomatic mild stent stenosis (<50%) were observed and were related to in-stent intimal hyperplasia (1 case of mild stent stenosis is depicted in the On-line Figure).

### Angiographic Outcome of Covered Arteries and Perforators

All of the included patients underwent DSA at follow-up (mean DSA follow-up, 14 months; median, 13.5 months; range, 11–24 months, IQR, 13–14 months). Overall, 76 (77.5%) anterior circulation and 22 (22.5%) posterior circulation side branches were covered with LEO stents (On-line Table 1). Among 15 patients,

the superimposition of other arteries or bone structures hampered the angiographic visualization of some branching vessels that were not included in the analysis. During follow-up, 89 covered arteries (91%) were normal, whereas 7 showed a reduction in diameter (7%) (Figs 2 and 3) and 2 arteries (2%) were occluded (Fig 3). There were no symptomatic or asymptomatic associated complications.

All except 1 group of perforators (17 Sylvian perforators and 7 basilar perforators) were patent at the last follow-up. One patient (4%) with an MCA aneurysm treated with Y-stent placement had asymptomatic occlusion of some of the M1 perforators during 13 months of follow-up (Fig 1). The M1 perforators were covered with 2 overlapped LEOs.

### Factors Associated with Arterial Remodeling

The factors tested as predictors of arterial occlusion/narrowing are reported in On-line Table 4. There was a trend toward lower mean age among patients presenting with flow remodeling (47.8 vs 54.7 years,  $P = .06$ ). However, the univariate analysis showed that the only factors associated with an increased risk of arterial narrowing/occlusion were the length of radiologic follow-up ( $P < .001$ , OR = 1.85) and smoking ( $P < .001$ , OR = 18.4), which were confirmed with multivariate

analysis (smoking: OR > 20,  $P = .03$ ) (length of follow-up: OR = 1.99,  $P = .002$ ).

### Angiographic Outcome of Aneurysms Treated with LEO Stents as Stent Monotherapy

Overall, the LEO stent was used as flow-diversion treatment among 10 aneurysms (On-line Table 5). Five of them were recanalized after coiling (3 previously ruptured and 2 unruptured); the others were directly treated with LEO stents (4 unruptured aneurysms and 1 dissecting ruptured aneurysm) (Fig 3 and On-line Figure). Reasons behind the treatment with the sole stent-placement technique are detailed in On-line Table 5. The mean size of this group of aneurysms was 3.5 mm (median, 3.5 mm; range, 2–5 mm). Complete occlusion (RR I) was achieved in 70% of aneurysms. There were no differences in the size of aneurysms completely and incompletely occluded (RR III) ( $P = .33$ ). RR I occlusion was 60% and 80% among lesions directly treated with LEO stents versus aneurysms previously coiled, respectively ( $P = .9$ ). The mean length of follow-up was 14 months; the mean length of follow-up of the groups of completely occluded and incompletely occluded aneurysms was 22 months and 15 months, respectively ( $P = .6$ ).

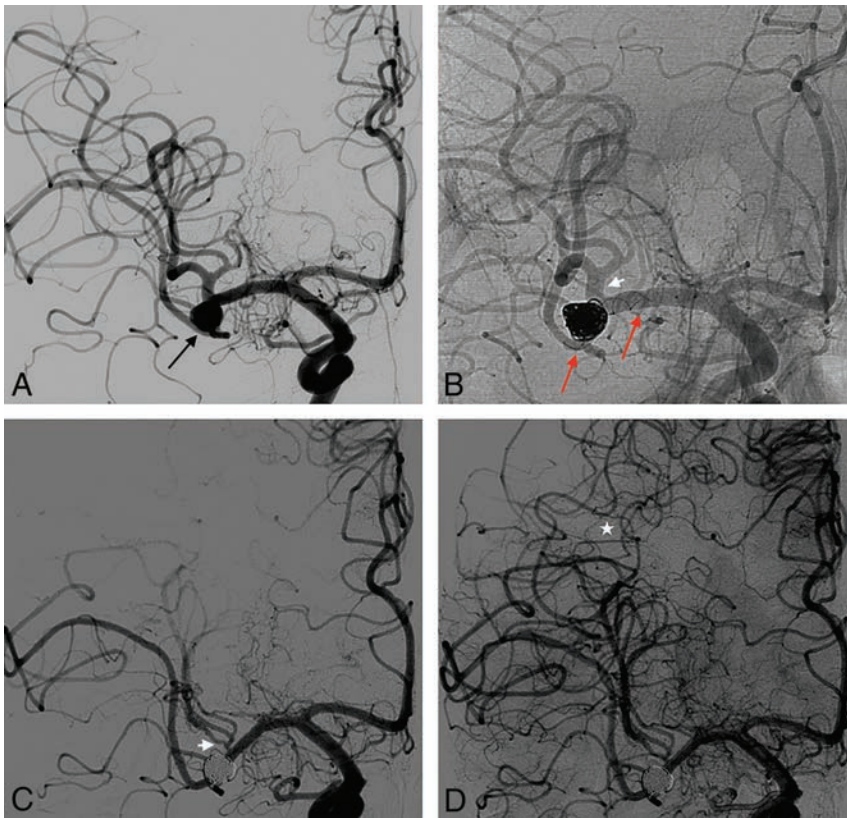


**FIG 2.** A, Procedural angiogram of a 49-year-old male patient with a 7-mm unruptured aneurysm on the right MCA bifurcation (*black arrow*). B, A nonsubtracted angiographic image obtained during treatment demonstrates the successful SAC embolization of the aneurysm with a LEO stent (2.5 × 18 mm) deployed from the M1 to the inferior M2 segment (*red arrows*). The M2 superior branch is covered by the stent (*short white arrow*). C, A 20-month follow-up DSA reveals complete aneurysm occlusion and asymptomatic narrowing of the covered superior M2 branch. D, Blood flow compensation is provided by the collateral circulation (*white star*).

## DISCUSSION

Compared with laser-cut stents, LEO devices are braided from a single nitinol wire with closed cells that can change size on the basis of the stent deployment.<sup>10</sup> The braided stents have relatively higher pore density (0.979 and 0.782 pore/mm<sup>2</sup>) than the laser-cut stents (0.276 pore/mm<sup>2</sup> for both Enterprise [Codman & Shurtleff, Raynham, Massachusetts] and Neuroform [Stryker Neurovascular, Kalamazoo, Michigan] stents), giving greater metal coverage (14% for LEO stents versus 5%–10% for Enterprise and Neuroform stents).<sup>2</sup> These characteristics may have important therapeutic implications. Indeed, although their metal surface coverage is lower than that in a flow diverter (30% for the Pipeline Embolization Device; Covidien, Irvine, California), LEO stents have been successfully used as stent monotherapy, especially for distal and complex small aneurysms.<sup>3,11</sup> In addition, computational fluid dynamics studies revealed that a double-overlapped braided stent resulted in greater flow diversion than a single Pipeline device, supporting the flow-diversion capacity of these stents.<sup>12</sup> However, while the hemodynamic effect of flow diverters has been largely studied, the potential flow remodeling of LEO stents on the aneurysm, covered side branches, and perforator arteries has been poorly investigated.

## Angiographic Outcome of Covered Side Branches and Perforators

To the best of our knowledge, our series is the first study that provides angiographic and clinical data about the perianeurysmal flow remodeling of LEO devices. The rates of arterial narrowing and occlusion were close to 7% and 2%, respectively. Among series of flow diverters covering ICA branches, the rate of arterial occlusion and related symptoms ranged widely in relation to the type of covered artery. The rate of PcomA occlusion is reported between 7% and 50% without related symptoms and with lower rates of occlusion in the fetal variant (due to the major supply to the posterior cerebral artery).<sup>13–15</sup> The rate of ophthalmic artery occlusion ranged from 0% to 17%, with <1% associated symptoms.<sup>16–19</sup> Finally, occlusion of the anterior choroidal artery has been described between 0% to 5%, without neurologic sequelae in most of the reported series.<sup>20–22</sup> Arterial occlusion and remodeling are influenced by the high density of the mesh. The pressure gradient across the jailed branch is reduced, and if the “flow competition” from the collateral supply is well-represented, the artery can be occluded.<sup>23</sup> In our series, occlusion occurred in 1 PcomA (20%) (Fig 3) and 1 MCA (5%), without related symptoms. In a recent meta-analysis of

MCA aneurysms treated with flow-diverter stents, nearly 10% of jailed arteries were occluded during follow-up, with approximately 5% related neurologic events.<sup>24</sup>

Most interesting, in our series, the mean follow-up time among patients with arterial narrowing and occlusion was higher (19 and 21 months, respectively) compared with the group of normal arteries (13 months). Indeed, multivariate analysis confirmed the length of radiologic follow-up as an independent factor associated with arterial remodeling ( $P = .002$ ). Accordingly, it is likely that a longer follow-up time would demonstrate a higher incidence of vessel remodeling. In addition, arterial narrowing and occlusion were strongly related to smoking. Data regarding the influence of smoking on arterial occlusion after flow diversion are scant. In a series of 30 PcomAs covered with Pipeline devices, smoking was not a risk factor for occlusion in the multivariate analysis.<sup>13</sup> Rouchaud et al,<sup>25</sup> in a series of nearly 600 patients treated with the Pipeline, demonstrated that tobacco does not affect aneurysm occlusion or thromboembolic complications after flow diversion. However, other studies have shown that smoking is associated with worse clinical outcomes after stent treatment in other locations. In a study of 9000 patients undergoing percutaneous coronary implantation of drug-eluting stents, Matteau et al<sup>26</sup> found that smoking was an independent risk factor for ischemic events and bleeding. Similarly, after percutaneous cor-

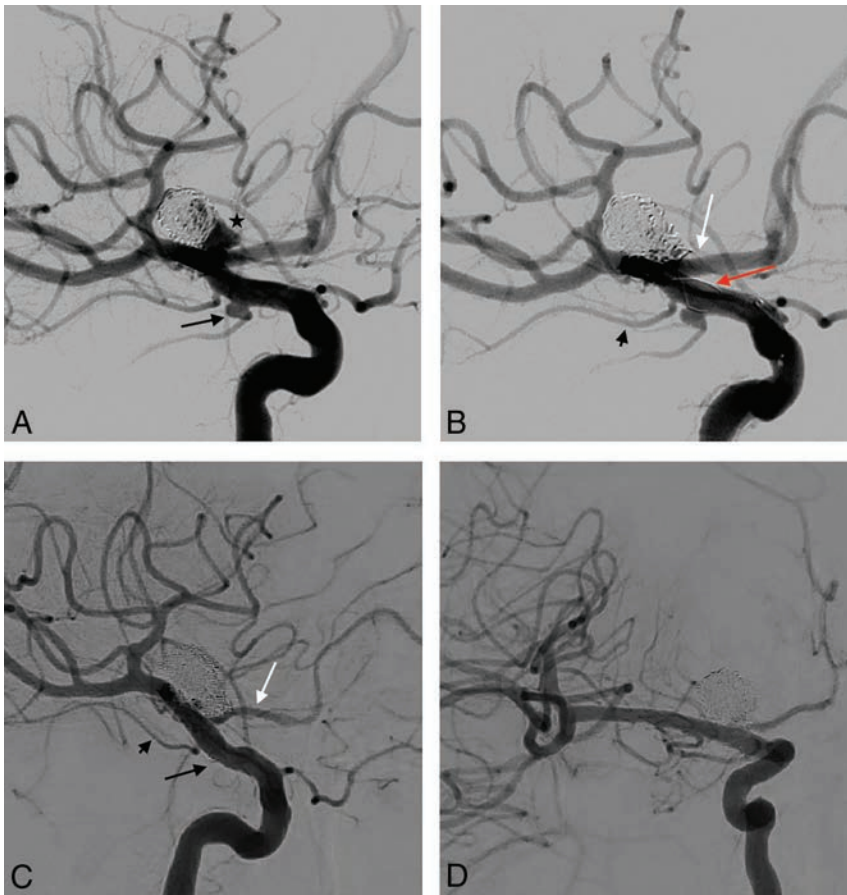


**FIG 3.** A, Procedural angiogram depicting a right, previously coiled, and recanalized ICA bifurcation aneurysm (*black star*), and a 3-mm PcomA aneurysm (*black arrow*). B, The ICA bifurcation aneurysm is treated with SAC with a LEO stent (3.5 × 18 mm) implanted from the ICA to the M1 (*red arrow*). The right AI (*white arrow*) and the right anterior choroidal artery (*short black arrow*) are covered by the stent. The PcomA artery and the small related aneurysm are covered with the LEO without additional coils. The working (C) and frontal (D) projections during a 24-month follow-up DSA demonstrate a small residual neck of the ICA bifurcation aneurysm (RR II), flow remodeling of the covered AI segment (*white arrow*), and occlusion of the PcomA artery and aneurysm (*black arrow*). The anterior choroidal artery is still patent (*short black arrow*).

onary intervention, Yeo et al<sup>27</sup> found that active smoking was associated with a higher risk of in-stent thrombosis. After stent deployment, the cellular responses related to the mechanical vascular injury included the following: 1) platelet activation and inflammation, 2) granulation tissue and smooth-muscle cell proliferation, and 3) tissue remodeling and neoendothelialization.<sup>28</sup> Smoking negatively influences the coagulation system, stimulating platelet aggregation, promoting a pre-coagulatory state, and causing endothelial dysfunction.<sup>27,28</sup> These factors potentially stimulate an exuberant healing response leading to intimal hyperplasia at the level of the ostium of the branching arteries. Theoretically, this mechanism can explain the higher rate of occlusion of covered arteries in smoking patients found in our series.

Contrariwise, location, age, and sex were not statistically associated with arterial flow changes. Although few patients were treated with double LEO stents, multiple stents were not related to a higher risk of arterial occlusion. Similarly, multiple flow diverters were reported to be associated with greater occlusion in some series,<sup>18,29</sup> while in other studies, the number of devices was not a significant predictor of sluggish flow.<sup>30</sup> This result highlights the complexity of the flow-remodeling process, which involves the mechanical proper-

ties of the stent as well as biologic (neoenendothelialization) and hemodynamic factors (collateral circulation).<sup>14</sup>

In case of tortuous parent arteries (carotid siphon or bifurcations), the local stent deformation can influence the density of the pores, resulting in tighter mesh in the inner curves, with higher flow density and lower density of the pores in the outer curve.<sup>31</sup> Rouchaud et al<sup>32</sup> reported 75% optic nerve atrophy when the ophthalmic artery originated from the inner curve of the flow diverter, probably based on the higher local density of the stent. However, in our series, there was no statistically significant correlation between the different origins of the covered artery (from the inner or outer curve or from a linear stent) and the angiographic outcome.

Another important factor associated with flow diverters is the risk of perforating injury due to coverage of lenticulostriate or basilar perforators. Accordingly, flow-diversion treatment of MCA or posterior circulation aneurysms is associated with higher complications, mostly related to perforating injury.<sup>6,24,33,34</sup> In our series, we observed only 1 case (4%) of asymptomatic flow remodeling of lenticulostriate arteries covered with 2 overlapped LEO stents (Fig 1). Similarly, Aydin et al<sup>3</sup> reported 1 patient with a small and clinically transient lacunar infarct in the basal ganglia due to Sylvian perforator occlusion during follow-up.

### Angiographic Outcome of Aneurysms Treated with the LEO Stent as Stent Monotherapy

The first experience of flow-diverter treatment with LEO stents was described by Pumar et al,<sup>4</sup> reporting 75% complete occlusion after treatment of 20 intracranial fusiform aneurysms. Recently, Aydin et al<sup>3</sup> reported 73% complete occlusion of complex and small aneurysms located behind the circle of Willis and treated with braided stents as stent monotherapy. In our series, 70% of aneurysms treated with the LEO as a flow diverter showed complete occlusion (RR I) during 14 months of follow-up, showing the flow-diversion capacity of these stents. We reported a slightly higher occlusion rate among aneurysms previously coiled (80%) compared with lesions directly treated with sole stent-placement therapy (60%). Stent monotherapy has also been reported with open-cell laser-cut stents. Fiorella et al<sup>35</sup> reported 10 ruptured uncoilable aneurysms treated with Neuroform stents, showing 50% and 40% complete and near-complete occlusion, respectively. Comparable results reported by Nyberg and Larson<sup>36</sup> showed a 45% complete or near-complete occlusion of small sac-

cular aneurysms treated with a single low-porosity stent. Indeed, aneurysm occlusion is influenced by both the flow disruption of the intra-aneurysmal flow and the endothelialization of the stent with subsequent intravascular remodeling.<sup>3,5</sup> The main factor influencing neointimalization is the vessel wall apposition of the stent; LEO devices, with their braided morphology, provide high conformability and wall apposition, promoting, together with their flow-diversion effect, thrombosis of the aneurysm. As with in vitro studies showing good conformability and vessel wall apposition,<sup>37</sup> in our series, successful stent deployment and wall apposition were achieved in 97% of cases and were confirmed by the VasoCT. This outcome is in accordance with other recent series of LEO stent embolization reporting rates of successful stent delivery ranging from 90% to 100%.<sup>3,4,38</sup>

### Limitations of the Study

Our study has limitations intrinsic to single-center series. The data were analyzed retrospectively. The imaging outcome was assessed by operators and not independently. Although all patients received the same dual-antiplatelet therapy, the influence of the platelet responsiveness of each patient was not assessed in the univariate and multivariate analyses. Accordingly, we were not able to establish whether the platelet responsiveness was a risk factor of arterial narrowing/occlusion after stent coverage.

### CONCLUSIONS

The rate of flow remodeling on the covered arteries and perforators was 9% and 4%, respectively, and was clinically irrelevant in all cases. Flow changes on the covered side branches were directly related to the length of follow-up and influenced by smoking habits. Complete occlusion of aneurysms treated with sole stent-placement therapy was 70%. These data stress the flow-diversion properties of LEO stents.

### ACKNOWLEDGMENTS

We thank Beth De Felici for the English revision.

Disclosures: Pierre-Henri Lefevre—UNRELATED: Payment for Development of Educational Presentations: Balt, Medtronic, Stryker, MicroVention. Alain Bonafe—UNRELATED: Consultancy: Medtronic, Stryker, MicroVention. Vincent Costalat—UNRELATED: Consultancy: Stryker, Balt; Grants/Grants Pending: Medtronic, MicroVention, Stryker\*; Payment for Development of Educational Presentations: Medtronic, Stryker, Balt, MicroVention. \*Money paid to the institution.

### REFERENCES

- Lubicz B, Kadou A, Morais R, et al. **Leo stent for endovascular treatment of intracranial aneurysms: very long-term results in 50 patients with 52 aneurysms and literature review.** *Neuroradiology* 2017;59:271–76 CrossRef Medline
- Cho SH, Jo WI, Jo YE, et al. **Bench-top comparison of physical properties of 4 commercially-available self-expanding intracranial stents.** *Neurointervention* 2017;12:31–39 CrossRef Medline
- Aydin K, Barburuglu M, Sencer S, et al. **Flow diversion with low-profile braided stents for the treatment of very small or uncoilable intracranial aneurysms at or distal to the circle of Willis.** *AJNR Am J Neuroradiol* 2017;38:2131–37 CrossRef Medline
- Pumar JM, Arias-Rivas S, Rodriguez-Yanez M, et al. **Using Leo Plus stent as flow diverter and endoluminal remodeling in endovascular treatment of intracranial fusiform aneurysms.** *J Neurointerv Surg* 2013;5(Suppl 3):iii22–27 CrossRef Medline
- Bhogal P, Ganslandt O, Bazner H, et al. **The fate of side branches covered by flow diverters: results from 140 patients.** *World Neurosurg* 2017;103:789–98 CrossRef Medline
- Gawlitza M, Januel AC, Tall P, et al. **Flow diversion treatment of complex bifurcation aneurysms beyond the circle of Willis: a single-center series with special emphasis on covered cortical branches and perforating arteries.** *J Neurointerv Surg* 2016;8:481–87 CrossRef Medline
- Clarençon F, Di Maria F, Gabrieli J, et al. **Clinical impact of flat panel volume CT angiography in evaluating the accurate intraoperative deployment of flow-diverter stents.** *AJNR Am J Neuroradiol* 2017;38:1966–72 CrossRef Medline
- Poncyłjusz W, Zwarzany L, Safranow K. **Visualization of novel microstents in patients with unruptured intracranial aneurysms with contrast-enhanced flat panel detector CT.** *Eur J Radiol* 2015;84:1313–17 CrossRef Medline
- Roy D, Milot G, Raymond J. **Endovascular treatment of unruptured aneurysms.** *Stroke* 2001;32:1998–2004 CrossRef Medline
- Gross BA, Frerichs KU. **Stent usage in the treatment of intracranial aneurysms: past, present and future.** *J Neurol Neurosurg Psychiatry* 2013;84:244–53 CrossRef Medline
- Lv X, Li Y, Jiang C, et al. **Potential advantages and limitations of the Leo stent in endovascular treatment of complex cerebral aneurysms.** *Eur J Radiol* 2011;79:317–22 CrossRef Medline
- Wang C, Tian Z, Liu J, et al. **Flow diverter effect of LVIS stent on cerebral aneurysm hemodynamics: a comparison with Enterprise stents and the Pipeline device.** *J Transl Med* 2016;14:199 CrossRef Medline
- Daou B, Valle-Giler EP, Chalouhi N, et al. **Patency of the posterior communicating artery following treatment with the Pipeline Embolization Device.** *J Neurosurg* 2017;126:564–69 CrossRef Medline
- Vedantam A, Rao VY, Shaltoni HM, et al. **Incidence and clinical implications of carotid branch occlusion following treatment of internal carotid artery aneurysms with the Pipeline embolization device.** *Neurosurgery* 2015;76:173–78; discussion 178 CrossRef Medline
- Brinjikji W, Lanzino G, Cloft HJ, et al. **Patency of the posterior communicating artery after flow diversion treatment of internal carotid artery aneurysms.** *Clin Neurol Neurosurg* 2014;120:84–88 CrossRef Medline
- Yu SC, Kwok CK, Cheng PW, et al. **Intracranial aneurysms: midterm outcome of Pipeline embolization device: a prospective study in 143 patients with 178 aneurysms.** *Radiology* 2012;265:893–901 CrossRef Medline
- Burrows AM, Brinjikji W, Puffer RC, et al. **Flow diversion for ophthalmic artery aneurysms.** *AJNR Am J Neuroradiol* 2016 Jun 2. [Epub ahead of print] CrossRef Medline
- Chalouhi N, Daou B, Kung D, et al. **Fate of the ophthalmic artery after treatment with the Pipeline Embolization Device.** *Neurosurgery* 2015;77:581–84; discussion 584 CrossRef Medline
- Griessenauer CJ, Ogilvy CS, Foreman PM, et al. **Pipeline Embolization Device for small paraophthalmic artery aneurysms with an emphasis on the anatomical relationship of ophthalmic artery origin and aneurysm.** *J Neurosurg* 2016;125:1352–59 CrossRef Medline
- Brinjikji W, Kallmes DF, Cloft HJ, et al. **Patency of the anterior choroidal artery after flow-diversion treatment of internal carotid artery aneurysms.** *AJNR Am J Neuroradiol* 2015;36:537–41 CrossRef Medline
- Raz E, Shapiro M, Becske T, et al. **Anterior choroidal artery patency and clinical follow-up after coverage with the Pipeline embolization device.** *AJNR Am J Neuroradiol* 2015;36:937–42 CrossRef Medline
- Rangel-Castilla L, Munich SA, Jaleel N, et al. **Patency of anterior circulation branch vessels after Pipeline embolization: longer-term results from 82 aneurysm cases.** *J Neurosurg* 2017;126:1064–69 CrossRef Medline
- Saleme S, Iosif C, Ponomarjova S, et al. **Flow-diverting stents for intracranial bifurcation aneurysm treatment.** *Neurosurgery* 2014; 75:623–31; quiz 631 CrossRef Medline
- Cagnazzo F, Mantilla D, Lefevre PH, et al. **Treatment of middle ce-**

- rebral artery aneurysms with flow-diverter stents: a systematic review and meta-analysis. *AJNR Am J Neuroradiol* 2017;38:2289–94 CrossRef Medline
25. Rouchaud A, Brinjikji W, Cloft HJ, et al. **Smoking does not affect occlusion rates and morbidity-mortality after Pipeline embolization for intracranial aneurysms.** *AJNR Am J Neuroradiol* 2016;37:1122–26 CrossRef Medline
  26. Matteau A, Yeh RW, Camenzind E, et al. **Balancing long-term risks of ischemic and bleeding complications after percutaneous coronary intervention with drug-eluting stents.** *Am J Cardiol* 2015;116:686–93 CrossRef Medline
  27. Yeo KK, Armstrong EJ, Soni K, et al. **Long-term outcomes of angiographically confirmed coronary stent thrombosis: results from a multicentre California registry.** *EuroIntervention* 2015;11:188–95 CrossRef Medline
  28. Inoue T, Croce K, Morooka T, et al. **Vascular inflammation and repair: implications for re-endothelialization, restenosis, and stent thrombosis.** *JACC Cardiovasc Interv* 2011;4:1057–66 CrossRef Medline
  29. Puffer RC, Kallmes DF, Cloft HJ, et al. **Patency of the ophthalmic artery after flow diversion treatment of paraclinoid aneurysms.** *J Neurosurg* 2012;116:892–96 CrossRef Medline
  30. Durst CR, Starke RM, Clopton D, et al. **Endovascular treatment of ophthalmic artery aneurysms: ophthalmic artery patency following flow diversion versus coil embolization.** *J Neurointerv Surg* 2016;8:919–22 CrossRef Medline
  31. Makoyeva A, Bing F, Darsaut TE, et al. **The varying porosity of braided self-expanding stents and flow diverters: an experimental study.** *AJNR Am J Neuroradiol* 2013;34:596–602 CrossRef Medline
  32. Rouchaud A, Leclerc O, Benayoun Y, et al. **Visual outcomes with flow-diverter stents covering the ophthalmic artery for treatment of internal carotid artery aneurysms.** *AJNR Am J Neuroradiol* 2015;36:330–36 CrossRef Medline
  33. Kallmes DF, Hanel R, Lopes D, et al. **International retrospective study of the Pipeline embolization device: a multicenter aneurysm treatment study.** *AJNR Am J Neuroradiol* 2015;36:108–15 CrossRef Medline
  34. Wang CB, Shi WW, Zhang GX, et al. **Flow diverter treatment of posterior circulation aneurysms: a meta-analysis.** *Neuroradiology* 2016;58:391–400 CrossRef Medline
  35. Fiorella D, Albuquerque FC, Deshmukh VR, et al. **Endovascular reconstruction with the Neuroform stent as monotherapy for the treatment of uncoilable intradural pseudoaneurysms.** *Neurosurgery* 2006;59:291–300; discussion 291–300 CrossRef Medline
  36. Nyberg EM, Larson TC. **Beneficial remodeling of small saccular intracranial aneurysms after staged stent only treatment: a case series.** *J Stroke Cerebrovasc Dis* 2014;23:80–85 CrossRef Medline
  37. Valdivia y Alvarado M, Ebrahimi N, Benndorf G. **Study of conformability of the new LEO Plus stent to a curved vascular model using flat-panel detector computed tomography (DynaCT).** *Neurosurgery* 2009;64:ons130–134; discussion ons134 CrossRef Medline
  38. Machi P, Costalat V, Lobotesis K, et al. **LEO Baby Stent use following balloon-assisted coiling: single- and dual-stent technique—immediate and midterm results of 29 consecutive patients.** *AJNR Am J Neuroradiol* 2015;36:2096–103 CrossRef Medline

# Treatment of Intracranial Aneurysms with Self-Expandable Braided Stents: A Systematic Review and Meta-Analysis

F. Cagnazzo, M. Cappucci, P.-H. Lefevre, C. Dargazanli, G. Gascou, R. Morganti, V. Mazzotti, D. di Carlo, P. Perrini, D. Mantilla, C. Riquelme, A. Bonafe, and V. Costalat



## ABSTRACT

**BACKGROUND:** The safety and efficacy of treatment with self-expandable braided stents (LEO and LVIS) required further investigation.

**PURPOSE:** Our aim was to analyze the outcomes after treatment with braided stents.

**DATA SOURCES:** A systematic search of 3 databases was performed for studies published from 2006 to 2017.

**STUDY SELECTION:** According to Preferred Reporting Items for Systematic Reviews and Meta-Analyses guidelines, we included studies reporting patients treated with LEO or LVIS stents.

**DATA ANALYSIS:** Random-effects meta-analysis was used to pool the following: aneurysm occlusion rate, complications, and neurologic outcomes.

**DATA SYNTHESIS:** Thirty-five studies evaluating 1426 patients treated with braided stents were included in this meta-analysis. Successful stent delivery and complete aneurysm occlusion were 97% (1041/1095; 95% CI, 95%–98%) ( $I^2 = 44%$ ) and 88.3% (1097/1256; 95% CI, 85%–91%) ( $I^2 = 72%$ ), respectively. Overall, treatment-related complications were 7.4% (107/1317; 95% CI, 5%–9%) ( $I^2 = 44%$ ). Ischemic/thromboembolic events (48/1324 = 2.4%; 95% CI, 1.5%–3.4%) ( $I^2 = 27%$ ) and in-stent thrombosis (35/1324 = 1.5%; 95% CI, 0.6%–1.7%) ( $I^2 = 0%$ ) were the most common complications. Treatment-related morbidity was 1.5% (30/1324; 95% CI, 0.9%–2%) and was comparable between the LEO and LVIS groups. Complication rates between the anterior (29/322 = 8.8%; 95% CI, 3.4%–12%) ( $I^2 = 41%$ ) versus posterior circulation (10/84 = 10.5%; 95% CI, 4%–16%) ( $I^2 = 0%$ ) and distal (30/303 = 8%; 95% CI, 4.5%–12%) ( $I^2 = 48%$ ) versus proximal aneurysms (14/153 = 9%; 95% CI, 3%–13%) ( $I^2 = 46%$ ) were comparable ( $P > .05$ ).

**LIMITATIONS:** Limitations were selection and publication biases.

**CONCLUSIONS:** In this analysis, treatment with the LEO and LVIS stents was relatively safe and effective. The most common complications were periprocedural thromboembolisms and in-stent thrombosis. The rate of complications was comparable among anterior and posterior circulation aneurysms, as well as for proximal and distally located lesions.

**ABBREVIATIONS:** IQR = interquartile range; PRISMA = Preferred Reporting Items for Systematic Reviews and Meta-Analyses; SAC = stent-assisted coiling

The development of self-expandable stents has progressively changed the treatment strategy for most intracranial aneurysms, creating a mechanical scaffold that prevents coil protrusion and promoting neoendothelialization of the neck.<sup>1</sup> Several self-expandable stents were introduced in the past years,<sup>2,3</sup> including

laser-cut open-cell stents (such as the Neuroform; Stryker Neurovascular, Kalamazoo, Michigan) and laser-cut closed-cell stents (such as the Enterprise; Codman & Shurtleff, Raynham, Massachusetts).<sup>2</sup> The third generation of self-expandable closed stents was produced by braiding individual strands of nitinol onto a mandrel (LVIS, MicroVention, Tustin, California; and LEO, Balt Extrusion, Montmorency, France).<sup>4,5</sup> In addition to providing mechanical support, the braided morphology gives a relatively higher pore density than the laser-cut stents, theoretically improving the flow-diverting hemodynamic effect of these devices.

Received March 15, 2018; accepted after revision July 30.

From the Neuroradiology Department (F.G., M.C., P.-H.L., C.D., G.G., C.R., A.B., V.C.), University Hospital G u-de-Chauliac, Centre Hospitalier Universitaire de Montpellier, Montpellier, France; Department of Neurosurgery (D.d.C., P.P.), University of Pisa, Pisa, Italy; Section of Statistics (R.M., V.M.), University Hospital of Pisa, Pisa, Italy; and Neuroradiology Department (D.M.), Clinic FOSCAL, Universidad Autonoma de Bucaramanga, Andr s Bello National University, Santiago, Chile

Please address correspondence to Federico Cagnazzo, MD, Neuroradiology Department, CHU G u De Chauliac, 80 Ave Augustin Fliche, 34000 Montpellier, France; e-mail: f.cagnazzo86@gmail.com

Indicates article with supplemental on-line tables.

Indicates article with supplemental on-line photo.

<http://dx.doi.org/10.3174/ajnr.A5804>

es.<sup>6-8</sup> Recently, the low-profile design of the braided stents (LEO Baby and LVIS Jr) allowed delivery through a 0.0165-inch microcatheter and navigation in small vessels, with the possibility of treating distally located aneurysms.<sup>9,10</sup> Improved understanding of treatment-related outcomes of braided stents can help practitioners in the selection of lesions amenable to being effectively treated with these devices. Our meta-analysis examined occlusion rates and procedure-related complications after treatment with braided stents, focusing on the influence of aneurysm features, location, and treatment characteristics on the studied outcomes.

## MATERIALS AND METHODS

### Literature Search

A comprehensive literature search of PubMed, Ovid MEDLINE, and Ovid EMBASE was conducted for studies published from January 2006 to February 2018. The Preferred Reporting Items for Systematic Reviews and Meta-Analyses (PRISMA) guidelines<sup>11</sup> were followed. The key words and the detailed search strategy are reported in On-line Table 1. The inclusion criteria were the following: studies reporting series of intracranial aneurysms treated with LEO and LVIS stents. Exclusion criteria were the following: 1) review articles, 2) studies published in languages other than English, 3) in vitro studies, and 4) animal studies. In cases of overlapping patient populations, only the series with the largest number of patients or the most detailed data was included. Two independent readers screened articles in their entirety to determine eligibility for inclusion. A third author solved discrepancies.

### Data Collection

From each study, we extracted the following: 1) treatment-related complications, 2) occlusion rate, and 3) clinical outcome. Occlusion and complication rates were analyzed on the basis of the influence of the following parameters: 1) unruptured-versus-ruptured aneurysms, 2) distal-versus-proximal location, 3) anterior-versus-posterior circulation, 4) first treatment versus retreatment, 5) stent alone versus stent-assisted coiling (SAC), and 6) single-versus-multiple stents. A subgroup analysis was performed for aneurysms treated with small low-profile braided stents (LEO Baby and LVIS Jr). Distal location was considered for lesions arising distal to the circle of Willis or located in small vessels: A2–3 segments, middle cerebral artery, posterior cerebral artery, posterior inferior cerebellar artery, anterior inferior cerebellar artery, and superior cerebellar artery. The occlusion rate was defined on the basis of the Raymond-Roy classification. Accordingly, we used the following terms: complete occlusion (class I), residual neck or near complete occlusion (class II), and incomplete occlusion or residual aneurysm (class III).<sup>12</sup> Treatment-related complications were divided into 2 groups: periprocedural/early events (within 30 days after treatment) and delayed events (after 30 days). Finally, good outcome was defined as a modified Rankin Scale score of 0–2 or a Glasgow Outcome Score of 4–5, or it was assumed if the study used terms such as “no morbidity,” “good recovery,” or “no symptoms.”

### Outcomes

The primary objectives of this meta-analysis were to define the safety (treatment-related complications, neurologic outcomes, mortality rate) and the efficacy (aneurysm occlusion rate) of the treatment of intracranial aneurysms with self-expanding braided stents (LEO and LVIS). The secondary objectives were to define the influence of aneurysm location, aneurysm characteristics, and factors related to the treatment on the analyzed outcomes.

### Quality Scoring

A modified version of the Newcastle-Ottawa Scale<sup>13</sup> was used for quality assessment of the included studies. The details are reported in On-line Tables 2 and 3. The quality assessment was performed by 2 authors independently, and a third author solved discrepancies.

### Statistical Analysis

We estimated, from each cohort, the cumulative prevalence (percentage) and 95% confidence interval for each outcome. Percentages were calculated with a random-effects meta-analysis. Heterogeneity across studies was evaluated using the  $I^2$  statistic: An  $I^2$  value of  $>50\%$  suggests substantial heterogeneity. To compare the percentages and to calculate the  $P$  values, we used the  $Z$ -test for 2 proportions. Meta-regression was not used in this study. Statistical analysis was performed using OpenMeta[Analyst] (<http://www.cebm.brown.edu/openmeta/>).

## RESULTS

### Literature Review

Studies included in our meta-analysis are summarized in On-line Table 4. The search flow diagram is shown in the On-line Figure.

A total of 35 studies and 1426 patients with 1518 intracranial aneurysms treated with LEO or LVIS stents were included in our review.

### Quality of Studies

Overall, 14 studies (40%) were rated “high quality” (On-line Tables 2 and 3). Three articles were prospective multicentric series, 5 studies were obtained from a prospectively maintained data base, 3 studies were retrospective multicentric, and 24 articles were single-center retrospective.

### Patient Population

Overall, 510 aneurysms (33.5%) were treated with LEO stents and 948 aneurysms (62.5%) were treated with LVIS devices. One study with 60 aneurysms (4%) reported patients treated with LEO and LVIS stents (On-line Table 5). The mean age of patients (54.5 years; range, 7–79 years) and the male/female ratio (0.47) were comparable between the 2 groups. Overall, 83% (1172/1410; 95% CI, 81%–84%) of aneurysms were located in the anterior circulation. The mean aneurysm size was 7.2 mm (range, 2–65 mm). Most aneurysms were found incidentally (572/954 = 60%; 95% CI, 56%–63%). The mean radiologic and clinical follow-up was 10.4 months (interquartile range [IQR], 6–12 months; median, 6.5 months) and 12 months (IQR, 6–13 months; median, 8 months), respectively.

### Angiographic Outcomes

Overall, the devices were successfully delivered in 97% (1041/1095; 95% CI, 95%–98%) ( $I^2 = 44\%$ ) of cases (On-line Table 6). The technical success rate was 97.5% (379/396; 95% CI, 95%–98%) ( $I^2 = 42\%$ ) and 97% (662/699; 95% CI, 95%–99%) ( $I^2 = 58\%$ ) for LEO and LVIS stents, respectively. During a mean angiographic follow-up of 10.4 months (median, 6.5 months; IQR, 6–12 months), the overall rate of complete/near-complete occlusion was 88.3% (1097/1256; 95% CI, 85%–91%) ( $I^2 = 72\%$ ): Complete/near-complete occlusion was achieved in 88.6% (410/463; 95% CI, 83%–93%) ( $I^2 = 69\%$ ) and 87.8% (687/793; 95% CI, 83%–92%) ( $I^2 = 74\%$ ) of aneurysms treated with LEO and LVIS stents, respectively.

### Treatment-Related Complications

The overall complication rate was 7.4% (107/1317; 95% CI, 5%–9%) ( $I^2 = 44\%$ ). Complications were higher among LEO stents (46/391 = 10.5%; 95% CI, 7%–13%) ( $I^2 = 0\%$ ) compared with LVIS stents (54/867 = 5.3%; 95% CI, 3%–7%) ( $I^2 = 34\%$ ) ( $P = .001$ ). The overall rate of permanent complications was 1.5% (30/1324; 95% CI, 0.9%–2%) ( $I^2 = 0\%$ ). Permanent complications were 2.7% (17/398; 95% CI, 1%–4%) ( $I^2 = 3\%$ ) and 1.3% (12/867; 95% CI, 0.6%–2.2%) ( $I^2 = 0\%$ ) after LEO and LVIS stent treatment, respectively ( $P = .002$ ).

Most complications were periprocedural or early events (85/1324 = 5%; 95% CI, 3%–6%) ( $I^2 = 36\%$ ), whereas delayed complications were 1% (27/1324; 95% CI, 0.5%–1.6%) ( $I^2 = 0\%$ ). Both periprocedural and delayed complications were higher in the LEO group (On-line Table 6). Overall, the most common complications were ischemic/thromboembolic events (48/1324 = 2.4%; 95% CI, 1.5%–3.4%) ( $I^2 = 27\%$ ), followed by in-stent thrombosis (35/1324 = 1.5%; 95% CI, 0.6%–1.7%) ( $I^2 = 0\%$ ). After treatment with LEO stents, there was a higher incidence of ischemic/thromboembolic events (21/398 = 3.6%; 95% CI, 1.8%–5% versus 24/867 = 1.6%; 95% CI, 0.6%–1.5%) ( $P = .03$ ) and in-stent thrombosis (19/398 = 3.2%; 95% CI, 1.5%–5% versus 15/867 = 0.8%; 95% CI, 0.2%–1.5%) ( $P = .003$ ). Ischemic complications were related to the following events: thromboembolism (44/48 = 91%; 95% CI, 79%–97%), perforating injury due to stent coverage of lenticulostriate arteries (1/48 = 2%; 95% CI, 0.1%–10%), and platelet aggregation in the side branches covered with the stent (3/48 = 6.5%; 95% CI, 1.5%–17%). The rate of aneurysm perforation/vessel dissection during treatment and the rate of intraparenchymal hemorrhage (unrelated to aneurysm rupture) were 1.3% (22/1324; 95% CI, 0.7%–1.8%) ( $I^2 = 0\%$ ) and 0.5% (1/1324; 95% CI, 0.1%–1.1%) ( $I^2 = 0\%$ ), respectively, without differences between the 2 groups. The incidence of aneurysm rupture after treatment was 0.7% (3/1324; 95% CI, 0.3%–1.1%) ( $I^2 = 0\%$ ). Treatment-related mortality was 0.7% (3/1357; 95% CI, 0.3%–1.2%) ( $I^2 = 0\%$ ), whereas the rate of good neurologic outcome was 98% (770/78; 95% CI, 97%–99%) ( $I^2 = 0\%$ ).

### Factors Related to Aneurysm Occlusion

Overall, the occlusion rate of distally located aneurysms and more proximal lesions was 89.5% (237/272; 95% CI, 86%–93%) ( $I^2 = 0\%$ ) and 77% (90/124; 95% CI, 66%–87%) ( $I^2 = 57\%$ ), respectively ( $P = .001$ ) (On-line Table 7). Complete/near-complete oc-

clusion in the anterior circulation (149/174 = 88.5%; 95% CI, 82%–94%) ( $I^2 = 34\%$ ) was higher compared with the posterior circulation (26/37 = 70%; 95% CI, 53%–86%) ( $I^2 = 47\%$ ) ( $P = .003$ ). Occlusion after retreatment with braided stents of aneurysms recanalized after previous treatments was lower (31/42 = 75%; 95% CI, 54%–94%) ( $I^2 = 57\%$ ) compared with the occlusion rate of the first treatment (179/203 = 88.9%; 95% CI, 83%–94%) ( $I^2 = 23\%$ ) ( $P = .01$ ). Differences in occlusion rates were not statistically significant in relation to single-versus-multiple overlapping devices. SAC was more effective compared with treatment with a stent alone: a complete/near-complete occlusion rate of 90% (807/898; 95% CI, 86%–93%) ( $I^2 = 67\%$ ) versus 63% (19/26; 95% CI, 40%–90%) ( $I^2 = 48\%$ ), respectively ( $P = .0001$ ). In the stent-alone group, 58% (15 aneurysms) and 42% (11 aneurysms) of patients were treated with single and double stents, respectively.

### Factors Related to Complications after Treatment

The complication rate was higher for ruptured aneurysms treated in the acute phase (12/75 = 14.5%; 95% CI, 7%–21%) ( $I^2 = 0\%$ ) compared with unruptured lesions (54/675 = 6.6%; 95% CI, 4.8%–4%) ( $I^2 = 0\%$ ) ( $P = .01$ ). There was no statistically significant difference in complication rates among distal-versus-proximal locations and anterior-versus-posterior circulation. Similarly, treatment-related complications were comparable among first treatment versus retreatment, SAC versus stent alone, and single-versus-multiple stents.

### Angiographic Outcomes and Treatment-Related Complications for Low-Profile Braided Stents (LEO Baby and LVIS Jr)

Low-profile braided stents were successfully delivered in 96% (601/638; 95% CI, 94%–98%) ( $I^2 = 41\%$ ) of cases, without differences between the LEO Baby and LVIS Jr (On-line Table 8). Overall, 61% (318/521; 95% CI, 56%–65%) of low-profile braided stents were deployed in small and distal vessels, whereas 39% (203/521; 95% CI, 34%–43%) were used to treat proximally located aneurysms. In addition, LEO Baby and LVIS Jr were mostly used for the treatment of anterior circulation aneurysms (296/399 = 74%; 95% CI, 69%–78%) compared with posterior circulation lesions (103/399 = 26%; 95% CI, 21%–30%). Overall, complete/near-complete occlusion was 88.6% (507/580; 95% CI, 84%–92%) ( $I^2 = 63\%$ ) and was higher with the LEO Baby (135/143 = 96.3%; 95% CI, 93%–99%) ( $I^2 = 0\%$ ) compared with LVIS Jr (372/437 = 86%; 95% CI, 80%–91%) ( $I^2 = 65\%$ ) ( $P = .005$ ). The overall complication rate was 7.2% (54/636; 95% CI, 5%–9%) ( $I^2 = 0\%$ ) with 1.9% (13/636; 95% CI, 0.9%–2.9%) ( $I^2 = 0\%$ ) permanent events. LEO Baby devices were associated with a 3.7% (4/148; 95% CI, 0.7%–6%) ( $I^2 = 0\%$ ) permanent complication rate, whereas LVIS Jr stents had 1.6% (9/488; 95% CI, 0.5%–2.8%) ( $I^2 = 0\%$ ) ( $P = .7$ ). The most common complications were ischemic/thromboembolic (22/636 = 1.8%; 95% CI, 0.7%–2.8%) ( $I^2 = 0\%$ ) and in-stent thrombosis (21/636 = 1.6%; 95% CI, 0.6%–2.6%) ( $I^2 = 4\%$ ). In-stent thrombosis was higher among LEO Baby (9/148 = 5%; 95% CI, 2%–8%) ( $I^2 = 0\%$ ) compared with LVIS Jr (12/488 = 1.1%; 95% CI, 0.2%–2%) ( $I^2 = 0\%$ ). Treatment-related mortality and good neurologic outcome

were 0.8% (1/636; 95% CI, 0.4%–1.5%) ( $I^2 = 0\%$ ) and 98.3% (406/415; 95% CI, 96%–99%) ( $I^2 = 0\%$ ), respectively.

### Study Heterogeneity

Analysis of the angiographic outcomes and treatment-related complications showed high heterogeneity in 10% of the reported results (4 of 39 studied outcomes) (On-line Table 6). The analysis of the factors related to complications and occlusion (On-line Table 5) showed high heterogeneity in 18% of the studied events (4 of 22 reported outcomes). The rate of high heterogeneity among complications and angiographic outcomes after LEO Baby and LVIS Jr (On-line Table 7) was 9% (3 of 33 reported results).

## DISCUSSION

With the advent of the SAC technique, most complex, wide-neck intracranial aneurysms can be efficiently treated endovascularly.<sup>14</sup> Compared with other intracranial stents that are laser-cut from nitinol hypotubes, LEO and LVIS stents are braided from a single nitinol wire with a closed-cell design.<sup>6,8</sup> Because of the increased use of these devices, understanding the safety and efficacy of treatment with braided stents is important in the management of lesions amenable to SAC treatment.

### Angiographic Outcomes

In combining aneurysmal occlusion rates from 35 series, our analysis provides more representative data on angiographic outcomes than any single study. We demonstrated high rates of complete/near-complete occlusion for both LEO (88.6%; 95% CI, 83%–93%) and LVIS devices (87.8%; 95% CI, 83%–92%). Meta-analysis of aneurysms treated with SAC using different devices showed 61% long-term occlusion.<sup>15</sup> The high rates of occlusion after treatment with braided stents can be related to the smaller cell size, higher metal coverage and flow-diversion effect than other conventional self-expandable stents.<sup>6,8,16</sup> Computational fluid dynamics studies showed that LVIS stents allowed more flow reduction than laser-cut devices, and double LVIS stents resulted in a better flow-diverting effect than the Pipeline Embolization Device (PED; Covidien, Irvine, California).<sup>8</sup> Aydin et al,<sup>16</sup> investigating the flow-diversion effect of low-profile braided stents used as stent monotherapy, reported 75% complete occlusion during follow-up. In the subgroup of aneurysms treated with double stents, the authors showed a slightly higher rate of complete occlusion (82%). In our study, braided stents used as stent monotherapy allowed a 63% (95% CI, 40%–90%) complete occlusion rate, which was significantly lower compared with the treatment with stent plus coiling (90%; 95% CI, 86%–93%) ( $P = .0001$ ). Most interesting, lesions treated with SAC with single or multiple stents had comparable rates of occlusion, showing that in most cases, a single stent is enough to achieve complete aneurysm occlusion, avoiding the ischemic complications related to the higher metal density in the vessel.

### Treatment-Related Complications

In general, treatment-related complications and morbidity after SAC are 12% and 5%, respectively.<sup>17,18</sup> In our analysis, treatment with braided stents was relatively safe, with overall rates of complications and morbidity of 7.4% (95% CI, 5%–9%) and 1.5%

(95% CI, 0.9%–2%), respectively. This is in accordance with a recent prospective, multicentric study of LVIS devices that reported approximately 5% treatment-related morbidity.<sup>19</sup> Most interesting, the overall complication rate was higher after treatment with LEO (10.5%; 95% CI, 7%–13%) compared with LVIS stents (5.3%; 95% CI, 3%–7%). The higher rate of complications was related to higher ischemic/thromboembolic events (3.6%; 95% CI, 1.5%–5% versus 1.6%; 95% CI, 0.6%–2.5%) and in-stent thrombosis (3.2%; 95% CI, 1.5%–5% versus 0.8%; 95% CI, 0.2%–1.5%). After we investigated the literature, the rate of in-stent thrombosis after treatment with laser-cut stents was 1%,<sup>2</sup> which is lower compared with the overall rate of both braided stents and low-profile braided stents (1.5% and 1.6%, respectively). Similar to that in flow-diverter stents, the higher incidence of acute occlusion of braided stents compared with laser-cut devices can be explained, at least in part, by the higher mesh density and more condensed pores of these devices. However, in our meta-analysis, LVIS and LVIS Jr had a low incidence of acute in-stent occlusion (0.8% and 1.1%, respectively), which appears quite comparable with that in the laser-cut stents.

Knowledge of the safety of braided stents in relation to the location and characteristics of the aneurysms has important therapeutic implications. Most interesting, we found comparable rates of complications between proximal (ICA and circle of Willis) and distal aneurysms beyond the circle of Willis or in small vessels. The rate of complications for distal aneurysms treated with flow-diverter stents ranges between 15% and 20%.<sup>20,21</sup> Feng et al<sup>22</sup> reported 5% complications after SAC of MCA aneurysms with LVIS Jr stents. Similarly, Aydin et al<sup>16</sup> reported a high occlusion rate and a low incidence (5%) of complications after flow-diversion treatment of aneurysms at or distal to the circle of Willis, with low-profile braided stents used as stent monotherapy.

Although the occlusion rate was lower in the posterior circulation (70%; 95% CI, 53%–86% versus 88.5%; 95% CI, 82%–94%), treatment-related complications were comparable between anterior (8.8%; 95% CI, 3.4%–12%) and posterior circulation aneurysms (10.5; 95% CI, 4%–16%) ( $P = .7$ ). Similarly, Johnson et al,<sup>23</sup> in a large series of 486 aneurysms treated with Neuroform and Enterprise stents, reported comparable rates of complications among anterior (11.5%) and posterior circulation lesions (12.7%). Contrariwise, flow diversion in the posterior circulation is associated with not negligible rates of ischemic complications related to perforators infarcts. In the International Retrospective Study of Pipeline Embolization Device, the rates of morbidity and mortality after flow diversion treatment were higher among posterior circulation (16.5%) compared with anterior circulation lesions (5%–9%).<sup>24</sup>

Finally, our subgroup analysis of >600 aneurysms treated with low-profile braided stents (LEO Baby and LVIS Jr) demonstrated comparable results in terms of the safety (complication rate = 7.2%; 95% CI, 5%–9%) and efficacy (complete/near-complete occlusion = 96.3%; 95% CI, 93%–99%) of these devices usually used in smaller and distal vessels because of the possibility of being delivered through a 0.0165-inch microcatheter.

## Strength and Limitations

Our study has limitations. Most series are retrospective studies and single-institution experiences. Details of the antiplatelet therapy were infrequently specified. The smaller number of cases in some subgroup analyses may not provide sufficient power to demonstrate a statistically significant difference among the studied outcomes. However, although retrospective data are low in quality, our meta-analysis is the best available evidence to guide the treatment management of aneurysms with braided stents.

## CONCLUSIONS

In our study, treatment with the LEO and LVIS stents was relatively safe and effective. Most of the complications were related to periprocedural thromboembolic events and in-stent thrombosis. We found comparable rates of treatment-related complications among anterior-versus-posterior circulation aneurysms and for proximal-versus-distally located lesions. These findings can guide practitioners in the treatment, management, and selection of aneurysms amenable to treatment with braided stents.

## ACKNOWLEDGMENTS

We thank Beth De Felici for the English revision.

Disclosures: Federico Cagnazzo—UNRELATED: Employment: University of Florence.\* Pierre-Henri Lefevre—UNRELATED: Payment for Development of Educational Presentations: Medtronic, Stryker.\* Paolo Perrini—UNRELATED: Employment: Azienda Ospedaliero Universitaria Pisana. Comments: I work as Associate Professor of Neurosurgery, University of Pisa, Italy, and as a consultant neurosurgeon at Azienda Ospedaliero-Universitaria Pisana, Pisa, Italy. Carlos Riquelme—UNRELATED: Employment: Hopital Gui de Chauliac, service de neuroradiology.\* Vincent Costalat—UNRELATED: Consultancy: Stryker, Medtronic\*; Grants/Grants Pending: Stryker, Medtronic\*; Payment for Development of Educational Presentations: Medtronic, Stryker, Balt Extrusion. \*Money paid to the Institution.

## REFERENCES

1. Wanke I, Forsting M. **Stents for intracranial wide-necked aneurysms: more than mechanical protection.** *Neuroradiology* 2008; 50:991–98 CrossRef Medline
2. King B, Vaziri S, Singla A, et al. **Clinical and angiographic outcomes after stent-assisted coiling of cerebral aneurysms with Enterprise and Neuroform stents: a comparative analysis of the literature.** *J Neurointerv Surg* 2015;7:905–09 CrossRef Medline
3. Brinjikji W, Murad MH, Lanzino G, et al. **Endovascular treatment of intracranial aneurysms with flow diverters: a meta-analysis.** *Stroke* 2013;44:442–47 CrossRef Medline
4. Fiorella D, Arthur A, Boulous A, et al. **Final results of the US humanitarian device exemption study of the low-profile visualized intraluminal support (LVIS) device.** *J Neurointerv Surg* 2016;8:894–97 CrossRef Medline
5. Lubicz B, Kadou A, Morais R, et al. **Leo stent for endovascular treatment of intracranial aneurysms: very long-term results in 50 patients with 52 aneurysms and literature review.** *Neuroradiology* 2017;59:271–76 CrossRef Medline
6. Cho SH, Jo WI, Jo YE, et al. **Bench-top comparison of physical properties of 4 commercially-available self-expanding intracranial stents.** *Neurointervention* 2017;12:31–39 CrossRef Medline
7. Gross BA, Frerichs KU. **Stent usage in the treatment of intracranial aneurysms: past, present and future.** *J Neurol Neurosurg Psychiatry* 2013;84:244–53 CrossRef Medline
8. Wang C, Tian Z, Liu J, et al. **Flow diverter effect of LVIS stent on cerebral aneurysm hemodynamics: a comparison with Enterprise stents and the Pipeline device.** *J Transl Med* 2016;14:199 CrossRef Medline
9. Aydin K, Arat A, Sencer S, et al. **Stent-assisted coiling of wide-neck intracranial aneurysms using low-profile LEO Baby stents: initial and midterm results.** *AJNR Am J Neuroradiol* 2015;36:1934–41 CrossRef Medline
10. Möhlenbruch M, Herweh C, Behrens L, et al. **The LVIS Jr. microstent to assist coil embolization of wide-neck intracranial aneurysms: clinical study to assess safety and efficacy.** *Neuroradiology* 2014;56: 389–95 CrossRef Medline
11. Moher D, Liberati A, Tetzlaff J, et al. **Preferred Reporting Items for Systematic Reviews and Meta-Analyses: the PRISMA statement.** *Int J Surg* 2010;8:336–41 CrossRef Medline
12. Roy D, Milot G, Raymond J. **Endovascular treatment of unruptured aneurysms.** *Stroke* 2001;32:1998–2004 CrossRef Medline
13. Wells G, Shea B, O'Connell D, et al. **The Newcastle-Ottawa Scale (NOS) for assessing the quality of nonrandomized studies in meta-analyses.** Ottawa: Ottawa Hospital Research Institute; 2011. [http://www.evidencebasedpublichealth.de/download/Newcastle\\_Ottawa\\_Scale\\_Pope\\_Bruce.pdf](http://www.evidencebasedpublichealth.de/download/Newcastle_Ottawa_Scale_Pope_Bruce.pdf). Accessed February 5, 2018
14. Chalouhi N, Jabbour P, Singhal S, et al. **Stent-assisted coiling of intracranial aneurysms: predictors of complications, recanalization, and outcome in 508 cases.** *Stroke* 2013;44:1348–53 CrossRef Medline
15. Shapiro M, Becks T, Sahlein D, et al. **Stent-supported aneurysm coiling: a literature survey of treatment and follow-up.** *AJNR Am J Neuroradiol* 2012;33:159–63 CrossRef Medline
16. Aydin K, Barbuoglu M, Sencer S, et al. **Flow diversion with low-profile braided stents for the treatment of very small or uncoilable intracranial aneurysms at or distal to the circle of Willis.** *AJNR Am J Neuroradiol* 2017;38:2131–37 CrossRef Medline
17. Feng MT, Wen WL, Feng ZZ, et al. **Endovascular embolization of intracranial aneurysms: to use stent (s) or not? Systematic review and meta-analysis.** *World Neurosurg* 2016;93:271–78 CrossRef Medline
18. Phan K, Huo YR, Jia F, et al. **Meta-analysis of stent-assisted coiling versus coiling-only for the treatment of intracranial aneurysms.** *J Clin Neurosci* 2016;31:15–22 CrossRef Medline
19. Iosif C, Piotin M, Saleme S, et al; TRAIL Investigators. **Safety and effectiveness of the Low Profile Visualized Intraluminal Support (LVIS and LVIS Jr) devices in the endovascular treatment of intracranial aneurysms: results of the TRAIL multicenter observational study.** *J Neurointerv Surg* 2018;10:675–81 CrossRef Medline
20. Gawlitza M, Januel AC, Tall P, et al. **Flow diversion treatment of complex bifurcation aneurysms beyond the circle of Willis: a single-center series with special emphasis on covered cortical branches and perforating arteries.** *J Neurointerv Surg* 2016;8:481–87 CrossRef Medline
21. Cagnazzo F, Mantilla D, Lefevre PH, et al. **Treatment of middle cerebral artery aneurysms with flow-diverter stents: a systematic review and meta-analysis.** *AJNR Am J Neuroradiol* 2017;38:2289–94 CrossRef Medline
22. Feng Z, Li Q, Zhao R, et al. **Endovascular treatment of middle cerebral artery aneurysm with the LVIS Junior stent.** *J Stroke Cerebrovasc Dis* 2015;24:1357–62 CrossRef Medline
23. Johnson AK, Munich SA, Tan LA, et al. **Complication analysis in nitinol stent-assisted embolization of 486 intracranial aneurysms.** *J Neurosurg* 2015;123:453–59 CrossRef Medline
24. Kallmes DF, Hanel R, Lopes D, et al. **International retrospective study of the Pipeline embolization device: a multicenter aneurysm treatment study.** *AJNR Am J Neuroradiol* 2015;36:108–15 CrossRef Medline
25. Kis B, Weber W, Berlit P, et al. **Elective treatment of saccular and broad-necked intracranial aneurysms using a closed-cell nitinol stent (Leo).** *Neurosurgery* 2006;58:443–50; discussion 443–50 CrossRef Medline
26. Juszkat R, Nowak S, Smól S, et al. **Leo stent for endovascular treatment of broad-necked and fusiform intracranial aneurysms.** *Interv Neuroradiol* 2007;13:255–69 CrossRef Medline
27. Yang P, Liu J, Huang Q, et al. **Endovascular treatment of wide-neck middle cerebral artery aneurysms with stents: a review of 16 cases.** *AJNR Am J Neuroradiol* 2010;31:940–46 CrossRef Medline

28. Luo J, Lv X, Jiang C, et al. **Preliminary use of the Leo stent in the endovascular treatment of wide-necked cerebral aneurysms.** *World Neurosurg* 2010;73:379–84 CrossRef Medline
29. Lv X, Li Y, Jiang C, et al. **Potential advantages and limitations of the Leo stent in endovascular treatment of complex cerebral aneurysms.** *Eur J Radiol* 2011;79:317–22 CrossRef Medline
30. Akmangit I, Aydin K, Sencer S, et al. **Dual stenting using low-profile LEO baby stents for the endovascular management of challenging intracranial aneurysms.** *AJNR Am J Neuroradiol* 2015;36:323–29 CrossRef Medline
31. Machi P, Costalat V, Lobotesis K, et al. **LEO Baby stent use following balloon-assisted coiling: single- and dual-stent technique—immediate and midterm results of 29 consecutive patients.** *AJNR Am J Neuroradiol* 2015;36:2096–103 CrossRef Medline
32. Negrotto M, Crosa R, Casagrande W. **Assisted coiling using LEO Baby or LVIS Jr stents: report of six cases.** *Interv Neuroradiol* 2015; 21:566–74 CrossRef Medline
33. Chau Y, Mondot L, Sacht M, et al. **Modification of cerebral vascular anatomy induced by Leo stent placement depending on the site of stenting: a series of 102 cases.** *Interv Neuroradiol* 2016;22:666–73 CrossRef Medline
34. Voigt P, Schob S, Jantschke R, et al. **Stent-assisted coiling of ruptured and incidental aneurysms of the intracranial circulation using moderately flow-redirecting, braided LEO stents: initial experience in 39 patients.** *Front Neurol* 2017;8:602 CrossRef Medline
35. Sedat J, Chau Y, Gaudart J, et al. **Stent-assisted coiling of intracranial aneurysms using LEO stents: long-term follow-up in 153 patients.** *Neuroradiology* 2018;60:211–19 CrossRef Medline
36. Poncyłjusz W, Biliński P, Safranow K, et al. **The LVIS/LVIS Jr. stents in the treatment of wide-neck intracranial aneurysms: multicentre registry.** *J Neurointerv Surg* 2015;7:524–29 CrossRef Medline
37. Cho YD, Sohn CH, Kang HS, et al. **Coil embolization of intracranial saccular aneurysms using the Low-profile Visualized Intraluminal Support (LVIS) device.** *Neuroradiology* 2014;56:543–51 CrossRef Medline
38. Behme D, Weber A, Kowoll A, et al. **Low-profile Visualized Intraluminal Support device (LVIS Jr) as a novel tool in the treatment of wide-necked intracranial aneurysms: initial experience in 32 cases.** *J Neurointerv Surg* 2015;7:281–85 CrossRef Medline
39. Feng Z, Zhang L, Li Q, et al. **Endovascular treatment of wide-neck anterior communicating artery aneurysms using the LVIS Junior stent.** *J Clin Neurosci* 2015;22:1288–91 CrossRef Medline
40. Samaniego EA, Abdo G, Hanel RA, et al. **Endovascular treatment of PICA aneurysms with a Low-profile Visualized Intraluminal Support (LVIS Jr) device.** *J Neurointerv Surg* 2016;8:1030–33 CrossRef Medline
41. Alghamdi F, Mine B, Morais R, et al. **Stent-assisted coiling of intracranial aneurysms located on small vessels: midterm results with the LVIS Junior stent in 40 patients with 43 aneurysms.** *Neuroradiology* 2016;58:665–71 CrossRef Medline
42. Du EH, Shankar JJ. **LVIS Jr ‘shelf’ technique: an alternative to Y stent-assisted aneurysm coiling.** *J Neurointerv Surg* 2016;8:1256–59 CrossRef Medline
43. Shankar JJ, Quateen A, Weill A, et al. **Canadian Registry of LVIS Jr for Treatment of Intracranial Aneurysms (CaRLA).** *J Neurointerv Surg* 2017;9:849–53 CrossRef Medline
44. Grossberg JA, Hanel RA, Dabus G, et al. **Treatment of wide-necked aneurysms with the Low-profile Visualized Intraluminal Support (LVIS Jr) device: a multicenter experience.** *J Neurointerv Surg* 2017; 9:1098–102 CrossRef Medline
45. Lim JW, Lee J, Cho YD. **Progressive occlusion of small saccular aneurysms incompletely occluded after stent-assisted coil embolization: analysis of related factors and long-term outcomes.** *Clin Neuroradiol* 2017 Aug 8. [Epub ahead of print] CrossRef Medline
46. Wang CC, Fang YB, Zhang P, et al. **Reconstructive endovascular treatment of vertebral artery dissecting aneurysms with the Low-profile Visualized Intraluminal Support (LVIS) device.** *PLoS One* 2017;12:e0180079 CrossRef Medline
47. Feng X, Qian Z, Liu P, et al. **Comparison of recanalization and in-stent stenosis between the Low-profile Visualized Intraluminal Support stent and Enterprise stent-assisted coiling for 254 intracranial aneurysms.** *World Neurosurg* 2018;109:e99–104 CrossRef Medline
48. Santillan A, Boddu S, Schwarz J, et al. **LVIS Jr. stent for treatment of intracranial aneurysms with parent vessel diameter of 2.5 mm or less.** *Interv Neuroradiol* 2018;24:246–53 CrossRef Medline
49. Yoo DH, Cho YD, Moon J, et al. **Long-term outcomes of Low-Profile Visualized Intraluminal Support device usage in stent-assisted coiling of intracranial aneurysm.** *J Clin Neurosci* 2018; 50:287–91 CrossRef Medline
50. Gao BL, Li TX, Li L, et al. **Tiny cerebral aneurysms can be treated safely and effectively with Low-Profile Visualized Intraluminal Support stent-assisted coiling or coiling alone.** *World Neurosurg* 2018;113:e426–30 CrossRef Medline
51. Cheung NK, Chiu AH, Cheung A, et al. **Long term follow-up of bifurcation aneurysms treated with braided stent assisted coiling and complex T- and Y- stent constructs.** *J Neurointerv Surg* 2018;10: 560–65 CrossRef Medline

# Outcomes of Stent Retriever versus Aspiration-First Thrombectomy in Ischemic Stroke: A Systematic Review and Meta-Analysis

 C.O.A. Tsang,  I.H.W. Cheung,  K.K. Lau,  W. Brinjikji,  D.F. Kallmes, and  T. Krings



## ABSTRACT

**BACKGROUND:** There is ongoing debate regarding the optimal first-line thrombectomy technique for large-vessel occlusion.

**PURPOSE:** We performed a systematic review and meta-analysis of comparative studies on stent retriever–first and aspiration–first thrombectomy.

**DATA SOURCES:** We searched Ovid MEDLINE, PubMed, and EMBASE from 2009 to February 2018.

**STUDY SELECTION:** Two reviewers independently selected the studies. The primary end point was successful reperfusion (TICI 2b/3).

**DATA ANALYSIS:** Random-effects meta-analysis was used for analysis.

**DATA SYNTHESIS:** Eighteen studies including 2893 patients were included. There was no significant difference in the rate of final successful reperfusion (83.9% versus 83.3%; OR = 0.87; 95% CI, 0.62%–1.27%) or good functional outcome (mRS 0–2) at 90 days (OR = 1.07; 95% CI, 0.80–1.44) between the stent-retriever thrombectomy and aspiration groups. The stent-retriever thrombectomy–first group achieved a statistically significant higher TICI 2b/3 rate after the first-line device than the aspiration–first group (74.9% versus 66.4%; OR = 1.53; 95% CI, 1.14%–2.05%) and resulted in lower use of a rescue device (19.9% versus 32.5%; OR = 0.36; 95% CI, 0.14%–0.90%). The aspiration–first approach resulted in a statistically shorter groin-to-reperfusion time (weighted mean difference, 7.15 minutes; 95% CI, 1.63–12.67 minutes). There was no difference in the number of passes, symptomatic intracerebral hemorrhage, vessel dissection or perforation, and mortality between groups.

**LIMITATIONS:** Most of the included studies were nonrandomized. There was significant heterogeneity in some of the outcome variables.

**CONCLUSIONS:** Stent-retriever thrombectomy–first and aspiration–first thrombectomy were associated with comparable final reperfusion rates and functional outcome. Stent-retriever thrombectomy was superior in achieving reperfusion as a stand-alone first-line technique, with lower use of rescue devices but a longer groin-to-reperfusion time.

**ABBREVIATIONS:** ADAPT = A Direct Aspiration, First Pass Technique for the Endovascular Treatment of Stroke; PRISMA = Preferred Reporting Items for Systematic Reviews and Meta-Analyses; RCT = randomized controlled trial; SRT = stent-retriever thrombectomy

Endovascular thrombectomy is recommended as a standard of care for anterior circulation acute ischemic stroke secondary to large-vessel occlusion.<sup>1</sup> This treatment was established in 2015

when multiple randomized controlled trials (RCTs) established the clinical efficacy and safety of modern stent-retriever thrombectomy (SRT) in removing the obstructing thrombus in acute ischemia.<sup>2–6</sup> A Direct Aspiration, First Pass Technique for the Endovascular Treatment of Stroke (ADAPT) is an alternative thrombectomy technique that has become the standard of care at many centers.<sup>7</sup> This is performed by advancing a large-bore catheter (typically with an inner diameter of  $\geq 0.060$  inch) to the face of the thrombus, followed by its removal by aspiration alone or withdrawal of the catheter while aspirating. Previous observational studies focusing on ADAPT reported a higher rate of com-

Received April 19, 2018; accepted after revision August 16.

From the Division of Neurosurgery (C.O.A.T.), Department of Surgery, and Division of Neurology (K.K.L.), Department of Medicine, University of Hong Kong, Hong Kong; Department of Medical Imaging (C.O.A.T., W.B., T.K.), Toronto Western Hospital, Toronto, Ontario, Canada; Department of Diagnostic Radiology (I.H.W.C.), Queen Mary Hospital, Hong Kong; and Department of Radiology (W.B., D.F.K.), Mayo Clinic, Rochester, Minnesota.

This study was supported by the Health and Medical Research Fund of Hong Kong (01150027).

Please address correspondence to Chun On Anderson Tsang, Room 701, Administrative Block, Department of Neurosurgery, Queen Mary Hospital, 102 Pokfulam Rd, Hong Kong; e-mail: acotsang@hku.hk

 Indicates open access to non-subscribers at [www.ajnr.org](http://www.ajnr.org)

<http://dx.doi.org/10.3174/ajnr.A5825>

plete revascularization and potentially a shorter time from groin puncture to reperfusion compared with stent-retriever thrombectomy.<sup>8</sup> However, recent randomized trials comparing SRT with ADAPT have failed to demonstrate the superiority of ADAPT in technical or clinical outcomes.<sup>9</sup> To address the ongoing debate of the optimal first-line thrombectomy technique, we performed a meta-analysis of comparative studies reporting outcomes on SRT versus ADAPT as a first-line approach.

## **MATERIALS AND METHODS**

### **Search Strategy and Selection Criteria**

A systematic literature review was performed following the Preferred Reporting Items for Systematic Reviews and Meta-Analyses (PRISMA) guidelines.<sup>10</sup> The English literature was searched with Ovid MEDLINE, PubMed, and EMBASE from January 2009 to February 2018. The following terms and their combinations were used as keywords or Medical Subject Headings terms: “mechanical thrombectomy,” “endovascular,” “stroke,” “ADAPT,” “aspiration,” “stent retriever,” and “first-pass.” We also searched the references of relevant articles and contacted experts in the field to identify additional studies pertaining to the outcome of different thrombectomy techniques that were not included in the initial literature search.

Studies identified were then evaluated to meet the following inclusion criteria: 1) studies comparing the outcomes of the SRT-first and aspiration-first strategies; 2) studies reporting separately the clinical and technical outcomes of the SRT and aspiration groups; and 3) studies with at least 10 patients each in the SRT or aspiration group. The exclusion criteria were the following: 1) noncomparative studies reporting outcomes only on 1 group (SRT or aspiration); 2) studies that predominantly used the first generation of aspiration catheters (eg, Penumbra Separator 0.041 [Penumbra, Alameda, California] or smaller catheters, with or without the Separator) in the aspiration arm; and 3) studies that did not separate outcomes by the first-line thrombectomy technique adopted. Both randomized and observational studies were included.

### **Data Items and Extraction**

Patients were divided into 2 groups: SRT-first and aspiration-first. For this study, patients were considered to have SRT-first if any stent retriever was used in the first thrombectomy attempt, with or without balloon-guiding catheters or simultaneous distal aspiration (ie, Solumbra technique). Those receiving only direct aspiration with large-bore distal-access catheters in the first thrombectomy attempt were considered aspiration-first.

The primary end point was the rate of successful reperfusion defined as the final Thrombolysis in Cerebral Infarction score of 2b/3. Other clinical outcomes included the following: good functional outcome defined as a modified Rankin Scale 0–2 at 90 days, 90-day mortality, symptomatic intracerebral hemorrhage, and complications of vessel dissection or perforation. Other technical outcomes studied included the following: the rate of complete reperfusion (TICI 3), the rate of TICI 2b/3 achieved with only the first device, the use of a rescue device, the number of thrombectomy passes, and the time from groin puncture to reperfusion.

### **Risk of Bias Assessment**

The included studies were assessed for risk of bias by 2 independent readers (A.C.O.T. and I.H.W.C.) with the Newcastle Ottawa Scale.<sup>11</sup> This is an 8-item tool for nonrandomized studies included in systematic reviews and meta-analyses, in which the selection, comparability, and ascertainment of outcomes of the study groups are assessed. The scale ranges from 0 to 9, with the higher score indicating lower risk of bias. Studies that used well-defined selection criteria, with comparable baseline stroke severity; patient demographics; onset-to-groin puncture time, with contemporaneous use of SRT; and aspiration thrombectomy and those that had an independent assessment of clinical and technical outcomes are considered to have a low risk of bias.

### **Statistical Analysis**

We extracted from each study a 2 × 2 table for binary outcomes and the mean group sample size and a variability measure for continuous outcomes. The pooled outcomes were meta-analyzed using a random-effects model.<sup>12</sup> Heterogeneity of the studies not attributable to chance was quantified with the I<sup>2</sup> statistic.<sup>13</sup> The 95% confidence intervals of the odds ratios for binary outcomes and the weighted mean differences for continuous outcomes were reported. Some included studies reported continuous outcomes with median and interquartile range; these were converted to a mean and SD value based on the assumption of a log-normal distribution of the original measure. When the SD or the interquartile range for a specific outcome was not reported in the article, it was extrapolated from other studies when such data were available. If >10 studies were identified, a funnel plot was constructed to explore the impact of publication bias.

Only 3 of the 18 included studies were randomized by the first thrombectomy strategy. To address the potential heterogeneity between the 2 study groups, we conducted meta-regression to test the influence of moderators, including baseline stroke severity measured by the National Institutes of Health Stroke Scale and age. Sensitivity analyses were performed by studying the comparative outcomes, including only those studies that were RCTs, those that included predominantly (>90%) anterior circulation thrombectomy, and those that used balloon-guiding catheters with SRT consistently. Meta-analysis and meta-regression were performed with OpenMeta[Analyst] (<http://www.cebm.brown.edu/openmeta/>).<sup>14</sup>

## **RESULTS**

### **Literature Search**

The initial literature search yielded 862 articles. The titles and abstracts of these were read, and 818 articles were excluded for irrelevance. Of the remaining 44 articles, 14 were excluded because they were conference abstracts, and 7 were excluded because they were review articles or editorials. After review, 2 articles were excluded for overlapping patient populations, and 4 studies were excluded for predominantly using a previous generation of thrombectomy devices. One additional study was identified by contacting experts in the field, yielding a total of 18 studies eligible for analysis.<sup>9,15–31</sup> The PRISMA flow diagram is provided in Fig 1.

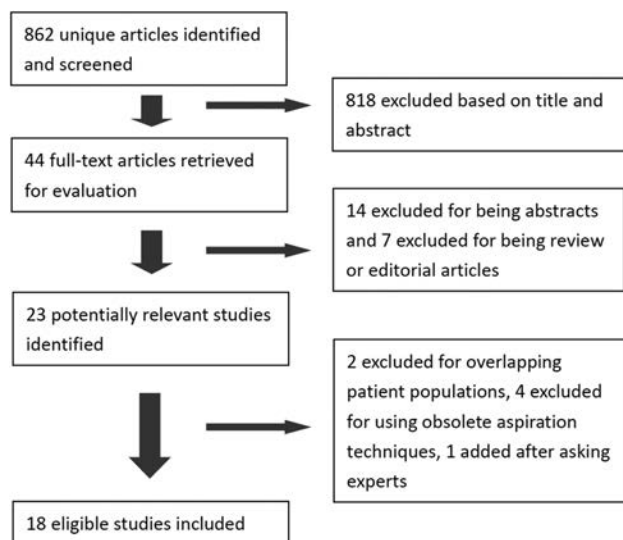


**FIG 1.** Literature search flowchart.

### Study and Patient Characteristics

A total of 2893 patients (1564 with SRT and 1329 with aspiration-first) in the 3 randomized multicenter trials and 15 retrospective studies were included. The mean age of patients in the SRT and aspiration group were 69.8 and 68.7 years, respectively. For the SRT group, the mean baseline NIHSS score was 15.8, and that in the aspiration group was 15.3. The median ASPECTS in both groups was 8.

Balloon-guiding catheters were routinely used in 5 studies, intermittently used in 2 studies, and not used in 11 studies. In 6 studies, simultaneous adjuvant distal aspiration with SRT was used in the first pass in a variable proportion of patients. All except 3 studies reported predominantly anterior circulation thrombectomy (>85%), including the 3 randomized trials. There were 4 retrospective single-center studies reporting only posterior circulation thrombectomy, comprising 138 patients (8.8%) in the SRT arm and 126 patients (9.5%) in the aspiration arm. Four studies had a low risk of bias, 12 had a moderate risk of bias, and 2 had a high risk of bias. The included studies are summarized in Table 1.

### Technical Outcomes

When we compared SRT-first and aspiration-first thrombectomy, there was no statistically significant difference in the rate of final successful reperfusion (TICI 2b/3) (83.9% versus 83.3%; OR = 0.87; 95% CI, 0.62%–1.27%) or complete reperfusion (TICI 3) (38.1% versus 40.3%; OR = 0.82; 95% CI, 0.49%–1.37%). The SRT-first group achieved a statistically significant higher TICI 2b/3 rate after the first-line strategy than the aspiration-first group (74.9% versus 66.4%; OR = 1.53; 95% CI, 1.14%–2.05%) and this resulted in lower use of the rescue device (19.9% versus 32.5%; OR = 0.36; 95% CI, 0.14%–0.90%) (Fig 2). The aspiration-first approach resulted in a statistically shorter groin-to-reperfusion time (weighted mean difference, 7.15 minutes; 95% CI, 1.63–12.67). There was no difference in the number of passes required to achieve reperfusion between groups.

### Clinical Outcomes

There was no statistical difference in the rate of good functional outcome (mRS 0–2) at 90 days between groups (OR = 1.07; 95% CI, 0.80–1.44). There was also no significant difference in the mortality rate, the rate of symptomatic intracerebral hemorrhage, emboli to new territories, vessel dissection, or perforation between the 2 groups. These results are summarized in Tables 2 and 3.

### Publication Bias and Study Heterogeneity

Funnel plot analysis did not suggest publication bias (Fig 3). There was low heterogeneity ( $I^2 < 50\%$ ) for the following outcomes: the TICI 2b/3 rate after the first-line approach ( $I^2 = 31\%$ ), mortality rate ( $I^2 = 28\%$ ), risk of symptomatic intracerebral hemorrhage ( $I^2 = 0\%$ ), emboli to new territories ( $I^2 = 0\%$ ), and vessel dissection or perforation ( $I^2 = 26\%$ ). There was moderate substantial heterogeneity ( $I^2 > 50\%$ ) for the following outcomes: final rate of TICI 2b/3 ( $I^2 = 54\%$ ), final rate of TICI 3 ( $I^2 = 79.5\%$ ), mRS 0–2 at 90 days ( $I^2 = 62\%$ ), the need for a rescue device ( $I^2 = 93\%$ ), groin-to-reperfusion time ( $I^2 = 79\%$ ), and the number of passes required ( $I^2 = 77\%$ ).

Meta-regression analyses performed on outcomes with high heterogeneity (final TICI 2b/3 and mRS 0–2 at 90 days) did not identify variables explaining differences between studies.

### Sensitivity Analysis

We performed a subgroup analysis to determine whether the outcomes were different in anterior circulation stroke versus posterior circulation stroke. In the 9 studies that included predominantly (>90%) anterior circulation stroke, there was no statistically significant difference in the final TICI 2b/3 rate between groups (OR = 0.892; 95% CI, 0.59–1.35). Four studies reporting posterior circulation stroke only were included. The use of the SRT-first approach in posterior circulation stroke was associated with a statistically significant lower successful reperfusion (OR = 0.47; 95% CI, 0.25–0.91).

When we included only the 3 randomized controlled trials, we found no difference in the final TICI 2b/3 rate (OR = 1.05; 95% CI, 0.58–1.90) and good functional outcome (OR = 1.04; 95% CI, 0.79–1.37). There was a non-statistically significant higher chance in the SRT-first group of achieving TICI 2b/3 after the first-line approach (OR = 1.26; 95% CI, 0.85–1.86).

When including only the 5 studies that consistently used balloon-guiding catheters with SRT, we again found no difference in the final TICI 2b/3 rate (OR = 0.95; 95% CI, 0.54–1.67) and good functional outcome (OR = 1.22; 95% CI, 0.91–1.64). There was a non-statistically significant higher chance in the SRT-first group of achieving TICI 2b/3 after the first-line approach (OR = 1.26; 95% CI, 0.92–1.73).

When we excluded the study that used the Penumbra 3D Separator device,<sup>28</sup> which was different in design from other conventional stent retrievers, there were no differences in the final TICI 2b/3 rate (OR = 0.88; 95% CI, 0.62–1.25). When we included only the 3 studies that reported TICI 2c/3 outcomes, there were no differences in the final TICI 2c/3 rate (OR = 1.10; 95% CI, 0.61–1.89) between groups.

**Table 1: Studies included in the meta-analysis**

Author	Year	No. of Patients, SRT/Asp	Mean Age (yr), SRT/Asp	Mean Baseline NIHSS, SRT/Asp	Mean Baseline ASPECTS, SRT/Asp	Anterior Circulation (%)	Study Design	Risk of Bias (NOS)
Delgado Almandoz et al <sup>17</sup>	2016	55/45	69.6/66.1	16.8/19.2	8.2/9.1	94%	Retrospective, single-center, case-control	7
Turk et al <sup>18</sup>	2015	30/64	62.5/68.5	17/16.5	NA	90%	Retrospective, single-center, case-control	7
Son et al <sup>29</sup>	2016	13/18	68.9/66.4	27.3/21.3	NA	0%	Retrospective, single-center, case-control	6
Kim et al <sup>20</sup>	2017	16/25	76.5/71	10.5/15	7/8	100%	Retrospective, single-center, case-control	7
Lapergue et al (a) <sup>19</sup>	2016	119/124	65.5/64.3	15.9/15.9	8/9	100%	Retrospective, multicenter, case-control	7
Mokin et al (a) <sup>16</sup>	2016	58/42	NA	NA	NA	0%	Retrospective, multicenter, case-control	7
Gerber et al <sup>22</sup>	2017	13/20	63.2/62.8	25/18	6.5/7.5	0%	Retrospective, single-center, case-control	6
Hentschel et al <sup>15</sup>	2017	67/69	66.2/66.1	NA	NA	90%	Retrospective, single-center, case-control	7
Hesse et al <sup>23</sup>	2018	286/164	74/72	15.5/15.3	8/8	100%	Retrospective, multicenter, case-control	5
Jadhav et al <sup>24</sup>	2017	195/112	69/66	17/17	9/9	87%	Retrospective, single-center, case-control	6
Lapergue et al (b) <sup>9</sup>	2017	189/192	68.1/71.7	16.1/16.3	7/7	100%	Randomized controlled trial, multicenter	9
Maergerlein et al <sup>25</sup>	2017	61/36	75.8/72.4	NA	NA	89%	Retrospective, multicenter, case-control	5
Mokin et al (b) <sup>21</sup>	2017	62/51	NA	NA	NA	100%	Retrospective, multicenter, case-control	8
Stapleton et al <sup>31</sup>	2018	70/47	69.4/63.5	16.5/16.5	8.3/8	100%	Retrospective, single-center, case-control	7
Gory et al <sup>26</sup>	2018	54/46	67/61	20/14	8/7	0%	Retrospective, multicenter, case-control	7
Mocco et al <sup>27</sup>	2018	136/133	71.1/71.8	7/6	NA	100%	Randomized controlled trial, multicenter	9
Nogueira et al <sup>28</sup>	2018	95/97	67.3/66.5	18/18	8/8	98%	Randomized controlled trial, multicenter	9
Nishi et al <sup>30</sup>	2018	45/44	73.1/77.8	19/17	NA	88%	Retrospective, single-center, case-control	7

**Note:**—NOS indicates Newcastle-Ottawa Scale; NA, not available; Asp, aspiration.

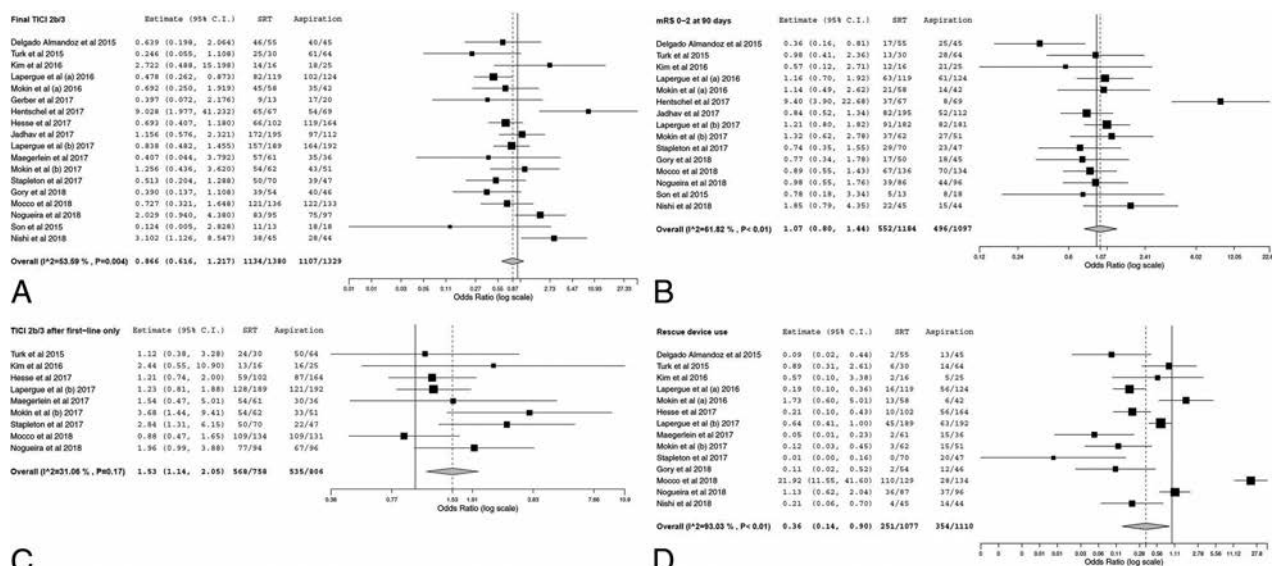


**FIG 2.** Forest plot of meta-analysis results. A, Final successful reperfusion was TIC1 2b/3. B, Good functional outcome mRS 0–2 at 90 days. Successful reperfusion TIC1 2b/3 after the first-line approach (C) and the use of a rescue device (D).

**Table 2: Summary of meta-analysis outcomes**

Outcome	Odds Ratio	95% CI	$I^2$
Final TIC1 2b/3	0.87	0.62–1.27	53.6%
Final TIC1 3	0.82	0.49–1.37	79.5%
First-line approach, TIC1 2b/3	1.53	1.14–2.05	31.1%
mRS 0–2 at 90 days	1.07	0.80–1.44	61.8%
Mortality	0.91	0.69–1.20	28.1%
Rescue device	0.36	0.14–0.90	93.0%
Dissection or perforation	1.26	0.52–3.08	26.3%
ENT	1.11	0.70–1.74	0%
sICH	1.20	0.78–1.84	0%

**Note:**—ENT indicates emboli to new territories; sICH, symptomatic intracranial hemorrhage.

**DISCUSSION**

Our meta-analysis of 2893 patients from 18 studies found no significant difference in terms of the final revascularization rate and functional outcome between aspiration-first and SRT-first thrombectomy for large-vessel occlusion stroke. Notably, stent retriever use was superior in achieving successful reperfusion as a stand-alone technique, compared with aspiration. The need for a

**Table 3: Summary of meta-analysis outcomes**

	Weighted Mean Difference	95% CI	$I^2$
Groin to perfusion (min)	7.15	1.63–12.67	79.0%
No. of passes	0.06	–0.40–0.52	77.0%

rescue device was also significantly less when SRT was adopted as a first approach instead of aspiration. The comparable final reperfusion rate in the aspiration group was achieved with the use of a rescue device after the initial failed attempts with contact aspiration, which was necessary in 32.5% of patients. These findings are important because they suggest that despite SRT and aspiration-first strategies being able to achieve similar final revascularization rates and functional outcomes, SRT appears to be more effective than aspiration as a primary treatment technique for achieving TIC1 2b/3 revascularization.

Endovascular thrombectomy with stent retrievers for large-vessel occlusion stroke has been established as the standard of care since 2015.<sup>32</sup> The use of direct-contact aspiration thrombectomy

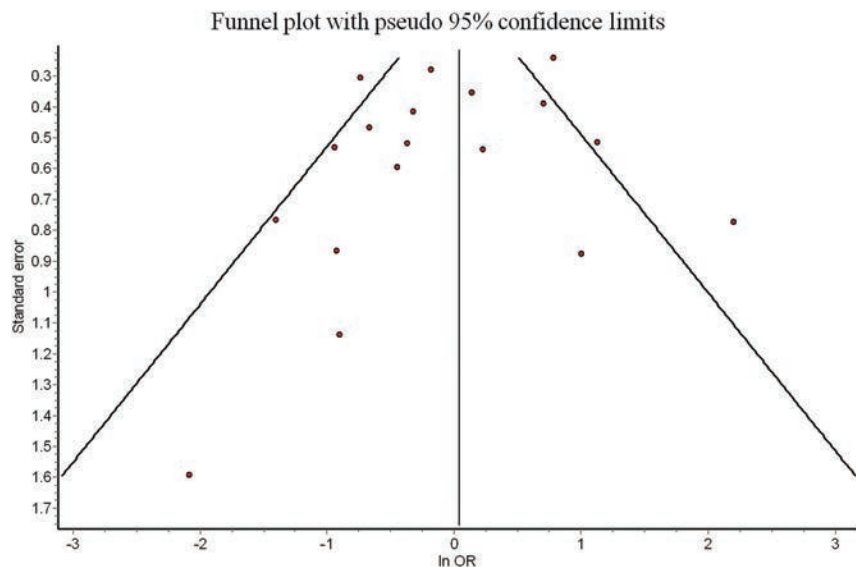


**FIG 3.** Funnel plot for publication bias.

is another common technique but was not supported by class I evidence. Nevertheless, aspiration thrombectomy as a first-line approach is widely practiced in the United States, Hong Kong, and Italy despite the availability of the proved and efficacious stent-retriever thrombectomy.<sup>33-35</sup> The THERAPY (The Randomized, Concurrent Controlled Trial to Assess the Penumbra System's Safety and Effectiveness in the Treatment of Acute Stroke; NCT01429350) trial, which compared aspiration thrombectomy with best medical therapy, was halted early and did not demonstrate efficacy.<sup>36</sup> While recent meta-analyses of uncontrolled observational studies focusing solely on the aspiration technique reported higher complete reperfusion rates and shorter procedure times than SRT,<sup>8,37</sup> these conclusions were confounded by the different patient-selection criteria and baseline stroke severity in the included single-arm studies. The published RCTs on this subject demonstrated noninferiority of aspiration thrombectomy compared with SRT in the final reperfusion rate but were underpowered to compare other clinical outcomes such as functional status and complication rates.<sup>8,37</sup> To address these limitations, the present review included only studies that compared both SRT-first and aspiration-first approaches in the same patient cohort, as well as the 3 recently published/presented RCTs investigating these 2 groups.

One of the notable findings from our study is that SRT could achieve higher rates of TICI 2b/3 reperfusion without the help of rescue therapy than aspiration thrombectomy alone. This is important because the literature has focused more on the first-pass effect during thrombectomy for acute ischemic stroke, defined as achieving complete recanalization with a single pass. In a recently published post hoc analysis of the North American Solitaire Acute Stroke Registry, Zaidat et al<sup>38</sup> found that patients who achieved TICI 2b/3 on a first pass had significantly better clinical outcomes than those who did not. Independent predictors of a first-pass effect included the use of a balloon-guiding catheter and noninternal carotid artery terminus occlusion. While we were not able to examine first-pass recanalization rates between SRT and aspiration in this meta-analysis, SRT alone achieved higher recanalization rates than aspiration alone. Ultimately, the fact that SRT

was used as a rescue therapy in nearly one-third of aspiration cases while aspiration was needed as rescue therapy in nearly one-fifth of SRT cases suggests that SRT has some technical advantages in clot retrieval.

There are a number of advantages to aspiration thrombectomy compared with SRT. With contact aspiration thrombectomy, it is not necessary to traverse the occluding thrombus, thus theoretically reducing the risk of vessel perforation and downstream emboli. While cases of catastrophic vessel perforation with the use of SRT have been reported, the incidence was low.<sup>39</sup> Our review did not show any significant difference in the safety profiles between the 2 groups. Rates of vessel perforation, dissection, and symptomatic ICH were comparable. Another proposed advantage of

aspiration over SRT is the shorter procedural time. The aspiration-first approach was associated with a 7-minute advantage in groin-to-reperfusion time in the meta-analysis. In the 3 randomized studies comparing the 2 approaches, the aspiration-first approach also resulted in a shorter procedural time of 10–13 minutes.<sup>9,27,28</sup> Nevertheless, this advantage in rapidity did not translate to improved patient outcome in any of those trials.

While the overall final reperfusion rate is comparable, there remain uncertainties about whether SRT or aspiration is superior in selected vessel locations or the etiology of stroke. Subgroup analysis of the 4 posterior circulation stroke studies including 264 patients showed that SRT was inferior to aspiration in terms of reperfusion rates. However, the sample size was too small to draw any definitive conclusions. None of the included studies reported the comparative efficacy of aspiration and SRT stratified by the specific occluded vessel to allow subgroup analysis. The etiology of large-vessel occlusion may also affect the efficacy of thrombectomy. In large-vessel occlusion secondary to intracranial artery stenosis, early experience with stent retrievers in this group of patients resulted in a lower reperfusion rate and poorer outcome. In addition, rescue therapy with balloon angioplasty or intra-arterial thrombolytic infusion was frequently required.<sup>40</sup> The shearing force exerted over the atherosclerotic plaque during stent retrieval may be the culprit, and the optimal first-line thrombectomy strategy in this group of patients needs further investigation. Techniques combining SRT and aspiration have been increasingly used, but their superiority over SRT or aspiration alone remains to be defined in randomized studies.<sup>17,41,42</sup> Future studies on the optimal thrombectomy technique should also adopt more robust outcome variables, including TICI 2c/3 angiographic outcome and the first-pass success rate,<sup>38,43</sup> and should consider other aspects such as delayed effects on the vessel wall and the relative cost-effectiveness of different techniques.

### Limitations

Our study has limitations. Apart from the 3 RCTs, most of the included studies were nonrandomized, thus introducing selection

bias. When performing subgroup analysis on only the 3 recent RCTs, we found results similar to those in our meta-analysis. We limited the review to comparative studies with control groups to compare the relative efficacy of SRT and aspiration and excluded those studies that used predominantly previous generations of thrombectomy catheters or devices. There was significant statistical heterogeneity in some of the outcome variables that can impact the validity of our results. Another limitation is that in some cases SRT was performed with simultaneous aspiration (ie, Solumbra technique) and we could not perform subgroup analyses of Solumbra versus SRT-alone versus aspiration. While TICI 2c/3 is increasingly recognized as a better angiographic outcome measure and correlates better with clinical outcome, only 3 of the included studies reported TICI 2c/3 rates and the subgroup analysis on these studies showed similar results.

## CONCLUSIONS

This systematic review and meta-analysis of 18 studies and 2893 patients found that SRT-first and aspiration-first thrombectomy were associated with comparable final reperfusion rates and functional outcomes. SRT was superior in achieving reperfusion as a stand-alone first-line technique, with lower use of rescue devices but a longer groin-to-reperfusion time. There were no significant differences in complication rates and mortality. The optimal first-line thrombectomy approach for specific location or stroke etiology remains unclear.

Disclosures: Chun On Anderson Tsang—RELATED: Grant: Health and Medical Research Fund of Hong Kong (01150027), Comments: a peer-reviewed medical research grant provided by the Hong Kong government through the Food and Health Bureau.\* David F. Kallmes—UNRELATED: Consultancy: Medtronic, Comments: clinical trials\*; Grants/Grants Pending: Medtronic, Neuravi, Comments: preclinical and clinical research\*; Patents (Planned, Pending or Issued): Mayo Clinic, Comments: balloon-guided devices; Stock/Stock Options: Marblehead Medical, Comments: stroke access device development. \*Money paid to the institution.

## REFERENCES

1. Powers WJ, Rabinstein AA, Ackerson T, et al; American Heart Association Stroke Council. **2018 Guidelines for the Early Management of Patients with Acute Ischemic Stroke: A Guideline for Healthcare Professionals from the American Heart Association/American Stroke Association.** *Stroke* 2018;49:e46–110 CrossRef Medline
2. Berkhemer OA, Fransen PS, Beumer D, et al; MR CLEAN Investigators. **A randomized trial of intraarterial treatment for acute ischemic stroke.** *N Engl J Med* 2015;372:11–20 CrossRef Medline
3. Campbell BC, Mitchell PJ, Kleinig TJ, et al; EXTEND-IA Investigators. **Endovascular therapy for ischemic stroke with perfusion-imaging selection.** *N Engl J Med* 2015;372:1009–18 CrossRef Medline
4. Goyal M, Demchuk AM, Menon BK, et al; ESCAPE Trial Investigators. **Randomized assessment of rapid endovascular treatment of ischemic stroke.** *N Engl J Med* 2015;372:1019–30 CrossRef Medline
5. Jovin TG, Chamorro A, Cobo E, et al; REVASCAT Trial Investigators. **Thrombectomy within 8 hours after symptom onset in ischemic stroke.** *N Engl J Med* 2015;372:2296–306 CrossRef Medline
6. Saver JL, Goyal M, Bonafe A, et al; SWIFT PRIME Investigators. **Stent-retriever thrombectomy after intravenous t-PA vs. t-PA alone in stroke.** *N Engl J Med* 2015;372:2285–95 CrossRef Medline
7. Turk AS, Frei D, Fiorella D, et al. **ADAPT FAST study: a direct aspiration first pass technique for acute stroke thrombectomy.** *J Neurointerv Surg* 2014;6:260–64 CrossRef Medline
8. Phan K, Dmytriw AA, Teng I, et al. **A direct aspiration first pass technique vs standard endovascular therapy for acute stroke: a systematic review and meta-analysis.** *Neurosurgery* 2018;83:19–28 CrossRef Medline
9. Lapergue B, Blanc R, Gory B, et al; ASTER Trial Investigators. **Effect of endovascular contact aspiration vs stent retriever on revascularization in patients with acute ischemic stroke and large vessel occlusion: the ASTER randomized clinical trial.** *JAMA* 2017; 318: 443–52 CrossRef Medline
10. Moher D, Liberati A, Tetzlaff J, et al; PRISMA Group. **Preferred reporting items for systematic reviews and meta-analyses: the PRISMA statement.** *J Clin Epidemiol* 2009;62:1006–12 CrossRef Medline
11. Wells GA, Shea B, O'Connell D, et al. **The Newcastle-Ottawa Scale (NOS) for assessing the quality of nonrandomised studies in meta-analyses.** 2013. [http://www.ohri.ca/programs/clinical\\_epidemiology/oxford.asp](http://www.ohri.ca/programs/clinical_epidemiology/oxford.asp). Accessed February 6, 2018
12. DerSimonian R, Laird N. **Meta-analysis in clinical trials revisited.** *Contemp Clin Trials* 2015;45(Pt A):139–45 CrossRef Medline
13. Higgins JP, Thompson SG, Deeks JJ, et al. **Measuring inconsistency in meta-analyses.** *BMJ* 2003;327:557–60 CrossRef Medline
14. Wallace BC, Dahabreh IJ, Trikalinos TA, et al. **Closing the gap between methodologists and end-users: R as a computational backend.** *J Stat Softw* 2012;19:1–15
15. Hentschel KA, Daou B, Chalouhi N, et al. **Comparison of non-stent retriever and stent retriever mechanical thrombectomy devices for the endovascular treatment of acute ischemic stroke.** *J Neurosurg* 2017;126:1123–30 CrossRef Medline
16. Mokin M, Sonig A, Sivakanthan S, et al. **Clinical and procedural predictors of outcomes from the endovascular treatment of posterior circulation strokes.** *Stroke* 2016;47:782–88 CrossRef Medline
17. Delgado Almandoz JE, Kayan Y, Young ML, et al. **Comparison of clinical outcomes in patients with acute ischemic strokes treated with mechanical thrombectomy using either Solumbra or ADAPT techniques.** *J Neurointerv Surg* 2016;8:1123–28 CrossRef Medline
18. Turk AS, Turner R, Spiotta A, et al. **Comparison of endovascular treatment approaches for acute ischemic stroke: cost effectiveness, technical success, and clinical outcomes.** *J Neurointerv Surg* 2015;7: 666–70 CrossRef Medline
19. Lapergue B, Blanc R, Guédin P, et al. **A direct aspiration, first pass technique (ADAPT) versus stent retrievers for acute stroke therapy: an observational comparative study.** *AJNR Am J Neuroradiol* 2016; 37:1860–65 CrossRef Medline
20. Kim YW, Son S, Kang DH, et al. **Endovascular thrombectomy for M2 occlusions: comparison between forced arterial suction thrombectomy and stent retriever thrombectomy.** *J Neurointerv Surg* 2017;9:626–30 CrossRef Medline
21. Mokin M, Primiani CT, Ren Z, et al. **Endovascular treatment of middle cerebral artery M2 occlusion strokes: clinical and procedural predictors of outcomes.** *Neurosurgery* 2017;81:795–802 CrossRef Medline
22. Gerber JC, Daubner D, Kaiser D, et al. **Efficacy and safety of direct aspiration first pass technique versus stent-retriever thrombectomy in acute basilar artery occlusion—a retrospective single center experience.** *Neuroradiology* 2017;59:297–304 CrossRef Medline
23. Hesse AC, Behme D, Kemmling A, et al. **Comparing different thrombectomy techniques in five large-volume centers: a 'real world' observational study.** *J Neurointerv Surg* 2018;10:525–29 CrossRef Medline
24. Jadhav AP, Aghaebrahim A, Horev A, et al. **Stent retriever-mediated manual aspiration thrombectomy for acute ischemic stroke.** *Interv Neurol* 2017;6:16–24 CrossRef Medline
25. Maegerlein C, Prothmann S, Lucia KE, et al. **Intraprocedural thrombus fragmentation during interventional stroke treatment: a comparison of direct thrombus aspiration and stent retriever thrombectomy.** *Cardiovasc Intervent Radiol* 2017;40:987–93 CrossRef Medline
26. Gory B, Mazighi M, Blanc R, et al; Endovascular Treatment in Ischemic Stroke (ETIS) Research Investigators. **Mechanical thrombectomy in basilar artery occlusion: influence of reperfusion on clinical outcomes.** *AJNR Am J Neuroradiol* 2018;39:2070–76

- cal outcome and impact of the first-line strategy (ADAPT vs stent retriever). *J Neurosurg* 2018 Jan 12:1–10. [Epub ahead of print] CrossRef Medline
27. Mocco JSA, Turk A III. **A Comparison of Direct Aspiration vs. Stent Retriever as a First Approach (“COMPASS”): a randomized trial.** In: *Proceedings of the International Stroke Conference*, Los Angeles, CA, January 25, 2018
  28. Nogueira RG, Frei D, Kirmani JF, et al; Penumbra Separator 3D Investigators. **Safety and efficacy of a 3-dimensional stent retriever with aspiration-based thrombectomy vs aspiration-based thrombectomy alone in acute ischemic stroke intervention: a randomized clinical trial.** *JAMA Neurol* 2018;75:304–11 CrossRef Medline
  29. Son S, Choi DS, Oh MK, et al. **Comparison of Solitaire thrombectomy and Penumbra suction thrombectomy in patients with acute ischemic stroke caused by basilar artery occlusion.** *J Neurointerv Surg* 2016;8:13–18 CrossRef Medline
  30. Nishi H, Ishii A, Nakahara I, et al. **Different learning curves between stent retrieval and a direct aspiration first-pass technique for acute ischemic stroke.** *J Neurosurg* 2018 Jan 5:1–8. [Epub ahead of print] CrossRef Medline
  31. Stapleton CJ, Leslie-Mazwi TM, Torok CM, et al. **A direct aspiration first-pass technique vs stentriever thrombectomy in emergent large vessel intracranial occlusions.** *J Neurosurg* 2018;128:567–74 CrossRef Medline
  32. Powers WJ, Derdeyn CP, Biller J, et al; American Heart Association Stroke Council. **2015 American Heart Association/American Stroke Association Focused Update of the 2013 Guidelines for the Early Management of Patients with Acute Ischemic Stroke Regarding Endovascular Treatment: A Guideline for Healthcare Professionals from the American Heart Association/American Stroke Association.** *Stroke* 2015;46:3020–35 CrossRef Medline
  33. Fargen KM, Arthur AS, Spiotta AM, et al. **A survey of neurointerventionalists on thrombectomy practices for emergent large vessel occlusions.** *J Neurointerv Surg* 2017;9:142–46 CrossRef Medline
  34. Tsang AC, Yeung RW, Tse MM, et al. **Emergency thrombectomy for acute ischaemic stroke: current evidence, international guidelines and local clinical practice.** *Hong Kong Med J* 2018;24:85–92 CrossRef Medline
  35. Romano DG, Cioni S, Vinci SL, et al. **Thromboaspiration technique as first approach for endovascular treatment of acute ischemic stroke: initial experience at nine Italian stroke centers.** *J Neurointerv Surg* 2017;9:6–10 CrossRef Medline
  36. Mocco J, Zaidat OO, von Kummer R, et al; THERAPY Trial Investigators. **Aspiration thrombectomy after intravenous alteplase versus intravenous alteplase alone.** *Stroke* 2016;47:2331–38 CrossRef Medline
  37. Gory B, Armoiry X, Sivan-Hoffmann R, et al. **A direct aspiration first pass technique for acute stroke therapy: a systematic review and meta-analysis.** *Eur J Neurol* 2018;25:284–92 CrossRef Medline
  38. Zaidat OO, Castonguay AC, Linfante I, et al. **First pass effect: a new measure for stroke thrombectomy devices.** *Stroke* 2018;49:660–66 CrossRef Medline
  39. Mokin M, Fargen KM, Primiani CT, et al. **Vessel perforation during stent retriever thrombectomy for acute ischemic stroke: technical details and clinical outcomes.** *J Neurointerv Surg* 2017;9:922–28 CrossRef Medline
  40. Lee JS, Hong JM, Kim JS. **Diagnostic and therapeutic strategies for acute intracranial atherosclerosis-related occlusions.** *J Stroke* 2017;19:143–51 CrossRef Medline
  41. Maus V, Behme D, Kabbasch C, et al. **Maximizing first-pass complete reperfusion with SAVE.** *Clin Neuroradiol* 2018;28:327–38 CrossRef Medline
  42. McTaggart RA, Tung EL, Yaghi S, et al. **Continuous aspiration prior to intracranial vascular embolectomy (CAPTIVE): a technique which improves outcomes.** *J Neurointerv Surg* 2017;9:1154–59 CrossRef Medline
  43. Tung EL, McTaggart RA, Baird GL, et al. **Rethinking Thrombolysis in Cerebral Infarction 2b: which Thrombolysis in Cerebral Infarction scales best define near complete recanalization in the modern thrombectomy era?** *Stroke* 2017;48:2488–93 CrossRef Medline

# Balloon-Guide Catheters Are Needed for Effective Flow Reversal during Mechanical Thrombectomy

O. Nikoubashman, D. Wischer, H.M. Hennemann, J. Sandmann, T. Sichtermann, F.S. Mischenich, A. Reich, and M. Wiesmann

## ABSTRACT

**BACKGROUND AND PURPOSE:** Blood flow management in the carotid artery during mechanical thrombectomy is crucial for safety and effectiveness. There is an ongoing discussion about whether balloon-guide catheters or large-bore sheaths are needed for effective flow management. We compared general flow characteristics of proximal aspiration through a large-bore sheath and a balloon-guide catheter in a porcine in vivo model.

**MATERIALS AND METHODS:** We investigated blood flow in a porcine common carotid artery with and without aspiration (VacLok syringe and Penumbra pump, Pump MAX) through an 8F-long sheath and an 8F balloon-guide catheter. Blood hemodynamics were assessed via continuous duplex sonography.

**RESULTS:** Average vessel diameter and baseline blood flow were  $4.4 \pm 0.2$  mm and  $244 \pm 20$  mL/min, respectively. For the 8F sheath, pump aspiration resulted in a significant flow reduction ( $225 \pm 25$  mL/min,  $P < .001$ ), but with a persisting antegrade stream. Manual aspiration resulted in collapse of the vessel in 2 of 7 measurements and oscillatory flow with antegrade systolic and retrograde diastolic components in the remaining 5 measurements. Net flow was antegrade ( $52 \pm 44$  mL/min) in 3 and retrograde ( $-95 \pm 52$  mL/min) in the remaining 2 measurements. For balloon-guide catheters, balloon inflation always resulted in flow arrest. Additional pump or manual aspiration resulted in significant flow reversal of  $-1100 \pm 230$  and  $-468 \pm 46$  mL/min, respectively (both,  $P < .001$ ).

**CONCLUSIONS:** Only balloon-guide catheters allow reliable blood flow arrest and flow reversal in combination with aspiration via syringes or high-flow pump systems. Aspiration through an 8F sheath results in either collapse of the vessel or oscillatory flow, which can result in a net antegrade or retrograde stream.

**ABBREVIATIONS:** BGC = balloon-guide catheter; CCA = common carotid artery

Endovascular mechanical thrombectomy has been established as the standard treatment option for acute ischemic stroke caused by large-vessel occlusion.<sup>1</sup> Even though the basic principle of mechanical thrombectomy is established, actual procedures differ in many ways, ranging from the choice of stent retrievers to the choice of access catheters.<sup>2-4</sup> Recent clinical studies imply better procedural and clinical outcomes for patients who are treated with balloon-guide catheters (BGCs) compared with other carotid-access catheters such as large-bore sheaths.<sup>5,6</sup> Zaidat et al<sup>5</sup> found, in their analysis of the Systematic Evaluation of Patients Treated With Stroke Devices for Acute Ischemic Stroke (STRA-

TIS) Registry data, that BGCs are associated with higher rates of good clinical outcome (mRS  $\leq 2$ ), successful revascularization, a trend toward higher rates of complete first-pass revascularization, and a lower number of overall passes.<sup>7</sup> Because these data are not derived from randomized prospective trials, it is possible that the superiority of BGCs simply reflects their being used by more experienced interventionalists. Nonetheless, it is reasonable that blood flow management in the carotid artery is crucial for safety and effectiveness during mechanical thrombectomy.<sup>8</sup> It has been shown that thrombectomy maneuvers produce thousands of small clot fragments that may occlude small arterioles and capillaries.<sup>4</sup> The result can be small infarctions that can have a relevant clinical impact despite being invisible on MR imaging.<sup>9,10</sup> Hence, flow arrest is important regardless of the specific thrombectomy technique (eg, classic stent-retriever thrombectomy, A Direct Aspiration First Pass Technique [ADAPT], Solumbra, or other techniques). Antegrade blood flow should be reversed during mechanical thrombectomy to prevent embolization of clot frag-

Received April 30, 2018; accepted after revision August 13.

From the Departments of Diagnostic and Interventional Neuroradiology (O.N., D.W., H.M.H., J.S., T.S., F.S.M., M.W.) and Neurology (A.R.), RWTH Aachen University Hospital, Aachen, Germany.

Please address correspondence to Omid Nikoubashman, MD, Klinik für Neuroradiologie, Universitätsklinikum Aachen, Pauwelsstr 30, 52074 Aachen, Germany; e-mail: onikoubashman@ukaachen.de

<http://dx.doi.org/10.3174/ajnr.A5829>

ments.<sup>8</sup> This is usually attempted via blood aspiration through an access catheter in the internal carotid artery. There is a variety of access catheters, ranging from small (5F–7F) guiding catheters to large-bore sheath catheters (8F) and BGCs, but there is no consensus about which access catheter is most suitable.<sup>4,8,11–13</sup>

Mechanical thrombectomy is becoming more common, and many interventionalists must decide which technique to choose. Because empiric data are lacking and large randomized prospective studies are needed to resolve this issue from a clinical point of view, we addressed this question with a simple technical approach. To reflect basic principles of flow management in real-life settings, we quantified and compared flow characteristics and aspiration volumes of proximal aspiration through a large-bore sheath and a BGC with both manual and pump aspiration. Because it is practically impossible to quantify blood flow during mechanical thrombectomy in the ICA, let alone in the cerebral arteries, we decided to investigate flow characteristics in an in vivo porcine model.

### MATERIALS AND METHODS

All experiments were performed on 4 female Landrace swine (weight, 50–60 kg) with peri- and intrainterventional management as reported previously.<sup>14</sup> The experiments were performed in accordance with the German legislation governing animal studies following the “Guide for the Care and Use of Laboratory Animals” (<https://grants.nih.gov/grants/olaw/Guide-for-the-Care-and-use-of-laboratory-animals.pdf>) and the “Directive 2010/63/EU on the Protection of Animals Used for Scientific Purposes” ([https://www.researchgate.net/publication/233428185\\_DIRECTIVE\\_201063EU\\_on\\_the\\_protection\\_of\\_animals\\_used\\_for\\_scientific\\_purposes](https://www.researchgate.net/publication/233428185_DIRECTIVE_201063EU_on_the_protection_of_animals_used_for_scientific_purposes)). Official permission was granted from the governmental animal care and use office, Landesamt für Natur, Umwelt und Verbraucherschutz Nordrhein-Westfalen, Recklinghausen, Germany.

We investigated flow in a porcine common carotid artery (CCA) with and without aspiration through a large-bore sheath and a BGC. We chose the CCA because its diameter is comparable with that of the human ICA.<sup>15</sup> We adapted flow in the CCA, which has a physiologic blood flow that is twice as high the human ICA blood flow, by injecting blood clots into the subsequent arteries. This procedure was repeated until a blood flow between 200 and 280 mL/min was achieved in the target vessel. We assessed blood flow via duplex sonography (LOGIQ S8; GE Healthcare, Milwaukee, Wisconsin) by measuring vessel diameter and flow speed using the built-in software and GraphClick software (Arizona Software, Neuchâtel, Switzerland).

Instead of testing all possible access catheters ranging from 5F guide catheters to large-bore sheaths, we chose 1 large-bore sheath and 1 large-bore BGC to investigate flow characteristics in 2 setups that supposedly allow maximum flow control. We used an 8F-long sheath, Shuttle Select (Cook, Bloomington, Indiana; outer diameter, 3 mm; inner diameter, 2.87 mm) and an 8F Flow-Gate II BGC (Concentric Medical, Mountain View, California; outer diameter, 2.7 mm; inner diameter, 2.1 mm), which are currently the largest of the most commonly used proximal access catheters. Sheaths and BGCs were introduced through a femoral access and placed 5–7 cm behind the CCA origin. Blood flow was

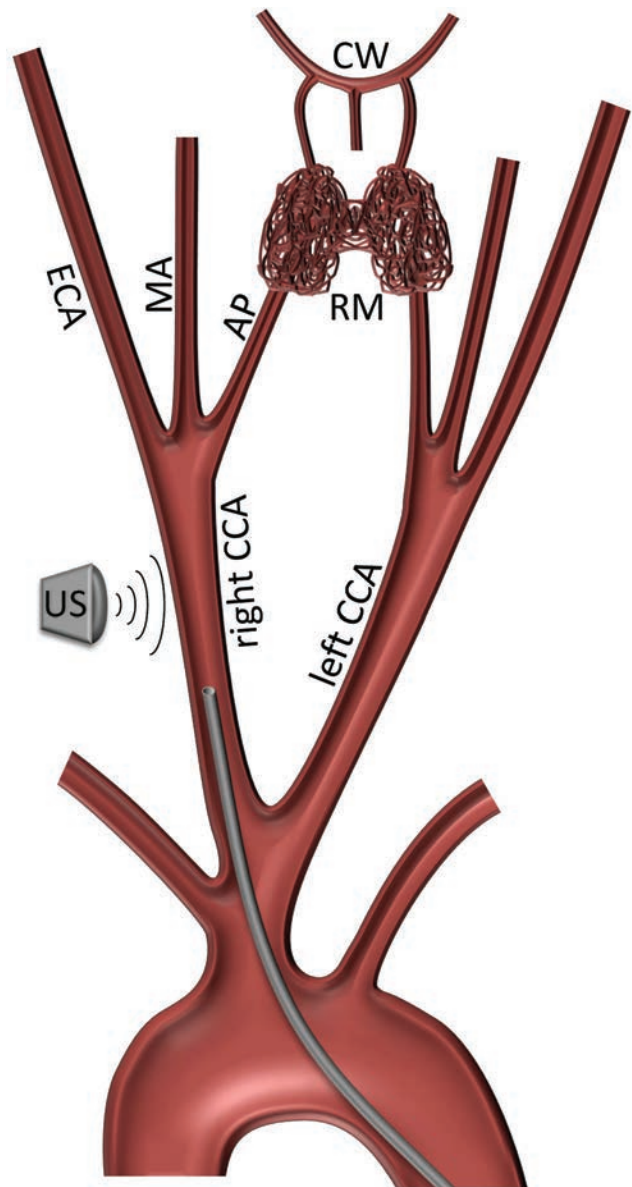


**FIG 1.** Schematic illustration of the porcine anatomy and the experimental setup. The catheter (*thick gray line*) is placed in the common carotid artery, which has a diameter comparable with that of the human internal carotid artery. The flow in the CCA was reduced to comparable values by clogging the subsequent vessels. US indicates sonography probe; ECA, external carotid artery; MA, maxillary artery; AP, ascending pharyngeal artery; RM, rete mirabile; CW, circle of Willis. Note that swine have a true bovine arch and that the internal carotid arteries arise from the rete mirabile, which is a spongiform conglomerate of blood vessels that serves as a filter for clots.

assessed 7–10 cm distal to the sheath/BGC tips (Fig 1). We did not measure immediately behind the catheter tips to avoid measuring blood flow in areas of turbulent flow. After quantifying the baseline blood flow in the CCA, we quantified blood flow with and without aspiration through the sheath and the inflated BGC. Aspiration was performed manually with a 60-mL VacLok syringe (Merit Medical Systems, South Jordan, Utah) and with a Penumbra pump, Pump MAX (Penumbra, Alameda, California), which is the most common aspiration pump, with the recommended vacuum pressure of  $-25.5$  Hg. All experiments were performed at least 7 times, and all measurements were included in our final

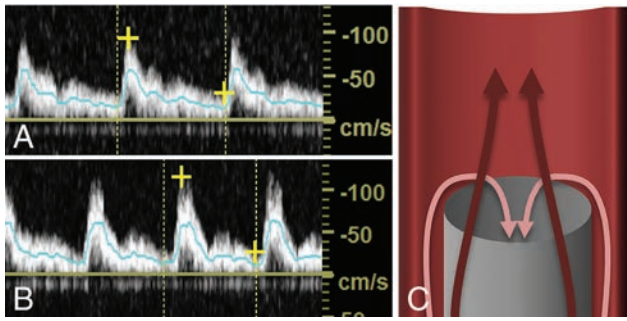


**FIG 2.** A, Typical sonography blood flow profile in the common carotid artery in our model. B, Typical flow profile in the common carotid artery during pump aspiration through an 8F sheath. Note that the profile is almost unchanged and flow remains antegrade. C, This feature is likely because aspiration results in an additional pressure gradient that mobilizes additional flow from the aortic arch into the CCA along the catheter (C, light arrows), while antegrade flow in the distal CCA is maintained (C, dark arrows).

analysis. Because our experiments resulted in considerable blood loss, not all experiments were repeated in all swine. However, every setup was performed in at least 2 swine to increase the variance. To restrict aspirated blood volume, we performed only 3 aspiration experiments with an inflated BGC as a proof of principle. Blood flow was assessed regularly between experiments to anticipate unnoticed shifts of baseline values.

### Statistical Analysis

Student *t* tests were used for comparison of flow volumes after testing our data for normal distribution with a Shapiro-Wilk test. *P* values of an  $\alpha$  level of  $\leq .05$  were significant. All statistical analyses were performed with SPSS 23 software (IBM, Armonk, New York).

### RESULTS

The average diameter of the CCA and baseline blood flow were  $4.4 \pm 0.2$  mm and  $244 \pm 20$  mL/min, respectively (Fig 1). The 8F sheath resulted in an average reduction of vessel diameter and cross-sectional area of 61% and 37%, respectively, and the sheath did not significantly reduce blood flow ( $236 \pm 25$  mL/min,  $P = .19$ ). Pump aspiration resulted in a significant flow reduction with a net flow of  $225 \pm 25$  mL/min ( $P < .001$ ) (Fig 2). However, flow always remained antegrade, and there was no flow arrest or reversal. Manual aspiration through the 8F sheath resulted in collapse of the vessel in 2 of 7 measurements. In the remaining 5 measurements, there was an oscillatory flow with antegrade flow in systole and retrograde flow in diastole (Fig 3). Net flow was antegrade ( $52 \pm 44$  mL/min) in 3 of 5 measurements and retrograde ( $-95 \pm 52$  mL/min) in the remaining 2 measurements.

The noninflated 8F BGC in the CCA led to an average reduction of vessel diameter and cross-sectional area of 61% and 37%, respectively, and slightly reduced blood flow (from  $244 \pm 20$  to  $228 \pm 22$  mL/min,  $P = .02$ ). Balloon inflation always resulted in arrest of antegrade flow (Fig 4). Additional pump aspiration and manual aspiration through an inflated BGC resulted in a constant and significant flow reversal with a flow of  $-1100 \pm 230$  and  $-468 \pm 46$  mL/min, respectively (both,  $P < .001$ ) (Fig 4). Net flow in the carotid artery was significantly lower when blood was

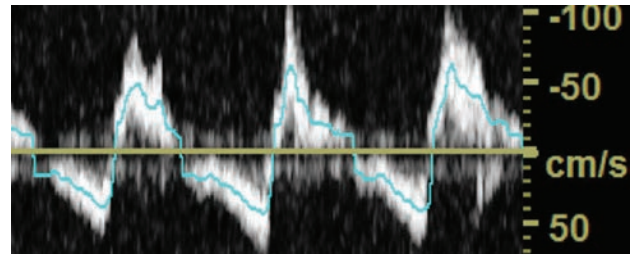


**FIG 3.** Oscillatory blood flow with antegrade flow in systole and retrograde flow in diastole after manual aspiration through the 8F sheath.

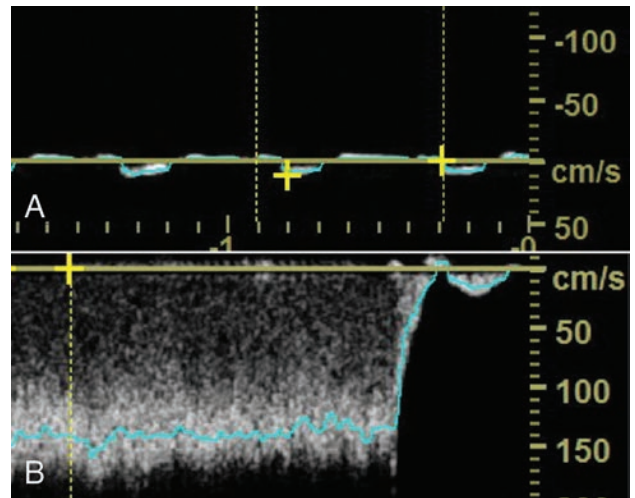


**FIG 4.** A, Balloon inflation results in flow arrest in the CCA. B, Manual aspiration through an inflated BGC results in a constant and significant flow reversal.

aspirated through an inflated BGC compared with the 8F sheath, regardless of pump or syringe aspiration (both,  $P < .001$ ).

### DISCUSSION

Ever since mechanical stroke treatment has been established as a standard treatment technique, the focus of neurointerventional stroke research has shifted to finding the optimal treatment techniques.<sup>1,2,4,16-18</sup> Proximal aspiration in the ICA to achieve flow reversal has been established as a standard technique for mechanical thrombectomy. In an average patient and without application of a balloon-guide catheter, which restricts antegrade flow, the amount of aspirated blood in the ICA should surpass its normal flow of 240 mL/min to achieve reliable flow reversal.<sup>19</sup> There is an ongoing discussion of whether BGCs or large-bore sheaths are needed for effective flow management. Large-bore sheaths allow aspiration of high-flow volumes up to approximately 1000 mL/min.<sup>20</sup> However, the handling of these sheaths is rather complicated because their stiffness necessitates additional guiding catheters for placement. BGCs allow reliable occlusion of the respective artery and consecutive reduction of antegrade flow. However, rather difficult handling and their comparably small inner diameters, which restrict the choice of catheters/devices that can be introduced through the BGC, prevent many interventionalists from using BGCs.

Our results show that the choice of carotid access catheter has an important impact on blood flow in the target vessel. We have

found that only BGCs allow reliable flow arrest in our in vivo porcine model. In a patient, this does not mean that balloon inflation results in arrest of cerebral perfusion because collaterals may maintain cerebral blood flow distal to the occlusion site. As long as the clot is located above the circle of Willis, flow from the posterior and anterior communicating arteries and the ophthalmic artery can sustain the full physiologic flow volume of the ICA and may cause embolization of clot fragments.<sup>21</sup> Consequently, aspiration of blood through an inflated BGC is necessary for reliable retrograde flow and control of peripheral embolization. Aspiration through the BGC with the syringe and with the Penumbra pump resulted in constant retrograde flow. However, only the syringe achieved high flow that surpassed the required antegrade flow rate of 240 mL/min for reliably reverting blood flow at the level of the terminal segment of the internal carotid artery. Therefore, we discourage using the Penumbra pump if flow reversal during mechanical thrombectomy is intended.

Surprisingly, aspiration with large-bore sheaths did not necessarily result in flow arrest or reversal, despite high-aspiration flow volumes. Aspiration through an 8F sheath with a syringe or a Penumbra pump results in flow volumes of  $\approx 800$  and  $\approx 240$  mL/min, respectively.<sup>20</sup> By simply adding antegrade and retrograde flow, we would have expected a net backward flow of  $>500$  mL/min with the syringe and flow arrest with the Penumbra pump. However, aspiration through an 8F sheath did not result in reliable flow reversal. At best, there was oscillatory flow with small net backward flow volumes, which would not suffice to reverse blood flow above the circle of Willis. This behavior is likely because aspiration results in an additional pressure gradient that mobilizes additional flow from the aortic arch into the CCA along the catheter while antegrade flow in the ICA is maintained (Fig 2). In the worst-case scenario, aspiration resulted in vessel collapse, which coincides with our clinical experience: During our interventions, we have found that when too much suction is applied, blood cannot be aspirated until the suction is decreased either because the catheter tip has engaged the vessel wall or—as we surmise—the vessel collapsed. Vessel collapse in perfused vessels is mainly due to the Bernoulli effect, which causes the vessel walls to converge during aspiration of high flow volumes. This issue is relevant in clinical practice because it is almost impossible to predict vessel collapse: Many factors such as flow volume, position of the catheter, occlusion site, and the diameter of the vessel and its rigidity have an impact on the applied forces that cause vessel collapse. Given that aspiration with large-bore sheaths did not reliably result in flow arrest or reversal, we discourage using large-bore catheters or sheaths for flow arrest in the ICA, regardless of syringe or pump aspiration. Furthermore, we specifically discourage using smaller guiding catheters (5F–7F), which are very common because of their easy handling and low cost but face the same issue of insufficient aspiration like the larger sheath tested in our experiment. Notably, even under ideal conditions (perfect vacuum and no external resistors), aspiration flow through a 6F catheter with a stent retriever in its lumen does not reach 240 mL/min.<sup>17</sup>

### Limitations

A major limitation of our study is that it does not allow assessing whether cerebral blood flow above the circle of Willis is reversed.

Such an experiment would need transcranial Doppler measurements in patients during thrombectomy, which is impossible due to the artifacts caused by the microcatheter and stent retriever in place. As an approximation, we estimated the following: Physiologic blood flow in an internal carotid artery is approximately 240 mL/min. It has been shown that aspiration flow through an 8F BGC with pump and syringe aspiration can surpass 350 mL/min (pump) and 500 mL/min (syringe), which again should be sufficient to allow flow arrest despite collateral flow. Nonetheless, there remains the possibility that collateral flow through the circle of Willis may be enough to maintain antegrade cerebral blood flow despite high-aspiration flow volumes.<sup>20</sup> Also, due to the nature of our study, we could not investigate whether flow reversal has an effect on clinical outcome, but our results may serve as a foundation for future research that specifically addresses this question. Also, even though the porcine cardiovascular system serves as an excellent model, it may be arguable whether our quantitative results can be translated to patients without restrictions. Nonetheless, because it is impossible to conduct such an experiment in patients the porcine model is the best approximation to real life.<sup>22</sup> Last, flow volume measurements based on duplex sonography may not always reflect actual flow volumes and are a minor limitation of our study.<sup>23</sup> However, even if flow volumes are over- or underestimated, our results remain valid on a qualitative level because the direction of flow is unaffected by the measuring method.

### CONCLUSIONS

Only BGCs allow reliable flow reversal and should be used with syringes or high-flow pump systems. Aspiration through an 8F sheath in the ICA results in either collapse of the vessel or oscillatory flow with antegrade flow in systole and retrograde flow in diastole, which can result in a net antegrade or retrograde flow.

Disclosures: Martin Wiesmann—UNRELATED: Consultancy: Stryker Neurovascular; Payment for Lectures Including Service on Speakers Bureaus: Bracco, Medtronic, Siemens, Stryker Neurovascular; Payment for Development of Educational Presentations: Abbott, ab medica, Acandis, Bayer HealthCare, Bracco, B. Braun, Codman Neurovascular, Kaneka Pharma Europe, Medtronic, Dahlhausen Medizintechnik, Microvention, Penumbra, phenox, Philips Healthcare, Route 92, Siemens, Silk Road Medical, St. Jude, Stryker Neurovascular.\* \*Money paid to the institution.

### REFERENCES

1. Goyal M, Menon BK, van Zwam WH, et al; HERMES collaborators. **Endovascular thrombectomy after large-vessel ischaemic stroke: a meta-analysis of individual patient data from five randomised trials.** *Lancet* 2016;387:1723–31 CrossRef Medline
2. Maus V, Behme D, Kabbasch C, et al. **Maximizing first-pass complete reperfusion with SAVE.** *Clin Neuroradiol* 2018;28:327–38 CrossRef Medline
3. Turk AS, Frei D, Fiorella D, et al. **ADAPT FAST study: a direct aspiration first pass technique for acute stroke thrombectomy.** *J Neurointerv Surg* 2014;6:260–64 CrossRef Medline
4. Chueh JY, Puri AS, Wakhloo AK, et al. **Risk of distal embolization with stent retriever thrombectomy and ADAPT.** *J Neurointerv Surg* 2016;8:197–202 CrossRef Medline
5. Zaidat O, Liebeskind D, Jahan R, et al. **O-005 influence of balloon, conventional, or distal catheters on angiographic and technical outcomes in STRATIS.** *J Neurointerv Surg* 2016;8(Suppl 1):A3.2–4 CrossRef
6. Velasco A, Buerke B, Stracke CP, et al. **Comparison of a balloon**

- guide catheter and a non-balloon guide catheter for mechanical thrombectomy. *Radiology* 2016;280:169–76 CrossRef Medline
7. Mueller-Kronast NH, Zaidat OO, Froehler MT, et al. **Systematic evaluation of patients treated with neurothrombectomy devices for acute ischemic stroke: primary results of the STRATIS Registry.** *Stroke* 2017;48:2760–68 CrossRef Medline
  8. Chueh JY, Kühn AL, Puri AS, et al. **Reduction in distal emboli with proximal flow control during mechanical thrombectomy: a quantitative in vitro study.** *Stroke* 2013;44:1396–401 CrossRef Medline
  9. Jouvent E, Poupon C, Gray F, et al. **Intracortical infarcts in small vessel disease: a combined 7-T postmortem MRI and neuropathological case study in cerebral autosomal-dominant arteriopathy with subcortical infarcts and leukoencephalopathy.** *Stroke* 2011;42:e27–30 CrossRef Medline
  10. Shih AY, Blinder P, Tsai PS, et al. **The smallest stroke: occlusion of one penetrating vessel leads to infarction and a cognitive deficit.** *Nat Neurosci* 2013;16:55–63 CrossRef Medline
  11. Eesa M, Almekhlafi MA, Mitha AP, et al. **Manual aspiration thrombectomy through balloon-tipped guide catheter for rapid clot burden reduction in endovascular therapy for ICA L/T occlusion.** *Neuroradiology* 2012;54:1261–65 CrossRef Medline
  12. Lally F, Soorani M, Woo T, et al. **In vitro experiments of cerebral blood flow during aspiration thrombectomy: potential effects on cerebral perfusion pressure and collateral flow.** *J Neurointerv Surg* 2016;8:969–72 CrossRef Medline
  13. Madjidyar J, Hermes J, Freitag-Wolf S, et al. **Stent-thrombus interaction and the influence of aspiration on mechanical thrombectomy: evaluation of different stent retrievers in a circulation model.** *Neuroradiology* 2015;57:791–97 CrossRef Medline
  14. Nikoubashman O, Pjontek R, Brockmann MA, et al. **Retrieval of migrated coils with stent retrievers: an animal study.** *AJNR Am J Neuroradiol* 2015;36:1162–66 CrossRef Medline
  15. Mühlenbruch G, Nikoubashman O, Steffen B, et al. **Endovascular broad-neck aneurysm creation in a porcine model using a vascular plug.** *Cardiovasc Intervent Radiol* 2013;36:239–44 CrossRef Medline
  16. Wiesmann M, Brockmann MA, Heringer S, et al. **Active push deployment technique improves stent/vessel-wall interaction in endovascular treatment of acute stroke with stent retrievers.** *J Neurointerv Surg* 2017;9:253–56 CrossRef Medline
  17. Nikoubashman O, Alt JP, Nikoubashman A, et al. **Optimizing endovascular stroke treatment: removing the microcatheter before clot retrieval with stent-retrievers increases aspiration flow.** *J Neurointerv Surg* 2017;9:459–62 CrossRef Medline
  18. Massari F, Henninger N, Lozano JD, et al. **ARTS (Aspiration-Retriever Technique for Stroke): initial clinical experience.** *Interv Neuroradiol* 2016;22:325–32 CrossRef Medline
  19. Schöning M, Walter J, Scheel P. **Estimation of cerebral blood flow through color duplex sonography of the carotid and vertebral arteries in healthy adults.** *Stroke* 1994;25:17–22 CrossRef Medline
  20. Nikoubashman O, Wischer D, Hennemann HM, et al. **Under pressure: comparison of aspiration techniques for endovascular mechanical thrombectomy.** *AJNR Am J Neuroradiol* 2018;39:905–09 CrossRef Medline
  21. Eckard DA, Purdy PD, Bonte FJ. **Temporary balloon occlusion of the carotid artery combined with brain blood flow imaging as a test to predict tolerance prior to permanent carotid sacrifice.** *AJNR Am J Neuroradiol* 1992;13:1565–69 Medline
  22. Gralla J, Schroth G, Remonda L, et al. **A dedicated animal model for mechanical thrombectomy in acute stroke.** *AJNR Am J Neuroradiol* 2006;27:1357–61 Medline
  23. Burns PN, Jaffe CC. **Quantitative flow measurements with Doppler ultrasound: techniques, accuracy, and limitations.** *Radiol Clin North Am* 1985;23:641–57 Medline

# Low Wall Shear Stress Is Associated with Local Aneurysm Wall Enhancement on High-Resolution MR Vessel Wall Imaging

W. Xiao, T. Qi, S. He, Z. Li, S. Ou, G. Zhang, X. Liu, Z. Huang, and F. Liang



## ABSTRACT

**BACKGROUND AND PURPOSE:** Some retrospective studies have found that the aneurysm wall enhancement on high-resolution MR vessel wall postgadolinium T1WI has the potential to distinguish unstable aneurysms. This study aimed to identify hemodynamic characteristics that differ between the enhanced and nonenhanced areas of the aneurysm wall on high-resolution MR vessel wall postgadolinium T1WI.

**MATERIALS AND METHODS:** TOF-MRA and high-resolution MR vessel wall T1WI of 25 patients were fused to localize the enhanced area of the aneurysm wall. Using computational fluid dynamics, we studied the aneurysm models. Mean static pressure, mean wall shear stress, and oscillatory shear index were compared between the enhanced and nonenhanced areas.

**RESULTS:** The aneurysmal enhanced area had lower wall shear stress ( $P < .05$ ) and a lower oscillatory shear index ( $P = .021$ ) than the nonenhanced area. In addition, the whole aneurysm had lower wall shear stress ( $P < .05$ ) and a higher oscillatory shear index ( $P = .007$ ) than the parent artery.

**CONCLUSIONS:** This study suggests that there are hemodynamic differences between the enhanced and nonenhanced areas of the aneurysm wall on high-resolution MR vessel wall postgadolinium T1WI.

**ABBREVIATIONS:** HR-VWI = high-resolution MR vessel wall imaging; OSI = oscillatory shear index; P = mean static pressure; WSS = wall shear stress

An intracranial aneurysm is regarded as the most common culprit for nontraumatic subarachnoid hemorrhage, a devastating clinical situation that is usually followed by the risks of aneurysm rebleeding, cerebral vascular spasm, and hydrocephalus. Imaging examinations, one of which is high-resolution MRI, have been used to discover, diagnose, estimate, and evaluate aneurysms. For instance, as a noninvasive examination, high-resolution MRI can be used as a screening method and a tool for follow-up visits, and it can help visualize dissecting aneurysms.<sup>1</sup> Moreover, it can be used to evaluate the depth of aneurysm location before open surgery such as the clipping of middle cerebral bifurcation aneurysms. In patients with subarachnoid hemor-

rhage and multiple aneurysms, MR imaging can help discriminate the responsible aneurysm. Fu et al<sup>2</sup> proposed that circumferential aneurysmal wall enhancement on high-resolution MR vessel wall imaging (HR-VWI) is correlated with headaches and third nerve palsy caused by unruptured aneurysms. Two previous studies indicated that as an indicator of inflammation, the aneurysm wall enhancement on HR-VWI postgadolinium T1WI has the potential for discriminating unstable aneurysms from stable ones.<sup>3,4</sup> Wang et al<sup>5</sup> found that all partial wall enhancement of 16 aneurysms was in the irregularly shaped portions or daughter sacs in their study.

Computational fluid dynamics has been used to investigate hemodynamic parameters that are linked with cerebral aneurysm formation, progression, and rupture, one of which is wall shear stress (WSS), the most highlighted but controversial parameter.<sup>6-8</sup> However, to our knowledge, no published investigations have revealed the association between hemodynamic characteristics and aneurysm wall enhancement on HR-VWI postgadolinium T1WI.

Therefore, we designed a retrospective study into hemodynamic parameters on aneurysm models with local wall enhancement on HR-VWI postgadolinium T1WI, to provide a new idea for the future investigation into wall enhancement.

Received May 3, 2018; accepted after revision July 30.

From the Departments of Neurosurgery (W.X., T.Q., S.O., G.Z., X.L., Z.H., F.L.) and Radiology (S.H., Z.L.), The First Affiliated Hospital, Sun Yat-sen University, Guangzhou, China.

Weiping Xiao and Tiewei Qi contributed equally to this work.

Please address correspondence to Feng Liang, MD, First Affiliated Hospital of Sun Yat-sen University, Department of Neurosurgery, 58 Zhongshan Er Rd, Guangzhou, Guangdong, 510080, China; e-mail: liangf6@mail.sysu.edu.cn

 Indicates article with supplemental on-line appendix and table.

 Indicates article with supplemental on-line photos.

<http://dx.doi.org/10.3174/ajnr.A5806>

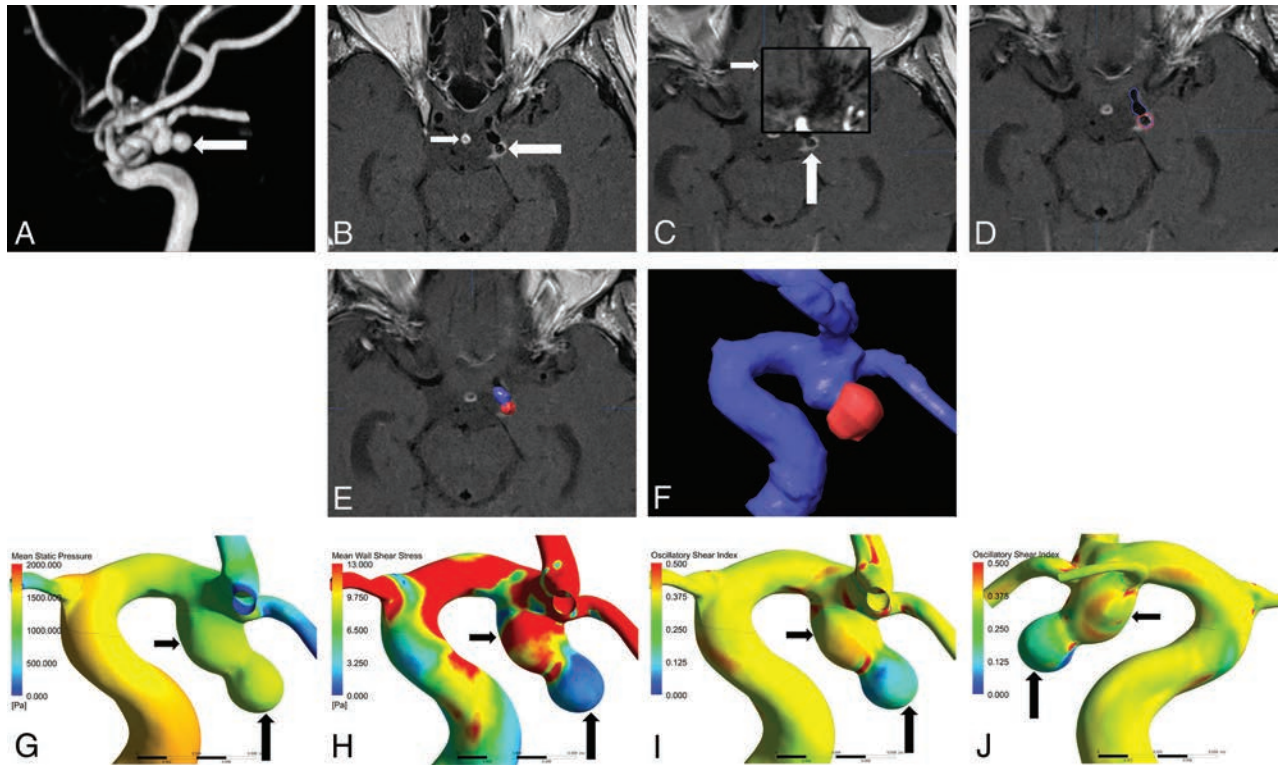


**FIG 1.** A, MRA shows a posterior communicating artery aneurysm (*white arrow*). B, Local enhancement on the aneurysmal wall on HR-VWI postgadolinium T1WI (*large white arrow*) compared with that of the pituitary infundibulum (*small white arrow*). C, Auto Fusion of HR-VWI T1WI (*large white arrow*) and TOF-MRA (*small white arrow*) images. D–F, Location of the enhanced area (highlighted in red) on the aneurysm (displayed in blue). G, Mean static pressure distribution. H, WSS distribution. The enhanced area has lower mean WSS (*large black arrow*) than the nonenhanced area (*small black arrow*). I and J, OSI distribution. The enhanced area has lower OSI (*large black arrow*) than the nonenhanced area (*small black arrow*).

## MATERIALS AND METHODS

### Patient Selection

This retrospective study protocol was approved by the ethics committees of the First Affiliated Hospital, Sun Yat-sen University, and informed consent was exempted. Patients with aneurysms who underwent an HR-VWI examination before an operation or conservative treatment from January 2015 to March 2016 were reviewed. The inclusion criteria were as follows: 1) intracranial aneurysms diagnosed by CTA, MRA, or DSA; 2) anterior circulation aneurysms; 3) HR-VWI postgadolinium T1WI revealing wall enhancement; and 4) available HR-VWI and DSA 3D rotational angiography data. The exclusion criteria were the following: 1) fusiform, dissecting aneurysms or pseudoaneurysms; 2) anterior communicating artery aneurysms or posterior circulation artery aneurysms; and 3) HR-VWI and 3D rotational angiography data unavailable.

### Imaging Analysis

Two experienced neurovascular radiologists (with >5 years' experience in neurovascular imaging) analyzed pre- and postcontrast T1-weighted images, retrospectively and respectively, to determine whether there was local enhancement. They were blinded to the patients' clinical data and other sequences except for 3D-TOF imaging before the analysis. Discordance between 2 readers was resolved by consensus. One of the readers performed a second analysis after 3 weeks. By comparing pre- and postcontrast T1WI, we defined the wall enhancement as circumferential when the whole aneurysm wall was enhanced after contrast agent infusion;

otherwise, it was defined as partial when only part of the aneurysm wall was enhanced. Only aneurysms with local enhancement were enrolled into this study. Protocols of HR-VWI and 3D rotational angiography are provided in the On-line Appendix.

### Location of Aneurysm Wall Enhanced Area

DICOM files of HR-VWI were imported into iPlan cranial 3.0 (BrainLab, Munich, Germany). Then, in the projection of Image Fusion, the HR-VWI T1WI and TOF-MRA images were chosen and paired (Fig 1C and Fig 2C). They were then merged using the function of Auto Fusion. After Auto Fusion, merged images were checked on the axial view and fine manual fusion was performed for tiny adjustments, which ensured the precision of Image Fusion. Aneurysm models were reconstructed with TOF-MRA using Auto Segmentation. Irrelevant arteries were cut off manually, with aneurysms, parent arteries, and the important branches preserved. Aneurysm wall enhanced areas were also reconstructed using manual segmentation with T1WI (Fig 1D and Fig 2D). The aneurysm models and aneurysm wall enhanced area were displayed simultaneously to locate the enhanced area (Fig 1E, -F and Fig 2E, -F).

### Aneurysm Modeling

The patients' 3D rotational angiography DICOM files were imported into Mimics 17.0 (Materialise, Leuven, Belgium) for a rough model reconstruction by threshold segmentation. Then the unconnected regions were manually removed with the region-

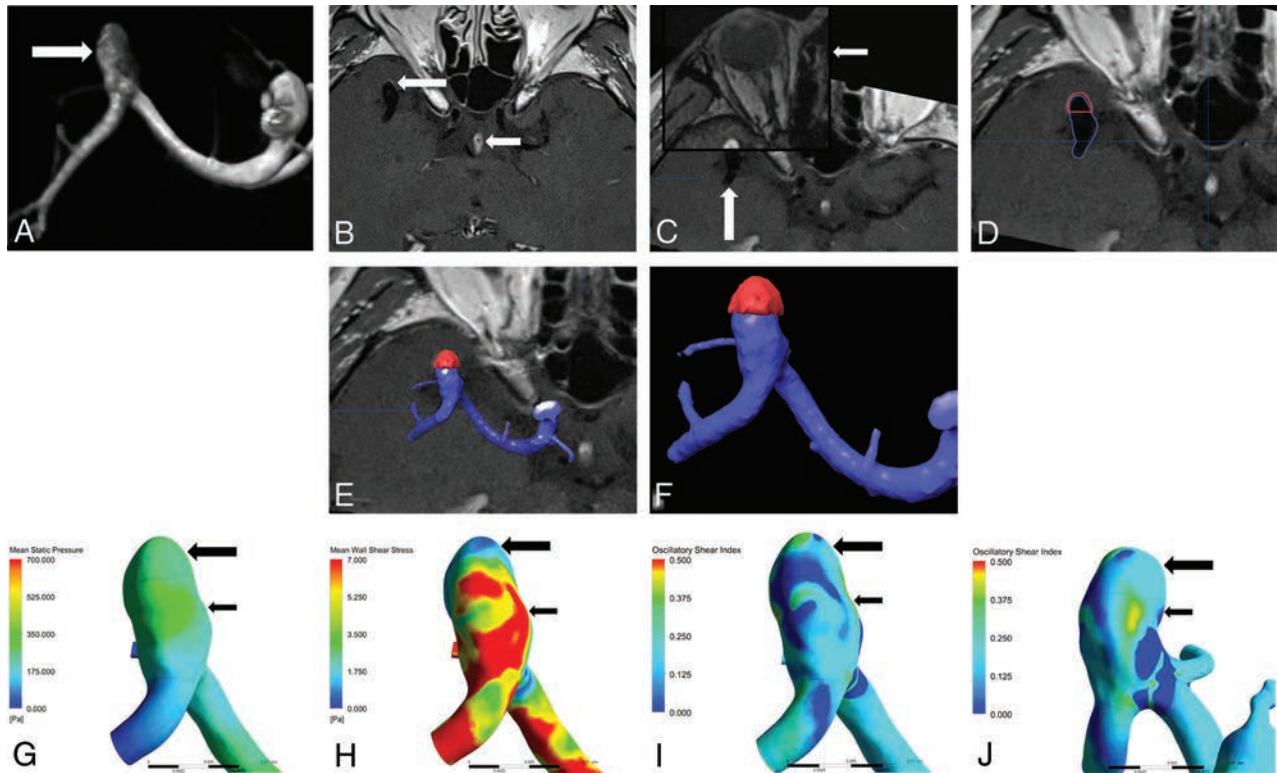


**FIG 2.** A, MRA shows a middle cerebral artery bifurcation aneurysm (*white arrow*). B, Local enhancement on the aneurysmal wall on HR-VWI postgadolinium TIWI (*large white arrow*) compared with that of the pituitary infundibulum (*small white arrow*). C, Auto Fusion of HR-VWI TIWI (*large white arrow*) and TOF-MRA (*small white arrow*) images. D–F, Location of enhanced area (highlighted in red) on the aneurysm (displayed in blue). G, Mean static pressure distribution. H, WSS distribution. The enhanced area has lower mean WSS (*large black arrow*) than the nonenhanced area (*small black arrow*). I and J, OSI distribution. The enhanced area has lower OSI (*large black arrow*) than the nonenhanced area (*small black arrow*).

growing algorithm. Meanwhile, branches extending from the parent artery and the aneurysm were preserved.<sup>9</sup> Then, the vascular models were converted to a stereolithography format and imported into Geomagic Studio 2013 (Geomagic, Research Triangle Park, North Carolina) and SolidWorks 2012 (Dassault Systemes, Waltham, Massachusetts) successively for smoothing, surface construction, cutting off distal redundant arteries along with cutting out vascular inlets and outlets, and keeping the proximal parent artery at least 2 cm long to ensure the numeric stability.

### Computational Fluid Dynamics Analysis

All the aneurysm models were loaded into Fluent Software 17.0 (ANSYS Corporation, Canonsburg, Pennsylvania) for meshing. In addition, the aneurysm wall-enhanced area and the whole aneurysm area were calculated, and the enhanced area ratio was defined as aneurysm wall enhanced area divided by the whole aneurysm area. The enhanced area, nonenhanced area, parent artery, inlets, and outlets of the aneurysm models were selected and defined. Computational fluid dynamics simulations were performed under the transient status, by setting the solver type as pressure-based, the velocity formulation as absolute, and the solver time as transient. The vessel was disposed as a rigid wall with no-slip boundary conditions, neglecting the gravity effect. A laminar and incompressible blood flow, with density and viscosity set as  $1060 \text{ kg/m}^3$  and  $0.004 \text{ Pa} \cdot \text{s}$ , respectively, was used in the calculation.<sup>10</sup> The pulsatile velocity profile of the ICA, which was

obtained from a middle-aged female patient with carotid duplex sonography, was imposed at the inlets, with all the vascular outlets defined as zero pressure boundary conditions. Time-step size was set at 0.02 seconds; the number of time-steps was set at 40. In addition, maximum iterations ranged from 40 to 100. Detailed information about pulsatile ICA velocity can be seen in the Online Appendix.

### Hemodynamic Analysis

Three hemodynamic parameters, which were time-averaged over a cardiac cycle of enhanced area, nonenhanced area, the whole aneurysm, and parent artery, respectively, were calculated, namely mean static pressure (P), mean wall shear stress, and oscillatory shear index (OSI).<sup>8</sup> To compare hemodynamic differences between ruptured and unruptured aneurysms, we calculated the P and WSS of the enhanced area and the whole aneurysm normalized by the parent artery P and WSS.

### Statistical Analysis

Statistical analysis was performed using SPSS 20.0 (IBM, Armonk, New York). The agreement between 2 observers for the presence of local enhancement was evaluated by a  $\kappa$  value. Normally distributed variables were expressed as mean  $\pm$  SD and analyzed with a paired-samples *t* test. Non-normally distributed variables were expressed as the median (interquartile range) and analyzed using a nonparametric paired Wilcoxon rank sum test. Statistical significance was indicated at the .05 level.

**Table 1: Hemodynamic comparison between enhanced and nonenhanced areas<sup>a</sup>**

Variables	Enhanced Area	Nonenhanced Area	P Value <sup>b</sup>
P (Pa)	183.2600 (97.4100–242.9950)	158.8200 (103.5900–220.2000)	.115
WSS (Pa)	3.7255 (1.8487–8.3531)	7.5342 (4.6062–11.1105)	.000 <sup>c</sup>
OSI	0.2288 ± 0.0918	0.3008 ± 0.0890	.021 <sup>c</sup>

<sup>a</sup>Data are expressed as means for normally distributed continuous variables, and as the median for non-normally distributed variables. Numbers in parentheses are interquartile range.

<sup>b</sup>A P value < .05 was statistically significant.

<sup>c</sup>Statistically significant.

**Table 2: Hemodynamic comparison between the whole aneurysm and parent artery<sup>a</sup>**

Variables	Whole Aneurysm	Parent Artery	P Value <sup>b</sup>
P (Pa)	161.4600 (106.7050–220.5200)	181.3400 (104.2630–268.1350)	.313
WSS (Pa)	6.8341 ± 3.7246	9.0612 ± 3.3256	.000 <sup>c</sup>
OSI	0.3402 ± 0.0629	0.2859 ± 0.0560	.007 <sup>c</sup>

<sup>a</sup>Data are expressed as means for normally distributed continuous variables, and as the median for non-normally distributed variables. Numbers in parentheses are interquartile range.

<sup>b</sup>A P value < .05 was statistically significant.

<sup>c</sup>Statistically significant.

## RESULTS

The 2 readers' diagnoses on local enhancement were well-matched ( $\kappa = 0.87$ ). The readers' first and second diagnoses were also consistent ( $\kappa = 0.90$ ). Among 87 patients with 94 aneurysms reviewed, 34 aneurysms had circumferential wall enhancement, while 25 exhibited local enhancement (7 men and 18 women; 8 ruptured and 17 unruptured; mean age, 54.7 years; 8 middle cerebral artery bifurcation aneurysms, 14 posterior communicating artery aneurysms, and 3 ophthalmic artery aneurysms). The aneurysm sizes ranged from 3.2 to 12.9 mm, with a mean enhanced area ratio of 0.37. The number of mean nodes and elements of the aneurysm models were 666,351 and 3,698,735.

### Comparison between Enhanced and Nonenhanced Areas

As is shown in Table 1, the WSS and OSI of the aneurysmal enhanced area were both significantly lower than those of the non-enhanced area (median, 3.7255 vs 7.5342;  $P < .05$ ; mean, 0.2288 ± 0.0918 vs 0.3008 ± 0.0890;  $P = .021$ , respectively). No difference was found regarding mean static pressure.

### Comparison between the Whole Aneurysm and Parent Artery

There were lower WSS (mean, 6.8341 ± 3.7246 vs 9.0612 ± 3.3256;  $P < .05$ ) and higher OSI (mean, 0.3402 ± 0.0629 vs 0.2859 ± 0.0560,  $P = .007$ ) on the whole aneurysm wall than on the parent artery (Table 2). No difference was found regarding mean static pressure.

### Comparison between the Ruptured and Unruptured Aneurysms

There were no statistically significant hemodynamic differences between the ruptured and unruptured aneurysms, either at the enhanced region or on the whole aneurysm (On-line Table).

## DISCUSSION

To our knowledge, our study is the first to reveal the association between hemodynamic characteristics and aneurysm wall enhancement on HR-VWI postgadolinium T1WI.

High-resolution MRI has been used for intracranial aneurysm evaluation and assessment in the past few years.<sup>2,4,11</sup> Several studies have reported the predicting role of high-resolution MRI in distinguishing unstable intracranial aneurysms.<sup>2,4,12</sup> As previ-

ously reported,<sup>13</sup> the aneurysm wall enhancement on HR-VWI postgadolinium T1WI could serve as an independent risk factor for the prediction of aneurysm rupture. On the other hand, hemodynamic forces are believed to act as a prominent factor in aneurysm initiation, progression, and rupture but are poorly understood.<sup>7</sup> Specifically, WSS, one of the most frequently explored but still controversial and puzzling hemodynamic parameters, either high or low, has been shown to be correlated with aneurysm progression and rupture.<sup>7,14,15</sup> However, the hemodynamic characteristics correlated with the enhanced area of the aneurysm wall on HR-VWI post-

gadolinium T1WI have still not been investigated. Therefore, in this study, computational fluid dynamics was performed on aneurysm models generated from 25 patients with local aneurysm enhancement on HR-VWI postgadolinium T1WI, for hemodynamic simulation and parameter calculation.

In our study, the WSS and OSI of the aneurysmal enhanced area were both significantly lower than those of the nonenhanced area (Fig 1H–J and Fig 2H–J). In addition, higher WSS was found in the parent artery in contrast to the whole aneurysm sac due to arterial curvature and tortuosity.<sup>15</sup> The abrupt geometric change caused aneurysm blood turbulence, thus resulting in higher aneurysmal OSI. There were no statistically significant hemodynamic differences between the ruptured and unruptured aneurysms, either at the enhanced region or in the whole aneurysm.

Because WSS is the tangential force exerted by the horizontally moving fluid on the surface<sup>7</sup> and OSI denotes WSS fluctuation magnitude and the tangential force oscillation in a cardiac cycle,<sup>8</sup> low WSS with low OSI may reflect a concentrated blood inflow jet at the enhanced area. We assume that a regional concentrated inflow jet is likely to damage the endothelial cell layer and lead to inflammation, thus changing the aneurysm geometry and promoting its tendency to grow or rupture. In fact, local enhancement of 17 aneurysms in our study was present in the irregularly shaped portions or in daughter sacs, both of which are normally regarded as risk factors for aneurysm rupture. The endothelial damage could possibly cause contrast agent adhesion or uptake or leakage.

Exposure to low WSS has been demonstrated to promote vascular permeability in some studies.<sup>16–18</sup> Conklin et al<sup>16</sup> performed porcine experiments and proposed that low WSS could decrease occludin expression and thus increase vascular permeability. Himgburg et al<sup>18</sup> also discovered that being exposed to high WSS, the endothelial permeability to albumin decreased in porcine models. Thus, intra-aneurysmal sites being exposed to low WSS are likely to exhibit elevated permeability to contrast agent, which is presented as local enhancement on HR-VWI postgadolinium T1WI. More advanced studies are needed to confirm this hypothesis.

Several studies also suggested that applying directly to the en-

endothelial cells and acting as a mechanobiological trigger, low WSS may predispose the region to the dysfunction of flow-induced nitric oxide, upregulate endothelial surface adhesion molecules, promote the permeability of endothelial cells, and, thus, facilitate atherosclerotic and inflammatory cell infiltration.<sup>10,14,19-21</sup> Edjlali et al<sup>3</sup> proposed the potential of low WSS in monitoring the aneurysm wall inflammatory process. Hu et al<sup>4</sup> collected a specimen of the aneurysm wall from a patient intraoperatively, which had exhibited local wall enhancement on the high-resolution MRI, and the following histologic study revealed phagocyte and lymphocyte invasion. In our study, we found that the whole aneurysm wall had lower mean WSS than the parent artery. In addition, the enhanced area had lower WSS than the nonenhanced region in the aneurysm as a whole. Low WSS may, therefore, underlie the aneurysm wall local enhancement on HR-VWI postgadolinium T1WI hemodynamically, which is summarized in On-line Fig 4. Future larger studies and further histologic investigation are needed to support this hypothesis.

In an unruptured aneurysm study, low WSS was found to colocalize with thin, easily visualized translucent regions of the aneurysm sac.<sup>22</sup> These regions were thought to be fragile locations of the aneurysm wall that lead to rupture. In addition, in studies on ruptured aneurysms, low WSS was associated with the aneurysm rupture point.<sup>10,20,22,23</sup> In our study, low WSS was also associated with a local enhanced area of the aneurysm wall; the association indicates that the enhanced area may also be the weak part of aneurysm wall. In addition, there were no statistically significant hemodynamic differences between the ruptured and unruptured aneurysms, which indicates that these unruptured aneurysms with local wall enhancement may have a potential risk similar to that of ruptured aneurysms.

### Limitations

In our study, all the aneurysm models were analyzed using the same pulsatile velocity profile of the ICA instead of patient-specific analysis because carotid duplex sonography is not a clinical routine examination. However, it may be able to reflect the hemodynamic differences in various areas of the same model, which we are trying to find. Moreover, we have normalized the aneurysmal values by the parent vessel values to reduce the influence of inlet boundary conditions when making comparisons between different aneurysms.

Moreover, the small number of the patients enrolled into this study may also introduce bias. This may be partly due to the difficulties and risks for patients with unstable and ruptured aneurysms undergoing time-consuming MR imaging examinations. The developing technique discussed here will shorten the examination time and help solve this problem to some extent.

### CONCLUSIONS

The results of this study indicate that hemodynamic differences exist between the enhanced and nonenhanced areas of the aneurysm wall on HR-VWI postgadolinium T1WI. The mean WSS of the aneurysm enhanced area is lower than that of the nonenhanced area, suggesting that low WSS may be an important hemodynamic factor that contributes to the aneurysm wall local

enhancement. In addition, the OSI of the aneurysm enhanced area was lower than that of the nonenhanced area, reflecting a comparatively concentrated inflow jet.

### REFERENCES

1. Matouk CC, Cord BJ, Yeung J, et al. **High-resolution vessel wall magnetic resonance imaging in intracranial aneurysms and brain arteriovenous malformations.** *Top Magn Reson Imaging* 2016;25:49–55 Medline
2. Fu Q, Guan S, Liu C, et al. **Clinical significance of circumferential aneurysmal wall enhancement in symptomatic patients with unruptured intracranial aneurysms: a high-resolution MRI study.** *Clin Neuroradiol* 2017 Jun 27. [Epub ahead of print] CrossRef Medline
3. Edjlali M, Gentric JC, Régent-Rodriguez C, et al. **Does aneurysmal wall enhancement on vessel wall MRI help to distinguish stable from unstable intracranial aneurysms?** *Stroke* 2014;45:3704–06 CrossRef Medline
4. Hu P, Yang Q, Wang DD, et al. **Wall enhancement on high-resolution magnetic resonance imaging may predict an unsteady state of an intracranial saccular aneurysm.** *Neuroradiology* 2016;58:979–85 CrossRef Medline
5. Wang GX, Wen L, Lei S, et al. **Wall enhancement ratio and partial wall enhancement on MRI associated with the rupture of intracranial aneurysms.** *J Neurointerv Surg* 2018;10:566–70 CrossRef Medline
6. Qiu T, Jin G, Bao W, et al. **Intercorrelations of morphology with hemodynamics in intracranial aneurysms in computational fluid dynamics.** *Neurosciences (Riyadh)* 2017;22:205–12 CrossRef Medline
7. Qiu T, Jin G, Xing H, et al. **Association between hemodynamics, morphology, and rupture risk of intracranial aneurysms: a computational fluid modeling study.** *Neurol Sci* 2017;38:1009–18 CrossRef Medline
8. Longo M, Granata F, Racchiusa S, et al. **Role of hemodynamic forces in unruptured intracranial aneurysms: an overview of a complex scenario.** *World Neurosurg* 2017;105:632–42 CrossRef Medline
9. Ren Y, Chen GZ, Liu Z, et al. **Reproducibility of image-based computational models of intracranial aneurysm: a comparison between 3D rotational angiography, CT angiography and MR angiography.** *Biomed Eng Online* 2016;15:50 CrossRef Medline
10. Zhang Y, Jing L, Zhang Y, et al. **Low wall shear stress is associated with the rupture of intracranial aneurysm with known rupture point: case report and literature review.** *BMC Neurol* 2016;16:231 CrossRef Medline
11. Arai D, Satow T, Komuro T, et al. **Evaluation of the arterial wall in vertebralbasilar artery dissection using high-resolution magnetic resonance vessel wall imaging.** *J Stroke Cerebrovasc Dis* 2016;25:1444–50 CrossRef Medline
12. Yalo B, Pop R, Zinchenko I, et al. **Aneurysmal wall imaging in a case of cortical superficial siderosis and multiple unruptured aneurysms.** *BMJ Case Report* 2016;2016 CrossRef Medline
13. Liang F, Qi T, Li F, et al. **High-resolution magnetic resonance vessel wall imaging evaluates intracranial aneurysms: preliminary results.** *Chin J Nerv Ment Dis* 2016;42:175–79
14. Zhang Y, Tian Z, Jing L, et al. **Bifurcation type and larger low shear area are associated with rupture status of very small intracranial aneurysms.** *Front Neurol* 2016;7:169 CrossRef Medline
15. Brinjikji W, Chung BJ, Jimenez C, et al. **Hemodynamic differences between unstable and stable unruptured aneurysms independent of size and location: a pilot study.** *J Neurointerv Surg* 2017;9:376–80 CrossRef Medline
16. Conklin BS, Vito RP, Chen C. **Effect of low shear stress on permeability and occludin expression in porcine artery endothelial cells.** *World J Surg* 2007;31:733–43 CrossRef Medline
17. LaMack JA, Himborg HA, Li XM, et al. **Interaction of wall shear stress magnitude and gradient in the prediction of arterial macromolecular permeability.** *Ann Biomed Eng* 2005;33:457–64 CrossRef Medline
18. Himborg HA, Grzybowski DM, Hazel AL, et al. **Spatial comparison**

- between wall shear stress measures and porcine arterial endothelial permeability.** *Am J Physiol Heart Circ Physiol* 2004;286:H1916–22 CrossRef Medline
19. Sano T, Ishida F, Tsuji M, et al. **Hemodynamic differences between ruptured and unruptured cerebral aneurysms simultaneously existing in the same location: 2 case reports and proposal of a novel parameter oscillatory velocity index.** *World Neurosurg* 2017;98:865–68 CrossRef Medline
  20. Tian Z, Zhang Y, Jing L, et al. **Rupture risk assessment for mirror aneurysms with different outcomes in the same patient.** *Front Neurol* 2016;7:219 CrossRef Medline
  21. Meng H, Tutino VM, Xiang J, et al. **High WSS or low WSS? Complex interactions of hemodynamics with intracranial aneurysm initiation, growth, and rupture: toward a unifying hypothesis.** *AJNR Am J Neuroradiol* 2014;35:1254–62 CrossRef Medline
  22. Kadasi LM, Dent WC, Malek AM. **Colocalization of thin-walled dome regions with low hemodynamic wall shear stress in unruptured cerebral aneurysms.** *J Neurosurg* 2013;119:172–79 CrossRef Medline
  23. Miura Y, Ishida F, Umeda Y, et al. **Low wall shear stress is independently associated with the rupture status of middle cerebral artery aneurysms.** *Stroke* 2013;44:519–21 CrossRef Medline

# Usefulness of Vessel Wall MR Imaging for Follow-Up after Stent-Assisted Coil Embolization of Intracranial Aneurysms

S. Kim, M. Kang, D.W. Kim, and J.-H. Choi



## ABSTRACT

**BACKGROUND AND PURPOSE:** Follow-up with MRA for intracranial aneurysms after stent-assisted coiling is complicated by imaging artifacts. We evaluated the usefulness of an alternative method: vessel wall MR imaging.

**MATERIALS AND METHODS:** We conducted a single-center, retrospective review of medical records of 47 patients who underwent 3D TOF-MRA, vessel wall MRI, and DSA after stent-assisted coiling between March 2016 and January 2018. We evaluated the mean value of the signal intensity in the stented artery and the contralateral normal artery on vessel wall MRI. The quality of visualization was further compared between TOF-MRA and vessel wall MRI. Furthermore, we evaluated the diagnostic accuracy and concordance rate of TOF-MRA and vessel wall MRI for assessing the patency of the stented parent artery. DSA was used as a reference test.

**RESULTS:** The mean signal intensities of the stented and normal arteries on vessel wall MRI were not significantly different ( $P = .133$ ). The mean scores for the visualization of the stented parent artery on vessel wall MRI were significantly superior to those of TOF-MRA images ( $P < .001$ ). Vessel wall MRI reached an excellent positive predictive value (100%). However, TOF-MRA had a poor positive predictive value (11%; 95% CI, 9%–12%). The likelihood ratios of vessel wall MRI and TOF-MRA were 27.36 ( $P < .001$ ) and 2.98 ( $P = .225$ ), respectively. The concordance rate of vessel wall MRI and TOF-MRA with DSA for evaluating the state of the stented artery was 100% ( $\kappa = 1$ ) and 28% ( $\kappa = 0.038$ ), respectively.

**CONCLUSIONS:** Vessel wall MRI may be useful in evaluating the patency of stented arteries after stent-assisted coil embolization for intracranial aneurysms.

**ABBREVIATIONS:** SI = signal intensity; VWMRI = vessel wall MRI

Endovascular coil embolization has become an established treatment method for intracranial aneurysms.<sup>1</sup> Intracranial stents are used to treat wide-neck aneurysms using the neck-remodeling technique.<sup>2</sup> However, stents cause endothelial hyperplasia and thrombosis, which can lead to stenosis or stented artery occlusion. The incidence of in-stent stenosis is approximately 1%.<sup>3,4</sup> In-stent thrombosis may be more common—reported to be as high as 4% in 1 series—and may account for as much as 29% of thromboembolic complications.<sup>3</sup> The criterion standard for evaluating this complication and the outcome of aneurysm treatment is DSA. There has been a move toward noninvasive fol-

low-up using MR imaging due to the risks inherent in the invasive DSA procedure.

A widely used noninvasive alternative to DSA is 3D TOF-MRA.<sup>5</sup> However, it is difficult to interpret the patency and/or degree of stenosis on TOF-MRA because of susceptibility artifacts and radiofrequency shielding of intracranial nitinol stents.<sup>6</sup> Contrast-enhanced MRA has been reported to yield better results than TOF-MRA for the evaluation of aneurysm occlusions, but the ability of contrast-enhanced MRA to evaluate stented-artery status remains unclear.<sup>7</sup> Furthermore, the use of contrast materials in contrast-enhanced MRA is associated with anaphylactic shock and nephrogenic systemic fibrosis; the frequency of all acute, adverse events after an injection of 0.1 or 0.2 mmol/kg of gadolinium chelate ranges from 0.07% to 2.4%.<sup>8</sup> To reduce this risk, we attempted to find a useful imaging technique to evaluate the stented parent artery as an alternative to both contrast agents and DSA.

Vessel wall MR imaging (VWMRI) has been increasingly used to study intracranial vascular lesions, such as atherosclerosis, vasculitis, and aneurysms.<sup>9</sup> In practice, the signal loss caused by the

Received April 15, 2018; accepted after revision July 30.

From the Departments of Radiology (S.K., M.K., D.W.K.) and Neurosurgery (J.-H.C.), Dong-A University Medical Center, Busan, Korea.

Please address correspondence to Myongjin Kang, MD, Department of Radiology, Dong-A University Medical Center, 1,3-ga, Dongdaeshin-dong, Seo-gu, Busan 602-715, Korea; e-mail: myongjinkang1@gmail.com

Indicates article with supplemental on-line photo.

<http://dx.doi.org/10.3174/ajnr.A5824>

stent on TOF-MRA makes evaluation of the parent artery difficult. However, VWMRI is closely related to fast spin-echo techniques with variable flip angle refocusing pulses, which use radio-frequency refocusing pulses to return a T2' decay of transverse magnetization to a longer T2 decay, thus reducing signal loss.<sup>10</sup> We hypothesized that even without contrast administration, VWMRI could provide good image quality for evaluating stented parent arteries. Thus, the present study evaluated the usefulness of VWMRI after stent-assisted coil embolization for intracranial aneurysms and compared its efficacy with that of TOF-MRA.

## MATERIALS AND METHODS

### Patients

This study was approved by our institutional review board, and the requirement for written informed consent was waived. We retrospectively reviewed the medical records of patients who had an intracranial aneurysm treated by stent-assisted coiling between March 2016 and January 2018. Before patient discharge, our institution performs an initial MR imaging with TOF-MRA and VWMRI after stent-assisted coil embolization. Follow-up is performed by MR imaging with TOF-MRA and VWMRI. Conventional angiography is performed if there is suspicion of aneurysm recanalization or stent-related complications (eg, thromboembolism, stenosis, or occlusion).

### MR Imaging Protocol

MR imaging was performed with a 3T MR imaging system (Discovery MR750; GE Healthcare, Milwaukee, Wisconsin) using a 32-channel head coil. The VWMRI consisted of 3D fast spin-echo proton-density imaging with variable flip angles (Cube; GE Healthcare) and motion-sensitized driven equilibrium. The imaging parameters for 3D proton-density images were as follows: TR, 1500 ms; TE, 21.3 ms; bandwidth, 62.5 kHz; FOV, 190 × 190 mm; matrix, 384 × 384; in-plane resolution, 0.49 × 0.49 mm; slice thickness, 0.8 mm (interpolated to 0.4 mm); NEX, 1; Auto-calibrating Reconstruction for Cartesian imaging acceleration factor, 1.5; scan time, 7 minutes, 53 seconds. We obtained 3D TOF-MRA with the following parameters: TR, 23 ms; TE, 2.5 ms; flip angle, 20°; bandwidth, 50 kHz; FOV, 210 × 180 mm; matrix, 416 × 224; slice thickness/slice overlap, 1.2 mm/16%; 3 slabs using multiple overlapping thin-slab acquisition; asset factor, 2; scan time, 4 minutes, 32 seconds. For 3D TOF-MRA, maximum-intensity-projection reconstructions and source images were used. For VWMRI, minimum-intensity-projection reconstructions and source images were used.

### DSA

Intra-arterial DSA was performed with a biplane neuroangiographic system (AXIOM Artis dBA; Siemens, Erlangen, Germany). Using transfemoral catheterization, selective injections of the internal carotid or vertebral arteries were performed according to the aneurysm location. All DSA examinations included anteroposterior, lateral, and working views.

### Image Analysis

We performed quantitative analyses of relative signal intensity (SI) and visualization of the stented parent arteries on the images obtained by VWMRI after the procedures.

One observer manually drew an ROI of at least 1 mm<sup>2</sup> on the single-slice source images (On-line Figure). An ROI was placed at the stented artery adjacent to the aneurysm neck on the basis of the assumption that an aneurysm would be located in the middle of the stented artery in most cases because we consistently placed the center of the stent at the aneurysm neck site during stent-assisted coiling. DSA and VWMRI are different imaging modalities, and it is difficult to match the exact position of the stent by comparing the VWMRI with DSA. Moreover, the stent strut is not visible on VWMRI.

The mean value of the SI in the stented artery was compared with that in the contralateral normal artery. The relative SI of the stented artery was calculated as follows: SI of the Stented Artery/SI of the Contralateral Normal Artery. In the case of the basilar artery, the proximal normal artery was referred to as the contralateral normal artery.

The image quality of the stented parent artery was graded subjectively on a 3-point scale: 1 = poor (evaluation could not be made), 2 = moderate (evaluation could be made but information was lacking compared with the DSA), and 3 = good (image could be evaluated similar to DSA).<sup>11</sup>

Furthermore, we evaluated the status of the stented parent artery by comparing the VWMRI, TOF-MRA, and the DSA. The patency status of the parent artery was evaluated on a 3-point scale: 1 = patent (no change in the parent artery diameter), 2 = stenosis (narrowing of the parent artery), 3 = parent artery occlusion. A simplified 2-grade scale was used to assess the diagnostic accuracies for parent vessel patency: normal and pathologic (stenosis, occlusion, or thrombosis).

Two interventional neuroradiologists (one with 10 years of experience and the other with 5 years) independently evaluated all images in a random order. In case of disagreement, a third experienced neuroradiologist with 17 years of experience helped to establish consensus. DSA findings were considered the standard reference and were interpreted independently by 1 neurosurgeon who was unaware of the MR imaging findings.

### Statistical Analysis

A Wilcoxon signed rank test was used to analyze the subjective scores for the quality of the stented artery images. *P* values < .05 were considered statistically significant. The Mann-Whitney *U* test was used to compare the mean relative SI value for the stented arteries with those of the contralateral normal arteries. The weighted  $\kappa$  statistic was used to evaluate interobserver agreement for each technique and the concordance rate for evaluating the patency of the parent vessel using the results of DSA as a standard of reference. Statistical analyses were performed with MedCalc for Windows, Version 18.2.1 (MedCalc Software, Mariakerke, Belgium). Diagnostic accuracy was calculated with SPSS software, Version 11.5 (IBM, Armonk, New York).

## RESULTS

Before discharge, 84 patients underwent stent-assisted coiling and an initial MR imaging; 2 patients were excluded from our study because the intraluminal signal intensity was too high, even in normal arteries, due to motion or flow artifacts; and 35 patients were excluded because the follow-up DSA was not available after

discharge. The sample of the present study, therefore, totaled 47 patients (female/male ratio, 33:14; mean age,  $57.2 \pm 8.9$  years; age range, 39–78 years) who underwent TOF-MRA, VWMRI, and DSA after their respective procedures. A Neuroform 3 stent (Stryker Neurovascular, Kalamazoo, Michigan) was used for 31 aneurysms, while a Solitaire AB stent (Covidien, Irvine, California) was used for 16. The clinical characteristics of the patients are shown in Table 1.

All 47 patients underwent both follow-up MR imaging and DSA with an interval gap of <7 days. The mean period between coil embolization and follow-up DSA was  $266 \pm 98$  days; the interval between the follow-up MR imaging and follow-up DSA was  $3.3 \pm 1.8$  days.

### Relative Signal Intensity in the Stent

We performed quantitative analyses of relative SI of the arteries in the images obtained by initial VWMRI after the procedures in 46 of the 47 patients; 1 patient was excluded due to signal intensity contamination in the parent artery by acute in-stent thrombosis. The mean SIs for the stented artery and normal artery were  $167 \pm 20$  and  $174 \pm 20$ , respectively, and were not significantly different ( $P = .133$ ). The mean relative SIs for the stented arteries using the Neuroform and Solitaire stents was  $0.97 \pm 0.04$  and  $0.94 \pm 0.05$ , respectively; the mean relative SI of the stented artery fitted with Solitaire stents was lower than that of stented arteries fitted with Neuroform stents ( $P < .013$ ).

**Table 1: Characteristics of the 47 patients and 47 aneurysms that underwent stent-assisted coiling**

Characteristics	
Mean age (range) (yr)	$57.2 \pm 8.9$ (39–78)
Sex (female/male)	33:14
Ruptured aneurysms	6 (13%)
Location	
Internal carotid artery	27
Middle cerebral artery	9
Anterior cerebral artery/anterior communicating artery	5
Vertebrobasilar artery	6
Aneurysm size	
<5 mm	24
5–10 mm	21
>10 mm	2
Initial occlusion result	
Complete occlusion	38
Remnant neck	7
Residual aneurysm	2
Stent	
Neuroform	31
Solitaire	16

**Table 2: Concordance rate of vessel wall MRI findings and TOF-MRA using results of DSA as a standard of reference**

	Vessel Wall MRI			MRA		
	Patent	Stenosis	Occlusion	Patent	Stenosis	Occlusion
DSA						
Patent	43	0	0	9	29	5
Stenosis	0	4	0	0	4	0
Occlusion	0	0	0	0	0	0
Concordance rate	100% ( $\kappa = 1$ )			28% ( $\kappa = 0.038$ )		

### Image Quality

For the Neuroform stent cases, the image quality of the stented parent artery on VWMRI was significantly superior to that obtained by TOF-MRA ( $P < .001$ ). The average scores were  $3 \pm 0$  for VWMRI and  $2.2 \pm 0.69$  for MRA. In cases of Solitaire stents, the image quality was equally poor for the stented parent artery on VWMRI and MRA. A proximal marker near the detachment zone of the Solitaire stent caused significant signal loss of the lumen due to susceptibility artifacts in both imaging modalities. When the evaluations were performed in the Solitaire stents and the proximal portion of the stented artery was excluded, the mean scores for the stented artery were  $3 \pm 0$  and  $1.7 \pm 0.7$  for VWMRI and TOF-MRA, respectively ( $P < .001$ ). Therefore, the quality for the stented artery images obtained by VWMRI was significantly superior to that observed in 3D TOF-MRA images. With the exception of the proximal portion in the Solitaire stent, this finding was consistent regardless of the type of stent used. The overall mean scores for image quality, in terms of visualization of the stented artery, were  $3 \pm 0$  and  $2 \pm 0.7$  for VWMRI and 3D TOF-MRA, respectively ( $P < .001$ ).

### Patency of the Parent Vessel

It was difficult to evaluate the patency of the parent artery near the detachment zone in Solitaire stents due to signal loss on VWMRI and MRA. However, apart from the marker region in the Solitaire stent, VWMRI showed results consistent with those of DSA. The statuses of the parent vessel artery assessed with VWMRI, TOF-MRA, and DSA are shown in Table 2.

Interobserver agreement was very good for VWMRI ( $\kappa = 1$ ) and good for TOF-MRA ( $\kappa = 0.64$ ). The concordance rate of VWMRI and TOF-MRA with DSA for evaluating the state of the stented artery was 100% ( $\kappa = 1$ ) and 28% ( $\kappa = 0.038$ ), respectively. The likelihood ratios of VWMRI and TOF-MRA were 27.36 ( $P < .001$ ) and 2.98 ( $P = .225$ ), respectively. By means of the simplified 2-grade scale (normal-versus-pathologic vessels), VWMRI reached an excellent positive predictive value (100%). However, TOF-MRA featured a poor positive predictive value (11%; 95% CI, 9%–12%). False stenosis was prevalent on TOF-MRA. Normal vessels on DSA were overestimated as pathologic vessels on TOF-MRA in 34/47 patients.

There were 4 cases of stent-related complications. An in-stent thrombus occurred after stent-assisted coiling for a paraclinoid ICA aneurysm (Fig 1). According to the 3-point scale, this case was classified as a stenosis, but 2 readers interpreted it as a thrombus on VWMRI. An angiogram obtained immediately after the final coil insertion revealed the acute small in-stent thrombosis. A 30-minute-delayed DSA performed after rescue use of tirofiban demonstrated no thrombus growth and uncompromised distal arterial flow velocity. Thus, we decided to follow-up without further interventional treatment.

VWMRI revealed that the thrombosis had increased in size in the stent 2 days after the procedure. However, TOF-MRA showed luminal narrowing of the stented parent artery. Immediate, same-day follow-up DSA confirmed the thrombus growth in the stent, consistent with the VWMRI findings. The other stent-re-

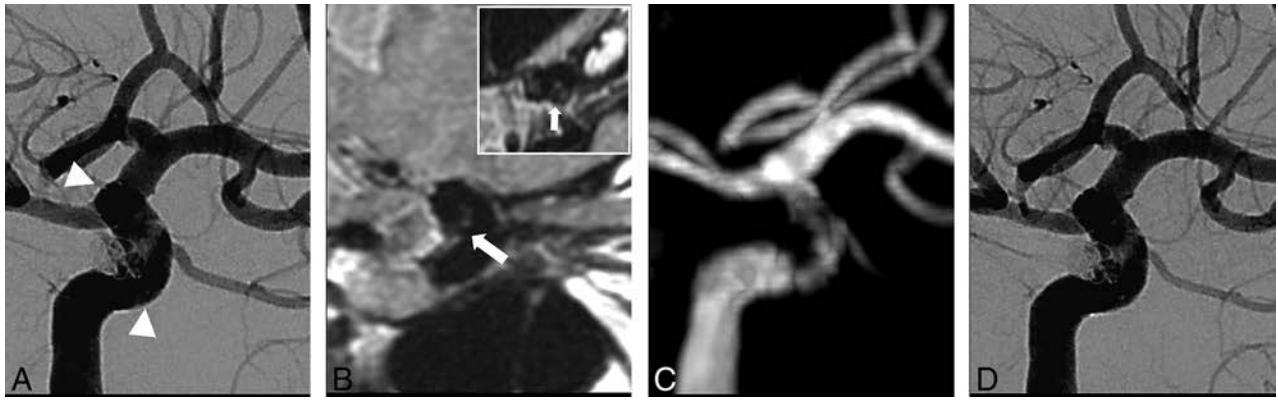


**FIG 1.** A 60-year-old woman with a paraclinoid internal carotid artery aneurysm. *A*, Cerebral angiography performed immediately after stent-assisted coiling shows an acute in-stent thrombus. The *arrowheads* indicate the proximal and distal markers of the stent. *B*, Oblique and axial (*upper right image*) reformatted images of the proton-density image obtained from a vessel wall MR imaging performed 2 days after coiling reveal the in-stent thrombus. *C*, Time-of-flight MR angiography demonstrates artifactual luminal narrowing of the stented parent artery. *D*, Cerebral angiography on the same day shows the thrombus within the stent, consistent with vessel wall MR imaging results.

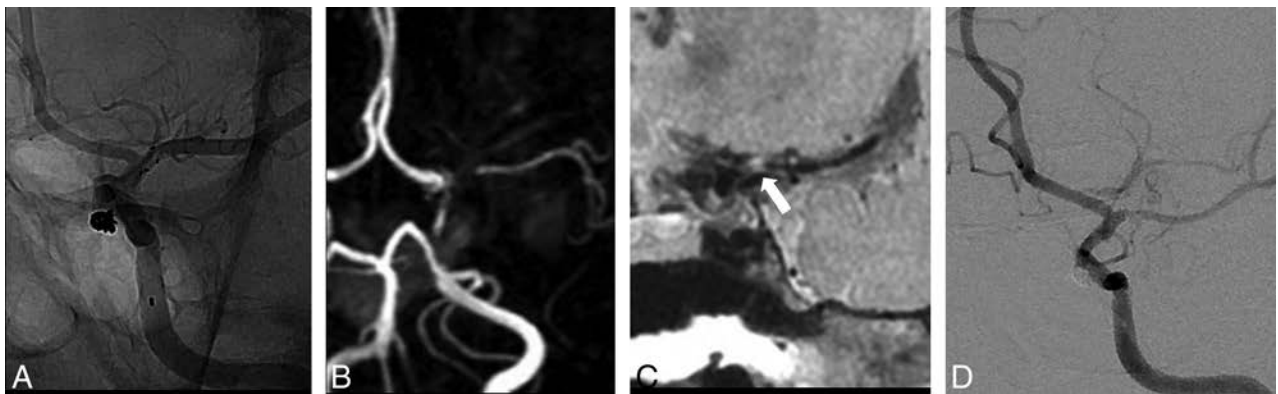


**FIG 2.** A 50-year-old man with a paraclinoid internal carotid artery aneurysm. *A*, Cerebral angiography performed immediately after stent-assisted coiling shows the normal parent artery. *B*, Time-of-flight MR angiography obtained at a 1-year follow-up examination shows signal drop-out with a decreased diameter and signal intensity of distal vessels in the left middle cerebral artery. *C*, Oblique reformatted images of vessel wall MR imaging reveal stenosis in the left proximal middle cerebral artery (*arrow*). *D*, Follow-up cerebral angiography confirms stenosis of the left proximal middle cerebral artery.

lated complication observed in 3 cases was in-stent restenosis following stent-assisted coiling. VWMRI assisted in the identification of the 3 stenosis cases (Fig 2). All 3 cases were also classified as pathologic vessels on TOF-MRA, but we were unable to determine whether this represented artifactual luminal narrowing or a true lesion.

### Additional Results

In our preliminary study, we evaluated coiled aneurysm stability with VWMRI. On the basis of the evolution of blood clots, the signal of clots decreases in the chronic phase on T1WI. Even in the chronic phase, the SI of hematoma is higher than the dark SI of blood.<sup>12</sup> Thus, we hypothesized that SI in the coiled aneurysm would appear higher than that in the parent artery and that the residual flow signal in the coiled aneurysm would appear dark on the proton-density image. We therefore sought to evaluate aneurysm stability with VWMRI using SI differences between treated aneurysms and residual flow. Of the 47 patients, follow-up DSA results showed complete occlusion in 42 patients, a remnant neck in 4 patients, and residual aneurysm in 1 patient. Regarding the depiction of residual flow in the coiled aneurysms, the concordance rate of VWMRI was lower than that of TOF-MRA (38%

versus 96%). In 42 cases of complete occlusion identified via DSA, 25 were erroneously interpreted as residual neck or residual aneurysm on VWMRI. In 2 patients whose TOF-MRA results were underestimated relative to DSA, a tiny residual neck was erroneously interpreted as complete occlusion.

### DISCUSSION

An intracranial stent is a powerful tool for the endovascular treatment of wide-neck and fusiform aneurysms. However, stent-related complications can cause permanent neurologic complications. Identifying these complications is important for patient diagnosis, management, and prognosis. Although DSA is standard for the follow-up of coiled aneurysms, it is invasive and exposes patients to procedure-related complications, such as cerebral thromboembolism, contrast nephrotoxicity, and radiation.<sup>13</sup> Thus, follow-up imaging after endovascular treatment is vital. We evaluated the usefulness of VWMRI after stent-assisted coil embolization of intracranial aneurysms. The primary finding of our study was that VWMRI could reliably identify in-stent complications.

First, we evaluated the relative SI of the stented parent arteries

on VWMRI after performing stent-assisted coiling with 2 types of intracranial nitinol stents: Neuroform and Solitaire. The signal intensity of the stented artery was different according to stent type. The relative SI for stented arteries fitted with Neuroform stents was higher than that for the stented arteries fitted with Solitaire stents in our VWMRI study. These findings are consistent with an *in vivo* study that used a silicone tube to reveal that the mean relative in-stent signal for Neuroform stents was higher than that for the Solitaire stents.<sup>14</sup> The extent of stent-induced signal loss on TOF-MRA has been shown to depend on the thickness of the strut and cell design.<sup>14</sup> The Neuroform stent has an open-cell design and a strut thickness of 65  $\mu\text{m}$ , while the Solitaire stent has a closed cell design and a thickness of 60  $\mu\text{m}$ . Open-cell-design stents have been shown to have lower susceptibility to artifacts compared with closed-cell stents.<sup>14</sup> Moreover, the partially overlapping strut in the Solitaire stent may cause more in-stent signal reduction than in Neuroform stents.

Second, we evaluated the image quality of the stented artery on VWMRI versus TOF-MRA. An intracranial stent can compromise the evaluation of the patency of the vessel on TOF-MRA.<sup>15</sup> Contrast administration can improve vessel lumen visualization.<sup>16,17</sup> Lövlblad et al<sup>16</sup> assessed 19 patients with stent-assisted coil embolization using noncontrast TOF-MRA and contrast-enhanced TOF-MRA with 1.5T MR imaging; the contrast administration allowed better visualization of the vessel lumen in the cases that used nitinol stents. Furthermore, the in-stent signal loss was present in all TOF-MRA cases except for contrast-enhanced MRA images. Thamburaj et al<sup>17</sup> assessed 42 patients with stent-assisted coiling and found that contrast-enhanced MRA showed a tendency to demonstrate superior in-stent flow, smoother margins, and minimal-to-no stenosis relative to noncontrast TOF-MRA. However, although complications of contrast agent administration for contrast-enhanced MRA are rare, contrast dye can cause severe allergic reactions and adverse effects. To avoid administration of contrast, we compared VWMRI with TOF-MRA: VWMRI provided better image quality compared with TOF-MRA. The latter method is based on a gradient-echo sequence. Image artifacts due to metal are caused by inhomogeneity in the static magnetic field, and gradient-echo-based sequences are therefore more prone to these artifacts. In contrast, VWMRI is based on a spin-echo sequence, and its use of 3D techniques allows very thin slices; compared with thin 2D slices, susceptibility artifacts are reduced because of the (fast) spin-echo technique.<sup>9</sup> In contrast to cases in which Neuroform stents were used, neither TOF-MRA nor VWMRI could evaluate the segment near the proximal marker of Solitaire stents. This issue is because the relatively thick, proximal marker near the detachment zone of the Solitaire stent caused complete signal loss of the lumen due to the susceptibility artifacts. However, when the proximal marker was excluded, the image quality of the stented artery on VWMRI was superior to that of TOF-MRA. Agid et al<sup>18</sup> reported a “marker band effect” appearing in arteries  $\leq 2$  mm in diameter. The markers of Neuroform stents are made of platinum, which creates strong magnetic susceptibility artifacts. We observed this effect on TOF-MRA in cases in which the Neuroform stent was used in the middle cerebral or posterior cerebral artery. However, this phenomenon did not occur on VWMRI.

Third, we compared VWMRI and TOF-MRA with DSA to evaluate the status of the stented parent artery. Several studies found that MRA with or without contrast material does not seem to provide an effective alternative to DSA for assessing parent artery patency.<sup>18-21</sup> In a direct comparison between contrast-enhanced MRA and DSA in 27 patients with 28 aneurysms, Agid et al<sup>18</sup> reported 6 cases of false stenosis and 2 of exaggerated stenosis on contrast-enhanced MRA, suggesting that the contrast-enhanced MRA did not depict the true status of the artery. Marciano et al<sup>19</sup> compared TOF-MRA and contrast-enhanced MRA with DSA in 33 patients with 35 aneurysms treated by stent-assisted coiling. The intermodality agreement was poor for 3D TOF-MRA ( $\kappa = 0.12$ ) and null for contrast-enhanced MRA ( $\kappa = -0.01$ ). TOF-MRA ( $\kappa = 0.05$ ) and contrast-enhanced MRA ( $\kappa = -0.04$ ) were not able to detect pathologic vessels better than DSA: No difference in accuracy was found ( $P = .68$ ). Recently, Akkaya et al<sup>20</sup> evaluated the usefulness of contrast-enhanced MRA and TOF-MRA in 24 aneurysms treated with low-profile stent-assisted coiling. Although interobserver agreement was substantial in both TOF-MRA ( $\kappa = 0.71$ ,  $P < .001$ ) and contrast-enhanced MRA ( $\kappa = 0.64$ ,  $P = .001$ ), intermodality agreement values of TOF-MRA and contrast-enhanced MRA with DSA were insignificant in terms of stent patency ( $\kappa = 0.065$ ,  $P = .27$ ) and contrast-enhanced MRA ( $\kappa = 0.158$ ,  $P = .15$ ). Choi et al<sup>21</sup> compared 4D-MRA and 3D TOF-MRA in a group of 26 patients with aneurysms treated with stents. Although the visualization of the stented arteries on 4D-MRA was significantly superior to that on 3D TOF-MRA ( $P < .001$ ), the investigators doubted whether the degree of in-stent restenosis was accurately measured by 4D-MRA. The ability of 4D-MRA to evaluate in-stent stenosis thus remains undetermined.

Recent studies have demonstrated that Silent MRA (Discovery MR750w; GE Healthcare) might be useful for follow-up imaging after stent-assisted coil embolization.<sup>22,23</sup> In Silent MRA, an ultrashort TE can minimize the phase dispersion of the labeled blood flow signal in the voxel and decrease magnetic-susceptibility artifacts; accordingly, the artifacts from stents or coils are theoretically decreased.<sup>23</sup> Thus, Silent MRA could improve visualization of the stent without contrast administration more clearly than could 3D TOF-MRA.<sup>22,23</sup> However, in Silent MRA, the angiographic image is obtained by subtraction of images scanned before and after labeling. Thus, static tissue such as a thrombus cannot be detected in Silent MRA.<sup>22</sup>

In contrast to previous studies that found that MRA techniques were unable to provide a precise evaluation of the stent lumen, our study showed that diagnostic accuracy and the concordance rate between VWMRI and DSA were excellent. VWMRI is helpful in identifying the morphology of intracranial vessels.<sup>15</sup> The present study found that VWMRI was more accurate than TOF-MRA for evaluating the status of the stented parent artery. VWMRI assisted the identification of 3 cases of stenosis and 1 of thrombosis, and its images demonstrated features similar to those shown by DSA.

In our preliminary study, VWMRI did not appear to be useful for evaluating aneurysm stability. We observed that in most cases, the SI of coiled aneurysms on VWMRI was heterogeneous regardless of follow-up duration. Thus, completeness of the coil embolization

lization was overestimated by VWMRI. Various factors such as thrombus organization, fibrosis, and coil-related low SI seem to contribute to heterogeneous SI in the coiled aneurysm. TOF-MRA (particularly with contrast) is good at detecting residual flow and aneurysm recurrence. It would seem that the techniques could be complementary.

The in-stent complication rates in our study were high. We observed that 3 of 4 patients were asymptomatic at follow-up. When a follow-up was performed with only TOF-MRA, DSA was recommended in cases of suspected abnormal findings with associated symptoms. In asymptomatic cases, follow-up was recommended but was often rejected by patients. However, after we used VWMRI, a subsequent DSA test was highly recommended and consequently less often rejected by patients. We speculate that this bias could be attributed to the high incidence of complications.

Asymptomatic in-stent stenosis can change into symptomatic stenosis, or spontaneous resolution of stenosis can occur.<sup>24</sup> These events have important clinical implications for the continuation of dual-antiplatelet medication, close observation of neurologic symptoms, and follow-up. For clinical purposes, if MRA with or without contrast material depicts in-stent stenosis or stent occlusion, DSA should be performed to rule out in-stent stenosis or stent occlusion due to false-positive results. Our findings indicate that VWMRI provides a clear depiction of the patency of the parent artery. Accordingly, it is possible to avoid performing DSA in a group of patients in whom there are no particular clinical concerns for stent stenosis/occlusion. In practice, we believe that noninvasive imaging techniques such as VWMRI could be used more frequently than invasive conventional angiography as a follow-up technique.

This retrospective study has several limitations. First, follow-up MR imaging and DSA evaluations were not performed on the same day in most cases. Therefore, these 2 modalities might not reflect the exact same conditions in terms of the state of aneurysms and stented parent arteries. Second, intracranial stents were limited to the Neuroform and Solitaire varieties. Multiple flow diverters or flow-disruption devices are currently available for the treatment of cerebral aneurysms. Several series have reported the usefulness of MRA with contrast material in the follow-up of flow diverters or flow-disruption devices.<sup>25,26</sup> These studies showed that contrast-enhanced MRA yielded better accuracy than TOF-MRA for the status of the parent artery. However, intraluminal evaluation remains difficult due to artifacts in MRA, regardless of the sequence used. This difficulty may be explained by the difference in composition but also porosity, metal coverage, and pore density between stents and flow diverters.<sup>25</sup> The usefulness of VWMRI for variable flow diverters or flow-disruption devices should be determined in future studies.

Third, the goal of VWMRI is to reduce the intraluminal signal to zero. Intraluminal SI is not always suppressed fully on VWMRI. Visually, intraluminal SI appeared to be dark in our study. However, intraluminal signals were not zero. Thrombus was assumed if visual assessment revealed higher SI than intraluminal SI. However, there are limitations to visual evaluation when blood suppression is less effective in the presence of slow or complex flow. Novel blood-suppression techniques, including the Delay Alter-

nating with Nutation for Tailored Excitation, can be used to reduce artifacts.<sup>27</sup>

Fourth, there are limitations concerning the TOF acquisition techniques. The SNR in the stent can be improved by a higher flip angle on the TOF technique.<sup>14</sup> However, we did not use these techniques to improve image acquisition. With the optimization of MR imaging parameters of TOF-MRA according to the various intracranial stents, the luminal visualization of stents could be improved. We performed multislab TOF-MRA with multiple overlapping thin-slab acquisitions. The slab boundaries typically show some artifacts and intensity variations, even if acquired with a generous slab overlap. In our study, the slab artifacts did not significantly affect the reader's interpretation of the image quality. However, the slab boundary artifacts may reduce image quality if the stent is located directly in a slab boundary zone. The single-slab or sliding interleaved projection reconstruction technique can be used to reduce slab boundary artifacts over the conventional TOF technique.<sup>28</sup>

## CONCLUSIONS

The present study performed quantitative and qualitative analyses of stented parent artery imaging using VWMRI and TOF-MRA. Even without contrast administration, VWMRI provided better image quality and higher accuracy in the evaluation of stented parent arteries than TOF-MRA. The high concordance rate of VWMRI for the analysis of pathologic parent artery status suggests that VWMRI could be useful in evaluating the patency of stented arteries after stent-assisted coiling.

## ACKNOWLEDGMENTS

This work was supported by the Dong-A University Research Fund.

## REFERENCES

1. Molyneux A, Kerr R, Stratton I, et al; International Subarachnoid Aneurysm Trial (ISAT) Collaborative Group. **International Subarachnoid Aneurysm Trial (ISAT) of neurosurgical clipping versus endovascular coiling in 2143 patients with ruptured intracranial aneurysms: a randomised trial.** *Lancet* 2002;360:1267–74 [CrossRef Medline](#)
2. Kemp WJ 3rd, Fulkerson DH, Payner TD, et al. **Risk of hemorrhage from de novo cerebral aneurysms.** *J Neurosurg* 2013;118:58–62 [CrossRef Medline](#)
3. Kim SR, Vora N, Jovin TG, et al. **Anatomic results and complications of stent-assisted coil embolization of intracranial aneurysms.** *Interv Neuroradiol* 2008;14:267–84 [CrossRef Medline](#)
4. King B, Vaziri S, Singla A, et al. **Clinical and angiographic outcomes after stent-assisted coiling of cerebral aneurysms with Enterprise and Neuroform stents: a comparative analysis of the literature.** *J Neurointerv Surg* 2015;7:905–09 [CrossRef Medline](#)
5. Schaafsma JD, Velthuis BK, Majoie CB, et al. **Intracranial aneurysms treated with coil placement: test characteristics of follow-up MR angiography—multicenter study.** *Radiology* 2010; 256:209–18 [CrossRef Medline](#)
6. Wang Y, Truong TN, Yen C, et al. **Quantitative evaluation of susceptibility and shielding effects of nitinol, platinum, cobalt-alloy, and stainless steel stents.** *Magn Reson Med* 2003;49:972–76 [CrossRef Medline](#)
7. Soize S, Gawlitza M, Raoult H, et al. **Imaging follow-up of intracranial aneurysms treated by endovascular means: why, when, and how?** *Stroke* 2016;47:1407–12 [CrossRef Medline](#)

8. The American College of Radiology. *ACR Manual on Contrast Media*. Version 10.3, 2018. [https://www.acr.org/-/media/ACR/Files/Clinical-Resources/Contrast\\_Media.pdf](https://www.acr.org/-/media/ACR/Files/Clinical-Resources/Contrast_Media.pdf). Accessed August 29, 2018
9. Mandell DM, Mossa-Basha M, Qiao Y, et al; Vessel Wall Imaging Study Group of the American Society of Neuroradiology. **Intracranial vessel wall MRI: principles and expert consensus recommendations of the American Society of Neuroradiology.** *AJNR Am J Neuroradiol* 2017;38:218–29 CrossRef Medline
10. Bitar R, Leung G, Perng R, et al. **MR pulse sequences: what every radiologist wants to know but is afraid to ask.** *Radiographics* 2006;26:513–37 CrossRef Medline
11. Takayama K, Taoka T, Nakagawa H, et al. **Usefulness of contrast-enhanced magnetic resonance angiography for follow-up of coil embolization with the Enterprise stent for cerebral aneurysms.** *J Comput Assist Tomogr* 2011;35:568–72 CrossRef Medline
12. Park KJ, Jung SC, Kim HS, et al. **Multi-contrast high-resolution magnetic resonance findings of spontaneous and unruptured intracranial vertebral artery dissection: qualitative and quantitative analysis according to stages.** *Cerebrovasc Dis* 2016;42:23–31 CrossRef Medline
13. Willinsky RA, Taylor SM, TerBrugge K, et al. **Neurologic complications of cerebral angiography: prospective analysis of 2,899 procedures and review of the literature.** *Radiology* 2003;227:522–28 CrossRef Medline
14. Choi JW, Roh HG, Moon WJ, et al. **Optimization of MR parameters of 3D TOF-MRA for various intracranial stents at 3.0T MRI.** *Neurointervention* 2011;6:71–77 CrossRef Medline
15. Wong JH, Mitha AP, Willson M, et al. **Assessment of brain aneurysms by using high-resolution magnetic resonance angiography after endovascular coil delivery.** *J Neurosurg* 2007;107:283–89 CrossRef Medline
16. Lövblad KO, Yilmaz H, Chouiter A, et al. **Intracranial aneurysm stenting: follow-up with MR angiography.** *J Magn Reson Imaging* 2006;24:418–22 CrossRef Medline
17. Thamburaj K, Cockroft K, Agarwal AK, et al. **A comparison of magnetic resonance angiography techniques for the evaluation of intracranial aneurysms treated with stent-assisted coil embolization.** *Cureus* 2016;8:e909 CrossRef Medline
18. Agid R, Willinsky RA, Lee SK, et al. **Characterization of aneurysm remnants after endovascular treatment: contrast-enhanced MR angiography versus catheter digital subtraction angiography.** *AJNR Am J Neuroradiol* 2008;29:1570–74 CrossRef Medline
19. Marciano D, Soize S, Metaxas G, et al. **Follow-up of intracranial aneurysms treated with stent-assisted coiling: comparison of contrast-enhanced MRA, time-of-flight MRA, and digital subtraction angiography.** *J Neuroradiol* 2017;44:44–51 CrossRef Medline
20. Akkaya S, Akca O, Arat A, et al. **Usefulness of contrast-enhanced and TOF MR angiography for follow-up after low-profile stent-assisted coil embolization of intracranial aneurysms.** *Interv Neuroradiol* 2018 Jan 1. [Epub ahead of print] CrossRef Medline
21. Choi JW, Roh HG, Moon WJ, et al. **Time-resolved 3D contrast-enhanced MRA on 3.0T: a non-invasive follow-up technique after stent-assisted coil embolization of the intracranial aneurysm.** *Korean J Radiol* 2011;12:662–70 CrossRef Medline
22. Irie R, Suzuki M, Yamamoto M, et al. **Assessing blood flow in an intracranial stent: a feasibility study of MR angiography using a silent scan after stent-assisted coil embolization for anterior circulation aneurysms.** *AJNR Am J Neuroradiol* 2015;36:967–70 CrossRef Medline
23. Takano N, Suzuki M, Irie R, et al. **Usefulness of non-contrast-enhanced MR angiography using a silent scan for follow-up after Y-configuration stent-assisted coil embolization for basilar tip aneurysms.** *AJNR Am J Neuroradiol* 2017;38:577–81 CrossRef Medline
24. Raymond J, Guilbert F, Weill A, et al. **Long-term angiographic recurrences after selective endovascular treatment of aneurysms with detachable coils.** *Stroke* 2003;34:1398–403 CrossRef Medline
25. Attali J, Benaissa A, Soize S, et al. **Follow-up of intracranial aneurysms treated by flow diverter: comparison of three-dimensional time-of-flight MR angiography (3D-TOF-MRA) and contrast-enhanced MR angiography (CE-MRA) sequences with digital subtraction angiography as the gold standard.** *J Neurointerv Surg* 2016;8:81–86 CrossRef Medline
26. Patzig M, Forbrig R, Ertl L, et al. **Intracranial aneurysms treated by flow-diverting stents: long-term follow-up with contrast-enhanced magnetic resonance angiography.** *Cardiovasc Intervent Radiol* 2017;40:1713–22 CrossRef Medline
27. Zhu C, Haraldsson H, Faraji F, et al. **Isotropic 3D black blood MRI of abdominal aortic aneurysm wall and intraluminal thrombus.** *Magn Reson Imaging* 2016;34:18–25 CrossRef Medline
28. Choi J, Seo H, Lim Y, et al. **Sliding time of flight: sliding time of flight MR angiography using a dynamic image reconstruction method.** *Magn Reson Med* 2015;73:1177–83 CrossRef Medline

# Spinal Epidural Arteriovenous Fistula with Perimedullary Venous Reflux: Clinical and Neuroradiologic Features of an Underestimated Vascular Disorder

M. Mull, A. Othman, M. Dafotakis, F.-J. Hans, G.A. Schubert, and F. Jablawi



## ABSTRACT

**BACKGROUND AND PURPOSE:** The purpose of this study was to discuss the clinical and radiologic characteristics of spinal epidural arteriovenous fistulas (SEAVF) and demonstrate their specific angiomorphology in a single-center series.

**MATERIALS AND METHODS:** Thirteen consecutive patients were diagnosed with SEAVF at RWTH Aachen University Hospital between 2006 and 2018 and were included in this study. All patients had MR imaging and DSA before treatment; 10 of these 13 patients received contrast-enhanced MRA (CE-MRA).

**RESULTS:** The mean patient age was  $72 \pm 8$  years. Paraparesis was present in 12 (92%) patients. Sphincter dysfunction and sensory symptoms were observed in 7 (54%) and 6 (46%) patients, respectively. The mean duration of symptoms was  $6 \pm 8$  months. Congestive myelopathy on MR imaging was present in all patients. Prominent arterialized perimedullary veins were demonstrated in only 3 cases. CE-MRA revealed arterialized perimedullary veins and an arterialized epidural pouch in 9/10 (90%) patients, mostly located ventrolaterally. DSA demonstrated a multisegmental extension of the arterialized ventrolateral epidural pouch in 6 (46%) cases. An intradural radicular drainage vein was localized distant from the original fistula point in 3 (23%) patients.

**CONCLUSIONS:** Congestive myelopathy with an acute/subacute clinical course was the dominant finding in spinal epidural arteriovenous fistulas. CE-MRA is a powerful diagnostic tool for identifying arterialized perimedullary veins as well as an arterialized epidural pouch. While arterialized perimedullary veins frequently present with only mild enlargement and elongation in spinal epidural arteriovenous fistulas, the arterialized epidural pouch is frequently located ventrolaterally and may extend over several vertebral levels. DSA remains the criterion standard to precisely visualize a spinal epidural arteriovenous fistula and its intradural radicular drainage vein, which may be located distant from the fistulous point.

**ABBREVIATIONS:** AV = arteriovenous; CE-MRA = contrast-enhanced MRA; SDAVF = spinal dural arteriovenous fistula; SEAVF = spinal epidural arteriovenous fistula

Various classifications have been established for spinal vascular malformations and fistulas based on their vascular supply, venous drainage pattern, and nidus location and morphology. The most common classification of spinal vascular diseases was developed by Oldfield and Doppman in 1988.<sup>1</sup> They classified these

lesions into 4 types comprising classic spinal dural arteriovenous fistulas (SDAVFs), glomus arteriovenous malformations, congenital juvenile arteriovenous malformations, and perimedullary arteriovenous fistulas. The much rarer spinal epidural arteriovenous fistulas (SEAVFs) were not included in this classification.

In contrast to the SDAVF, the arteriovenous (AV) shunt in the SEAVF is located in the epidural space. The venous drainage of these AV shunts varies from pure epidural fistulas with extradural venous drainage to combined epidural and intradural venous reflux.<sup>2</sup>

A SEAVF with perimedullary venous reflux has been thought to present with nonspecific myelopathic symptoms comparable with those of a typical SDAVF.<sup>3,4</sup> However, their precise angiographic and clinical presentations have not yet been investigated in a large number of patients and might still be unfamiliar to most neurologic and radiologic physicians.

A clear recommendation for treatment technique and strategy

Received March 12, 2018; accepted after revision August 13.

From the Departments of Diagnostic and Interventional Neuroradiology (M.M., A.O., F.J.), Neurology (M.D.), and Neurosurgery (G.A.S.), University Hospital Aachen, RWTH Aachen University, Aachen, Germany; Department of Neurosurgery (F.J.), Justus-Liebig-University, Giessen, Giessen, Germany; Department of Diagnostic and Interventional Radiology (A.O.), University Hospital Tübingen, Tübingen, Germany; and Department of Neurosurgery (F.-J.H.), Paracelsus Kliniken, Osnabrück, Germany.

Michael Mull and Ahmad Othman contributed equally to this work.

Please address correspondence to Michael Mull, MD, University Hospital Aachen, RWTH Aachen University, Department of Diagnostic and Interventional Neuroradiology, Pauwelsestr 30, 52074 Aachen, Germany; e-mail: mmull@ukaachen.de

<http://dx.doi.org/10.3174/ajnr.A5854>

is also still lacking in the literature. The goal of treatment is, however, the interruption of the intradural radicular drainage vein to stop the arterialization of perimedullary veins and additionally the obliteration of the arterialized epidural pouch to decrease the risk of residual or recurrent fistula. These goals can be achieved either surgically or endovascularly.

To further characterize this extremely rare subgroup of fistulas, we identified 13 patients presenting with an SEAVF with perimedullary venous reflux to demonstrate their anatomic features and clinical and radiologic presentation.

## MATERIALS AND METHODS

After obtaining permission from our local ethics board, we retrospectively evaluated the medical and radiologic reports of patients with an SEAVF diagnosed between January 2006 and February 2018 in RWTH Aachen University Hospital. All clinical data, including demographics and clinical presentation, were assessed by the treating physicians and re-evaluated for this study. In particular, we re-evaluated the neurologic status at time of admission to our institution, the duration of symptoms from onset until diagnosis, as well as previous misdiagnoses and treatment. The documented functional condition at time of discharge was rated as worse, stable, or improved.

All patients underwent spinal MR imaging ( $n = 13$ ) and/or contrast-enhanced MRA (CE-MRA) ( $n = 10$ ) before spinal angiography. Five (39%) of these 13 patients underwent repetitive DSA for a definite diagnosis. As a rather new technique, C-arm flat panel CT was performed in the last 5 patients of this cohort.

Radiologic data were analyzed blinded to all clinical data by both the first and last author. The first author is an interventional neuroradiologist with >30 years' experience in spinal angiography and spinal vascular diseases; the last author is a consultant neurosurgeon with a many years' experience in clinical, radiologic, and surgical aspects of spinal vascular diseases. A reference standard for statistical analysis was established in a consensus reading. We retrospectively evaluated the arterial supply, venous drainage patterns, and location and extension of the arterialized epidural pouch in our DSA findings of all included patients.

### MR/CE-MRA Imaging

MR imaging was performed in 7 patients at 1.5T (Intera, Release 10:3; Philips Healthcare, Best, the Netherlands) and in 6 patients at 3T (Prisma; Siemens, Erlangen, Germany) ( $n = 6$ ) as part of the routine clinical work-up. Sagittal T2- and pre- and postcontrast T1-weighted images were obtained as well as axial T2- and contrast-enhanced T1 images of the thoracolumbar region. In 1 patient, examination was limited to the lumbar and deep thoracic regions only. The craniocaudal extension of the T2 signal hyperintensity and the medullary contrast enhancement were qualified by the number of vertebral levels shown to be affected on T1 and T2 MR images. The appearance of the perimedullary veins was rated subjectively as mild, moderate, or prominent due to their tortuous and dilated appearance in the T1 and T2 images.

Contrast-enhanced MR angiography was performed on a clinical 1.5T MR imaging system with a phased array spine coil in 4 patients. To emphasize the arterial phase of the bolus enhancement relative to the venous enhancement, we sampled the  $k$ -space

using elliptic centric ordering, which allowed separation into arterial and mixed arterial-venous enhancement. Further details about this CE-MRA technique have been previously described by our group elsewhere.<sup>5,6</sup>

In 6 patients, time-resolved angiography with stochastic trajectories was performed on a clinical 3T MR imaging system. This CE-MRA also divides  $k$ -space into 2 regions but samples them alternately using a semi-randomized method. It allows a rapid acquisition of multiple images during the passage of the contrast bolus.

### DSA

Selective spinal DSA was performed via a femoral approach in a dedicated biplanar neuroangiographic suite (Artis zee biplane; Siemens). Standardized angiography included selective manual injections of 4–5 mL of 300 mg/mL of iodinated nonionic contrast medium into the lumbar and intercostal arteries. If the preceding MRA examination suggested the level of a SEAVF, DSA protocol included at least injection of the segmental arteries, on both sides, 1 level above and below the suggested level. Imaging was in the anteroposterior direction with 2 frames per second. Oblique and lateral views were added to depict the morphology of the AV shunt as well as the intradural course of the draining vein. Film sequences of at least 5–20 seconds were obtained. Furthermore, 3D C-arm conebeam CT acquisitions (so-called Dyna-CT; Siemens) were performed in the last 5 patients in this cohort with a total acquisition time of 8 seconds. The arterial injection for the conebeam CT angiogram allowed both early and late opacification throughout the acquisition. MPRs were performed using an external postprocessing workstation.

The extension of the epidural pouch, the arterialized perimedullary veins, and the location of the perimedullary veins (dorsal, ventral) were analyzed on the basis of CE-MRA and DSA.

## RESULTS

### Clinical Presentations

Ten (77%) of 13 patients were men. The mean age was  $72 \pm 8$  years (median, 77 years; range, 59–83 years). Overall, 10 (77%) patients presented with a relatively short clinical course (<6 months) with progressive motor weakness in the lower extremities. The remaining 3 (23%) patients experienced a gradual onset and progressive deterioration of neurologic function. The mean interval between symptom onset and diagnosis was  $6 \pm 8$  months (median, 3 months; range, 1–24 months) when excluding 1 statistical outlier in this series with a symptom duration of 60 months (Table 1).

The most common neurologic findings at admission in our institution were gait disturbances due to paraparesis in 12 (92%) patients. The remaining 1 (8%) patient had neurogenic claudication without manifest motor deficits. Eight (62%) patients reported sphincter dysfunction at admission to our institution. Sensory symptoms in various severities were documented in 7 (54%) patients and comprised diffuse loss of sensation and/or paresthesia in the lower extremities.

All 13 patients underwent microsurgical interruption at our center. Microsurgical dorsal lumbar decompressions and discectomies due to assumption of a spinal degenerative disease were

**Table 1: Clinical presentation of patients with spinal epidural arteriovenous fistula**

Patient No.	Age (yr)/Sex	Duration of Symptoms (mo)	Symptoms at Diagnosis	Status at Discharge
1	78, M	6	Paraparesis, sphincter dysfunction	Improved
2	63, M	1	Paraparesis, sphincter dysfunction, hypesthesia below T10	Stable
3	77, M	1.5	Paraparesis, hypesthesia L4, ataxia, sphincter dysfunction	Stable
4	60, F	1.5	Paraplegia, hypesthesia disturbances below T10	Improved
5	68, F	24	Neurogenic claudication <100 m	Improved
6	77, M	1.5	Paraplegia, hypesthesia below L1, sphincter dysfunction	Stable
7	64, F	1	Paraparesis, sphincter dysfunction	Improved
8	83, M	60	Paraparesis, hypesthesia, sphincter dysfunction	Stable
9	72, M	0	Paraparesis, hypesthesia, sphincter dysfunction	Stable
10	80, M	12	Paraparesis, sphincter dysfunction	Stable
11	77, M	2	Paresis of left foot, ataxia	Stable
12	78, M	3	Paraparesis, hypesthesia	Stable
13	59, M	5	Ataxia	Stable

**Table 2: Angiomorphologic characteristics of spinal epidural arteriovenous fistulas**

Patient No.	Arterial Feeder <sup>a</sup>	Origin of Intradural Radicular Drainage Vein <sup>a</sup>	Extension of Epidural Pouch <sup>b</sup>	Extension of Arterialized Perimedullary Veins <sup>b</sup>	Location of Arterialized Perimedullary Veins <sup>b</sup>	No. of DSAs until Diagnosis
1	L3 R	L3 L	L3–L4	T8–T12	D = V	2
2	L3 bilateral, L4 L	L3 L	L2–L4	T3–T12	D = V	2
3	L1 R	L1 R	L1	ND	D < V	1
4	L3 bilateral	L3 R	L3	T9–L1	D > V	1
5	Left iliolumbar artery	S1	S1	T7–T12	D > V	3
6	T10 L and T11 L	L2 L	T10–L3	T6–L1	D = V	3
7	L1 L	L2 L	L1–L2	T3–T12	D = V	1
8	T12 L	T12 L	T12 L	T11	D > V	3
9	L3 L	L3 L	L3 L	T6–T12	D < V	1
10	L4 R	L4 R	L2–L4	T3–T10	D = V	1
11	L3 L	S1 bilateral	L3–S1	T10–L1	D > V	1
12	L3 R	L3 R	L3 R	T9–T12	D < V	1
13	L1 R	L1 R	L1 R	T10–L1	D > V	1

**Note:**—D indicates dorsal to spinal cord; V, ventral to spinal cord; L, left; R, right; ND, no data.

<sup>a</sup> DSA.

<sup>b</sup> MRA/DSA.

performed elsewhere before a definite diagnosis in 3 (23%) of these 13 patients.

### Radiologic Findings

Data of preoperative MR images were available in all 13 patients (Table 2). There was a centromedullary multisegmental T2WI hyperintense signal with involvement of the conus medullaris in all patients (mean, 7 vertebral levels; range, 1–13 vertebral levels). Intramedullary contrast enhancement was present in 10/12 (83%) patients (mean, 3 vertebral levels; range, 1–10 vertebral levels).

Enlargement and elongation of arterialized perimedullary veins in the thoracic and/or thoracolumbar region were detected in various manifestations in all patients, mild in 6 (50%), moderate in 3 (25%), and prominent in the remaining 3 (25%) patients. The arterialized perimedullary veins were localized predominantly dorsal to the spinal cord in 5 (42%) and ventrally in 3 (25%). In the other 5 patients, arterialized perimedullary veins were observed dorsal and ventral to the spinal cord. In 9 (90%) of 10 patients who underwent CE-MRA before DSA at our center, the arterialized ventrolateral epidural pouch was additionally detected, triggering the diagnosis of an SEAVF.

In 5 patients, >2 DSA examinations were necessary to establish the diagnosis of SEAVF (Table 2).

Angiographically, 10 (77%) of the 13 fistulas were in the lum-

bar region, and 2, (15%) in the lower thoracic region below T10, respectively. The remaining (8%) fistula was located in the sacral region. The arterialized ventrolateral epidural pouch in 6 (46%) of 13 patients extended over several vertebral levels (mean, 2 vertebral levels; range, 1–3 vertebral levels). Multiple arterial feeders were detected in 3 (23%) patients.

Furthermore, the intradural radicular drainage vein originated in 3 (23%) patients distant from the level of the fistula-feeding segmental artery, ipsilaterally in 2, patients 6 and 7, and bilaterally in patient 11 (range, 1–3 vertebral levels) (Table 2).

## DISCUSSION

### Definition and Pathogenic Aspects of SEAVF

Arteriovenous disorders of the epidural venous plexus have been rarely reported in the literature.<sup>2,7,8</sup> Paraspinal AV shunts were first clearly described by Cognard et al<sup>9</sup> in 2 patients with retrograde filling of intradural veins. The first SEAVF in our institution was diagnosed in 2006 and reported elsewhere.<sup>10</sup> Since then, SEAVFs have been more frequently diagnosed in our center. The finding might reflect a better understanding of this particular vascular disorder as well as the growing diagnostic impact of spinal MR angiography.

The angioarchitecture, namely the feeding arteries, the venous

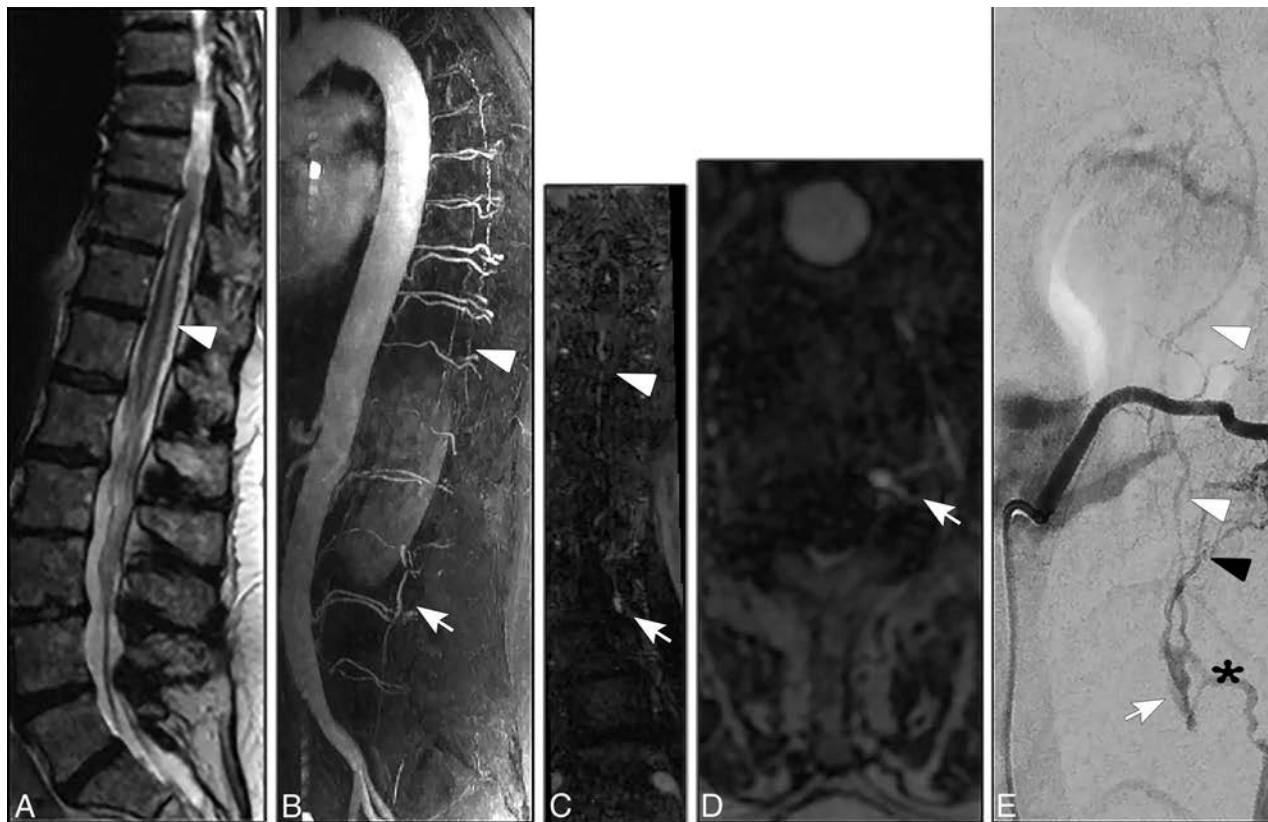


**FIG 1.** A, Sagittal T2-weighted images (3T; T2-TSE; slice thickness, 3 mm) reveal extensive congestive myelopathy (*white arrowhead*). B–D, Spinal CE-MRA (3T; time-resolved imaging with stochastic trajectories (TWIST); sagittal MIP; coronal and axial MPR) shows arterIALIZED pouch in the lumbar ventrolateral epidural space (*white arrows*) in association with arterIALIZED perimedullary veins in the thoracic region (*white arrowheads*) suspicious for a SEAVF in the lumbar region. E, DSA in lateral projection shows a SEAVF (*white arrow*) supplied via branches of the left L2 segmental artery (*black arrowhead*) and drained via the respective intradural radicular vein (*white arrowheads*). Note the extraspinal venous outlet (*asterisk*).

drainage pattern, and the location of the AV shunt itself, differentiate these SEAVFs from the more frequent SDAVF.<sup>8</sup>

Concerning the angioarchitecture in SEAVF, the blood supply of the epidural arterial arcade is usually derived from numerous osseous and epidural branches of the segmental arteries with multisegmental and/or collateral anastomoses running along the spinal epidural space.<sup>7,11</sup> In contrast, SDAVFs are usually supplied via radiculomeningeal branches of the radicular arteries, which run within the dural sleeve of the respective nerve roots.<sup>12</sup>

The venous drainage in SEAVF can occur epidurally and transdurally via an intradural radicular drainage vein into the perimedullary venous plexus, in contrast to the venous drainage in classic SDAVF, which occurs exclusively transdurally into the perimedullary venous plexus.<sup>2</sup>

Concerning the location of the AV shunt, the fistulous zone in all our patients was in the ventral and ventrolateral epidural spaces with variable craniocaudal extension of the arterIALIZED epidural pouch along several vertebral levels (Fig 1).

In 1 patient, the epidural shunt was even more complex, crossing the midline; multiple compartments of the epidural plexus were filled ventrally as well as the contralateral intradural radicular vein on the same vertebral level (Fig 2).

The frequent ventral/ventrolateral location of the arterIALIZED ventrolateral epidural pouch in an SEAVF could be explained by the rich venous anastomoses of the relatively wide ventral epidural

space in the thoracic and lumbar regions.<sup>13</sup> The posterior venous plexus is not well-appreciated angiographically and is not regularly involved in any pathologic process.<sup>3,14</sup> In contrast to the SEAVF, the AV shunt in a classic SDAVF is usually located within the dural sleeve of the nerve root dorsolaterally in the thoracolumbar region and mainly ventrolaterally in the deep lumbosacral region.<sup>5,15</sup>

Nonetheless, the precise pathomechanism of the transdural venous drainage in both SDAVFs and SEAVFs is still unclear.<sup>15,16</sup> An anti-reflux-impeding mechanism between both the epidural and perimedullary venous systems has been a matter of dispute in various anatomic studies.<sup>12,17-21</sup> Tadić et al<sup>17</sup> reported an anti-backflow system within the transdural course of the radicular veins, resulting from narrowing and zigzagging of the vein walls while crossing the dura. Thron et al<sup>12</sup> differentiated 2 types of transdural venous courses: a slit-like and a zigzag bulgy type. Both types of transdural venous courses might act as a valve protecting against reflux from the epidural into the coronal venous plexus.<sup>10,12</sup> Nonetheless, due to the valveless venous walls of the epidural plexus, it is also conceivable that this anti-reflux mechanism might decompensate under high-pressure conditions and the venous blood could flow in either direction.<sup>18,19,21-23</sup> A retrograde filling of radicular veins from the epidural venous plexus has also been observed in a few anatomic studies.<sup>10,12,17,19,24,25</sup> Moreover, during spinal DSAs and epidural phlebography, epidural shunts without reflux into the perimedullary veins have been occasionally visualized.<sup>15</sup>

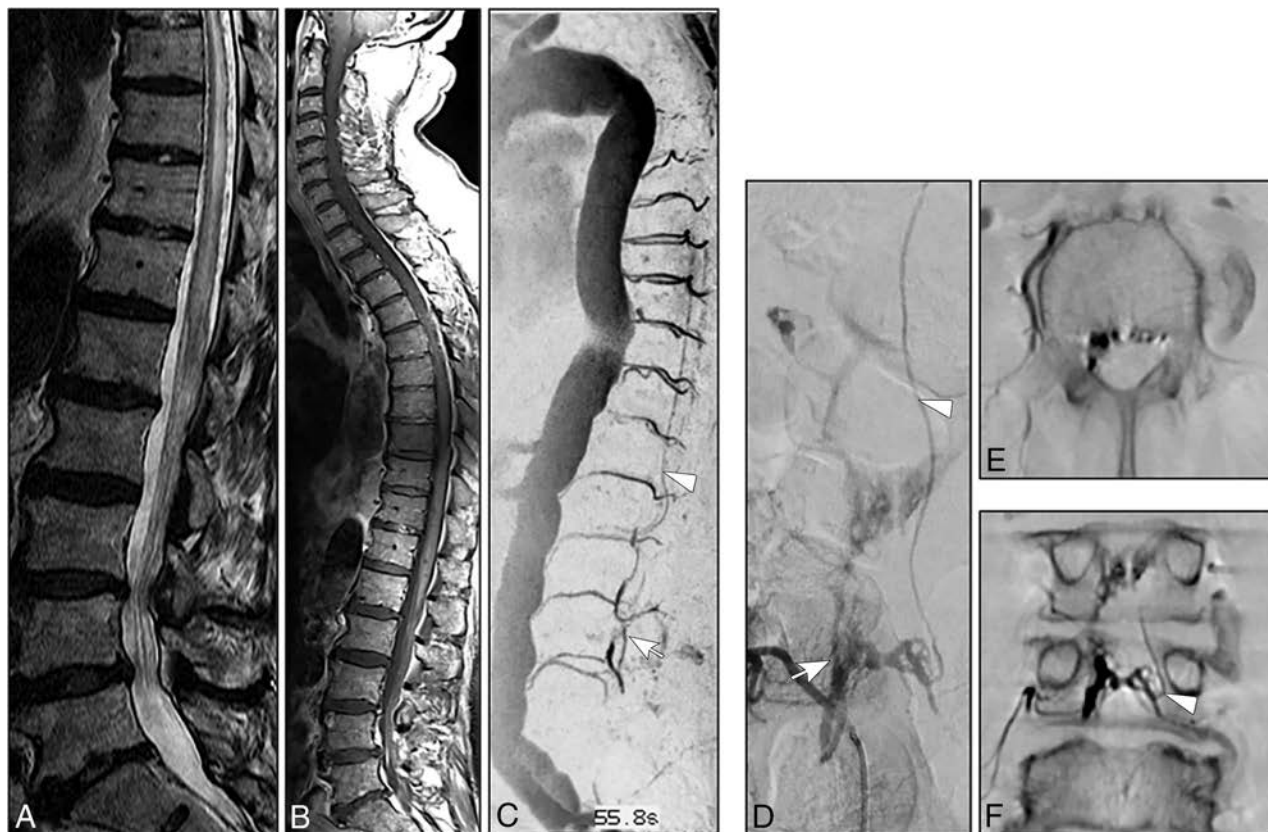


**FIG 2.** A–B, Sagittal T2- and contrast-enhanced T1-weighted images (3T; T2-TSE; T1-TSE; slice thickness, 3 mm) show extensive congestive thoracic myelopathy. C, Spinal CE-MRA (sagittal MIP) reveals an abnormal arterIALIZED epidural pouch in the lumbar region (*white arrow*) in addition to thoracic arterIALIZED perimedullary veins (*white arrowhead*). D, DSA (posteroanterior projection) exams identify the fistula in the epidural space on the vertebral level of L4 (*white arrow*), supplied via the right L4 segmental artery and drained by the contralateral L4 intradural radicular vein (*white arrowhead*). E and F, Axial and coronal MPR of DynaCT, 2 mm, 8 seconds rotation: Note the multisegmental and bilateral extension of the arterIALIZED epidural pouch and the left sided origin of the intradural radicular drainage vein crossing the dura at the contralateral neural foramen (*white arrowhead*).

On the basis of these observations, one could assume that epidural shunts might occur more frequently than previously thought, but they often remain asymptomatic as long as the transdural anti-reflux mechanism remains intact.<sup>10,12</sup>

An intravenous stasis and/or acute hydrostatic disturbances within these arterIALIZED elongated epidural compartments might reinforce the development of venous thrombosis. This may, in turn, induce acute disruption of the dural anti-reflux mechanisms causing transdural venous drainage and subsequent congestive myelopathy.<sup>26</sup> Supporting this hypothesis, the origin of the arterIALIZED radicular vein in 3 (23%) patients in our series was caudal to the epidural AV shunt (Fig 3).

### Clinical Presentation

Due to the extremely low incidence of SEAVFs, clinical presentations of these lesions have been rarely reported systematically in larger sample series.<sup>14,27</sup> Most patients in our study presented with motor weakness of the lower extremities, sphincter dysfunction, and sensory disturbances (Table 1) at admission. After treatment, clinical symptoms of most patients in our study stabilized or were mildly improved at discharge.<sup>14,27</sup> This result is in accordance with those in case series reported by Kiyosue et al<sup>14</sup> and Nasr et al.<sup>27</sup>

Due to the arterIALIZATION of the perimedullary venous plexus,

several progressive pathophysiologic changes can occur in the spinal cord and its vessels, such as hyalinization, vascular calcification, necrosis, and gliosis, all potential contributors to irreversible functional deterioration of the spinal cord.<sup>28-30</sup>

One major finding in our current analysis was the relatively rapid clinical course of SEAVFs compared with classic SDAVFs. This might be triggered by acute hemodynamic changes of the venous outflow of the spinal cord caused by thrombosis and/or hydrostatic changes in the epidural and perimedullary venous plexus.<sup>7</sup>

### Radiologic Findings

The hallmarks of SEAVFs on MR imaging in our current cohort were the following: 1) congestive thoracolumbar myelopathy with a high rate of conus medullaris involvement, 2) a predominantly nonprominent appearance of the pathologically arterIALIZED perimedullary veins in most cases (75%), and 3) the presence of ventrally/ventrolaterally located arterIALIZED epidural venous pouches detected in 9 of 10 patients with CE-MRA preceding DSA.

The value of CE-MRA in diagnosing an SDAVF has been previously reported by our group.<sup>6</sup> In a series of 19 patients with SDAVFs, the correct localization could be achieved in 14 (74%) patients. In the remaining 5 patients, a mismatch of only 1 vertebral level was noted.<sup>6</sup> Our current findings are supported by

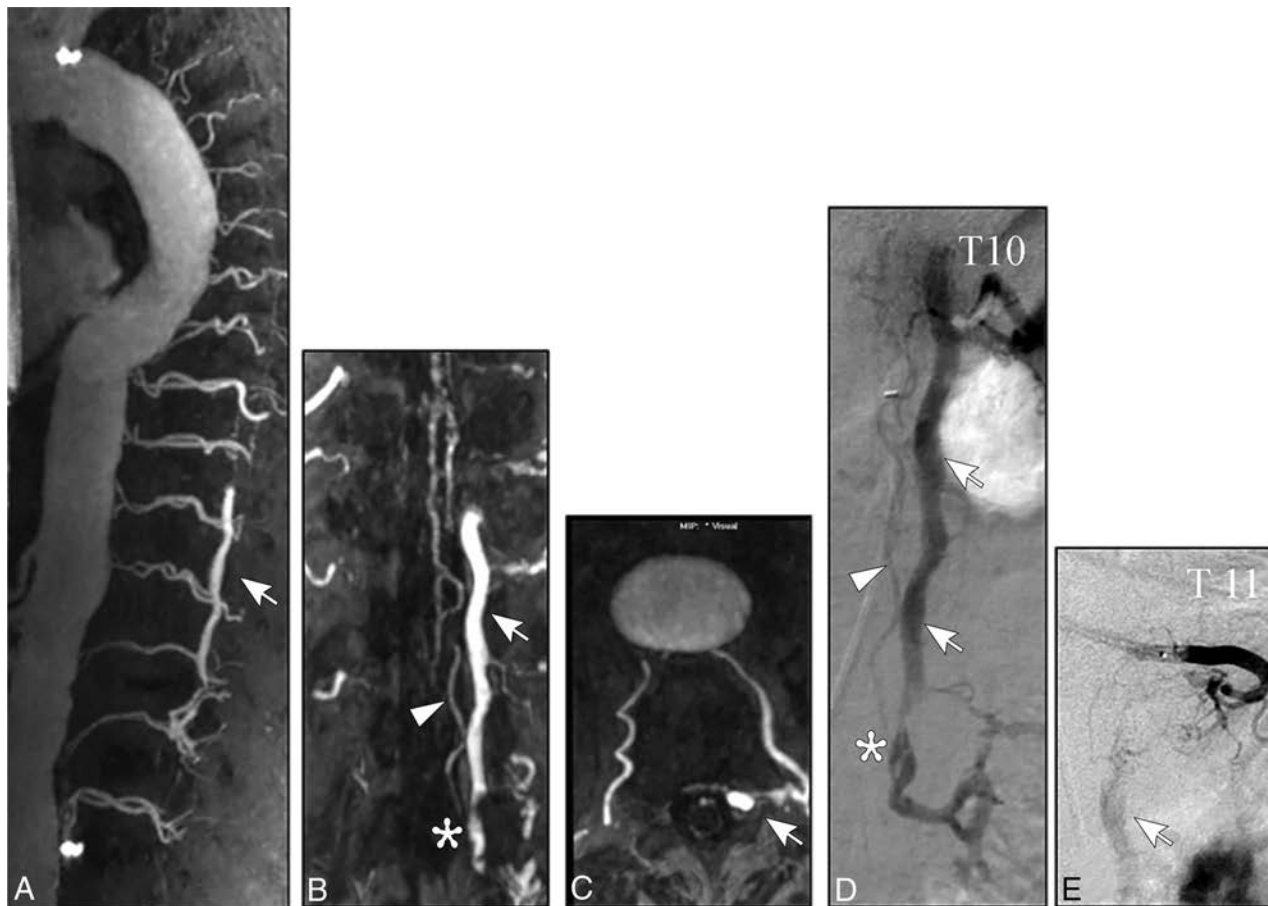


**FIG 3.** A, Spinal CE-MRA (1.5 T, sagittal MIP) reveals an extensive pathological arterialization of a ventrolateral epidural venous pouch extending over four vertebral levels (*white arrow*). B–C, Further reconstructions of the source MRA images (coronal and axial MPR) demonstrate precisely the epidural pouch (*white arrow*) and show the filling of the intradural radicular drainage vein (*white arrowhead*). D–E, DSA exams (posteroanterior projections) identify the multisegmental ventrolateral epidural pouch of the SEAVF (*white arrow*) with multiple left-sided arterial feeders supplied by the thoracic segmental arteries T 10 and T 11. Note the distant origin of the intradural radicular drainage vein (*asterisk*).

Mathur et al,<sup>31</sup> who recently observed, in a series of 7 patients with SEAVFs, a high accuracy and reliability of CE-MRA for identification and localization of these lesions.

DSA is, however, still regarded as a basic diagnostic tool for the angiomorphic, pretherapeutic evaluation in spinal AV fistulas and malformations.<sup>6,32–34</sup> In 5 (38%) of 13 patients, even repetitive spinal DSA remained inconclusive and did not sufficiently depict the suspected AV shunt before referral to our center.

Based on our experience, reasons for this failure rate were insufficient opacification of the respective segmental artery based on atherosclerosis and anatomic obstacles and a too-short DSA series, resulting in missing the intradural radicular and/or perimedullary veins. Moreover, 4 of these 5 patients did not undergo spinal CE-MRA initially, which may have facilitated the diagnosis via subsequent DSA.

Spinal angiography offers a dynamic visualization of the angioarchitecture of vascular malformations, including the arterial feeders, the morphology of AV shunts/venous pouches, and the draining veins.<sup>32</sup>

Overall, 12 (92%) fistulas were located in the thoracolumbar region and were supplied by segmental arteries. The remaining (8%) fistula was located in the sacral region and was supplied by branches of the left iliolumbar artery. Also, multisegmental or

collateral arterial feeders of the arterialized ventrolateral epidural pouch were present in 3 (23%) of our patients. In contrast, of 196 patients with SDAVFs treated at our center between 1990 and 2017, only 9 (4.6%) fistulas presented with a multisegmental or bilateral arterial supply.<sup>5,35</sup>

The predominant thoracolumbar location of SEAVFs and the higher rate of multiple arterial feeders of SEAVFs compared with classic SDAVFs could also be explained by the wide epidural space and the rich epidural anastomotic arterial network in this region.<sup>3,7,13</sup>

The arterialized epidural pouch extended over several vertebral levels in 6 (46%) patients. The intradural radicular drainage vein in 3 of these 6 patients was distant from the epidural fistulous point. This multisegmental distance between the fistulous feeding artery and the origin of the intradural radicular drainage vein has never been previously observed in any classic SDAVF at our center.<sup>15,35</sup>

Because the main goal of treatment of SEAVF is the disconnection of the intradural radicular drainage vein as well as the complete interruption of arterialized epidural compartments, the precise localization of the intradural radicular drainage vein in SEAVF is essential to reduce the risk of residual or recurrent fistulas irrespective of the treatment technique and strategy.

## Limitations

A major limitation of our study is the small sample size and the retrospective approach. Because spinal epidural arteriovenous fistulas are a very rare but clinically relevant entity, our results may, nevertheless, serve as an orientation for future studies, in particular because there are scarce data concerning this topic in large cohorts in the literature.

## CONCLUSIONS

Congestive myelopathy with an acute or subacute clinical course is a dominant finding in SEAVFs. The presence of myelopathic symptoms combined with medullary venous congestion with or without contrast enhancement on MR imaging should require CE-MRA, even in cases of nonprominent perimedullary veins. In SEAVFs, CE-MRA is a powerful noninvasive diagnostic tool to identify the epidural AV shunt itself and detect arterialized perimedullary veins. DSA remains obligatory for the angiomorphic analysis of the epidural AV shunt, which frequently extends ventrolaterally over several vertebral levels. DSA is mandatory for identifying the origin of the intradural radicular drainage vein that may be located distant from the epidural fistulous point.

Disclosures: Ahmed Othman—UNRELATED: Grants/Grants Pending: Bayer Healthcare, unrestricted grant\*; Payment for Lectures Including Service on Speakers Bureaus: GE Healthcare, speakers bureaus. Gerrit Alexander Schubert—UNRELATED: Payment for Lectures Including Service on Speakers Bureaus: Braun Aesculap. \*Money paid to the institution.

## REFERENCES

1. Oldfield EH, Doppman JL. **Spinal arteriovenous malformations.** *Clin Neurosurg* 1988;34:161–83 Medline
2. Clarke MJ, Patrick TA, White JB, et al. **Spinal extradural arteriovenous malformations with parenchymal drainage: venous drainage variability and implications in clinical manifestations.** *Neurosurg Focus* 2009;26:E5 CrossRef Medline
3. Brinjikji W, Yin R, Nasr DM, et al. **Spinal epidural arteriovenous fistulas.** *J Neurointerv Surg* 2016;8:1305–10 CrossRef Medline
4. Aminoff MJ, Logue V. **The prognosis of patients with spinal vascular malformations.** *Brain* 1974;97:211–18 CrossRef Medline
5. Jablawi F, Nikoubashman O, Schubert GA, et al. **Clinical and radiologic characteristics of deep lumbosacral dural arteriovenous fistulas.** *AJNR Am J Neuroradiol* 2018;39:392–98 CrossRef Medline
6. Mull M, Nijenhuis RJ, Backes WH, et al. **Value and limitations of contrast-enhanced MR angiography in spinal arteriovenous malformations and dural arteriovenous fistulas.** *AJNR Am J Neuroradiol* 2007;28:1249–58 CrossRef Medline
7. Silva N Jr, Januel AC, Tall P, et al. **Spinal epidural arteriovenous fistulas associated with progressive myelopathy: report of four cases.** *J Neurosurg Spine* 2007;6:552–58 CrossRef Medline
8. Rangel-Castilla L, Holman PJ, Krishna C, et al. **Spinal extradural arteriovenous fistulas: a clinical and radiological description of different types and their novel treatment with Onyx.** *J Neurosurg Spine* 2011;15:541–49 CrossRef Medline
9. Cognard C, Semaan H, Bakchine S, et al. **Paraspinal arteriovenous fistula with perimedullary venous drainage.** *AJNR Am J Neuroradiol* 1995;16:2044–48 Medline
10. Krings T, Mull M, Bostroem A, et al. **Spinal epidural arteriovenous fistula with perimedullary drainage: case report and pathomechanical considerations.** *J Neurosurg Spine* 2006;5:353–58 CrossRef Medline
11. Lasjaunias P, Berenstein A, Raybaud C. *Surgical Neuroangiography.* Berlin: Springer-Verlag; 1990
12. Thron A, Krings T, Otto J, et al. **The transdural course of radicular spinal cord veins: a microangiographical and microscopical study.** *Clin Neuroradiol* 2015;25:361–69 CrossRef Medline
13. Takai K, Taniguchi M. **Comparative analysis of spinal extradural arteriovenous fistulas with or without intradural venous drainage: a systematic literature review.** *Neurosurg Focus* 2012;32:E8 CrossRef Medline
14. Kiyosue H, Tanoue S, Okahara M, et al. **Spinal ventral epidural arteriovenous fistulas of the lumbar spine: angioarchitecture and endovascular treatment.** *Neuroradiology* 2013;55:327–36 CrossRef Medline
15. Thron AK. **Applications in spinal dural AV fistulas.** In: Thron A. *Vascular Anatomy of the Spinal Cord: Radioanatomy as the Key to Diagnosis and Treatment.* 2nd ed. Cham: Springer International Publishing; 2016
16. Jablawi F, Nikoubashman O, Mull M. **Arterial hypertension is associated with symptomatic spinal dural arteriovenous fistulas.** *World Neurosurg* 2017;103:360–63 CrossRef Medline
17. Tadié M, Hemet J, Freger P, et al. **Morphological and functional anatomy of spinal cord veins [in French].** *J Neuroradiol* 1985;12:3–20 Medline
18. Merland JJ, Riche MC, Chiras J. **Intraspinal extramedullary arteriovenous fistulae draining into the medullary veins [in French].** *J Neuroradiol* 1980;7:271–320 Medline
19. van der Kuip M, Hoogland PV, Groen RJ. **Human radicular veins: regulation of venous reflux in the absence of valves.** *Anat Rec* 1999;254:173–80 CrossRef Medline
20. Groen RJ, du Toit DF, Phillips FM, et al. **Anatomical and pathological considerations in percutaneous vertebroplasty and kyphoplasty: a reappraisal of the vertebral venous system.** *Spine* 2004;29:1465–71 CrossRef Medline
21. Groen RJ, Grobbelaar M, Muller CJ, et al. **Morphology of the human internal vertebral venous plexus: a cadaver study after latex injection in the 21–25-week fetus.** *Clin Anat* 2005;18:397–403 CrossRef Medline
22. Clemens HJ, Vogelsang H. **Transosseous phlebography of the vertebral column and spinal canal: morphological and clinical aspects [in German].** *Verh Anat Ges* 1970;64:179–80 Medline
23. Vogelsang H, Pia HW. **Importance of spinal angiography for the diagnosis of spinal angioma [in German].** *Fortschr Geb Rontgenstr Nuklearmed* 1965;102:661–66 Medline
24. Behrens S, Thron A. **Long-term follow-up and outcome in patients treated for spinal dural arteriovenous fistula.** *J Neurol* 1999;246:181–85 CrossRef Medline
25. Jürgen O. *Morphologie des Sperrmechanismus am Duradurchtritt der Venae Radiculares des Menschen: neuroradiologische und histologische Befunde* [doctoral thesis]. Aachen: Faculty of Medicine, RWTH Aachen University; 1990
26. Jablawi F, Schubert GA, Hans FJ, et al. **Anticoagulation therapy after surgical treatment of spinal dural arteriovenous fistula: effectiveness and long-term outcome analysis.** *World Neurosurg* 2018;114:e698–705 CrossRef Medline
27. Nasr DM, Brinjikji W, Clarke MJ, et al. **Clinical presentation and treatment outcomes of spinal epidural arteriovenous fistulas.** *J Neurosurg Spine* 2017;26:613–20 CrossRef Medline
28. Hurst RW, Kenyon LC, Lavi E, et al. **Spinal dural arteriovenous fistula: the pathology of venous hypertensive myelopathy.** *Neurology* 1995;45:1309–13 CrossRef Medline
29. Benhaïem N, Poirier J, Hurth M. **Arteriovenous fistulae of the meninges draining into the spinal veins: a histological study of 28 cases.** *Acta Neuropathol* 1983;62:103–11 CrossRef Medline
30. Rodriguez FJ, Crum BA, Krauss WE, et al. **Venous congestive myelopathy: a mimic of neoplasia.** *Mod Pathol* 2005;18:710–18 CrossRef Medline
31. Mathur S, Symons SP, Huynh TJ, et al. **First-pass contrast-enhanced MRA for pretherapeutic diagnosis of spinal epidural arteriovenous fistulas with intradural venous reflux.** *AJNR Am J Neuroradiol* 2017;38:195–99 CrossRef Medline

32. Thron A. **Spinal dural arteriovenous fistulas [in German]**. *Radiologe* 2001;41:955–60 Medline
33. Gilbertson JR, Miller GM, Goldman MS, et al. **Spinal dural arteriovenous fistulas: MR and myelographic findings**. *AJNR Am J Neuroradiol* 1995;16:2049–57 Medline
34. Thron A, Mull M, Reith W. **Spinal arteriovenous malformations [in German]**. *Radiologe* 2001;41:949–54 CrossRef Medline
35. Mull M. **Durchblutungsstörungen des Rückenmarks: Neurologische Untersuchungen zur Pathogenese und Strategien der Diagnosesicherung**. Department of Diagnostic and Interventional Neuroradiology, University Hospital Aachen. 2004 [https://www.researchgate.net/publication/33987973\\_Durchblutungsstorungen\\_des\\_Ruckenmarks\\_neuroradiologische\\_Untersuchungen\\_zur\\_Pathogenese\\_und\\_Strategien\\_der\\_Diagnosesicherung](https://www.researchgate.net/publication/33987973_Durchblutungsstorungen_des_Ruckenmarks_neuroradiologische_Untersuchungen_zur_Pathogenese_und_Strategien_der_Diagnosesicherung). Accessed January 20, 2004

# Facial Venous Malformations Are Associated with Cerebral Developmental Venous Anomalies

W. Brinjikji, C.A. Hilditch, A.C. Tsang, P.J. Nicholson, T. Krings, and R. Agid



## ABSTRACT

**BACKGROUND AND PURPOSE:** A number of studies have demonstrated the existence of segmental vascular disorders affecting soft tissues of the head and neck along with the intracranial vasculature. The purpose of this study was to determine whether there is an association between cerebral developmental venous anomalies and venous malformations of the face, head, and neck.

**MATERIALS AND METHODS:** A consecutive series of patients with head and neck venous malformations who underwent MR imaging of the brain with postcontrast T1- or T2\*-weighted imaging were included. Developmental venous anomaly prevalence in this patient population was compared with an age- and sex-matched control group without venous malformations at a ratio of 1:2. All images were interpreted by 2 neuroradiologists. Data were collected on venous malformation location, developmental venous anomaly location, developmental venous anomaly drainage pattern, and metameric location of venous malformations and developmental venous anomalies. Categorical variables were compared using  $\chi^2$  tests.

**RESULTS:** Forty-two patients with venous malformations were included. The mean age was  $38.1 \pm 11.1$  years, and 78.6% of patients were female. The prevalence of developmental venous anomalies in this patient population was 28.6%. The control population of 84 patients had a mean age of  $40.0 \pm 5.9$  years, and 78.6% of patients were female. The prevalence of developmental venous anomalies in this patient population was 9.5% ( $P = .01$ ). In 83.3% of cases, developmental venous anomalies were ipsilateral to the venous malformation, and in 75% of cases, they involved the same metamere.

**CONCLUSIONS:** Our case-control study demonstrated a significant association between brain developmental venous anomalies and superficial venous malformations. These findings suggest that there may be a similar pathophysiologic origin for these 2 entities.

**ABBREVIATIONS:** CVMS = Cerebrofacial venous metameric syndrome; DVA = developmental venous anomaly; VM = venous malformation

With increased use of cross-sectional imaging, developmental venous anomalies (DVAs) are discovered more frequently. DVAs consist of dilated intramedullary veins that converge into a larger draining vein, which then drains into either the superficial or deep venous system. Population-based studies have found that up to 10% of the general population has incidental DVAs.<sup>1</sup>

While DVAs are generally common, superficial venous vascular malformations of the head and neck are quite rare. Venous malformations (VMs) are slow-flow vascular malformations that manifest as soft-tissue swellings under normal or bluish skin.

These lesions are exacerbated by increased central venous pressure such as a Valsalva maneuver. Pathologically, VMs consist of dilated venous channels in the dermis or muscular tissues that usually drain into larger tributaries of the external jugular venous system.<sup>2</sup>

During the past several years, we have noticed a possible association between the presence of VMs and intracranial DVAs on cross-sectional imaging. This may be a logical association given that the presence of metameric disorders in which patients have vascular malformations involving the brain and soft tissues of the head, face, and neck is well-established.<sup>3</sup> Identification of such an association could also be important because it could provide some insight into the pathogenesis of both of these entities. In order to study the association between DVAs and VMs, we performed a case-control study examining the prevalence of DVAs on MR imaging of a consecutive population of patients with VMs compared to a group of age- and sex-matched controls.

Received June 30, 2018; accepted after revision August 6.

From the Departments of Radiology (W.B.) and Neurosurgery (W.B.), Mayo Clinic, Rochester, Minnesota; and Joint Department of Medical Imaging (W.B., C.A.H., A.C.T., P.J.N., T.K., R.A.), Toronto Western Hospital, Toronto, Ontario, Canada.

Please address correspondence to Waleed Brinjikji, MD, Mayo Clinic, 200 1st St SW, Rochester, MN 55905; e-mail: brinjikji.waleed@mayo.edu; @wbrinjikji

Indicates article with supplemental on-line table.

<http://dx.doi.org/10.3174/ajnr.A5811>

## MATERIALS AND METHODS

### Patient Population

Following institutional review board approval at Toronto Western Hospital, we queried our data base of >250 patients with VMs for patients who had an MR imaging of the brain including either T2\*-weighted imaging and/or postcontrast T1-weighted imaging. VMs were confirmed by a combination of physical examination and imaging-based findings.<sup>4,5</sup> Imaging criteria for a VM on MR imaging were the following: 1) a septate lobulated T2 hyperintense and T1 hypointense mass without mass effect; 2) phleboliths, which are characteristically hypointense on T1/T2; 3) the presence of fluid-fluid levels; 4) no flow voids on spin-echo sequences; 5) the lesion infiltrating tissue planes; 6) no arterial or early venous enhancement; and 7) diffuse enhancement on delayed images. On clinical examination, VMs appear as faint blue, soft, and easily compressible nonpulsatile masses. The lesions characteristically enlarge with a Valsalva maneuver and in dependent positions and decompress with local compression. Only adult patients with VMs were included in this study because our institution is not a pediatric center. We also selected a group of age- and sex-matched controls (case:control ratio of 1:2) from a data base used to estimate the prevalence of brain DVAs in the general population, which was reviewed by 2 board-certified neuroradiologists. Age matching was performed with an error margin of  $\pm 1$  year. Thus, a 37-year-old woman could be matched with a 36- to 38-year-old woman.

### Imaging Analysis

For the VM population, all images were analyzed by 2 neuroradiologists. Images were reviewed to document the following: 1) the presence or absence of a DVA, 2) the location and side of the DVA if present, and 3) the location and side of the VM. Locations were categorized by metamere as well. The 3 metameres of the craniofacial system include the medial prosencephalic group (olfactory) with involvement of the forehead, nose hypothalamus, corpus callosum, and hypophysis (cerebrofacial venous metameric syndrome [CVMS] 1); the lateral prosencephalic group (optic) with involvement of the temporoparieto-occipital lobes, optic nerve, retina, thalamus, eye, cheek, and maxilla (CVMS 2); and the rhombencephalic/mesencephalon (otic) group with involvement of the cerebellum, brain stem, lower face, mandible, petrous bone, and maxilla (CVMS 3).<sup>6</sup>

### Statistical Analysis

The primary outcome of this study was the prevalence of DVAs in the VM population and in controls. Prevalence rates were compared using a  $\chi^2$  test. A Student *t* test was used to compare continuous variables. All statistical analyses were performed using JMP 13.0 (SAS Institute, Cary, North Carolina).

## RESULTS

### Patient Population

Forty-two patients with VMs were included along with 84 controls. In the VM population, the mean age was  $38.1 \pm 11.1$  years, and 78.6% of patients were women (33/42). The control population had a mean age of  $40.0 \pm 5.9$  years, and 78.6% of patients were women (66/84). Among the patients with VMs, 3 patients

had bilateral VMs and 39 patients had unilateral facial VMs. Of the patients in the control group, 11 patients underwent MR imaging for evaluation of seizure, 7 patients underwent MR imaging for evaluation of an intracranial mass, and 66 patients underwent MR imaging for other causes, including headache, metastatic disease screening, and other indications such as ruling out ischemia.

### DVA Prevalence and Characteristics

Of the 42 patients with VMs, a diagnosis of DVA was made in 12 patients (28.6%). The prevalence of DVAs in the control population was 9.5% (8/84). This difference was statistically significant ( $P = .01$ ).

Of the patients with VMs and DVAs, none were men and 12 were women. All 12 had extensive cutaneous VMs. DVAs were unilateral in 8 patients and bilateral in 4 patients. There were 35 DVAs, with 7 patients having multiple DVAs. Thirty DVAs had deep drainage, and 5 had superficial venous drainage. In 23 cases, DVAs were supratentorial, and in 12 cases, they were infratentorial. In 83.3% of cases, DVAs were ipsilateral to the VM, and in 75% of cases, they involved the same metamere. The On-line Table summarizes the characteristics of all patients with VMs with associated DVAs. Case examples are provided in Figs 1–3.

## DISCUSSION

Our case-control study examining the prevalence of DVAs in patients with VMs and a group of control patients demonstrated a number of interesting findings. First, the prevalence of DVAs in the VM population was >2 times higher than that in the general population. Most interesting, more often than not, DVAs were located along the same metamere and/or side as the VM. These findings are important because they suggest that there may be a similar pathophysiologic or embryologic basis to both craniofacial VMs and intracranial DVAs.

Prior studies have demonstrated a possible association between DVAs and VMs. However, no case-control studies have been performed to date comparing the prevalence of DVAs in patients with VMs and in a group of patient controls without VMs. In a series of 40 patients who underwent cerebral angiography as part of the evaluation of facial venous vascular malformations, Boukobza et al<sup>7</sup> identified 8 patients (20%) with complex DVAs, with most patients having multiple DVAs. Unlike Sturge-Weber Syndrome, these complex DVAs were associated with a normal superficial cortical venous system. Most DVAs were supratentorial and had large flaming venous radicles that drained into a tortuous deep venous system, and most were ipsilateral to the facial VM. One patient had a symptomatic cavernoma that required resection.<sup>7</sup> Overall, the DVA prevalence rate and clinical presentation of these VM-associated DVAs are very similar to those seen in our patient population. A number of additional case reports have been published concerning patients with extensive facial venous malformations and associated ipsilateral DVAs. Such an association hardly appears to be coincidental.<sup>2,3,6,8-10</sup>

DVAs are thought to form in later periods of cerebral venous development as functional adaptations to thrombosis or failure

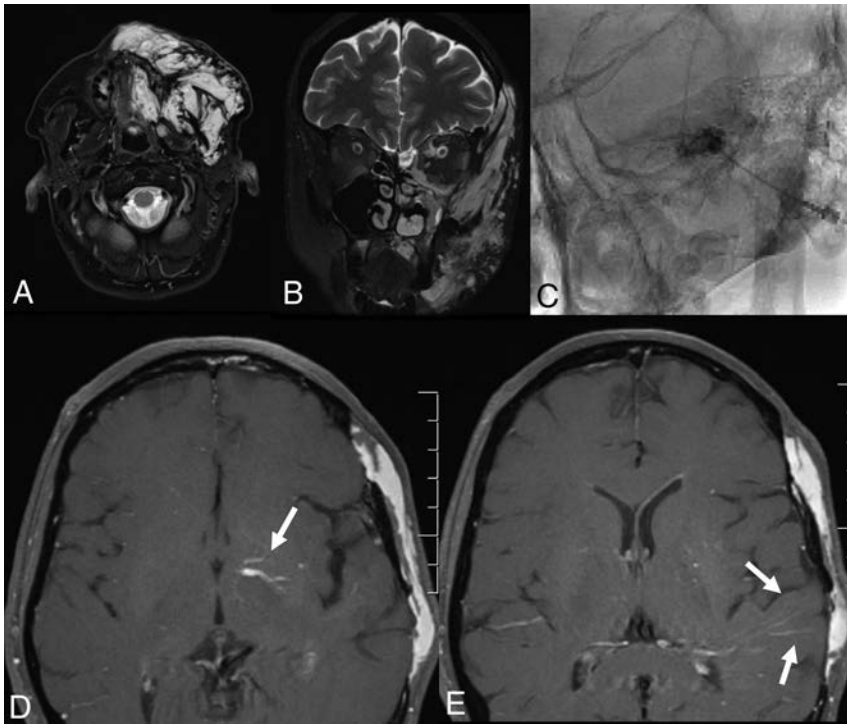


**FIG 1.** A 49-year-old woman with VMs and DVAs. VMs are in the left temporal region, orbit, zygomaticofacial region, and mandible (A and B). The patient underwent bleomycin sclerotherapy for treatment of the VMs with good results (C). She also had an extensive DVA of the left temporal lobe, basal ganglia, and left cerebellar hemisphere (D and E). Findings would be consistent with CVMS 1–3.

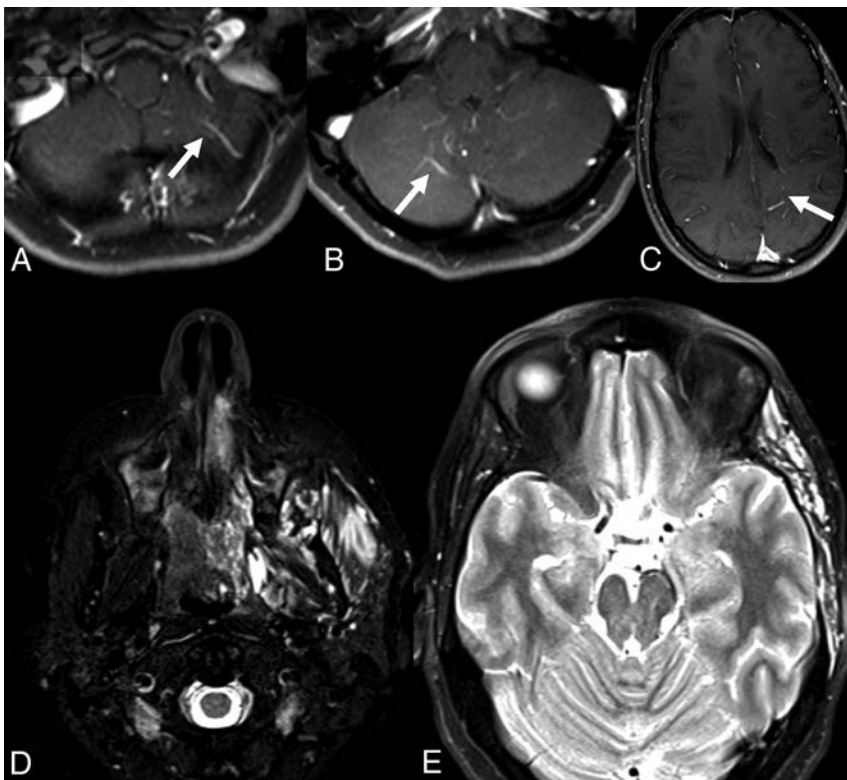


**FIG 2.** A 30-year-old man with facial VMs and left supratentorial DVAs. A–C, Postcontrast T1-weighted MRIs show DVAs in the bilateral cerebellar hemispheres, left parietal lobe, and left temporal lobe. D and E, T2-weighted MR imaging shows extensive VMs of the left zygomatico-temporal region and masticator spaces.

of development of superficial or deep veins.<sup>11</sup> It is possible that early postnatal venous occlusion could trigger remodeling of medullary veins, thus resulting in DVA formation. Furthermore, when DVAs become symptomatic, it is invariably due to thrombosis of the collector vein or a venous radicle.<sup>11</sup> Nonetheless, the common final pathway is an error in vascular embryogenesis resulting in occlusion and maldevelopment of normal venous structures in a given part of the brain. To date, there have been no genetic mutations associated with DVA development.

Some authors have postulated that a similar error in vascular embryogenesis (ie, thrombosis resulting in occlusion and maldevelopment) affecting the craniofacial venous vasculature could result in the formation of VMs as well. Like DVAs, VMs generally do not develop de novo or proliferate and spread to other vascular beds in adult life. Most interesting, some authors have suggested that VMs are also thought to form due to a procoagulable state.<sup>12,13</sup> In a case-control study of patients with and without VMs, Domp Martin et al<sup>12,13</sup> found that 43% of patients with VMs have an elevated D-dimer level compared with just 4% of patients without VMs. Up to one-third of children with VMs have some form of prothrombotic coagulopathy.<sup>14</sup> In another study, Domp Martin et al<sup>12,13</sup> found that almost 50% of patients with VMs have local intravascular coagulation, a factor thought to be responsible for VM enlargement and pain. So how can we explain the link between DVAs and extensive facial VMs in a more or less unilateral distribution in this patient population? Given that both VMs and DVAs are associated with some degree of prothrombotic state, we hypothesize that VMs and DVAs may develop due to an increased predilection for local venous thrombosis and occlusion, possibly due to a metamer disorder related to venous endothelial dysfunction.

Our study has both practical implications and implications for future research. First, on the basis of these findings, one might consider a whole-head MR imaging for patients with VMs to evaluate intracranial vascular abnormalities. Two patients had DVA-associated cavernomas, one of which developed de novo and was associated with clinical

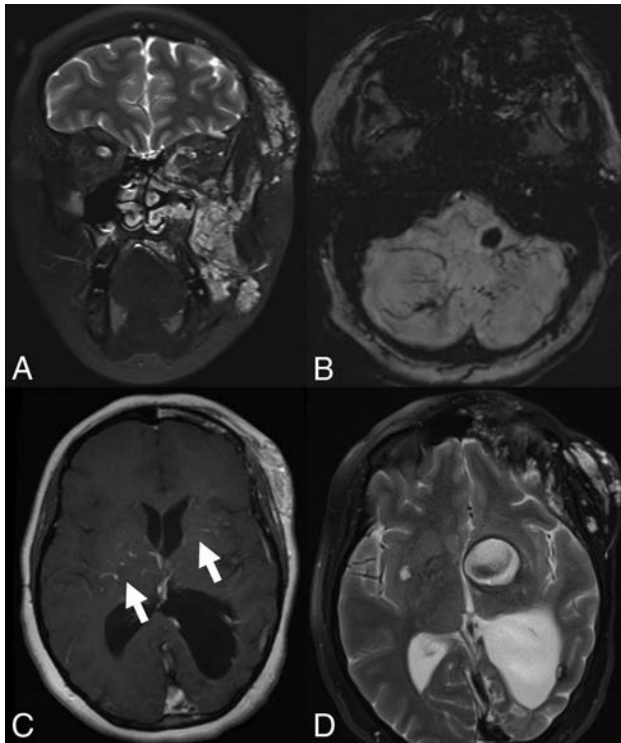


**FIG 3.** A 22-year-old woman with a left facial DVA, bilateral VMs, and a de novo cavernoma. **A**, Coronal T2-weighted MR imaging demonstrates a vascular malformation involving the soft tissues overlying the left zygomatico-orbital region with extension to the left maxillary region. **B**, Axial SWI MR imaging of the brain demonstrates extensive DVAs of the bilateral cerebellar hemispheres and a cavernoma of the left medulla. **C**, Postcontrast MR imaging demonstrates venous radicles of 2 DVAs involving the bilateral basal ganglia. **D**, T2-weighted MR imaging 2 years later demonstrates a large cavernoma that developed in one of the venous radicles of the left basal ganglia DVA.

symptoms. Identification of extensive DVAs in the patient population with VMs could be used to select patients who may require closer imaging surveillance. Regarding implications for future research, the genetic and pathophysiologic mechanisms that result in the codevelopment of DVAs and VMs should be further studied. Three patients in our study had either a classic Sturge-Weber syndrome or a form fruste of Sturge-Weber. It is now well-established that Sturge-Weber is due to a somatic mutation in the *GNAQ* gene, which plays a role in expression of the endothelin in vascular endothelial cells.<sup>15</sup> Meanwhile, somatic mutations in vascular endothelial cells of the *PIK3CA* gene are associated with the development of venous vascular malformations.<sup>16</sup> Discovery of these genetic associations has led to promising research in targeted therapy for these diseases. It may be that patients with DVAs and head and neck VMs carry a common vascular endothelial cell somatic mutation. Further research into identifying genetic mutations in this patient population may provide insight into disease pathophysiology and targeted treatment of venous vascular malformations.

#### Limitations

Our study has limitations. First, this was a retrospective study and is prone to selection bias. It is possible that the prevalence of DVAs in both the VM and control groups is artificially high due to variations in the indications for imaging. Routine intracranial T2\*

and postcontrast imaging are no longer performed at our institution for evaluation of patients with VMs, and often, these imaging studies are performed for evaluation of orbital vascular malformations or in patients with VMs with neurologic symptoms such as headaches. Another limitation is that while all patients in the control group underwent a postcontrast T1-weighted sequence, this was not the case in our patient population with VMs. Postcontrast T1-weighted imaging is more sensitive than T2\*-weighted imaging for the detection of smaller DVAs. Thus, we could have underestimated the DVA prevalence in the VM population. On the other hand, it is possible that our study is prone to selection bias because only a subset of patients presented with brain MR imaging. Last, our study is small, including only 42 patients with VMs.

#### CONCLUSIONS

Our case-control study demonstrated a significant association between DVAs and superficial VMs. More often than not, DVAs were located along a similar metamere or side as the VMs. These findings suggest that there may be a similar pathophysiologic origin for these 2 entities.

#### REFERENCES

1. Brinjikji W, El-Masri AE, Wald JT, et al. **Prevalence of cerebral cavernous malformations associated with developmental venous anomalies increases with age.** *Childs Nerv Syst* 2017;33:1539–43 [CrossRef Medline](#)
2. Agid R, Terbrugge KG. **Cerebrofacial venous metamerism syndrome 2 plus 3: facial and cerebral manifestations.** *Interv Neuroradiol* 2007;13:55–58 [CrossRef Medline](#)
3. Krings T, Geibprasert S, Luo CB, et al. **Segmental neurovascular syndromes in children.** *Neuroimaging Clin N Am* 2007;17:245–58 [CrossRef Medline](#)
4. Flors L, Leiva-Salinas C, Maged IM, et al. **MR imaging of soft-tissue vascular malformations: diagnosis, classification, and therapy follow-up.** *Radiographics* 2011;31:1321–40; discussion 1340–41 [CrossRef Medline](#)
5. Wassef M, Blei F, Adams D, et al; VA Board and Scientific Committee. **Vascular anomalies classification: recommendations from the International Society for the Study of Vascular Anomalies.** *Pediatrics* 2015;136:e203–14 [CrossRef Medline](#)
6. Bhattacharya JJ, Luo CB, Suh DC, et al. **Wyburn-Mason or Bonnet-Dechaume-Blanc as Cerebrofacial Arteriovenous Metameric Syndromes (CAMS): a new concept and a new classification.** *Interv Neuroradiol* 2001;7:5–17 [CrossRef Medline](#)
7. Boukobza M, Enjolras O, Guichard JP, et al. **Cerebral developmental venous anomalies associated with head and neck venous malformations.** *AJNR Am J Neuroradiol* 1996;17:987–94 [Medline](#)
8. Goulaou A, Alvarez H, Garcia Monaco R, et al. **Venous anomalies and abnormalities of the posterior fossa.** *Neuroradiology* 1990;31:476–82 [CrossRef Medline](#)
9. Portilla P, Husson B, Lasjaunias P, et al. **Sturge-Weber disease with repercussion on the prenatal development of the cerebral hemisphere.** *AJNR Am J Neuroradiol* 2002;23:490–92 [Medline](#)
10. Ramli N, Sachet M, Bao C, et al. **Cerebrofacial venous metamerism syndrome (CVMS) 3: Sturge-Weber syndrome with bilateral lymphatic/venous malformations of the mandible.** *Neuroradiology* 2003;45:687–90 [CrossRef Medline](#)
11. Pereira VM, Geibprasert S, Krings T, et al. **Pathomechanisms of symptomatic developmental venous anomalies.** *Stroke* 2008;39:3201–15 [CrossRef Medline](#)
12. DompMartin A, Acher A, Thibon P, et al. **Association of localized intravascular coagulopathy with venous malformations.** *Arch Dermatol* 2008;144:873–77 [Medline](#)

13. Domp Martin A, Ballieux F, Thibon P, et al. **Elevated D-dimer level in the differential diagnosis of venous malformations.** *Arch Dermatol* 2009;145:1239–44 Medline
14. Hung JW, Leung MW, Liu CS, et al. **Venous malformation and localized intravascular coagulopathy in children.** *Eur J Pediatr Surg* 2017;27:181–84 CrossRef Medline
15. Shirley MD, Tang H, Gallione CJ, et al. **Sturge-Weber syndrome and port-wine stains caused by somatic mutation in GNAQ.** *N Engl J Med* 2013;368:1971–79 CrossRef Medline
16. Limaye N, Kangas J, Mendola A, et al. **Somatic activating PIK3CA mutations cause venous malformation.** *Am J Hum Genet* 2015;97:914–21 CrossRef Medline

# MR Venous Flow in Sigmoid Sinus Diverticulum

M.R. Amans, H. Haraldsson, E. Kao, S. Kefayati, K. Meisel, R. Khangura, J. Leach, N.D. Jani, F. Faraji, M. Ballweber, W. Smith, and D. Saloner



## ABSTRACT

**BACKGROUND AND PURPOSE:** Case reports demonstrate that coiling of a sigmoid sinus diverticulum can treat pulsatile tinnitus. We hypothesized that MR imaging 4D flow and computational fluid dynamics would reveal distinct blood flow patterns in the venous outflow tract in these patients.

**MATERIALS AND METHODS:** Patients with pulsatile tinnitus of suspected venous etiology underwent MR imaging at 3T, using venous phase contrast-enhanced MR angiography, 4D flow, and 2D phase contrast. The contrast-enhanced MRA contours were evaluated to determine the presence and extent of a sigmoid sinus diverticulum. Computational fluid dynamics analysis was performed using the 4D flow inlet flow and the luminal contours from contrast-enhanced MRA as boundary conditions. In addition, computational fluid dynamics was performed for the expected post treatment conditions by smoothing the venous geometry to exclude the sigmoid sinus diverticulum from the anatomic boundary conditions. Streamlines were generated from the 4D flow and computational fluid dynamics velocity maps, and flow patterns were examined for the presence of rotational components.

**RESULTS:** Twenty-five patients with pulsatile tinnitus of suspected venous etiology and 10 control subjects were enrolled. Five (20%) of the symptomatic subjects had sigmoid sinus diverticula, all associated with an upstream stenosis. In each of these patients, but none of the controls, a stenosis-related flow jet was directed toward the opening of the sigmoid sinus diverticulum with rotational flow patterns in the sigmoid sinus diverticulum and parent sigmoid sinus on both 4D flow and computational fluid dynamics.

**CONCLUSIONS:** Consistent patterns of blood flow can be visualized in a sigmoid sinus diverticulum and the parent sinus using 4D flow and computational fluid dynamics. Strong components of rotational blood flow were seen in subjects with sigmoid sinus diverticula that were absent in controls.

**ABBREVIATIONS:** CFD = computational fluid dynamics; 4DF = 4D flow; PT = pulsatile tinnitus; SSD = sigmoid sinus diverticulum; SSIJ = sigmoid sinus and internal jugular vein; UCSF = University of California, San Francisco

Tinnitus is the auditory perception of sound in the absence of an extracorporeal source, which affects millions of Americans.<sup>1</sup> Patients' lives can be severely impacted by tinnitus, and it is not uncommon for patients to have insomnia, depression, or even

suicidal ideations because of their tinnitus.<sup>2-9</sup> A subset of tinnitus is rhythmic, termed "pulsatile tinnitus" (PT). PT accounts for up to 10% of patients with tinnitus.<sup>10-12</sup> Some causes of PT are associated with a very high risk of intracranial hemorrhage, stroke, or blindness. Even the more benign causes of PT have a very high association with debilitating comorbid psychiatric disease. Some causes of PT can be treated. In our experience, treating an underlying cause of PT not only alleviates the risks of hemorrhage, stroke, or blindness but can also mitigate the comorbid psychiatric disease. Thus, identifying and treating causes of PT can be very beneficial to patients.

PT may be related to abnormal flow in vascular structures near

Received March 27, 2018; accepted after revision August 20.

From the Departments of Radiology and Biomedical Imaging (M.R.A., H.H., E.K., S.K., R.K., J.L., N.D.J., F.F., M.B., D.S.) and Neurology (K.M., W.S.), University of California, San Francisco, San Francisco, California.

This work was supported by the National Center for Advancing Translational Sciences, National Institutes of Health, through UCSF-CTSI Grant Number B27552C. In addition, the research reported in this publication was supported by the National Institutes of Health under award number R21 DC016087-01A1.

The content of this article is solely the responsibility of the authors and does not necessarily represent the official views of the National Institutes of Health.

Paper previously presented, in part, at: Annual Meeting of the American Academy of Otolaryngology–Head and Neck Surgery Foundation, September 18–21, 2016; San Diego, California; and another portion of these data were presented at: Annual Meeting of the Society of NeuroInterventional Surgery, July 25–29, 2016; Boston, Massachusetts.

Please address correspondence to Matthew Amans, MD, MSc, UCSF, Department of Radiology and Biomedical Imaging, 505 Parnassus Ave, Room L349, San Francisco, CA, 94143; e-mail: matthew.amans@ucsf.edu.

Indicates open access to non-subscribers at [www.ajnr.org](http://www.ajnr.org)

<http://dx.doi.org/10.3174/ajnr.A5833>

the cochlea and is often pulse-synchronous.<sup>1,11</sup> The vascular structures with aberrant flow can be either venous or arterial. Approximately 40% of PT etiologies are venous, approximately 35% are arterial, and in nearly 25%, the cause of PT is never identified.<sup>13</sup> One of the venous etiologies of PT is a sigmoid sinus diverticulum (SSD). SSD is an outpouching from the sigmoid dural venous sinus that is usually laterally or anteriorly oriented and is often associated with an upstream transverse or sigmoid sinus stenosis.<sup>1,13-16</sup> Altering the flow of venous blood through the SSD and the parent sinus by manual compression of the ipsilateral internal jugular vein is known to mitigate symptoms. Patients report an increase in symptoms in high-flow states such as contralateral internal jugular vein compression, after exercise, or during pregnancy.<sup>13,17</sup> Treatment of the offending SSD, which has been reported with both endovascular and open surgical techniques, can resolve PT.<sup>17-22</sup>

However, the exact pattern of blood flow in patients with SSD has not been studied. Two recent approaches provide the ability to explore the flow patterns in complex vascular geometries. One is direct measurement of the velocity field using MR imaging techniques; the other is using a numeric simulation approach to compute the velocity field. Advances in MR imaging have facilitated the visualization of the 3D velocity field of blood flow through the cardiac cycle. We have adapted these techniques for imaging the flow patterns in the transverse sinus, sigmoid sinus, and the internal jugular vein near to and including the jugular bulb (a region of venous sinus anatomy we will refer to as the SSIJ) using 3T MR imaging.<sup>23-25</sup> Alternatively, with known boundary conditions (ie, the luminal surface and the inlet flow waveform), numeric simulations (computational fluid dynamics [CFD]) can be used to calculate the velocity field. The aim of this study was to apply these techniques to subjects with SSD and evaluate the blood flow patterns in this venous anomaly. We hypothesize that subjects with PT with SSD demonstrate a distinct flow pattern in the SSIJ and SSD that is absent in control subjects.

## MATERIALS AND METHODS

We prospectively performed MR imaging analysis on adult patients with suspected venous etiology of pulsatile tinnitus and control subjects without pulsatile tinnitus using a study protocol approved by our institutional review board. All patients signed written informed consent to participate in this study.

### Patient Selection

Patients were recruited from the University of California, San Francisco (UCSF) Pulsatile Tinnitus Clinic. The UCSF Pulsatile Tinnitus Clinic is a multispecialty clinic that evaluates patients with PT. PT was suspected to be of venous etiology if the patient described a low-pitched, pulse-synchronous PT that improved with ipsilateral neck compression and potential arterial (or other) etiologies (such as carotid atherosclerosis, fibromuscular dysplasia, tumor, or dural arteriovenous fistula) were not identified on prior imaging studies. All patients underwent the UCSF Pulsatile Tinnitus Clinic MR imaging and MRA protocol, which included brain MR imaging with fat-saturated postcontrast sequences, time-of-flight MRA of the head, time-resolved contrast-enhanced MRA of the neck

through the circle of Willis, and postcontrast spoiled gradient-recalled imaging to evaluate venous sinus anatomy.

### Imaging

The imaging protocol used in this study is an adaptation of contrast-enhanced MRA and 4D flow (4DF) described in prior articles.<sup>23-25</sup> High-resolution contrast-enhanced MRA was performed on a 3T Magnetom Skyra scanner (Siemens, Erlangen, Germany). A 3D time-resolved imaging with a stochastic trajectory timing run with a 2-mL gadolinium bolus was used to determine the venous phase of contrast opacification as the point when the contrast first appears in the distal transverse sinus. The full contrast-enhanced MRA study was then performed with a 20-mL injection of gadolinium-based contrast agent at 2 mL/s with an acquisition time of 35 seconds. Images had 0.7-mm isotropic resolution covering an FOV of 280 × 180 mm with an 84-mm-thick slab. Image acquisition used an elliptic centric *k*-space ordering with the center of *k*-space synchronized to the venous phase as determined from the timing run. Following acquisition of the MRA, a finger-pulse-triggered 4D MR velocimetry study (4DF) was acquired at a 1.3-mm isotropic resolution and 32-mm slab coverage. Subsequently, 2D phase contrast was acquired in a slice transverse to the vessel in the mid-transverse sinus and proximal to any stenosis if one was present. Phase contrast in-plane resolution was 0.65 × 0.65 mm.

### Postprocessing

The contrast-enhanced MRA vein and 4D MR velocimetry datasets were segmented using Clem-volume, an in-house software package. The velocity field, streamlines, path lines, vorticity, and helicity maps were generated from these data using Paraview (Kitware, Clifton Park, New York). In addition, a numeric simulation of the velocity field (ie, a CFD analysis) was performed using the contrast-enhanced MRA for the luminal surface boundary conditions and the inlet flow condition as acquired from the 2D phase contrast study. Several assumptions were made in our CFD analysis, including Newtonian flow, steady flow conditions, pressure of 0 cm H<sub>2</sub>O at the outlet of the modeled segment, and rigid walls, as per our previously published method.<sup>24</sup> To investigate the effects of an interventional treatment on the velocity field, we altered the geometry to provide a simulated, smooth, and continuous luminal surface that excluded the SSD. Path lines and streamlines were generated from the CFD-predicted velocity field.

### Flow Pattern Analysis

The streamlines were extracted and visualized in Paraview, using seed points dispersed throughout the flow domain. As can be seen in the figures, regions of recirculating or vortical flow were identified by visual inspection.

## RESULTS

Twenty-five patients with a suspected venous etiology of PT and 10 control subjects without PT were imaged using our protocol. Of the 25, five (20%) had an SSD identified on MRA (Table). Streamlines of the CFD- and 4DF-resolved velocity field images for the 5 patients with SSD and 1 control subject are shown in

### Anatomic characteristics and treatments performed for the identified sigmoid sinus diverticula

Subject	SSD Dimensions (mm)	Neck Maximum Width (mm)	Orientation of Long Axis of SSD		Associated Upstream Stenosis	Treatment
			Laterality	Laterality		
1	6.0 × 2.8 × 3.2	3.2	Lateral	Left	Yes	None
2	6.8 × 8.0 × 4.2	3.4	Lateral	Right	Yes	Coiled
3	7.4 × 5.5 × 6.3	5.1	Anterior	Right	Yes	Surgical resurfacing
4	8.8 × 5.7 × 8.4	6.4	Anterior	Right	Yes	None
5	8.3 × 3.9 × 6.9	6.6	Lateral	Right	Yes	None
5	6.8 × 7.5 × 5.6	4.1	Lateral	Left	Yes	Stent

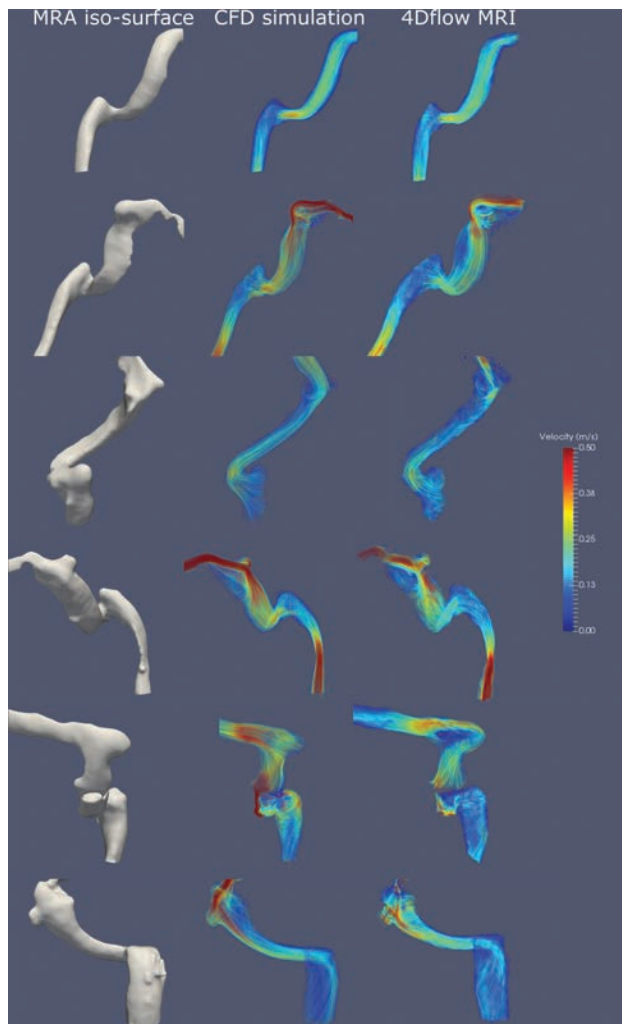


**FIG 1.** MRA isosurface MIP rendering, CFD-predicted flow fields, and 4D-flow MR imaging from 6 subjects. The first subject is a control subject. The other 5 are subjects clinically suspected of having a venous cause for pulsatile tinnitus who were found to have a sigmoid sinus diverticulum on MRA. The following observations are made in symptomatic subjects with a sigmoid diverticulum: 1) high velocity flow jet in an upstream stenosis in the transverse sinus directed at the SSD opening; 2) a flow jet into the SSD along the long axis of the SSD, either anteriorly or laterally directed; 3) a vortex of flow in the SSD; and 4) a strong vortex component of flow in the sigmoid sinus from the SSD. In the control subject, none of these flow components were present.

Fig 1. All SSDs had a bulbous shape directed away from the flow in the upstream sinus, either laterally or anteriorly, and all were associated with an upstream stenosis with a flow jet directed toward the SSD opening.

### Observations of Blood Flow from 4DF (In Vivo Measurement)

In vivo measurement of blood flow in the SSIJ revealed some commonalities among patients with SSD: 1) a high-velocity flow jet is demonstrated at the stenosis in the transverse sinus, directed distally at the SSD opening; 2) the flow jet into the SSD is oriented along the long axis of the SSD (either anteriorly or laterally directed); 3) there is a vortical flow in the SSD; 4) a large component of rotational flow is present in the sigmoid sinus downstream from the SSD; and 5) none of these flow features were seen in the SSIJ of control subjects.

### Observations from CFD Flow Analysis

The flow patterns observed in the CFD analysis were very similar to those identified by 4DF. The flow jets through the stenoses, the vortices of flow in the SSD, and the flow recirculation in the sigmoid sinuses were all comparable between modalities. While the gross flow features were similar, there were some minor differences in the velocity fields resolved by 4DF and CFD in certain locations.

### Observations from Post treatment

CFD analysis was performed on the expected post treatment geometries lacking SSDs and demonstrated the absence of flow recirculation in the parent sinus. Subject 2 elected to have surgical resurfacing of her SSD, which resulted in resolution of her PT symptoms. This subject subsequently underwent repeat MR imaging evaluation using our protocol. No flow was identified at the site of the prior SSD, and recirculation was no longer present in the parent sinus. The pre- and post treatment 4DF and CFD flow fields based on the pre- and post treatment MRA are shown in Fig 2. The SSD was excluded from the flow domain to simulate resurfacing of the pretreatment sinus geometry, and CFD was performed. For this simulated post-treatment geometry, the flow jet through the stenosis remained unchanged but the vortices in the sigmoid sinus downstream from the diverticulum remained.

### DISCUSSION

We present a case series of 5 subjects with suspected venous PT and SSD in whom we imaged the anatomy and blood flow of the venous anomaly as well as the parent sinus using contrast-enhanced MRA and 4DF, and we also performed CFD analysis. All SSDs had similar anatomic and flow imaging, consisting of a bulbous outpouching projecting anteriorly or laterally from the sigmoid sinus, with the long axis of the SSD in the direction of a flow jet through the upstream transverse sinus stenosis. This study was an observational analysis that provides an illustration of the ability of imaging and computational methods to visualize complex

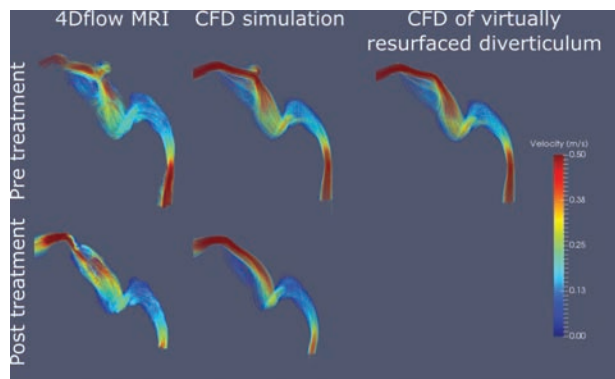


**FIG 2.** MRA, CFD simulation, and 4D-flow MR imaging from subject 2 before and after surgical exclusion of her sigmoid sinus diverticulum, which resulted in resolution of symptoms. There was an absence of flow in the SSD as well as lack of a vortex in the downstream sigmoid sinus. Only the SSD was excluded from the CFD flow domain. Thus, the flow jet through the proximal stenosis is unchanged.

flow patterns present in patients with venous diverticula. To have a clinical impact, inclusion of a broader range of geometrically varying SSDs is needed to provide a definitive link between geometry and flow and subsequently to the manifestation of PT symptoms.

While 4DF has been used fairly extensively in the vasculature, it has found the greatest application on the arterial side. To develop confidence in the 4DF measurement of the velocity field in the tortuous venous anatomy, we also performed numeric simulations of the flow fields using a CFD approach. Both 4DF and CFD demonstrated comparable flow patterns consisting of a flow jet through the stenosis, a vortex of flow in the SSD, and an additional vortex of flow in the parent sigmoid sinus. One case of repeat 4DF and CFD after SSD surgical exclusion, which resulted in cessation of PT, demonstrated an absence of flow in the SSD as well as resolution of the vortex of flow in the sigmoid sinus.

Previous publications have demonstrated the ability to evaluate flow in the SSIJ of patients with pulsatile tinnitus using both *in vivo* and patient-specific flow models,<sup>23</sup> evaluate flow differences in the SSIJ of subjects with and without PT using CFD,<sup>24</sup> and provide an overview of the varying flow patterns that can be seen in subjects with PT with different SSIJ anatomies using 4DF.<sup>25</sup> Levitt et al<sup>26</sup> used patient-specific MR imaging and catheter-obtained pressure measurements to generate CFD models of transverse sinus stenoses. The current work expands on prior articles by systematically reviewing a series of subjects with an anatomic aberration, SSD. In addition, we are the first group to evaluate flow in the dural venous sinuses of patients to establish the boundary conditions for the inlet flow conditions of our CFD analysis. This work also includes pre- and postsurgical evaluation of flow using both 4DF and CFD. In keeping with our group's prior publications of blood flow evaluation in the cerebral venous structures, we have again identified several interesting flow features in these patients.

The role that these flow patterns, specifically the vortices in the SSD and parent sinus, play in sound generation in patients with SSD and PT is unclear, and in fact, they may play no role at all. It is conceivable that turbulent flow downstream of the stenosis, within the SSD or at the outlet of the SSD, may contribute to

sound generation. However, the unique pattern of flow presented in this work has not been previously demonstrated, to our knowledge. Our hope is to eventually use this technique to prospectively identify patients whose PT would be well-treated with surgical or endovascular exclusion of the SSD.

All subjects with SSDs had a concomitant transverse sinus stenosis. Transverse sinus stenosis has also been shown to be a cause of PT, and the high rate of comorbid sinus stenosis and SSD has been previously reported.<sup>18,20,22,27-32</sup> The stenosis and subsequent flow jet may cause the SSD, similar to the effects of complex patterns of wall shear stress and spatial wall shear stress gradients previously reported in intracranial bifurcation aneurysms such as at the basilar tip.<sup>33,34</sup> Our observation that the long axis of the SSD is coincident with the flow jet from the stenosis would seem to lend credence to this hypothesis; however, the relationship between the entities remains speculative.

To establish the role that geometric features of the diverticulum, such as maximal diameter and neck width, have in defining specific flow patterns such as vortices in the SSD and parent sinus, it will be necessary to expand this study to include a broader spectrum of geometric conditions. Expanding the study will similarly contribute to defining the link between flow patterns and sound generation in patients with SSD and PT. The unique pattern of flow presented in this work has not been previously demonstrated.

It is also unclear whether the stenosis, the SSD, or both are causing patients' symptoms. Many authors have treated both the stenosis and the diverticulum and reported resolution of symptoms<sup>27,31,32</sup>; others have treated only the SSD and also reported resolution of symptoms.<sup>18,22,28-30</sup> We suspect that sound generation in these patients with PT is multifactorial, and the source of sound generation remains a focus of ongoing research.

All 5 patients with PT found to have an SSD were women. This may be simply a result of the small sample size, though there may be a component of idiopathic intracranial hypertension contributing to the transverse sinus stenosis in these patients, and idiopathic intracranial hypertension is more common in females.<sup>35</sup> In fact, subject 5 was found to have idiopathic intracranial hypertension based on standard criteria,<sup>36</sup> and her symptoms greatly improved with stent placement in a transverse sinus stenosis, which decreased the pretreatment pressure gradient across the stenosis from 13 to 3 mm Hg.

There are several limitations to our study. Our small sample size limits the extent of the conclusions we can derive. Several assumptions were made in our CFD analysis, including Newtonian flow, steady flow conditions, zero pressure at the outflow, and a noncompliant vessel wall. While Newtonian flow is a reasonable assumption in capacious vessels such as the sigmoid sinus and jugular vein, the flow may be non-Newtonian in transverse-sigmoid junction stenosis. Steady flow conditions have been used in our prior work and have previously captured most flow information with a high degree of fidelity.<sup>24</sup> Rigid wall conditions are likely a reasonable assumption in the transverse and sigmoid sinuses, which are encased by the thick dura and bone. However, the validity of this assumption is challenged by known changes in PT with lumbar puncture and removal of CSF, particularly in patients with idiopathic intracranial hypertension.<sup>37</sup> In addition,

the jugular vein has a very high capacitance and is known to not be a rigid structure. Our models in this work include only the jugular bulb that is, at least partly, bounded by the skull base.

## CONCLUSIONS

This prospective case series applied 4DF and CFD analysis to patients suspected of having a venous etiology of PT and identified a consistent pattern of blood flow that was absent in controls. The flow pattern consists of a high-velocity jet through a transverse sinus stenosis directed into the SSD, vortical flow in the SSD, and a vortex of flow returning to the sigmoid sinus from the SSD. 4DF and CFD of the post treatment state show resolution of flow in the SSD and resolution of the vortex in the sigmoid sinus. The role the vortices play in sound generation for PT is unclear and remains a subject of future investigation.

Disclosures: Matthew R. Amans—*RELATED: Grant:* National Institutes of Health, *Comments:* This project was supported by the National Center for Advancing Translational Sciences, National Institutes of Health, through UCSF-CTSI Grant Number B27552C. In addition, the research reported in this publication was supported by the National Institutes of Health under award number R21 DC016087–01A1. Its content is solely the responsibility of the authors and does not necessarily represent the official views of the National Institutes of Health\*. *UNRELATED: Consultancy:* Covidien, *Comments:* I have worked as a proctor for Pipeline embolization procedures. The total annual compensation is less than \$25,000. David Saloner—*RELATED: Grant:* National Institutes of Health\*, *UNRELATED: Grants/Grants Pending:* National Institutes of Health, *Comments:* The National Institutes of Health is funding a grant related to this article. \*Money paid to the institution.

## REFERENCES

- Krishnan A, Mattox DE, Fountain AJ, et al. **CT arteriography and venography in pulsatile tinnitus: preliminary results.** *AJNR Am J Neuroradiol* 2006;27:1635–38 Medline
- Belli S, Belli H, Bahcebası T, et al. **Assessment of psychopathological aspects and psychiatric comorbidities in patients affected by tinnitus.** *Eur Arch Otorhinolaryngol* 2008;265:279–85 CrossRef Medline
- Weidt S, Delsignore A, Meyer M, et al. **Which tinnitus-related characteristics affect current health-related quality of life and depression? A cross-sectional cohort study.** *Psychiatry Res* 2016;237:114–21 CrossRef Medline
- Xu Y, Yao J, Zhang Z, et al. **Association between sleep quality and psychiatric disorders in patients with subjective tinnitus in China.** *Eur Arch Otorhinolaryngol* 2016;273:3063–72 CrossRef Medline
- Pridmore S, Walter G, Friedland P. **Tinnitus and suicide: recent cases on the public record give cause for reconsideration.** *Otolaryngol Head Neck Surg* 2012;147:193–95 CrossRef Medline
- Jacques D, Nozeret Y, Zdanowicz N, et al. **Tinnitus and psychiatric comorbidities in liaison psychiatry analysis of three years in an audiology centre.** *Psychiatr Danub* 2013;25(Suppl 2):S102–04 Medline
- Zirke N, Seydel C, Arsoy D, et al. **Analysis of mental disorders in tinnitus patients performed with Composite International Diagnostic Interview.** *Qual Life Res* 2013;22:2095–104 CrossRef Medline
- Seo JH, Kang JM, Hwang SH, et al. **Relationship between tinnitus and suicidal behavior in Korean men and women: a cross-sectional study.** *Clin Otolaryngol* 2016;41:222–27 CrossRef Medline
- Seydel C, Haupt H, Szczepek AJ, et al. **Three years later: report on the state of well-being of patients with chronic tinnitus who underwent modified tinnitus retraining therapy.** *Audiol Neurootol* 2015;20:26–38 CrossRef Medline
- Liyanage SH, Singh A, Savundra P, et al. **Pulsatile tinnitus.** *J Laryngol Otol* 2006;120:93–97 Medline
- Madani G, Connor SE. **Imaging in pulsatile tinnitus.** *Clin Radiol* 2009;64:319–28 CrossRef Medline
- Harvey RS, Hertzano R, Kelman SE, et al. **Pulse-synchronous tinnitus and sigmoid sinus wall anomalies: descriptive epidemiology and the idiopathic intracranial hypertension patient population.** *Otol Neurotol* 2014;35:7–15 CrossRef Medline
- Mattox DE, Hudgins P. **Algorithm for evaluation of pulsatile tinnitus.** *Acta Otolaryngol* 2008;128:427–31 CrossRef Medline
- Weissman JL, Hirsch BE. **Imaging of tinnitus: a review.** *Radiology* 2000;216:342–49 CrossRef Medline
- Sonmez G, Baskim CC, Ozturk E, et al. **Imaging of pulsatile tinnitus: a review of 74 patients.** *Clin Imaging* 2007;31:102–08 CrossRef Medline
- Hou ZQ, Han DY. **Pulsatile tinnitus in perimenopausal period.** *Acta Otolaryngol* 2011;131:896–904 CrossRef Medline
- Otto KJ, Hudgins PA, Abdelkafy W, et al. **Sigmoid sinus diverticulum: a new surgical approach to the correction of pulsatile tinnitus.** *Otol Neurotol* 2007;28:48–53 CrossRef Medline
- Houdart E, Chapot R, Merland JJ. **Aneurysm of a dural sigmoid sinus: a novel vascular cause of pulsatile tinnitus.** *Ann Neurol* 2000;48:669–71 CrossRef Medline
- Eisenman DJ. **Sinus wall reconstruction for sigmoid sinus diverticulum and dehiscence: a standardized surgical procedure for a range of radiographic findings.** *Otol Neurotol* 2011;32:1116–19 CrossRef Medline
- Liu Z, Chen C, Wang Z, et al. **Sigmoid sinus diverticulum and pulsatile tinnitus: analysis of CT scans from 15 cases.** *Acta Radiol* 2013;54:812–16 CrossRef Medline
- Santa Maria PL. **Sigmoid sinus dehiscence resurfacing as treatment for pulsatile tinnitus.** *J Laryngol Otol* 2013;127(Suppl 2):S57–S59 CrossRef Medline
- Amans MR, Stout C, Dowd CF, et al. **Resolution of pulsatile tinnitus after coil embolization of sigmoid sinus diverticulum.** *J Cerebrovasc Dis & Stroke* 2014;1:1010
- Acevedo-Bolton G, Amans MR, Kefayati S, et al. **Four-dimensional magnetic resonance velocimetry for complex flow in the jugular vein.** *Quant Imaging Med Surg* 2015;5:635–37 CrossRef Medline
- Kao E, Kefayati S, Amans MR, et al. **Flow patterns in the jugular veins of pulsatile tinnitus patients.** *J Biomech* 2017;52:61–67 CrossRef Medline
- Kefayati S, Amans M, Faraji F, et al. **The manifestation of vortical and secondary flow in the cerebral venous outflow tract: an in vivo MR velocimetry study.** *J Biomech* 2017;50:180–87 CrossRef Medline
- Levitt MR, McGah PM, Moon K, et al. **Computational modeling of venous sinus stenosis in idiopathic intracranial hypertension.** *AJNR Am J Neuroradiol* 2016;37:1876–82 CrossRef Medline
- Zenteno M, Murillo-Bonilla L, Martínez S, et al. **Endovascular treatment of a transverse-sigmoid sinus aneurysm presenting as pulsatile tinnitus: case report.** *J Neurosurg* 2004;100:120–22 CrossRef Medline
- Gard AP, Klopper HB, Thorell WE. **Successful endovascular treatment of pulsatile tinnitus caused by a sigmoid sinus aneurysm: a case report and review of the literature.** *Intervent Neuroradiol* 2009;15:425–28 CrossRef Medline
- Mehanna R, Shaltoni H, Morsi H, et al. **Endovascular treatment of sigmoid sinus aneurysm presenting as devastating pulsatile tinnitus: a case report and review of literature.** *Intervent Neuroradiol* 2010;16:451–54 CrossRef Medline
- Park YH, Kwon HJ. **Awake embolization of sigmoid sinus diverticulum causing pulsatile tinnitus: simultaneous confirmative diagnosis and treatment.** *Intervent Neuroradiol* 2011;17:376–79 CrossRef Medline
- Santos-Franco JA, Lee A, Nava-Salgado G, et al. **Hybrid carotid stent for the management of a venous aneurysm of the sigmoid sinus treated by sole stenting.** *Vasc Endovascular Surg* 2012;46:342–46 CrossRef Medline
- Signorelli F, Mahla K, Turjman F. **Endovascular treatment of two concomitant causes of pulsatile tinnitus: sigmoid sinus stenosis and ipsilateral jugular bulb diverticulum: case report and literature review.** *Acta Neurochir (Wien)* 2012;154:89–92 CrossRef Medline
- Meng H, Wang Z, Hoi Y, et al. **Complex hemodynamics at the apex of an arterial bifurcation induces vascular remodeling re-**

- sembling cerebral aneurysm initiation.** *Stroke* 2007;38:1924–31 CrossRef Medline
34. Kulcsár Z, Ugron A, Marosfoi M, et al. **Hemodynamics of cerebral aneurysm initiation: the role of wall shear stress and spatial wall shear stress gradient.** *AJNR Am J Neuroradiol* 2011;32:587–94 CrossRef Medline
35. Satti SR, Leishangthem L, Chaudry MI. **Meta-analysis of CSF diversion procedures and dural venous sinus stenting in the setting of medically refractory idiopathic intracranial hypertension.** *AJNR Am J Neuroradiol* 2015;36:1899–904 CrossRef Medline
36. Friedman DI, Jacobson DM. **Diagnostic criteria for idiopathic intracranial hypertension.** *Neurology* 2002;59:1492–95 CrossRef Medline
37. Wall M. **Idiopathic intracranial hypertension.** *Neurol Clin* 2010;28:593–617 CrossRef Medline

# MR Imaging in Menière Disease: Is the Contact between the Vestibular Endolymphatic Space and the Oval Window a Reliable Biomarker?

G. Conte, L. Caschera, S. Calloni, S. Barozzi, F. Di Bernardino, D. Zanetti, C. Scuffi, E. Scola, C. Sina, and F. Triulzi



## ABSTRACT

**BACKGROUND AND PURPOSE:** No reliable MR imaging marker for the diagnosis of Menière disease has been reported. Our aim was to investigate whether the obliteration of the inferior portion of the vestibule and the contact with the stapes footplate by the vestibular endolymphatic space are reliable MR imaging markers in the diagnosis of Menière disease.

**MATERIALS AND METHODS:** We retrospectively enrolled 49 patients, 24 affected by unilateral sudden hearing loss and 25 affected by definite Menière disease, who had undergone a 4-hour delayed 3D-FLAIR sequence. Two readers analyzed the MR images investigating whether the vestibular endolymphatic space bulged in the third inferior portion of the vestibule contacting the stapes footplate. This sign was defined as the vestibular endolymphatic space contacting the oval window.

**RESULTS:** We analyzed 98 ears: 27 affected by Menière disease, 24 affected by sudden sensorineural hearing loss, and 47 that were healthy. The vestibular endolymphatic space contacting the oval window showed an almost perfect interobserver agreement (Cohen  $\kappa$  = 0.87; 95% CI, 0.69–1). The vestibular endolymphatic space contacting oval window showed the following: sensitivity = 81%, specificity = 96%, positive predictive value = 88%, and negative predictive value = 93% in differentiating Menière disease ears from other ears. The vestibular endolymphatic space contacting the oval window showed the following: sensitivity = 81%, specificity = 96%, positive predictive value = 96%, negative predictive value = 82% in differentiating Menière disease ears from sudden sensorineural hearing loss ears.

**CONCLUSIONS:** The vestibular endolymphatic space contacting the oval window has high specificity and positive predictive value in differentiating Menière disease ears from other ears, thus resulting in a valid tool for ruling in Menière disease in patients with mimicking symptoms.

**ABBREVIATIONS:** AAO-HNS = American Academy of Otolaryngology–Head and Neck Surgery; BLB = blood-labyrinthine barrier; CH = cochlear hydrops; HC = healthy control; MD = Menière disease; nMD = normal in a patient with MD; NPV = negative predictive value; PPV = positive predictive value; SSHL = sudden sensorineural hearing loss; VEH = vestibular endolymphatic hydrops; VES = vestibular endolymphatic space; VESCO = vestibular endolymphatic space contacting the oval window

Menière disease (MD) is a relatively common disorder, with a prevalence of 200–500 per 100,000, characterized by fluctuating hearing loss, intermittent vertigo, tinnitus, and aural fullness.<sup>1</sup> MD is characterized by the presence of vestibular endolymphatic hydrops (VEH), a distension of the vestibular endolymphatic space (VES) of the inner ear. However, VEH might

not represent the sole cause of the symptoms. Following the assumption of Merchant et al, “It seems that all patients with classical symptoms of Menière’s disease have VEH, but not vice versa, as not all patients with hydrops have Menière’s disease symptoms.”<sup>2</sup> A diagnosis of definite MD is made by the presence of  $\geq 2$  episodes of vertigo, audiometrically documented low-to-medium frequency sensorineural hearing loss in 1 ear, or fluctuating aural fullness.<sup>3</sup>

MR imaging has recently been used in the diagnosis of MD because the presence of VEH can be demonstrated in vivo with a 3D-FLAIR sequence 4 hours after the intravenous administration of a contrast agent.<sup>4</sup> Data emerging from the literature about MR imaging of VEH in patients with MD are still discordant/uneven. Several diagnostic criteria have been proposed to evaluate the degree of the VEH, the most relevant/common being those of Nakashima et al,<sup>5</sup> a quantitative method that assesses the VES,

Received May 9, 2018; accepted after revision August 20.

From the Neuroradiology Unit (G.C., E.S., C. Sina, F.T.), Fondazione IRCCS Ca’Granda Ospedale Maggiore Policlinico, Milan, Italy; Postgraduation School of Radiodiagnosics (L.C., S.C.) and Departments of Medicine and Surgery (C. Scuffi) and Pathophysiology and Transplantation (F.T.), Università degli Studi di Milano, Milan, Italy; and Audiology Unit (S.B., F.D.B., D.Z.), Department of Clinical Sciences and Community, Fondazione IRCCS Ca’Granda Ospedale Maggiore Policlinico, Università degli Studi di Milano, Milan, Italy.

Please address correspondence to Giorgio Conte, MD, Neuroradiology Unit, Fondazione IRCCS Ca’Granda Ospedale Maggiore Policlinico, Via Francesco Sforza 35, 20122 Milan, Italy; e-mail: giorgioconte.unimed@gmail.com; @GiorgioConte86

<http://dx.doi.org/10.3174/ajnr.A5841>

**Table 1: Scanning parameters (3T)**

	Pre- and Postcontrast TI FSE	Pre- and Postcontrast 3D-FLAIR	3D T2-SSFP	Delayed Postcontrast 3D-FLAIR
Plane	Axial	Axial	Axial	Axial
TR (ms)	500	6000	1500	7600
TE (ms)	10	350	194	345
TI (ms)	/	2350	/	2100
Fat saturation	SPIR	SPIR	/	SPAIR
TSE factor	3	182	40	100
Flip angle	90°	90°	90°	90°
Slice thickness (mm)	1.5	1	0.6	0.6
Slices (no.)	15	30	22	40
FOV (mm <sup>2</sup> )	180 × 160	230 × 190	140 × 140	200 × 255
Matrix	256 × 205	232 × 229	264 × 248	250 × 252
Parallel imaging	No	Yes	No	Yes
Averages	4	6	1	4
Scan time	2 min 51 sec	10 min 6 sec	6 min 35 sec	9 min 15 sec

**Note.**—SSFP indicates steady-state free precession; SPIR, spectral presaturation with inversion recovery; SPAIR, spectral attenuated inversion recovery; 3D FLAIR, Three dimensionally Fluid Attenuated Inversion Recovery; FSE, Fast spin echo; TR, time of repetition; TE, time of echo; TI, time of inversion; TSE, Turbo Spin-Echo; FOV, field of view; /, specific parameter is not available.

calculating the ratio of the area of the VES to the entire vestibule (VES/vestibule ratio) in the axial plane and defining VEH as present if this ratio is >33%. More recently, Attyé et al<sup>6</sup> have established a morphology-based method: Saccular hydrops is considered when a sacculle-to-utricle ratio of  $\geq 1$  is present. However, both of these scores seem to lack high accuracy in differentiating MD from other otologic disorders.<sup>7</sup>

There is an unmet clinical need to understand the role of the contact between the VES and the stapes footplate. Our aim was to investigate whether the obliteration of the inferior portion of the vestibule with the contact between the ES and the stapes footplate is a reliable MR imaging marker in differentiating MD ears from healthy ears and from those affected by other otologic disorders. In addition, we assessed whether the blood-labyrinthine barrier (BLB) breakdown is associated with the presence of symptoms on the MR image.

## MATERIALS AND METHODS

### Subject Enrollment

This study was approved by the Fondazione IRCCS Ca' Granda Ospedale Maggiore Policlinico institutional review board; patient informed consent was waived. We retrospectively enrolled consecutive patients affected by unilateral sudden sensorineural hearing loss (SSHL) and uni-/bilateral definite MD, who had undergone MR imaging at our department from July 2016 to January 2018. According to the American Academy of Otolaryngology–Head and Neck Surgery (AAO-HNS) guidelines, SSHL was defined by a sensorineural hearing loss of at least 30 decibels over 3 contiguous frequencies occurring within a 72-hour period.<sup>8,9</sup> The diagnosis of definite MD fulfilled the criteria of both the Bárány Society and the AAO-HNS. According to the Bárány Society guidelines, definite MD was diagnosed if there was a history of at least 2 definitive spontaneous episodes of vertigo lasting 20 minutes or longer, tinnitus, or aural fullness and audiometrically documented sensorineural hearing loss of at least 30 dB (or low-to-medium frequency sensorineural hearing loss).<sup>3</sup> According to the AAO-HNS, definite MD was diagnosed if there was a history of at least two spontaneous episodes of vertigo lasting 20 minutes to 12 hours; audiometrically documented low-to-medium frequency senso-

rineural hearing loss in 1 ear, defining the affected ear on at least 1 occasion before, during, or after one of the episodes of vertigo; and fluctuating aural symptoms (hearing, tinnitus, or fullness) in the affected ear, not better accounted for by another vestibular diagnosis.<sup>10</sup>

Exclusion criteria were the following: a history of neurologic or psychiatric disorders; systemic autoimmune diseases; previous otosurgical procedures; middle ear pathologies; and other causes of sensorineural hearing loss, such as inherited hearing loss, the use of ototoxic drugs, noise trauma, exposure to industrial solvents, labyrinthine fistula, and/or previous episodes of SSHL.

### Audiologic Assessment

Diagnoses of SSHL and definite MD were made by an otolaryngologist by otomicroscopy, vestibular evaluation, complete audiologic examination by pure-tone audiometry with measurement of air conduction at all octave frequencies between 125 and 8000 Hz and of bone conduction thresholds at 250–4000 Hz, immittance audiometry, speech audiometry, and distortion product otoacoustic emissions. The functional level score of MD was measured on the day of MR imaging for each patient.<sup>10</sup> In patients with unilateral SSHL and unilateral MD, the unaffected contralateral ear was defined as the healthy control (HC) and normal in a patient with MD (nMD), respectively, if the audiologic assessment revealed normal hearing, including the presence of distortion product otoacoustic emissions. Thus, after the audiologic assessment, ears could be categorized to 4 types: HC, SSHL, MD, and nMD.

### MR Imaging Acquisition and Image Analysis

All patients were imaged on a 3T Achieva scanner (Philips Healthcare, Best, the Netherlands) using a 32-channel head coil. The imaging protocol consisted of sequences performed for whole-brain evaluation (axial diffusion-weighted sequence and 3D FLAIR) and specific sequences for temporal bone assessment (Table 1). Contrast-agent (gadoteridol, ProHance; Bracco Diagnostics, Princeton, New Jersey) was administered intravenously at the recommended dose (0.2 mmol/kg). MR imaging acquisition data are listed in Table 1. According to our protocol, all patients with SSHL were scanned within 10 days after onset.

Two observers, a senior neuroradiologist and a radiology resident with 6 years and 6 months of experience in otoradiology, respectively, assessed the delayed 3D-FLAIR images independently and, in a second reading session, in consensus. Multiplanar reconstructions were obtained using the local PACS viewer with a slice thickness of 0.33 mm. Image analysis was conducted using 2 oblique planes: parasagittal, parallel to the superior semicircular canal; para-axial, parallel to the lateral semicircular canal (Fig 1). According to our new proposed method, readers had to report when the VES bulged in the third inferior portion of the vestibule, which meant below the para-axial plane at the level of the lateral

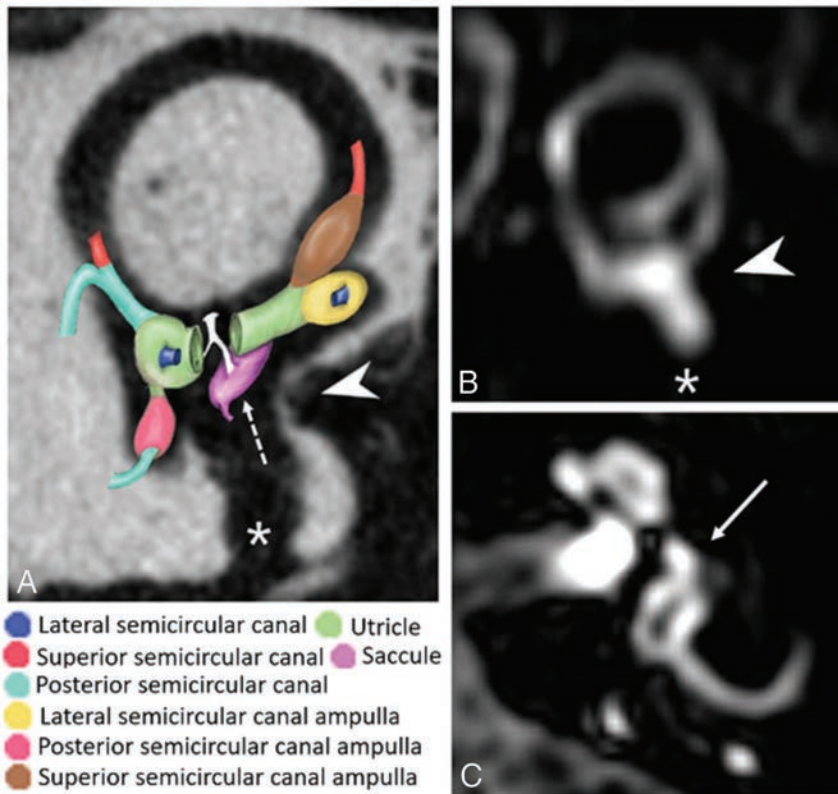


**FIG 1.** Left ear. A, Flat panel CT scan (isotropic voxel, 0.15-mm resolution) of a cadaver temporal bone specimen with a superimposed 3D colored schematic representation of the normal VES on the oblique sagittal plane parallel to the superior semicircular canal. On this plane, the normal sacculle (dotted arrow) is more medially and posteriorly located compared with the utricle. The utricle does not protrude into the inferior portion of the vestibule, and the VES does not contact the round (asterisk) and oval (arrowhead) windows. B, MR imaging oblique sagittal reconstruction parallel to the superior semicircular canal of a healthy ear shows superiorly the VES and inferiorly the perilymph filling the inferior third of the vestibule with preservation of the perilymph signal medial to the oval window (arrowhead) and round window (asterisk). C, MR imaging axial reconstruction parallel to the lateral semicircular canal at the inferior third of the vestibule in a healthy subject, showing the vestibule filled by the perilymph (arrow).

semicircular canal (Fig 2), and contacted the oval window as indicated by the disappearance of the gadolinium-enhanced perilymph behind the oval window on the parasagittal plane at the level of the superior semicircular canal. This sign was defined as the vestibular endolymphatic space contacting the oval window (VESCO).

In addition, only in the in-consensus reading section, the readers assessed the presence of cochlear hydrops (CH) and VEH according to the classic criteria by Nakashima et al.<sup>5</sup> VEH was assessed by calculating the ratio of the area of the VES to that of the vestibular space. VEH was defined as “absent” if the ratio was <33.3%; “mild,” from 33.3% to 50%; and “significant,” if >50%. CH was defined as “absent” if no displacement of the Reissner membrane was detected; “mild” if a displacement of the Reissner membrane was detected but the area of the cochlear endolymphatic space did not exceed the area of the scala vestibuli; and “significant” if the area of the endolymphatic space exceeded the area of the scala vestibuli.

The presence or absence of BLB breakdown of the inner ear structures was also assessed in patients with MD. The BLB breakdown was defined as a higher perilymph gadolinium-enhancement of the inner ear structures compared with the contralateral

ones (Fig 3). If the enhancement was symmetric in a subject, BLB breakdown was judged absent.

### Statistical Analysis

The interobserver agreement was calculated with the Cohen  $\kappa$  coefficient. The clinical examination was used as a reference standard. Because we performed a per-ear analysis, we calculated the intraclass correlation coefficient to demonstrate the independence of measurements within a subject. Using the in-consensus reading for VESCO, the Nakashima method, and both combined, we calculated the sensitivity, specificity, positive predictive value (PPV), and negative predictive value (NPV) in differentiating MD ears from other ears (HC, nMD, SSSL). The McNemar test was used to compare the sensitivity and specificity between VESCO alone and VESCO combined with CH according to the Nakashima method. We used the Mann-Whitney  $U$  test to investigate the association between BLB breakdown and the functional level score in patients with MD. Statistical analysis was performed using SPSS, Version 20.0 (IBM, Armonk, New York). Significance was defined at  $P < .05$ .

### RESULTS

We included 24 patients affected by unilateral SSSL (male/female: 11:13; mean age, 54.9  $\pm$  11.7 years) and 25 patients affected by definite MD (male/female: 15:10; mean age, 60.6  $\pm$  18.6 years). There were no significant differences in the mean ages ( $P = .08$ ) or sex ( $P = .48$ ) of the SSSL and MD groups. Twenty-three of 25 patients with MD had unilateral disease (10 right, 13 left), and 2 had bilateral disease. The mean interval of disease duration in the patients with MD was 6.4 years (range, 1–25 years). No MD ears showed an air-bone gap at the audiometric examination. The functional level score at the time of MR imaging was 1 in 7 patients, 2 in 6 patients, 3 in 4 patients, 4 in 3 patients, 5 in 6 patients, and 6 in 1 patient.

We therefore analyzed 98 ears: 27 with MD, 24 with SSSL, 24 HC, and 23 nMDs. VESCO was detected in 22 of 27 MD ears (true-positives), 1 of 24 SSSL ears, 1 of 24 HC ears, and 1 of 23 nMD ears (false-positives). The intraclass correlation coefficient of within-subject ear measurements was 0.07 with a 95% CI,  $-0.20-0.35$  [null-hypothesis intraclass correlation coefficient = 0;  $F(48,48) = 1.16, P = .30$ ]. Data on the sensitivity, specificity, PPV, and NPV in differentiating MD ears from other ears are shown in Table 2. The interreader agreement was almost perfect (Cohen  $\kappa = 0.867$ ; 95% CI, 0.689–1).

According to the Nakashima score, VEH (32 mild, 10 severe)

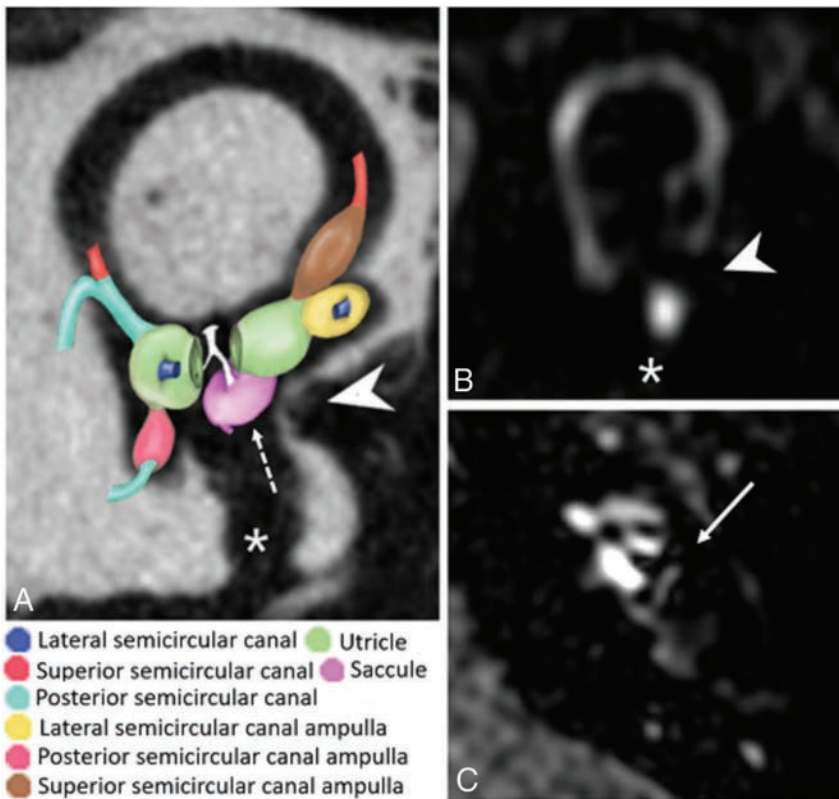


**FIG 2.** Left ear. **A**, Flat panel CT scan (isotropic voxel, 0.15-mm resolution) of a cadaver temporal bone specimen with superimposed 3D colored schematic representation of the VES on the oblique sagittal plane parallel to the superior semicircular canal, as suggested in patients with MD. The utricle bulges into the inferior third of the vestibule, and the saccule (*dotted arrow*) bulges more medially; thus, the VES contacts the oval window (*arrowhead*). The *asterisk* indicates the round window and the *dotted arrow* indicates the saccule. **B**, MR imaging oblique sagittal reconstruction parallel to the superior semicircular canal of an MD ear shows enlargement of the VES bulging into the inferior third of the vestibule and contacting the oval window (*arrowhead*), with the consequent absence of the normal perilymph signal behind the stapes footplate (*asterisk* indicates the round window). **C**, MR imaging axial reconstruction parallel to the lateral semicircular canal at the inferior third of the vestibule in a patient with MD shows the VES contacting the oval window (*arrow* indicates enlargement of the VES bulging into the inferior third of the vestibule and contacting the oval window).

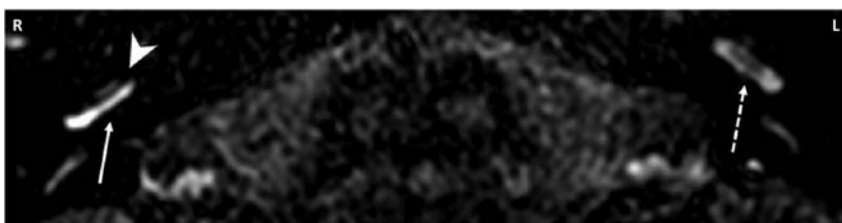


**FIG 3.** Four-hour-delayed postcontrast 3D-FLAIR MR axial image through the basal turns of the cochleae. The right (R) MD ear shows cochlear hydrops (*arrowhead*) and marked contrast enhancement (*arrow*) compared with the contralateral (L) healthy ear (*dotted arrow*), suggesting BLB breakdown.

**Table 2: Contact between the oval window and the saccule in sagittal oblique plane (VESCO)**

	SE (%) (95% CI)	SP (%) (95% CI)	PPV (%) (95% CI)	NPV (%) (95% CI)
Symptomatic MD vs asymptomatic MD	81 (61–93)	96 (76–100)	96 (76–100)	81 (61–93)
Symptomatic MD vs healthy	81 (61–93)	96 (77–100)	96 (76–100)	82 (62–93)
Symptomatic MD vs SSHL	81 (61–93)	96 (77–100)	96 (76–100)	82 (62–93)
Symptomatic MD vs other	81 (61–93)	96 (87–99)	88 (68–97)	93 (84–97)

**Note:**—SE indicates sensitivity; SP, specificity; PPV, positive predictive value; NPV, negative predictive value.

was correctly detected in 20 of 27 MD ears (true-positives) and misdiagnosed (in all cases as mild hydrops) in 10 SSHL ears, 4 HC ears, and 8 nMD ears (false-positives). Furthermore, CH was correctly detected in 20 of 27 MD ears (true-positives) and misdiagnosed in 4 SSHL ears, 1 HC ear, and 5 nMD ears (false-positives). Data on the sensitivity, specificity, PPV, and NPV in differentiating MD ears from other ears are shown in Tables 3 and 4.

In Table 5, the comparison between VESCO and VEH and CH according to the Nakashima criteria is reported in patients with MD. VESCO or CH or both were detected in 24 of 27 MD ears and in 11 of 71 other ears (HC, SSHL, nMD). Thus, the presence of at least 1 of these imaging biomarkers did not show a significant difference in terms of sensitivity (89%; 95% CI, 70%–97%; McNemar test,  $P = .50$ ) compared with VESCO alone, but it caused a significant reduction of the specificity (85%; 95% CI, 74%–92%; McNemar test,  $P = .008$ ) in differentiating MD ears from the others.

BLB breakdown was identified in 14 of 23 patients with unilateral MD, always on the side of the affected ear, and in 1 of 2 patients with bilateral MD. The functional level score at the time of the MR imaging study was significantly higher in patients with BLB breakdown ( $P = .03$ ).

## DISCUSSION

Our study showed that VESCO alone has high specificity (96%) and PPV (88%) in differentiating MD ears from other ears. On the contrary, the combined evaluation of VESCO and CH according to the Nakashima method resulted in a significant reduction of the specificity (85%; McNemar test,  $P = .008$ ), without a significant advantage in terms of sensitivity (89%; McNemar test,  $P = .50$ ). These results suggest that VESCO could be used to confirm MD after clinical examination. However, the good but not excellent sensitivity of VESCO (81%) prevents radiologists from using it as biomarker to definitively rule out MD.

Most studies published on MR imaging of MD used the Nakashima score to identify VEH and CH, but this method showed low specificity in the diagnosis

**Table 3: Vestibular endolymphatic hydrops according to Nakashima grading**

	SE (%) (95% CI)	SP (%) (95% CI)	PPV (%) (95% CI)	NPV (%) (95% CI)
Symptomatic MD vs asymptomatic MD	74 (53–88)	65 (43–83)	71 (51–86)	68 (45–85)
Symptomatic MD vs healthy	74 (53–88)	83 (62–95)	83 (62–95)	74 (53–88)
Symptomatic MD vs SSHL	74 (53–88)	58 (37–77)	67 (47–82)	67 (43–85)
Symptomatic MD vs other	74 (53–88)	69 (57–79)	48 (32–63)	88 (75–94)

Note:—SE indicates sensitivity; SP, specificity.

**Table 4: Cochlear hydrops according to Nakashima grading**

	SE (%) (95% CI)	SP (%) (95% CI)	PPV (%) (95% CI)	NPV (%) (95% CI)
Symptomatic MD vs asymptomatic MD	74 (53–88)	78 (56–92)	80 (59–92)	72 (50–87)
Symptomatic MD vs healthy	74 (53–88)	96 (77–100)	95 (74–100)	77 (57–89)
Symptomatic MD vs SSHL	74 (53–88)	83 (62–95)	83 (62–95)	74 (53–88)
Symptomatic MD vs other	74 (53–88)	86 (75–93)	67 (47–82)	90 (79–95)

Note:—SE indicates sensitivity; SP, specificity.

**Table 5: Presence of VESCO versus VEH and CH according to the Nakashima criteria in patients with MD**

VESCO	VEH			CH	
	No (n = 7)	Mild (n = 11)	Severe (n = 9)	No (n = 7)	Yes (n = 20)
No (n = 5)	2 (40%)	3 (60%)	0 (0%)	3 (60%)	2 (40%)
Yes (n = 22)	5 (23%)	8 (36%)	9 (41%)	4 (18%)	18 (82%)

of MD, resulting in poor utility in clinical practice. The main limitations of this method are the following: 1) the conspicuity of the endolymphatic space depends on the MR image parameters such as TI, making results from different imaging centers less comparable; and 2) the endolymphatic space is a volume, with extreme variability in morphology<sup>11</sup>; therefore, the evaluation of its expansion simply on a single axial plane is not a suitable method to obtain a reliable estimate of the hydrops state.

However, MR imaging evidence from the literature using the Nakashima score is in line with the pathologic findings that have been described in cadavers, suggesting that CH and VEH are not exclusive findings in patients with MD and are probably not always pathologic. Thus, the ambitious objective for radiologists is to determine a method to distinguish clinically relevant hydrops. We support the idea that morphology-based imaging methods, such as ours, can be more accurate than quantitative-based ones, such as the Nakashima score, to reach this goal. Attyé et al<sup>6</sup> pursued this objective using a saccule-to-utricle ratio of  $\geq 1$  as a biomarker for MD, reaching low sensitivity (50%) but high specificity (100%) in differentiating the symptomatic ears of patients with MD from the asymptomatic ears of healthy volunteers. However, it remains unclear what the diagnostic role of the saccule-to-utricle ratio is in differentiating MD ears from ears affected by other otologic disorders. We find the saccule-to-utricle ratio difficult to apply in clinical practice for the following reasons: 1) When there is VEH, there is the effacement of the perilymph between the saccule and the utricle, thus making it impossible to delineate the boundaries of these structures; and 2) Attyé et al calculated the saccule-to-utricle ratio in a parasagittal plane along the major axis of the vestibule, but the saccule and the utricle are not visible together in this plane because the saccule is more medially located.

Attyé et al<sup>6</sup> reported the contact of the VES with the oval window in 9/30 patients with MD, all with the saccule-to-utricle ratio. Our data disagree with this observation. The discrepancy could be due to technical differences in the imaging analysis. Attyé et al did not clearly state their method of defining the contact between the saccule and the stapes footplate, which is surely different from ours: We used a parasagittal plane parallel to the lateral semicircular canal, which does not correspond to the parasagittal plane along the long axial axis of the vestibule as represented by these authors. Recently, some authors reported that patients with significant VEH adjacent to the stapes footplate showed

higher average air-bone gaps at 250 Hz compared with patients with nonadjacent significant VEH.

In contrast, we did not find air-bone gaps in our patients with MD.<sup>12</sup> First, audiograms of patients with MD showed unexplained air-bone gaps at low frequencies from 13% to 32% in the literature, even though no middle ear pathology could be demonstrated.<sup>13,14</sup> In addition, some methodologic differences between our study and the aforementioned study<sup>12</sup> should be stated to understand why the results are in disagreement. The authors of this study enrolled not only patients with MD (66% of the total) but also patients with other otologic disorders who presented with severe hydrops according to the Nakashima score. As evidenced by our results, severe hydrops was found only in 9/22 (41%) patients with MD with VESCO. According to these observations, the populations of the studies are not comparable. In addition, the authors used “HYDROPS” imaging, performed by subtracting the positive endolymph images from the positive perilymph images. This type of postprocessing transformation can alter the MR imaging anatomy of the endolymphatic space by inducing researchers to incorrectly locate the endolymph liquid within the inner ear structures for problems of registration between the 2 MR images. This limitation could be more relevant when VEH should be defined as “nonadjacent” or “adjacent” according to the presence or absence of a black area of endolymph underneath the stapes footplate.

Our study showed that patients with MD with BLB breakdown have a higher functional level at the time of the MR imaging than those without BLB breakdown. Similar to our results, in a recent MR imaging study, it was noted that the permeability of the capillaries in the inner ear of patients with MD was significantly greater than that in the inner ear of patients with SSHL.<sup>15</sup> These findings are in agreement with the hypothesis that MD may be caused by dysfunction in the BLB as confirmed by the pathologic changes that were described in the capillary lumens of MD cadavers.<sup>16</sup> The finding of increased vesicular transport in the endothelial cells of the capillaries, vascular endothelial cell degenerative changes, and the thickening of the basement membrane of the capillaries in Menière disease raises the possibility of an inflam-

matory pathology similar to that proposed as causative in autoimmune inner ear disease.<sup>17</sup>

Some limitations of our study should be acknowledged. Our standard reference for the definition of MD was clinical instead of histopathologic. Furthermore, while enrolling only patients with definite MD, we did not test the accuracy of VESCO in those clinical conditions, such as possible or probable MD or MD-mimicking disorders, which represent the true diagnostic challenges in clinical practice. Thus, the reported specificity of VESCO could be overestimated. For example, is VESCO accurate in early differentiate recurrent peripheral vestibulopathy from MD? Future studies should therefore aim to answer this question using clinical follow-up or histology as a reference standard. Because in SSHL we performed MR imaging within 10 days after the onset of the pathology, we cannot exclude the possibility that these patients could develop late vestibular hydrops and that VESCO could be detected in them later.

We did not correlate imaging results with audiometric tests, the duration of MD, or vestibular-evoked myogenic potentials. In particular, the vestibular-evoked myogenic potentials are a reliable tool for the investigation of saccular function<sup>18</sup>; thus, they can elucidate the role of the saccule in the definition of VESCO, considering that in our opinion, it is impossible to clearly delineate the saccule from the other endolymphatic structures when marked hydrops is present. Some technical aspects in the imaging acquisition could have influenced our results; a recent study has shown that it is easy to shift from the normal condition to VEH disease simply by varying the TI sequence by 100 ms.<sup>19</sup> The same group of researchers suggested that different contrast agents can provide different anatomic details regarding endolymphatic space and the semicircular canals.<sup>19</sup>

## CONCLUSIONS

VESCO is a promising MR imaging biomarker for MD and BLB breakdown, as depicted by the enhancement on MR imaging, to identify patients with higher functional levels probably due to florid inflammatory activity within the inner ear structures.

Disclosures: Diego Zanetti—UNRELATED: Payment for Lectures Including Service on Speakers Bureaus: Advanced Bionics, Staefa (Switzerland), Comments: honorarium and travel expenses for lecturing at an international course on cochlear implants, Hannover, Germany 2017.

## REFERENCES

1. Gürkov R. **Menière and friends: imaging and classification of hydroptic ear disease.** *Otol Neurotol* 2017;38:e539–44 CrossRef Medline
2. Merchant SN, Rauch SD, Nadol JB Jr. **Meniere's disease.** *Eur Arch Otorhinolaryngol* 1995;252:63–75 Medline
3. Lopez-Escameza JA, Carey J, Chung WH, et al. **Diagnostic criteria for Menière's disease: consensus document of the Bárány Society, the Japan Society for Equilibrium Research, the European Academy of Otolology and Neurotology (EAONO), the American Academy of Otolaryngology-Head and Neck Surgery (AAO-HNS) and the Korean Balance Society [in Spanish].** *Acta Otorrinolaringol Esp* 2016;67:1–7 CrossRef Medline
4. Sepahdari AR, Ishiyama G, Vorasubin N, et al. **Delayed intravenous contrast-enhanced 3D FLAIR MRI in Meniere's disease: correlation of quantitative measures of endolymphatic hydrops with hearing.** *Clin Imaging* 2015;39:26–31 CrossRef Medline
5. Nakashima T, Naganawa S, Pyykko I, et al. **Grading of endolymphatic hydrops using magnetic resonance imaging.** *Acta Otolaryngol Suppl* 2009;5–8 CrossRef Medline
6. Attyé A, Eliezer M, Boudiaf N, et al. **MRI of endolymphatic hydrops in patients with Meniere's disease: a case-controlled study with a simplified classification based on saccular morphology.** *Eur Radiol* 2017;27:3138–46 CrossRef Medline
7. Conte G, Lo Russo FM, Calloni SF, et al. **MR imaging of endolymphatic hydrops in Menière's disease: not all that glitters is gold.** *Acta Otorhinolaryngol Ital* 2018;38:369–76.
8. Stachler RJ, Chandrasekhar SS, Archer SM, et al; American Academy of Otolaryngology-Head and Neck Surgery. **Clinical practice guideline: sudden hearing loss.** *Otolaryngol Head Neck Surg* 2012;146(3 Suppl): S1–35 CrossRef Medline
9. Rauch SD. **Clinical practice: idiopathic sudden sensorineural hearing loss.** *N Eng J Med* 2008;359:833–40 CrossRef Medline
10. **Committee on Hearing and Equilibrium guidelines for the diagnosis and evaluation of therapy in Meniere's disease: American Academy of Otolaryngology-Head and Neck Foundation, Inc.** *Otolaryngol Head Neck Surg* 1995;113:181–85 CrossRef Medline
11. Pender DJ. **Membrane stress in the human labyrinth and Meniere disease: a model analysis.** *Int Arch Otorhinolaryngol* 2015;19:336–42 CrossRef Medline
12. Sugimoto S, Yoshida T, Teranishi M, et al. **The relationship between endolymphatic hydrops in the vestibule and low-frequency air-bone gaps.** *Laryngoscope* 2018;128:1658–62 CrossRef Medline
13. Lee HJ, Jeon JH, Park S, et al. **Prevalence and clinical significance of spontaneous low-frequency air-bone gaps in Meniere's disease.** *Otol Neurotol* 2014;35:489–94 CrossRef Medline
14. Muchnik C, Hildesheimer M, Rubinstein M, et al. **Low frequency air-bone gap in Menière's disease without middle ear pathology: a preliminary report.** *Am J Otol* 1989;10:1–4 CrossRef Medline
15. Pakdaman MN, Ishiyama G, Ishiyama A, et al. **Blood-labyrinth barrier permeability in Meniere's disease and idiopathic sudden sensorineural hearing loss: findings on delayed postcontrast 3D-FLAIR MRI.** *AJNR Am J Neuroradiol* 2016;37:1903–08 CrossRef Medline
16. Ishiyama G, Lopez IA, Ishiyama P, et al. **The blood labyrinthine barrier in the human normal and Meniere's disease macula utriculi.** *Sci Rep* 2017;7:253 21 CrossRef Medline
17. Neng L, Zhang F, Kachelmeier A, et al. **Endothelial cell, pericyte, and perivascular resident macrophage-type melanocyte interactions regulate cochlear intrastrial fluid-blood barrier permeability.** *J Assoc Res Otolaryngol* 2013;14:175–85 CrossRef Medline
18. de Waele C, Tran Ba Huy P, Diard JP, et al. **Saccular dysfunction in Meniere's patients: a vestibular-evoked myogenic potential study.** *Ann N Y Acad Sci* 1999;871:392–97 CrossRef
19. Eliezer M, Gillibert A, Tropres I, et al. **Influence of inversion time on endolymphatic hydrops evaluation in 3D-FLAIR imaging.** *J Neuro-radiol* 2017;44:339–43 CrossRef Medline

# Corticopallidal Connectome of the Globus Pallidus Externus in Humans: An Exploratory Study of Structural Connectivity Using Probabilistic Diffusion Tractography

S.S. Grewal, V.M. Holanda, and E.H. Middlebrooks

## ABSTRACT

**BACKGROUND AND PURPOSE:** Electrophysiologic abnormalities of the globus pallidus externus have been shown in several disease processes including Parkinson disease, dystonia, and Huntington disease. However, the connectivity, nuclear structure, and function of the globus pallidus externus are still not well-understood. Increasing evidence for the existence of direct corticopallidal connections challenges traditional understanding of the connectivity of the globus pallidus externus; nevertheless, these corticopallidal connections have yet to be fully characterized in humans. The objective of this study was to assess the corticopallidal connections of the globus pallidus externus by means of probabilistic diffusion-weighted MR imaging tractography using high-resolution, multishell data.

**MATERIALS AND METHODS:** Imaging data from the open-access Human Connectome Project data base were used to perform probabilistic tractography between the globus pallidus externus and the cerebral cortex using 34 distinct cortical regions. Group averages were calculated for normalized percentages of tracts reaching each of the cortical targets, and side-to-side comparison was made.

**RESULTS:** Cortical connectivity was demonstrated between the globus pallidus externus and multiple cortical regions, including direct connection to putative sensorimotor, associative, and limbic areas. Connectivity patterns were not significantly different between the right and left hemispheres with the exception of the frontal pole, which showed a greater number of connections on the right ( $P = .004$ ).

**CONCLUSIONS:** Our in vivo study of the human globus pallidus externus using probabilistic tractography supports the existence of extensive corticopallidal connections and a tripartite functional division, as found in animal studies. A better understanding of the connectivity of the globus pallidus externus may help to understand its function and elucidate the effects of programming the higher contacts in pallidal deep brain stimulation.

**ABBREVIATIONS:** DBS = deep brain stimulation; GPe = globus pallidus externus

The globus pallidus externus (GPe) is the lateral component of the globus pallidus known to have extensive connections with other basal ganglia nuclei.<sup>1</sup> Traditionally thought to primarily function in motor control,<sup>2</sup> more recent evidence has challenged this belief, showing additional function in associative and limbic processes.<sup>3-5</sup> GPe dysfunction has been shown in several disease processes, including a decreased spontaneous discharge rate in

Parkinson disease<sup>6</sup> and dystonia<sup>7</sup> and an increased spontaneous discharge rate in Huntington disease.<sup>8</sup> These findings suggest an important role of the GPe in the pathophysiology of several disease processes and a potential clinical relevance.<sup>9,10</sup>

In 2003, Silberstein et al<sup>11</sup> showed that the local field potentials recorded in the globus pallidus externus in patients who underwent deep brain stimulation (DBS) were greater in patients with Parkinson disease (11–30 Hz) than in those with dystonia (4–10 Hz). This finding indicated the importance of understanding the GPe connections to help in elucidating the mechanistic basis of DBS when treating these diseases. Fifteen years later, the connectivity, nuclear structure, and function of the GPe are still not well-understood.<sup>1,5</sup>

Traditionally, the basal ganglia circuitry has been thought to involve 2 pathways, a “direct” and an “indirect” pathway, with the striatum being the main input source for cortical efferents.<sup>12,13</sup> Nevertheless, this model was challenged with the postulation of a “hyperdirect” pathway, connecting the subthalamic nucleus to

Received February 11, 2018; accepted after revision August 7.

From the Departments of Neurosurgery (S.S.G., E.H.M.) and Radiology (E.H.M.), Mayo Clinic, Jacksonville, Florida; and Center of Neurology and Neurosurgery Associates (V.M.H.), BP-A Beneficência Portuguesa de São Paulo, São Paulo, Brazil.

Data were provided, in part, by the Human Connectome Project, WU-Minn Consortium (Principal Investigators: David Van Essen and Kamil Ugurbil, 1U54MH091657) funded by the 16 National Institutes of Health institutes and centers that support the National Institutes of Health Blueprint for Neuroscience Research, and by the McDonnell Center for Systems Neuroscience at Washington University.

Please address correspondence to Erik H. Middlebrooks, MD, Mayo Clinic, Department of Neurosurgery, 4500 San Pablo Rd, Jacksonville, FL 32224; e-mail: Middlebrooks.Erik@mayo.edu

<http://dx.doi.org/10.3174/ajnr.A5816>

the cortex.<sup>14-16</sup> Subsequently, there was increasing work in both animal and in vivo human models highlighting the existence of direct corticopallidal connections; however, these corticopallidal connections specific to the globus pallidus externus have yet to be fully characterized in humans.<sup>17-23</sup> The objective of this study was to assess corticopallidal connections of the GPe by means of probabilistic diffusion-weighted MR imaging tractography, using high-resolution, multishell data.

## MATERIALS AND METHODS

### Data Acquisition

Imaging data from the open-access Human Connectome Project data base were used (<https://www.humanconnectome.org>). Twenty healthy subjects were consecutively selected from the data base. Full imaging acquisition details are freely available at the Human Connectome Project data base Web site (<https://www.humanconnectome.org>), but briefly, the imaging was obtained using a modified 3T Magnetom Skyra scanner (Siemens, Erlanger, Germany). The multidirection diffusion-weighted imaging used a spin-echo EPI sequence with an isotropic resolution of 1.25 mm<sup>3</sup>. Diffusion b-values were acquired at 1000, 2000, and 3000 s/mm<sup>2</sup> in 90 diffusion directions for each shell. A multiband factor of 3 with 6/8 phase partial Fourier was used, and 111 axial slices were obtained with no gap. The parameters were the following: TR = 5520 ms, TE = 89.5 ms, flip angle = 78°. Images were obtained in both the left-to-right and right-to-left phase-encoding directions. Total imaging time for the diffusion data was 59 minutes. The T1-weighted 3D MPRAGE structural scan used an isotropic resolution of 0.7 mm<sup>3</sup>. Additional acquisition parameters included the following: TR = 2400 ms, TE = 2.14 ms, TI = 1000 ms, flip angle = 8°, generalized autocalibrating partially parallel acquisition = 2, and bandwidth = 210 Hz/Px for an acquisition time of 7 minutes and 40 seconds.

Preprocessing of the diffusion data included realignment, B<sub>0</sub> image-intensity normalization, EPI distortion correction with the FSL Topup algorithm (<https://fsl.fmrib.ox.ac.uk/fsl/fslwiki/topup>), gradient nonlinearity correction, and eddy current correction.<sup>24</sup> The diffusion data were co-registered to the structural MPRAGE images using a boundary-based registration method (BBR) implemented in the FMRIB Linear Registration Tool (FLIRT; <http://www.fmrib.ox.ac.uk/fsl/wiki/FLIRT>) followed by the “bbregister” function in FreeSurfer (<https://surfer.nmr.mgh.harvard.edu>). All preprocessing steps used standard options as detailed in the Human Connectome Project data base preprocessing pipeline.<sup>24</sup>

### Data Processing

Segmentation of the MPRAGE data was performed with FreeSurfer (<https://surfer.nmr.mgh.harvard.edu>). The left and right cerebral cortices were segmented into 34 distinct volumes of interest in FreeSurfer based on the Desikan-Killiany cortical atlas using the FreeSurfer `mri_label2vol` function.<sup>25</sup> VOIs were also generated of the right and left GPe in the Montreal Neurological Institute template space from the Montreal Neurological Institute Basal Ganglia Human Area Template.<sup>26</sup> The GPe VOIs were then transformed from Montreal Neurological Institute space to Free-

Surfer space using a linear registration implemented in FSL FLIRT.

Voxelwise diffusion parameters were estimated via a Markov Chain Monte Carlo sampling implemented in FSL `bedpostx` (<http://fsl.fmrib.ox.ac.uk/fsl/fslwiki/FDT/UserGuide#BEDPOSTX>). A multifiber approach (2 fiber orientations) was used along with a multishell model. Next, probabilistic tractography was performed using the FSL `probtrackx2` function (<https://fsl.fmrib.ox.ac.uk/fsl/fslwiki/FDT/UserGuide>) with the network option to estimate the connectivity between each GPe VOI and the 34 ipsilateral cortical targets. Standard tracking parameters include a 0.2 curvature threshold, 2000 steps per sample, a step length of 0.5 mm, and 5000 samples per side.

### Data Analysis

For each subject, the weighted connectivity was calculated between each of the 34 cortical ROIs and the ipsilateral GPe ROI by means of bidirectional fiber tracking between the GPe ROIs and each cortical target ROI. Because the distance traveled has a positive correlation with fiber-tract uncertainty, the tracts were normalized by the distance traveled, as implemented in FSL `probtrackx2`. To account for potential tracking bias due to variable sizes of the ROIs, we normalized the connectivity matrix by the surface area of the ROIs according to the method proposed by Hagmann et al.<sup>27</sup> The number of paths was normalized among all patients by dividing the total number of paths by the waytotal for each subject to facilitate between-subject comparison. Group averages were calculated for normalized percentages of tracts reaching each of the cortical targets. In an attempt to account for false fibers generated by probabilistic tractography, a normalized fiber threshold level was set to exclude all target VOIs. Appropriate threshold levels remain a point of contention in the literature; therefore, we have selected a probabilistic threshold that is in the range of that used in prior studies of  $\geq 2\%$  of the total (98% confidence level) in either hemisphere.<sup>17,28</sup> The VOIs exceeding the threshold were used to generate a connectogram for both the left and right GPe in Matlab 9.1 (MathWorks, Natick, Massachusetts). Last, differences between the connectivity profile of the left and right GPe were assessed for each cortical target in GraphPad Prism 7.0 software (GraphPad Software, San Diego, California) by means of a Mann-Whitney *U* test to account for non-normality in distribution.

## RESULTS

Of the 34 cortical targets evaluated (Table), 17 exceeded the fiber count threshold on either side (Figure). The right GPe exhibited maximal cortical connectivity to the frontal pole (14.4%  $\pm$  9.4%), and the left GPe had maximal cortical connectivity to the temporal pole (10.5%  $\pm$  8.0%). The greatest difference in the connectivity profile between sides was related to the frontal pole (14.4%  $\pm$  9.4% on the right and 7.7%  $\pm$  5.4% on the left), insula (11.0%  $\pm$  4.2% on the right and 8.5%  $\pm$  4.6% on the left), and entorhinal cortex (5.1%  $\pm$  4.4% on the right and 7.4%  $\pm$  6.6% on the left). The side-to-side variation was also only significant for the frontal pole (*P* = .004). The remaining targets showed no significant variation between sides (*P* > .05).

### Cortical ROIs meeting the tract threshold for connectivity to the globus pallidus externus for both hemispheres<sup>a</sup>

Cortical Region	Right Hemisphere (% Tract Probability) (SD)	Left Hemisphere (% Tract Probability) (SD)	P Value
Frontal pole	14.4% (9.4%)	7.7% (5.4%)	.004
Insula	11.0% (4.2%)	8.5% (4.6%)	.1
Temporal pole	9.2% (7.7%)	10.5% (8.0%)	.49
Medial orbitofrontal	6.7% (5.9%)	8.3% (4.9%)	.21
Entorhinal	5.1% (4.4%)	7.4% (6.6%)	.22
Superior frontal	4.3% (3.5%)	4.8% (3.2%)	.56
Pars orbitalis	3.8% (2.6%)	3.2% (2.6%)	.4
Lateral orbitofrontal	3.8% (3.9%)	4.1% (3.9%)	.72
Paracentral	3.4% (2.9%)	3.9% (2.9%)	.5
Postcentral	3.2% (2.2%)	4.3% (2.2%)	.1
Pars triangularis	3.1% (4.1%)	3.2% (3.7%)	.96
Precentral	2.9% (1.9%)	4.4% (2.5%)	.07
Rostral anterior cingulate	2.7% (2.8%)	1.2% (1.2%)	.06
Superior parietal	2.3% (1.3%)	2.9% (1.2%)	.1
Rostral middle frontal	2.3% (1.4%)	2.0% (1.2%)	.83
Isthmus cingulate	2.2% (1.2%)	3.5% (3.2%)	.27
Parahippocampal	1.4% (1.2%)	2.1% (1.5%)	.12

<sup>a</sup>The P value is reported for left-to-right tract comparison.

### DISCUSSION

Our probabilistic tractography study highlights the potential widespread direct cortical connectivity of the GPe. As predicted from prior animal functional studies, direct cortical connections were found between the GPe and areas functioning in sensorimotor, associative, and limbic tasks.<sup>3,4</sup> These direct corticopallidal connections challenge the traditional hypotheses regarding the GPe as merely a subcortical relay within the indirect pathway of the basal ganglia.<sup>1</sup>

Initial descriptions of basal ganglia connectivity were largely based on the work of DeLong<sup>13</sup> and Albin et al<sup>12</sup>, elucidated through a combination of both immunohistochemistry and *in situ* hybridization techniques.<sup>12,13</sup> These models defined 2 corticofugal networks, a direct and indirect pathway of basal ganglia circuitry, and considered the dorsal striatum as the main input area for cortical efferent neurons to these pathways.<sup>12</sup> More recently, a third network, a hyperdirect pathway, has been discovered in which glutamatergic cortical efferents synapse directly on the subthalamic nucleus.<sup>16</sup> The existence of this hyperdirect pathway challenged the traditional hypotheses of basal ganglia connectivity. Indeed, evidence has mounted for additional subpopulations of efferent neurons with direct cortical connection to basal ganglia nuclei outside the dorsal striatum, including the GPe.<sup>17-23</sup>

Direct cortical connection to the GPe was described as early as 1977 in primates.<sup>29</sup> It was again described in an anterograde tracing study in rodents, linking the precentral cortex of rodents to the GPe.<sup>20</sup> Additional studies have also described both cholinergic and GABAergic neurons within the GPe, sending direct efferent connections to the cortex.<sup>18,21</sup> One *in vivo* human study used constrained spherical deconvolution to assess the existence of a corticopallidal network with connections from the GP to Brodmann areas 2, 11, 46, 48, 6, 4, and 5; however, distribution of fiber densities between areas was not assessed.<sup>19</sup> Using a similar technique, Cacciola et al<sup>17</sup> described 2 separate corticopallidal networks: an anatomic pallidal-temporal network involving the hippocampus and amygdala and a sensorimotor-pallidal network mainly involving the precentral, postcentral, and paracentral gyri, in addition to higher order functional areas, such as the superior

frontal gyrus. Unfortunately, due to grouping the GPe and globus pallidus internus as 1 ROI (pallidum), it is uncertain how the GPe and globus pallidus internus connectivity profiles differ.<sup>17</sup> Our current study clarifies the distribution and density of corticopallidal connections specifically to the GPe.

The GPe is classically considered as part of the indirect pathway and extensively connected to deep brain structures.<sup>1,13</sup> Animal studies of bicuculline injections into various regions of the GPe have elicited behavioral disturbances that can be functionally segmented into 3 zones: the ventrolateral “sensorimotor territory,” the middle “associative territory,” and the anterior ventral “limbic territory.”<sup>3,4</sup> To assess the potential role of direct corticopallidal

connections in these functional areas, prior studies used rabies virus injections to trace these potential connections.<sup>3,4</sup> An injection into the limbic GPe labeled areas with known cortical projections: the rostromedial prefrontal cortex, insula, and orbitofrontal cortex, among others.<sup>3,4</sup> Injection in the associative GPe labeled areas with known cortical projections to the supplementary motor area and pre-supplementary motor area as well as the associative parietal, motor, and premotor cortices. Finally, injection into the sensorimotor GPe labeled areas with known cortical projections to the premotor, primary motor, and somatosensory cortices.<sup>3,4</sup>

In line with these animal studies, we were able to illustrate GPe direct cortical connectivity to similar putative associative, sensorimotor, and limbic areas.<sup>3,4</sup> Direct cortical connections corresponding to the limbic GPe include the rostral middle frontal region (presumed dorsolateral prefrontal cortex), entorhinal cortex, parahippocampal gyrus, isthmus of the cingulate cortex, insula, and orbitofrontal cortex.<sup>3,4</sup> Likewise, associative connections to the supplementary motor area/pre-supplementary motor area regions, superior parietal cortex, primary motor cortex, and premotor cortex were found. Last, as suggested by the sensorimotor function, we found corticopallidal connections between the GPe and the premotor, primary motor, and somatosensory cortices.

Animal studies have revealed attention deficits and hyperactivity induced by regional damage to the GPe, raising the possibility of a GPe role in the symptoms of attention deficit/hyperactivity disorder.<sup>3,4</sup> The symptomatology of attention deficit/hyperactivity disorder would suggest dysfunction in attention processing as well as motor planning. Although the role of the frontal pole is not well-understood, it has been implicated in the process of managing multiple cognitive tasks and attention.<sup>30</sup> Spatial attention has also been attributed to function within the premotor and dorsolateral prefrontal cortices.<sup>31,32</sup> Additionally, the rostral cingulate and supplementary motor area, both showing GPe connectivity in our study, have been implicated in the hyperactive symptoms seen in attention deficit/hyperactivity dis-

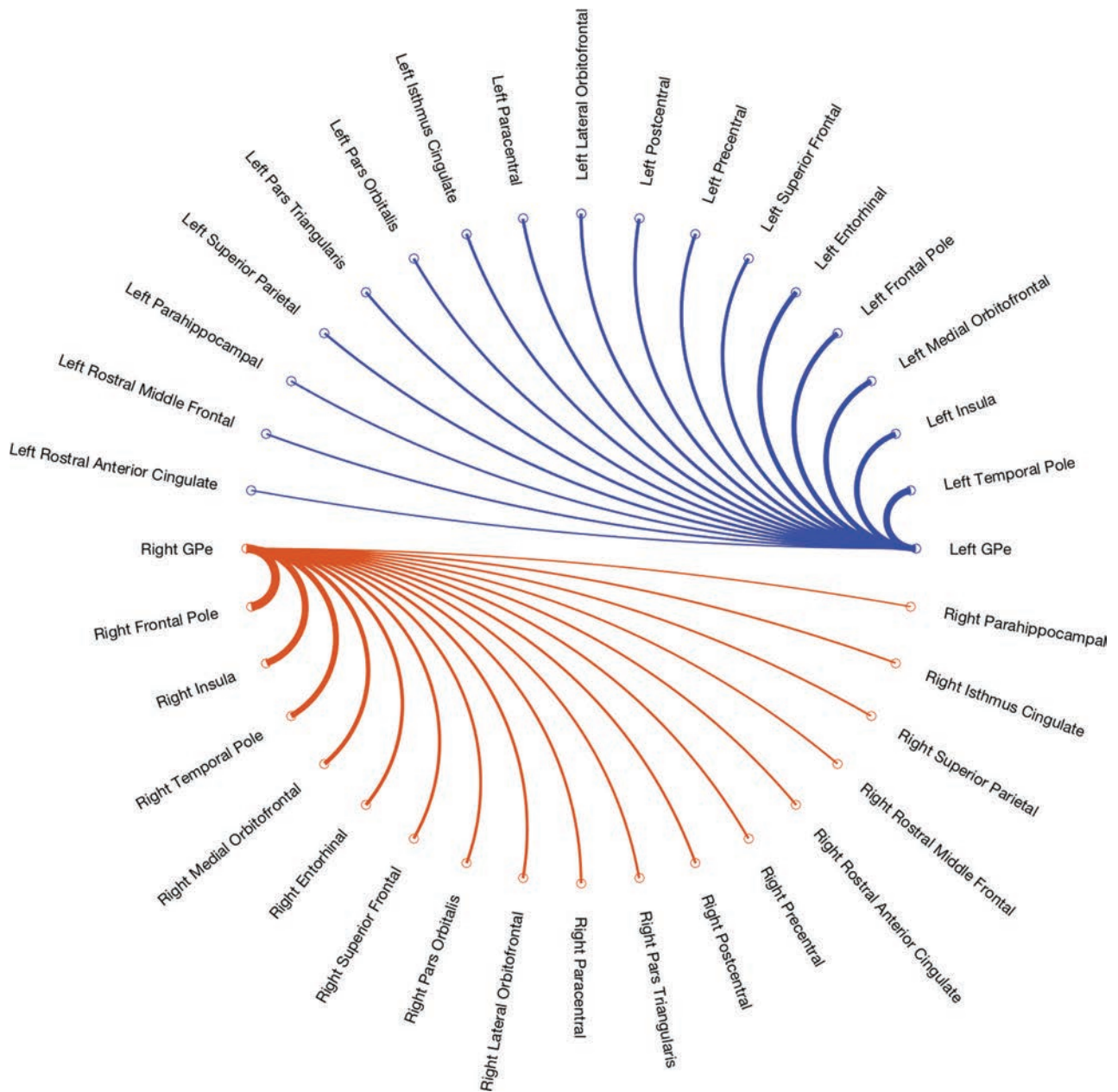


**FIGURE.** Connectogram showing the connectivity profile for the right and left globus pallidus externus. Lines are weighted by tract count.

order.<sup>33</sup> Taken together, the connectivity between the GPe and these cortical regions in our study would corroborate the attention and hyperactivity symptoms elicited in animal studies of the GPe.<sup>3,4</sup>

Animal studies have also implicated the GPe in movement symptoms, such as dyskinesia, as well as stereotyped behavioral symptoms. Although they are not fully understood, it has been suggested that the ventral pallidum and striatal projections to the orbitofrontal cortex, insula, anterior cingulate, and amygdalohippocampal complex (regions functioning in the processing of motivation and emotion) may facilitate such behavioral symptoms.<sup>3,34-40</sup> In addition to these known projections from other portions of the striatum, our study suggests the existence of direct corticopallidal connections originating from the GPe to similar regions, which could also contribute to the behaviors observed in

obsessive-compulsive disorder and Tourette syndrome. Support that these symptoms are also mediated through the GPe includes reports that pallidal lesions can result in obsessive-compulsive-type behavior.<sup>41,42</sup> Additionally, DBS of the GPe has been shown to reduce tics in patients with Tourette syndrome.<sup>43,44</sup>

Broad connectivity of the GPe to primary and secondary sensorimotor regions, including the superior frontal, precentral, and postcentral gyri may play an additional role in mediating symptoms of movement disorders, such as Parkinson disease, Huntington disease, and dystonia.<sup>45-47</sup> In fact, DBS of the GPe has been shown as a potential treatment for both Parkinson disease and dystonia.<sup>46,47</sup> Whether these treatment effects are, in part, mediated by direct corticopallidal connectivity remains to be determined, but they could potentially provide an additional treatment targeting for these debilitating conditions.

In summary, the connectivity and function of the GPe are not as well-understood compared with other components of the basal ganglia.<sup>1</sup> Current evidence supports a role of the GPe in limbic, associative, and sensorimotor processes.<sup>3,4</sup> Animal tracer studies have demonstrated connectivity of the GPe to additional sites in the basal ganglia that have secondary cortical connections to areas of matching function<sup>3,4</sup>; however, we were also able to demonstrate primary connections to similar cortical areas from corticopallidal fibers. A more complete understanding of the function of the GPe may help shed light on its role in pathologic conditions, including Parkinson disease, Huntington disease, obsessive-compulsive disorder, attention deficit/hyperactivity disorder, and dystonia.<sup>6,8,9</sup> In the future, the knowledge of connectivity beyond the motor network may also reveal a role of the GPe in other disorders of the limbic and associative networks.

Several limitations of this study are noteworthy. Firstly, limitations of diffusion-based tractography itself include the inability to determine the directionality (afferent-efferent) of fiber tracts, the limited resolution of crossing fibers, and the potential for “false fibers.”<sup>48,49</sup> Probabilistic tractography is a more sensitive and robust method compared with deterministic tractography; however, probabilistic tractography is associated with a higher incidence of false fiber detection.<sup>50</sup> Additionally, the selection of thresholds for fiber tract probabilities has pitfalls.<sup>51</sup> For instance, a very small bundle of true fibers may be rejected as a statistical error simply due to the small number of fibers, effectively biasing the results to larger fiber bundles. Second, the diffusion-based tractography method is unable to directly provide any functional information regarding the fiber tracts; therefore, the function of the identified tracts is merely speculative. Nevertheless, the anatomic connectivity illustrated in our study is well-aligned with functional deficits identified in prior animal studies.<sup>3,4</sup>

## CONCLUSIONS

Our in vivo study of the human GPe using probabilistic tractography supports the existence of extensive corticopallidal connections. Direct cortical connections to putative sensorimotor, associative, and limbic areas support this tripartite functional division found in animal studies. A better understanding of the connectivity of the GPe may help to understand its function and elucidate the effects of programming the higher contacts in pallidal DBS. Further electrophysiologic studies are needed to investigate the significance of these connections and their ultimate role in basal ganglia circuitry.

## REFERENCES

- Hegeman DJ, Hong ES, Hernández VM, et al. **The external globus pallidus: progress and perspectives.** *Eur J Neurosci* 2016;43:1239–65 CrossRef Medline
- Mouton S, Xie-Brustolin J, Mertens P, et al. **Chorea induced by globus pallidus externum stimulation in a dystonic patient.** *Mov Disord* 2006;21:1771–73 CrossRef Medline
- François C, Grabli D, McCairn K, et al. **Behavioural disorders induced by external globus pallidus dysfunction in primates, II: anatomical study.** *Brain* 2004;127:2055–70 CrossRef Medline
- Grabli D, McCairn K, Hirsch EC, et al. **Behavioural disorders induced by external globus pallidus dysfunction in primates, I: behavioural study.** *Brain* 2004;127:2039–54 CrossRef Medline
- Gittis AH, Berke JD, Bevan MD, et al. **New roles for the external globus pallidus in basal ganglia circuits and behavior.** *J Neurosci* 2014;34:15178–83 CrossRef Medline
- Filion M, Tremblay L. **Abnormal spontaneous activity of globus pallidus neurons in monkeys with MPTP-induced parkinsonism.** *Brain Res* 1991;547:142–51 Medline
- Stoessel AJ, Lehericy S, Strafella AP. **Imaging insights into basal ganglia function, Parkinson’s disease, and dystonia.** *Lancet* 2014;384:532–44 CrossRef Medline
- Starr PA, Kang GA, Heath S, et al. **Pallidal neuronal discharge in Huntington’s disease: support for selective loss of striatal cells originating the indirect pathway.** *Exp Neurol* 2008;211:227–33 CrossRef Medline
- Starr PA, Rau GM, Davis V, et al. **Spontaneous pallidal neuronal activity in human dystonia: comparison with Parkinson’s disease and normal macaque.** *J Neurophysiol* 2005;93:3165–76 CrossRef Medline
- Nambu A, Chiken S, Shashidharan P, et al. **Reduced pallidal output causes dystonia.** *Front Syst Neurosci* 2011;5:89 CrossRef Medline
- Silberstein P, Kühn AA, Kupsch A, et al. **Patterning of globus pallidus local field potentials differs between Parkinson’s disease and dystonia.** *Brain* 2003;126:2597–608 CrossRef Medline
- Albin RL, Young AB, Penney JB. **The functional anatomy of basal ganglia disorders.** *Trends Neurosci* 1989;12:366–75 CrossRef Medline
- DeLong MR. **Primate models of movement disorders of basal ganglia origin.** *Trends Neurosci* 1990;13:281–85 CrossRef Medline
- Brunenberg EJ, Moeskops P, Backes WH, et al. **Structural and resting state functional connectivity of the subthalamic nucleus: identification of motor STN parts and the hyperdirect pathway.** *PLoS One* 2012;7:e39061 CrossRef Medline
- Forstmann BU, Keuken MC, Jahfari S, et al. **Cortico-subthalamic white matter tract strength predicts interindividual efficacy in stopping a motor response.** *Neuroimage* 2012;60:370–75 CrossRef Medline
- Nambu A, Tokuno H, Takada M. **Functional significance of the cortico-subthalamo-pallidal ‘hyperdirect’ pathway.** *Neurosci Res* 2002;43:111–17 CrossRef Medline
- Cacciola A, Calamuneri A, Milardi D, et al. **A connectomic analysis of the human basal ganglia network.** *Front Neuroanat* 2017;11:85 CrossRef Medline
- Chen MC, Ferrari L, Sacchet MD, et al. **Identification of a direct GABAergic pallidocortical pathway in rodents.** *Eur J Neurosci* 2015;41:748–59 CrossRef Medline
- Milardi D, Gaeta M, Marino S, et al. **Basal ganglia network by constrained spherical deconvolution: a possible cortico-pallidal pathway?** *Mov Disord* 2015;30:342–49 CrossRef Medline
- Naito A, Kita H. **The cortico-pallidal projection in the rat: an anterograde tracing study with biotinylated dextran amine.** *Brain Res* 1994;653:251–57 CrossRef Medline
- Saunders A, Oldenburg IA, Berezovskii VK, et al. **A direct GABAergic output from the basal ganglia to frontal cortex.** *Nature* 2015;521:85–89 CrossRef Medline
- Neumann WJ, Jha A, Bock A, et al. **Cortico-pallidal oscillatory connectivity in patients with dystonia.** *Brain* 2015;138:1894–906 CrossRef Medline
- Hoover JE, Strick PL. **Multiple output channels in the basal ganglia.** *Science* 1993;259:819–21 CrossRef Medline
- Glasser MF, Sotiropoulos SN, Wilson JA, et al; WU-Minn HCP Consortium. **The minimal preprocessing pipelines for the Human Connectome Project.** *Neuroimage* 2013;80:105–24 CrossRef Medline
- Desikan RS, Ségonne F, Fischl B, et al. **An automated labeling system for subdividing the human cerebral cortex on MRI scans into gyral based regions of interest.** *Neuroimage* 2006;31:968–80 CrossRef Medline
- Prodoehl J, Yu H, Little DM, et al. **Region of interest template for the human basal ganglia: comparing EPI and standardized space approaches.** *Neuroimage* 2008;39:956–65 CrossRef Medline
- Hagmann P, Cammoun L, Gigandet X, et al. **Mapping the structural**

- core of human cerebral cortex. *PLoS Biol* 2008;6:e159 CrossRef Medline
28. van Wijk BC, Stam CJ, Daffertshofer A. Comparing brain networks of different size and connectivity density using graph theory. *PLoS One* 2010;5:e13701 CrossRef Medline
  29. Leichnetz GR, Astruc J. The course of some prefrontal corticofugals to the pallidum, substantia innominata, and amygdaloid complex in monkeys. *Exp Neurol* 1977;54:104–09 CrossRef Medline
  30. Koehlin E, Hyafil A. Anterior prefrontal function and the limits of human decision-making. *Science* 2007;318:594–98 CrossRef Medline
  31. Corbetta M, Miezin FM, Dobmeyer S, et al. Selective and divided attention during visual discriminations of shape, color, and speed: functional anatomy by positron emission tomography. *J Neurosci* 1991;11:2383–402 CrossRef Medline
  32. Boussaoud D. Attention versus intention in the primate premotor cortex. *Neuroimage* 2001;14:S40–45 CrossRef Medline
  33. Takada M, Tokuno H, Hamada I, et al. Organization of inputs from cingulate motor areas to basal ganglia in macaque monkey. *Eur J Neurosci* 2001;14:1633–50 CrossRef Medline
  34. Chikama M, McFarland NR, Amaral DG, et al. Insular cortical projections to functional regions of the striatum correlate with cortical cytoarchitectonic organization in the primate. *J Neurosci* 1997;17:9686–705 CrossRef Medline
  35. Haber SN, Kunishio K, Mizobuchi M, et al. The orbital and medial prefrontal circuit through the primate basal ganglia. *J Neurosci* 1995;15:4851–67 CrossRef Medline
  36. Kunishio K, Haber SN. Primate cingulostriatal projection: limbic striatal versus sensorimotor striatal input. *J Comp Neurol* 1994;350:337–56 CrossRef Medline
  37. Ferry AT, Ongür D, An X, et al. Prefrontal cortical projections to the striatum in macaque monkeys: evidence for an organization related to prefrontal networks. *J Comp Neurol* 2000;425:447–70 CrossRef Medline
  38. Friedman DP, Aggleton JP, Saunders RC. Comparison of hippocampal, amygdala, and perirhinal projections to the nucleus accumbens: combined anterograde and retrograde tracing study in the Macaque brain. *J Comp Neurol* 2002;450:345–65 CrossRef Medline
  39. Russchen FT, Bakst I, Amaral DG, et al. The amygdalostriatal projections in the monkey: an anterograde tracing study. *Brain Res* 1985;329:241–57 CrossRef Medline
  40. Fudge JL, Haber SN. Defining the caudal ventral striatum in primates: cellular and histochemical features. *J Neurosci* 2002;22:10078–82 CrossRef Medline
  41. Laplane D, Baulac M, Widlöcher D, et al. Pure psychic akinesia with bilateral lesions of basal ganglia. *J Neurol Neurosurg Psychiatry* 1984;47:377–85 CrossRef Medline
  42. Laplane D, Levasseur M, Pillon B, et al. Obsessive-compulsive and other behavioural changes with bilateral basal ganglia lesions: a neuropsychological, magnetic resonance imaging and positron tomography study. *Brain* 1989;112(Pt 3):699–725 CrossRef Medline
  43. Filho OV, Ragazzo PC, Silva DJ, et al. Bilateral globus pallidus externus deep brain stimulation (GPe-DBS) for the treatment of Tourette syndrome: an ongoing prospective controlled study. *Stereotact Funct Neurosurg* 2007;85:42–43 CrossRef
  44. Piedimonte F, Andreani JC, Piedimonte L, et al. Behavioral and motor improvement after deep brain stimulation of the globus pallidus externus in a case of Tourette's syndrome. *Neuromodulation* 2013;16:55–58; discussion 58 CrossRef Medline
  45. Singh-Bains MK, Waldvogel HJ, Faull RL. The role of the human globus pallidus in Huntington's disease. *Brain Pathol* 2016;26:741–51 CrossRef Medline
  46. Vitek JL, Zhang J, Hashimoto T, et al. External pallidal stimulation improves parkinsonian motor signs and modulates neuronal activity throughout the basal ganglia thalamic network. *Exp Neurol* 2012;233:581–86 CrossRef Medline
  47. Houeto JL, Yelnik J, Bardinet E, et al; French Stimulation du Pallidum Interne dans la Dystonie Study Group. Acute deep-brain stimulation of the internal and external globus pallidus in primary dystonia: functional mapping of the pallidum. *Arch Neurol* 2007;64:1281–86 CrossRef Medline
  48. Chung HW, Chou MC, Chen CY. Principles and limitations of computational algorithms in clinical diffusion tensor MR tractography. *AJNR Am J Neuroradiol* 2011;32:3–13 CrossRef Medline
  49. Parker GD, Marshall D, Rosin PL, et al. A pitfall in the reconstruction of fibre ODFs using spherical deconvolution of diffusion MRI data. *Neuroimage* 2013;65:433–48 CrossRef Medline
  50. Maier-Hein KH, Neher PF, Houde JC, et al. The challenge of mapping the human connectome based on diffusion tractography. *Nat Commun* 2017;8:1349 CrossRef Medline
  51. Schlaier JR, Beer AL, Faltermeier R, et al. Probabilistic vs. deterministic fiber tracking and the influence of different seed regions to delineate cerebellar-thalamic fibers in deep brain stimulation. *Eur J Neurosci* 2017;45:1623–33 CrossRef Medline

# Expanding the Distinctive Neuroimaging Phenotype of *ACTA2* Mutations

F. D'Arco, C.A. Alves, C. Raybaud, W.K.K. Chong, G.E. Ishak, S. Ramji, M. Grima, A.J. Barkovich, and V. Ganesan



## ABSTRACT

**BACKGROUND AND PURPOSE:** *Arg179His* mutations in *ACTA2* are associated with a distinctive neurovascular phenotype characterized by a straight course of intracranial arteries, absent basal Moyamoya collaterals, dilation of the proximal internal carotid arteries, and occlusive disease of the terminal internal carotid arteries. We now add to the distinctive neuroimaging features in these patients by describing their unique constellation of brain malformative findings that could flag the diagnosis in cases in which targeted cerebrovascular imaging has not been performed.

**MATERIALS AND METHODS:** Neuroimaging studies from 13 patients with heterozygous *Arg179His* mutations in *ACTA2* and 1 patient with pathognomonic clinoradiologic findings for *ACTA2* mutation were retrospectively reviewed. The presence and localization of brain malformations and other abnormal brain MR imaging findings are reported.

**RESULTS:** Characteristics bending and hypoplasia of the anterior corpus callosum, apparent absence of the anterior gyrus cinguli, and radial frontal gyration were present in 100% of the patients; flattening of the pons on the midline and multiple indentations in the lateral surface of the pons were demonstrated in 93% of the patients; and apparent “squeezing” of the cerebral peduncles in 85% of the patients.

**CONCLUSIONS:** Because  $\alpha$ -actin is not expressed in the brain parenchyma, only in vascular tissue, we speculate that rather than a true malformative process, these findings represent a deformation of the brain during development related to the mechanical interaction with rigid arteries during the embryogenesis.

The cerebral arteriopathy associated with *Arg179His* mutations in *ACTA2* is a prototypical example of nonatherosclerotic cerebral arteriopathies, some of which are Mendelian disorders.<sup>1</sup> Patients

with the *ACTA2* mutation have distinctive clinical (multisystem smooth-muscle involvement) and angiographic features<sup>2</sup>—specifically, a combination of ectasia and stenosis, a straight arterial course, absence of basal collaterals, and more widespread cerebrovascular involvement in comparison with Moyamoya disease.<sup>2</sup> The diagnosis is suggested by these imaging features and has important implications for the management of the patient (increased risks associated with arterial instrumentation) and other family members, but it also provides important mechanistic insights that may be more generalizable.<sup>1</sup> Previously, the imaging phenotype associated with *ACTA2* mutations had been confined to cerebrovascular abnormalities and associated leukoencephalopathy,<sup>3</sup> apart from a single case report of a patient with a dysmorphic corpus callosum.<sup>4</sup>

Here we expand the neuroimaging phenotype and describe characteristic brain parenchymal abnormalities that could flag the diagnosis when targeted cerebrovascular imaging has not been performed.

## MATERIALS AND METHODS

We reviewed in detail the brain MR imaging findings in a cohort of patients with *ACTA2* mutations to describe the characteristics of brain congenital abnormalities in addition to known neuroan-

Received June 13, 2018; accepted after revision August 16.

From the Departments of Radiology (F.D.A., W.K.K.C.) and Neurology (V.G.), Great Ormond Street Hospital for Children National Health Service Foundation Trust, London, UK; Radiology Department (C.A.A.), Hospital Das Clinicas, Sao Paulo, Brazil; Department of Diagnostic Imaging (C.R.), Hospital for Sick Children, Toronto, Ontario, Canada; Department of Radiology (G.E.I.), Seattle Children's Hospital, University of Washington School of Medicine, Seattle, Washington; Department of Radiology (S.R.), Imperial College Healthcare National Health Service Trust, London, UK; Department of Radiology (M.G.), University Hospital of North Staffordshire National Health Service Trust, Stoke-on-Trent, UK; Department of Radiology and Diagnostic Imaging (A.J.B.), University of California, San Francisco, San Francisco, California; and Neuroscience Unit (V.G.), UCL Great Ormond Street Institute of Child Health, London, UK.

Felice D'Arco and Cesar A. Alves contributed equally to the article.

This project was supported by the National Institute for Health Research Biomedical Research Centre at Great Ormond Street Hospital for Children National Health Service Foundation Trust and University College London.

Please address correspondence to Felice D'Arco, MD, Great Ormond St Hospital for Children NHS Trust, Department of Radiology, London WC1N 3JH, UK; e-mail: darcofel@gmail.com; @FeliceDArco

Indicates open access to non-subscribers at [www.ajnr.org](http://www.ajnr.org)

Indicates article with supplemental on-line table.

<http://dx.doi.org/10.3174/ajnr.A5823>

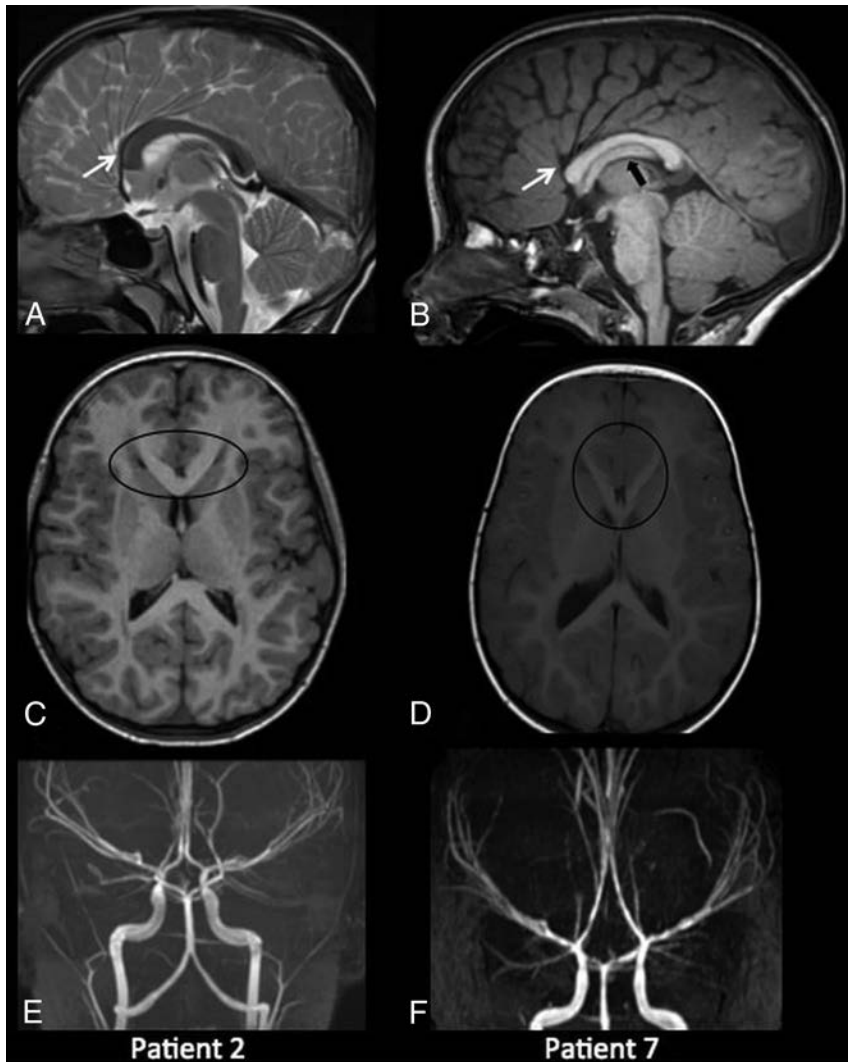


**FIG 1.** Supratentorial abnormalities in patients with the *ACTA2* mutation. *Upper row:* sagittal T2-weighted image (A) and sagittal T1WI (B) show typical hypoplasia and bending of the anterior corpus callosum with associated abnormal radial gyration of the frontal lobes and a deficient anterior cingulate gyrus (white arrows). In patient 7, there is a horizontal orientation of the fornix (black arrow in B), which is also markedly thick. *Middle row:* axial T1WI (C and D) demonstrates characteristic V-shaped anterior corpus callosum (black circle). *Lower row:* MR angiography maximum-intensity-projection anteroposterior view (E and F) shows typical neurovascular abnormalities in patients with *ACTA2* mutation.

geographic findings previously described.<sup>2</sup> Clinically acquired, anonymized brain and cerebrovascular imaging studies from 13 unrelated patients with heterozygous *Arg179His* mutations in *ACTA2* were retrospectively included from 4 pediatric hospitals and 3 general university hospitals (University Hospital of North Midlands; Hospital Das Clinicas, Sao Paulo, Brazil; Imperial College Healthcare National Health Service Trust, London, UK), with appropriate governance permissions from each site. The patients were selected after a search for *ACTA2* mutation in the electronic data management systems of the centers involved in the study (past 10 years). Inclusion criteria were confirmed mutation and/or pathognomonic neuroradiologic and clinical findings and availability of MR imaging of diagnostic quality.

This included re-analysis of 8 patients already published by Munot et al.<sup>2</sup> All 13 patients had the genetic diagnosis confirmed in a clinically accredited laboratory as part of their clinical evaluation.

Another patient had no genetic confirmation (lost at follow-up) but showed typical radiologic and clinical phenotypes that are considered pathognomonic for *ACTA2* mutation<sup>2,5</sup> and thus was included in the study.

Images were reviewed for quality and co-reported by 2 pediatric neuroradiologists (F.D'A. and W.K.K.C.), who reported the presence and localization of brain malformations (ie, the presence of cortical malformations; abnormal shape of the brain stem; abnormal relative size of the midbrain, pons, and medulla oblongata; abnormal shape and size of the corpus callosum; and abnormal gyration) (On-line Table). MR angiography or digital subtraction angiography or both, when available, were also reviewed for typical *ACTA2*-related cerebrovascular anomalies as described in literature.<sup>2</sup>

The presence of associated ischemic brain damage was also reported and divided into large territorial infarction of the brain and evidence of watershed infarctions/small vessel disease.

The presence of specific brain malformations found in our cohort was compared with known similar brain malformation patterns and analyzed in view of known embryologic knowledge<sup>6</sup> to elucidate possible pathogenetic mechanisms.

Review through the electronic data management systems of the MR imaging scans and clinical data of all the patients from the main institution (ie, Great Ormond Street Hospital for Children) with a diagnosis of other forms of neurovascular dysplasia (eg, Moyamoya disease) excluded the presence of similar brain abnormalities.

## RESULTS

Clinical, radiologic, and genetic findings in our patients are summarized in the On-line Table. Thirteen patients had heterozygous missense *Arg179His* in *ACTA2*, and 1 patient without genetic confirmation had clinical and radiologic findings pathognomonic for *ACTA2* mutation (subject 14) and was included in the case series.

All patients had the neuroangiographic features previously described in the *ACTA2 Arg179His* mutation: namely, dilation of the proximal internal carotid arteries, occlusion or narrowing of the distal internal carotid arteries, straight “broomstick-like” arteries of the circle of Willis, and absence of Moyamoya collaterals (Fig 1E, -F). Multiple areas of abnormal signal in keeping with small vessel disease and sometimes frank supratentorial infarctions in a different stage of maturation were commonly observed.

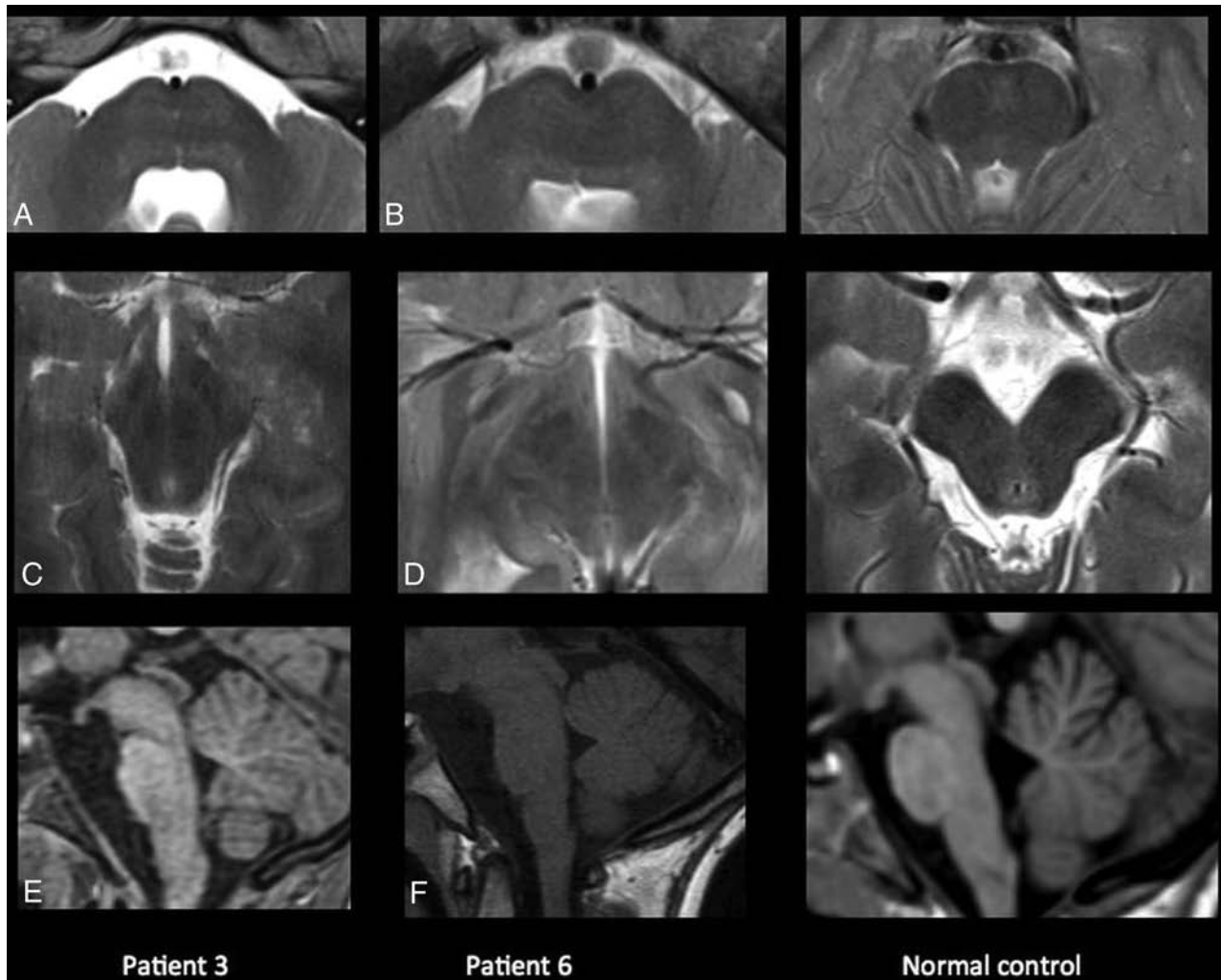


**FIG 2.** Infratentorial malformations in *ACTA2* mutation. *Upper row:* axial T2WI (A and B) at the level of the pons. The twin peaks sign is demonstrated; the pons is flattened with reduction of the anteroposterior diameter and an impression of the basilar artery on the anterior surface with consequent presence of 2 symmetric prominences resembling twin mountains. *Middle row:* axial T2WI at the level of the cerebral peduncles (C and D) shows mild antero-posterior elongation of the midbrain with reduction of the laterolateral diameter and squeezing of the cerebral peduncles. *Right column:* normal for comparison.



**FIG 3.** In the parasagittal slice, the patients show multiple indentations on the surface of the pons. We speculate that these may be due to stretching of the straightened pontine arterial branches.

All patients showed different degrees of abnormal brain morphology, namely the following:

1) Bending (excessive curvature inferiorly and anteriorly) and hypoplasia (rostrum not well-formed and flattened genu) of the anterior corpus callosum (Fig 1A, -B) with a relatively normal or mildly hypoplastic posterior corpus callosum were present. On

axial images, the anterior corpus callosum demonstrates a characteristic V-shaped appearance (Fig 1C, -D). This finding was present in all (100%) patients.

2) Abnormal radial gyration of the frontal lobes and a deficient anterior cingulate gyrus (Fig 1A, -B) (100%) was present.

3) “Twin peaks” pons (appreciable in all the patients with the exception of patient 1: 93%): The pons was flattened with subjective reduction of the anteroposterior diameter noted on the midline and an impression of the basilar artery

on the anterior surface with the consequent presence of 2 symmetric prominences resembling twin mountains (Fig 2). In the parasagittal slice, the patients had multiple indentations on the surface of the pons (Fig 3), probably due to the straightened pontine arterial branches creating compression of the pontine surface (see the “Discussion”).

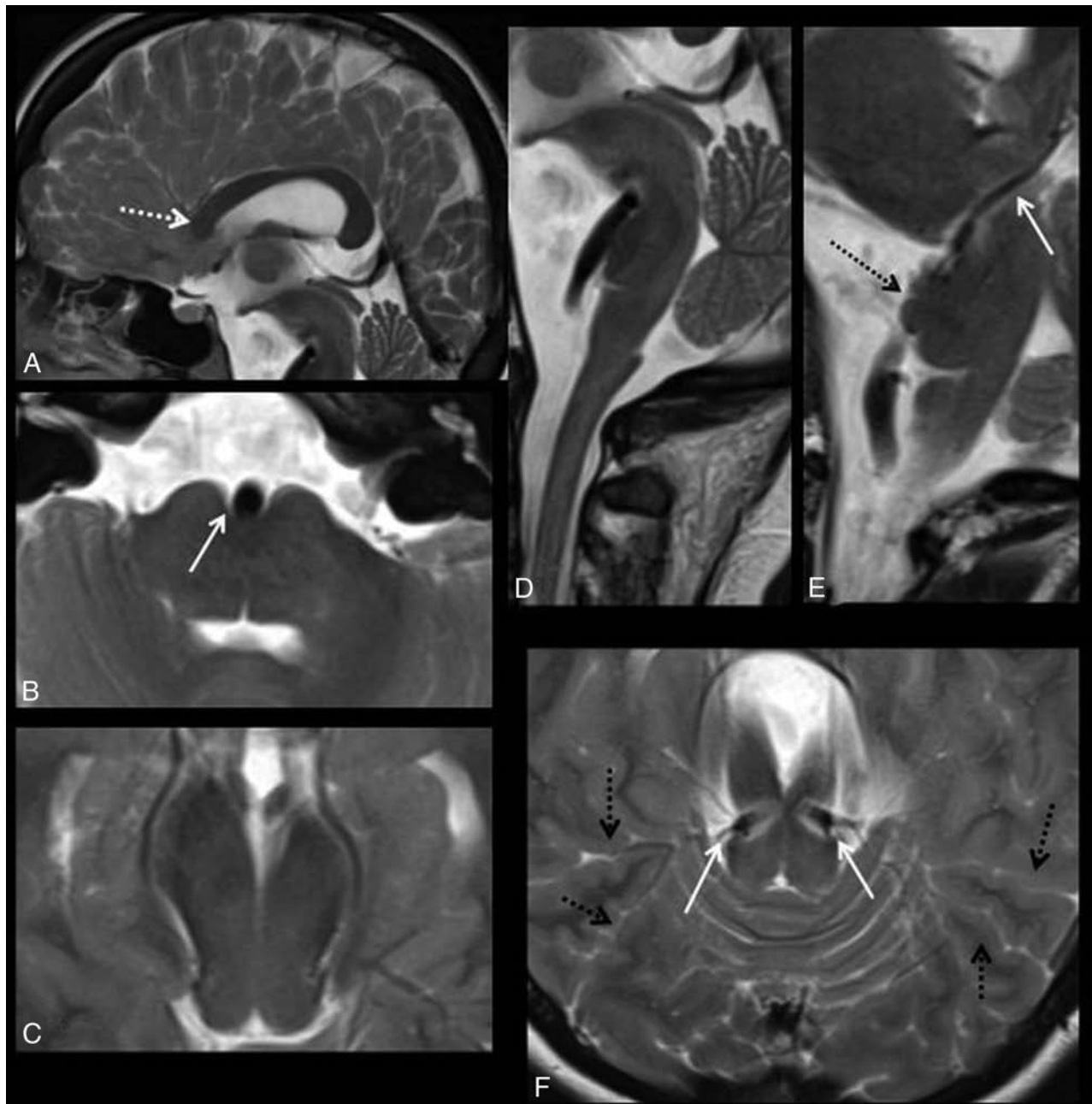


**FIG 4.** Neuroradiologic findings in an adult patient without a confirmed *ACTA2* mutation (patient 15). Sagittal T2WI (A) and axial T2WI at the level of the pons (B) and the midbrain (C) show marked callosal anterior bending (dotted arrow in A), the twin peaks pontine sign (arrow in B), and reduction of the laterolateral diameter of the midbrain with a squeezed cerebral peduncle. D, Sagittal T2WI demonstrates a marked basilar impression on the pons and anterior bending of the midbrain. The parasagittal right slice (E) demonstrates indentation of the lateral surface of the pons (dotted black arrow) and a straight course of the posterior cerebral arteries (white arrow). Axial T2WI (F) at the level of the proximal segment of the posterior cerebral arteries (pontomesencephalic junction) shows marked compression of the brain stem at that level related to straightening of the arteries (white arrows) and radial gyration of the posterior temporal lobes (black dotted arrows).

4) Apparent “squeezing” of the cerebral peduncles in the midbrain (Fig 2C, -D) was present in 12 patients (85%).

5) A variable degree of horizontal orientation and thickening of the fornix (ie, fornix parallel to the corpus callosum) was present in all patients (Fig 1A, -B).

The radiologic and clinical findings of the patient without confirmed mutations were similar to those in the confirmed cases, with the typical *ACTA2* cerebrovascular changes.<sup>2</sup>

Most interesting, we also found an adult patient with a similar and pronounced *ACTA2*-like cerebrovascular phenotype (patient

15 in the On-line Table), which showed the same spectrum of brain abnormalities, straightening of posterior circulation arteries, and abnormal radial gyration also involving the posterior temporal lobes (Fig 4). This patient refused genetic testing and did not have pathognomonic clinical findings associated with *ACTA2* mutation. Nevertheless, this case is extremely interesting for understanding the possible pathophysiology of the brain abnormalities related to vascular dysplasia (see the “Discussion”).

In 8 subjects (patients 1, 5, 8, 10, 11, 12, 13, and 15), follow-up MR imaging was not available. The others had a different evolu-

tion of the ischemic cerebral lesions. In all patients with follow-up available, the abnormalities in the corpus callosum, gyration, and brain stem were stable with time as well as the degree of arteriopathy. None of the patients showed cortical malformations such as focal cortical dysplasia, polymicrogyria, agyria, or pachygyria, as described in literature.<sup>7</sup>

## DISCUSSION

Actin is an abundant protein in eukaryotic organisms and plays an essential role in the protein-protein interactions. The actin protein represents a monomeric subunit of 2 main varieties of filaments in cells that make up the cytoskeleton and form part of the contractile apparatus in muscle cells. The mammalian genome comprises 6 distinct actin isoforms ( $\alpha$ -skeletal,  $\alpha$ -cardiac,  $\alpha$ -smooth,  $\beta$ -cytoplasmic,  $\gamma$ -smooth, and  $\gamma$ -cytoplasmic actin) encoded by 6 different genes.<sup>8</sup> Alpha-smooth-muscle actin, encoded by *ACTA2*, located on 10q22-q24,<sup>9</sup> is a principal element of the contractile units of vascular smooth-muscle cells but is not expressed in the brain parenchyma. However,  $\alpha$ -actin cross-reacts with  $\gamma$ -actin to reinforce the cytoskeleton.<sup>10</sup> The arterial phenotype in *Arg179His ACTA2* mutations, with ectasia of the large arteries and occlusive disease in the small arteries, appears to reflect the local influence on the presence or absence of elastin within the arterial wall on the vascular phenotype.<sup>2</sup> These arterial features are also observed in the mouse model.<sup>11</sup> Vascular smooth-muscle cells are derived from the mesoderm in the posterior fossa/brain stem/thalami and form the neural crest supratentorially (anterior neural plate)<sup>12</sup>; however, there are no data, to the best of our knowledge, to suggest differences in expression of *ACTA2* related to different embryologic origins.

The occlusive disease observed in intracranial vessels is a result of fibrosis, thickening of the vascular wall, flattening and disorganization of the internal lamina, and proliferation of smooth-muscle cells.<sup>13</sup> We previously postulated that this process renders the arteries more rigid and less deformable.<sup>2</sup> Arterial growth follows the contours of brain growth and gyration during normal development.<sup>12</sup> Thus, we speculate that in patients with these *ACTA2* mutations, the increased rigidity of the intracranial arteries results in both the characteristic “straight” appearance and the morphologic brain changes that we have described as a consequence of the local mechanical effect from these vessels. Interestingly, the muscular layers do not appear in the basal perforator vessels until the gestational age of 27 weeks and, progressively, until term over the convexity. However studies on rat embryos show that actin expression in the vasculature starts very early,<sup>14</sup> and histologic specimens in subjects with *ACTA2* mutations demonstrate that the rigidity is also due to abnormality in elastic and intima laminae.<sup>13</sup> Furthermore, although the shape of the corpus callosum is complete by the gestational age of 20 weeks, this structure enlarges together with the connectivity and the development of the cortex<sup>6</sup>; thus, it is still possible that interaction with abnormally formed vessels is responsible for the observed deformity despite these differences in the embryologic age of development. In addition, because the actin cytoskeleton participates directly or indirectly in almost every aspect of neuronal development and function,<sup>15</sup> any instability in the cytoskeleton resulting from abnormal cross-linkage between actin subtypes could also influence

neuronal migration.<sup>8</sup> Alpha-actin is not expressed in the brain parenchyma but only in vessels (different from other isoforms), so it is unlikely that a mutation of this isoform will directly influence brain development, but it is possible that cross-regulation between different isoforms may play a role in subjects with the *ACTA2* mutation.

There are other examples of malformative disorders being related to local mechanical factors, for example, arachnoid cysts with surrounding brain hypoplasia and Chiari I malformation, in which a small posterior fossa results in distortion and inferior displacement of the cerebellar tonsils, which is why the term “Chiari I deformity” was proposed instead of “malformation.”<sup>16</sup>

In patients with the *ACTA2* mutation, the abnormal arterial morphology and structural brain abnormalities parallel each other in both supratentorial and infratentorial parenchyma—universally so in the anterior part of the corpus callosum, anterior cingulate gyrus, and abnormal radial frontal gyration, and variably in the brain stem. In fact, the characteristic twin peaks appearance of the pons in the axial plane seems to be related to impression by the basilar artery as well as the indentation of the lateral pontine surface that may be due to the impression by the pontine arteries coming from the basilar artery (Fig 3).

We have observed a particularly extreme example of this phenotype in a genetically untested patient who showed neuroradiologic features similar to those in *ACTA2* mutations (patient 15). In this patient, the posterior cerebral arteries are also severely straightened and are associated with abnormal radial gyration involving the posterior temporal lobes and marked brain stem compression (Fig 4). The vascular phenotype present in this patient is similar to that in the others and is only described in patients with *ACTA2* mutation, with the exception of an isolated case report<sup>17</sup> in which a mutation was not found and brain images were very similar to those in our patient. Thus, even though it is possible that this patient (despite neurovascular findings) does not have an *ACTA2* mutation, we think that the striking association between severe vascular and brain phenotypes in this subject is supportive of our hypothesis that brain abnormalities are secondary to vessel rigidity.

The apparent absence/definition of a segment of the anterior cingulate and the frontal radial pattern are both likely associated with a callosal abnormality at that level, which itself probably translates into the axial callosal V-shape. The horizontal fornix (or rather, the fornix that is parallel to the anterior callosum) results from an abnormally developed septum pellucidum (ie, too thick), which itself may well relate to the abnormal cingulate.<sup>6</sup>

The brain malformation features do not appear to have a clear clinical correlate in patients with *Arg179His ACTA2* mutations; epilepsy is rare, other than in the context of brain ischemia, and intellectual outcomes again seem related to brain injury rather than to developmental abnormalities per se. However, the extreme reproducibility of the brain phenotype could represent an asset in the diagnosis when neuroangiographic studies are not available; for instance, in patient 8, standard MR imaging sequences showed typical bending of corpus callosum and radial frontal gyration that triggered the addition of an MRA sequence, which confirmed the radiologic diagnosis.

These observations contribute to defining the distinctive neu-

roradiologic features of *ACTA2* mutations, as well to shedding light on mechanisms, both genetic and mechanical, that result in structural changes to the brain and its vasculature.

## CONCLUSIONS

We describe a characteristic and potentially pathognomonic (in specific clinical context) brain phenotype in patients with *ACTA2* mutations and/or the typical clinical and neurovascular picture. A possible explanation for these brain imaging findings, which can be helpful in diagnosis, is a mechanical effect on the brain parenchyma during development by abnormal rigid vessels with possible contribution of cross-regulation between different actin isoforms.

Disclosures: Marius Grima—UNRELATED: Employment: University Hospitals of North Midlands, Comments: I am a salaried doctor in this institution; Travel/Accommodations/Meeting Expenses Unrelated to Activities Listed: University Hospitals of North Midlands, Comments: study-leave budget.

## REFERENCES

1. Ganesan V, Prengler M, Wade A, et al. **Clinical and radiological recurrence after childhood arterial ischemic stroke.** *Circulation* 2006;114:2170–77 Medline
2. Munot P, Saunders DE, Milewicz DM, et al. **A novel distinctive cerebrovascular phenotype is associated with heterozygous Arg179 *ACTA2* mutations.** *Brain* 2012;135(Pt 8):2506–14 CrossRef Medline
3. Moosa AN, Traboulsi EI, Reid J, et al. **Neonatal stroke and progressive leukoencephalopathy in a child with an *ACTA2* mutation.** *J Child Neurol* 2013;28:531–34 CrossRef Medline
4. Meuwissen ME, Lequin MH, Bindels-de Heus K, et al. ***ACTA2* mutation with childhood cardiovascular, autonomic and brain anomalies and severe outcome.** *Am J Med Genet A* 2013;161A:1376–80 CrossRef Medline
5. Milewicz DM, Østergaard JR, Ala-Kokko LM, et al. **De novo *ACTA2* mutation causes a novel syndrome of multisystemic smooth muscle dysfunction.** *Am J Med Genet A* 2010;152A:2437–43 CrossRef Medline
6. Raybaud C. **The corpus callosum, the other great forebrain commissures, and the septum pellucidum: anatomy, development, and malformation.** *Neuroradiology* 2010;52:447–77 CrossRef Medline
7. Di Donato N, Chiari S, Mirzaa GM, et al. **Lissencephaly: expanded imaging and clinical classification.** *Am J Med Genet A* 2017;173:1473–88 CrossRef Medline
8. Perrin BJ, Ervasti JM. **The actin gene family: function follows isoform.** *Cytoskeleton (Hoboken)* 2010;67:630–34 CrossRef Medline
9. Ueyama H, Bruns G, Kanda N. **Assignment of the vascular smooth muscle actin gene *ACTSA* to human chromosome 10.** *Jinrui Iden-gaku Zasshi* 1990;35:145–50 CrossRef Medline
10. Belyantseva IA, Perrin BJ, Sonnemann KJ, et al. **Gamma-actin is required for cytoskeletal maintenance but not development.** *Proc Natl Acad Sci U S A* 2009;106:9703–08 CrossRef Medline
11. Yuan SM. **α-Smooth muscle actin and *ACTA2* gene expressions in vasculopathies.** *Braz J Cardiovasc Surg* 2015;30:644–49 CrossRef Medline
12. Raybaud C. **Normal and abnormal embryology and development of the intracranial vascular system.** *Neurosurg Clin N Am* 2010;21:399–426 CrossRef Medline
13. Georgescu MM, Pinho Mda C, Richardson TE, et al. **The defining pathology of the new clinical and histopathologic entity *ACTA2*-related cerebrovascular disease.** *Acta Neuropathol Commun* 2015;3:81 CrossRef Medline
14. de Ruiter MC, Poelmann RE, van Iperen L, et al. **The early development of the tunica media in the vascular system of rat embryos.** *Anat Embryol (Berl)* 1990;181:341–49 Medline
15. Cheever TR, Ervasti JM. **Actin isoforms in neuronal development and function.** *Int Rev Cell Mol Biol* 2013;301:157–213 CrossRef Medline
16. Poretti A, Ashmawy R, Garzon-Muvdi T, et al. **Chiari type 1 deformity in children: pathogenetic, clinical, neuroimaging, and management aspects.** *Neuropediatrics* 2016;47:293–307 CrossRef Medline
17. Nagarajan K, Swamiappan E, Anbazhagan S, et al. **“Twig-like” cerebral vessels are not pathognomonic for *ACTA2* mutations: a case report.** *Interv Neuroradiol* 2018;24:463–68 CrossRef Medline

# Cerebral Blood Flow and Marrow Diffusion Alterations in Children with Sickle Cell Anemia after Bone Marrow Transplantation and Transfusion

M.T. Whitehead, A. Smitthimedhin, J. Webb, E.S. Mahdi, Z.P. Khademian, J.L. Carpenter, and A. Abraham

## ABSTRACT

**BACKGROUND AND PURPOSE:** Hematopoietic marrow hyperplasia and hyperperfusion are compensatory mechanisms in sickle cell anemia. We have observed marrow diffusion and arterial spin-labeling perfusion changes in sickle cell anemia following bone marrow transplantation. We aimed to compare arterial spin-labeling perfusion and marrow diffusion/ADC values in patients with sickle cell anemia before and after bone marrow transplantation or transfusion.

**MATERIALS AND METHODS:** We reviewed brain MRIs from patients with sickle cell anemia obtained during 6 consecutive years at a children's hospital. Quantitative marrow diffusion values were procured from the occipital and sphenoid bones. Pseudocontinuous arterial spin-labeling perfusion values (milliliters/100 g of tissue/min) of MCA, anterior cerebral artery, and posterior cerebral artery territories were determined. Territorial CBF, whole-brain average CBF, and marrow ADC values were compared for changes before and after either bone marrow transplantation or transfusion. Bone marrow transplantation and transfusion groups were compared. Two-tailed paired and unpaired Student *t* tests were used;  $P < .05$  was considered significant.

**RESULTS:** Fifty-three examinations from 17 patients with bone marrow transplantation and 29 examinations from 9 patients with transfusion were included. ADC values significantly increased in the sphenoid and occipital marrow following bone marrow transplantation in contrast to patients with transfusion ( $P > .83$ ). Whole-brain mean CBF significantly decreased following bone marrow transplantation ( $77.39 \pm 13.78$  to  $60.39 \pm 13.62$  ml/100 g tissue/min;  $P < .001$ ), without significant change thereafter. CBF did not significantly change following the first ( $81.11 \pm 12.23$  to  $80.25 \pm 8.27$  ml/100 g tissue/min;  $P = .47$ ) or subsequent transfusions. There was no significant difference in mean CBF between groups before intervention ( $P = .22$ ).

**CONCLUSIONS:** Improved CBF and marrow diffusion eventuate following bone marrow transplantation in children with sickle cell anemia in contrast to transfusion therapy.

**ABBREVIATIONS:** ACA = anterior cerebral artery; ASL = arterial spin-labeling; BMT = bone marrow transplantation; PCA = posterior cerebral artery; SCA = sickle cell anemia; TI = relaxation time

Sickle cell anemia (SCA) is an inherited hematopoietic disorder, rare in the general US population but more common in African Americans (0.3%; 1/365).<sup>1</sup> The mutated hemoglobin contained in the red blood cells of patients with SCA (HbSS) forms insoluble polymers under low oxygen conditions and deforms the cells, giving them their sickle shape. The "sickle cells" have decreased deformability, rendering them unable to easily

pass through small vessels, and can reduce or occlude blood flow to tissues. Enhanced red blood cell production and blood flow are compensatory mechanisms used by the body in an attempt to maintain homeostasis. Hematopoietic marrow hyperplasia causes marrow signal alterations on MR imaging, including T1 lengthening, T2 shortening, and reduced diffusion.<sup>2-4</sup> Elevated cardiac output, increased arterial blood flow, and vasodilation contribute to cerebral hyperperfusion.<sup>5</sup> However, end organs remain vulnerable to ischemic injury because these compensatory adjustments are often insufficient. Furthermore, small- and large-vessel vasculopathy can potentiate this rather tenuous situation.<sup>6</sup> In the brain, injury may take the form of borderzone ischemia, focal small-vessel lacunar infarcts (symptomatic or silent), or large vascular territory infarctions.

Arterial spin-labeling (ASL) perfusion is a noninvasive MR imaging technique that uses flowing blood as an intrinsic tracer to

Received June 17, 2018; accepted after revision August 15.

From the Departments of Radiology (M.T.W., A.S., E.S.M., Z.P.K.), Hematology (J.W., A.A.), and Neurology (J.L.C.), Children's National Medical Center, Washington, DC; and George Washington University Hospital (M.T.W., J.W., Z.P.K., J.L.C., A.A.), Washington, DC.

Please address correspondence to Matthew T. Whitehead, MD, Department of Radiology, Children's National Medical Center, 111 Michigan Ave NW, Washington, DC 20010; e-mail: MWhitehe@childrensnational.org

<http://dx.doi.org/10.3174/ajnr.A5830>

assess cerebral blood flow in milliliters/100 g of tissue/min.<sup>7-9</sup> Thus, it is an MR imaging technique well-suited to the SCA population because it readily depicts the present state of blood flow to the brain without the need for intravenous gadolinium. In compensated patients with SCA, the combination of hyperperfusion and anemia leads to a generalized increase in ASL brain signal. The signal is then reduced in patients with cerebrovascular disease, including delayed arterial transit (eg, vasculopathy) and hypoperfusion (eg, ischemia or encephalomalacia), or increased in states of hyperperfusion (eg, luxury perfusion or seizure-related).<sup>8,10,11</sup> Notable limitations of the ASL technique include a relatively poor signal-to-noise ratio and variables often represented as estimations in calculating the ASL perfusion equation, such as tagging efficiency, postlabel delay, the cortex-blood partition coefficient, and the T1 of blood.<sup>8</sup> The latter, however, can be measured directly or calculated with knowledge of the magnetic field strength, hemoglobin, and oxygen saturation.<sup>12</sup>

Primary therapeutic measures in symptomatic patients with SCA include hydroxyurea, red blood cell transfusions, and, in the appropriate population, bone marrow transplantation (BMT), which is curative if successful. Human leukocyte antigen-matched sibling donors offer the best hope for a cure with BMT, with a success rate as high as 98%.<sup>13</sup> However, failure can occur in up to 10% and is more common with nonsibling human leukocyte antigen-matched donors and nonmatched donors.<sup>14-20</sup> Repeat transplantation would be necessary under these circumstances to achieve success. Imaging markers for transplantation failure would thus be useful adjuncts to guide early treatment decisions.

We have observed changes in brain blood flow and marrow diffusion values following bone marrow transplant in SCA, potentially representing imaging biomarkers of a favorable therapeutic response. The aim of this study was to compare and contrast alterations in ASL perfusion and bone marrow diffusion/ADC values in patients with SCA before and after BMT or initiation of chronic, monthly transfusion therapy.

## MATERIALS AND METHODS

This Health Insurance Portability and Accountability Act-compliant retrospective study was performed after institutional review board approval. The brain MR imaging data base from a single academic children's hospital was queried for all examinations performed in patients with sickle cell anemia during a consecutive 6-year period (January 1, 2012, to December 31, 2017) using the terms "sickle cell," "ASL," and "arterial spin-labeling" to build a cohort for retrospective analysis. Each patient's medical record was reviewed to confirm a diagnosis of sickle cell disease, record demographic information, and determine the clinical course of the disease, including time points for transfusions and/or bone marrow transplantation. Each patient's most recent hematocrit and oxygen saturation levels relative to the time of the brain MR imaging were documented to correct for the longitudinal relaxation (T1) value of arterial blood. MR imaging examinations with excessive motion artifacts and technical limitations and without ASL images were excluded. Excessive motion artifacts were determined at the discretion of the board-certified neuroradiologist who reviewed each of the scans (M.T.W.) on the basis of training and experience. Motion artifacts were considered exces-

sive when they limited either the ASL and/or DWI datasets more than a minimal-to-mild degree. Additional exclusion criteria included acute chest syndrome, acute stroke, posterior reversible encephalopathy syndrome, active infection, recent seizure, and vasculopathy based on MRA or transcranial Doppler (when MRA was unavailable). Cerebral hemispheres containing any chronic lesions larger than a lacunar infarct were excluded from analysis; in these cases, the contralateral hemisphere was evaluated in isolation. ASL perfusion images were evaluated qualitatively and quantitatively by a board-certified neuroradiologist with >6 years of clinical experience after board certification who was blinded to the type of therapy/intervention at the time of assessment.

Studies were performed on either a 1.5T (Discovery MR450 or Optima MR450W) or 3T (Discovery MR750) MR imaging scanner (GE Healthcare, Milwaukee, Wisconsin). The following sequences were performed through the brain in each examination: arterial spin-labeling perfusion, sagittal spoiled gradient-echo T1WI, axial T2WI, axial T2 FLAIR, axial DWI, and coronal fat-saturated T2WI. 3D TOF-MRA of the circle of Willis was also acquired concurrently with each brain MR imaging examination.

### DWI: Technique, Processing, and Assessment

The bone marrow was evaluated qualitatively on T1, T2, and diffusion-weighted sequences. The T1WI and T2WI were assessed first to ensure lack of substantial marrow hypointensity reflecting transfusion-related iron deposition, which would interfere with the assessment of the DWI due to susceptibility. We excluded from further evaluation those with substantial marrow hypointensity defined as hypointense marrow signal with respect to muscle on all pulse sequences.

DWI acquisition parameters were as follows: TR, 10,000 ms; TE, 83-94 ms; flip angle, 90°; matrix, 128 × 128 mm; FOV, 24 × 27 cm; 1-2 excitations; section thickness, 5 mm; spacing, 0. Qualitative marrow diffusion abnormalities were documented using a 3-point scale: 1, within normal limits; 2, mild-to-moderate restricted diffusion; and 3, marked restricted diffusion. Quantitative apparent diffusion coefficient values (in square millimeters/second) were measured using 4-mm circular ROIs placed manually in the marrow cavity of the right greater sphenoid wing and midline occipital bones; these representative sites were selected because the marrow cavity here is reliably thicker than in many other locations of the skull.

### ASL: Technique, Processing, and Assessment

Each subject underwent pseudocontinuous ASL with background suppression and a segmented 3D fast spin-echo readout in accordance with current consensus guidelines<sup>7</sup> using the following scan parameters: flip angle, 111°-155°; inversion time/postlabel delay, 1025-1525 ms; labeling duration, 1500-2000 ms; TR, 4300-4600 ms; TE, 11 ms; ETL (echo train length), 1; NEX, 2-3; matrix, 512 × 8; FOV, 24-55 × 24-29 cm; 32-35 slices; 3- to 4-mm slice thickness; 3- to 4-mm spacing; total sequence acquisition time, 4-5 minutes. Anatomic landmarks were used to select the labeling plane just below the inferior margin of the cerebellum. ASL post-processing was performed on the MR imaging scanner. Grayscale ASL perfusion images and pseudocolor images were generated and displayed with age-dependent scaling based on the

**Table 1: Transplant group—hemoglobinopathy subtype, transplant data, and MR imaging data analyzed<sup>a</sup>**

Pt	Diagnosis	Source	Donor	HLA Match	Scans (No.)	Age (yr)	DWI (No.)	ASL (Right Cerebrum) (No.)	ASL (Left Cerebrum) (No.)
1	HbSS	BM	R	8/8	2	18,19	2	2	2
2	HbSS	BM	R	8/8	4	15,16,16,18	4	4	4
3	HbS-B0Th	PBSC	R, H	4/8	2	12,13	2	2	2
4	HbSC	BM	R	8/8	5	13,14,14,16,17	5	5	5
5	HbSS	BM	R	8/8	4	7,10,11	3	3	3
6	HbSS	BM	R	8/8	2	7,9	2	2	2
7	HbS-B0Th	BM	R	8/8	2	10,12	2	2	2
8	HbSS	BM	R	8/8	3	11,11,12	3	2	2
9	HbSS	BM	R	8/8	4	5,7,8,9	4	4	4
10	HbSS	UCB	R	5/6	4	8,8,9,10	4	0	4
11	HbSS	BM	R	8/8	3	8,9,10	3	3	3
12	HbSS	PBSC	R, H	3/6	3	4,5,5	3	0	3
13	HbSS	BM	U	8/8	5	18,18,18,19,20	5	3	3
14	HbSS	BM	R	8/8	2	1,2	2	2	2
15	HbSS	BM	R	10/10	3	3,3,3	2	3	3
16	HbSS	BM	R	8/8	2	15,16	2	2	2
17	HbSS	UCB	U	6/6	3	3,3,4	3	3	3

**Note:**—Pt indicates patient; BM, bone marrow; PBSC, peripheral blood stem cell; UCB, umbilical cord blood; R, related; H, haploidentical; U, unrelated; HbSS, homozygous hemoglobin S; HbSC, sickle cell hemoglobin C; HbS-B0Th, hemoglobin S-β-thalassemia disease; HLA, human leukocyte antigen.

<sup>a</sup> SCA subtype, transplant information, total MRI scans, number of DWIs, and number of ASL sequences analyzed (right and left cerebral hemispheres) from 17 patients with transplants.

**Table 2: Chronic transfusion group—hemoglobinopathy subtype and MR imaging data analyzed<sup>a</sup>**

Pt	Diagnosis	Scans (No.)	Age (yr)	DWI (No.)	ASL (Right Cerebrum) (No.)	ASL (Left Cerebrum) (No.)
1	HbSS	3	7,9,11	0	3	0
2	HbSS	6	0,1,2,5,6	3	1	5
3	HbSS	2	7,8	0	2	2
4	HbSS	2	8,11	2	0	2
5	HbSS	6	2,3,4,5,6,7	0	6	6
6	HbSS	2	4,6	1	2	2
7	HbSS	2	6,8	1	2	2
8	HbSS	3	3,4,5	1	3	3
9	HbSS	3	9,10,11	0	3	3

**Note:**—Pt indicates patient; HbSS, homozygous hemoglobin S.

<sup>a</sup> SCA subtype, total MRI scans, number of DWIs, and number of ASL sequences analyzed (right and left cerebral hemispheres) from 9 patients with transfusion.

magnitude of normal cerebral blood flow from the neonatal-to-early childhood period (younger than 1 year: 0–60 mL/100 g of tissue/min; older than 1 year: 0–100 mL/100 g of tissue/min).<sup>21</sup>

Arterial territory-specific quantitative ASL data in milliliters/100 g of tissue/min were procured using an AW workstation with Func-Tool software (GE Healthcare). The T1 value of arterial blood was calculated in each patient using patient-specific hematocrit levels, oxygen saturation at or around the time of imaging (median, 2 days; range, 0–71 days), and the magnetic field strength according to previously published guidelines.<sup>12</sup> Then, 6 distinct manual ROIs were drawn around the cerebral cortex and subcortical white matter at the level of the basal ganglia to approximate each of the following vascular territories: anterior cerebral artery (right and left), middle cerebral artery (right and left), and posterior cerebral artery (right and left), using a previously established technique.<sup>22</sup> Cerebral blood flow was calculated from the following equation:

$$CBF = \frac{\lambda(1 - e^{-\frac{t_{sat}}{T_{1b}}})}{2\alpha T_{1b}(1 - e^{-\frac{\tau}{T_{1b}}})} \frac{PW}{PD} e^{-\frac{PLD}{T_{1b}}}$$

where  $\lambda$  indicates the cortex-blood partition coefficient (0.9, assumed);  $t_{sat}$ , time of saturation before imaging (2000 ms);  $T_{1b}$ , T1

of gray matter (1200 ms, assumed);  $\alpha$ , labeling efficiency (0.8, assumed);  $T_{1b}$ , T1 of the blood (calculated for each patient using the hematocrit, oxygen saturation, and magnetic field strength based on Hales et al<sup>12</sup>);  $\tau$ , labeling duration (1500 ms); PW, perfusion weighted signal intensity; PD, proton density signal intensity; and PLD, postlabeling delay time. Mean whole-brain perfusion was estimated in each examination by averaging CBF values from all 6 evaluated territories. Gray-scale and corresponding postprocessed pseudocolor data were also evaluated together qualitatively. Qualitative cerebral signal magnitude was recorded using a 3-point scale: 1, hypoperfusion; 2, within normal limits; and 3, hyperperfusion.

### Statistical Methods

The normal Gaussian distribution of the data mean was determined and confirmed by a Shapiro-Wilk test. Subsequently, 2-tailed paired *t* tests were used separately in each group of patients with SCA before and after BMT and transfusion, respectively. Two-tailed unpaired *t* tests were then performed to evaluate differences in the mean cerebral blood flow and marrow diffusion values between the posttransplantation and posttransfusion arms. The Wilcoxon signed rank test was used to evaluate paired samples of qualitative ordinal data. Observed power was calculated on the basis of the postintervention whole-brain CBF mean and SD differences between groups.  $P \leq .05$  was considered significant.

### RESULTS

Fifty-three brain MR imaging examinations from 17 patients with BMT (mean, 3; range, 2–5; mean length of follow-up,  $1.9 \pm 0.9$  years; range, 0.7–4.2 years) (9 male, 8 female) and 29 brain MR

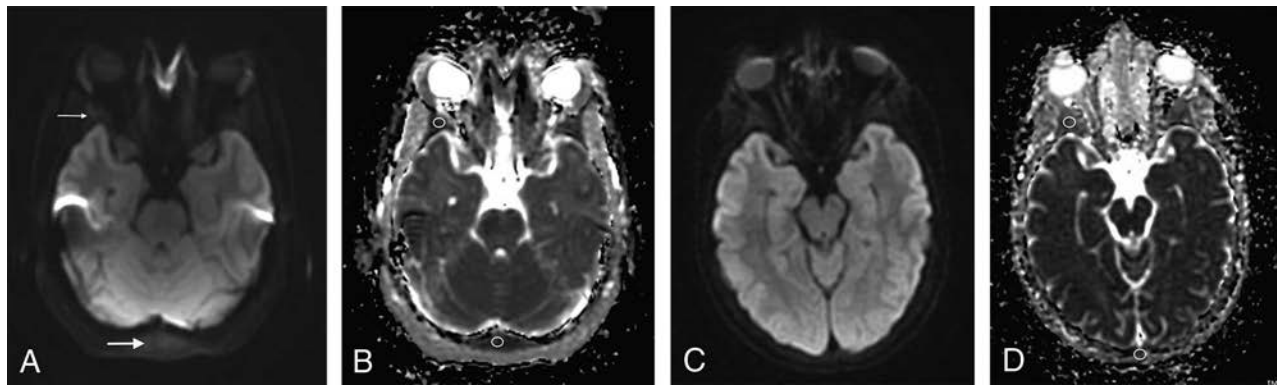


**FIG 1.** A 13-year-old girl with sickle cell disease. Pre-bone marrow transplantation axial DWI (A) (TR/TE = 10,000/83 ms, slice thickness = 5 mm) through the greater sphenoid wing (*thin arrow*) and occipital bone (*thick arrow*) and corresponding quantitative ADC map with ROIs (B) placed demonstrating reduced diffusion of the bone marrow. Follow-up MR imaging at 14 years of age from the same patient post-bone marrow transplantation with axial DWI (C) (TR/TE = 10,000/79.8 ms, slice thickness = 5 mm) at the same level as A and corresponding quantitative ADC map (D) demonstrating facilitated diffusion with respect to the pretransplantation scan.

**Table 3: Pre- and posttransplantation ASL perfusion changes<sup>a</sup>**

Pt	Pretransplantation							Posttransplantation							P Value
	MCA (R)	MCA (L)	ACA (R)	ACA (L)	PCA (R)	PCA (L)	Avg	MCA (R)	MCA (L)	ACA (R)	ACA (L)	PCA (R)	PCA (L)	Avg	
1	71	70	68	73	55	60	66	78	79	69	75	58	68	71	.02 <sup>b</sup>
2	92	82	88	85	96	89	89	74	78	70	73	61	65	70	.008 <sup>c</sup>
3	82	80	79	83	92	90	84	60	63	62	64	64	64	63	<.001 <sup>c</sup>
4	66	63	64	60	50	51	59	34	35	37	38	28	30	34	<.001 <sup>c</sup>
5	100	80	93	85	97	83	90	62	61	62	61	63	54	61	<.001 <sup>c</sup>
6	90	89	96	93	87	91	91	81	77	74	70	71	73	74	<.001 <sup>c</sup>
7	68	65	68	63	63	59	64	69	62	37	59	51	57	56	.14
8	76	72	73	67	73	73	72	59	54	56	52	48	46	53	<.001 <sup>c</sup>
9	84	65	77	64	86	77	76	97	87	86	84	79	71	84	.16
10	NA	57	NA	56	NA	55	56	NA	45	NA	48	NA	40	44	.03 <sup>c</sup>
11	73	81	76	77	72	74	76	78	73	75	74	71	74	74	.47
12	89	NA	77	NA	100	NA	95	82	NA	72	NA	87	NA	80	.07
13	63	66	59	68	66	37	60	61	60	67	55	58	67	61	.82
14	85	81	79	76	77	74	79	77	79	65	70	62	63	69	.006 <sup>c</sup>
15	68	71	67	72	63	64	68	64	65	63	62	53	50	60	.004 <sup>c</sup>
16	76	73	76	71	75	71	74	66	66	57	58	45	47	57	.005 <sup>c</sup>
17	100	99	101	94	91	94	97	40	40	37	37	35	37	38	<.001 <sup>c</sup>
T	81	76	79	75	78	72	<b>77</b>	66	63	60	60	57	55	60	<.001 <sup>c</sup>

**Note:**—Pt indicates patient; R, right; L, left; Avg, average/mean whole-brain CBF; NA, not applicable/excluded; T, mean of each arterial territory.

<sup>a</sup> Arterial territory–specific and mean whole-brain CBF values (in milliliters/100 g of tissue/min) from 17 patients with BMT prior to (left columns) and at the first scan after (right columns) transplantation. In the interest of space and simplicity, CBF values were rounded to the nearest whole number for this display.

<sup>b</sup> Significant increase in mean whole-brain CBF.

<sup>c</sup> Significant.

imaging examinations from 9 patient with transfusion (mean, 3; range, 2–6; mean length of follow-up,  $3 \pm 1.4$  years; range, 1.1–5.6 years) (3 male, 6 female) met the inclusion criteria (Tables 1 and 2). Two patients with transfusion were excluded; one lacked ASL, and the other had a severe vasculopathy with multiple infarctions and excessive motion artifacts. Three follow-up examinations after BMT were excluded from 2 different patients due to posterior reversible encephalopathy syndrome. One hemisphere was excluded from ASL analysis due to infarctions or vasculopathy in 4 cases from 2 patients in the transplant group and in 5 cases from 3 patients in the transfusion group; however, there was no significant difference between pre- and posttransfusion and pre- and posttransplantation CBF values between the subgroups that underwent unilateral and bilateral cerebral analysis. At the time of the initial MR imaging, the mean age of the BMT group was  $9.8 \pm 5$  years (range, 1–18 years), while the mean age of the transfusion group was  $6.3 \pm 4$  years (range, 0–9 years) ( $P = .13$ ). Transfu-

sions were initiated 20 days before the follow-up MR imaging on average (range, 4–60 days). The mean time between BMT and the first follow-up MR imaging was  $281 \pm 170$  days (range, 3–875 days). No patients who underwent BMT had graft failure.

#### Marrow ADC Values

ADC values significantly increased in the marrow of the greater sphenoid wing ( $0.97 \pm 0.34$  to  $1.59 \pm 0.55 \times 10^{-3}$  mm<sup>2</sup>/s;  $P = .025$ ) and occipital bone ( $1.11 \pm 0.27$  to  $1.44 \pm 0.51 \times 10^{-3}$  mm<sup>2</sup>/s;  $P = .043$ ) following bone marrow transplantation (Fig 1). Qualitatively, ADC sequences also demonstrated visually brighter marrow following BMT (the mean score decreased from 3 to 1), representing more facilitated diffusion ( $P = .01428$ ) (Fig 1). These changes were sustained across time on follow-up examinations, with no significant difference in the interval mean ADC values ( $P > .05$ ). There was no significant difference in sphenoid wing and occipital marrow mean ADC values be-

tween patients pre- and posttransfusion ( $P > .83$ ); however, only 2 patients could be evaluated posttransfusion due to MR imaging evidence of marrow iron deposition. Post-BMT and posttransfusion

marrow ADC values were significantly different from one another ( $P = .0323$ ). There was no significant difference between marrow ADC values obtained at 1.5T and 3T in either group ( $P > .05$ ).

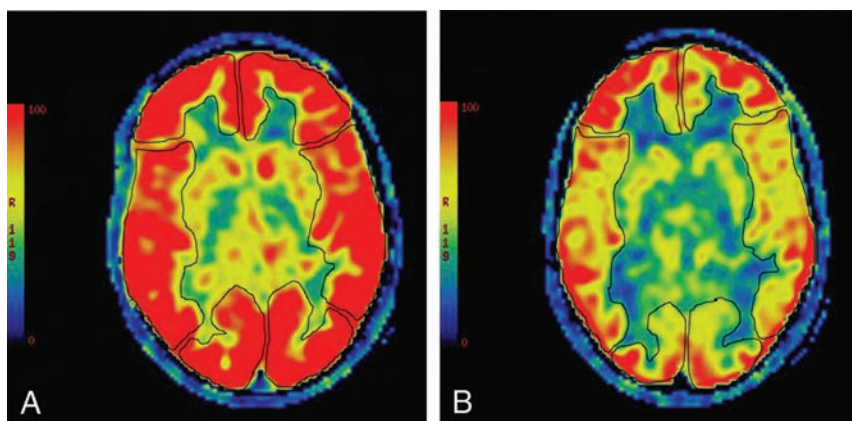


**FIG 2.** An 11-year-old boy with sickle cell disease. Pre-bone marrow transplantation, axial pseudocolor ASL (A) depicts manual ROIs drawn to interrogate CBF from the bilateral ACA, MCA, and PCA territories. Diffusely increased signal is present throughout the cerebrum, consistent with elevated cerebral blood flow. Follow-up MR imaging at 12 years of age from the same patient, post-bone marrow transplantation, with axial pseudocolor ASL (B) depicting persistent-but-improved/decreased hyperperfusion.

### Cerebral Blood Flow

Preintervention mean whole-brain perfusion for both groups combined was  $78.43 \pm 11.18$  mL/100 g of tissue/min. CBF values obtained at 1.5T were not significantly different from those obtained at 3T in either group ( $P > .05$ ). There was no significant difference in mean quantitative cerebral blood flow between the BMT and transfusion groups before intervention ( $P = .22$ ). Mean whole-brain cerebral blood flow was significantly lower after BMT compared with transfusion ( $P = .0004$ ). The observed power was strong at 99.6%.

Whole-brain mean quantitative cerebral blood flow significantly decreased following BMT, from  $77.39 \pm 13.78$  to  $60.39 \pm 13.62$  mL/100 g tissue/min (first scan;  $P = .00004$ ), and did not significantly change thereafter (Table 3 and Figs 2 and 3). The mean CBF significantly decreased in all bilateral vascular territories (anterior cerebral artery [ACA], MCA, posterior cerebral artery [PCA]) on the first scan following BMT, and most of these significant differences were sustained across time. On an individual level, most patients (11/17) had a significant drop in whole-brain CBF on the first scan following BMT. Half of the patients who did not experience significantly decreased CBF on the first scan were reimaged at  $\geq 1$  later time point; CBF ultimately decreased significantly in two-thirds of these patients. The first posttransplantation scan was performed at  $0.8 \pm 6$  years on average

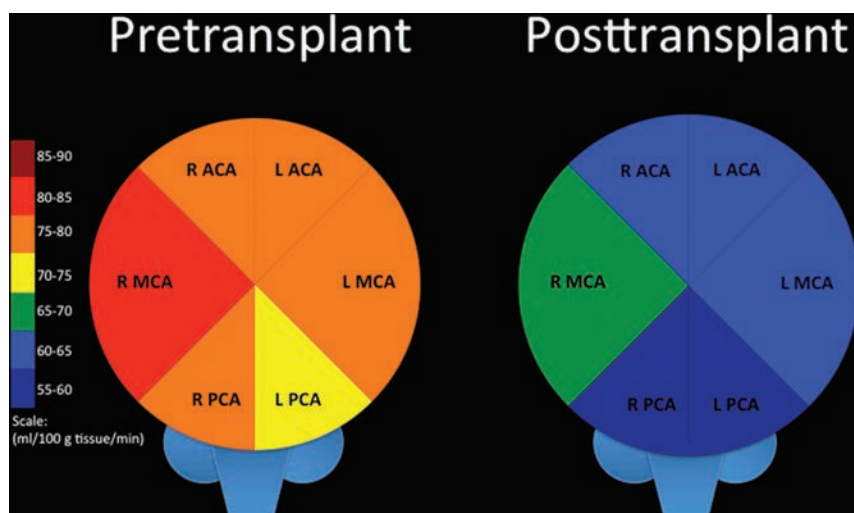


**FIG 3.** Comparison of arterial territory-specific quantitative mean CBF in patients with SCA before BMT (left) and at the first scan after BMT (right). R indicates right; L, left.

**Table 4: Pre- and postinitiation of chronic transfusion therapy ASL perfusion changes<sup>a</sup>**

Pt	Pretransfusion							Posttransfusion							P Value
	MCA (R)	MCA (L)	ACA (R)	ACA (L)	PCA (R)	PCA (L)	Avg	MCA (R)	MCA (L)	ACA (R)	ACA (L)	PCA (R)	PCA (L)	Avg	
1	96	NA	78	NA	93	NA	89	95	NA	94	NA	87	NA	92	.69
2	79	71	64	65	62	73	69	NA	87	NA	84	NA	80	84	.06
3	103	91	102	98	111	107	102	75	78	76	76	73	75	76	<.001 <sup>b</sup>
4	NA	89	NA	80	NA	80	83	NA	75	NA	82	NA	76	78	.37
5	90	96	81	93	82	88	88	93	96	95	101	91	93	95	.02 <sup>c</sup>
6	84	102	88	100	78	83	90	79	96	81	86	78	76	83	.02 <sup>b</sup>
7	98	93	88	90	92	88	92	81	84	74	85	74	83	81	.005 <sup>b</sup>
8	70	68	70	65	65	64	67	74	79	64	71	60	60	68	.74
9	70	70	64	66	63	71	67	69	74	77	85	73	80	87	.02 <sup>c</sup>
T	86	78	79	82	81	82	81	81	84	80	80	77	78	80	.47

**Note:**—Pt indicates patient; R, right; L, left; Avg, average/mean whole-brain CBF; NA, not applicable/excluded; T, mean of each arterial territory.

<sup>a</sup> Arterial territory-specific and mean whole-brain CBF values (in milliliters/100 g of tissue/min) from 9 patients with transfusion prior to (left columns) and at the first scan after (right columns) transfusion initiation. In the interest in space and simplicity, CBF values were rounded to the nearest whole number for this display.

<sup>b</sup> Significant.

<sup>c</sup> Significant increase in mean whole-brain CBF.

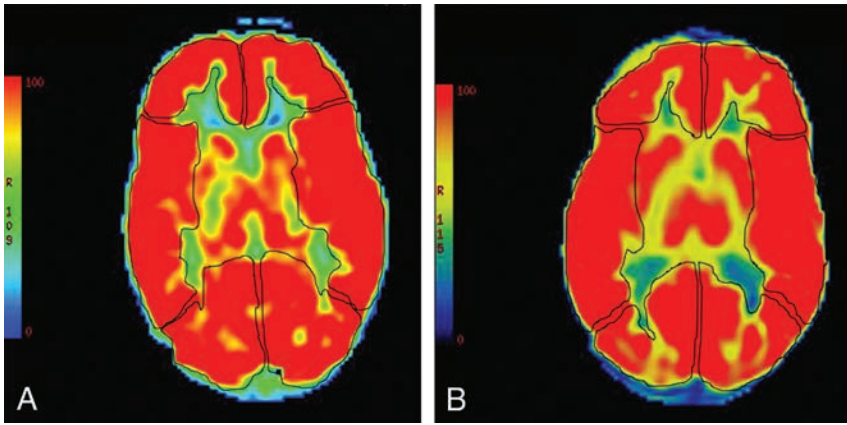


**FIG 4.** A 31-month-old girl with sickle cell disease. Pretransfusion axial pseudocolor ASL (A) depicts manual ROIs drawn to interrogate CBF from the bilateral ACA, MCA, and PCA territories. Diffusely increased signal is present throughout the cerebrum, consistent with elevated cerebral blood flow. Follow-up MR imaging at 36 months of age from the same patient at the same level posttransfusion with axial pseudocolor ASL (B) depicting persistent hyperperfusion without significant change.

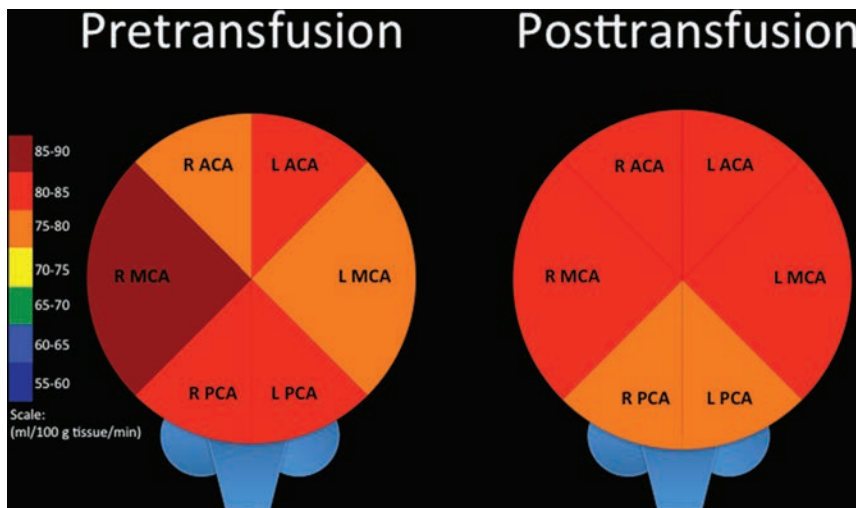


**FIG 5.** Comparison of arterial territory–specific quantitative mean CBF in patients with SCA before initial transfusion (left) and at the first scan after transfusion initiation (right). R indicates right; L, left.

after BMT. There was no significant difference in the time interval between transplant and the first posttransplantation brain MR imaging between patients who did and did not experience decreased CBF ( $P = .5$ ). One of the 6 patients without significant CBF alteration had an unrelated BMT without myeloablative preconditioning.

Whole-brain mean perfusion values did not significantly change following the first transfusion ( $81.11 \pm 12.23$  to  $80.25 \pm 8.27$  mL/100 g tissue/min;  $P = .47$ ) or across time after subsequent transfusions (Table 4 and Figs 4 and 5). Whole-brain CBF did not significantly decline in 6 of the 9 patients and actually significantly increased in 2 of these patients. A minority of patients (3/9) did experience significantly decreased whole-brain CBF after transfusion; unfortunately, none of these patients had further follow-up imaging to determine the duration of the change.

## DISCUSSION

Marrow diffusion and cerebral perfusion significantly improved in patients with sickle cell anemia following bone marrow trans-

plantation and did not change significantly after transfusion alone. Because marrow ADC values negatively correlate and CBF positively correlates with the severity of anemia, these may be useful surrogate imaging biomarkers for therapeutic success.<sup>2-4,12</sup>

Apparent diffusion coefficient values of bone marrow are inversely proportional to the degree of hematopoietic constituents. Red marrow hyperplasia causes T1 prolongation, T2 shortening, and reduced diffusion.<sup>2-4</sup> Proliferative hematopoietic marrow changes in SCA are an attempt to compensate for the diminished oxygen-carrying capacity of the sickled erythrocytes and to replenish red blood cells prematurely removed from circulation. All patients in our cohort had evidence of reduced diffusion in the sphenoid and occipital bone marrow before intervention. Although SCA-associated quantitative ADC values in the skull have not been previously assessed in the literature to our knowledge, the significant increase in ADC and facilitated diffusion following BMT raises the possibility that marrow diffusion is reduced at baseline compared with age-expected values. These increased marrow ADC values were sustained across time on follow-up examinations after BMT, suggesting diminished or resolved hematopoietic marrow proliferation. No significant change in marrow ADC values was found in patients with SSA pre- to posttransfusion. However, interpretation was confounded because transfusion causes increased bone marrow T1 pro-

longation and T2 shortening due to iron deposition.<sup>2,3</sup> Thus, we excluded examinations with qualitative marrow hypointensity from marrow DWI assessment. Unfortunately, in the transfusion group, this exclusion left only 2 patients for analysis.

The ASL signal magnitude is influenced by a number of factors in addition to blood flow, namely the spin-lattice relaxation time (T1) of arterial blood, blood flow velocity, labeling efficiency, and the brain-blood partition coefficient of water. The latter variable is difficult to accurately measure and is therefore typically estimated at 0.9 mL/g for averaged brain gray and white matter.<sup>7</sup> Labeling efficiency is inversely related to blood flow velocity and requires additional measurements for calculation, such as with phase-contrast imaging. However, the T1 of blood can and should be adjusted on a patient-to-patient basis, especially if there are known deviations from normal hematocrit. Anemia will prolong the T1 value of blood and cause spuriously increased ASL signal that, all other factors being equal, would be interpreted as hyper-

perfusion. Arterial T1 values can be measured directly, but specific sequences are required at the time of MR imaging.<sup>23-25</sup> Alternatively, as used in our study, the T1 value can be calculated after determining the hematocrit, O<sub>2</sub> saturation, and magnetic field strength.<sup>12</sup>

Cerebral perfusion decreases during childhood in normal states.<sup>26</sup> It has been shown that anemia positively correlates with cerebral blood flow and negatively correlates with cerebrovascular reserve and that these relationships are strongly associated with anemia severity in children with SCA.<sup>5</sup> In untreated patients with asymptomatic sickle cell anemia, cerebral blood flow is diffusely elevated relative to aged-matched healthy subjects without regard for age, manifested on ASL as diffusely increased brain signal.<sup>6</sup> Before intervention, we estimated the mean whole-brain CBF in our SCA cohort (transfusion and BMT groups combined) to be elevated at 78 ± 11 mL/100 g of tissue/min (64 ± 14 mL/100 g of tissue/min is considered normal).<sup>27</sup> Previous literature reported quantitative whole-brain CBF values in patients with SCA to be in a similar range (83–87 ± 24 mL/100 g of tissue/min), though different ASL techniques were used and anemia-related blood T1 value adjustments were not made in that study, possibly accounting for slightly higher reported values.<sup>6,28</sup>

Therapeutic measures in SCA include blood transfusions and allogenic bone marrow transplantation. The improved O<sub>2</sub> delivery conferred by transfused normal red blood cells enhances cerebrovascular reserve, decreases the oxygen extraction fraction, and decreases CBF.<sup>5,23</sup> Williams et al<sup>23</sup> reported a significant mean CBF drop following transfusion, from 88 to 82 mL/100 g of tissue/min. A minority of patients in our cohort also experienced decreased CBF posttransfusion; however, the mean whole-brain CBF encompassing the entire group did not change significantly (from 81 to 80 mL/100 g of tissue/min). It is unclear whether this finding could relate to a smaller sample size and/or differences in techniques among studies. In contrast, whole-brain CBF significantly decreased after BMT (from 76 to 63 mL/100 g of tissue/min) and was sustained across time on follow-up MR imaging. This change occurred as early as 3 days after transplantation and, therefore, could be a neuroimaging marker heralding favorable engraftment. Engraftment can be observed clinically from 1 to 4 weeks posttransplantation with the definition based on a sustained rebound in the absolute neutrophil count of ≥500/μL and platelet count of ≥20,000/μL.<sup>29</sup>

Several study limitations should be noted. The sample size is relatively small due to the rarity of SCA-related BMT, the high prevalence of brain and vascular pathology factoring into exclusions, and the novelty of ASL. The posttransfusion bone marrow diffusion data were particularly sparse because iron deposition precluded accurate interpretation in most cases. In the few cases that required single cerebral hemisphere exclusion from analysis, contralateral cerebral ASL perfusion data could have been unreliable to some extent; however, there was no significant difference between pre- and posttransfusion and pre- and posttransplantation CBF values between the subgroups that underwent unilateral and bilateral cerebral analysis to suggest that unilateral cerebral hemisphere exclusion from analysis had any bearing on the results. Future studies with a larger number of subjects will be useful to confirm our findings. Increased blood velocity due to chronic

anemia is a known cause of decreased labeling efficiency using ASL, which may have resulted in underestimation of absolute CBF.<sup>30,31</sup> Because this was a retrospective study, we did not have corresponding phase data available to approximate labeling efficiency in each case. However, relative changes across time and between groups would be unaffected. In addition, we used a single rather than a multicompartamental model for quantitative ASL calculation, and we did not account for venous outflow effects in SSA.<sup>24,30</sup>

## CONCLUSIONS

Improved cerebral blood flow and marrow diffusion ensue following bone marrow transplantation in children with sickle cell anemia. We found no significant alteration in CBF or marrow diffusion in patients with SCA who underwent transfusion therapy, though the sample size is a limitation. ASL perfusion and quantitative marrow diffusion values are useful posttherapeutic imaging biomarkers.

Disclosures: Allistair Abraham—UNRELATED: Grant: American Society of Hematology\*. \*Money paid to the institution.

## REFERENCES

1. Sickle Cell Disease (SCD). Centers for Disease Control and Prevention. Updated August 31, 2016. <https://www.cdc.gov/ncbddd/sicklecell/data.html>. Accessed September 14, 2018.
2. Elias EJ, Liao JH, Jara H, et al. Quantitative MRI analysis of craniofacial bone marrow in patients with sickle cell disease. *AJNR Am J Neuroradiol* 2013;34:622–27 CrossRef Medline
3. Saito N, Nadgir RN, Flower EN, et al. Clinical and radiologic manifestations of sickle cell disease in the head and neck. *Radiographics* 2010;30:1021–34 CrossRef Medline
4. Park S, Kwack KS, Chung NS, et al. Intravoxel incoherent motion diffusion-weighted magnetic resonance imaging of focal vertebral bone marrow lesions: initial experience of the differentiation of nodular hyperplastic hematopoietic bone marrow from malignant lesions. *Skeletal Radiol* 2017;46:675–83 CrossRef Medline
5. Kosinski PD, Croal PL, Leung J, et al. The severity of anaemia depletes cerebrovascular dilatory reserve in children with sickle cell disease: a quantitative magnetic resonance imaging study. *Br J Haematol* 2017;176:280–87 CrossRef Medline
6. Arkuszewski M, Krejza J, Chen R, et al. Sickle cell anemia: reference values of cerebral blood flow determined by continuous arterial spin labeling MRI. *Neuroradiol J* 2013;26:191–200 CrossRef Medline
7. Alsop DC, Detre JA, Golay X, et al. Recommended implementation of arterial spin-labeled perfusion MRI for clinical applications: a consensus of the ISMRM perfusion study group and the European consortium for ASL in dementia. *Magn Reson Med* 2015;73:102–16 CrossRef Medline
8. Grade M, Hernandez Tamames JA, Pizzini FB, et al. A neuroradiologist's guide to arterial spin labeling MRI in clinical practice. *Neuroradiology* 2015;57:1181–202 CrossRef Medline
9. Deibler AR, Pollock JM, Kraft RA, et al. Arterial spin-labeling in routine clinical practice, Part 1: techniques and artifacts. *AJNR Am J Neuroradiol* 2008;29:1228–34 CrossRef Medline
10. Deibler AR, Pollock JM, Kraft RA, et al. Arterial spin-labeling in routine clinical practice, Part 2: hypoperfusion patterns. *AJNR Am J Neuroradiol* 2008;29:1235–41 CrossRef Medline
11. Deibler AR, Pollock JM, Kraft RA, et al. Arterial spin-labeling in routine clinical practice, Part 3: hyperperfusion patterns. *AJNR Am J Neuroradiol* 2008;29:1428–35 CrossRef Medline
12. Hales PW, Kirkham FJ, Clark CA. A general model to calculate the spin-lattice (T1) relaxation time of blood, accounting for haemat-

- ocrit, oxygen saturation and magnetic field strength. *J Cereb Blood Flow Metab* 2016;36:370–74 CrossRef Medline
13. Gluckman E, Cappelli B, Bernaudin F, et al; Eurocord, the Pediatric Working Party of the European Society for Blood and Marrow Transplantation, and the Center for International Blood and Marrow Transplant Research. **Sickle cell disease: an international survey of results of HLA-identical sibling hematopoietic stem cell transplantation.** *Blood* 2017;129:1548–56 CrossRef Medline
  14. Shenoy S, Eapen M, Panepinto JA, et al. **A trial of unrelated donor marrow transplantation for children with severe sickle cell disease.** *Blood* 2016;128:2561–67 CrossRef Medline
  15. Dalle JH. **Hematopoietic stem cell transplantation in SCD.** *C R Biol* 2013;336:148–51 CrossRef Medline
  16. Walters MC. **Update of hematopoietic cell transplantation for sickle cell disease.** *Curr Opin Hematol* 2015;22:227–33 CrossRef Medline
  17. Fitzhugh CD, Abraham AA, Tisdale JF, et al. **Hematopoietic stem cell transplantation for patients with sickle cell disease: progress and future directions.** *Hematol Oncol Clin North Am* 2014;28:1171–85 CrossRef Medline
  18. Angelucci E, Matthes-Martin S, Baronciani D, et al; EBMT Inborn Error and EBMT Paediatric Working Parties. **Hematopoietic stem cell transplantation in thalassemia major and sickle cell disease: indications and management recommendations from an international expert panel.** *Haematologica* 2014;99:811–20 CrossRef Medline
  19. Dedeken L, Lè PQ, Azzi N, et al. **Haematopoietic stem cell transplantation for severe sickle cell disease in childhood: a single centre experience of 50 patients.** *Br J Haematol* 2014;165:402–08 CrossRef Medline
  20. Gluckman E. **Allogenic transplantation strategies including haploidentical transplantation in sickle cell disease.** *Hematol Am Soc Hematol Educ Program* 2013;2013:370–76 CrossRef Medline
  21. Wintermark M, Lepori D, Cotting J, et al. **Brain perfusion in children: evolution with age assessed by quantitative perfusion computed tomography.** *Pediatrics* 2004;113:1642–52 CrossRef Medline
  22. Goetti R, O’Gorman R, Khan N, et al. **Arterial spin labeling MRI for assessment of cerebral perfusion in children with moyamoya disease: comparison with dynamic susceptibility contrast MRI.** *Neuroradiology* 2013;55:639–47 CrossRef Medline
  23. Williams KP, Fields ME, Ragan DK, et al. **Red cell exchange transfusions lower cerebral blood flow and oxygen extraction fraction in pediatric sickle cell anemia.** *Blood* 2018;131:1012–21 CrossRef Medline
  24. Wu WC, St Lawrence KS, Licht DJ, et al. **Quantification issues in arterial spin labeling perfusion magnetic resonance imaging.** *Top Magn Reson Imaging* 2010;21:65–73. CrossRef Medline
  25. Václavů L, van der Land V, Heijtel DF, et al. **In vivo T1 of blood measurements in children with sickle cell disease improve cerebral blood flow quantification from arterial spin-labeling MRI.** *AJNR Am J Neuroradiol* 2016;37:1727–32 CrossRef Medline
  26. Hales PW, Kawadler JM, Aylett SE, et al. **Arterial spin labeling characterization of cerebral perfusion during normal maturation from late childhood into adulthood: normal ‘reference range’ values and their use in clinical studies.** *J Cereb Blood Flow Metab* 2014;34:776–84 CrossRef Medline
  27. Wang J, Licht DJ. **Pediatric perfusion MR imaging using arterial spin labeling.** *Neuroimaging Clin N Am* 2006;16:149–67, ix Medline
  28. Helton KJ, Paydar A, Glass J, et al. **Arterial spin-labeled perfusion combined with segmentation techniques to evaluate cerebral blood flow in white and gray matter of children with sickle cell anemia.** *Pediatr Blood Cancer* 2009;52:85–91 CrossRef Medline
  29. Dallas MH, Triplett B, Shook DR, et al. **Long-term outcome and evaluation of organ function in pediatric patients undergoing haploidentical and matched related hematopoietic cell transplantation for sickle cell disease.** *Biol Blood Marrow Transplant* 2013;19:820–30 CrossRef Medline
  30. Bush A, Chai Y, Choi SY, et al. **Pseudo continuous arterial spin labeling quantification in anemic subjects with hyperemic cerebral blood flow.** *Magn Reson Imaging* 2018;47:137–46 CrossRef Medline
  31. Gevers S, Nederveen AJ, Fijnvandraat K, et al. **Arterial spin labeling measurement of cerebral perfusion in children with sickle cell disease.** *J Magn Reson Imaging* 2012;35:779–87 CrossRef Medline

# Aberrant Structural Brain Connectivity in Adolescents with Attentional Problems Who Were Born Prematurely

 O. Tymofiyeva,  D. Gano,  R.J. Trevino Jr,  H.C. Glass,  T. Flynn,  S.M. Lundy,  P.S. McQuillen,  D.M. Ferriero,  A.J. Barkovich, and  D. Xu



## ABSTRACT

**BACKGROUND AND PURPOSE:** Differences in structural brain connectivity that underlie inattention have been previously investigated in adolescents with attention deficit/hyperactivity disorder, but not in the context of premature birth, which is often associated with attentional problems. The purpose of this study was to identify the neural correlates of attentional problems in adolescents born prematurely and determine neonatal predictors of those neural correlates and attention problems.

**MATERIALS AND METHODS:** The study included 24 adolescents ( $12.5 \pm 1.8$  years of age; 12 girls, 12 boys) who were born prematurely and underwent MR imaging of the brain and cognitive assessment, both shortly after birth and as adolescents. Structural connectivity was assessed at adolescence using diffusion tensor imaging and tractography.

**RESULTS:** Of the 24 subjects, 12 had attention deficits. A set of axonal pathways connecting the frontal, parietal, temporal, and occipital lobes had significantly lower fractional anisotropy in subjects with attentional problems. The temporoparietal connection between the left precuneus and left middle temporal gyrus was the most significantly underconnected interlobar axonal pathway. Low birth weight and ventriculomegaly, but not white matter injury or intraventricular hemorrhage on neonatal MR imaging, predicted temporoparietal hypoconnectivity in adolescence. However, neither birth weight nor other neonatal characteristics were associated with attention deficits directly.

**CONCLUSIONS:** We identified an aberrant structural brain connectivity pattern, involving temporoparietal hypoconnectivity, in prematurely born adolescents with attentional problems. We also identified birth weight as a potential neonatal predictor of the temporoparietal hypoconnectivity. These findings add to our understanding of the neural basis and etiology of inattention in adolescents after premature birth.

**ABBREVIATIONS:** ADHD = attention deficit/hyperactivity disorder; AAL = Automated Anatomical Labeling; FA = fractional anisotropy; FDR = false discovery rate; TOVA = Test of Variables of Attention; WMI = white matter injury

About 1 in 10 children are born prematurely and, as a result, enter the world with a higher risk of several health problems as well as early death.<sup>1</sup> Those who survive often have life-long

neurodevelopmental problems, with attention deficit being among the most consistently reported cognitive impairment related to prematurity.<sup>2</sup> This deficit impacts daily functioning, and many individuals meet the formal diagnostic criteria for attention deficit/hyperactivity disorder (ADHD).<sup>3</sup> It is essential to better understand the underlying neurologic causes of attentional problems and their etiologies to develop effective interventions.

Diffusion tensor imaging allows noninvasive assessment of white matter microstructure.<sup>4</sup> This methodology enables 3D visualization of white matter properties and has been used for several decades to study neurologic and psychiatric disorders in an attempt to relate white matter abnormalities to clinical manifestations.<sup>5</sup> A commonly used metric derived from DTI is fractional anisotropy (FA). A general, simplified interpretation is that higher FA represents higher white matter integrity in specific brain regions. With regard to attentional problems, several studies have focused on the FA in the brains of individuals with ADHD, reporting both higher<sup>6-8</sup> and lower<sup>9-11</sup> FA values compared with healthy controls. The effects of premature birth on

Received May 11, 2018; accepted after revision August 16.

From the Departments of Radiology & Biomedical Imaging (O.T., R.J.T., T.F., A.J.B., D.X.), Neurology (D.G., H.C.G., D.M.F.), and Pediatrics (D.G., H.C.G., S.M.L., P.S.M., D.M.F.), University of California, San Francisco, San Francisco, California.

This study was supported by P01NS082330 to D.M.F., P.S.M., D.X., and A.J.B.; NICHD R01HD072074 to D.X. and O.T.; NCCIH R21AT009173 to O.T.; and the University of California, San Francisco, Research Evaluation and Allocation Committee and the J. Jacobson Fund to O.T. and D.X.

The content of this article is solely the responsibility of the authors and does not necessarily represent the official views of the National Institutes of Health or other funding agencies. The funding agencies did not play any role in study design or in the collection, analysis, and interpretation of data; in the writing of the report; and in the decision to submit the article for publication.

Please address correspondence to Olga Tymofiyeva, PhD, Department of Radiology & Biomedical Imaging, University of California, San Francisco, 1700 4th St, Byers Hall, Suite 102, San Francisco, CA 94158; e-mail: Olga.Tymofiyeva@ucsf.edu

 Indicates open access to non-subscribers at [www.ajnr.org](http://www.ajnr.org)

<http://dx.doi.org/10.3174/ajnr.A5834>

DTI parameters have also been investigated, showing that children born prematurely tend to have lower FA values in several regions of the brain consistently from infancy to adulthood.<sup>12-16</sup>

Recently, neurologic and psychiatric disorders, including ADHD, are increasingly being viewed not as anomalies of focal brain regions but rather as disorders arising from disruption of distributed brain networks (connectomes).<sup>17</sup> These networks are modeled as sets of nodes, with pairs of nodes connected by edges. In a structural connectivity study, cortical and subcortical gray matter structures typically play the role of nodes, whereas tractography-derived white matter connections between them serve as edges. This network approach differs in an important way from the voxel-based DTI approaches in that it moves away from focal abnormalities to network-level disruptions and offers new explanations of observed dysfunctions.

To date, there are 3 studies examining white matter network properties in youth with ADHD.<sup>18-20</sup> The main findings include aberrant connectivity of the frontal and striatal regions,<sup>18-20</sup> but also parietal,<sup>18,20</sup> occipital,<sup>18,20</sup> temporal,<sup>20</sup> and cerebellar regions.<sup>19</sup> One additional study used T1-weighted images and showed differences in topologic properties of structural covariance networks in youth with ADHD compared with controls.<sup>21</sup> However, there have been no studies examining structural connectivity associated with inattention in adolescents born prematurely. This is an important gap in knowledge because understanding the underlying mechanisms of attentional dysfunction is crucial for the development of targeted interventions. The purpose of this study was to identify network-level neural correlates of attentional problems in adolescents born prematurely and assess neonatal predictors of those neural correlates.

## **MATERIALS AND METHODS**

### **Participants and Clinical Information**

The study was approved by the local institutional review board, and all participants in the study provided written informed assent, and their parents or legal guardians provided written informed consent in accordance with the Declaration of Helsinki. Prematurely born adolescents who were enrolled in a longitudinal MR imaging study of preterm infants were invited to return for optional MR imaging and neuropsychological testing at 10–14 years of age. Inclusion criteria for the cohort were birth before 33 weeks' gestation. Exclusion criteria included clinical evidence of a congenital malformation or syndrome, congenital infection, or clinical status too unstable for MR imaging. The group included in this study consisted of 24 adolescents (10–14 years of age; average age, 12.5 ± 1.8 years; 12 girls and 12 boys) who were born prematurely (including 11 extremely premature subjects, <28 weeks' gestation) and came for the 10- to 14-year follow-up visit and had both neuropsychological and diffusion MR imaging data available.

### **Neonatal Clinical Assessments**

Trained research nurses blinded to the MR imaging findings reviewed medical records and extracted clinical data. Maternal and antenatal variables included exposure to prenatal steroids as well as maternal age, primiparity, maternal smoking, placenta previa, preeclampsia, and twin gestation.

Demographic variables included gestational age at birth, birth weight, and sex. The z score for birth weight was calculated. Perinatal variables included placental abruption, chorioamnionitis, and mode of delivery, which was classified as vaginal or cesarean delivery. Chorioamnionitis was diagnosed clinically (maternal fever, >38°C during labor or fetal tachycardia with uterine tenderness, treated with antibiotics).<sup>22</sup> Neonatal variables included duration of mechanical ventilation, infection, hypotension, symptomatic patent ductus arteriosus, necrotizing enterocolitis, neonatal surgery, and chronic lung disease. Neonates with culture-positive sepsis, clinical signs of sepsis with blood culture negative for sepsis, or meningitis were classified as having infection. Hypotension was defined as a period of sustained low blood pressure treated with intravenous fluid bolus and/or inotropes. Neonates with clinical signs of patent ductus arteriosus (prolonged systolic murmur, bounding pulses, and hyperdynamic precordium) and evidence of left-to-right flow through the patent ductus arteriosus on echocardiogram were classified as having symptomatic patent ductus arteriosus. Necrotizing enterocolitis was diagnosed according to the Bell stage 2 criteria.<sup>23</sup> Chronic lung disease was defined as an oxygen requirement at 36 weeks' postmenstrual age.

### **Neonatal MR Imaging**

MR imaging scans were obtained after birth as soon as the neonates were clinically stable and again near term-equivalent age when possible. A custom MR imaging-compatible incubator with a specialized neonatal head coil was used to provide a quiet, well-monitored environment for the neonates, minimizing patient movement and improving the signal-to-noise ratio.<sup>24</sup> MR imaging scans were acquired using a 1.5T scanner and a specialized, high-sensitivity, neonatal head coil built into the MR imaging-compatible incubator. MR imaging scans included axial spin-echo T2-weighted images (TR = 3 seconds; TE = 60 and 120 ms; FOV = 240 mm with a 256 × 256 matrix; slice thickness = 4 mm; gap = 2 mm) and sagittal volumetric 3D spoiled gradient-echo T1-weighted images (TR = 36 ms; minimum TE; FOV = 180 mm; 1.0-mm isotropic). A single pediatric neuroradiologist (A.J.B.) blinded to the clinical history (other than premature birth) evaluated all MR images. The severity of the white matter injury (WMI) on T1-weighted MR imaging was scored according to our published criteria as none, mild (≤3 areas of signal abnormality, each <2 mm in diameter), moderate (>3 areas of signal abnormality or areas of signal abnormality of >2 mm but <5% of the hemisphere involved), or severe (>5% of hemisphere involved).<sup>25</sup> WMI was further classified as absent/mild or moderate/severe. Neonates were diagnosed with mild ventriculomegaly if the largest atrial ventricular diameter (at the level of the glomus of the choroid plexus) measured 8–10 mm and with moderate/severe ventriculomegaly if it measured >10 mm.<sup>26</sup> Intraventricular hemorrhage was classified according to the Papile grading system.<sup>27</sup>

### **Adolescent Attention Assessments**

A psychologist blinded to imaging findings administered performance-based measures and parent report forms targeting attention. Attentional problems in most subjects (*n* = 17 of the 24

**Table 1: Neonatal clinical characteristics of the study participants<sup>a</sup>**

	Abnormal Attention		P Value <sup>b</sup>
	No (n = 12)	Yes (n = 12)	
Male	6	6	1.0
Gestational age at birth (mean) (wk)	29.4 ± 1.83	27.8 ± 2.9	.093
BW (median) (IQR) (g)	1167 (900–1365)	875 (708–898)	.043
BW z score, (median) (IQR)	−0.35 (−1.05–0.48)	−0.22 (−0.73–0.34)	.82
Cesarean delivery	6	4	.41
Intubated at birth	5	11	.027
Apgar 5 (median) (IQR)	8 (6.5–8)	5.5 (3.5–8)	.84
Apgar 10 (median) (IQR)	7 (4–7)	6.5 (5–8)	.56
Hypotension	5	10	.089
Patent ductus arteriosus	2	7	.089
Necrotizing enterocolitis	0	5	.037
Chronic lung disease	1	6	.069
Neonatal surgery	2	8	.036
Infection	2	10	.022

**Note:**—BW indicates birth weight; IQR, interquartile range.

<sup>a</sup> All neonates with necrotizing enterocolitis had surgery.

<sup>b</sup> Kruskal-Wallis for continuous variables; Fisher exact test for categoric variables.

subjects included in this study) were evaluated using the Test of Variables of Attention (TOVA), a continuous performance test used to measure the speed and accuracy of attentional processing.<sup>28</sup> Negative TOVA Attention Comparison Scores were interpreted as indicative of attentional problems. Six subjects were evaluated using the Conners Comprehensive Behavior Rating Scales, suitable for assessing children ages 6–18. Conners attention *t*-scores of >60 were interpreted as indicative of attentional problems. One subject was evaluated using the Child Behavior Checklist.<sup>29</sup> The Child Behavior Checklist attention *t*-scores of >66 were interpreted as indicative of attentional problems. The comparability of ADHD-related metrics has been previously reported for the TOVA and Child Behavior Checklist,<sup>30</sup> for the Conners Rating Scales and Child Behavior Checklist,<sup>31,32</sup> and for the TOVA and Conners Rating Scales.<sup>33</sup>

### Adolescent MR Imaging Data Acquisition and Processing

Each adolescent underwent an hour-long MR imaging protocol using a 3T MR750 MR imaging scanner (GE Healthcare, Milwaukee, Wisconsin) and a 32-channel Nova Medical head coil (Siemens, Erlangen, Germany). The scan included a standard T1-weighted sequence and a spin-echo echo-planar DTI sequence (TR = 7.5 seconds, minimum TE, FOV = 25.6 cm with a 128 × 128 matrix, slice thickness = 2 mm). Diffusion-sensitizing gradients were applied at a b-value of 1000 s/mm<sup>2</sup> along 30 noncollinear directions. An array spatial sensitivity encoding technique acceleration factor was set to 2, resulting in a sequence scan time of 4 minutes.

Preprocessing was performed using the FMRIB Software Library (FSL 5.0.8; <http://www.fmrib.ox.ac.uk/fsl>)<sup>34</sup> and Matlab (MathWorks, Natick, Massachusetts). A quality-assurance step was performed, in which diffusion volumes affected by motion were rejected<sup>35</sup> and the remaining images were corrected for eddy current distortions, affine head motion, and b-vector rotation. DTI reconstruction and deterministic whole-brain streamline fiber tractography were performed using the Diffusion Toolkit (TrackVis; <http://www.trackvis.org/dtk/>).<sup>36</sup> For whole-brain tractography, the Fiber Assignment by Continuous Tracking algorithm<sup>37</sup> with 1 seed per voxel was applied using the entire dif-

fusion-weighted volume as the mask image. Streamlines were terminated if the tract curvature exceeded 35°, a value chosen on the basis of previous work in adolescents.<sup>38</sup>

Each brain was segmented into ROIs using the Automated Anatomical Labeling (AAL; <https://omictools.com/aal-tool>) atlas.<sup>39</sup> Only 90 cerebral regions were considered, because the cerebellum is often affected by stronger artifacts and is not always fully covered in the FOV.<sup>38</sup> T1-weighted data were registered to the B<sub>0</sub> volume of the DTI dataset and to the Montreal Neurological Institute space template using the FMRIB Linear Image Registration Tool (FLIRT; <http://www.fmrib.ox.ac.uk/fsl/fslwiki/FLIRT>).<sup>40,41</sup>

This step allowed the application of the AAL atlas in the DTI space to produce the 90 nodes of the network. The registration and segmentation results were visually inspected for errors. The resultant ROIs were dilated by 1 voxel. To define the connections between the ROIs, we considered only streamlines with at least 5 points, and we used the average FA value within voxels along streamlines connecting the ROIs as a proxy for the connectivity strength.

### Statistical Analysis

**Adolescent Structural Connectivity Analysis.** Our main assumption was that aberrant connectivity underlies attentional problems. To test whether significant associations between connectivity and attention exists, we performed *t* tests using attention as the grouping variable. We did not assume that the connections associated with this contrast of interest form a connected component. To control for the massive number of multiple comparisons, we applied a standard link-based controlling procedure, the false discovery rate (FDR). We used the implementation in Matlab by Zalesky et al<sup>42</sup> with default parameters (a significance value of .05 and 1000 permutations). In this context, the FDR is referred to as a link-based controlling procedure because each link is treated independently for the sake of the family-wise error rate control.

The rest of the statistical analyses were performed using SPSS Statistics software (Version 25; IBM, Armonk, New York). Neonatal predictors of attentional problems in adolescence were tested using the Kruskal-Wallis test for continuous variables and the Fisher exact test for categoric variables. Neonatal predictors of abnormal structural connectivity associated with attentional problems in teens were investigated using a linear regression model with abnormal connectivity as the dependent variable and neonatal clinical and imaging metrics and the age at the adolescent MR imaging visit as independent variables. Additionally, the number of rejected diffusion volumes affected by motion was compared between the groups of adolescents with normal and abnormal attention using the independent-samples *t* test.

No matching of intelligence quotient (IQ) was performed in the analyses because this can be problematic in the case of children

**Table 2: Neonatal scan results for study participants**

	Abnormal Attention		P Value
	No (n = 12)	Yes (n = 12)	
Scan 1	12	12	
WMI <sup>a</sup>			.05
Absent	6	8	
Mild	1	3	
Moderate	5	0	
Severe	0	1	
IVH			.32
Absent	8	11	
Grade I	4	1	
Grade II	0	0	
Grade III	0	0	
Grade IV	0	0	
VM			1.0
Absent	11	12	
Mild	1	0	
Moderate/severe	0	0	
Scan 2	10	8	
WMI			.57
Absent	7	6	
Mild	1	2	
Moderate	2	0	
Severe	0	0	
IVH			.35
Absent	6	6	
Grade I	4	1	
Grade II	0	1	
Grade III	0	0	
Grade IV	0	0	
VM			.64
Absent	9	8	
Mild	0	0	
Moderate/severe	1	0	

**Note:**—IVH indicates intraventricular hemorrhage; VM, ventriculomegaly.  
<sup>a</sup>Note for WMI, scan 1, when dichotomized as absent/mild vs moderate/severe,  $P = .16$ .

with attentional problems. On the traditional Wechsler IQ tests, the subtests tend to be rote, repetitive, and require attention and memory and are difficult for a child with attentional problems, and he or she may therefore perform slowly and/or inaccurately.<sup>43</sup>

## RESULTS

Of the 24 adolescents, 12 have been determined to have attention deficits (6 girls/6 boys). There were no statistically significant differences in the number of rejected diffusion-weighted volumes, indicating that adolescents' movements during the MR imaging scan did not differ depending on the attentional problems ( $t = 1.1, P = .28$ ).

### Neonatal Predictors of Attentional Problems in Adolescence

Details about the participants' neonatal characteristics grouped by attentional deficits can be found in Tables 1 and 2. The groups did not differ significantly by sex, gestational age at birth, or birth weight z scores (Table 1). However, there was a group difference in variables that denote increased illness severity, with infection, necrotizing enterocolitis, neonatal surgery, and intubation at birth reaching statistical significance (Table 1). Among neonatal scan results, only WMI at the first neonatal scan indicated a potential difference between the 2 groups with normal and abnormal attention ( $P = .05$ ) (Table 2).

### Adolescent Structural Connectivity Correlates of Attentional Problems

A set of tracts connecting frontal, parietal, temporal, and occipital lobes, including frontal cortices and subcortical regions, had significantly lower FA values in adolescents with attentional problems compared with those with normal attention. Connections

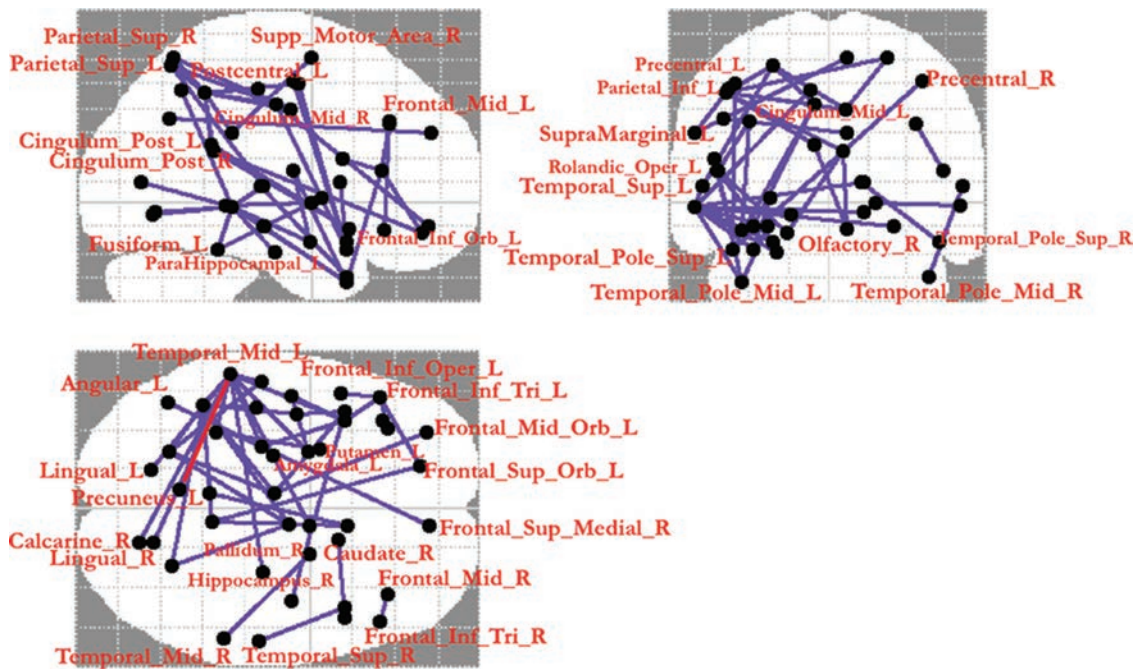


**FIG 1.** Results of the connection-wise group comparison of connectivity matrices using an FDR-corrected  $t$  test with 1000 permutations ( $P = .05$ ). The connections highlighted in blue (46 edges, involving 44 nodes) were statistically significantly weaker in the attention deficit group. The connection highlighted in red, between the left precuneus and left middle temporal gyrus, was the most statistically significantly hypoconnected interlobular connection.

**Table 3: Structural connectivity analysis results (FDR-corrected)—connections with weaker connectivity in the inattention group that survived the FDR correction<sup>a</sup>**

	Connection (AAL Abbreviation)	Test Statistic
1	Frontal_Sup_Orb_L to Frontal_Inf_Tri_L	3.39
2	Frontal_Mid_L to Frontal_Inf_Tri_L	4.12
3	Frontal_Inf_Oper_L to Frontal_Inf_Tri_L	4.16
4	Frontal_Mid_R to Frontal_Inf_Tri_R	3.61
5	Frontal_Mid_L to Frontal_Inf_Orb_L	3.75
6	Frontal_Mid_Orb_L to Cingulum_Mid_L	2.82
7	Olfactory_R to Cingulum_Post_L	4.56
8	Frontal_Sup_Orb_L to Cingulum_Post_R	3.72
9	Olfactory_R to Cingulum_Post_R	4.01
10	Rolandic_Oper_L to Amygdala_L	2.74
11	Cingulum_Mid_L to Parietal_Sup_L	4.12
12	Cingulum_Mid_R to Parietal_Sup_L	3.87
13	Cingulum_Mid_R to Parietal_Sup_R	3.52
14	Precentral_L to Parietal_Inf_L	4.31
15	Cingulum_Mid_L to Parietal_Inf_L	4.10
16	Cingulum_Mid_R to Parietal_Inf_L	4.72
17	Cingulum_Post_L to Parietal_Inf_L	4.11
18	Cingulum_Post_R to Parietal_Inf_L	4.48
19	Postcentral_L to Parietal_Inf_L	4.44
20	Parietal_Sup_L to Parietal_Inf_L	5.40
21	Parietal_Sup_R to Parietal_Inf_L	3.45
22	Supp_Motor_Area_R to SupraMarginal_L	2.34
23	Parietal_Inf_L to SupraMarginal_L	3.48
24	Frontal_Sup_Medial_R to Angular_L	2.6
25	Fusiform_L to Putamen_L	3.49
26	Parietal_Sup_L to Temporal_Sup_L	2.37
27	Precentral_L to Temporal_Pole_Sup_L	3.73
28	Precentral_R to Temporal_Pole_Sup_L	2.30
29	Cingulum_Mid_L to Temporal_Pole_Sup_L	2.41
30	Caudate_R to Temporal_Pole_Sup_R	3.33
31	Hippocampus_L to Temporal_Mid_L	3.56
32	Hippocampus_R to Temporal_Mid_L	3.75
33	ParaHippocampal_L to Temporal_Mid_L	3.16
34	Amygdala_L to Temporal_Mid_L	3.38
35	Calcarine_R to Temporal_Mid_L	3.81
36	Lingual_L to Temporal_Mid_L	3.65
37	Lingual_R to Temporal_Mid_L	3.21
38	Fusiform_L to Temporal_Mid_L	3.45
39	Precuneus_L to Temporal_Mid_L	4.18
40	Temporal_Sup_L to Temporal_Mid_L	4.35
41	Pallidum_R to Temporal_Mid_R	3.44
42	Frontal_Inf_Tri_L to Temporal_Pole_Mid_L	2.33
43	Rolandic_Oper_L to Temporal_Pole_Mid_L	2.08
44	Hippocampus_L to Temporal_Pole_Mid_L	3.46
45	Temporal_Mid_L to Temporal_Pole_Mid_L	3.59
46	Temporal_Sup_R to Temporal_Pole_Mid_R	3.25

<sup>a</sup> AAL abbreviations can be found in Table 4.

that survived the FDR correction are presented in Fig 1 and Tables 3 and 4. Connections of the left middle temporal gyrus were the most prevalent hypoconnected connections (10 connections), and among them, the most statistically significantly hypoconnected interlobular connection was the left precuneus–left middle temporal gyrus connection (test statistic: 4.18; average FA of 0.34 in the inattention group compared with 0.37 in the group with normal attention), which we explored further. Figure 2 shows an example of the participant’s tractography streamlines going through the left precuneus and left middle temporal gyrus. None of the connections were stronger in the inattention group compared with the group with normal attention.

**Table 4: AAL abbreviations and standardized names of the corresponding brain regions**

AAL Abbreviation	Standardized Name of the Brain Region
Amygdala	Amygdala
Angular	Angular gyrus
Calcarine	Calcarine fissure and surrounding cortex
Caudate	Caudate nucleus
Cingulum_Mid	Median cingulate and paracingulate gyri (>20% overlap with anterior cingulate)
Cingulum_Post	Posterior cingulate gyrus
Frontal_Inf_Oper	Inferior frontal gyrus, opercular part
Frontal_Inf_Orb	Inferior frontal gyrus, orbital part
Frontal_Inf_Tri	Inferior frontal gyrus, triangular part
Frontal_Mid	Middle frontal gyrus
Frontal_Mid_Orb	Middle frontal gyrus, orbital part
Frontal_Sup_Medial	Superior frontal gyrus, medial
Frontal_Sup_Orb	Superior frontal gyrus, orbital part
Fusiform	Fusiform gyrus
Hippocampus	Hippocampus
Lingual	Lingual gyrus
Olfactory	Olfactory cortex
Pallidum	Lenticular nucleus, pallidum
ParaHippocampal	Parahippocampal gyrus
Parietal_Inf	Inferior parietal, excluding supramarginal and angular gyri
Parietal_Sup	Superior parietal gyrus
Postcentral	Postcentral gyrus
Precentral	Precentral gyrus
Precuneus	Precuneus
Putamen	Lenticular nucleus, putamen
Rolandic_Oper	Rolandic operculum
Supp_Motor_Area	Supplementary motor area
SupraMarginal	Supramarginal gyrus
Temporal_Mid	Middle temporal gyrus
Temporal_Pole_Mid	Temporal pole, middle temporal gyrus
Temporal_Pole_Sup	Temporal pole, superior temporal gyrus
Temporal_Sup	Superior temporal gyrus

**Neonatal Predictors of Abnormal Structural Connectivity Associated with Attentional Problems in Adolescents**

Linear regression analysis was performed with left precuneus–left middle temporal gyrus connectivity as the dependent variable and neonatal clinical and imaging metrics and the age at the adolescent MR imaging visit as independent variables. Only low birth weight in grams and ventriculomegaly detected at the second neonatal scan independently and statistically significantly predicted hypoconnectivity between the left precuneus and left middle temporal gyrus ( $t = 4.874, P < .000$  and  $t = 4.617, P < .000$ , respectively). None of the other variables showed statistical significance (neonatal clinical characteristics listed in Table 1 or neonatal scan results listed in Table 2, or age at the adolescent MR imaging visit). Similar results were obtained using the average FA as the dependent variable: Low birth weight and ventriculomegaly at the second neonatal scan independently and statistically significantly predicted average FA ( $t = 2.929, P = .010$  and  $t = 2.385, P = .031$ , respectively). While low birth weight was associated with lower FA, ventriculomegaly was associated with higher FA.

Because only 1 subject had ventriculomegaly, we excluded this subject and performed linear regression with left precuneus–left middle temporal gyrus connectivity as the dependent variable and only birth weight as an independent variable. The results were  $t = 2.382, P = .027; R^2 = 0.213$ . Figure 3 shows a scatterplot of the

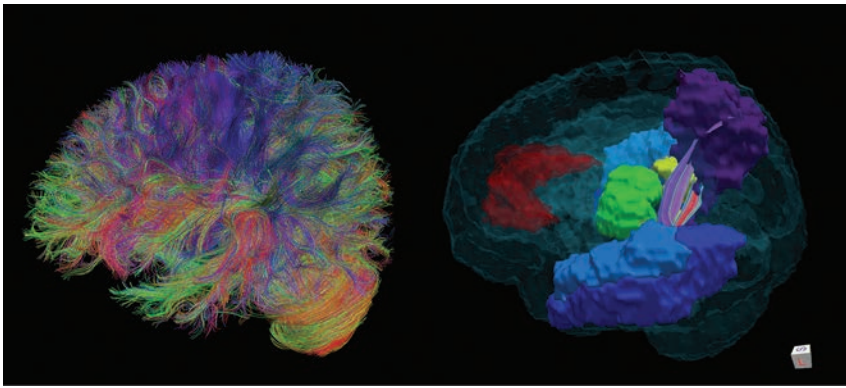


**FIG 2.** Left: example of study participant's whole-brain tractography. Right: tractography streamlines going through the left precuneus (purple) and left middle temporal gyrus (blue). The anterior cingulate cortex is shown in red; the thalamus, in green.

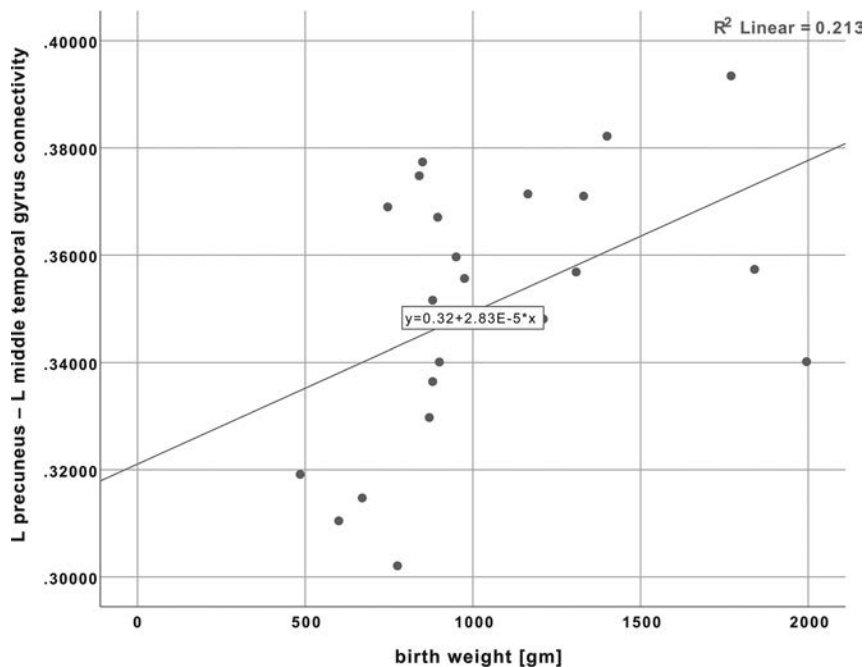


**FIG 3.** Linear regression: left precuneus–left middle temporal gyrus connectivity as a dependent variable and birth weight as independent variable.



**FIG 4.** A model that describes the relationship between neonatal characteristics of prematurely born children, structural brain connectivity at adolescence, and attention at adolescence. The model is supported by the findings of this study.

variables. The result remained significant when using birth weight z scores.

## DISCUSSION

The results of this study indicate that attentional problems in adolescents who were born prematurely may be associated with a weaker structural connectivity among the frontal, parietal, temporal, and occipital lobes, including frontal cortices and subcortical regions. The resulting hypoconnected edges linked to atten-

tional problems in our study are known to underlie general attentional processes. Specifically, the frontoparietal attentional network is known to facilitate voluntary spatial attention, whereas re-orienting of attention recruits other brain areas, such as the temporoparietal junction and lateral inferior frontal cortex.<sup>44</sup>

Our findings are generally supported by previous literature reporting microstructural abnormalities in children formally diagnosed with ADHD and in prematurely born children, as well as by the structural network analysis literature in children with ADHD,<sup>18,19</sup> though contradictory results have been reported.<sup>20</sup> Among other regions, we detected lower connectivity of the left middle temporal gyrus to other regions in the subjects with attentional deficits. This finding is aligned with results published by Lei et al,<sup>45</sup> who observed microstructural abnormalities in the left middle temporal gyrus in children with ADHD, inattentive type. Most interesting, they also observed microstructural disruptions within the right middle temporal gyrus in children with the combined ADHD types compared with controls. Our results indicate a weaker connectivity between the right pallidum and the right middle temporal gyrus in the group with attentional deficits, which is also consistent with those findings.

The conflicting findings within the ADHD literature are, however, of particular interest. Different etiologies might be the reason for some of these differences. Specifically, in a study by

Beare et al,<sup>20</sup> individuals with ADHD presented with a subnetwork of stronger connectivity encompassing bilateral frontostriatal connections as well as left occipital, temporal, and parietal regions, in which the white matter microstructure was associated with ADHD symptom severity. This result differs from those in 2 previous studies,<sup>18,19</sup> as well as from the study described here. The prematurity status was, however, not reported in these prior studies. The only previous study linking prematurity, ADHD, and white matter metrics is the one by Skranes et al,<sup>14</sup> which investigated the relationship between clinical findings and FA measurements in white matter of 34 adolescents born prematurely with very low birth weights compared with 47 age-matched controls born at term. In their study, high inattention scores on the ADHD Rating Scale (based on mothers' reports) correlated with low FA values in the right superior and left middle fasciculus.

Previous studies have reported that adolescents with very low birth weights are more likely to have attention and/or executive

function deficits compared with controls,<sup>46,47</sup> which is consistent with our findings. In our study, low birth weight and ventriculomegaly (but not white matter injury or intraventricular hemorrhage) detected on the neonatal MR imaging were associated with altered temporoparietal connectivity in adolescence. Because ventriculomegaly was only detected in 1 study participant, we do not draw any conclusions. The obtained results are summarized in the model in Fig 4. A potential explanation for the association of low birth weight (but not gestational age) with temporoparietal hypoconnectivity is the substantial risk of children with very low birth weights for perinatal hemorrhages and injury.<sup>48</sup> The subsequent hypoconnectivity can be caused by perinatal white matter damage that has long-term effects on myelin disturbances, disorganization, or a reduced number of axons in projectional, commissural, and association tracts.<sup>14</sup> Although neonatal white matter injury or intraventricular hemorrhage was not associated with hypoconnectivity in adolescence in our study, this may relate to the lower resolution of MR images 14 years ago when some of the neonatal scans were performed, as well as limited power to detect a difference between groups, given the small sample size. Lower birth weight was also associated with other markers of illness severity, which, in turn, were also linked to inattention, and it is likely that unmeasured variables are a source of residual confounding. Additionally, other factors (eg, parenting style, adverse events, and so forth) may have a strong influence on performance in attentional tasks.

Several methodologic limitations need to be considered when interpreting our findings. First, a DTI-based tractography method was used to reconstruct structural brain networks, which is the most widely used tractography method but is limited in terms of its capacity for resolving crossing fibers.<sup>49</sup> Second, our study did not include a typically developing control group or a group of term-born adolescents with attentional problems. Third, the assessment of attention in creating the binary variable of the attention/inattention group was nonuniform across subjects. Finally, the study sample was limited and included only 24 adolescents who came for the 10- to 14 year follow-up visit and had diffusion MR imaging data. Nevertheless, the main result of an aberrant structural connectivity associated with attentional problems was statistically significant after correction for multiple comparisons. This result contributes to our understanding of the mechanisms underlying the development of attentional deficits in children born prematurely and can help direct future studies.

It would be advantageous if future studies of aberrant neural networks in ADHD included information about the gestational age at birth (prematurity) of study participants. Another important step would be a comparison of 4 groups in 1 study: term-born adolescents without attention deficits, term-born adolescents with attention deficits, pre-term-born adolescents without attention deficits, and pre-term-born adolescents with attention deficits.

## CONCLUSIONS

In this study, we examined network-level neural correlates of attentional deficits in adolescents born prematurely as well as neonatal predictors of those neural correlates and attentional problems. Our major findings are the hypoconnected axonal tracts in the frontal, parietal, temporal, and occipital lobes in adolescents with attentional problems, with temporoparietal connection be-

ing the most prominent and low birth weight being a predictor of this hypoconnectivity. This knowledge could lead to a better understanding of the mechanisms that play a role in the development of attentional deficits in children/adolescents born prematurely and could possibly lead to new therapeutic agents and additional interventions.

## ACKNOWLEDGMENTS

We would like to thank all of the study participants and their parents who made this work possible. We also thank Drs Bridget Johnson and Elizabeth Rogers for their help with the psychological assessments of the study participants. Finally, we thank Laurel Haeusslein, Veronica de Santiago, Shrey Goel, and Kristyn Casalino for the study coordination.

Disclosures: Olga Tymofiyeva—*RELATED: Grant:* National Institutes of Health, *Comments:* National Institutes of Health grants P01NS082330, R01HD072074, and R21AT009173\*; *Support for Travel to Meetings for the Study or Other Purposes:* National Institutes of Health, *Comments:* National Institutes of Health grants P01NS082330, R01HD072074, and R21AT009173\*. Dawn Gano—*RELATED: Grant:* National Institutes of Health\*; *UNRELATED: Grants/Grants Pending:* PERF\*. Robert J. Trevino—*UNRELATED: Other:* Summer Research Training Program at the University of California, San Francisco; Maximizing Access to Research Careers—Undergraduate Student Training for Academic Research (MARC U-STAR), *Comments:* During my time at the University of California, San Francisco, I was in a living arrangement provided by the Summer Research Training Program at the University of California, San Francisco. I am also partly funded by the MARC U-STAR Program through National Institutes of Health/National Institute of General Medical Sciences MARC U-STAR GM07717. Hannah C. Glass—*UNRELATED: medicolegal consulting: various Grants/Grants Pending:* National Institutes of Health, Cerebral Palsy Alliance, Pediatric Epilepsy Research Foundation. Donna M. Ferriero—*RELATED: Grant:* National Institutes of Health\*; *UNRELATED: Grants/Grants Pending:* National Institutes of Health, Cerebral Palsy Alliance\*; *Royalties:* Elsevier for an edited book\*. A. James Barkovich—*RELATED: Grant:* National Institutes of Health, *Comments:* grant to look at differences in brain injuries and brain structure in children born before 32 weeks' gestational age\*. Duan Xu—*RELATED: Grant:* National Institutes of Health\*; *UNRELATED: Grants/Grants Pending:* National Institutes of Health\*. \*Money paid to the institution.

## REFERENCES

1. Blencowe H, Cousens S, Oestergaard MZ, et al. **National, regional, and worldwide estimates of preterm birth rates in the year 2010 with time trends since 1990 for selected countries: a systematic analysis and implications.** *Lancet* 2012;379:2162–72 CrossRef Medline
2. Aylward GP. **Neurodevelopmental outcomes of infants born prematurely.** *Dev Behav Pediatr* 2005;26:427–40 CrossRef
3. Lindström K, Lindblad F, Hjern A. **Preterm birth and attention-deficit/hyperactivity disorder in schoolchildren.** *Pediatrics* 2011; 127:858–65 CrossRef Medline
4. Alexander AL, Lee JE, Lazar M, et al. **Diffusion tensor imaging of the brain.** *Neurotherapeutics* 2007;4:316–29 CrossRef Medline
5. Chanraud S, Zahr N, Sullivan EV, et al. **MR diffusion tensor imaging: a window into white matter integrity of the working brain.** *Neuropsychol Rev* 2010;20:209–25 CrossRef Medline
6. Silk TJ, Vance A, Rinehart N, et al. **White-matter abnormalities in attention deficit hyperactivity disorder: a diffusion tensor imaging study.** *Hum Brain Mapp* 2009;30:2757–65 CrossRef Medline
7. Peterson DJ, Ryan M, Rimrodt SL, et al. **Increased regional fractional anisotropy in highly screened attention-deficit hyperactivity disorder (ADHD).** *J Child Neurol* 2011;26:1296–302 CrossRef Medline
8. Tamm L, Barnea-Goraly N, Reiss AL. **Diffusion tensor imaging reveals white matter abnormalities in attention-deficit/hyperactivity disorder.** *Psychiatry Res* 2012;202:150–54 CrossRef Medline
9. Ashtari M, Kumra S, Bhaskar SL, et al. **Attention-deficit/hyperactivity disorder: a preliminary diffusion tensor imaging study.** *Biol Psychiatry* 2005;57:448–55 CrossRef Medline
10. Makris N, Buka SL, Biederman J, et al. **Attention and executive systems**

- abnormalities in adults with childhood ADHD: a DT-MRI study of connections. *Cereb Cortex* 2008;18:1210–20 CrossRef Medline
11. Bouziane C, Caan MW, Tamminga HG, et al. **ADHD and maturation of brain white matter: A DTI study in medication naive children and adults.** *Neuroimage Clin* 2018;17:53–59 CrossRef Medline
  12. Nagy Z, Westerberg H, Skare S, et al. **Preterm children have disturbances of white matter at 11 years of age as shown by diffusion tensor imaging.** *Pediatr Res* 2003;54:672–79 CrossRef Medline
  13. Vangberg TR, Skranes J, Dale AM, et al. **Changes in white matter diffusion anisotropy in adolescents born prematurely.** *Neuroimage* 2006;32:1538–48 CrossRef Medline
  14. Skranes J, Vangberg TR, Kulseng S, et al. **Clinical findings and white matter abnormalities seen on diffusion tensor imaging in adolescents with very low birth weight.** *Brain* 2007;130(Pt 3):654–66 CrossRef Medline
  15. Allin MP, Kontis D, Walshe M, et al. **White matter and cognition in adults who were born preterm.** *PLoS One* 2011;6:e24525 CrossRef Medline
  16. Mullen KM, Vohr BR, Katz KH, et al. **Preterm birth results in alterations in neural connectivity at age 16 years.** *Neuroimage* 2011;54:2563–70 CrossRef Medline
  17. Meskaldji DE, Fischi-Gomez E, Griffa A, et al. **Comparing connectomes across subjects and populations at different scales.** *Neuroimage* 2013;80:416–25 CrossRef Medline
  18. Cao Q, Shu N, An L, et al. **Probabilistic diffusion tractography and graph theory analysis reveal abnormal white matter structural connectivity networks in drug-naive boys with attention deficit/hyperactivity disorder.** *J Neurosci* 2013;33:10676–87 CrossRef Medline
  19. Hong SB, Zalesky A, Fornito A, et al. **Connectomic disturbances in attention-deficit/hyperactivity disorder: a whole-brain tractography analysis.** *Biol Psychiatry* 2014;76:656–63 CrossRef Medline
  20. Beare R, Adamson C, Bellgrove MA, et al. **Altered structural connectivity in ADHD: a network-based analysis.** *Brain Imaging Behav* 2017;11:846–58 CrossRef Medline
  21. Bethlehem RA, Romero-Garcia R, Mak E, et al. **Structural covariance networks in children with autism or ADHD.** *Cereb Cortex* 2017;27:4267–76 CrossRef Medline
  22. Rouse DJ, Landon M, Leveno KJ, et al; National Institute of Child Health and Human Development, Maternal-Fetal Medicine Units Network. **The Maternal-Fetal Medicine Units cesarean registry: chorioamnionitis at term and its duration-relationship to outcomes.** *Am J Obstet Gynecol* 2004;191:211–16 CrossRef Medline
  23. Kliegman RM, Hack M, Jones P, et al. **Epidemiologic study of necrotizing enterocolitis among low-birth-weight infants: absence of identifiable risk factors.** *J Pediatr* 1982;100:4404 Medline
  24. Dumoulin CL, Rohling KW, Piel JE, et al. **Magnetic resonance imaging compatible neonate incubator.** *Concepts Magn Reson* 2002;15:117–28 CrossRef
  25. Miller SP, Cozzio CC, Goldstein RB, et al. **Comparing the diagnosis of white matter injury in premature newborns with serial MR imaging and transfontanel ultrasonography findings.** *AJNR Am J Neuroradiol* 2003;24:1661–69 Medline
  26. Miller SP, Ferriero DM, Leonard C, et al. **Early brain injury in premature newborns detected with magnetic resonance imaging is associated with adverse early neurodevelopmental outcome.** *J Pediatr* 2005;147:609–16 CrossRef Medline
  27. Papile LA, Burstein J, Burstein R, et al. **Incidence and evolution of subependymal and intraventricular hemorrhage: a study of infants with birth weights less than 1,500 gm.** *J Pediatr* 1978;92:529–34 CrossRef Medline
  28. Greenberg LM. *Test of Variables of Attention.* Los Alamitos: The Tova Company; 1991
  29. Achenbach TM, Rescorla LA. *Manual for the ASEBA School-Age Forms and Profiles: An Integrated System of Multi-Informant Assessment.* Burlington: ASEBA; 2001
  30. Wu YY, Huang YS, Chen YY, et al. **Psychometric study of the test of variables of attention: preliminary findings on Taiwanese children with attention-deficit/hyperactivity disorder.** *Psychiatry Clin Neurosci* 2007;61:211–18 CrossRef Medline
  31. Chang LY, Wang MY, Tsai PS. **Diagnostic accuracy of rating scales for attention-deficit/hyperactivity disorder: a meta-analysis.** *Pediatrics* 2016;137:e20152749 CrossRef Medline
  32. Morales-Hidalgo P, Hernández-Martínez C, Vera M, et al. **Properties of the Conners-3 and Conners Early Childhood Indexes in a Spanish school population.** *International Journal of Clinical and Health Psychology* 2017;17:85–96 CrossRef
  33. Forbes GB. **Clinical utility of the Test of Variables of Attention (TOVA) in the diagnosis of attention-deficit/hyperactivity disorder.** *J Clin Psychol* 1998;54:461–76 CrossRef Medline
  34. Smith SM, Jenkinson M, Woolrich MW, et al. **Advances in functional and structural MR image analysis and implementation as FSL.** *Neuroimage* 2004;23(Suppl 1):S208–19 CrossRef Medline
  35. Tymofiyeva O, Hess CP, Ziv E, et al. **Towards the “baby connectome”: mapping the structural connectivity of the newborn brain.** *PLoS One* 2012;7:e31029 CrossRef Medline
  36. Wang R, Benner T, Sorensen AG, et al. **Diffusion Toolkit: a software package for diffusion imaging data processing and tractography.** In: *Proceedings of Annual Meeting of the International Society for Magnetic Resonance in Medicine and the European Society for Magnetic Resonance in Medicine and Biology and Society for MR Radiographers & Technologists*, Berlin, Germany. May 19–25, 2007:3720
  37. Mori S, Crain BJ, Chacko VP, et al. **Three-dimensional tracking of axonal projections in the brain by magnetic resonance imaging.** *Ann Neurol* 1999;45:265–69 CrossRef Medline
  38. Tymofiyeva O, Connolly CG, Ho TC, et al. **DTI-based connectome analysis of adolescents with major depressive disorder reveals hypoconnectivity of the right caudate.** *J Affect Disord* 2017;207:18–25 CrossRef Medline
  39. Tzourio-Mazoyer N, Landeau B, Papathanassiou D, et al. **Automated anatomical labeling of activations in SPM using a macroscopic anatomical parcellation of the MNI MRI single-subject brain.** *Neuroimage* 2002;15:273–89 CrossRef Medline
  40. Jenkinson M, Smith S. **A global optimisation method for robust affine registration of brain images.** *Med Image Anal* 2001;5:143–56 CrossRef Medline
  41. Jenkinson M, Bannister P, Brady M, et al. **Improved optimization for the robust and accurate linear registration and motion correction of brain images.** *Neuroimage* 2002;17:825–41 CrossRef Medline
  42. Zalesky A, Fornito A, Bullmore ET. **Network-based statistic: identifying differences in brain networks.** *Neuroimage* 2010;53:1197–207 CrossRef Medline
  43. Nass RD. **Evaluation and assessment issues in the diagnosis of attention deficit hyperactivity disorder.** *Semin Pediatr Neurol* 2005;12:200–16 CrossRef Medline
  44. Gazzaniga MS, Ivry RB, Mangun GR. *Cognitive Neuroscience: The Biology of the Mind.* 3rd ed. Rockville: W.W. Norton & Company; 2008:553
  45. Lei D, Ma J, Du X, et al. **Microstructural abnormalities in the combined and inattentive subtypes of attention deficit hyperactivity disorder: a diffusion tensor imaging study.** *Sci Rep* 2014;4:6875 CrossRef Medline
  46. Indredavik MS, Vik T, Heyerdahl S, et al. **Psychiatric symptoms in low birth weight adolescents, assessed by screening questionnaires.** *Eur Child Adolesc Psychiatry* 2005;14:226–36 CrossRef Medline
  47. Kulseng S, Jennekens-Schinkel A, Naess P, et al. **Very-low-birth-weight and term small-for-gestational-age adolescents: attention revisited.** *Acta Paediatr* 2006;95:224–30 CrossRef Medline
  48. Volpe JJ. **Brain injury in the premature infant: neuropathology, clinical aspects, pathogenesis, and prevention.** *Clin Perinatol* 1997;24:567–87 CrossRef Medline
  49. Farquharson S, Tournier JD, Calamante F, et al. **White matter fiber tractography: why we need to move beyond DTI.** *J Neurosurg* 2013;118:1367–77 CrossRef Medline

# Spinal Coccidioidomycosis: MR Imaging Findings in 41 Patients

R.N. Crete,<sup>1</sup> W. Gallmann,<sup>2</sup> J.P. Karis,<sup>3</sup> and J. Ross<sup>4</sup>

## ABSTRACT

**BACKGROUND AND PURPOSE:** *Coccidioides immitis* is a dimorphic fungus endemic to the Southwest United States and Mexico, and at our institution, it is a relatively common pathogen presenting with a broad spectrum of associated spine diseases. We describe the various spinal manifestations resulting from coccidioidal infection and provide MR imaging examples from 41 pathologically proved cases.

**MATERIALS AND METHODS:** Retrospective electronic medical record and PACS searches were performed. Patients found to have both MR imaging findings positive for infection and confirmative biopsy and/or CSF studies were included. Abnormal MR imaging findings were identified, categorized, and quantified. Patient demographics and associated intracranial involvement if present were also recorded.

**RESULTS:** Forty-one patients were included. Positive findings were categorized as leptomeningeal enhancement (26 patients, 63%), arachnoiditis (22 patients, 54%), osteomyelitis-discitis (14 patients, 34%), cord edema (11 patients, 27%), and true syrinx (3 patients, 7%). Thirty patients had documented brain involvement (73%), most commonly in the form of basilar meningitis. Four patients were positive for HIV (10%). Fifteen patients had pulmonary manifestations at presentation (37%).

**CONCLUSIONS:** *C immitis* results in various spinal manifestations, most commonly leptomeningeal enhancement and arachnoiditis/adhesive disease followed by osteomyelitis, which may resemble tuberculous or pyogenic infection on MR imaging.

**ABBREVIATION:** T1+C = T1-weighted images with contrast

*Coccidioides immitis* is a dimorphic fungus well-known to be endemic to the Southwest United States and Mexico.<sup>1,2</sup> At our institution, we experience *C immitis* as a relatively common pathogen, presenting with variable pulmonary, intracranial, and spinal diseases regardless of immune status. The spectrum of spine disease reported in the literature is extensive, with involvement of the leptomeninges, epidural/paraspinal space, vertebral bodies both with and without disc involvement, and, rarely, the spinal cord. Although previous case reports and articles have discussed the imaging appearance of spinal coccidioidomycosis, to our knowledge, there has not been a comprehensive review of both intrathecal and vertebral/paraspinal involvement of this magnitude.<sup>3-9</sup>

We describe the spinal MR imaging findings from 41 patients with pathologically proved *Coccidioides* infection.

## MATERIALS AND METHODS

This retrospective study was approved by the St. Joseph Hospital and Medical Center institutional review board and was conducted in accordance with Health Insurance Portability and Accountability Act guidelines.

A broad retrospective search was performed using the electronic medical record for patients with a history of coccidioidomycosis during a 6-year period. Key words used for the search included “*Coccidioides*,” “coccidioidomycosis,” “cocci,” and “valley fever.” Patients were screened with spinal MR imaging and individually overread to evaluate abnormal findings. Patients with an abnormal spine MRI were then cross-referenced for evidence of true coccidioidal infection. True infection was defined as culture positive for *C immitis* obtained from a paraspinal mass, fluid collection, or vertebral body or positive CSF complement fixation titers. Only patients found to have both MR imaging findings positive for infection and laboratory evidence of true infection were included. Abnormal MR imaging findings were categorized as cord edema, syrinx, cord enhancement, leptomeningeal

Received April 29, 2018; accepted after revision August 9.

From the Department of Neuroradiology (R.N.C., W.G., J.P.K.), Barrow Neurological Institute, Phoenix, Arizona; and Department of Radiology (J.R.), Mayo Clinic College of Medicine, Phoenix, Arizona.

Paper previously presented at: Annual Meeting of the Western Neuroradiological Society, October 25–28, 2017; Koloa, Hawaii.

Please address correspondence to Ryan N. Crete, MD, Barrow Neurological Institute, Department of Neuroradiology, Dignity Health/St. Joseph's Hospital and Medical Center, 350 West Thomas Rd, Phoenix, AZ 85013; e-mail: Danielle.Andazola@dignityhealth.org

<http://dx.doi.org/10.3174/ajnr.A5818>

**Table 1: Patient demographics**

	No. (%)
Ethnicity	
White	17 (41)
African American	12 (29)
Latino	7 (17)
Native American	3 (7)
Asian	2 (5)
Sex	
Male	34 (83)
Female	7 (17)
Patient age (mean) (SD) (yr)	42.0 (14.7)

**Table 2: Abnormal findings on spinal MR imaging**

	No. of Patients (%)
Leptomeningeal enhancement	26 (63)
Arachnoid adhesive disease	22 (54)
Osteomyelitis/discitis	14 (34)
Cord edema	11 (27)
Syrinx	3 (7)

**Table 3: Distribution of intrathecal disease**

	Leptomeningeal Enhancement	Adhesive Arachnoiditis	Cord Edema/Syrinx
Cervical	23	14	9
Thoracic	20	11	9
Lumbar	19	18	NA

**Note:**—NA indicates not applicable.

enhancement, arachnoiditis, and osteomyelitis-discitis with or without epidural/paraspinal abscess/phlegmon. Cord edema and syrinx were differentiated from one another by the degree of hypointensity on T1, in which syrinx more closely followed the CSF signal. Patient demographics, immune status, and the presence of associated intracranial or pulmonary involvement were also recorded.

During the 6-year period, patients were scanned using either GE (GE Healthcare, Milwaukee, Wisconsin) or Phillips (Phillips Healthcare, Best, the Netherlands) magnets at 1.5 or 3T. All patients included received intravenous gadolinium. Patients did not require total spine imaging to be included in the study.

Patients with intrathecal disease were screened for brain MR imaging and intracranial involvement. In patients without brain MR imaging, the posterior fossa was reviewed on cervical spine MR imaging to assess basilar meningitis.

## RESULTS

Forty-one patients with confirmed *C immitis* were identified as having abnormalities on spinal MR imaging. Of the 41 patients, 34 were men (83%) and 7 were women (17%). Seventeen patients were white (41%); 12, African American (29%); 7, Latino (17%); 3, Native American (7%); and 2, Asian (5%) (Table 1). The average patient age was 42.0 ± 14.7 years.

Abnormal findings on intrathecal, vertebral/spinal, and intracranial MR imaging are addressed below and are summarized in Tables 2–5.

The most common finding was leptomeningeal enhancement (26 of 41 patients, 63%) (Fig 1), often associated with arachnoiditis/adhesive disease (22 of 41, 54%) (Fig 2). Cord edema was observed in 11 patients (27%) (Fig 3A), and true syrinx was ob-

**Table 4: Osteomyelitis-discitis distribution and characteristics**

	No. of Patients (%)
Segment	
Cervical	5 (36)
Thoracic	11 (79)
Lumbar	9 (64)
Characteristic	
Paraspinal involvement	11 (78)
Disc involvement	7 (50)
Skip levels	7 (50)
Destructive (osseous)	7 (50)
Epidural involvement	6 (43)
Well-circumscribed (osseous)	5 (36)
Well-circumscribed (paraspinal)	4 (29)
Disc sparing with involvement of adjacent levels	2 (14)
Gibbus deformity	1 (7)

**Table 5: Disease involvement and overlap**

Abnormality	No. of Patients (%)
Intrathecal disease	30 (73)
Discitis-osteomyelitis	14 (34)
Overlap	3 (7)

served in 3 patients (7%) (Fig 3B–D). Cord enhancement was not definitively observed.

The distribution of intrathecal findings is summarized in Table 3. Leptomeningeal enhancement was most often diffuse and affected the cervical cord, thoracic cord, and conus medullaris/cauda equina fairly evenly (23, 20, and 19 patients, respectively). Adhesive arachnoiditis was most common in the lumbar spine where nerve root clumping was the most common finding (18 patients). Cervical and thoracic cord adhesive disease was observed in 14 and 11 patients, respectively. Collectively, cord edema and syrinx were observed equally in the cervical and thoracic cord (9 patients each). In total, 30/41 (73%) patients had intrathecal involvement.

Fourteen of 41 patients presented with vertebral osteomyelitis and/or discitis (34%, Fig 4). Disease distribution and characteristics are summarized in Table 4. Paraspinal involvement (Figs 5 and 6) was most common, occurring in 11 patients. Disc involvement, osseous destruction (Fig 4A), and skip lesions involving noncontiguous vertebral bodies occurred in 7 patients each. Epidural involvement (Figs 5 and 6) was identified in 6 patients. Well-circumscribed osteomyelitis was observed in 5 patients; 2 instances involved the disc space. Four patients had a well-circumscribed pattern of paravertebral/epidural phlegmon as well (Fig 4B). Sparing of the disc space and involvement of adjacent vertebral levels in a pattern resembling tuberculosis was observed in 2 patients (Fig 4C). Gibbus deformity (focal kyphosis) was observed in 1 patient (Fig 6). The thoracic spine was most commonly involved (11 patients).

Intracranial disease was identified in each (30/30) patient with intrathecal disease. Twenty-seven of 30 patients had MR imaging of the brain performed, while 3 other patients had evidence of posterior fossa involvement by cervical MR imaging. Nineteen of 30 (63%) had either exclusively basilar or basilar-predominant leptomeningeal enhancement, while 4 patients (13%) had diffuse leptomeningeal enhancement. Less typical intracranial manifestations identified included the following: middle cranial fossa

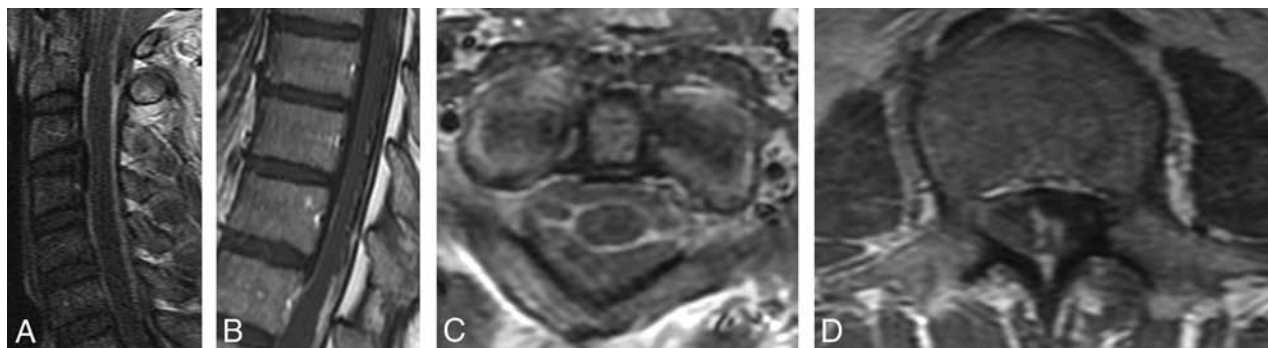


**FIG 1.** Leptomeningeal enhancement. Sagittal cervical (A) and thoracic (B) spine T1+C MR T1-weighted imaging with contrast show abnormal leptomeningeal enhancement, confluent in the cervical spine and patchy in the thoracic spine. Axial cervical (C) and lumbar (D) spine T1+C MR imaging show cord, cervical nerve root, and cauda equina nerve root leptomeningeal enhancement.



**FIG 2.** Arachnoiditis/adhesive disease. Sagittal T2 (A) and T1+C (B) MR imaging of the lumbar spine show cauda equina nerve root clumping and enhancement. Note the dependent, nonenhancing purulent debris in the thecal sac on T2WI. Axial T1+C of the cervical spine (C) shows tethering and deformity of the cord in addition to leptomeningeal enhancement. Axial T2 of the lumbar spine (D) shows adhesive cauda equina nerve root clumping.

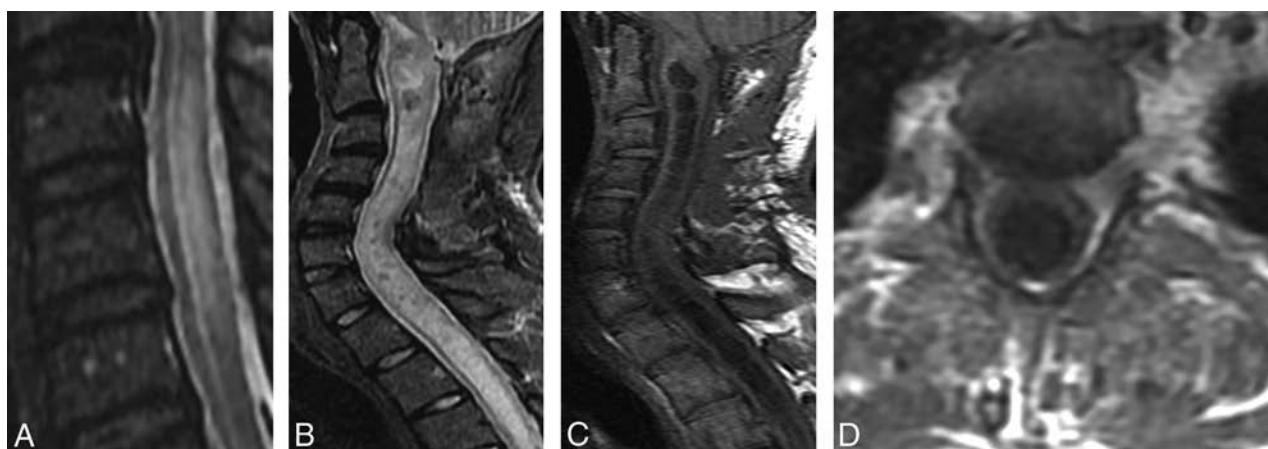


**FIG 3.** Cord edema and syrinx. Sagittal STIR images of the cervical spine show cord edema (A) and true syrinx (B). Sagittal T1 (C) shows true syrinx and exemplifies the utility of T1WI to differentiate true syrinx from edema states. Axial T1+C (D) shows no associated cord enhancement. Paraspinous enhancement in this image is related to postsurgical decompression.

pachymeningeal enhancement, diffuse pachymeningeal enhancement, prepontine abscess, suprasellar leptomeningeal enhancement, Sylvian fissure leptomeningeal enhancement, interpeduncular/infundibular enhancement, and right temporal lobe intra-axial and leptomeningeal enhancement.

Only three (7%) patients in our study group had both intra-

thecal and vertebral disease (Table 5). Each of these 3 patients had intracranial disease.

Four patients were positive for HIV (10%). Fifteen patients had documented pulmonary involvement (36%).

Patient clinical manifestations varied. Four patients (4/30) with intrathecal disease presented with acute myelopathy. Clinical

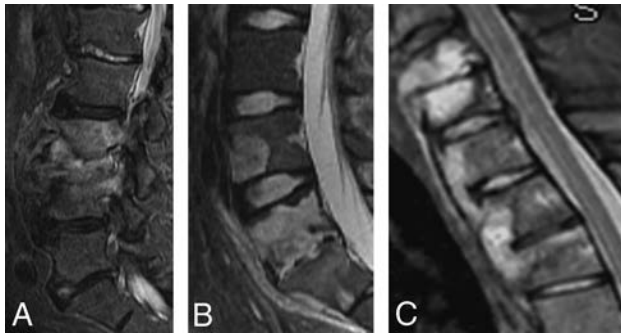


**FIG 4.** Osteomyelitis-discitis. Sagittal STIR of the lumbar spine (A) shows destructive endplate changes similar to pyogenic disease at L3/4 with paravertebral phlegmon. Sagittal STIR of the lumbar spine (B) shows destructive endplate changes of L5/S1, but note the well-circumscribed nature of L5 and the L4 skip lesion. Sagittal STIR of the cervicothoracic junction (C) shows a well-circumscribed signal abnormality of the vertebral bodies with paravertebral phlegmon that appears to skip disc spaces, similar to tuberculous disease.

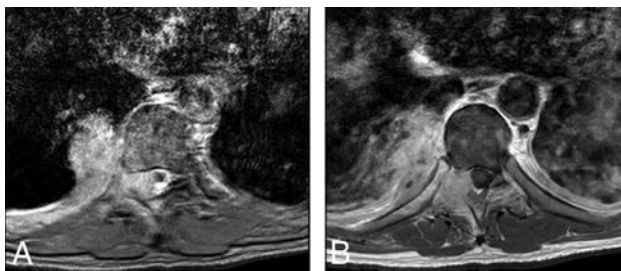


**FIG 5.** Axial T2 (A) and TIC+ (B) sequences demonstrate right T8–9 paraspinous and epidural phlegmon, producing mild effacement of the thecal sac and leftward cord displacement.

history was considered incomplete for 5 patients with intrathecal disease (25 had sufficient information obtainable via the electronic medical record). The 4 are summarized as follows: quadriplegia secondary to severe cervical cord deformity/adhesive disease (Fig 7), quadriparesis secondary to a large loculated cervical cord syrinx (Fig 3C), neuropathic pain and quadriparesis secondary to cord edema and intermittent syrinx, and bilateral foot numbness secondary to extensive cord edema and arachnoid adhesive disease. Many other patients with ataxia had hydrocephalus along with other symptoms that could not be attributed solely to spinal disease.

## DISCUSSION

Spinal infection with *C immitis* is relatively common at our institution due to its location within a highly endemic region. Morbidity is high, and treatment strategies are complex and often lengthy.<sup>10,11</sup> These observations illustrate the importance of understanding characteristic imaging findings to aid in diagnosis, especially in areas where a high index of suspicion must be maintained.

Osteomyelitis-discitis is a well-known association of infection with *C immitis*.<sup>3,4,7,8</sup> However, leptomeningeal disease is a more common manifestation. Extensive leptomeningeal enhancement involving the entire neural axis is common and requires complete spinal and brain imaging to evaluate the full extent. Only 5 patients with leptomeningeal enhancement did not have evidence of adhesive disease, but all patients with adhesive disease had lepto-

meningeal enhancement, implicating both as related processes in which the antigen incites inflammation and inflammation plus exudate formation across time leads to adhesions.

The pathophysiology of the relationship to syrinx and cord edema is controversial. The Gardner hydrodynamic theory proposes that pulsatile ventricular CSF pressure is transmitted from the fourth ventricle to the central canal, eventually resulting in a progressive dilation (water-hammer effect).<sup>4</sup> Only 1 case in our review demonstrated a dilated connection from the fourth ventricle to the central canal; however, it is most likely that syrinx and cord edema in the remainder of our patients are better explained by the theory that increased subarachnoid pressure due to CSF flow disturbances results in excess interstitial intramedullary fluid via the perivascular spaces.<sup>12</sup> Increased intramedullary pulse pressures also promote circulatory disturbances within the cord and further intramedullary fluid accumulation. All patients with cord signal abnormality and syrinx had evidence of leptomeningeal disease.

Many patients with extensive leptomeningeal enhancement and cord edema were not myelopathic. This is congruent with the findings of Lammering et al,<sup>4</sup> who noted that 7 of 8 patients with intrathecal disease were without back pain or radiculopathy. The 4 patients with myelopathy had syrinx formation or severe adhesion/cord deformity.

Meningitis is the most common and lethal form of disseminated coccidioidal disease, consisting of pyogranulomatous and fibroblastic processes affecting the meninges as well as the small vessels and perivascular zones.<sup>13</sup> Once the intracranial meninges are involved, CSF dissemination can and often does occur. In our case review, 30/30 patients with intrathecal disease had evidence of intracranial involvement, most commonly in the form of basilar leptomeningitis (19/30). Lammering et al<sup>4</sup> documented intracranial disease in 19/19 patients with intrathecal disease. It would appear that intrathecal involvement either does not or is highly unlikely to occur in the absence of intracranial involvement.

Osteomyelitis-discitis seen in the study population often resembled pyogenic spondylitis with aggressive endplate destruction and paravertebral phlegmon formation (7/14) (Fig 4A).<sup>6</sup> A common misconception is that coccidioidal spondylitis is identical to tuberculous disease. Osteomyelitis that clearly spares the disc space commonly evokes the differential diagnosis of tuberculosis/fungal infection. This is not altogether incorrect; however, it leads to secondary misperception by affiliation. It suggests that because *C immitis* is a fungus, it cannot appear similar to pyogenic disease. The origin of this error may stem from a survey report in the 1960s in which the authors observed only a single *Trichophyton* among 30 different fungal species that were capable of collagen digestion. The group included all major dimorphic mycotic pathogens, with the exception of *C immitis*.<sup>14,15</sup> It was not until 1985 that a group in Nevada using different culture media observed that *C immitis* could, in fact, digest collagen.<sup>16</sup> The authors postulated that a fungal-specific collagenase or a more broadly functioning protease may be responsible. This finding appears to be unique to *C immitis* among fungal species and explains the appearance often similar to pyogenic osteomyelitis-discitis.

Spinal infection with *Coccidioides* uncommonly resembled tuberculous spondylitis in our population, with sparing of the disc

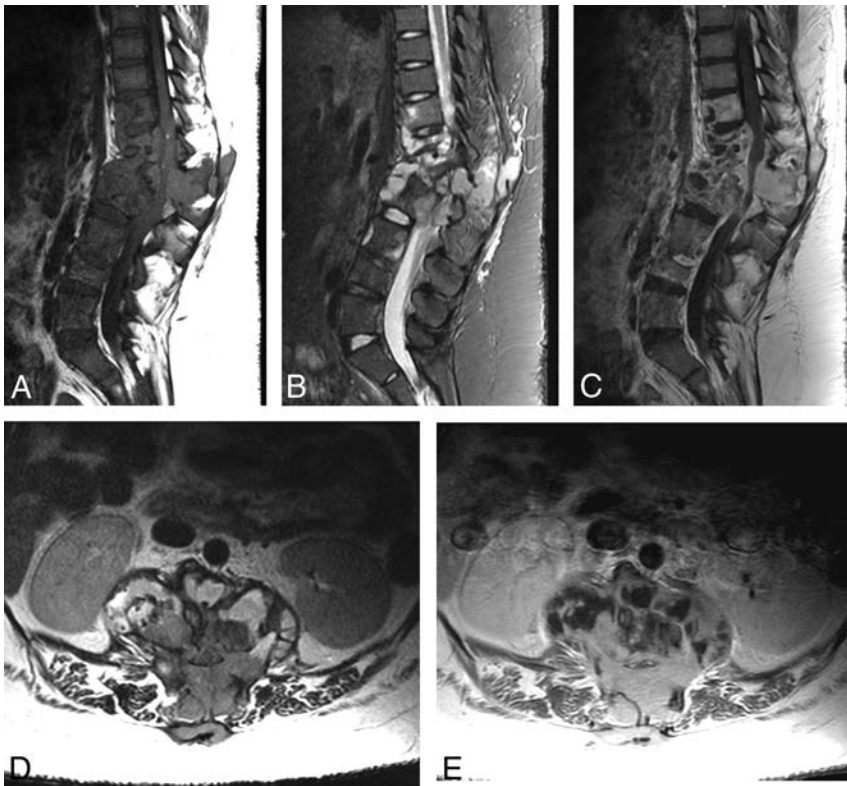


**FIG 6.** Sagittal T1 (A), STIR (B), and TIC+ (C) images depict destructive thoracolumbar spondylodiscitis with obliteration of the central canal, multilevel height loss, and associated kyphosis (Gibbus deformity).



**FIG 7.** Sagittal T2-weighted image reveals severe multifocal cord tethering and deformity with associated intramedullary T2 signal at the C3 level.

spaces and involvement of adjacent vertebral levels (2/14) (Fig 4C).<sup>17</sup> Most interesting, a common finding was that of a well-circumscribed osteomyelitis that does indeed involve the disc space (5/14) (Fig 4B), contrasting with typical aggressive pyogenic bone destruction. The authors of this study suggest the terminology of

“clean” osteomyelitis-discitis when observing this pattern and considering coccidioid disease, especially in endemic areas. Skip lesions are common, supporting the need for entire neuraxis imaging. Gibbus deformity, historically associated with tuberculous spondylitis, was observed in 1 patient.

Overlapping intrathecal/intracranial disease and spondylitis were observed in only 3 patients (7%). The lack of overlap suggests alternate routes of infection (eg, CSF seeding versus hematogenous spread).

Intramedullary spinal cord enhancement was not a finding associated with coccidioid infection in our study population. Such involvement has been reported rarely in the form of intramedullary abscess and enhancing intramedullary lesions.<sup>18,19</sup>

Men are much more commonly affected, potentially secondary to environmental/work exposure. The military has studied this extensively due to marine base locations in the San Joaquin Valley and frequent engagement in outdoor exercises.<sup>20,21</sup> According to the 2016 US Census Bureau, 5% of the greater Phoenix, Arizona, population is composed of African Americans, and our study population was composed of 29% African Americans.<sup>22</sup>

This suggests a disproportionate amount of African Americans in the study group, implicating a predisposition, possibly due to genetics or secondary to occupational/environmental exposure. This finding is in concordance with other observations.<sup>2</sup> Associated pulmonary disease is common and agrees with other investigations.<sup>4</sup> Immunocompromised state is not required. In fact, only a minority of patients in our study were immunocompromised, suggesting complex host-pathogen interactions.

A recent neurosurgical review of spinal coccidioidomycosis included 140 patients and yielded similar patient characteristics. Males were disproportionately affected (95%) as were African Americans (52%). One-third of patients had concurrent pulmonary disease.<sup>23</sup>

## CONCLUSIONS

The pathology associated with *C immitis* infection is most commonly manifested as leptomenigeal enhancement and arachnoiditis, followed by osteomyelitis. Osteomyelitis and leptomenigeal disease are uncommonly seen simultaneously, suggesting different pathophysiology leading to infection. Cord edema and true syrinx states are secondary findings commonly seen in association with leptomenigeal disease. Coccidioid spondylitis is protean and can mimic pyogenic spondylodiscitis, though it can also appear as well-circumscribed spondylitis with or without discitis. Skip lesions are common, necessitating imaging of the entire neuraxis. Myelopathy was an uncommon clinical presentation in

our patient population, only documented in patients with syrinx or severe arachnoid adhesive disease.

## REFERENCES

1. Pappagianis D. **Epidemiology of coccidioidomycosis.** In: Stevens DA, ed. *Coccidioidomycosis: A Text (Current Topics in Infectious Disease)*. New York: Plenum Medical Book Company; 1980
2. Huntington RW, Waldmann WJ, Sargent JA, et al. **Pathologic and clinical observations on 142 cases of fatal coccidioidomycosis.** In: Ajello L, ed. *Arizona State Department of Health. Coccidioidomycosis: Papers*. Tucson: University of Arizona Press; 1967:221–25
3. Olson EM, Duberg AC, Herron LD, et al. **Coccidioidal spondylitis: MR findings in 15 patients.** *AJR Am J Roentgenol* 1998;171:785–89 CrossRef Medline
4. Lammering JC, Iv M, Gupta N, et al. **Imaging spectrum of CNS coccidioidomycosis: prevalence and significance of concurrent brain and spinal disease.** *AJR Am J Roentgenol* 2013;200:1334–46 CrossRef Medline
5. Zeppa MA, Laorr A, Greenspan A, et al. **Skeletal coccidioidomycosis: imaging findings in 19 patients.** *Skeletal Radiol* 1996;25:337–43 CrossRef Medline
6. Thrush A, Enzmann D. **MR imaging of infectious spondylitis.** *AJNR Am J Neuroradiol* 1990;11:1171–80 Medline
7. McGahan JP, Graves DS, Palmer PE. **Coccidioidal spondylitis: usual and unusual radiographic manifestations.** *Radiology* 1980;136:5–9 CrossRef Medline
8. Halpern AA, Rinsky LA, Fountain S, et al. **Coccidioidomycosis of the spine: unusual roentgenographic presentation.** *Clin Orthop Relat Res* 1979;78–79 Medline
9. Wesselius LJ, Brooks RJ, Gall EP. **Vertebral coccidioidomycosis presenting as Pott's disease.** *JAMA* 1977;238:1397–98 Medline
10. Kakarla UK, Kalani MY, Sharma GK, et al. **Surgical management of coccidioidomycosis of the spine: clinical article.** *J Neurosurg Spine* 2011;15:441–46 CrossRef Medline
11. Lewicky YM, Roberto RF, Curtin SL. **The unique complications of coccidioidomycosis of the spine: a detailed time line of disease progression and suppression.** *Spine (Phila Pa 1976)* 2004;29:E435–41 CrossRef Medline
12. Klekamp J. **The pathophysiology of syringomyelia: historical overview and current concept.** *Acta Neurochir (Wien)* 2002;144:649–64 CrossRef Medline
13. Mischel PS, Vinters HV. **Coccidioidomycosis of the central nervous system: neuropathological and vasculopathic manifestations and clinical correlates.** *Clin Infect Dis* 1995;20:400–05 CrossRef Medline
14. Rippon JW, Lorincz AL. **Collagenase activity of Streptomyces (Nocardia) madurae.** *J Invest Dermatol* 1964;43:483–86 CrossRef Medline
15. Rippon JW, Varadi DP. **The elastases of pathogenic fungi and actinomycetes.** *J Invest Dermatol* 1968;50:54–58 CrossRef Medline
16. Lupan DM, Nziramasanga P. **Collagenolytic activity of Coccidioides immitis.** *Infect Immun* 1986;51:360–61 Medline
17. Smith AS, Weinstein MA, Mizushima A, et al. **MR imaging characteristics of tuberculous spondylitis vs vertebral osteomyelitis.** *AJNR Am J Neuroradiol* 1989;10:619–25 Medline
18. Bajema KL, Dalesandro M, Fredricks DN, et al. **Disseminated coccidioidomycosis presenting with intramedullary spinal cord abscesses: management challenges.** *Med Mycol Case Rep* 2016;15:1–4 CrossRef Medline
19. Tan LA, Kasliwal MK, Nag S et al. **Rapidly progressive quadriplegia heralding disseminated coccidioidomycosis in an immunocompetent patient.** *J Clin Neurosci* 2014;21:1049–51 CrossRef Medline
20. Standaert SM, Schaffner W, Galgiani JN, et al. **Coccidioidomycosis among visitors to a Coccidioides immitis-endemic area: an outbreak in a military reserve unit.** *J Infect Dis* 1995;171:1672–75 CrossRef Medline
21. Brown J, Benedict K, Park BJ, et al. **Coccidioidomycosis: epidemiology.** *Clin Epidemiol* 2013;5:185–97 CrossRef Medline
22. 2017 U.S. Census Bureau QuickFacts: Arizona. <https://www.census.gov/quickfacts/AZ>. Accessed September 11, 2018
23. Martinez-Del-Campo E, Kalb S, Rangel-Castilla L, et al. **Spinal coccidioidomycosis: a current review of diagnosis and management.** *World Neurosurg* 2017;108:69–75 CrossRef Medline

# MR Neurography of the Lumbosacral Plexus for Lower Extremity Radiculopathy: Frequency of Findings, Characteristics of Abnormal Intra-neural Signal, and Correlation with Electromyography

J.L. Chazen, J. Cornman-Homonoff, Y. Zhao, M. Sein, and N. Feuer

## ABSTRACT

**BACKGROUND AND PURPOSE:** MR neurography enables high resolution imaging of peripheral nerves. Our aim was to evaluate the utility of MR neurography in lumbosacral radiculopathy and correlate abnormal intra-neural signal with history, physical examination, and abnormal electrodiagnostic study findings.

**MATERIALS AND METHODS:** Retrospective review of lumbosacral MR neurography examinations performed from December 2014 through January 2017 on a 3T scanner was undertaken. MR neurography examinations were independently reviewed in a blinded fashion by 2 radiologists, and the intra-neural signal was graded on a 0–2 scale relative to adjacent vasculature. Abnormal nerve signal was correlated with subjective and objective findings from clinical notes in the electronic medical record and compared with results of electrodiagnostic studies (nerve conduction study/electromyography).

**RESULTS:** Three hundred three lumbosacral MR neurography examinations were performed during the study period, 64 of which met the inclusion criteria, including symptoms of radiculopathy on electromyography performed within 3 months of MR neurography. Twenty-nine (45%) MR neurography examinations had abnormal intra-neural signal. There was no statistically significant correlation between subjective clinical findings and intra-neural signal abnormality on MR neurography. There was a statistically significant correlation between abnormal intra-neural T2 signal and findings of active radiculopathy on electromyography ( $P < .001$ ).

**CONCLUSIONS:** Lumbosacral MR neurography appears to demonstrate abnormal intra-neural signal in a substantial portion of patients with clinical symptoms of lower extremity radiculopathy and correlates with findings of active radiculopathy on electromyography. This finding further bolsters the growing body of evidence on the utility of MR neurography and suggests that abnormal intra-neural signal may provide a useful adjunct to electrodiagnostic testing. Further research is required to evaluate the prognostic value of MR neurography, which may help guide therapeutic decision-making.

**ABBREVIATIONS:** EMG = electromyography; MRN = MR neurography; MUAP = motor unit action potential; NCS = nerve conduction study; SPAIR = spectral adiabatic inversion recovery

Lumbosacral radiculopathy has a prevalence of approximately 3%–5% in the general population.<sup>1</sup> It affects men and women equally, though the onset in men is, on average, a decade earlier than in women.<sup>1</sup> Clinical evaluation relies predominantly on history and physical examination. Electrodiagnostic testing including needle electromyography (EMG) has been described as an “extension” of the clinical examination but remains an imperfect

test with a sensitivity ranging from 49% to 86% for lumbosacral radiculopathy.<sup>2,3</sup> Despite its limitations, EMG can be a useful adjunct examination, given the high rate of false-positive findings on spinal MR imaging in asymptomatic individuals.<sup>4,5</sup>

MR neurography (MRN), first described in 1992, is a novel technique increasingly used in clinical practice to evaluate extraspinal neuropathy.<sup>6</sup> The MRN technique relies on high-field-strength magnets, anisotropic diffusion along the nerve path, and fat-suppressed T2-based imaging with long TEs to optimize intra-neural signal. Endoneural fluid and T2 signal are increased with nerve irritation and compression.<sup>7</sup> A variety of neuropathies can be evaluated with MRN, including neoplastic, traumatic, and inflammatory/autoimmune disease.<sup>8</sup> MRN of extraspinal nerve entrapment has generated particular interest. In an investigation by Lewis et al,<sup>9</sup> abnormal sciatic nerve signal and findings of entrapment were seen in 12 of 14 patients on MRN, with sciatica symptoms and unrevealing lumbar spine MR

Received April 17, 2018; accepted after revision July 27.

From the Departments of Radiology (J.L.C.), Resident Physician (J.C.-H.), Rehabilitation Medicine (M.S.), and Neurology (N.F.), Center for Comprehensive Spine Care, Weill Cornell Medicine, New York-Presbyterian Hospital, New York, New York; and Department of Healthcare Policy & Research (Y.Z.), Weill Cornell Medicine, New York, New York.

Please address correspondence to J. Levi Chazen, MD, Weill Cornell Medicine, New York-Presbyterian Hospital, Department of Radiology, 525 East 68th St, Starr 631, New York, NY 10065; e-mail: jlc2008@med.cornell.edu

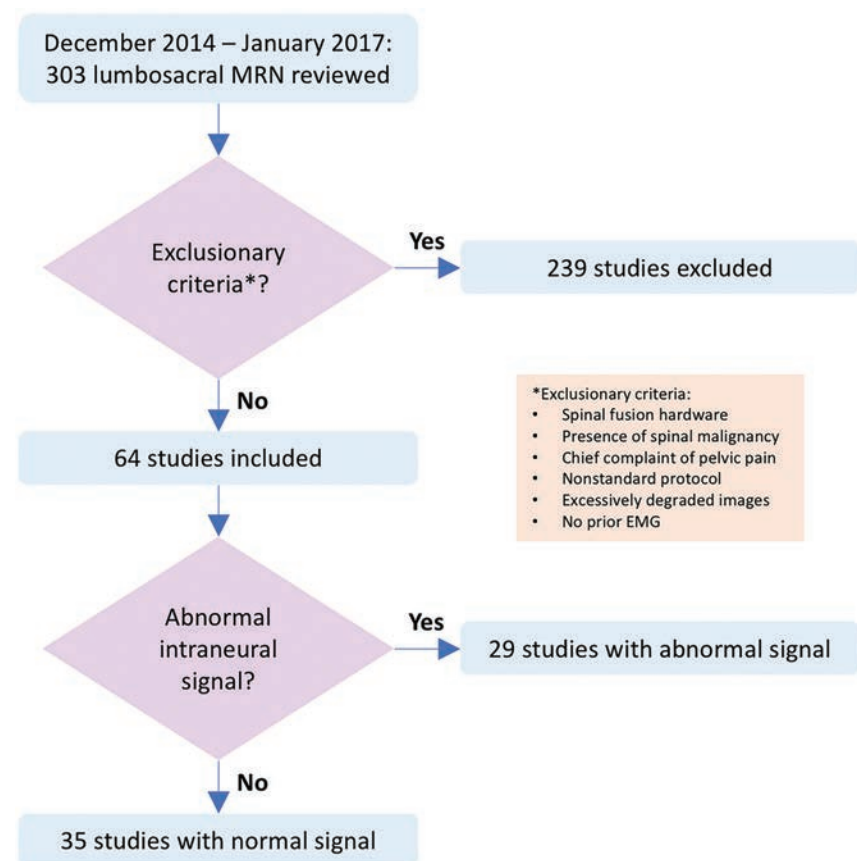
<http://dx.doi.org/10.3174/ajnr.A5797>

**Table 1: MR imaging parameters<sup>a</sup>**

Sequence	Matrix	TR (ms)	TE (ms)	NEX	FOV (cm)	In-Plane Resolution (mm)	Slice Thickness (mm)	Acquisition Time (min: sec)
Axial T1 TSE	320 × 240	663	12	2	31	1.0 × 1.3	3.5	6:18
Axial T2 FS SPAIR	320 × 192	6220	83	2	31	1.0 × 1.6	3.5	7:52
Coronal T1	384 × 216	3160	9.9	1	36	1.0 × 1.7	3	3:49
Coronal PD SPAIR	320 × 224	4380	35	2	36	1.1 × 1.6	3	4:10
3D Coronal SPACE STIR	256 × 256	1500	119	1.4	38	1.5 × 1.5	1.5	8:23
Sagittal T2 Dixon (lumbar spine)	448 × 300	4160	83	2	28	0.6 × 0.9	3	3:59

**Note:**—PD indicates proton density; SPACE, sampling perfection with application-optimized contrasts by using different flip angle evolution (Siemens); FS, fat suppressed.

<sup>a</sup> All lumbosacral plexus MR imaging was performed on a 3T Magnetom Skyra (Siemens) scanner without contrast.

**FIG 1.** Flowchart illustrating study selection.

imaging. Furthermore, additional important anatomic findings such as a split piriformis muscle belly and aberrant sciatic nerve course can be evaluated at the time of MRN, influencing interventional and surgical decision-making.<sup>10</sup>

The role of MRN in the work-up of radiculopathy has been recently explored with promising results.<sup>11</sup> There are scattered reports correlating MRN and EMG findings in individuals; however, it remains difficult to draw reliable conclusions about the agreement between MRN and EMG based on limited research studies in the literature with small sample sizes. Retrospective investigations suggest a significant rate of extraspinal pathology in patients with lower extremity radicular symptoms that can be detected with MRN sequences.<sup>12</sup> The frequency of abnormal intraneural signal in patients presenting with lower extremity radiculopathy is not known.

This study evaluated the frequency of abnormal intraneural T2 signal abnormality in patients presenting with lumbosacral radicu-

lopathy and correlates MRN abnormalities with those described on EMG. MRN can precisely identify abnormal signal in extraspinal nerves as they exit the neuroforamen and traverse anatomic corridors to join the lumbosacral plexus. This extraspinal signal abnormality may allow more accurate and specific evaluation of abnormal nerves responsible for clinical symptoms than traditional methods. Furthermore, extraspinal extraneural causes for symptomatology (eg, hip osteoarthritis masquerading as high lumbar “radicular” symptoms) can be identified at the time of MRN.

## MATERIALS AND METHODS

### Study Participants

Weill Cornell Medicine institutional review board approval was obtained for this retrospective study with a waiver of informed consent. Patients included in the analysis had clinical signs of active lower extremity radiculopathy and both a MR neurogram and EMG performed within a 3-month timeframe at our institution. Patients were excluded if they had spinal fusion hardware, which could limit the MR neurogram evaluation from susceptibility artifact.

### MR Imaging Protocol and Evaluation

MR imaging was performed at 3T on a Magnetom Skyra platform (Siemens, Erlangen, Germany). The MRN imaging protocol is described in Table 1 and consisted of limited sagittal lumbar spine imaging along with axial and coronal T1 and fat-suppressed T2 sequences through the lumbosacral plexus. Imaging studies were evaluated by a radiologist with a Certificate of Added Qualification in neuroradiology (J.L.C.), and scores were recorded for statistical analysis. Following a 10-case training session, MRN examinations were independently evaluated by a radiology senior resident (J.C.-H.) to determine interrater reliability. The radiologists were blinded to clinical history, including the laterality of pain. Abnormal nerves were graded on a categorical scale from 0–2 with 0 representing normal signal; 1, increased intraneural signal but less than adjacent vasculature; and 2, marked increased intraneural signal similar to that in adjacent vascular structures. If multiple abnormal nerves were iden-

**Table 2: Demographics/clinical characteristics and MRN/EMG findings**

Variable	Value	Range/Percentage
Subjects	64	
Age (yr)	57	20–84
Sex (male)	33	51.6%
Symptom duration (mo)	26	1–312
Diabetes	12	18.8%
Prior surgery	9	14.1%
Weakness	29	45.3%
Numbness	31	48.4%
Leg pain	48	75.0%
Back pain	28	43.8%
Tingling	23	35.9%
MRN intraneural T2 signal abnormality (grade I or II)	28	43.8%
MRN evidence of muscular denervation	8	12.5%
EMG findings of active radiculopathy	20	31.3%

tified, the most pronounced signal abnormality was recorded and the proximal nerve was considered for analysis (for example, if the ipsilateral L4 and femoral nerves were abnormal, it was graded as an L4 radiculopathy).

Imaging findings of muscular denervation were rated as positive if T2 hyperintense edema was present in the substance of the paraspinous, psoas, iliacus, gluteal, piriformis, adductor, or proximal thigh musculature.

#### **Nerve Conduction Studies/EMG Protocol and Evaluation**

Nerve conduction studies (NCSs) and needle EMG were performed by board-certified neuromuscular neurologists at our institution. Reports were individually reviewed by an experienced neuromuscular neurologist (N.F.). Nerve conduction studies included standard tested sensory (superficial peroneal and sural) and motor (peroneal and tibial) nerves in the legs. These were analyzed by measuring the waveform latency, amplitude, duration, and conduction velocity. Late responses were also evaluated, including the F-Responses and H-reflex, to aid in the evaluation of the proximal nerve segments.

Needle electromyography was performed using a concentric needle in leg muscles representing L2–S1 myotomes. Muscles were evaluated for the presence of active denervation, motor unit action potential (MUAP) morphology, and MUAP recruitment and activation patterns. When present, active denervation was determined by fibrillation potentials and positive sharp waves. Chronic re-innervation changes in a muscle were defined by the decreased activation and recruitment of neurogenic (long duration and high amplitude) MUAPs.

#### **Electronic Medical Record Review**

The electronic medical records of the included subjects were reviewed for subjective findings of lower extremity weakness, numbness, leg pain, back pain, tingling, burning, pain quality, and severity (Visual Analog Scale 1–10). Patient history was recorded, including the inciting event, history of surgery, diabetes mellitus, and symptom duration. Physical examination findings were collected, including the presence of atrophy, weakness, decreased sensation, decreased reflexes, and positive findings on straight leg raises.

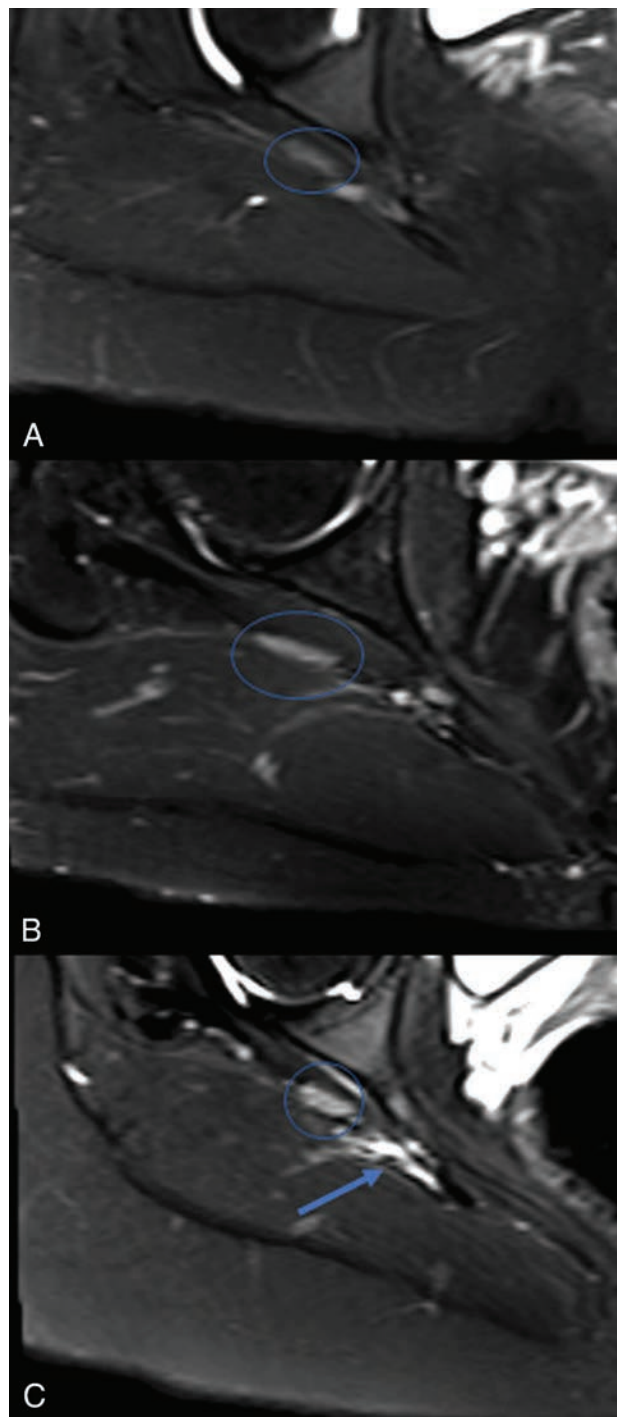


**FIG 2.** Axial fat-suppressed T2-weighted spectral adiabatic inversion recovery (SPAIR) images just distal to the greater sciatic foramen. A, Grade 0 nerve signal in a normal right sciatic nerve (circle). B, Grade I nerve signal abnormality shows a mildly hyperintense right sciatic nerve but less intense than the adjacent vasculature. C, Grade II nerve signal abnormality, similar to that of adjacent veins.

#### **Statistical Analysis**

Demographic variables and MR imaging parameters were summarized by mean/SD (continuous variables) and frequency/percentage (categorical variables). The comparison between ordinal variables (ie, signal, in 2 groups) was achieved with a Wilcoxon rank sum test. The association between categorical variables was

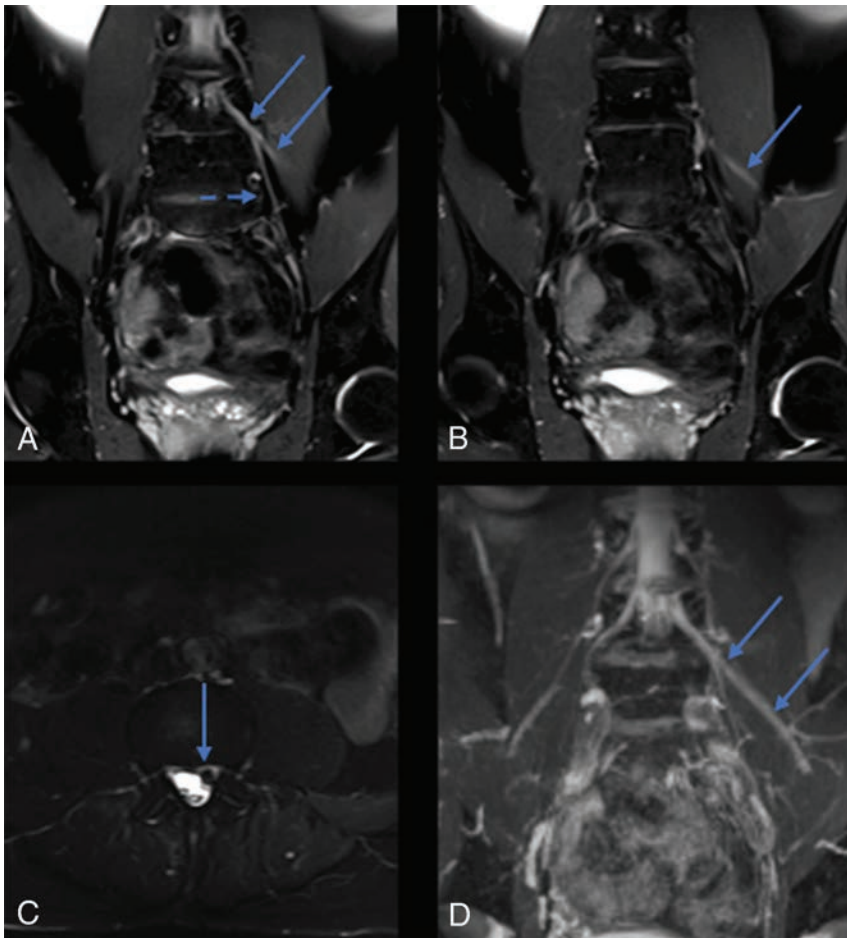


**FIG 3.** Coronal fat-suppressed T2 SPAIR (A and B), axial fat-suppressed T2 SPAIR (C), and maximum-intensity reconstruction of 3D coronal fat-suppressed T2 STIR (D) reveal marked asymmetric signal involving the left L4 nerve root extending to the left femoral nerve (arrows, A, B, and D). Signal abnormality also extends along the left obturator nerve (dashed arrow, A), also supplied by the L4 nerve root. An axial slice through the L3–L4 level (C) shows a disc extrusion (arrow, C) compressing the left L4 nerve root, accounting for the nerve inflammation.

**Table 3: Statistical association**

Correlations	$\phi$ Coefficient/ Cramér V	P Value
Denervation/subjective weakness	0.13	.30
Denervation/objective weakness	0.21	.10
Denervation/objective atrophy	0.33	.02
MRN intraneural signal/EMG active radiculopathy	0.79	<.001
MRN laterality/EMG laterality	1.00	<.001

measured by the  $\phi$  coefficient under a Pearson  $\chi^2$  test or a Fisher exact test. A  $\kappa$  statistic was calculated for interrater reliability between the 2 interpreters of MRN examinations. All the statistical analyses were performed by R statistical and computing software, Version 3.4.3 (<http://www.r-project.org/>). For the statistical tests, relevant *P* values are reported with a significant level of .05.

## RESULTS

Three hundred three MRN studies were performed during the study period from December 2014 through January 2017. Of these, 64 patients were included in the final analysis when both MR neurograms and EMG were acquired within a 3-month timeframe and exclusion criteria were not met (Fig 1). The mean sub-

ject age was 57 years (range, 20–84 years), 52% were male, and 75% reported leg pain. Demographics and clinical characteristics are described in Table 2. Half of the patients had decreased lower extremity sensation on physical examination, and 36% showed some signs of objective weakness. On MRN, 28 of 64 patients (44%) of the cohort had at least 1 nerve with abnormal intraneural signal on the fat-suppressed T2-weighted images (Fig 2). Of the 28 patients with abnormal intraneural T2 signal, 18 (64%) had a grade 2 signal abnormality, similar to that in adjacent vasculature (Fig 3). Eight patients (13%) had MRN findings of active muscular denervation. On NCS and EMG evaluations, 20 of 64 patients (31%) had findings of an active radiculopathy with denervation changes (Table 2). There was substantial agreement between readers with a  $\kappa$  statistic of 0.71 (confidence boundary, 0.41, 1) on blinded MRN interpretation. Ten subjects with suspicious findings on MRN had normal electrodiagnostic test findings without evidence of active radiculopathy.

Abnormal intraneural signal was not significantly associated with subjective clinical abnormalities. The association between patient-reported symptom duration, weakness, numbness, leg pain, back pain, or tingling and abnormal intraneural signal on MRN was not significant. Similarly, no significant

association was identified between physician-reported findings of weakness, decreased sensation, decreased deep tendon reflexes, the presence of positive straight leg raises, and abnormal intraneural signal. However, there was a statistically significant correlation between objective findings of muscle atrophy and denervation changes on MRN (*P* = .02).

There was a statistically significant association between abnormal intraneural T2 signal and findings of active radiculopathy on EMG with a mean intraneural signal score of 0.3 in patients without findings of active radiculopathy versus 1.7 in patients with EMG findings of active radiculopathy (*P* < .001). Furthermore, when abnormal intraneural signal was treated as a binary variable (normal or abnormal), there was a statistically significant association between signal abnormality on MRN and active radiculopathy on EMG (*P* < .001) (Table 3).

## DISCUSSION

This study revealed a statistically significant correlation between abnormal intraneural signal on MRN and findings of active denervation on NCS/EMG performed within 3 months. To our knowledge, this correlation has not been demonstrated previ-

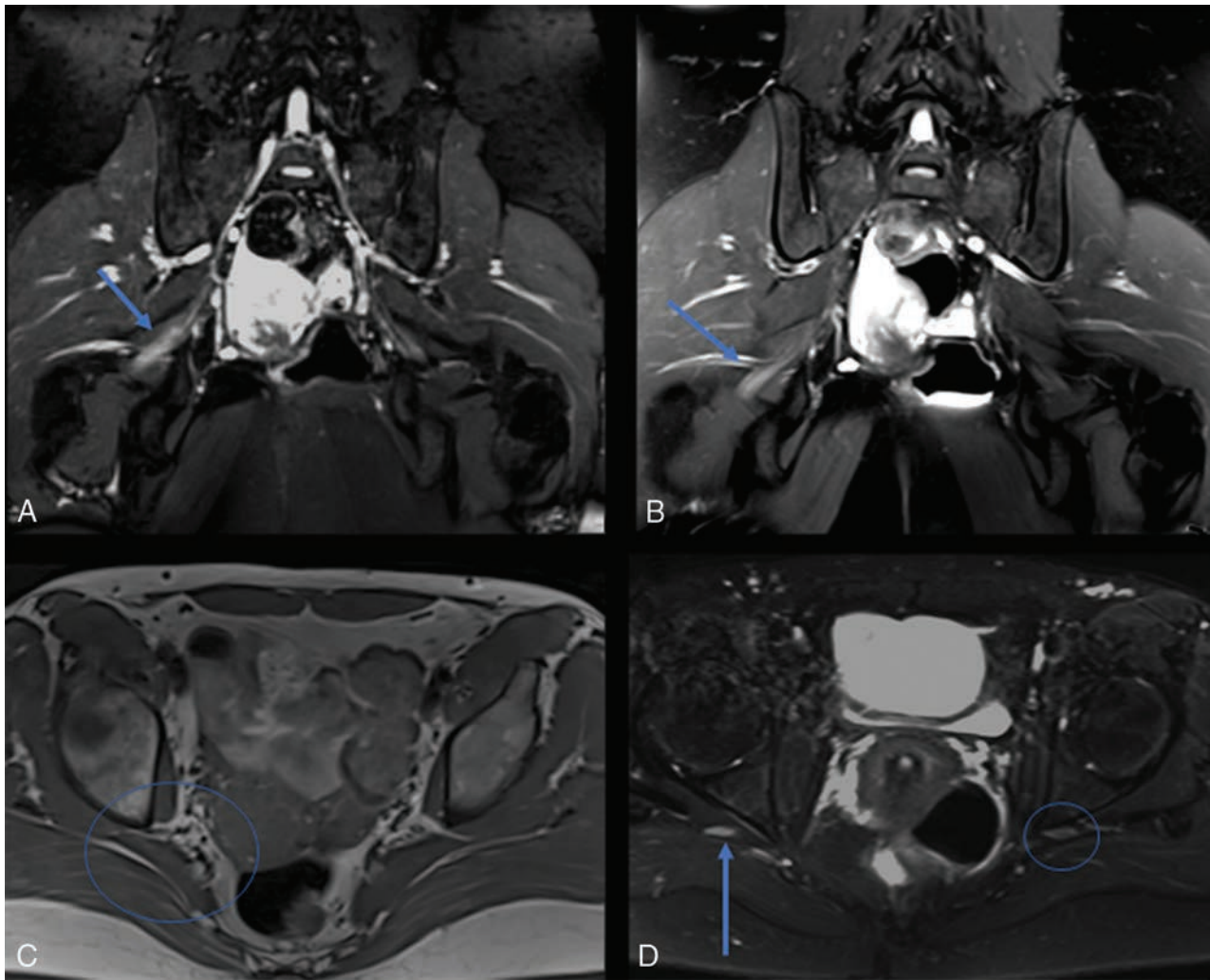


**FIG 4.** 3D coronal fat-suppressed T2 STIR (A), coronal fat-suppressed T2 SPAIR (B), axial T1 (C), and axial fat-suppressed T2 SPAIR (D) images show a typical example of right sciatic neuropathy. There is abnormal signal in the right sciatic nerve (arrows) through the greater sciatic foramen (circle, C), a characteristic location of piriformis-related sciatic nerve compression. There is corresponding asymmetric signal of the right sciatic nerve compared with the left (circle, D).

ously for lumbosacral radiculopathy. Furthermore, this imaging-electrodiagnostic correlation was one of the only statistically significant findings in our cohort despite the consideration of multiple subjective and physical examination findings. Lumbar radiculopathy is notoriously difficult to diagnose with history or physical examination findings alone.<sup>13,14</sup> MRN appears to provide useful diagnostic information, and the statistical correlation with EMG further reinforces its accuracy.

A study by Crim and Ingalls<sup>15</sup> revealed a moderate sensitivity (41.2%–70.6%) and very high specificity (97.7%–100%) in the interpretation of brachial plexus MRN when EMG was used as a criterion standard. This study was not limited to radiculopathy and included MRN studies performed at both 1.5T and 3T. A study by Chhabra et al<sup>16</sup> revealed a measurable impact of 3T MRN on diagnostic thinking and therapeutic choices. MRN is a recommended study for presurgical planning in patients with peripheral neuropathy. The observed interrater reliability ( $\kappa = 0.71$ ) demonstrates substantial agreement between readers, in line with studies of lumbar spine imaging.<sup>17</sup>

This study evaluated the intraneural T2 signal as a marker for

nerve abnormality on MRN. The authors do not find nerve caliber to be a useful metric in this setting because the abnormal nerves in this cohort had a size similar to that of normal nerves (Figs 2 and 4). Furthermore, it is difficult to reproducibly measure the caliber of nerve fascicles, given their oblique orientation, while excluding the perineural fat and soft tissues. Findings of acute or subacute muscular denervation were recorded when T2 hyperintense signal was seen within the lumbosacral musculature, as described by others.<sup>8</sup> Imaging findings of muscular denervation were seen in a minority of patients (12.5%) but were helpful findings to confirm a neuropathy when observed. For example, in 1 subject with an L4 radiculopathy extending to the femoral nerve, ipsilateral denervation changes were observed in the iliacus, a muscle innervated by the femoral nerve (Fig 5). The relatively low rate of observed denervation changes may be related to the timing of imaging to the active period of radiculopathy and the exclusion of lower thigh and lower extremity muscles from the imaging FOV.

Diffusion-weighted imaging or diffusion tensor imaging was not part of the imaging protocol in this study. The authors have not found that DTI provides useful information when evaluating

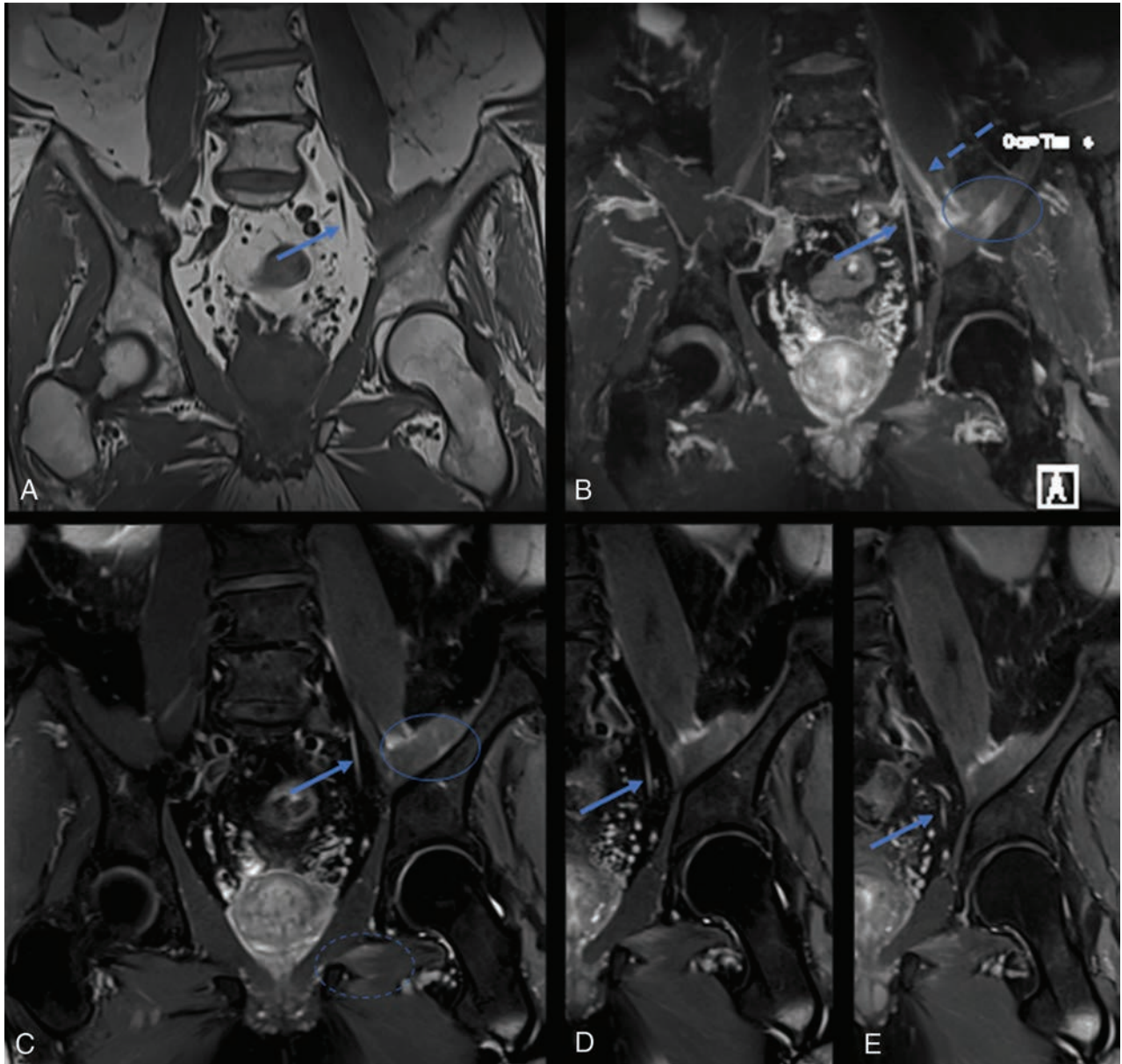


**FIG 5.** Coronal T1 (A), maximum-intensity reconstruction of 3D coronal fat-suppressed T2 STIR (B), and sequential coronal fat-suppressed T2 SPAIR (C–E) images show abnormal signal of the left L4, left femoral (dashed arrow, B) and left obturator (arrows) nerves. There is also abnormal intramuscular T2 hyperintense signal in the left iliopsoas muscle (circle, B). This patient had a long-standing history of type 2 diabetes, and signal abnormality was attributed to diabetic amyotrophy.

the lumbosacral plexus despite initially acquiring a coronal reversed fast imaging with steady-state precession diffusion sequence as part of the imaging protocol. DWI/DTI may have utility in imaging of peripheral nerves where surface coils can be placed close to the nerves of interest for an improved signal-to-noise ratio.<sup>18</sup>

Electrodiagnostic studies are not a perfect criterion standard, and there are variabilities inherent in the performance and interpretation of NCS and EMG. In patients with active radiculopathy, electrodiagnostic studies classically demonstrate a combination of normal NCS and abnormal needle EMG.<sup>19</sup> This pattern is thought to result from the common lateral recess or subarticular location of a disc herniation proximal to the dorsal root ganglion, thus sparing the sensory nerve fibers. Needle EMG reveals fibril-

lation potentials and positive sharp waves when a neuropathic lesion is present. These denervation potentials represent the spontaneous depolarization of an individual muscle fiber from ongoing or active axonal drop-out. The time course of radiculopathy is not always clear on NCS/EMG, but certain findings can narrow the window, including the MUAP morphology. Active denervation may take some time to be apparent on NCS/EMG; it is only evident following axonal injury once Wallerian degeneration begins. Evidence of active denervation with normal MUAP morphology suggests a subacute time course in which the muscles have not yet undergone reinnervation. Regardless, by the time a patient with true radiculopathy comes to clinical attention, there are typically electrodiagnostic findings.

Electrodiagnostic testing has several limitations and may dem-

onstrate confounding results, for example, when a superimposed peripheral neuropathy or primary myopathy is present. Furthermore, the NCS/EMG is highly operator-dependent, and false-negative studies with equivocal findings are common despite true radiculopathy for a variety of reasons, including a fascicular phenomenon and variations in electromyographer technique and experience. Despite these limitations, EMG remains a useful examination to evaluate active radiculopathy as class II evidence and level B recommendation by the American Association of Neuro-muscular and Electrodiagnostic Medicine in lumbosacral radiculopathy in an analysis of 119 articles.<sup>20</sup>

This study is limited by its retrospective nature and variations in the timing of clinical notes, though all notes reviewed were from neuromuscular neurologists who performed the electrodiagnostic testing. There are also variabilities inherent in MRN interpretation, though the interreader variability was substantial between interpreters. Despite these limitations, it is the largest study performed, to the authors' knowledge, that correlates MRN and electrodiagnostic findings in patients with lumbosacral radiculopathy.

## CONCLUSIONS

In this cohort of patients with lower extremity radiculopathy who had both MRN and electrodiagnostic studies performed within 3 months, 44% had abnormal intraneural signal on MRN and 31% had electrodiagnostic findings of active radiculopathy with a statistically significant correlation between positive findings on these modalities. The role of MRN in the work-up and clinical management of patients with lumbosacral radiculopathy is still being explored. The presence of abnormal extraspinal intraneural signal on MRN may identify patients with a high likelihood of response to targeted therapy such as transforaminal epidural steroid injection. It is anticipated that this information will help guide clinical management of patients presenting with active radicular symptoms. These data may prove to be particularly useful in an era of overexuberant epidural injection treatment and personalized medicine with a focus on cost-benefit treatment algorithms.

Disclosures: Michael Sein—UNRELATED: Consultancy: CID Management Solutions.

## REFERENCES

1. Tarulli AW, Raynor EM. **Lumbosacral radiculopathy.** *Neurol Clin* 2007;25:387–405 CrossRef Medline
2. Dillingham TR. **Evaluating the patient with suspected radiculopathy.** *PM R* 2013;5:S41–49 CrossRef Medline
3. Tong HC, Haig AJ, Yamakawa KS, et al. **Specificity of needle electromyography for lumbar radiculopathy and plexopathy in 55- to 79-year-old asymptomatic subjects.** *Am J Phys Med Rehabil* 2006;85:908–12; quiz 913–15, 934 CrossRef Medline
4. Jensen MC, Brant-Zawadzki MN, Obuchowski N, et al. **Magnetic resonance imaging of the lumbar spine in people without back pain.** *N Engl J Med* 1994;331:69–73 CrossRef Medline
5. Boden SD, McCowin PR, Davis DO, et al. **Abnormal magnetic-resonance scans of the cervical spine in asymptomatic subjects: a prospective investigation.** *J Bone Joint Surg Am* 1990;72:1178–84 CrossRef Medline
6. Howe FA, Filler AG, Bell BA, et al. **Magnetic resonance neurography.** *Magn Reson Med* 1992;28:328–38 CrossRef Medline
7. Chhabra A, Flammang A, Padua A Jr, et al. **Magnetic resonance neurography: technical considerations.** *Neuroimaging Clin N Am* 2014;24:67–78 CrossRef Medline
8. Soldatos T, Andreisek G, Thawait GK, et al. **High-resolution 3-T MR neurography of the lumbosacral plexus.** *Radiographics* 2013;33:967–87 CrossRef Medline
9. Lewis AM, Layzer R, Engstrom JW, et al. **Magnetic resonance neurography in extraspinal sciatica.** *Arch Neurol* 2006;63:1469–72 CrossRef Medline
10. Filler AG, Haynes J, Jordan SE, et al. **Sciatica of nondisc origin and piriformis syndrome: diagnosis by magnetic resonance neurography and interventional magnetic resonance imaging with outcome study of resulting treatment.** *J Neurosurg Spine* 2005;2:99–115 CrossRef Medline
11. Yoshida T, Sueyoshi T, Suwazono S, et al. **Three-Tesla magnetic resonance neurography of the brachial plexus in cervical radiculopathy.** *Muscle Nerve* 2015;52:392–96 CrossRef Medline
12. Laporte C, Albert JD, Duvauferrier R, et al. **MRI investigation of radiating pain in the lower limbs: value of an additional sequence dedicated to the lumbosacral plexus and pelvic girdle.** *AJR Am J Roentgenol* 2014;203:1280–85 CrossRef Medline
13. Iversen T, Solberg TK, Romner B, et al. **Accuracy of physical examination for chronic lumbar radiculopathy.** *BMC Musculoskelet Disord* 2013;14:206 CrossRef Medline
14. Suri P, Rainville J, Katz JN, et al. **The accuracy of the physical examination for the diagnosis of midlumbar and low lumbar nerve root impingement.** *Spine* 2011;36:63–73 CrossRef Medline
15. Crim J, Ingalls K. **Accuracy of MR neurography in the diagnosis of brachial plexopathy.** *Eur J Radiol* 2017;95:24–27 CrossRef Medline
16. Chhabra A, Belzberg AJ, Rosson GD, et al. **Impact of high resolution 3 Tesla MR neurography (MRN) on diagnostic thinking and therapeutic patient management.** *Eur Radiol* 2016;26:1235–44 CrossRef Medline
17. Lurie JD, Tosteson AN, Tosteson TD, et al. **Reliability of readings of magnetic resonance imaging features of lumbar spinal stenosis.** *Spine (Phila Pa 1976)* 2008;33:1605–10 CrossRef Medline
18. Guggenberger R, Markovic D, Eppenberger P, et al. **Assessment of median nerve with MR neurography by using diffusion-tensor imaging: normative and pathologic diffusion values.** *Radiology* 2012;265:194–203 CrossRef Medline
19. Narayanaswami P, Geisbush T, Jones L, et al. **Critically re-evaluating a common technique: accuracy, reliability, and confirmation bias of EMG.** *Neurology* 2016;86:218–23 CrossRef Medline
20. Cho SC, Ferrante MA, Levin KH, et al. **Utility of electrodiagnostic testing in evaluating patients with lumbosacral radiculopathy: an evidence-based review.** *Muscle Nerve* 2010;42:276–82 CrossRef Medline

# Fluoroscopically Guided Facet Injections: Comparison of Intra-Articular and Periarticular Steroid and Anesthetic Injection on Immediate and Short-Term Pain Relief

L.M. Kershen, N.C. Nacey, J.T. Patrie, and M.G. Fox



## ABSTRACT

**BACKGROUND AND PURPOSE:** The effectiveness of facet injections is unclear in the literature. Our objective was to determine the immediate and short-term efficacy of intra-articular and periarticular steroid/anesthetic injections for facet-mediated lumbar pain.

**MATERIALS AND METHODS:** All outpatient fluoroscopically guided facet injections at a single institution during a 54-month period were retrospectively and independently reviewed by 2 musculoskeletal (MSK) trained radiologists. All intra-articular, all periarticular, and partial intra-/periarticular injection locations were determined. Periarticular and partial peri-/intra-articular injections were combined for analysis. Preinjection, immediate, and 1-week postinjection numeric pain scores, patient age, sex, anesthetic/steroid mixture, fluoroscopic time, and physician performing the procedure were recorded.

**RESULTS:** Seventy-seven patients (mean age, 51.1 years) had 100 procedures with 205 total facet joints injected. All intra-articular, all periarticular, and partial peri-/intra-articular injections constituted 54%, 20%, and 26% of the cases, respectively. The immediate and 1-week postprocedural change in pain was  $-3.7$  (95% CI,  $-4.5$  to  $-2.8$ ;  $P < .001$ ) and  $-1.4$  (95% CI,  $-2.2$  to  $-0.6$ ;  $P = .001$ ) for the all intra-articular and  $-3.6$  (95% CI,  $-4.4$  to  $-2.9$ ;  $P < .001$ ) and  $-1.2$  (95% CI,  $-1.9$  to  $-0.4$ ;  $P = .002$ ) for the combined group. Changes in immediate pain were significantly associated with the prepain level ( $P < .001$ ) and patient age ( $P = .024$ ) but not with the anesthetic used. Analyses revealed no significant difference in pain reduction between the groups either immediately or 1 week postinjection. Intra-articular injections required less fluoroscopic time (geometric mean, 39 versus 52 seconds) ( $P = .005$ ).

**CONCLUSIONS:** Intra-articular and periarticular fluoroscopically guided facet injections provide statistically significant and similar pain relief both immediately and 1 week postinjection.

Given the variety of presentations and factors that contribute to low back pain, determining the optimal treatment method may be challenging. The facet joint is 1 possible etiology of axial low back pain with both surgical and nonsurgical treatment methods used to provide pain relief.<sup>1</sup> Facet-mediated pain or “facet syndrome” may account for up to 45% of

cases of axial low back pain.<sup>2</sup> The characteristic pain in facet syndrome is located in the low back with involvement of the buttock/greater trochanteric region with occasional unilateral extension along the lateral thigh.<sup>1,2</sup> The pain is usually more pronounced after immobilization and with low back extension.<sup>2</sup> The injection of a local anesthetic is often used to both diagnose and manage facet-mediated pain.<sup>1,2</sup> Even though there is a paucity of literature to support the use of intra-articular steroid injections in this patient population, corticosteroids are often injected to provide longer term pain relief and restore functional status.<sup>3-12</sup> Whether intra-articular or periarticular placement of the injectate substantially alters the efficacy of the injection is also debated.<sup>4,7,8</sup> Therefore, we retrospectively evaluated patients with fluoroscopically guided facet injections for clinically suspected facet syndrome to determine the immediate and short-term efficacy of those injections and to evaluate whether an intra-articular or periarticular injection provided greater pain relief.

Received March 27, 2018; accepted after revision July 30.

From the Colorado Imaging Associates (L.M.K.), Golden, Colorado; Departments of Radiology and Medical Imaging (N.C.N.) and Public Health Sciences (J.T.P.), University of Virginia, Charlottesville Virginia; and Department of Radiology (M.G.F.), Mayo Clinic Arizona, Phoenix, Arizona. Drs. Fox and Kershen were previously affiliated with the Department of Radiology and Medical Imaging, University of Virginia, Charlottesville, Virginia.

Previously presented as an electronic scientific exhibit (O-476) at: Annual Meeting of the American Society of Neuroradiology and the Foundation of the ASNR Symposium, April 25–30, 2015; Chicago, Illinois.

Please address correspondence to Michael G. Fox, MD, MBA, Mayo Clinic Arizona, Department of Radiology, 5777 E Mayo Blvd, Phoenix, AZ 85054; e-mail: Fox.Michael@mayo.edu

<http://dx.doi.org/10.3174/ajnr.A5805>



**FIG 1.** Anteroposterior image of the lumbar spine demonstrates the straight anteroposterior approach to accessing the inferior articular recess (*arrow*) of the facet joint.

## MATERIALS AND METHODS

Institutional review board approval was obtained from The University of Virginia for the study. All outpatient fluoroscopically guided facet injections performed during a 4-year period (June 2010 to October 2014) at a single institution were retrospectively reviewed. More than 90% of the patients were referred by orthopedic spine specialists ( $n = 94$ ) for treatment of suspected facet syndrome or to help quantify the degree of back pain accounted for by the facet arthropathy; physical medicine and rehabilitation ( $n = 4$ ) and neurosurgery ( $n = 2$ ) accounted for the remainder of the patient referrals.

### Technique

After we obtained written informed consent, the patients were placed prone on the fluoroscopic table with a bolster placed under their lower abdomen to reduce lordosis. The patients were sterilely prepped and draped in the usual manner and a 22-ga 3.5-inch spinal needle was directed toward the inferior articular recess of the facet joint using fluoroscopic guidance (Fig 1).<sup>13</sup> Following needle placement, 0.5–1 mL of iohexol (Omnipaque 300) was injected to confirm placement. Opacification of the facet joint and/or superior articular recess was used as the criterion for determining an intra-articular injection (Fig 2). When contrast was not demonstrated in the facet joint, the injection was considered periarticular (Fig 3). The patients were then injected with either 0.5 mL of 0.25% bupivacaine ( $n = 29$  procedures); 0.5 mL of 0.5% bupivacaine ( $n = 39$  procedures); or 0.5 mL of 1% lidocaine ( $n = 32$  procedures) and either 20 mg (0.5 mL) of methylprednisolone acetate (Depo-Medrol) ( $n = 92$  procedures), 3 mg (0.5 mL) of betamethasone (Celestone) ( $n = 4$  procedures), or 20 mg (0.5

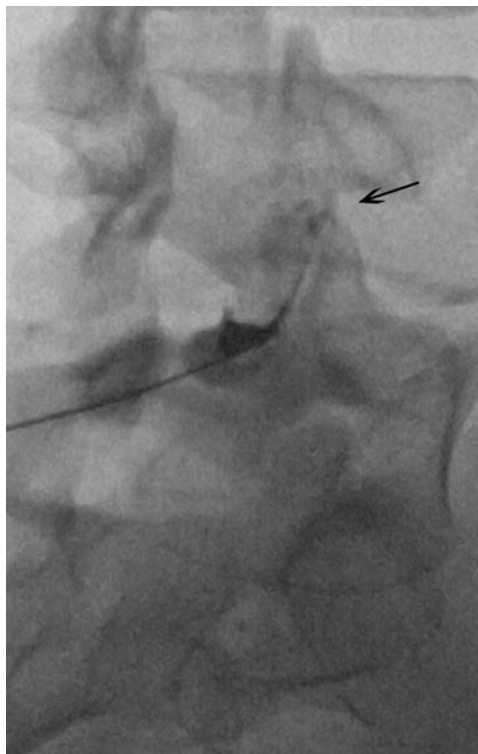


**FIG 2.** Oblique fluoroscopic image of the L4–L5 facet joint demonstrates an intra-articular injection. Contrast spreads from the injection into the inferior recess to the superior recess (*arrow*).



**FIG 3.** Oblique fluoroscopic image of the L4–L5 facet joint demonstrates a periarticular injection. Contrast pools around the needle tip adjacent to the hypertrophied facet joint. No contrast is identified within the joint or joint recess.

mL) of triamcinolone acetonide (Kenalog) ( $n = 4$  procedures). The injection was performed by either a musculoskeletal (MSK) fellow ( $n = 30$ ), an MSK faculty member ( $n = 2$ ), or an MSK fellow with an MSK faculty member present ( $n = 68$ ).

### **Pain Analysis**

All patients reported their preinjection and 5- to 10-minute postinjection pain scores to a radiology nurse using an 11-point Numeric Pain Rating Scale; 0 (no pain) to 10 (worst pain imaginable). In addition, patients were called 1 week postinjection, and the current pain score was recorded using the same 11-point scale. We were able to record a 1-week pain score for 49% (49/100) of the procedures. Patients were excluded if a different concentration of steroid was injected, if a preinjection or 5- to 10-minute postinjection pain score was not recorded, or if a pars defect was present. Patients younger than 16 years of age were also excluded from the study.

### **Image Analysis**

Two fellowship-trained MSK radiologists, with 2 and 16 years of experience in performing facet injections, independently reviewed the fluoroscopic images to determine whether the injections were intra-articular or periarticular. When a discrepancy was present, the discrepant cases were re-analyzed in a blinded fashion and a consensus interpretation was rendered. The consensus interpretation was used for the statistical analyses. If an injection of >1 facet joint was performed in the same setting, all injections needed to be within the facet joint for the injection to be considered “all-in.” Likewise, all the injected facet joints needed to be periarticular to be considered “all-out.” When bilateral or 2-level facet injections were performed, if  $\geq 1$  of the injections was determined to be periarticular and  $\geq 1$ , intra-articular, the injection was considered “partial.” Partial and all-out groups were combined for analysis.

### **Statistical Analysis**

**Data Summary.** Categorical data were summarized as frequencies and percentages, and continuous scaled data were generally summarized by the mean and SD of the distribution.

**Interreader Agreement.** The concordance between the 2 readers' assessments of whether the intra-articular injection was “all-in”, partially in, or “all-out” was evaluated by the  $\kappa$  statistic. An exact binomial confidence interval was used to establish a plausible range of values for the underlying level of concordance between the 2 readers' injection classifications.

### **Postprocedure Pain Analysis**

ANCOVA models were used to estimate the immediate and short-term postinjection mean changes in the pain scores. The ANCOVA model for examining the immediate change in pain was specified so that the partial variability in the immediate change in pain attributable to the injection site (“all-in” versus “partially in” or “all-out”) and the partial variability in the immediate change in pain attributable to the anesthetic type (0.5 mL of 0.25% bupivacaine, 0.5 mL of 0.50% bupivacaine, or 0.5 mL of 1% lidocaine) could be examined after accounting for the variabilities in immediate change in pain attributable to patient age, sex, prepain level, and procedure personnel (attending physician involvement). The ANCOVA model for examining short-term (1 week postinjection) change in pain was specified in the same way as the ANCOVA model for the immediate change in pain, except

that the “anesthetic type” was excluded. All null hypotheses related to the immediate and short-term changes in pain were tested via *F* tests, and a  $P < .05$  decision rule was used as the null hypothesis rejection rule.

### **Fluoroscopic Time**

Fluoroscopic time was analyzed on the natural logarithmic scale via ANCOVA, with the injection location the ANCOVA model factor of interest, and the personnel performing the procedure as the ANCOVA covariates. Comparison of fluoroscopic time was with the geometric mean fluoroscopic time, and a  $P < .05$  decision rule was used for testing the null hypothesis that the geometric mean ratio is equal to 1.

### **Statistical Software**

The statistical software package SAS, Version 9.4 (SAS Institute, Cary, North Carolina) was used to conduct the aforementioned statistical analyses.

## **RESULTS**

One hundred procedures were performed on 77 patients (29 males, 48 females; mean age, 51.1 years; range, 16–67 years) with a total of 205 facet joints injected. Sixty-six patients underwent 1 procedure, 8 patients underwent 2 procedures, and 1 patient each underwent 3, 4, and 11 procedures. Twenty-four procedures (24%, 24 facets) were single-facet injections, 61 (61%, 122 facets) procedures were 2-facet injections in the same sitting, 1 procedure had 3 facet injections (1%, 3 facets), and 14 (14%, 56 facets) procedures had 4 facets injected in the same sitting. We injected the following facet levels: T12–L1 ( $n = 4$ ), L1–L2 ( $n = 2$ ), L2–L3 ( $n = 9$ ), L3–L4 ( $n = 20$ ), L4–L5 ( $n = 104$ ), and L5–S1 ( $n = 66$ ).

The consensus interpretation in 54 of 100 procedures (100/205 facets injected) was all intra-articular; in 20 procedures (33/205 facets), it was all periarticular; and in 26 procedures (72/205 facets), it was partial intra-articular injection. Exact agreement between the 2 readers was present in 77% (77/100) (95% CI, 0.68–0.84) of the procedures with a  $\kappa$  statistic of 0.60 (95% CI, 0.46–0.75).

Analysis of the immediate (5- to 10-minute) change in pain yielded a statistically significant association with the prepain level ( $P < .001$ ) and patient age ( $P = .024$ ) (older patients experienced greater pain relief) but no significant association with the anesthetic used ( $P = .431$ ), sex ( $P = .205$ ), or the radiology team member performing the procedure ( $P = .153$ ). Analysis of the 1-week change in pain revealed no statistically significant association with the prepain level ( $P = .979$ ), patient age ( $P = .462$ ), sex ( $P = .979$ ), or the radiology team member performing the procedure ( $P = .672$ ).

The mean preinjection and 5- to 10-minute postinjection pain scores for the 54 procedures in the all intra-articular group were 6.3 and 2.7, respectively, with a mean change in pain of  $-3.7$  (95% CI,  $-4.5$  to  $-2.8$ ;  $P < .001$ ). The mean preinjection and 5- to 10-minute postinjection pain scores for the 46 periarticular/partial procedures were 5.8 and 2.1, respectively, with a mean change in pain of  $-3.6$  (95% CI,  $-4.4$  to  $-2.9$ ;  $P < .001$ ) (Table 1).

Twenty-four of the all intra-articular injections had a 1-week postprocedure pain score recorded with the mean 1-week postin-

**Table 1: Mean pain level in the 5- to 10-minute postinjection period when accounting for intra-articular-versus-periarticular/partial injections**

	No.	Prepain	Postpain	Change in Pain (95% CI)	P Value (Unadjusted)
All-in	54	6.3	2.7	-3.7 (-4.5 to -2.8)	<.001
All-out/partial	46	5.8	2.1	-3.6 (-4.4 to -2.9)	<.001

**Table 2: Mean pain level 1 week postinjection when accounting for intra-articular-versus-periarticular/partial injections**

	No.	Prepain	Postpain	Change in Pain (95% CI)	P Value (Unadjusted)
All-in	24	6.4	5.0	-1.4 (-2.2 to -0.6)	.001
All-out/partial	25	6.8	5.7	-1.2 (-1.9 to -0.4)	.002

**Table 3: ANCOVA summary of mean change in pain between the immediate and 1-week postinjection period when adjusting for prepain level, age, sex, and radiology team member performing the procedure**

	Difference in Mean Change in Pain between All-In and All-Out/Partial Groups (95% CI)	P Value (Adjusted)
Immediate	0.46 (-0.56-1.49)	.371
One week	0.27 (-0.94-1.48)	.652

jection change in pain of -1.4 (95% CI, -2.2 to -0.6;  $P = .001$ ). Twenty-five of the periarticular/partial injections had a 1-week postprocedural pain score recorded with a mean 1-week postinjection change in pain of -1.2 (95% CI, -1.9 to -0.4;  $P = .002$ ) (Table 2).

The mean difference in the change in pain 5–10 minutes postinjection between the intra-articular and periarticular/partial groups was 0.46 (95% CI, -0.56 to 1.49;  $P = .371$ ), and the mean difference in the change in pain between the intra-articular and periarticular/partial groups at 1 week postinjection was 0.27 (95% CI, -0.94 to 1.48;  $P = .652$ ) (Table 3).

The mean fluoroscopic time for intra-articular, periarticular, and partial injection was 44, 59, and 54 seconds, respectively. After adjusting for the person performing the injection (fellow alone, and so forth), a statistically significant difference in the ratio of geometric means between the intra-articular and periarticular/partial groups was noted (geometric mean ratio = 1.31; 95% CI, 1.08–1.58;  $P = .005$ ).

## DISCUSSION

The facet joint is a known contributor to axial low back pain. However, diagnosing facet-mediated pain can be challenging due to confounding factors in pain generation such as concomitant lumbar disk and sacroiliac joint degenerative changes. In addition, dual innervation of the facet joint by medial branches of the dorsal ganglion at and above the level of the target facet may further complicate the diagnosis and treatment of facet-mediated pain.

Even though injections have been used for decades to diagnose and manage facet-mediated pain, the utility of injections to relieve this pain as reported in the literature is inconclusive.<sup>14</sup> Local anesthetics inhibit nerve conduction and excitation to various degrees with the 3 most commonly used agents being lidocaine (shortest acting), bupivacaine, and ropivacaine (longest acting).<sup>15</sup> It is generally accepted that anesthetic-only injections are useful as a diagnostic test for facet-mediated pain in clinically unclear cases.

Mooney and Robertson<sup>1</sup> demonstrated that saline injected into the facet joint could reproduce facet-mediated pain and that the pain could be alleviated with a local anesthetic injection.

Corticosteroids can interrupt the inflammatory cascade, which is thought to contribute to axial back pain, ideally resulting in longer pain relief than that provided by local anesthetics. The 4 most commonly used corticosteroid agents include the following: methylprednisolone, triamcinolone, beta-

methasone, and dexamethasone, with only dexamethasone considered nonparticulate unless it is combined with ropivacaine, which will result in particulate formation.<sup>15</sup> While the use of corticosteroids in back injections is generally accepted, the specific use of intra-articular steroid injections for facet-mediated pain is less clear. Mooney and Robertson<sup>1</sup> reported that 20% of patients achieved complete and 33% of patients experienced partial pain relief 6 months following steroid injection. Similarly, Destouet et al<sup>3</sup> determined that 54% of patients, many of whom had prior spinal surgery, responded to facet steroid injections. In fact, 38% of the responders achieved long-term (6–12 months) clinical improvement. In contrast, Lilius et al<sup>4</sup> randomized patients into 3 facet-injection groups: steroid, anesthetic only, and normal saline. They found a significant improvement in the pain and disability scores for all 3 groups, with no significant difference among the groups. As a result, they questioned the utility of steroid and anesthetic injections for managing facet pain.

More recently, Manchikanti et al,<sup>5</sup> using a meta-analysis, concluded that there is limited evidence to support the use of intra-articular lumbar facet steroid injections based on 3 high-quality studies demonstrating effectiveness for follow-up <6 months and 2 moderate to high-quality studies demonstrating a lack of effectiveness. Similarly, Bogduk<sup>6</sup> concluded that the efficacy of intra-articular steroid injections was no better than that of sham treatments. Because there is limited evidence to support the routine use of steroid facet injections, Bykowski and Wong<sup>2</sup> advocated a more tailored use of steroid injections, reserving them for patients in whom radiofrequency ablation was refused or contraindicated.

We found no difference in the 1-week postinjection pain relief between the all intra-articular and the combined all periarticular and partial peri-/intra-articular groups, which is similar to the results reported by Lilius et al.<sup>4</sup> In contrast, Lynch and Taylor<sup>7</sup> reported that intra-articular injections were substantially better than periarticular injections in relieving facet-mediated pain 2 weeks postinjection.

The imaging guidance used to perform facet injections is often based on operator familiarity and the availability of equipment. In our experience, fluoroscopically guided facet injections can be performed with minimal radiation exposure. We found that intra-articular injections required less fluoroscopic time compared with periarticular injections, which is likely because some radiologists were more diligent in attempting to access to the facet joint. When accessing the joint or joint recess was more challenging, due to facet joint degeneration and hypertrophy, some perform-

ing radiologists were less concerned about being intra-articular because the efficacy of intra-articular compared with periarticular steroid injections remains unclear. We suspect that if a periarticular injection was the primary goal of all of the performing radiologists, the fluoroscopy time would be substantially lower in this group. Nevertheless, the mean fluoroscopic time in our study was <60 seconds in each group.

Our study is limited because it is retrospective and lacks a randomized control group. In addition, our 1-week response rate was only 49%, which limits our patient population in this category. However, the 1-week response rate was fairly equal between the 2 groups. The lack of follow-up beyond 1 week is also a limitation.

## CONCLUSIONS

Both intra-articular and periarticular facet injections provide similar and statistically significant immediate and 1-week postinjection relief of facet-mediated pain.

## ACKNOWLEDGMENTS

The data for this project originated from and were provided by the University of Virginia.

## REFERENCES

1. Mooney V, Robertson J. **The facet syndrome.** *Clin Orthop Relat Res* 1976;115:149–56 Medline
2. Bykowski JL, Wong WH. **Role of facet joints in spine pain and image-guided treatment: a review.** *AJNR Am J Neuroradiol* 2012;33:1419–26 CrossRef Medline
3. Destouet JM, Gilula LA, Murphy WA, et al. **Lumbar facet joint injection: indication, technique, clinical correlation, and preliminary results.** *Radiology* 1982;145:321–25 CrossRef Medline
4. Lilius G, Laasonen EM, Myllynen P, et al. **Lumbar facet joint syndrome: a randomised clinical trial.** *J Bone Joint Surg Br* 1989;71:681–84 Medline
5. Manchikanti L, Kaye AD, Boswell MV, et al. **A systemic review and best evidence synthesis of the effectiveness of therapeutic facet joint interventions in managing chronic spinal pain.** *Pain Physician* 2015;18:E535–82 CrossRef Medline
6. Bogduk N. **A narrative review of intra-articular corticosteroid injections for low back pain.** *Pain Med* 2005;6:287–96 CrossRef Medline
7. Lynch MC, Taylor JF. **Facet joint injection for low back pain: a clinical study.** *J Bone Joint Surg Br* 1986;68:138–41 Medline
8. Staal JB, de Bie R, de Vet HC, et al. **Injection therapy for subacute and chronic low back pain: an updated Cochrane review.** *Spine (Phila Pa 1976)* 2009;34:49–59 CrossRef Medline
9. Carotte S, Marcoux S, Truchon R, et al. **A controlled trial of corticosteroid injections into facet joints for chronic low back pain.** *N Engl J Med* 1991;325:1002–07 CrossRef Medline
10. Fuchs S, Erbe T, Fischer HL, et al. **Intraarticular hyaluronic acid versus glucocorticoid injections for nonradicular pain in the lumbar spine.** *J Vasc Interv Radiol* 2005;16:1493–98 CrossRef Medline
11. Murtagh FR. **Computed tomography and fluoroscopy guided anesthesia and steroid injection in facet syndrome.** *Spine (Phila Pa 1976)* 1988;13:686–89 CrossRef Medline
12. Lippitt AB. **The facet joint and its role in spine pain: management with facet joint injections.** *Spine (Phila Pa 1976)* 1984;9:746–50 CrossRef Medline
13. Sarazin L, Chevrot A, Pessis E, et al. **Lumbar facet joint arthrography with the posterior approach.** *Radiographics* 1999;19:93–104 CrossRef Medline
14. Vekaria R, Bhatt R, Ellard DR, et al. **Intra-articular facet joint injections for low back pain: a systematic review.** *Eur Spine J* 2016;25:1266–81 CrossRef Medline
15. MacMahon PJ, Huang AJ, Palmer WE. **Spine injectables: what is the safest cocktail?** *AJR Am J Roentgenol* 2016;207:526–33 CrossRef Medline

# Celebrating 35 Years of the AJNR

November 1983 edition

## NMR Imaging of the Spine

Jong S. Han<sup>1</sup>  
Benjamin Kaufman<sup>1</sup>  
Saba J. El Youssfi<sup>1</sup>  
Jane E. Benson<sup>1</sup>  
Charles T. Borstelle<sup>1</sup>  
Ralph J. Alfidi<sup>1</sup>  
John R. Haaga<sup>1</sup>  
Hong Young<sup>1</sup>  
Richard G. Huss<sup>1</sup>

The usefulness of nuclear magnetic resonance (NMR) images in the evaluation of spinal disorders below the craniocervical junction was studied. Six normal subjects and 41 patients with various spinal abnormalities were examined. NMR proved capable of demonstrating important normal and pathologic anatomic structures; it was useful in the evaluation of spondylomyeloma and cystic spinal cord tumors, and the bright signal intensity of lipoma was quite impressive. In the evaluation of herniated disk, NMR images offered a new perspective by visualizing abnormal degradation of the signal intensity of the nucleus pulposus itself. NMR images were least valuable in the evaluation of spondylolysis and spinal stenosis. Although NMR imaging of the spine is still in a very early developmental stage, the absence of both ionizing radiation and risks associated with contrast material makes it especially attractive as a new diagnostic method. This limited experience with currently available equipment suggests that, with technical refinement, the efficacy of NMR of the spine will increase.

Nuclear magnetic resonance (NMR) holds great promise as an imaging method, with its high theoretical limits in image detail and very low attendant risks. Clinical experience in the evaluation of the central nervous system, particularly the brain, is rapidly accumulating [1-5]. However, the normal anatomic features of the spine have not been established thus far with NMR. We summarize initial NMR studies of spinal anatomy in normal subjects at our institution and present NMR findings in a spectrum of spinal pathology.

### Subjects and Methods

During a 5-month period, six normal subjects and 41 patients with various spinal abnormalities underwent NMR examinations at Case Western Reserve University Hospitals of Cleveland. Normal adult volunteers included four men and two women with a mean age of 31 years. To delineate the normal morphologic images of the spine and its related structures, the entire spinal column of each normal subject was studied in a supine position. NMR studies were also performed on 41 patients (20 men and 21 women, age range, 12-77 years; mean age, 37 years) who had a confirmed diagnosis on the basis of clinical findings and/or preceding radiologic studies, including myelography and computed tomography (CT). Written informed consent was obtained from all participants.

Various radiofrequency pulse sequences were used to obtain the NMR images, including saturation-recovery (SR), inversion-recovery (IR), and T<sub>2</sub>-weighted spin-echo (SE) pulse sequences. The principles describing these sequences and the technique of NMR imaging have been described [6-8]. The NMR imaging system that we currently use is a Cryogenic Superconducting Magnet (Teleson, Technicon Corp., Solon, OH) with a 100 cm bore, operating at 3.0 kG. The NMR scan was generated using a two-dimensional Fourier transform technique with 128 phase-encoding data lines. The data acquisition time varies depending on the pulse sequences used. The SR technique (0.8 sec sequence interval, 30 msec echo delay) requires 2.3 min; the IR technique (1.3 sec sequence interval, 30 msec echo delay and 450 msec inversion time), 6.7 min; and the T<sub>2</sub>-weighted SE technique (1.0 sec sequence interval, 60 msec echo delay), 4.5 min. The slice thickness is about 10 mm.



This article appears in the November/December 1983 issue of AJNR and the December 1983 issue of AJNR.

Received May 5, 1983; accepted after revision July 19, 1983.

Presented at the annual meeting of the American Society of Neuroradiology, San Francisco, June 1982.

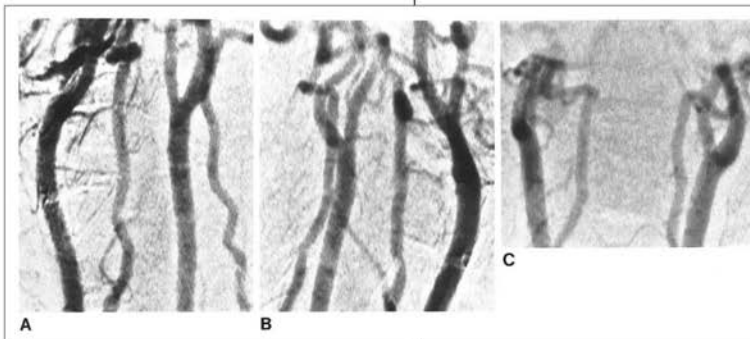
<sup>1</sup>Department of Radiology, Case Western Reserve University School of Medicine, University Hospitals of Cleveland, 2074 Abington Rd., Cleveland, OH 44106. Address reprint requests to J. S. Han.

<sup>2</sup>Technicon Corporation, Solon, OH 44138.  
AJNR 4:1151-1159, Nov/Dec 1983  
0195-6108/83/0408-1151\$00.00  
© American Neurological Association

## Limitations in the Interpretation of Intravenous Carotid Digital Subtraction Angiography

Michael G. Hoffman<sup>1</sup>  
Antoinette S. Gomez<sup>1</sup>  
S. Osher Pais<sup>1,2</sup>

To evaluate the limitations of intravenous carotid digital subtraction angiography (DSA) in the diagnosis of carotid disease, studies of 150 patients were reviewed. Factors that resulted in a nondiagnostic study included: (1) misregistration larynx artifact overlying the carotid bifurcation; (2) external carotid or vertebral artery overlying the internal carotid artery; and (3) poor arterial contrast density secondary to poor cardiac function. As a result of these limitations, the ideal of adequate demonstration of both carotid bifurcations in two opposite oblique projections or an oblique and anteroposterior projection was achieved in only 24 patients (26%). Of 126 carotid bifurcations that were seen adequately in two or more different projections, 19 (15%) showed an abnormality in one projection but appeared normal in another. These abnormalities would not have been detected had the vessel been visualized only in the spontaneously normal-appearing projection. These and other limitations of intravenous DSA, such as contrast load and morbidity, are discussed.



DSA) has become popular for screening for brachiocephalic vessels [1-3]. Avoidance of reliance on an outpatient basis account for the. Recent reports have indicated that clinical nonoperative treatment can be made on the cases [1]. Furthermore, it has been stated that oral aortic arch angiography [2]. However, we are, applied, carotid DSA studies may be hence not warranted by the quality or completeness, although the incidence of significant disease is not without risk and the associated cost.

A1, Lot 2, was used with a 0.7 mm focal spot and 6, 1 cm image intensifier modes. Exposure factors were 10 were generally 100-200 mA and 65-75 kVp. The 256 × 8 matrix. Imaging was performed using the 1/8 frame/sec, averaging eight frames. Some about 1 l. of fluid beginning the previous night procedure. With the Seldinger technique, a 5.0 French catheter was placed in the superior vena cava via an whom an arm vein could not be catheterized, the vena cava via a femoral vein. For each projection, 40 ml of contrast at 20 ml/sec. Exposures were initiated 4-5 sec after injection. The injection consisted of four projections: 45°-55° right anterior oblique (RAO) of neck, 55°-60° of aortic arch, and 15°-20° of aortic arch. Additional steeper oblique or anteroposterior projections of interest were obtained frequently. Postprocessing

# Standards of Practice in Acute Ischemic Stroke Intervention: International Recommendations

Laurent Pierot,<sup>1</sup> Mahesh V Jayaraman,<sup>2</sup> Istvan Szikora,<sup>3</sup> Joshua A Hirsch,<sup>4</sup> Blaise Baxter,<sup>5</sup> Shigeru Miyachi,<sup>6</sup> Jeyaledchumy Mahadevan,<sup>7</sup> Winston Chong,<sup>8</sup> Peter J Mitchell,<sup>9</sup> Alan Coulthard,<sup>10</sup> Howard A Rowley,<sup>11</sup> Pina C Sanelli,<sup>12</sup> Donatella Tampieri,<sup>13</sup> Patrick A Brouwer,<sup>14</sup> Jens Fiehler,<sup>15</sup> Naci Kocer,<sup>16</sup> Pedro Vilela,<sup>17</sup> Alex Rovira,<sup>18</sup> Urs Fischer,<sup>19</sup> Valeria Caso,<sup>20</sup> Bart van der Worp,<sup>21</sup> Nobuyuki Sakai,<sup>22</sup> Yuji Matsumaru,<sup>23</sup> Shin-ichi Yoshimura,<sup>24</sup> Rene Anxionnat,<sup>25</sup> Hubert Desal,<sup>25</sup> Luisa Biscoito,<sup>26</sup> José Manuel Pumar,<sup>27</sup> Orlando Diaz,<sup>28</sup> Justin F Fraser,<sup>29</sup> Italo Linfante,<sup>30</sup> David S Liebeskind,<sup>31</sup> Raul G Nogueira,<sup>32</sup> Werner Hacke,<sup>33</sup> Michael Brainin,<sup>34</sup> Bernard Yan,<sup>35</sup> Michael Soderman,<sup>14</sup> Allan Taylor,<sup>36</sup> Sirintara Pongpech,<sup>37</sup> Michihiro Tanaka,<sup>38</sup> Karel Terbrugge,<sup>39</sup> Asian-Australian Federation of Interventional and Therapeutic Neuroradiology (AAFITN), Australian and New Zealand Society of Neuroradiology (ANZSNR), American Society of Neuroradiology (ASNR), Canadian Society of Neuroradiology (CSNR), European Society of Minimally Invasive Neurological Therapy (ESMINT), European Society of Neuroradiology (ESNR), European Stroke Organization (ESO), Japanese Society for NeuroEndovascular Therapy (JSNET), the French Society of Neuroradiology (SFNR), Ibero-Latin American Society of Diagnostic and Therapeutic Neuroradiology (SILAN), Society of NeuroInterventional Surgery (SNIS), Society of Vascular and Interventional Neurology (SVIN), World Stroke Organization (WSO), World Federation of Interventional Neuroradiology (WFITN).

## PREAMBLE

After the five positive randomized controlled trials showing the benefit of mechanical thrombectomy (MT) in the management of acute ischemic stroke (AIS) with emergent large vessel occlusion (ELVO), a multisociety meeting was organized during the 16th Congress of the World Federation of Interventional and Therapeutic Neuroradiology (WFITN), October 2015, Gold Coast (Australia). This meeting was dedicated to the training of physicians performing MT, and recommendations were published thereafter in multiple scientific journals.<sup>1</sup>

The same group of scientific societies decided to organize a similar meeting during the 17th WFITN Congress, October 2017, Budapest (Hungary). This multisociety meeting was dedicated to standards of practice in acute ischemic stroke intervention (AISI), aiming for a consensus on the minimum requirements for centers providing such treatment.

In an ideal situation, all patients would be treated at a center offering a full spectrum of neuroendovascular care (a level 1 center). However, for geographical reasons, some patients are unable to reach such a center in a reasonable period of time. With this in mind, the group paid special attention to define recommendations on the prerequisites of organizing stroke centers providing MT for AIS, but not for other neurovascular diseases (a level 2 center). Finally, some centers will have a stroke unit and offer intravenous thrombolysis, but not any endovascular stroke therapy (a level 3 center). Together, these level 1, 2, and 3 centers form a complete stroke system of care. The requirements for these centers are summarized in Table 1.

Due to the relatively short time elapsed since the evidence in favor of MT has been published, some organizational aspects still

require scientific validation. However, considering the extremely fast growth of such activities around the world, the multisociety group considered it timely and rational to set-up recommendations and a framework for the development of MT services in all parts of the world. The requirements included in this document are proposed to help countries and centers to properly implement MT.

## COMPOSITION OF THE CONSENSUS GROUP

This working group is composed of delegates from the following societies: Asian-Australian Federation of Interventional and Therapeutic Neuroradiology (AAFITN), Australian and New Zealand Society of Neuroradiology (ANZSNR), American Society of Neuroradiology (ASNR), Canadian Society of Neuroradiology (CSNR), European Society of Minimally Invasive Neurologic Therapy (ESMINT), European Society of Neuroradiology (ESNR), European Stroke Organization (ESO), Japanese Society for NeuroEndovascular Therapy (JSNET), Ibero-Latin American Society of Diagnostic and Therapeutic Neuroradiology (SILAN), Society of NeuroInterventional Surgery (SNIS), Society of Vascular and Interventional Neurology (SVIN), World Stroke Organization (WSO), World Federation of Interventional Neuroradiology (WFITN).

## DEFINITIONS

*Neuroendovascular procedures:* minimally invasive, image guided procedures to treat diseases of the brain and spinal cord. These include embolization, for treatment of intracranial aneurysms, arteriovenous malformations, tumors, and revascularization techniques, such as angioplasty and stent placement for atherosclerotic disease.

*Acute ischemic stroke intervention (AISI)* involves percutaneous endovascular procedures to treat ischemic stroke in adults and children, and may involve thrombectomy, aspiration, percu-

This article was first published as: Pierot L, Jayaraman MV, Szikora I, et al. **Standards of practice in acute ischemic stroke intervention: international recommendations.** *Journal of Neuro Interventional Surgery* Published Online First: 28 August 2018; doi: 10.1136/neurintsurg-2018-014287 and is reprinted with permission.

<http://dx.doi.org/10.3174/ajnr.A5853>

**Table 1: General summary of capabilities of level 1, 2, and 3 centers**

	Level 1 Center		Level 2 Center	Level 3 Center
Offers full spectrum of neuroendovascular therapy (including aneurysm treatment, surgical and endovascular, arteriovenous malformations, arteriovenous fistulas, etc)	Yes	No		No
Offers endovascular stroke therapy	Yes	Yes		No
Offers intravenous tissue plasminogen activator	Yes	Yes		Yes
Minimum No of stroke patients per year	250	100		50
Minimum thrombectomy volume per year	50	50		N/A
Dedicated neuro-intensive care unit	Yes	Optional		Not needed
Dedicated stroke unit	Yes	Yes		Yes
Open neurosurgical services on site	Yes	Optional		Not needed
Geographic restriction?	No	Yes (should be more than 2 hours' transport time from a level 1 center)		No
Inter-facility transfers	Receives cases from level 1 and 2 centers	Will transfer some cases to a level 1 center. Will occasionally receive transfers from level 3 centers if no level 1 center is available within 2 hours from the level 3 center		Has standardized transfer processes in place with a level 1 center (preferable), or a level 2 center

taneous transluminal angioplasty, and stent implantation, as well as superselective drug infusion.

**Stroke unit:** a dedicated, geographically clearly defined area or ward in a hospital where stroke patients are admitted and cared for by a multi-professional team (medical, nursing, and therapy staff) who have specialist knowledge, training, and skills in stroke care with well defined individual tasks, regular interaction with other disciplines, and stroke leadership. This team shall coordinate stroke care through regular (weekly) multi-professional meetings (<http://stroke.ahajournals.org/content/44/3/828#T1>).

**Stroke center:** a hospital infrastructure and related processes of care that provide the full pathway of stroke unit care. A stroke center is the coordinating body of the entire chain of care. This covers prehospital care, emergency room assessment and diagnosis, emergency medical treatment, stroke unit care, ongoing rehabilitation, and secondary prevention, and access to related neurosurgical and vascular intervention. A stroke unit is the most important component of a stroke center. A stroke center provides stroke unit services for the population of its own catchment area and serves as a referral center for peripheral hospitals with stroke units in case their patients need services that are not locally available (<http://stroke.ahajournals.org/content/44/3/828#T1>).

## BACKGROUND AND SIGNIFICANCE

AIS caused by ELVO is the leading cause of adult disability in the world.<sup>2</sup> Strokes caused by occlusion of the large intracranial vessels, such as the internal carotid artery, proximal middle cerebral artery, or basilar artery have low rates of response to intravenous tissue plasminogen activator and, subsequently, poor outcomes.<sup>3</sup> The major revolution in acute stroke intervention began in 2015 when five randomized trials showed that rapid MT significantly improves outcomes in anterior circulation (internal carotid artery, M1) ELVO stroke patients.<sup>4-8</sup> The degree of benefit is profound, with a number needed to treat as low as 2.5 to have one patient be less disabled.<sup>9, 10</sup> Few, if any, therapies in medicine can

approach that level of benefit. Two additional trials have further confirmed that indeed rapid thrombectomy dramatically improves outcomes, including up to 24 hours from the last known normal.<sup>11-14</sup>

Training guidelines for physicians performing AISI were already proposed by the same working group.<sup>1</sup> Delivering the benefit of this therapy to a population that is applicable in diverse localities throughout the world, as reflected by the breath of international societies sponsoring this guideline, requires a concerted effort. Critical to this is ensuring the proper facility capabilities to deliver this treatment in a safe yet timely fashion.

The goal of this document is to provide recommendations that outline the minimum requirements to provide AISI to as large of a population as possible, including those that do not have timely access to a level 1 center, which is capable of treating all vascular diseases of the brain and spine.

## PURPOSE

This is a document which provides recommendations based on expert opinions and best available evidence, in relation to the optimal conditions for the safe practice of AISI.

In order to replicate the dramatic results of the major randomized trials, we must ensure patients throughout the world are treated in a center with the capabilities necessary to handle not just the procedural aspects, but also the medical management of the patient prior to, during, and post-thrombectomy.

These general recommendations are not a substitute for existing national and regional guidelines, recommendations, and regulations in the field of AIS. Rather, this describes the minimum organization and workload that, based on expert consensus, is necessary for a hospital to practice AISI.

The best option for the management of AIS is to have patients transferred to and treated in high volume, level 1 centers, as demonstrated by scientific evidence.<sup>15</sup> However, in some situations, specifically due to geographical, traffic, and transportation con-

ditions, access of patients to such centers in an acceptable time frame may not be possible. In that case, it would be wise to have a system of care that incorporates level 2 centers, able to provide AISI but not necessarily the full spectrum of neuroendovascular procedures.

### WHERE IS AISI PERFORMED?

The practice of AISI should ideally take place in healthcare institutions that routinely provide services for all neurological disorders and neurointerventional treatments to patients with all kinds of neurovascular disorders (level 1 centers). Recommendation for these centers have been recently published.<sup>16</sup>

However, if a level 1 center is not regionally available, a center treating only ischemic stroke (level 2) can be established under the following conditions:

- There is no level 1 center available within 2 hours of interfacility transport time.
- The level 2 center must care for a reasonable number of AISI treatments a year (at least 100 treatments, including intravenous thrombolysis and AISI).
- The institution must incorporate an acute stroke center or stroke unit with fully trained stroke physicians.
- It is highly recommended that the level 2 center is organized in cooperation with a level 1 center, and should pursue the objective of collaborative work with the level 1 center for neurointervention training, continuous medical education, mortality and morbidity rounds, expertise advice by tele-consultations or by practice, 24 hour/7 week day coverage, referrals, among other).

### LEVEL 2 CENTER: STANDARDS OF PRACTICE

For those centers established under these conditions the standards of practice described below apply.

#### 1. Facilities

Facilities that must be available on site include:

- Stroke unit beds: a sufficient number of stroke unit beds should be available in stroke units to accommodate interventionally treated stroke patients at any time.
- Intensive care unit.
- A radiology/neuroradiology service, with competence in neuroimaging, and a suitable angiography room (as defined below): high quality, rapidly available noninvasive imaging is vital to the management of the acute stroke patient. At a minimum, CT scanners should be available on a 24/7 basis to image patients with noncontrast CT and CT angiography. The availability of CT perfusion and/or MRI may also assist in patient selection for AISI beyond 6 hours from onset. The necessary technologists and support personnel for this imaging should be available and onsite at the time of patient admission. Diagnostic radiologists/neuroradiologists with sufficient training and experience in the interpretation of these imaging studies shall be available on a 24/7 basis. Finally, cerebrovascular ultrasound facilities will be available.
- A team of trained acute stroke neurointerventionists.

- A dedicated 'stroke unit' and a 'stroke team' with fully trained stroke physicians.
- A department of neurosurgery ideally in house or, if that is not possible, in a nearby hospital.

#### 2. Angiography Suite

A suitable interventional angiographic suite implies the ability to routinely accommodate general anesthesia. Optimally, procedures should be carried out under the image guidance of a biplane digital angiography unit with flat panel CT capabilities and necessary software and hardware to perform high quality cerebral angiography.

As a minimum, each suite should include a single plane high resolution digital subtraction angiography unit with road mapping capabilities.

Radiation protection measures in accordance with national regulations should be in place with designated individuals responsible for carrying out the necessary checks and audits.

#### 3. Treatment Availability

AISI should be offered to every appropriate patient according to international guidelines, not excluding/discriminating against any patient, appropriate at the right time to obtain the best results, with population treatment access equity, in centers providing safe, effective, and efficient treatment.

A suitable level 2 center should be able to provide the services defined in the definition section, on a full time basis, 24/7, all year around.

#### 4. Procedural Volume

The randomized trials demonstrating a clear benefit from thrombectomy were almost exclusively performed in high volume centers. It has been shown that high volume centers have a significantly lower mortality, even if the patient has to be transferred from a low volume center. Rinaldo et al found that centers performing 35 or more thrombectomy cases per year would classify as 'high volume' and offer the lowest mortality rate for patients.<sup>15</sup> Similarly, the American College of Cardiology Foundation, the American Heart Association, and the Society for Cardiovascular Angiography and Interventions suggest a minimum of 36 percutaneous coronary interventions for acute myocardial infarction per year per center as a minimum requirement.<sup>17</sup>

We acknowledge that the thresholds listed below are generally low. Multiple regional/national recommendations with higher limits are available and should be observed in regions/countries having already advanced healthcare networks providing services for AIS patients. The current recommendations are international and have to be compatible with the development of this new activity in areas and countries where there had been previously limited availability. Subsequently, these thresholds should be considered as the minimum caseload providing the lowest limit of safe operation. With the increased implementation of AISI in the world, it may be desirable to revise these thresholds in the future.

On the other hand, we also acknowledge that these thresholds are potentially difficult to reach in newly created level 2 centers and recognize that, during a transitory period, the activity can be

below the threshold numbers, as long as it is expected that the volumes would be reached within 12–24 months.

With all of the above in mind, the suggested thresholds for annual procedure volume to maintain the competence for AIS endovascular treatment are the following:

- Each level 2 center shall perform a minimum number of intracranial thrombectomy procedures for ELVO per year. The global consensus group recommends a minimum of 50 procedures per center per year.
- Including the aforementioned thrombectomy procedures, each level 2 center shall perform a minimum total number of neuroendovascular procedures (diagnostic and interventional) per year according to national requirements. The global consensus group recommends a minimum of 120 per center per year.
- Each neurointerventionist working in a level 2 center must perform a minimum number of acute intracranial thrombectomy procedures per year, in accordance with national requirements. The global consensus group recommends a minimum of 15 procedures per neurointerventionist per year.
- In addition to the aforementioned thrombectomy procedures, each neurointerventionist in a level 2 center should perform a minimum number of total neuroendovascular procedures per year according to national requirements. The global consensus group recommends a minimum of 50 procedures per neurointerventionist per year.

## **5. Operational Guidelines/Medical Personnel**

### **5.1 Stroke Team**

Outstanding stroke care does not exist in a vacuum solely focused on the procedure but instead is part of a successful multidisciplinary team. The stroke team comprises fully trained stroke physicians (vascular neurologists or neurointensivists), allied professionals, and nurse that are all led by a stroke physician with a strong background in the management of neurovascular disease.

### **5.2 Level 2 Stroke Intervention Team**

- The team should have a minimum of three clinicians with training and qualification in AISI.<sup>18</sup>
- The team should organize 24/7/365 acute ELVO stroke coverage (possibly in a rotation system organized with other level 2 centers or a level 1 center).
- It is recommended that stroke neurointerventionists involved in AISI maintain outpatient clinics for follow-up and have admitting privileges either in units/beds dedicated to Interventional neuroradiology or in other appropriate inpatient facilities.
- The stroke neurointerventionist/interventionist, in collaboration with the stroke team, should have shared responsibility for preoperative and postoperative patient care with input from the appropriate specialties.
- AISI should ideally be practiced in neurointerventional teams with the possibility to exchange experience and knowledge. Clinical research should be encouraged. The solitary practice of AISI is strongly discouraged.

### **5.3 Anesthesia Team**

There shall be 24/7 in hospital anesthesia coverage with anesthesiologists with experience in caring for patients undergoing AISI. At many centers, the use of anesthesia, whether monitored anesthetic care or general anesthesia, is routine during thrombectomy. Even at centers primarily using moderate sedation, patients may deteriorate clinically prior to, or during, the procedure such that immediate access to general anesthesia is necessary to safely complete the procedure.

### **5.4 Others**

Given the significant amount of assistance stroke patients need re-integrating into the community, the center should have access to physical therapy, speech therapy, occupational therapy services, as well as a coordinated plan for assessment for rehabilitation needs.

### **5.5 Individual Procedures**

With regard to individual procedures, ideally the following staff roles are present for each case:

- One first operator: a neurointerventionist
- One assistant: a second scrubbed individual (ie, a supporting AISI interventionist, physician in training (resident or fellow), nurse practitioner, physician assistant, a scrub nurse, or a radiographer)
- One radiographer
- One nurse or nurse assistant
- Regardless of the type of anesthesia, an anesthesiology service must be readily available 24/7.

As a minimum, a neurointerventionist, a radiographer, and appropriately trained nursing must be present.

### **5.6 Quality Improvement Processes**

Treatment of AIS by using AISI techniques is a novel method that involves the consumption of significant human and material resources and carries the risk of severe complications. Accurate documentation of medical and technical details as well as patient outcome and follow-up results is inevitable to ensure the highest benefit of such complex and demanding procedures.

To secure such documentation and data management, it is recommended that:

- The level 2 stroke center team includes a dedicated individual, preferably a stroke nurse or a stroke fellow, with the responsibility of data recording and data base management.
- All technical and clinical data of AISI procedures, patient outcomes, and follow-up must be entered into an electronic data base either locally or (preferably) nationally or internationally.
- The center shall establish target time metrics for all cases in accordance with the most recent requirements by international standards. Cases that exceed their chosen metrics should trigger an internal process for quality improvement.<sup>17</sup>
- The database should be regularly audited. At a minimum, process metrics such as time from arrival to intravenous tissue plasminogen activator, to start of angiography, and to recanalization, as well as overall recanalization rates, are to be reviewed and compared against reasonable published benchmarks.

- The center provides routine continuing education (suggested minimum of 8 hours per year) related to cerebrovascular disease and stroke for all core members of the center, as designated by the medical director.
- All cases of symptomatic intracranial hemorrhage shall be reviewed. For the purposes of this document, we broadly define symptomatic intracranial hemorrhage as the presence of new intracranial hemorrhage on post-treatment brain imaging, with clinical deterioration that is potentially attributable to the hemorrhage.
- Standardized care pathways should be implemented with clinical practice guidelines, order sets, and other tools to ensure consistent care delivery and minimize practice variability. This should apply to providers, and nursing and ancillary staff. These pathways should be developed by the multidisciplinary Asian-Australian Federation of Interventional and Therapeutic Neuroradiology (AAFITN), Australian and New Zealand Society of Neuroradiology (ANZSNR), American Society of Neuroradiology (ASNR), Canadian Society of Neuroradiology (CSNR), European Society of Minimally Invasive Neurologic Therapy (ESMINT), European Society of Neuroradiology (ESNR), European Stroke Organization (ESO), Japanese Society for NeuroEndovascular Therapy (JSNET), The French Society of Neuroradiology (SFNR) Ibero-Latin American Society of Diagnostic and Therapeutic Neuroradiology (SILAN), Society of NeuroInterventional Surgery (SNIS), Society of Vascular and Interventional Neurology (SVIN), World Stroke Organization (WSO), World Federation of Interventional Neuroradiology (WFITN) leadership of the center and reflect evidence based practice.

## 6. Community and EMS Outreach

Outstanding stroke care starts not in the hospital but in the field. Increasingly, operators will likely promote selection of the most appropriate destination for suspected ELVO patients based on distance to a center from the field.<sup>19</sup> Such a mechanism should decrease time to treatment. As such, the level 2 center should interface with local emergency medical services (EMS) in order to coordinate care in the prehospital arena.

Specifically, we feel there are some key items in this area.

- Representatives of the center shall work with local and regional EMS officials to ensure they are aware of the system's capabilities, as well as which patients (based on the region's chosen severity scale) are appropriate for direct field triage to the level 2 or 1 centers.
- Additionally, some patients may be distant from the level two (or 1) and present to a level 3 center. The level 2 center should work with these local centers to assist in identification of suspected or confirmed ELVO patients and facilitate rapid transfer as part of a 'hub and spoke' model of care. However, if a level 1 center is available in a similar transfer time, it is preferable that interfacility transfers are directed to the highest level facility.
- A mechanism should exist for providing feedback to the EMS and referring non-thrombectomy centers to highlight which aspects of care went well and identify areas for improvement. This would be similar to quality assessment work done on patients presenting directly to the level 2 and 1 centers.

## AUTHOR AFFILIATIONS

<sup>1</sup>Hôpital Maison-Blanche, Université Reims-Champagne-Ardenne (URCA), Reims, France; <sup>2</sup>Warren Alpert School of Medicine at Brown University, Providence, Rhode Island, USA; <sup>3</sup>National Institute of Clinical Neurosciences, Budapest, Hungary; <sup>4</sup>Massachusetts General Hospital, Harvard Medical School, Boston, Massachusetts, USA; <sup>5</sup>Erlanger Medical Center, Chattanooga, Tennessee, USA; <sup>6</sup>Neuroendovascular Therapy Centre, Aichi Medical University, Aichi-gun, Japan; <sup>7</sup>Pantai Hospital, Kuala Lumpur, Malaysia; <sup>8</sup>Monash University, Clayton, Victoria, Australia; <sup>9</sup>The University of Melbourne, The Royal Hospital of Melbourne, Parkville, Victoria, Australia; <sup>10</sup>University of Queensland, Royal Brisbane and Women's Hospital, Brisbane, Queensland, Australia; <sup>11</sup>University of Wisconsin, Madison, Wisconsin, USA; <sup>12</sup>Northwell Health Donald and Barbara Zucker School of Medicine, New York, New York, USA; <sup>13</sup>Queen's University, Kingston, Ontario, Canada; <sup>14</sup>Karolinska University Hospital, Stockholm, Sweden; <sup>15</sup>University Medical Centre Hamburg-Eppendorf, Hamburg, Germany; <sup>16</sup>Istanbul University, Cerrahpasa Medical School, Istanbul, Turkey; <sup>17</sup>Hospital Garcia de Orta, Hospital da Luz, Lisbon, Portugal; <sup>18</sup>Hospital Univesitari Vall d'Hebron, Barcelona, Spain; <sup>19</sup>Neurology, Inselspital, University Hospital Bern and University of Bern, Bern, Switzerland; <sup>20</sup>University of Perugia, Perugia, Italy; <sup>21</sup>University Medical Centre, Utrecht, The Netherlands; <sup>22</sup>Kobe City Medical Centre General Hospital, Kobe, Japan; <sup>23</sup>University of Tsukuba, Tsukuba, Japan; <sup>24</sup>Hyogo College of Medicine, Nishinomiya, Japan; <sup>25</sup>CHU Nantes, Nantes, France; <sup>26</sup>Hospital Universitário Santa Maria, Lisbon, Portugal; <sup>27</sup>Hospital Clinico Universitario, Santiago de Compostela, Espana; <sup>28</sup>The Methodist Hospital, Houston, Texas, USA; <sup>29</sup>University of Kentucky, Lexington, Kentucky, USA; <sup>30</sup>Herbert Wertheim College of Medicine, Florida International University, Miami Cardiac and Vascular Institute, Baptist Hospital, Miami, Florida, USA; <sup>31</sup>UCLA, Los Angeles, California, USA; <sup>32</sup>Marcus Stroke and Neuroscience Center, Grady Memorial Hospital, Emory University School of Medicine, Atlanta, Georgia, USA; <sup>33</sup>University of Heidelberg, Heidelberg, Germany; <sup>34</sup>Danube University Krems, Krems, Austria; <sup>35</sup>Melbourne Brain Centre at Royal Melbourne Hospital, University of Melbourne, Parkville, Victoria, Australia; <sup>36</sup>Groote Schuur Hospital, University of Cape Town, Cape Town, South Africa; <sup>37</sup>Ramathibodi Hospital, Mahidol University, Bangkok, Thailand; <sup>38</sup>Kameda Medical Center, Kamagawa City, Chiba, Japan; <sup>39</sup>University of Toronto, Toronto Western Hospital, Toronto, Ontario, Canada

## REFERENCES

1. Anon. **Training guidelines for endovascular ischemic stroke intervention: an international multi-society consensus document.** *J Neurointerv Surg* 2016;8:989–91
2. Leslie-Mazwi T, Chandra RV, Baxter BW, *et al.* **Society of Neuro-Interventional Surgery. ELVO: an operational definition.** *J Neurointerv Surg* 2018;10:507–9
3. Lima FO, Furie KL, Silva GS, *et al.* **Prognosis of untreated strokes due to anterior circulation proximal intracranial arterial occlusions detected by use of computed tomography angiography.** *JAMA Neurol* 2014;71:151–7
4. Saver JL, Goyal M, Bonafe A, *et al.* **Stent-retriever thrombectomy after intravenous t-PA vs. t-PA alone in stroke.** *N Engl J Med* 2015;372:2285–95
5. Jovin TG, Chamorro A, Cobo E, *et al.* **Thrombectomy within 8 hours after symptom onset in ischemic stroke.** *N Engl J Med* 2015;372:2296–306
6. Goyal M, Demchuk AM, Menon BK, *et al.* **Randomized assessment of rapid endovascular treatment of ischemic stroke.** *N Engl J Med* 2015;372:1019–30
7. Campbell BC, Mitchell PJ, Kleinig TJ, *et al.* **Endovascular therapy for ischemic stroke with perfusion-imaging selection.** *N Engl J Med* 2015;372:1009–18
8. Berkhemer OA, Fransen PS, Beumer D, *et al.* **A randomized trial of intraarterial treatment for acute ischemic stroke.** *N Engl J Med* 2015;372:11–20
9. Goyal M, Menon BK, van Zwam WH, *et al.* **Endovascular thrombectomy after large-vessel ischaemic stroke: a meta-analysis of individual patient data from five randomised trials.** *Lancet* 2016;387:1723–31
10. Saver JL, Goyal M, van der Lugt A, *et al.* **Time to treatment with endovascular thrombectomy and outcomes from ischemic stroke: a meta-analysis.** *JAMA* 2016;316:1279–88
11. Mocco J, Zaidat OO, von Kummer R, *et al.* **Aspiration thrombec-**

- tomy after intravenous alteplase versus intravenous alteplase alone. *Stroke* 2016;47:2331–8
12. Bracard S, Ducrocq X, Mas JL, *et al.* Mechanical thrombectomy after intravenous alteplase versus alteplase alone after stroke (THRACE): a randomised controlled trial. *Lancet Neurol* 2016;15:1138–47
  13. Nogueira RG, Jadhav AP, Haussen DC, *et al.* Thrombectomy 6 to 24 hours after stroke with a mismatch between deficit and infarct. *N Engl J Med* 2018;378:11–21
  14. Albers GW, Marks MP, Kemp S, *et al.* Thrombectomy for stroke at 6 to 16 hours with selection by perfusion imaging. *N Engl J Med* 2018;378:708–18
  15. Rinaldo L, Brinjikji W, Rabinstein AA. Transfer to high-volume centers associated with reduced mortality after endovascular treatment of acute stroke. *Stroke* 2017;48:1316–21
  16. Jansen O, Szikora I, Causin F, *et al.* Standards of practice in interventional neuroradiology. *Neuroradiology* 2017;59:541–4
  17. Harold JG, Bass TA, Bashore TM, *et al.* ACCF/AHA/SCAI 2013 update of the clinical competence statement on coronary artery interventional procedures: a report of the American College of Cardiology Foundation/American Heart Association/American College of Physicians Task Force on Clinical Competence and Training (writing committee to revise the 2007 clinical competence statement on cardiac interventional procedures). *Circulation* 2013;128:436–72
  18. McTaggart RA, Ansari SA, Goyal M, *et al.* Initial hospital management of patients with emergent large vessel occlusion (ELVO): report of the standards and guidelines committee of the Society of NeuroInterventional Surgery. *J Neurointerv Surg* 2017;9:316–23
  19. Zhao H, Coote S, Pesavento L, *et al.* Large vessel occlusion scales increase delivery to endovascular centers without excessive harm from misclassifications. *Stroke* 2017;48:568–73

## Comment on “Blood Flow Mimicking Aneurysmal Wall Enhancement: A Diagnostic Pitfall of Vessel Wall MRI Using the Postcontrast 3D Turbo Spin-Echo MR Imaging Sequence”

We read with interest the article “Blood Flow Mimicking Aneurysmal Wall Enhancement: A Diagnostic Pitfall of Vessel Wall MRI Using the Postcontrast 3D Turbo Spin-Echo MR Imaging Sequence”<sup>1</sup> published in the *American Journal of Neuroradiology* in 2018.

We would like to congratulate the authors for a very well-written article on a subject that may strongly affect the interpretation of vessel wall enhancement obtained on 3T brain MR imaging.

Several studies<sup>2,3</sup> performed on various MR imaging units have demonstrated that aneurysm wall enhancement may be a marker for instability, thus a noninvasive biomarker for patient counseling and therapeutic decision-making. In this article, the authors demonstrated that part of the enhancement may be due to intra-aneurysmal slow blood flow because the wall enhancement decreased and sometimes vanished when a motion-sensitized driven equilibrium sequence was used. We agree that T1-shortened enhanced blood signal near the wall may cause nonspecific wall enhancement-like signal. However, in our opinion, the observation that slow-flow artifacts may contribute to the observed wall enhancement does not invalidate the fact that contrast enhancement is strongly linked to aneurysm status.<sup>2</sup>

Computational fluid dynamics studies<sup>4</sup> demonstrated that slow flow contributes to low wall shear stress, hence promoting aneurysm wall inflammation. Slow flow, low wall shear stress, and wall inflammation probably all contribute to the observed enhancement. We agree that histopathologic confirmation is

strongly warranted to confirm the inflammatory nature of aneurysm wall enhancement.

### REFERENCES

1. Kalsoum E, Chabernaud Negrier A, Tuilier T, et al. **Blood flow mimicking aneurysmal wall enhancement: a diagnostic pitfall of vessel wall MRI using the postcontrast 3D turbo spin-echo MR imaging sequence.** *AJNR Am J Neuroradiol* 2018;39:1065–67 CrossRef Medline
2. Edjlali M, Ben Hassen W, Boulouis G, et al. **Circumferential thick enhancement on high resolution vessel wall MRI is a biomarker with high specificity of intracranial aneurysm instability.** *Radiology* 2018 Jul 3:172879. [Epub ahead of print] CrossRef Medline
3. Edjlali M, Gentric JC, Régent-Rodriguez C, et al. **Does aneurysmal wall enhancement on vessel wall MRI help to distinguish stable from unstable intracranial aneurysms?** *Stroke* 2014;45:3704–06 CrossRef Medline
4. Xiang J, Tutino VM, Snyder KV, et al. **CFD: computational fluid dynamics or confounding factor dissemination? The role of hemodynamics in intracranial aneurysm rupture risk assessment.** *AJNR Am J Neuroradiol* 2014;35:1849–57 CrossRef Medline

● M. Edjlali

Department of Neuroradiology  
Université Paris Descartes Sorbonne Paris Cité  
Centre Hospitalier Sainte-Anne  
Paris, France

● P. Turski

Departments of Radiology and Medical Physics  
University of Wisconsin  
Madison, Wisconsin

● C. Oppenheim

● O. Naggara

Department of Neuroradiology  
Université Paris Descartes Sorbonne Paris Cité, Centre Hospitalier Sainte-Anne  
Paris, France

<http://dx.doi.org/10.3174/ajnr.A5777>

## REPLY:

We thank our colleagues for their comments about our recent article, “Blood Flow Mimicking Aneurysmal Wall Enhancement: A Diagnostic Pitfall of Vessel Wall MRI Using the Postcontrast 3D Turbo Spin-Echo MR Imaging Sequence.”<sup>1</sup>

Black-blood techniques such as motion-sensitized driven equilibrium or delay alternating with nutation for tailored excitation (DANTE) offer new perspectives for a better understanding of the nature of intracranial aneurysm enhancement. In our experience, flow-related artifacts are frequently encountered using the postcontrast 3D-TSE sequence for a wide range of incidental aneurysms (at the center of the aneurysmal cavity but also in contact with the wall of the aneurysm). It is now clear that the slow-flowing blood near the aneurysmal wall may represent all or part of the visible enhancement using conventional 3D-TSE sequences. Such findings raise the question of the relevance of this parameter for the management of asymptomatic patients.

The relationship among contrast enhancement on 3D-TSE, slow-flowing blood, low shear stress, and aneurysmal instability is poorly reported and is still speculative. In addition, studies with a long-term follow-up and/or histologic correlation are lacking in the literature. Thus, it appears difficult to assume that the enhancement related to slow-flowing blood and that of the aneurysmal wall itself are both related to inflammation/instability. Quite on the opposite, we think that it would be interesting to independently analyze each component of the enhancement visible on conventional 3D-TSE, including slow-flowing blood. Such an approach would allow us to identify patients in whom the slow-flowing blood is predominant versus those in whom the addition of a black-blood technique has little or no influence on the en-

hancement already visible on conventional sequences (and therefore potentially related to a “true” enhancement of the wall).

A better understanding of the factors likely to promote slow-flowing blood near the aneurysmal wall (such as the size of the aneurysm?) also appears important. In our opinion, the real ability of the 3D-TSE sequence to assess arterial wall inflammation remains uncertain because we cannot formally exclude residual slow-flowing blood (even including the additional black-blood technique). Further studies are required to evaluate alternative/complementary MR sequences less sensitive to flow artifacts and with a higher spatial resolution.

We hope that this discussion will encourage other teams to continue evaluating the circumferential wall enhancement of intracranial aneurysms, which remains a particularly complex entity.

## REFERENCE

1. Kalsoum E, Chabernaud Negrier A, Tuilier T, et al. **Blood flow mimicking aneurysmal wall enhancement: a diagnostic pitfall of vessel wall MRI using the postcontrast 3D turbo spin-echo MR imaging sequence.** *AJNR Am J Neuroradiol* 2018;39:1065–67 CrossRef Medline

● J. Hodel

● E. Kalsoum

● T. Tuilier

● A. Benaïssa

Department of Neuroradiology  
Centre Hospitalier Universitaire Henri Mondor  
Créteil, France

● R. Blanc

Department of Interventional Neuroradiology  
Rothschild Foundation Hospital  
Paris, France

● P. Brugières

Department of Neuroradiology  
Centre Hospitalier Universitaire Henri Mondor  
Créteil, France

<http://dx.doi.org/10.3174/ajnr.A5789>

## MRI Findings Suggestive of Herpes Simplex Encephalitis in Patients with Anti-NMDA Receptor Encephalitis

We read with great interest the recent article by Zhang et al<sup>1</sup> regarding brain MR imaging characteristics of 53 patients with anti-N-methyl-D-aspartate (NMDA) receptor encephalitis. In their important analysis, the authors describe 4 distinct imaging patterns: normal MR imaging findings (type 1, 53% of patients), isolated hippocampal involvement (type 2, 13%), other brain lesions without hippocampal involvement (type 3, 13%), and other brain lesions with hippocampal involvement (type 4, 21%).

The authors provide representative images of these 4 imaging types. The image example for type 4 (lesions in both the hippocampus and other brain areas, Fig 1D1 and D2) shows an asymmetric T2/FLAIR hyperintense presentation of both medial temporal lobes and large parts of the left lateral temporal lobe as well as bilateral frontal, insular, and cingulate involvement. In our experience, this MRI pattern is very atypical for anti-NMDA receptor encephalitis, for which we have observed much more circumscribed hippocampal T2/FLAIR hyperintense signal alterations, and only in a few patients,<sup>2,3</sup> but would be compatible with herpes simplex encephalitis (HSE) imaging findings.

Recently, it has been shown that up to 20% of patients with HSE develop postviral anti-NMDA receptor encephalitis.<sup>4</sup> These patients have HSE followed by autoimmune encephalitis with NMDA receptor autoantibodies weeks to months after initial recovery. In light of these findings and the imaging pattern suggestive of HSE in the article by Zhang et al,<sup>1</sup> we would like to suggest that the presented patient did not have isolated anti-NMDA receptor encephalitis but rather HSE followed by anti-NMDA receptor encephalitis. In our opinion, it would be most important to discriminate these 2 patient groups, and it would therefore be very interesting to know how many patients with type 4 have an imaging pattern that would be compatible with HSE MR imaging findings. We would like to encourage the authors to present MR imaging examples of all group 4 patients in an article supplement. This would be of great interest to the readers and of immense help in clinical practice.

If some patients with type 4 presented by Zhang et al<sup>1</sup> indeed have post-HSE anti-NMDA receptor encephalitis, it would also affect the interpretation of the correlation analysis, in which a worse outcome was associated with hippocampal lesions. While most patients with anti-NMDA receptor encephalitis recover quite well and frequently do not show any specific MR imaging changes, most patients with HSE have persistent cognitive impairment associated with hippocampal/medial temporal lobe damage and corresponding MR imaging findings. Hence, including patients with post-HSE anti-NMDA receptor encephalitis in this correlation analysis could bias the analysis toward an association of hippocampal involvement with poor outcome. It would therefore also be very interesting to reconsider this correlation analysis.

Disclosures: Carsten Finke—UNRELATED: Grants/Grants Pending: Deutsche Forschungsgemeinschaft, German Ministry for Education and Research.\* \*Money paid to the institution.

### REFERENCES

1. Zhang T, Duan Y, Ye J, et al. **Brain MRI characteristics of patients with anti-N-methyl-D-aspartate receptor encephalitis and their associations with 2-year clinical outcome.** *AJNR Am J Neuroradiol* 2018;39:824–29
2. Heine J, Prüss H, Bartsch T, et al. **Imaging of autoimmune encephalitis: relevance for clinical practice and hippocampal function.** *Neuroscience* 2015;309:68–83 CrossRef Medline
3. Bacchi S, Franke K, Wewegama D, et al. **Magnetic resonance imaging and positron emission tomography in anti-NMDA receptor encephalitis: a systematic review.** *J Clin Neurosci* 2018;52:54–59 CrossRef Medline
4. Prüss H. **Postviral autoimmune encephalitis: manifestations in children and adults.** *Curr Opin Neurol* 2017;30:327–33 CrossRef Medline

● M. Scheel

NeuroCure Cluster of Excellence and NeuroCure Clinical Research Center  
Department of Neuroradiology  
Charité–Universitätsmedizin Berlin  
Berlin, Germany

● C. Finke

Department of Neurology  
Charité–Universitätsmedizin Berlin  
Berlin, Germany

Berlin School of Mind and Brain, Humboldt-Universität zu Berlin  
Berlin, Germany

<http://dx.doi.org/10.3174/ajnr.A5788>

**REPLY:**

**W**e thank Drs Scheel and Finke for their insightful comments and for sharing their opinions on our article, “Brain MR Imaging Characteristics of Patients with Anti-*N*-Methyl-D-Aspartate Receptor Encephalitis and Their Associations with 2-Year Clinical Outcome.” We agree with Drs Scheel and Finke’s important comments that it is crucial to differentiate isolated anti-*N*-methyl-D-aspartate (NMDA) receptor encephalitis from herpes simplex encephalitis (HSE) followed by anti-NMDA receptor encephalitis.

In this publication, we tried to investigate the brain MR imaging characteristics of patients with anti-NMDA receptor encephalitis. We classified the brain MR imaging manifestations into 4 types: type 1, normal MR imaging findings; type 2, only hippocampal lesions; type 3, lesions not involving the hippocampus; and type 4, lesions in both the hippocampus and other brain areas. Type 4 (11 patients) was relatively common in our study; we presented in this article the brain MRIs of the remaining 10 patients presenting with type 4 lesions (not including the sample figure in our article) (Figure).

In our study, the patients were diagnosed as having as anti-NMDA receptor encephalitis by 2 experienced neurologists (one with >20 years of experience and one with 5 years of experience in neurology) on the basis of the clinical symptoms, physical examinations, laboratory tests, and treatment responses. The neurologists were careful to exclude the herpes simplex virus followed by

anti-NMDA receptor encephalitis, and they reached a consensus that all the patients had isolated anti-NMDA receptor encephalitis. Furthermore, the virus antibody tests such as those for herpes simplex virus and cytomegalovirus antibodies in the CSF were regularly performed in our hospital when encephalitis was suspected, and the results of virus antibody tests were negative in all the patients in our group. Despite the above effort, it is still very difficult to fully exclude HSE followed by anti-NMDA receptor encephalitis from isolated anti-NMDA receptor encephalitis in the routine clinical setting. Thus, our results about the type 4 lesions of patients with anti-NMDA receptor encephalitis should be interpreted carefully and need to be further validated. Further studies are warranted to investigate the association between isolated anti-NMDA receptor encephalitis and HSE followed by anti-NMDA receptor encephalitis, and to develop a differential diagnosis strategy.

We thank Drs Michael Scheel and Carsten Finke again for their constructive comments on our article, as well as sharing their experience for a deeper understanding of this disease entity.

**T. Zhang**

Department of Radiology  
Xuanwu Hospital, Capital Medical University  
Beijing P. R. China

Department of Radiology  
Beijing Bo'ai Hospital, China Rehabilitation Research Center  
Beijing, P. R. China

**Y. Liu**

Department of Radiology  
Beijing Tiantan Hospital, Capital Medical University  
Beijing, P. R. China  
Tiantan Image Research Center  
China National Clinical Research Center for Neurologic Diseases  
Beijing, P. R. China

<http://dx.doi.org/10.3174/ajnr.A5800>

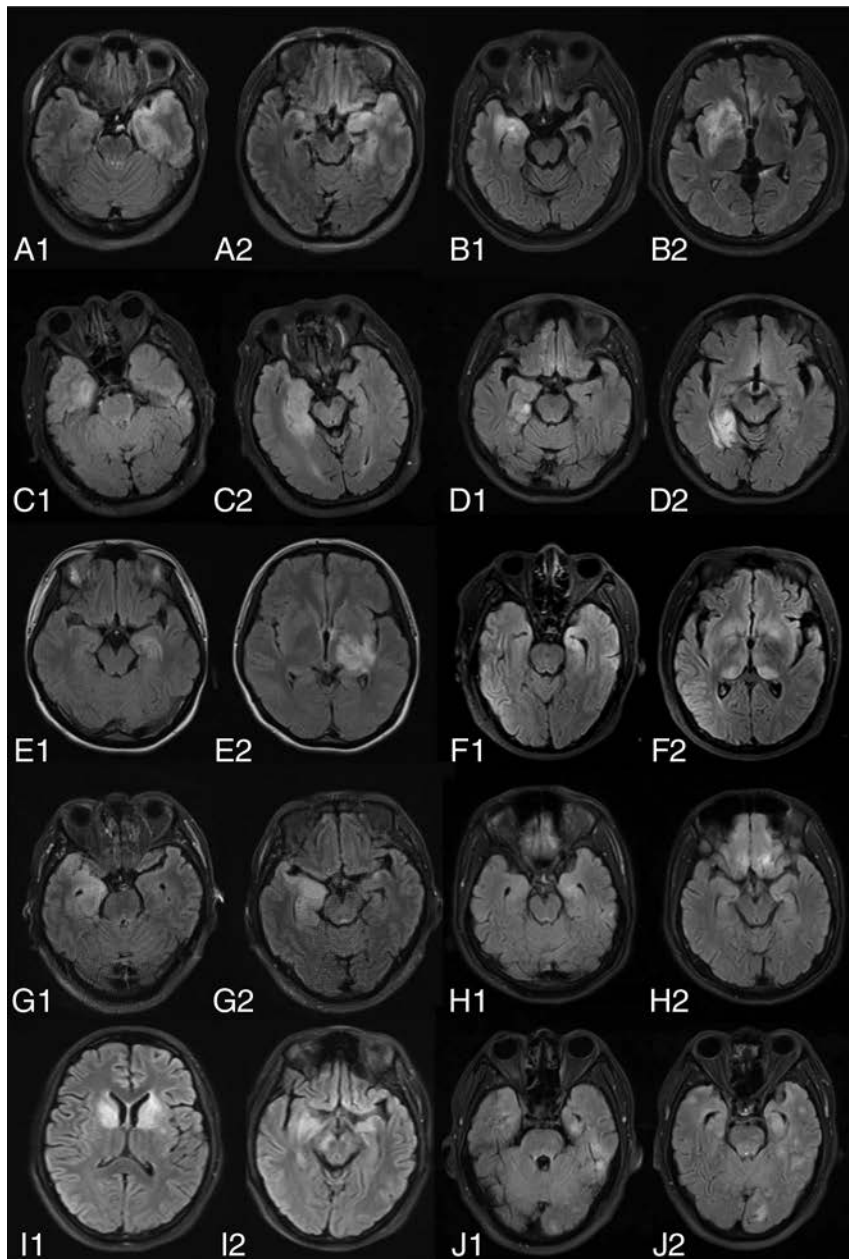


**FIGURE.** Axial FLAIR images of the 10 patients from A to J with anti-NMDA with type 4 lesions.

## Methodologic Issues on Interrater Reliability Regarding Structural and DTI-Based Corticospinal Tract Asymmetry

We read, with interest, the article by Foesleitner et al<sup>1</sup> published in the June 2018 issue of the *American Journal of Neuroradiology*. The purpose was to investigate a clinically feasible imaging approach to assess corticospinal tract (CST) asymmetry in unilateral polymicrogyria (PMG), check diffusion-based tractography as a guide to the presumed motor area within the dysplastic cortex, and investigate whether the “rule” of CST asymmetry as a good prognostic factor for postsurgical motor function preservation specifically applies to cases of unilateral PMG involving the central region. The interrater reliability was calculated by the Cohen coefficient.<sup>1</sup> The authors reported that the interrater reliability in the assessment of corticospinal tract asymmetry was most robust at the level of the cerebral crus. Also, excellent congruence was reached by categorizing the asymmetry degree into no or minimal asymmetry or moderate/severe asymmetry ( $\kappa = 1.0$ ) in the event that the other levels of assessment did not result in considerable agreement ( $\kappa = 0.21\text{--}0.6$ ).<sup>1</sup>

It is of crucial importance to know that the  $\kappa$  value cannot be a sign of good agreement. In assessing the agreement of a qualitative variable, the  $\kappa$  value has 2 major weaknesses: 1) It depends on the prevalence in each class—that is, there might be different  $\kappa$  values of the same percentages for concordant and discordant cells. As can be seen in the Table, the prevalence of concordant cells in both (a) and (b) situations is 90%, while that of discordant cells is 10%. However, we can get different values of  $\kappa$  (0.44 and 0.80) for concordant and discordant cells, respectively. 2) The  $\kappa$  value also depends on the number of classes. It is preferable to use a weighted  $\kappa$  in such situations to obtain unbiased results.<sup>2-4</sup>

They concluded that visual assessment of structural and diffusion tensor images of the corticospinal tract (especially at the cerebral crus) is a reliable and clinically feasible imaging approach in the preoperative work-up of patients with unilateral PMG affecting the central region. Also, in noncompliant patients, DTI-based

**Limitation of  $\kappa$  to assess the reliability of 2 raters' judgments with different prevalences in the 2 categories**

		Positive	Rater 1 Negative	Total (%)
Situation (a)	Positive	85	5	90
	Negative	5	5	10
	Total	90	10	100
$\kappa = 0.44$				
Situation (b)	Positive	45	5	50
	Negative	5	45	50
	Total	50	50	100
$\kappa = 0.80$				

tractography is a useful alternative to task-based fMRI and helps in the anatomic localization of the primary motor cortex. If one considered the above-mentioned limitations of the  $\kappa$  value to assess reliability, such a conclusion may be misleading. Therefore, misinterpretation cannot be avoided.<sup>2-4</sup>

In this letter, we discuss the limitations of the  $\kappa$  value to assess reliability. Therefore, any conclusion especially in reliability analysis should be supported by the above mentioned statistical and methodological issues.

### REFERENCES

1. Foesleitner O, Nenning KH, Traub-Weidinger T, et al. **Assessing corticospinal tract asymmetry in unilateral polymicrogyria.** *AJNR Am J Neuroradiol* 2018;39:1530–35 CrossRef Medline
2. Szklo M, Nieto FJ. *Epidemiology: Beyond the Basics*. 2nd ed. Sudbury: Jones and Bartlett Publisher; 2007
3. Naderi M, Jalalvandi F, Fatahi S. **Observer reproducibility of breast strain elastography in data acquisition and interpretation: a methodological issue.** *Eur J Radiol* 2018 May 2. [Epub ahead of print] CrossRef Medline
4. Sabour S, Dastjerdi EV. **Reliability of four different computerized cephalometric analysis programs: a methodological error.** *Eur J Orthod* 2013;35:848 CrossRef Medline

● F. Jalalvandi

● M. Naderi

Department of Operating Room

School of Paramedical

Kermanshah University of Medical Sciences

Kermanshah, I.R. Iran

<http://dx.doi.org/10.3174/ajnr.A5799>

REPLY:

We would like to comment on the letter to the Editor regarding our article on corticospinal tract asymmetries in unilateral polymicrogyria.<sup>1</sup> We thank Drs Jalalvandi and Naderi for their interest in our work and appreciate the opportunity to respond to their remarks.

In most radiologic studies, the  $\kappa$  value is commonly used to assess interrater reliability. However, as emphasized by the authors and initially shown by Byrt et al,<sup>2</sup> it has important weaknesses due to bias and prevalence issues. Byrt et al recommended using the bias and the prevalence indices to address these shortcomings. In addition to several other observations, we documented a high concordance in detecting the presence or absence of corticospinal tract asymmetry in cases of unilateral polymicrogyria by 2 independent observers (9/10 consistent ratings, Table). The low bias (0.22) and prevalence (0.11) indices support the validity of our  $\kappa$  values. If, however, one wanted to use the prevalence-adjusted bias-adjusted  $\kappa$ ,<sup>2</sup> in our case reaching 0.78, interrater agreement would still show a substantial strength of agreement.<sup>2,3</sup> Because the issues mentioned above do not apply to our sample, we opted for the classic  $\kappa$  value.

In conclusion, we support the call of the letter for caution when using the  $\kappa$  coefficient. However, the issue of neither prevalence nor bias is relevant for our study. Thus, our results allow the conclusion of reliable visual assessment of corticospinal tract asymmetry in unilateral polymicrogyria involving the motor cortex based on T1-weighted and color-coded diffusion tensor imaging maps at the level of the midbrain.

<http://dx.doi.org/10.3174/ajnr.A5822>

Assessment of the corticospinal tract asymmetry by raters A and B<sup>a</sup>

Patient	Rater A	Rater B	Agreement
1	1	1	Yes
2	0	1	No
3	0	0	Yes
4	1	1	Yes
5	0	0	Yes
6	1	1	Yes
7	1	1	Yes
8	1	1	Yes
9	0	0	Yes

<sup>a</sup>1 = asymmetry, 0 = symmetry (data published in Foesleitner et al<sup>1</sup>).

REFERENCES

1. Foesleitner O, Nenning KH, Traub-Weidinger T, et al. **Assessing corticospinal tract asymmetry in unilateral polymicrogyria.** *AJNR Am J Neuroradiol* 2018;39:1530–35 CrossRef Medline
2. Byrt T, Bishop J, Carlin JB. **Bias, prevalence and kappa.** *J Clin Epidemiol* 1993;46:423–29 CrossRef Medline
3. Sim J, Wright CC. **The kappa statistic in reliability studies: use, interpretation, and sample size requirements.** *Phys Ther* 2005;85:257–68 Medline

● O. Foesleitner

● K.-H. Nenning

● T. Traub-Weidinger

Departments of Biomedical Imaging and Image-Guided Therapy

● M. Feucht

Department of Pediatrics and Adolescent Medicine

● S. Bonelli

Department of Neurology

● T. Czech

● C. Dorfer

Department of Neurosurgery

● D. Prayer

● G. Kasprian

Departments of Biomedical Imaging and Image-Guided Therapy

Medical University of Vienna

Vienna, Austria